CHAPTER 2: STRUCTURAL EVALUATION

This chapter presents a synopsis of the evaluations carried out to establish the mechanical and structural characteristics of the HI-STAR 100 package as they pertain to demonstrating compliance with the provisions of 10CFR71. All required structural design analyses of the packaging, components, and systems Important to Safety (ITS) pursuant to the provisions of 10CFR71are documented in this chapter. The objectives of this chapter are twofold:

a. To demonstrate that the structural performance of the HI-STAR 100 package has been adequately evaluated for the conditions specified under normal conditions of transport and hypothetical accident conditions.

b. To demonstrate that the HI-STAR 100 package design has adequate structural integrity to meet the regulatory requirements of 10CFR71 [2.1.1].

To facilitate regulatory review, the assumptions and conservatism inherent in the analyses are identified along with a complete description of the analytical methods, models, and acceptance criteria. A summary of other considerations germane to satisfactory structural performance, such as corrosion and material fracture toughness is also provided.

This SAR is written to conform to the requirements of NUREG-1617 and 10CFR71 and follows the format of Regulatory Guide 7.9 [1.0.3]. It is noted that the areas of NRC staff technical inquiries with respect to 10CFR71 structural compliance span a wide array of technical topics within and beyond the material in this chapter. To facilitate the staff's review, Table 2.0.1 "Matrix of NUREG-1617/10CFR71 Compliance - Structural Review", is included in this chapter. A comprehensive cross-reference of the topical areas set forth in Section 2.3.2 (Regulatory Requirements) of the draft Regulatory Guide 1617, along with the sponsoring paragraphs in10CFR71, and the location of the required compliance information, within this SAR, is contained in Table 2.0.1.

Section 2.10.2 contains a summary of the evaluation findings derived from the technical information presented in this chapter.

TABLE 2.0.1- MATRIX OF NUREG-1617/10CFR71 COMPLIANCE – STRUCTURAL REVIEW†

SECTION IN NUREG-1617 AND APPLICABLE 10CFR71/REG.GUIDE (R.G.) SECTIONS	NUREG-1617/10CFR71 COMPLIANCE ITEM	LOCATION IN SAR CHAPTER 2	LOCATION OUTSIDE OF SAR CHAPTER
2.3.1 Description of Structural Design			
10CFR71.31(a)(1); 10CFR71.33	Description of Structural Design	2.1	1.2.3
10CFR71.33	Drawings		1.4
10CFR71.33	Weights and Center of Gravity	2.2	
10CFR71.31(c)	Applicable Codes/Standards		1.3
2.3.2 Material Properties			
10CFR71.33	Materials and Material Specifications	2.3	
10CFR71.33	Prevention of Chemical, Galvanic, or Other Reactions	2.4	
10CFR71.43(d)	Effects of Radiation on Materials	2.4.4	

TABLE 2.0.1- MATRIX OF NUREG-1617/10CFR71 COMPLIANCE – STRUCTURAL REVIEW (Continued)

SECTION IN NUREG-1617 AND APPLICABLE 10CFR71/REG.GUIDE (R.G.) SECTIONS	NUREG-1617/10CFR71 COMPLIANCE ITEM	LOCATION IN SAR CHAPTER 2	LOCATION OUTSIDE OF SAR CHAPTER
R.G 7.11, 7.12	Brittle Fracture	2.1.2.3	
2.3.3 Lifting and Tie Down Standards for All Packages			
10CFR71.45(a)	Lifting Devices	2.5	1.4
10CFR71.45(b)	Tie-Down Devices	2.5	1.4
2.3.4 General Considerations for Structural Evaluation of Packaging			
10CFR71, Subpart E,F	Evaluation by Analysis		
10CFR71.35(a), 71.41(a)	• Models, Methods, and Results	2.6, 2.7.1,2.7.2	
10CFR71, Subpart E,F	• Material Properties	2.3	
"	• Boundary Conditions	2.6	
"	• Dynamic Amplifiers	2.6, 2.7	
"	• Load Combinations	2.1	
"	• Margins of Safety	2.5, 2.6, 2.7	

TABLE 2.0.1- MATRIX OF NUREG-1617/10CFR71 COMPLIANCE – STRUCTURAL REVIEW (Continued)

SECTION IN NUREG-1617 AND APPLICABLE 10CFR71/REG.GUIDE (R.G.) SECTIONS	NUREG-1617/10CFR71 COMPLIANCE ITEM	LOCATION IN SAR CHAPTER 2	LOCATION OUTSIDE OF SAR CHAPTER
10CFR71, Subparts E,F	Evaluation by Test		
10CFR71.73(a)	• Procedures for Impact Testing	2.7.1 2.A	
"	• Test Specimens	2.7.1 2.A	
10CFR71.73(c)(1)	• Drop Orientations	2.7.1 2.A	
"	• Conclusions	2.7.1 2.A	
2.3.5 Normal Conditions of Transport			
10CFR71.71 with reference to 10CFR71 sections 71.35(a), 71.43(f), 71.51(a)(1), 71.55(d)(4)	Heat	2.6.1	
"	Cold	2.6.2	
"	Reduced External Pressure	2.6.3	
"	Increased External Pressure	2.6.4	
"	Vibration	2.6.5	
"	Water Spray	2.6.6	
"	Free Drop	2.6.1; 2.6.2; 2.6.7	
"	Corner Drop	NA	NA
"	Compression	NA	NA
"	Penetration	NA	NA

TABLE 2.0.1- MATRIX OF 10CFR71 COMPLIANCE – STRUCTURAL REVIEW (Continued)

SECTION IN NUREG-1617 AND APPLICABLE 10CFR71/REG.GUIDE (R.G.) SECTIONS	NUREG-1617/10CFR71 COMPLIANCE ITEM	LOCATION IN SAR CHAPTER 2	LOCATION OUTSIDE OF SAR CHAPTER
2.3.6 Hypothetical Accident Conditions			
10CFR71.73(c)(1)	Free Drop	2.7.1, 2.A	
10CFR71.73(c)(2)	Crush	NA	NA
10CFR71.73(c)(3)	Puncture	2.7.2	
10CFR71.73(c)(4)	Thermal	2.7.3	
10CFR71.73(c)(5)	Immersion-Fissile Material	2.7.4	NA
10CFR71.73(c)(6)	Immersion – All Material	2.7.5	
2.3.7 Special Requirements for Irradiated Nuclear Fuel Shipments			
10CFR71.61	Elastic Stability of Containment	2.7.5	
"	Closure Seal Region Below Yield Stress	2.7.1	
2.3.8 Internal Pressure Test			
10CFR71.85(b)	Internal Pressure Test – All stresses below yield	2.6.1.4.3	8.1

TABLE 2.0.1- MATRIX OF 10CFR71 COMPLIANCE – STRUCTURAL REVIEW (Continued)

SECTION IN 10CFR71	10CFR71 COMPLIANCE ITEM	LOCATION IN SAR CHAPTER 2	LOCATION OUTSIDE OF SAR CHAPTER
Appendices			
	Supplemental Information	2.10	

† Legend for Table 2.0.1

Per the nomenclature defined in Chapter 1, the first digit refers to the chapter number, the second digit is the section number within the chapter; an alphabetic character in the second place means it is an appendix to the chapter.

NA Not Applicable for this item

2.1 STRUCTURAL DESIGN

2.1.1 Discussion

The HI-STAR 100 System (also designated as the HI-STAR 100 Package) consists of three principal components: the multi-purpose canister (MPC), the overpack assembly, and a set of impact limiters. The overpack confines the MPC and provides the containment boundary for transport conditions. The MPC is a hermetically sealed, welded structure of cylindrical profile with flat ends and an internal honeycomb fuel basket for SNF. A complete description of the HI-STAR MPC is provided in Section 1.2.1.2.2 wherein its design and fabrication details are presented with the aid of figures. A discussion of the HI-STAR 100 overpack is presented in Subsection 1.2.1.2.1. Drawings for the HI-STAR 100 System are provided in Section 1.4. In this section, the discussion is directed to characterizing and establishing the structural features of the MPC and the transport overpack.

The design of the HI-STAR 100 MPC seeks to attain three objectives that are central to its functional adequacy, namely;

- Ability to Dissipate Heat: The thermal energy produced by the spent fuel must be transported to the outside surface of the MPC such that the prescribed temperature limits for the fuel cladding and the fuel basket metal walls are not exceeded.

- Ability to Withstand Large Impact Loads: The MPC with its payload of nuclear fuel must be sufficiently robust to withstand large impact loads associated with the hypothetical accident conditions during transportation of the system. Furthermore, the strength of the MPC must be sufficiently isotropic to assure structural qualification under a wide variety of drop orientations.

- Restraint of Free End Expansion: The membrane and bending stresses produced by restraint of free end expansion of the fuel basket are conservatively categorized as primary stresses. In view of the concentration of heat generation in the fuel basket, it is necessary to ensure that structural constraints to its external expansion do not exist.

Where the first two criteria call for extensive inter-cell connections, the last criterion requires the opposite. The design of the HI-STAR 100 MPC seeks to realize all of the above three criteria in an optimal manner.

As the description presented in Chapter 1 indicates, the MPC enclosure vessel is a spent nuclear fuel (SNF) pressure vessel designed to meet ASME Code, Section III, Subsection NB stress limits. The enveloping canister shell, the MPC baseplate, and the closure lid system form a complete closed pressure vessel referred to as the "enclosure vessel". This enclosure vessel serves as the helium retention boundary when the HI-STAR 100 is within the purview of 10CFR71. Within this cylindrical vessel is an integrally welded assemblage of cells of square cross sectional openings, referred to herein as the "fuel basket". The fuel basket is analyzed under the provisions of Subsection NG of Section III of the ASME Code. There are different multi-purpose canisters that are exactly alike in their external dimensions. The essential difference between the MPCs lies in the fuel

baskets. Each fuel storage MPC is designed to house fuel assemblies with different characteristics. Although all HI-STAR 100 MPC fuel baskets are configured to maximize structural ruggedness through extensive inter-cell connectivity, they are sufficiently dissimilar in structural details to warrant separate evaluations. Therefore, analyses for the different MPC types are presented, as appropriate, throughout this chapter.

The HI-STAR 100 overpack provides the containment function for the stored SNF. There is an undivided reliance on the structural integrity of this containment vessel to maintain complete isolation of its contained radioactive contents from the environment under all postulated accident scenarios, even though the MPC is a completely autonomous, ASME Section III Class 1 pressure vessel which provides an unbreachable enclosure for the fuel. The containment boundary is made up of the inner shell, the bottom plate, the top flange, and the closure plate.

Components of the HI-STAR 100 System that are important to safety and their applicable design codes are defined in Chapter 1.

The structural function of the MPC in the transport mode is:

1. To maintain position of the fuel in a sub-critical configuration.

2. To maintain a helium confinement boundary.

The structural function of the overpack in the transport mode is:

1. To serve as a penetration and puncture barrier for the MPC.

2. To provide a containment boundary.

3. To provide a structurally robust support for the radiation shielding.

The structural function of the impact limiters in the transport mode is:

1. To cushion the HI-STAR 100 overpack and the contained MPC with fuel during normal transport handling and in the event of a hypothetical drop accident during transport.

Some structural features of the MPCs that allow the system to perform their structural functions are summarized below:

- There are no external or gasketed ports or openings in the MPC. The MPC does not rely on any sealing arrangement except welding. The absence of any gasketed or flanged joints precludes joint leaks. The MPC enclosure vessel contains no valves or other pressure relief devices.

- The closure system for the MPCs consists of two components, namely, the MPC lid and the closure ring. The MPC lid is a thick circular plate continuously welded to the MPC shell along its circumference. The MPC closure system is shown in the drawings in Section 1.4. The MPC lid-to-MPC shell weld is a J-groove weld that is subject to root and final pass liquid penetrant examinations and finally, a volumetric examination to ensure the absence of unacceptable flaws and indications. The MPC lid is equipped with vent and drain ports which are utilized for evacuating moisture and air from the MPC following fuel loading and subsequent backfilling with an inert gas (helium) in a specified quantity. The vent and drain ports are covered by a cover plate and welded before the closure ring is installed. The closure ring is a thin circular annular plate edge-welded to the MPC shell and to the MPC lid. Lift points for the MPC are provided in the MPC lid.

- The MPC fuel basket consists of an array of interconnecting plates. The number of storage cells formed by this interconnection process varies depending on the type of fuel being transported. Basket designs for different PWR and BWR cell configurations have been designed and are explained in detail in Subsection 1.2. All baskets are designed to fit into the same MPC shell. Welding the plates along their edges essentially renders the fuel basket into a multi-flange beam. For example, Figure 2.1.1 provides an isometric illustration of a fuel basket for the MPC-68 design.

- The MPC basket is separated from the longitudinal supports installed in the enclosure vessel by a small gap. The gap size decreases as a result of thermal expansion (depending on the magnitude of internal heat generation from the stored spent fuel). The provision of a small gap between the basket and the basket support structure is consistent with the natural thermal characteristics of the MPC. The planar temperature distribution across the basket, as shown in Chapter 3, approximates a shallow parabolic profile. This profile will create high thermal stresses unless structural constraints at the interface between the basket and the basket support structure are removed.

  The MPCs will be loaded with fuel assemblies with widely varying heat generation rates. The basket/basket support structure gap tends to be reduced for higher heat generation rates due to increased thermal expansion rates. The basket/basket support structure gap tends to be reduced due to thermal expansion from decay heat generation. Gaps between the fuel basket and the basket support structure are specified to be sufficiently large such that a gap exists around the periphery under all normal or accident conditions of transport.

A small number of optional flexible thermal conduction elements (thin aluminum tubes) may be interposed between the basket and the MPC shell. The elements are designed to be resilient. They do not provide structural support for the basket, and thus their resistance to thermal growth is negligible.

Structural features of the overpack that allow the HI-STAR 100 package to perform its safety function are summarized below:

- The overpack features a thick inner shell welded to a bottom plate which forms a load bearing surface for the HI-STAR 100 System. A solid metal top flange welded at the top of the inner shell provides the attachment location for the lifting trunnions. The top flange is designed to provide a recessed ledge for the closure plate to protect the bolts from direct shear loading resulting from an impulsive load at the top edge of the overpack (Figure 2.1.2). In the transport mode the overpack

  inner shell, bottom plate, top flange, and closure plate with metallic seals constitute the containment boundary for the HI-STAR 100 System. The HI-STAR 100 overpack is subject to the stress limits of the ASME Code, Section III, Subsection NB [2.1.5].

- The inner shell (containment boundary) is reinforced by multi-layered intermediate shells. The multi-layer approach eliminates the potential for a crack in any one layer, developed by any postulated mechanical loading or material flaw, to travel uninterrupted through the vessel wall. The intermediate shells also buttress the overpack inner shell against buckling. The intermediate shells of the HI-STAR 100 overpack are subject to the stress limits of the ASME Code, Section III, Subsection NF, Class 3 [2.1.7].

- To facilitate handling of the loaded package, the HI-STAR 100 overpack is equipped with two lifting trunnions at the top of the overpack. The initial seven HI-STAR 100 overpacks are also equipped with pocket trunnions, embedded in the overpack intermediate shells, just above the bottom plate. HI-STAR 100 overpacks fabricated after the initial seven do not have pocket trunnions (see Subsection 2.5 for further discussion). Lifting trunnions are conservatively designed to meet the design safety factor requirements of NUREG-0612 [2.1.9] and ANSI N14.6-1993 [2.1.10] for single failure proof lifting equipment.

- A circular recess is incorporated on the inner surface of the overpack closure plate. The purpose of this recess is to reduce the moment applied to the flanged joint from MPC impact during a hypothetical top end drop accident. During a hypothetical drop accident where the top end of the overpack impacts first, the MPC contacts the inner surface of the overpack closure plate. Because of the recess, the MPC will only contact an annular region of the inner surface of the overpack closure plate. Thus, the load on the overpack closure plate from the MPC is located closer to the bolt circle, and the moment on the flanged joint is reduced.

- A small circular gap between the MPC external surface and the inside surface of the overpack is provided to allow insertion and removal of the MPC. This gap diminishes monotonically with the increase in the heat generation rate in the MPC, but is sized to avoid metal-to-metal contact between the MPC and the overpack cylindrical surface as a result of thermal expansion under the most adverse thermal conditions.

- There are no valves in the HI-STAR 100 overpack containment boundary. The vent and drain ports used during HI-STAR 100 overpack loading and unloading operations are closed with port plugs and metallic seals. The port plugs are recessed and are suitably protected with a cover plate with seal. These small penetrations equipped with dual seals are not deemed to be particularly vulnerable locations in the HI-STAR 100 System.

The HI-STAR 100 System is equipped with a set of impact limiters (AL-STAR) attached to the top and bottom ends of the overpack. The structural function of the impact limiters is to cushion the HI-STAR 100 overpack and the contained MPC with fuel in the event of a hypothetical drop accident during transport, and to provide the necessary resistance to the longitudinal decelerations experienced during normal rail transport. The design of the impact limiter is independent of the design of the MPC and overpack. This is achieved by establishing design basis deceleration limits for normal transport and for the hypothetical 30-foot drop accident and demonstrating that impact limiter performance limits the deceleration levels imposed on the cask.

Table 1.3.3 provides a listing of the applicable design codes for all structures, systems, and components that are designated as Important to Safety (ITS).

2.1.2 Design Criteria

Regulatory Guide 7.6 provides design criteria for the structural analysis of shipping casks [2.1.4]. Loading conditions and load combinations that must be considered for transport are defined in 10CFR71 [2.1.1] and in USNRC Regulatory Guide 7.8 [2.1.2]. Consistent with the provisions of these documents, the central objective of the structural analysis presented in this chapter is to ensure that the HI-STAR 100 System possesses sufficient structural capability to meet the demands of normal conditions and hypothetical accident conditions of transport.

The following table provides a synoptic matrix to demonstrate our explicit compliance with the seven regulatory positions stated in Regulatory Guide 7.6.

REGULATORY GUIDE 7.6 COMPLIANCE	
Regulatory Position	**Compliance in HI-STAR 100 SAR**
1. Material properties, design stress intensities, and fatigue curves are obtained from the ASME Code	Tables 2.1.12-2.1.20 for allowable stresses/stress intensities and Tables 2.3.1-2.3.5 for material properties are obtained from the ASME Code (the 1995 Code tables are used). Section 2.6.1.3.3 uses the appropriate fatigue data from the Code.
2. Under normal conditions of transport, the limits on stress intensity are those limits defined by the ASME Code for primary membrane and for primary membrane plus bending for Level A conditions.	Tables 2.1.3-2.1.5 define the correct stress intensity limits for normal conditions of transport as stated in the ASME Code for Level A conditions.
3. Perform fatigue analysis for normal conditions of transport using ASME Code Section III methodology (NB) and appropriate fatigue curves.	Section 2.6.1.3.3 considers the potential for fatigue using accepted ASME Code methodology and fatigue data from the ASME Code.
4. The stress intensity S_n associated with the range of primary plus secondary stresses under normal conditions should be less than $3S_m$ where S_m is the primary membrane stress intensity from the Code.	Section 2.6.1.3.3 considers the fatigue potential of the HI-STAR 100 Package based on the $3S_m$ limit.
5. Buckling of the containment vessel should not occur under normal or accident conditions.	The methodology used is Code Case N-284; this has been accepted by the NRC as an appropriate vehicle to evaluate buckling of the containment.

REGULATORY GUIDE 7.6 COMPLIANCE	
Regulatory Position	**Compliance in HI-STAR 100 SAR**
6. Under accident conditions, the values of primary membrane stress intensity should not exceed the lesser of $2.4S_m$ and $0.7S_u$ (ultimate strength), and primary membrane plus bending stress intensity should not exceed the lesser of $3.6S_m$ and S_u.	Tables 2.1.3-2.1.5 of the SAR state these requirements.
7. The extreme total stress intensity range should be less than S_a at 10 cycles as given by the appropriate fatigue curves.	Subsection 2.6.1.3.3 demonstrates compliance by conservatively bounding the total stress intensity range and demonstrating that the bounding value is less than S_a at 10 cycles as given by the appropriate fatigue curves.

Note that Regulatory Guide 7.6 references ASME Code Sections in the 1977 code year. This SAR has been prepared using the identical information on allowable stress intensities and fatigue data as listed in the 1995 ASME Code.

Table 1.3.1, in Chapter 1, summarizes the ASME pressure vessel code applicability to HI-STAR 100 components. Table 1.3.2 in Chapter 1 provides a statement of exceptions taken to the ASME Code requirements.

Stresses arise in the components of the HI-STAR 100 System due to various loads that originate under normal and hypothetical accident conditions of transport. These individual loads are combined to form load combinations. Stresses and stress intensities resulting from the load combinations are compared to allowable stresses and stress intensities. The following subsections present loads, load combinations, and allowable strengths for use in the structural analyses of the MPC and the HI-STAR 100 overpack.

2.1.2.1 Loading and Load Combinations

10CFR71 and Regulatory Guide 7.6 define two conditions that must be considered for qualification of a transport package. These are defined as "Normal Conditions of Transport" and "Hypothetical Accident Conditions", which are related herein to the ASME Code Service Levels for the purposes of quantifying allowable stress limits. In terms of the ASME terminology, the following parallels are applicable.

Normal Conditions of Transport = ASME Design Condition and ASME Level A or B Service Condition

Hypothetical Accident Condition = ASME Level D Service Condition

To establish the appropriate loadings and load combinations that require evaluation, the pressure and temperatures used for the design analyses must be defined. Table 2.1.1 establishes the design pressures for the two transport conditions that must be evaluated. Table 2.1.2 establishes reference hot temperature limits for the two conditions of transport. The ASME Code does not prescribe a metal temperature limit for Level D (also called "faulted") conditions. Under the provisions of the

ASME Code, large strains (such as deformations resulting from a thermal shock) are acceptable if the post-event structural configuration of the component is within the limits prescribed for it subsequent to the faulted event (ASME Code Section III, Subsection NCA-2142.4). In the case of the cask, it is required that the containment boundary continues to perform its function and that the outer skin continues to provide an enclosure for the radiation shielding. For conservatism, the peak metal bulk temperature during and after the fire transient in the overpack containment structure is required to be limited to the maximum temperature limit prescribed in the ASME Section II Part D allowable stress /stress intensity tables. That is, the maximum bulk metal temperature is equal to the maximum temperature for which the allowable stress intensity, S_m, is listed in the Code for the applicable Code Class. For the external skin of the overpack that is directly exposed to the fire no specific temperature limits are enforced by the governing documents. The performance expectation of the HI-STAR 100 package, however, is that the skin does not melt, slump, or sever from the overpack structure. This performance objective is considered to be fulfilled with adequate margin if the metal temperature of the enclosure shell at any section does not exceed 50% of the melting point of the shell material. Tables 2.1.3 and 2.1.4 set forth the allowable strength bases for the two conditions of transport based on their designation as Level A, B, or D.

For its qualification as an acceptable packaging component, the following types of loads are defined for the HI-STAR 100 MPC.

- Dead load (lb.), D;
- Internal design pressure (psi), P_i;
- External design pressure (psi), P_o;
- Accident internal pressure (psi), P_i*;
- Accident external pressure (psi), P_o*;
- Thermal load due to design basis heat generation in the MPC, T, and under most adverse external environmental conditions, T';
- Side drop at 0° basket circumferential orientation under normal conditions of transport, H;
- Side drop at 45° basket circumferential orientation under normal conditions of transport, H;
- Drop at 0° fuel basket circumferential orientation under design basis deceleration for hypothetical accident conditions, H' (angle of inclination that the package longitudinal axis makes with the horizontal plane varies);
- Drop at 45° fuel basket circumferential orientation under design basis deceleration for hypothetical accidental conditions, H'(angle of inclination that the package longitudinal axis makes with the horizontal plane varies);

- Vertical drop under design basis deceleration for hypothetical accident conditions, H'.

Insofar as the fuel basket is not radially symmetric, the orientation of the basket cross section with respect to the direction of side drop will affect the state of stress induced by the deceleration produced by the impact. Heretofore, two horizontal drop circumferential orientations are considered which are referred to as the 0 degree drop and 45 degree drop, respectively. Figures 2.1.3 and 2.1.4, showing an MPC-68 fuel basket, illustrate the two orientations. In the 0-degree drop, the basket drops with its two sets of panels, respectively, parallel and normal to the vertical (Figure 2.1.3). The 45-degree drop implies that the basket's honeycomb section is rotated meridionally by 45 degrees (Figure 2.1.4).

For the above loads, a series of load combinations for the fuel baskets and the enclosure vessel are compiled in Tables 2.1.6 and 2.1.7, respectively. These load combinations represent both normal conditions of transport and the hypothetical accident conditions.

The loadings and load combinations applicable to the overpack are more numerous, because all external loads directly bear on it and several potentially limiting oblique drop orientations exist. In the following, each individual overpack loading which enters in subsequent load combinations is explained.

- **Internal Design Pressure, P_i:** An internal design pressure is defined for the containment cavity of the overpack pressure vessel (Figure 2.1.5). The coincident external pressure is assumed to be atmospheric (0 psig) (Table 2.1.1). For conservatism, the design value is set equal to the MPC internal pressure under normal conditions of transport.

- **External Design Pressure, P_o:** An external design pressure with the cavity depressurized (0 psig) is defined for the overpack pressure vessel as the second design condition loading (Figure 2.1.6),(Table 2.1.1).

- **Accident External Pressure, P_o^*:** An external accident design pressure with cavity depressurized (Figure 2.1.6)(Table 2.1.1). This loading in conjunction with the buckling analysis of the overpack inner shell, is intended to demonstrate that the containment boundary is in compliance with the requirements of 10CFR71.61. This loading condition bounds the external pressure specified by 10CFR71.73(c)(5) and (6).

- **Accident Internal Pressure, P_i^*:** An internal accident design pressure is defined for the containment cavity of the overpack pressure vessel (Figure 2.1.5). The coincident external pressure is assumed to be atmospheric (0 psig) (Table 2.1.1). The design value is based on conservatively assuming that the MPC enclosure vessel is breached.

- **Thermal Conditions:** Thermal conditions pertain to the stresses that develop due to thermal gradient in the overpack. The temperature field in the overpack under the maximum heat generation scenario is developed in Chapter 3. The effect of this temperature field, T_h, is included in all load cases, as appropriate.

The condition where the overpack is subject to a -40°F ambient environment and maximum decay heat is labeled as T_s. Likewise, the condition when the overpack is subject to a -20°F ambient environment is denoted by T_c. Finally, the thermal load during and after 30 minutes of exposure to a 1475°F enveloping fire is referred to as T_f.

- **Overpack Joint Sealing Load, W_s:** The pre-load applied to the overpack closure plate bolts seat the metallic seals and create a contact pressure on the inside land which serves to protect the joint from leakage under postulated impact loading events. The bolt pre-load, however, produces a state of stress in the overpack top closure plate, the overpack top flange, and the overpack inner and intermediate shell region adjacent to the flange. The pre-load, W_s, is, therefore, treated as a distinct loading type.

- **Fabrication Loads, F:** The internal loads induced due to the method of fabrication employed in building the overpack are included in the load combinations.

- **Bottom End Drop, D_{ba}:** This is the first of six drop accident scenarios, wherein the packaging is assumed to drop vertically with its overpack bottom plate sustaining the impulsive load transmitted through the bottom impact limiter. The weight of the package is included in all drop load cases. A schematic of the external forces working on the overpack under this drop scenario is illustrated in Figure 2.1.7. The deceleration load under the 30 ft drop event (accident event) is labeled D_{ba}. (The design basis deceleration is given in Table 2.1.10).

- **Top End Drop, D_{ta}:** This drop condition is the opposite of the preceding case. The top closure plate withstands the impact load transmitted through the impact limiter. This loading is illustrated in Figure 2.1.8. The design basis deceleration is given in Table 2.1.10.

- **Side Drop, D_{sn} and D_{sa}:** The overpack along with its contents drops with its longitudinal axis horizontal. The loaded MPC bears down on the overpack as it decelerates under the resistance offered by the two impact limiters pressing against an essentially unyielding surface (Figure 2.1.9). The subscripts "n" and "a" denote normal transport and hypothetical accident conditions, respectively. The design basis deceleration is given in Table 2.1.10.

- **Bottom C.G.-Over-the-Corner Drop, D_{ca}:** In this drop scenario, the HI-STAR 100 System is assumed to impact an essentially unyielding surface with its center-of-gravity directly above its bottom corner (Figure 2.1.10) under the hypothetical drop accident condition. The design basis deceleration is given in Table 2.1.10.

- **Top Center-of-Gravity Over-the-Corner Drop, D_{ga}:** This loading case is identical to the preceding case, except that the package is assumed to be dropping with its top end down and its center-of-gravity is aligned with the corner of the top closure plate (Figure 2.1.11). The design basis deceleration is given in Table 2.1.10.

- **Side Puncture Force Event, P_s:** This event consists of a free drop of the packaging for 1 meter (40 in.) on to a stationary and vertical mild steel bar of 6 in. diameter with its leading edge (top edge) rounded to 1/4 in. radius. The bar is assumed to be of such a length as to cause maximum damage to the overpack. The package is assumed to be dropping horizontally with the penetrant force being applied at the mid-length of the cask (Figure 2.1.12).

- **Top End Puncture Force, P_t:** This event is similar to the preceding case except the penetrant force is assumed to act at the center of the top closure plate (Figure 2.1.13).

- **Bottom End Puncture Force, P_b:** This is the third of the bar puncture events configured to create a condition of maximum damage to the package. The loading event is identical to the preceding two cases, except that the puncture load acts on the center of the bottom plate of the overpack (Figure 2.1.14).

- **Vibration and Shock, V:** Vibration and shock loads arise during transport of the packaging. The vibratory loads transmitted to the HI-STAR 100 System will produce negligibly small stresses in comparison with stresses that will be produced by the loadings described previously. Therefore, this loading is neglected in the analyses performed herein.

The foregoing loadings are combined in the manner of Table 1 of Regulatory Guide 7.8 to form four (4) distinct load combinations for the normal condition of transport and nineteen (19) load combinations for the hypothetical accident conditions. These load combinations are summarized in Tables 2.1.8 and 2.1.9.

Two concluding observations are relevant with respect to a Flange Seating Condition and to the External Pressure Condition:

- **Flange Seating Condition:** The stress field in the overpack under the bolt pre-stress load condition is evaluated with the elastic constants of the finite element gridwork in the overpack set at its coincident hot environment condition (100°F ambient). The bolt pre-load and material elastic constants under the cold environment condition (-20°F) will be different, resulting in a slightly different stress field. However, the consequence of this refinement is considered to be a second order effect and is, therefore, neglected.

- **External Pressure Condition:** The condition of 20 psia external pressure in Table 1 of Regulatory Guide 7.8 is conservatively bounded by the deep submergence pressure under 200 meters of water. Likewise, the internal design pressure of 100 psig with outside at ambient is assumed to conservatively bound the minimum external pressure (3.5 psia) service condition.

In the load cases considered (Tables 2.1.6-2.1.9), material behavior is always considered to be linearly elastic. To facilitate review, the following matrix is provided to relate the load combinations specifically addressed in Table 1 of Regulatory Guide 7.8 to the load combinations defined in this SAR by Tables 2.1.6-2.1.9. Also included in the matrix are locations in the SAR where particular results are presented that are germane to demonstrating compliance with the intent of Regulatory Guide 7.8.

Compliance of HI-STAR 100 SAR With Regulatory Guide 7.8 Load Combinations		
Reg. Guide Load Combination	**HI-STAR 100 Explicit Load Combination (Tables 2.1.6-2.1.9)**	**Location in SAR for Results**
NORMAL CONDITIONS		
Hot Environment	Table 2.1.7(Case E1.c) Table 2.1.8(Case 1)	2.6.1.3.1.2; Tables 2.6.6,2.6.7 Table 2.6.5; Table 2.6.9
Cold Environment	Table 2.1.8(Case 2)	Table 2.6.12
Increased External Pressure	Table 2.1.9 (Case 18 bounds)	2.6.4
Minimum External Pressure	---	2.6.3
Vibration and Shock	---	2.6.5
One-Foot Free Drop	Table 2.1.6(Case F2) Table 2.1.7(Case E2) Table 2.1.8(Cases 3,4)	Tables 2.6.2,2.6.8 Table 2.6.3 Tables 2.6.9,2.6.12
ACCIDENT CONDITIONS		
Thirty-Foot Free Drop	Table 2.1.6(Case F3) Table 2.1.7(Case E3) Table 2.1.9(Cases 1-5;9-13)	Tables 2.7.1,2.7.4,2.7.7 Tables 2.7.2,2.7.4,2.7.7 Tables 2.7.3,2.7.5,2.7.6-2.7.8
Puncture by Bar	Table 2.1.9(Cases 6-8;14-16)	Tables 2.7.3,2.7.5,2.7.6-2.7.8
Fire Accident	Table 2.1.9(Cases 17,19)	Tables 2.7.3,2.7.8

2.1.2.2 Allowables

Components of the HI-STAR 100 System Important to Safety (ITS) are listed in Table 1.3.3. Allowable stresses are tabulated for these components for all applicable service levels. The applicable service level from the ASME Code for determination of allowables is listed in Subsection 2.1.2.1.

Allowable stress limits for the overpack containment structure and for the MPC enclosure vessel are obtained from the ASME Code, Section III, Division 1, Subsection NB [2.1.5]. The MPC fuel basket is subject to the stress limits of ASME Section III, Division 1, Subsection NG [2.1.6].

All noncontainment parts of the overpack (e.g., intermediate shells, outer enclosure shells, radial channels), are subject to the stress limits of ASME Section III, Subsection NF [2.1.7] for mechanical loadings. The overpack containment boundary and the MPC enclosure vessel are also evaluated for stability in accordance with ASME Code Case N-284 [2.1.8]. Overpack closure bolts are subject to the stress limits of ASME Section III, Subsection NB. Finally, lifting trunnions and other lifting components are subject to the stress limits of NUREG-0612 [2.1.9], which references ANSI N14.6 [2.1.10].

Allowable stresses and stress intensities are calculated using the data provided in the ASME Code, Section II, Part D [2.1.11] and Tables 2.1.3 through 2.1.5. Tables 2.1.11 through 2.1.20 contain numerical values of the allowable stresses/stress intensities for all MPC and overpack load-bearing materials as a function of temperature.

In all tables, the terms S_m, S_y, and S_u, respectively, denote the design stress intensity, minimum yield strength, and the ultimate strength. Property values at intermediate temperatures that are not reported in the ASME Code are obtained by linear interpolation as allowed by paragraph NB-3229. Property values are not extrapolated beyond the limits of the Code in any structural analysis.

Additional terms relevant to the analyses are extracted from the ASME Code (Figure NB-3222-1) as follows.

Symbol	Description	Notes
P_m	Average primary stress across a solid section.	Excludes effects of discontinuities and concentrations. Produced by pressure and mechanical loads.
P_L	Average stress across any solid section.	Considers effects of discontinuities but not concentrations. Produced by pressure and mechanical loads, including inertia earthquake effects.
P_b	Primary bending stress.	Component of primary stress proportional to the distance from the centroid of a solid section. Excludes the effects of discontinuities and concentrations. Produced by pressure and mechanical loads, including inertia earthquake effects.
P_e	Secondary expansion stress.	Stresses which result from the constraint of free-end displacement. Considers effects of discontinuities but not local stress concentration. (Not applicable to vessels.)
Q	Secondary membrane plus bending stress.	Self-equilibrating stress necessary to satisfy continuity of structure. Occurs at structural discontinuities. Can be caused by pressure, mechanical loads, or differential thermal expansion.
F	Peak stress.	Increment added to primary or secondary stress by a concentration (notch), or, certain thermal stresses that may cause fatigue but not distortion. This value is not used in the tables.

It is shown in this report that there is no interference between component parts due to free thermal expansion. Therefore, P_e does not develop within any HI-STAR 100 component. A summary of the allowable limits for normal conditions of transport and for the hypothetical accident conditions as they apply to various components of the package is presented in Table 2.1.3 for the overpack and MPC enclosure vessel (shell, lid, and baseplate), in Table 2.1.4 for the MPC fuel basket, and in Table 2.1.5 for the noncontainment parts of the overpack.

It is recognized that the planar temperature distribution in the fuel basket and the overpack under the maximum heat load condition is the highest at the cask center and drops monotonically, reaching its lowest value at the outside surface. Strictly speaking, the allowable stresses/stress intensities at any location in the basket, the enclosure vessel, or the overpack should be based on the coincident metal temperature under the specific operating condition. However, in the interest of conservatism, reference temperatures may be established for each component that are upper bounds on the metal temperature for each situational condition. Table 2.1.21 provides the reference temperatures for the MPC and the overpack and, utilizing Tables 2.1.11 through 2.1.20, provides conservative numerical limits for the stresses and stress intensities for all loading cases.

Summarizing the previous discussions, in accordance with the Regulatory Guide 7.6 and with ASME Code Section III, Subsection NB, the allowable stress limits for the overpack containment boundary are based on design stress intensities (S_m), yield strengths (S_y) and ultimate strengths (S_u). These limits govern the design of the overpack (including the inner shell, the top flange, the bottom plate, and the closure plate), and also govern the design of the MPC enclosure vessel. The stress limits for the MPC fuel basket are based on stress intensities as set forth in ASME, Section III, Subsection NG. For applicable accident conditions, Appendix F of the ASME Code applies [2.1.12]. Stress limits for closure bolts conform to those given in Table 2.1.24.

The lifting devices in the HI-STAR 100 overpack and the multi-purpose canisters, collectively referred to as "trunnions", are subject to specific limits set forth by NUREG-0612: the primary stresses in a trunnion must be less than the smaller of 1/10 of the material ultimate strength and 1/6 of the material yield strength while loaded by the lifted load that includes an appropriate dynamic load amplifier.

The region around the trunnion is part of the NF structure in HI-STAR 100 and an NB pressure boundary in the MPC, and as such, must satisfy the applicable stress (or stress intensity) limits for the load combination. In addition to meeting the applicable Code limits, it is further required that the local primary stresses at the trunnion/mother structure interface must not exceed the material yield stress at three times the handling condition load. This criterion eliminates the potential of local yielding at the trunnion/structure interface.

Impact limiters are not designed to any stress or deformation criteria. Rather, their function is solely to absorb the impact energy by plastic deformation. The impact limiter must perform its energy absorption function over the range of environmental temperatures.

Allowable stresses derived from other authoritative sources are summarized in Table 2.1.24.

2.1.2.3 Brittle Fracture Failure

The MPC canister and basket are constructed from a series of stainless steels termed Alloy X. These stainless steel materials do not undergo a ductile-to-brittle transition in the minimum temperature range of the HI-STAR 100 System. Therefore, brittle fracture is not a concern for the MPC components. However, the HI-STAR 100 overpack is composed of ferritic steel materials, which will be subject to impact loading in a cold environment and, therefore, must be evaluated and/or subjected to impact testing in accordance with the ASME Code to ensure protection against brittle fracture.

Tables 2.1.22 and 2.1.23 provide the fracture toughness test criteria for the HI-STAR 100 overpack components in accordance with the applicable ASME Codes and Regulatory Guide requirements for prevention of brittle fracture. Regulatory Guides 7.11 [2.1.13] and 7.12 [2.1.14] are used to determine drop test requirements for the containment boundary components, as discussed below.

All containment boundary materials subject to impact loading in a cold environment must be evaluated and/or tested for their propensity for brittle fracture. The overpack baseplate, top flange, and closure plate have thicknesses greater than four inches. Table 1 of Regulatory Guide 7.12 requires that the Nil Ductility Transition temperature, T_{NDT} (for the lowest service temperature of -20°F), be -129°F for 6-inch thick material, and linear interpolation of the table shows that for 7-inch thick material, the T_{NDT} is -132°F. SA350-LF3 has been selected as the material for these overpack components based on the material's capability to perform at low temperatures with excellent ductility properties.

The overpack inner shell has a thickness of 2.5 inches. SA203-E has been selected as the material for this item due to its capability to perform at low temperatures (Table A1.15 of ASME Section IIA. Regulatory Guide 7.11 requires that the T_{NDT} for this material be less than -70°F (at the lowest service temperature of -20°F).

The overpack closure plate bolts are fabricated from SB-637 Grade N07718, a high strength nickel alloy material. Section 5 of NUREG/CR-1815 [2.1.15] indicates that bolts are generally not considered a fracture critical component. Nevertheless, this material has a high resistance to fracture at low temperatures, as can be shown by calculating the transition temperature of the material and assessing its performance as indicated in NUREG/CR-1815.

The Aerospace Structural Metals Handbook [2.1.16] shows that minimum impact absorption energy for SB-637 Grade N07718 at -320°F is 18.5 ft-lb. This may be transferred into a fracture toughness value by using the relationship (presented in Section 4.2 of NUREG/CR-1815) between Charpy impact measurement, C_v (ft-lb), and dynamic fracture toughness, K_{ID} (psi $\sqrt{in.}$)

$$K_{ID} = (5\ E\ C_v)^{1/2}$$

where $E = 31 \times 10^6$ psi at -320°F and C_v (minimum) = 18.5 ft-lb.

Therefore,

$$K_{ID} = 53.5 \text{ ksi}\sqrt{\text{in.}}$$

Using Figure 2 of NUREG/CR-1815 yields

$$(T - T_{NDT}) = 32 \text{ degrees F}$$

Since the data used is for T = -320°F, then T_{NDT} = -320°F - 32°F = -352°F

Using Figure 3 of NUREG/CR-1815 where thickness is defined as the bolt diameter (1.5 inch), and $\sigma/\sigma_{yd} = 1$ per Regulatory Guide 7.11, A (degrees F) is found to be 60 degrees F. Therefore, the required maximum nil ductility transition temperature per NUREG/CR-1815 for the closure bolts is:

$$T_{NDT} = T_{LT} - A$$
$$= -40° - 60° = -100°F$$

where T_{LT} = lowest temperature of -40 °F (conservatively below the lowest service temperature).

The large margin between the calculated T_{NDT} and the required maximum Nil Ductility Transition temperature leads to the conclusion that SB-637 Grade N07718 possesses appropriate fracture toughness for use as closure lid bolting.

ASME Code Section III, Subsection NF requires Charpy V-notch tests for materials of certain noncontainment components of the overpack. The intermediate shells used for gamma shielding are fabricated from normalized SA516-70. Table A1.15 of ASME Section IIA shows that normalized SA516-70 should have minimum energy absorption of 12 ft-lb at -40 F for a Charpy V-notch test. The lowest anticipated temperature the overpack is to experience is conservatively set at -40°F. Therefore, these tests on the normalized SA516-70 materials of the intermediate shells will confirm the minimum energy absorption of 12 ft-lb at -40°F and the ability of the intermediate shells to perform their intended function at the lowest service temperature.

The pocket trunnions in the initial seven HI-STAR 100 overpacks are fabricated from 17-4PH (or equivalent) material that is precipitation hardened to condition H1150. ARMCO Product Data Bulletin S-22 [2.1.17] shows that Charpy V-notch testing of 17-4PH H1150 material at -110°F gives energy absorption values of approximately 48 ft-lbs. Using the same methodology as used for the closure bolts,

$K_{ID} = 83 \text{ ksi}\sqrt{\text{in.}}$

where $E = 28.7 \times 10^6$ psi and $C_v = 48$ ft-lbs.

Using Figure 2 of NUREG/CR-1815 yields

$T - T_{NDT} = 65°F$

and therefore

$T_{NDT} = -110°F - 65°F = -175°F$

While the optional pocket trunnions are not part of the containment for the overpack, Regulatory Guide 7.12 is used to define the required T_{NDT} for the trunnion pocket thickness ($T_{NDT} = -140°F$). The 35°F margin between the calculated T_{NDT} and the T_{NDT} defined in Regulatory Guide 7.12 provides assurance that brittle fracture failure of the 17-4 material will not occur at the lowest service temperature.

2.1.2.4 Impact Limiter

The impact limiters are designed as energy absorbers to ensure that the maximum impact deceleration applied to the package is limited to values less than the design basis deceleration, as applicable.

2.1.2.5 Buckling

Certain load combinations subject structural sections with relatively large slenderness ratios (such as the MPC enclosure vessel shell) to compressive stresses that may actuate buckling instability before the allowable stress is reached. Tables 2.1.7 and 2.1.9 list load combinations for the MPC enclosure vessel and the HI-STAR 100 overpack structure; the cases that warrant stability (buckling) check are listed therein.

Table 2.1.1

DESIGN PRESSURES

Pressure Location	Condition	Pressure (psig)
MPC Internal Pressure	Normal Condition of Transport	100
	Hypothetical Accident	200[†]
MPC External Pressure	Normal Condition of Transport	40
	Hypothetical Accident	60[††]
Overpack External Pressure	Normal Condition of Transport	(0) Ambient
	Hypothetical Accident	300
Overpack Internal Pressure	Normal Condition of Transport	-Same as MPC Internal Pressure
	Hypothetical Accident	Same as MPC Internal Pressure
Overpack Enclosure Shell Internal Pressure	Normal Condition of Transport	30
	Hypothetical Accident	30

[†] This pressure is only associated with the hypothetical accident where 100% rod rupture is assumed to occur. For all other accident events, such as a 30-ft drop, the applicable MPC internal pressure is the design pressure under normal conditions of transport.

[††] For transport, this represents the differential pressure limit for elastic/plastic stability calculations.

Table 2.1.2

NORMAL REFERENCE TEMPERATURES AND ACCIDENT BULK METAL TEMPERATURE LIMITS

HI-STAR 100 Component	Normal Operating Condition Reference Temp. Limits† (Deg.F)	Hypothetical Accident Condition Metal Bulk Temp. Limits†† (Deg.F)
MPC shell	450	550
MPC basket	725	950
MPC lid	550	775
MPC closure ring	400	775
MPC baseplate	400	775
MPC Boral	800	950
MPC heat conduction elements	725	950
Overpack inner shell	400	500
Overpack bottom plate	350	700
Overpack closure plate	400	700
Overpack top flange	400	700
Overpack closure plate seals	400	1200
Overpack closure plate bolts	350	600
Port plug seals (vent and drain)	400	1600
Port cover seals (vent and drain)	400	932
Neutron shielding	300	†††
Overpack Intermediate Shells	350	700
Overpack Outer Enclosure Shell	350	1350
Optional Pocket Trunnion	200	700
Impact Limiter	150	1105

† These temperatures are maximum possible temperatures for the normal operating condition. They bound the actual calculated temperatures.

†† These temperatures are maximum possible temperatures for the postulated fire accident. They must bound the actual calculated temperatures.

††† For shielding analysis, the neutron shield is conservatively assumed to be lost during the fire accident.

Table 2.1.3

OVERPACK CONTAINMENT STRUCTURE AND MPC ENCLOSURE VESSELSTRESS INTENSITY LIMITS FOR DIFFERENT LOADING CONDITIONS (ELASTIC ANALYSIS PER NB-3220)[†]

STRESS CATEGORY	NORMAL CONDITIONS OF TRANSPORT	HYPOTHETICAL ACCIDENT[††]
Primary Membrane, P_m	S_m	AMIN ($2.4S_m$, $.7S_u$)
Local Membrane, P_L	$1.5S_m$	150% of P_m Limit
Membrane plus Primary Bending	$1.5S_m$	150% of P_m Limit
Primary Membrane plus Primary Bending	$1.5S_m$	150% of P_m Limit
Membrane plus Primary Bending plus Secondary	$3S_m$	N/A
Average[†††] Primary Shear (Section in Pure Shear)	$0.6S_m$	$0.42S_u$

† Stress combinations including F (peak stress) apply to fatigue evaluations only.

†† Governed by Appendix F, Paragraph F-1331 of the ASME Code, Section III. Stress limited to S_u

††† Governed by NB-3227.2 or F-1331.1(d) of the ASME Code, Section III (NB or Appendix F)

Table 2.1.4

MPC BASKET STRESS INTENSITY LIMITS
FOR DIFFERENT LOADING CONDITIONS (ELASTIC ANALYSIS PER NG-3220)

STRESS CATEGORY	NORMAL CONDITIONS OF TRANSPORT	HYPOTHETICAL ACCIDENT[†]
Primary Membrane, P_m	S_m	AMIN ($2.4S_m$, $.7S_u$)[††]
Primary Membrane plus Primary Bending	$1.5S_m$	150% of P_m Limit (Limited to S_u)
Primary Membrane plus Primary Bending plus Secondary	$3S_m$	N/A

† Governed by Appendix F, Paragraph F-1331 of the ASME Code, Section III.

†† Average primary shear stress across a section loaded in pure shear shall not exceed $0.42S_u$.

Table 2.1.5

STRESS INTENSITY LIMITS FOR DIFFERENT
LOADING CONDITIONS FOR THE EXTERNAL STRUCTURALS IN THE HI-STAR OVERPACK
(ELASTIC ANALYSIS PER NF-3260 - CLASS 3)
(ELASTIC ANALYSIS PER NF-3220 - CLASS 1)

STRESS CATEGORY	NORMAL CONDITION OF TRANSPORT†	HYPOTHETICAL ACCIDENT††
Primary Membrane, P_m	S (Class 3) S_m (Class 1)	AMAX ($1.2S_y$, $1.5S_m$) but < $.7S_u$
Primary Membrane, P_m, plus Primary Bending, P_b	1.5S (Class 3) $1.5S_m$ (Class 1)	150% of P_m (Limited to S_u)
Shear Stress	N/A (Class 3) $.6S_m$ (Class 1)	$<0.42S_u$

Definitions:

S = Allowable Stress Value for Table 1A, ASME Section II, Part D
S_m = Allowable Stress Intensity Value from Table 2A, ASME Section II, Part D
S_u = Ultimate Strength

† Limits for Normal Condition of Transport are on stress for Class 3 and on stress intensity for Class 1, upper value in column is for Class 3; lower value in column is for Class 3.

†† Governed by Appendix F, Paragraph F-1332 of the ASME Code, Section III. Class 1 and Class 3 use same stress intensity limits.

Table 2.1.6

LOADING CASES FOR THE MPC FUEL BASKET

Case Number	Load Combination†	Notes
F1	T or T'	Demonstrate that the most adverse of the temperature distributions in the basket will not cause fuel basket to expand and contact the enclosure vessel wall. Compute the stress intensity and show that it is less than allowable.
F2		
F2.a	D+H	1 ft. side drop, 0 degrees circumferential orientation (Figure 2.1.3)
F2.b	D+H	1 ft. side drop, 45 degrees circumferential orientation (Figure 2.1.4)
F3		
F3.a	D + H'	30 ft. vertical axis drop
F3.b	D + H'	30 ft. side Drop, 0 degrees circumferential orientation (Figure 2.1.3)
F3.c	D + H'	30 ft. side Drop, 45 degrees circumferential orientation (Figure 2.1.4)

† The symbols used for loads are defined in Subsection 2.1.2.1.

Table 2.1.7

LOADING CASES FOR THE MPC ENCLOSURE VESSEL

Case Number	Load Combination[†]	Notes
E1		
E1.a	Design internal pressure, P_i	Primary Stress intensity
E1.b	Design external pressure, P_o	Primary stress intensity limits, buckling stability
E1.c	Design internal pressure plus Temperature, $P_i + T$	Primary plus secondary stress intensity under Level A condition
E2		
E2.a	(P_i, P_o) +D +H	1 ft. side drop, 0° circumferential orientation (Figure 2.1.3)
E2.b	(P_i, P_o) +D +H	1 ft. side drop, 45° circumferential orientation (Figure 2.1.4)

† The symbols used for loads are defined in Subsection 2.1.2.1. Note that in the analyses, the bounding pressure (P_i, P_o) is applied, e.g., in stability calculations P_o is bounding, whereas in stress calculations both P_o and P_i are appropriate.

Table 2.1.7 (continued)

Case Number	Load Combination†	Notes
E3		
E3.a	$D + H' + P_o$ (Stability of the shell considers internal pressure plus drop deceleration)	30 ft. vertical axis drop
E3.b	$D + H' + P_i$	30 ft. side drop, 0° circumferential orientation (Figure 2.1.3)
E3.c	$D + H' + P_i$	30 ft. side drop, 45° circumferential orientation (Figure 2.1.4)
E4	T or T'	Demonstrate that interference with the overpack will not develop for T
E5	$(P_i^*, P_o^*) + D + T'$	Demonstrate compliance with level D stress limits - buckling stability

† The symbols used for loads are defined in Subsection 2.1.2.1. Note that in the analyses, the bounding pressure (P_i, P_o) is applied, e.g., in stability calculations P_o is bounding, whereas in stress calculations both P_o and P_i are appropriate.

Table 2.1.8

OVERPACK LOAD CASES FOR NORMAL CONDITION OF TRANSPORT

Case Number	Load Combination†	Notes
1	$T_h + P_i + F + W_s$	Hot Environment
2	$T_s + P_o + F + W_s$	Super-Cold Environment
3	$T_h + D_{sn} + P_i + F + W_s$	Free One Foot Side Drop - Hot Environment
4	$T_c + D_{sn} + P_o + F + W_s$	Free One Foot Side Drop - Cold Environment
5	T_c and $T_h + P_i + V$	Rapid Ambient Temperature Change

Note that load case 5 is outside of the load combinations of Reg. Guide 7.8

† The symbols used here are defined in Subsection 2.1.2.1.

Table 2.1.9

OVERPACK LOAD CASES FOR HYPOTHETICAL ACCIDENT CONDITIONS OF TRANSPORT

Case Number	Load Combination†	Notes
1	$T_h + D_{ba} + P_i + F + W_s$	Bottom End 30 ft. Drop - Hot
2	$T_h + D_{ta} + P_i + F + W_s$	Top End 30 ft Drop - Hot
3	$T_h + D_{sa} + P_i + F + W_s$	Side 30 ft Drop - Hot
4	$T_h + D_{ca} + P_i + F + W_s$	30 ft C.G. Over-the-Bottom-Corner Drop - Hot
5	$T_h + D_{ga} + P_i + F + W_s$	30 ft C.G. Over-the-Top-Corner Drop Hot
6	$T_h + P_s + P_i + F + W_s$	Side Puncture - Hot
7	$T_h + P_t + P_i + F + W_s$	Top End Puncture - Hot
8	$T_h + P_b + P_i + F + W_s$	Bottom End Puncture - Hot
9	$T_c + D_{ba} + P_o + F + W_s$	Case 1 - Cold
10	$T_c + D_{ta} + P_o + F + W_s$	Case 2 - Cold
11	$T_c + D_{sa} + P_o + F + W_s$	Case 3 - Cold
12	$T_c + D_{ca} + P_o + F + W_s$	Case 4 - Cold
13	$T_c + D_{ga} + P_o + F + W_s$	Case 5 - Cold
14	$T_c + P_s + P_o + F + W_s$	Case 6 - Cold
15	$T_c + P_t + P_o + F + W_s$	Case 7 - Cold
16	$T_c + P_b + P_o + F + W_s$	Case 8 - Cold
17	$T_f + P_i + F + W_s$	Fire Event (Bolt unloading)
18	P_o^*	Containment Stability - Hot Deep Submergence
19	$P_i^* + T_f + F + W_s$	Fire Accident Internal Pressure - Hot
20	$T_h + D_{ga} + P_i + F + W_s$	30 ft C.G. Oblique Drop (30 Degree) on Top Forging - Hot
21	$T_c + D_{ga} + P_i + F + W_s$	30 ft C.G. Oblique Drop (30 Degree) on Top Forging - Cold
22	$T_c + D_{ga} + P_i + F + W_s$	30 ft Drop -Slapdown Secondary Impact Limiter at Top Forging - Hot

† The symbols used here are defined in Subsection 2.1.2.1.

Table 2.1.10
BOUNDING DECELERATIONS FOR DROP EVENTS

Event	Deceleration Value (in multiples of acceleration due to gravity)
Normal conditions of transport, drop from 1 ft. height (any circumferential orientations)	17
Transport hypothetical accident conditions; drop from 30 ft. height (any axial and circumferential orientations)	60

Table 2.1.11

DESIGN, LEVELS A AND B: STRESS INTENSITY

Code: ASME NB
Material: SA203-E
Service Conditions: Normal Conditions of Transport
Item: Stress Intensity

Temp. (degree F)	Classification and Value (ksi)					
	S_m	P_m†	P_L†	$P_L + P_b$†	$P_L + P_b + Q$	Pe††
-20 to 100	23.3	23.3	35.0	35.0	69.9	69.9
200	23.3	23.3	35.0	35.0	69.9	69.9
300	23.3	23.3	35.0	35.0	69.9	69.9
400	22.9	22.9	34.4	34.4	68.7	68.7
500	21.6	21.6	32.4	32.4	64.8	64.8

Definitions:

S_m = Stress intensity values per ASME Code
P_m = Primary membrane stress intensity
P_L = Local membrane stress intensity
P_b = Primary bending stress intensity
P_e = Expansion stress
Q = Secondary stress
$P_L + P_b$ = Either primary or local membrane plus primary bending

Definitions for Table 2.1.11 apply to all following tables unless modified.

† Evaluation required for Design condition only.

†† P_e not applicable to vessels.

Table 2.1.12

LEVEL D: STRESS INTENSITY

Code: ASME NB
Material: SA203-E
Service Condition: Hypothetical Accident
Item: Stress Intensity

Temp. (degree F)	Classification and Value (ksi)		
	P_m	P_L	$P_L + P_b$
-20 to 100	49.0	70.0	70.0
200	49.0	70.0	70.0
300	49.0	70.0	70.0
400	48.2	68.8	68.8
500	45.4	64.9	64.9

Notes:

1. Level D allowables per NB-3225 and Appendix F, Paragraph F-1331.

2. Average primary shear stress across a section loaded in pure shear may not exceed 0.42 S_u.

3. Limits on values are presented in Table 2.1.3.

Table 2.1.13

DESIGN, LEVELS A AND B: STRESS INTENSITY

Code: ASME NB
Material: SA350-LF3
Service Conditions: Normal Conditions of Transport
Item: Stress Intensity

Temp. (degree F)	Classification and Value (ksi)					
	S_m	P_m†	P_L†	$P_L + P_b$†	$P_L + P_b + Q$	P_e††
-20 to 100	23.3	23.3	35.0	35.0	69.9	69.9
200	22.8	22.8	34.2	34.2	68.4	68.4
300	22.2	22.2	33.3	33.3	66.6	66.6
400	21.5	21.5	32.3	32.3	64.5	64.5
500	20.2	20.2	30.3	30.3	60.6	60.6
600	18.5	18.5	27.75	27.75	55.5	55.5
700	16.8	16.8	25.2	25.2	50.4	50.4

Notes:

1. Source for S_m is ASME Code.

2. Limits on values are presented in Table 2.1.3.

† Evaluation required for Design condition only.

†† P_e not applicable to vessels.

Table 2.1.14

LEVEL D, STRESS INTENSITY

Code: ASME NB
Material: SA350-LF3
Service Conditions: Hypothetical Accident
Item: Stress Intensity

Temp. (degree F)	Classification and Value (ksi)		
	P_m	P_L	$P_L + P_b$
-20 to 100	49.0	70.0	70.0
200	48.0	68.5	68.5
300	46.7	66.7	66.7
400	45.2	64.6	64.6
500	42.5	60.7	60.7
600	38.9	58.4	58.4
700	35.3	53.1	53.1

Notes:

1. Level D allowables per NB-3225 and Appendix F, Paragraph F-1331.

2. Average primary shear stress across a section loaded in pure shear may not exceed 0.42 S_u.

3. Limits on values are presented in Table 2.1.3.

Table 2.1.15

DESIGN AND LEVEL A: STRESS AND STRESS INTENSITY

Code:	ASME NF (Class 3)	ASME NF (Class 1)
Material:	SA515, Grade 70 SA516, Grade 70	SA515, Grade 70 SA516, Grade 70
Service Conditions:	Normal Conditions of Transport	Normal Conditions of Transport
Item:	Stress	Stress Intensity

Temp. (degree F)	Classification and Value (ksi)					
	S (Class 3)	S_m (Class 1)	Membrane Stress (Class 3)	P_m (Class 1)	Membrane plus Bending Stress (Class 3)	P_m+P_b (Class 1)
-20 to 100	17.5	23.3	17.5	23.3	26.3	34.95
200	17.5	23.1	17.5	23.1	26.3	34.65
300	17.5	22.5	17.5	22.5	26.3	33.75
400	17.5	21.7	17.5	21.7	26.3	32.55
500	17.5	20.5	17.5	20.5	26.3	30.75
600	17.5	18.7	17.5	18.7	26.3	28.05
650	17.5	18.4	17.5	18.4	26.3	27.6
700	16.6	18.3	16.6	18.3	24.9	27.45

Notes:

1. S = Maximum allowable stress values from Table 1A of ASME Code, Section II, Part D.
2. Stress classification per Paragraph NF-3260.
3. Limits on values are presented in Table 2.1.5.
4. Level A allowable stress intensities per NF.3221.1.
5. S_m = Stress intensity values per Table 2A of ASME, Section II, Part D.

Table 2.1.16

LEVEL D: STRESS INTENSITY

Code: ASME NF
Material: SA515, Grade 70
SA516, Grade 70
Service Conditions: Hypothetical Accident
Item: Stress Intensity

Temp. (degree F)	Classification and Value (ksi)		
	S_m	P_m	$P_m + P_b$
-20 to 100	23.3	45.6	68.4
200	23.1	41.5	62.3
300	22.5	40.4	60.6
400	21.7	39.1	58.7
500	20.5	36.8	55.3
600	18.7	33.7	50.6
650	18.4	33.1	49.7
700	18.3	32.9	49.3

Notes:

1. Level D allowable stress intensities per Appendix F, Paragraph F-1332.

2. S_m = Stress intensity values per Table 2A of ASME, Section II, Part D.

3. Limits on values are presented in Table 2.1.5.

Table 2.1.17

DESIGN, LEVELS A AND B: STRESS INTENSITY

Code: ASME NB
Material: Alloy X
Service Conditions: Normal Conditions of Transport
Item: Stress Intensity

Temp. (degree F)	Classification and Numerical Value					
	S_m	P_m†	P_L†	$P_L + P_b$†	P_L+P_b+Q	P_e††
-20 to 100	20.0	20.0	30.0	30.0	60.0	60.0
200	20.0	20.0	30.0	30.0	60.0	60.0
300	20.0	20.0	30.0	30.0	60.0	60.0
400	18.7	18.7	28.1	28.1	56.1	56.1
500	17.5	17.5	26.3	26.3	52.5	52.5
600	16.4	16.4	24.6	24.6	49.2	49.2
650	16.0	16.0	24.0	24.0	48.0	48.0
700	15.6	15.6	23.4	23.4	46.8	46.8
750	15.2	15.2	22.8	22.8	45.6	45.6
800	14.9	14.9	22.4	22.4	44.7	44.7

Notes:

1. S_m = Stress intensity values per Table 2A of ASME II, Part D.
2. Alloy X S_m values are the lowest values for each of the candidate materials at temperature.
3. Stress classification per NB-3220.
4. Limits on values are presented in Table 2.1.3.

† Evaluation required for Design condition only.

†† P_e not applicable to vessels.

Table 2.1.18

LEVEL D: STRESS INTENSITY

Code: ASME NB
Material: Alloy X
Service Conditions: Hypothetical Accident
Item: Stress Intensity

Temp. (degree F)	Classification and Value (ksi)†		
	P_m	P_L	$P_L + P_b$
-20 to 100	48.0 (48.0)	72.0 (72.0)	72.0 (72.0)
200	48.0 (46.3)	72.0 (69.5)	72.0 (69.5)
300	46.2 (43.1)	69.3 (64.7)	69.3 (64.7)
400	44.9 (42.0)	67.4 (63.0)	67.4 (63.0)
500	42.0 (41.5)	63.0 (62.3)	63.0 (62.3)
600	39.4 (39.4)	59.1 (59.1)	59.1 (59.1)
650	38.4 (38.4)	57.6 (57.6)	57.6 (57.6)
700	37.4 (37.4)	56.1 (56.1)	56.1 (56.1)
750	36.5 (36.5)	54.8 (54.8)	54.8 (54.8)
800	35.8 (35.8)	53.7 (53.7)	53.7 (53.7)

Notes:
1. Level D stress intensities per ASME NB-3225 and Appendix F, Paragraph F-1331.
2. The average primary shear strength across a section loaded in pure shear may not exceed 0.42 S_u.
3. Limits on values are presented in Table 2.1.3.

† Values in parentheses apply strictly to the one-piece construction MPC lids, which are made from SA-336 forging material rather than SA-240 plate material.

Table 2.1.19

DESIGN, LEVELS A AND B: STRESS INTENSITY

Code: ASME NG
Material: Alloy X
Service Conditions: Normal Conditions of Transport
Item: Stress Intensity

Temp. (degree F)	Classification and Value (ksi)				
	S_m	P_m	P_m+P_B	P_m+P_b+Q	P_e
-20 to 100	20.0	20.0	30.0	60.0	60.0
200	20.0	20.0	30.0	60.0	60.0
300	20.0	20.0	30.0	60.0	60.0
400	18.7	18.7	28.1	56.1	56.1
500	17.5	17.5	26.3	52.5	52.5
600	16.4	16.4	24.6	49.2	49.2
650	16.0	16.0	24.0	48.0	48.0
700	15.6	15.6	23.4	46.8	46.8
750	15.2	15.2	22.8	45.6	45.6
800	14.9	14.9	22.4	44.7	44.7

Notes:
1. S_m = Stress intensity values per Table 2A of ASME, Section II, Part D.
2. Alloy X S_m values are the lowest values for each of the candidate materials at temperature.
3. Classifications per NG-3220.
4. Limits on values are presented in Table 2.1.4.

Table 2.1.20

LEVEL D: STRESS INTENSITY

Code: ASME NG
Material: Alloy X
Service Conditions: Hypothetical Accident
Item: Stress Intensity

Temp. (degrees F)	Classification and Value (ksi)		
	P_m	P_L	$P_L + P_b$
-20 to 100	48.0	72.0	72.0
200	48.0	72.0	72.0
300	46.2	69.3	69.3
400	44.9	67.4	67.4
500	42.0	63.0	63.0
600	39.4	59.1	59.1
650	38.4	57.6	57.6
700	37.4	56.1	56.1
750	36.5	54.8	54.8
800	35.8	53.7	53.7

Notes:
1. Level D stress intensities per ASME NG-3225 and Appendix F, Paragraph F-1331.
2. The average primary shear strength across a section loaded in pure shear may not exceed 0.42 S_u.
3. Limits on values are presented in Table 2.1.4.

Table 2.1.21

REFERENCE TEMPERATURES AND STRESS LIMITS
FOR THE VARIOUS LOAD CASES

Load Case Number	Material	Reference Temperature†, (°F)	Stress Intensity Allowables, ksi		
			P_m	$P_L + P_b$	$P_L + P_b + Q$
F1	Alloy X	725	15.4	23.1	46.2
F2	Alloy X	725	15.4	23.1	46.2
F3	Alloy X	725	36.9	55.4	NL††
E1	Alloy X	450†††	18.1	27.2	NL
E2	Alloy X	450†††	18.1	27.2	54.3
E3	Alloy X	450†††	43.4	65.2	NL
E4	Alloy X	450†††	18.1	27.2	54.3
E5	Alloy X	775†††	36.15	54.25	NL

† Values for reference temperatures are taken as the design temperatures (Table 2.1.2).

†† NL: No specific limit in the Code.

††† Levels used for enclosure vessel top closure and baseplate only.

Table 2.1.21 (continued)

REFERENCE TEMPERATURES AND STRESS LIMITS
FOR THE VARIOUS LOAD CASES

Condition	Material	Reference Temperature, (°F)	Stress Intensity Allowables, ksi		
			P_m	$P_L + P_b$	$P_L + P_b + Q$
Normal	SA203-E	400†	22.9	34.4	68.7
	SA350-LF3	400†	21.5	32.3	64.5
	SA516 Gr. 70 SA515 Gr. 70	400†	17.5	26.3	52.5
	SA203-E	-20	23.3	35.0	69.9
	SA350-LF3	-20	23.3	35.0	69.9
	SA516 Gr. 70 SA515 Gr. 70	-20	17.5	26.3	52.5
Hypothetical Accident - Mechanical Loads	SA203-E	400†	48.2	68.8	NL††
	SA350-LF3	400†	45.2	64.6	NL
	SA516 Gr. 70 SA515 Gr. 70	400†	39.1	58.7	NL
	SA203-E	-20	49.0	70.0	NL
	SA350-LF3	-20	49.0	70.0	NL
	SA516 Gr. 70 SA515 Gr. 70	-20	45.6	68.4	NL
Fire	SA203-E	500	45.4	64.9	NL
	SA350-LF3	700	35.3	53.1	NL
	SA516 Gr. 70	700	32.9	49.3	NL

† Values for reference temperatures are taken as the design temperatures (Table 2.1.2).

†† NL: No limit specified in the Code.

Table 2.1.22

FRACTURE TOUGHNESS TEST CRITERIA: CONTAINMENT BOUNDARY

Item	Material	Thickness (in.)	Charpy V-Notch Temperature†	Drop Test Temperature††
Weld Metal for NB Welds	As required	NA	As required per ASME Section III, Subsection NB, Article NB-2430 and Article NB-2330 Min. test temperature = -40°F	As required per ASME Section III, Subsection NB, Articles NB-2430 and Article NB-2330
Shell	SA203E	2-1/2	$T_{NDT} \leq -70$ °F with testing and acceptance criteria per ASME Section III, Subsection NB, Article NB-2330	$T_{NDT} \leq -70$ °F per Reg. Guide 7.11
Top Flange	SA350-LF3	8-3/4	$T_{NDT} \leq -136$ °F with testing and acceptance criteria per ASME Section III, Subsection NB, Article NB-2330	$T_{NDT} \leq -136$ °F per Reg. Guide 7.12

† Temperature is T_{NDT} unless noted.

†† Materials to be tested in accordance with ASTM E208-87a.

Table 2.1.22 (Continued)

FRACTURE TOUGHNESS TEST CRITERIA: CONTAINMENT BOUNDARY

Item	Material	Thickness (in.)	Charpy V-Notch Temperature†	Drop Test Temperature††
Bottom Plate	SA350-LF3	6	$T_{NDT} \leq -129$ °F with testing and acceptance criteria per ASME Section III, Subsection NB, Article NB-2330	$T_{NDT} \leq -129$ °F per Reg. Guide 7.12
Closure Plate	SA350-LF3	6	$T_{NDT} \leq -129$ °F with testing and acceptance criteria per ASME Section III, Subsection NB, Article NB-2330	$T_{NDT} \leq -129$ °F per Reg. Guide 7.12

† Temperature is T_{NDT} unless noted.

†† Materials to be tested in accordance with ASTM E208-87a.

Table 2.1.23

FRACTURE TOUGHNESS TEST CRITERIA: MISCELLANEOUS ITEMS

Item	Material	Thickness (in.)	Charpy V-Notch Temperature†	Drop Test Temperature
Intermediate Shells	SA516 Grade 70	1-1/4 and 1	Test temperature = -40 Deg. F with acceptance criteria per ASME Section III, Subsection NF, Table NF-2331(a)-3 and Figure NF-2331(a)-2, except BOM items 15 & 16 shall meet Table NF-2331(a)-1 and NF-2331 (a)-4	Not Required
Port Cover Plates	SA203-E	1-1/2	Test temperature = -40 Deg. F with acceptance criteria per ASME Section III, Subsection NF, Table NF-2331(a)-3 and Figure NF-2331(a)-2	Not Required
Weld Metal for NF Welds	As required	NA	As required per ASME Section III, Subsection NF, Article NF-2430 and Article NF-2330 Test temperature = -40 Deg. F	Not Required

† Temperature is T_{NDT} unless noted.

Table 2.1.24

ALLOWABLE STRESS CRITERIA FROM OTHER SOURCES

OVERPACK CLOSURE BOLTS[†]:

STRESS CATEGORY	NORMAL CONDITIONS OF TRANSPORT	HYPOTHETICAL ACCIDENT
Average Tensile Stress	2/3 S_y	AMIN(S_y, 0.7 S_u)
Average Shear Stress	0.6 (2/3 S_y)	AMIN(0.6 S_y, 0.42 S_u)
Combined Tensile and Shear Stress[††]	$R_t^2 + R_s^2 < 1.0$	$R_t^2 + R_s^2 < 1.0$

IMPACT LIMITER ATTACHMENT BOLTS:

STRESS CATEGORY	NORMAL CONDITIONS OF TRANSPORT	HYPOTHETICAL ACCIDENT
Average Tensile Stress	2/3 S_y	S_u
Average Shear Stress	0.6 (2/3 S_y)	S_u
Combined Tensile and Shear Stress	$R_t^2 + R_s^2 < 1.0$	$R_t^2 + R_s^2 < 1.0$

LIFTING TRUNNIONS AND LIFTING BOLTS:

The lifting trunnions and the lifting bolts, for the overpack closure plate and for the MPC lid, are designed in accordance with NUREG-0612 and ANSI N14.6. Specifically, the design must meet factors of safety of six based on the material yield stress and ten based on the material ultimate stress for non-redundant lifting devices.

[†] The overpack closure bolts are designed in accordance with NUREG/CR-6007, "Stress Analysis of Closure Bolts for Shipping Casks".

[††] Rt and Rs are the ratios of actual stress to shear stress, respectively.

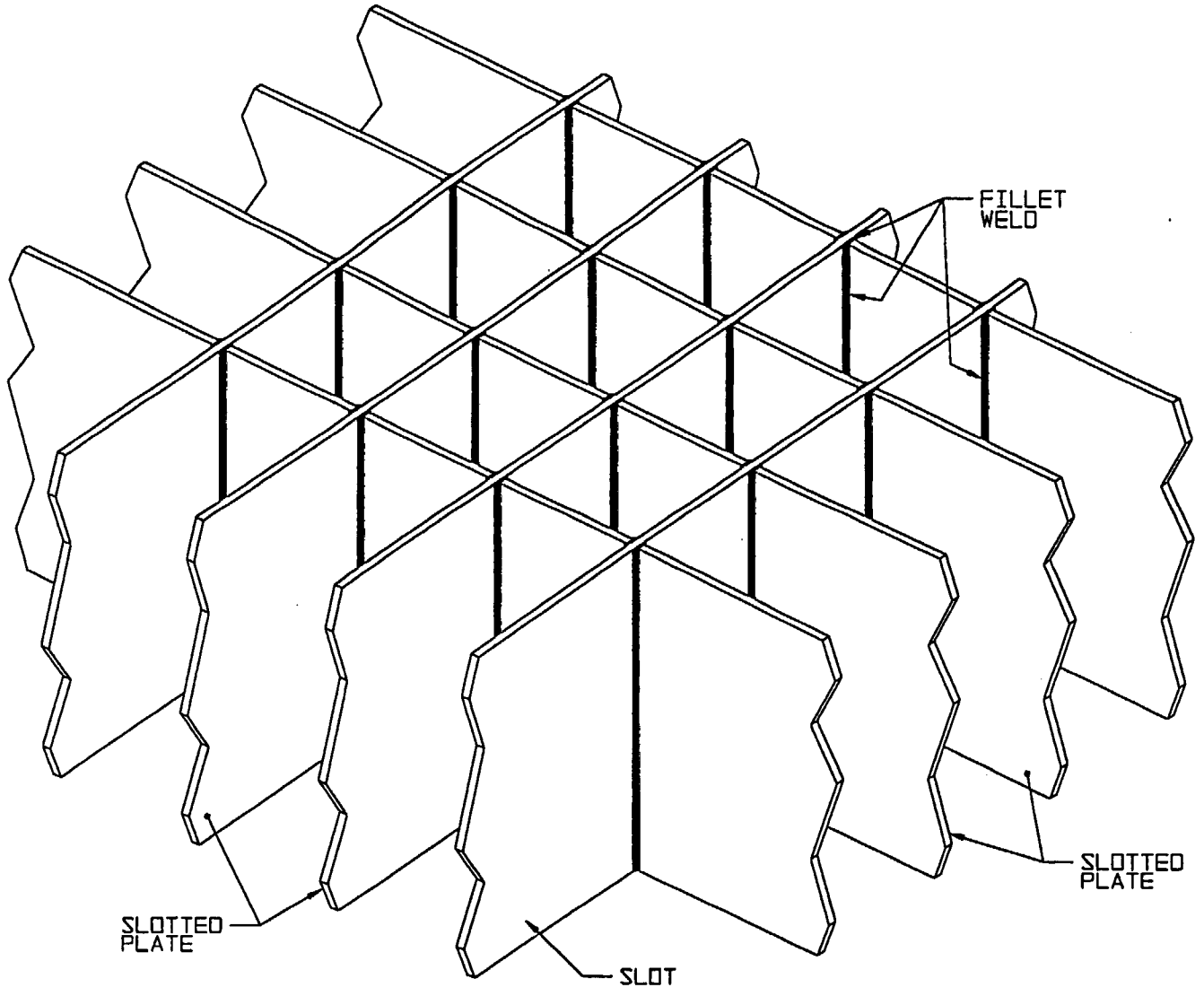

FIGURE 2.1.1; MPC FUEL BASKET GEOMETRY

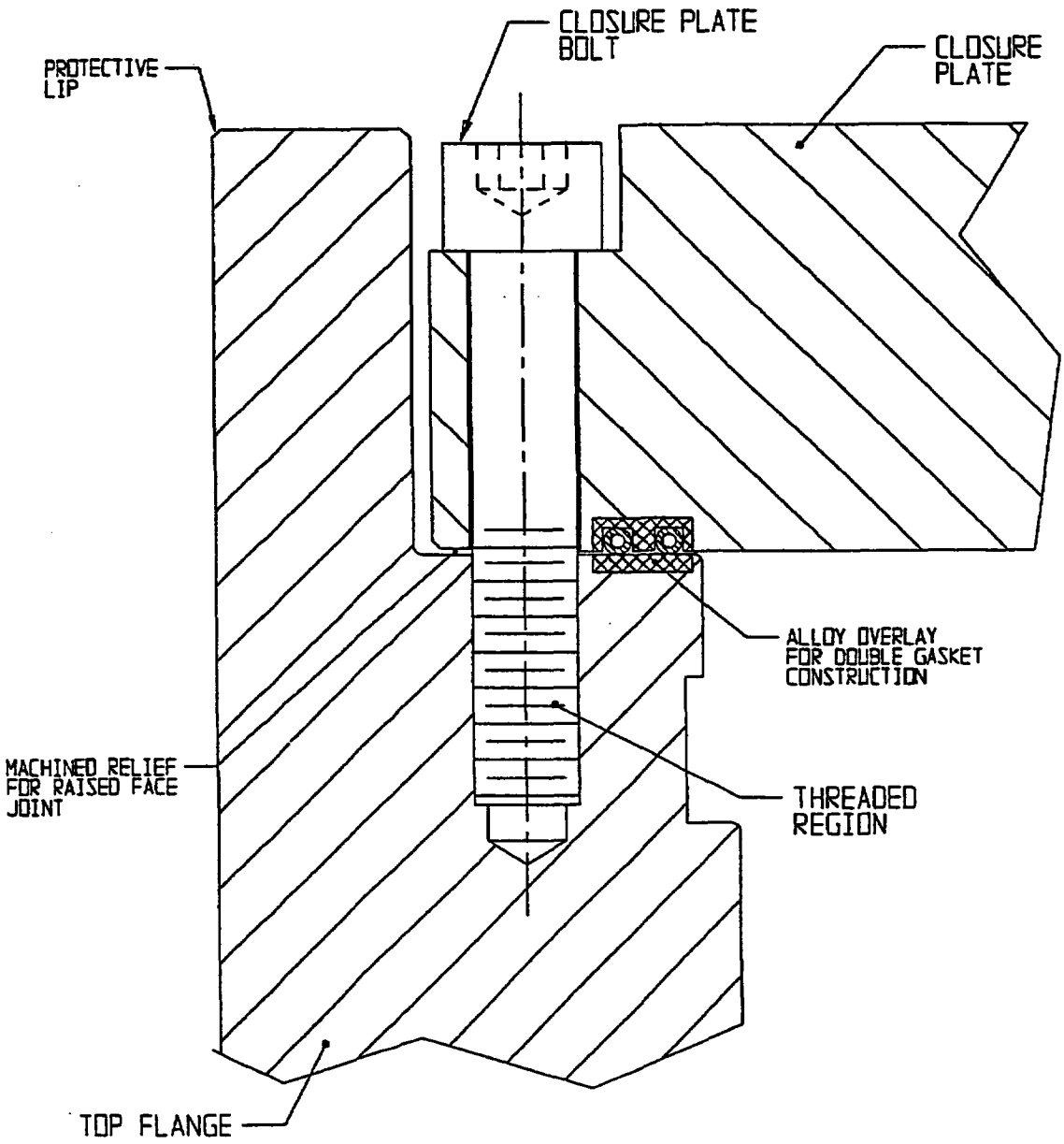

FIGURE 2.1.2; SCHEMATIC OF CLOSURE PLATE BOLTED JOINT

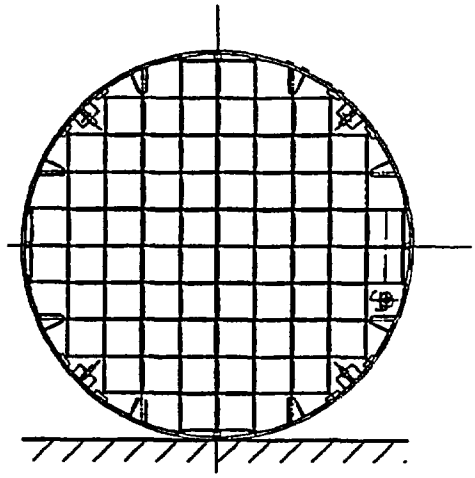

FIGURE 2.1.3; 0° DROP ORIENTATION FOR THE MPCs

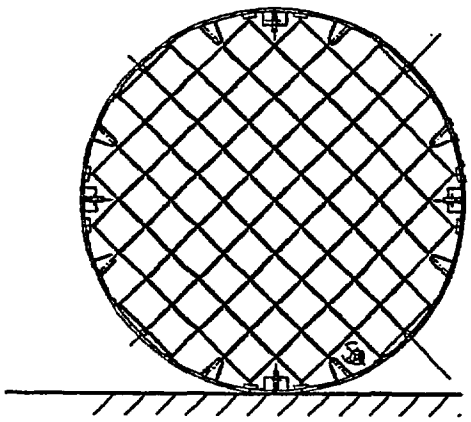

GRAVITY

FIGURE 2.1.4; 45° DROP ORIENTATION FOR THE MPCs

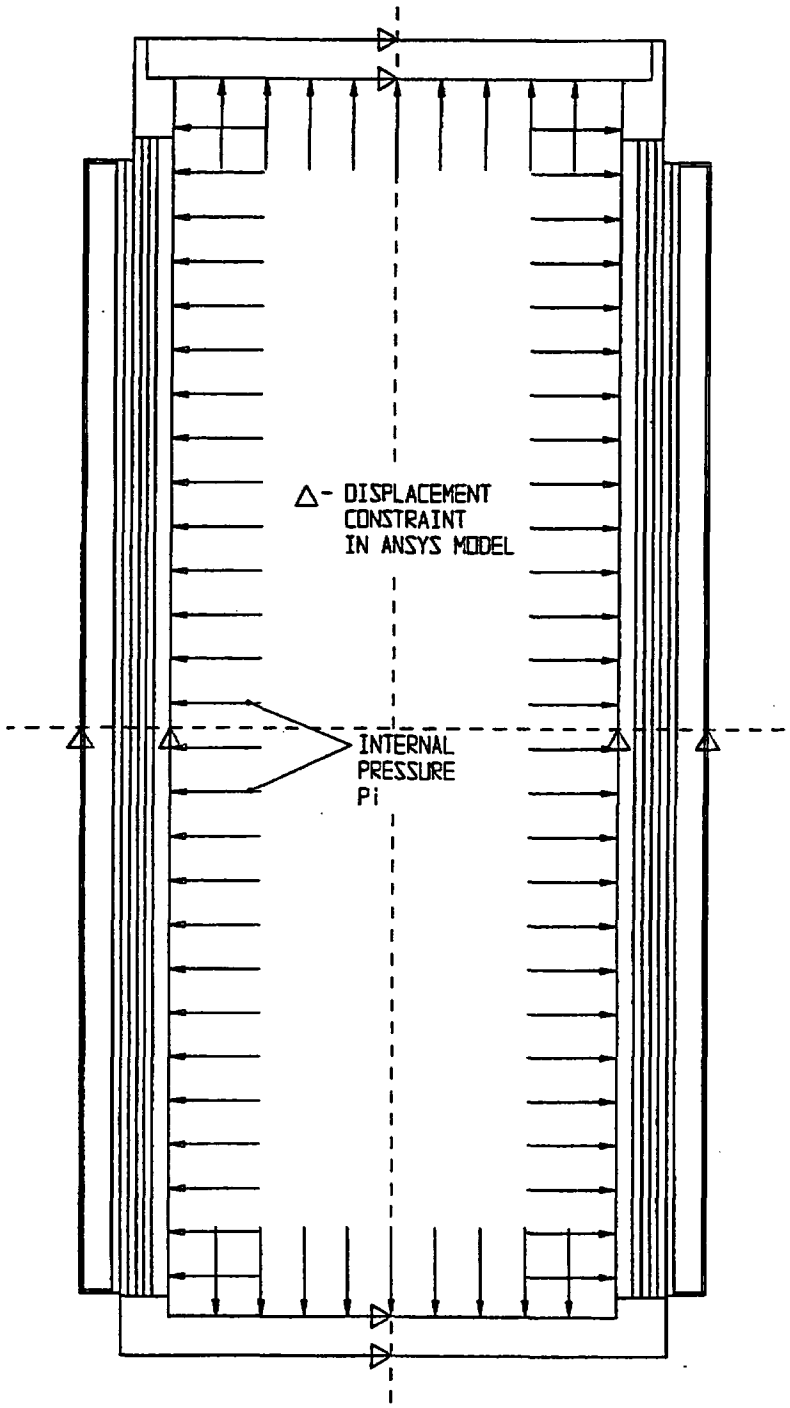

FIGURE 2.1.5; FREE BODY DIAGRAM OF OVERPACK - INTERNAL PRESSURE

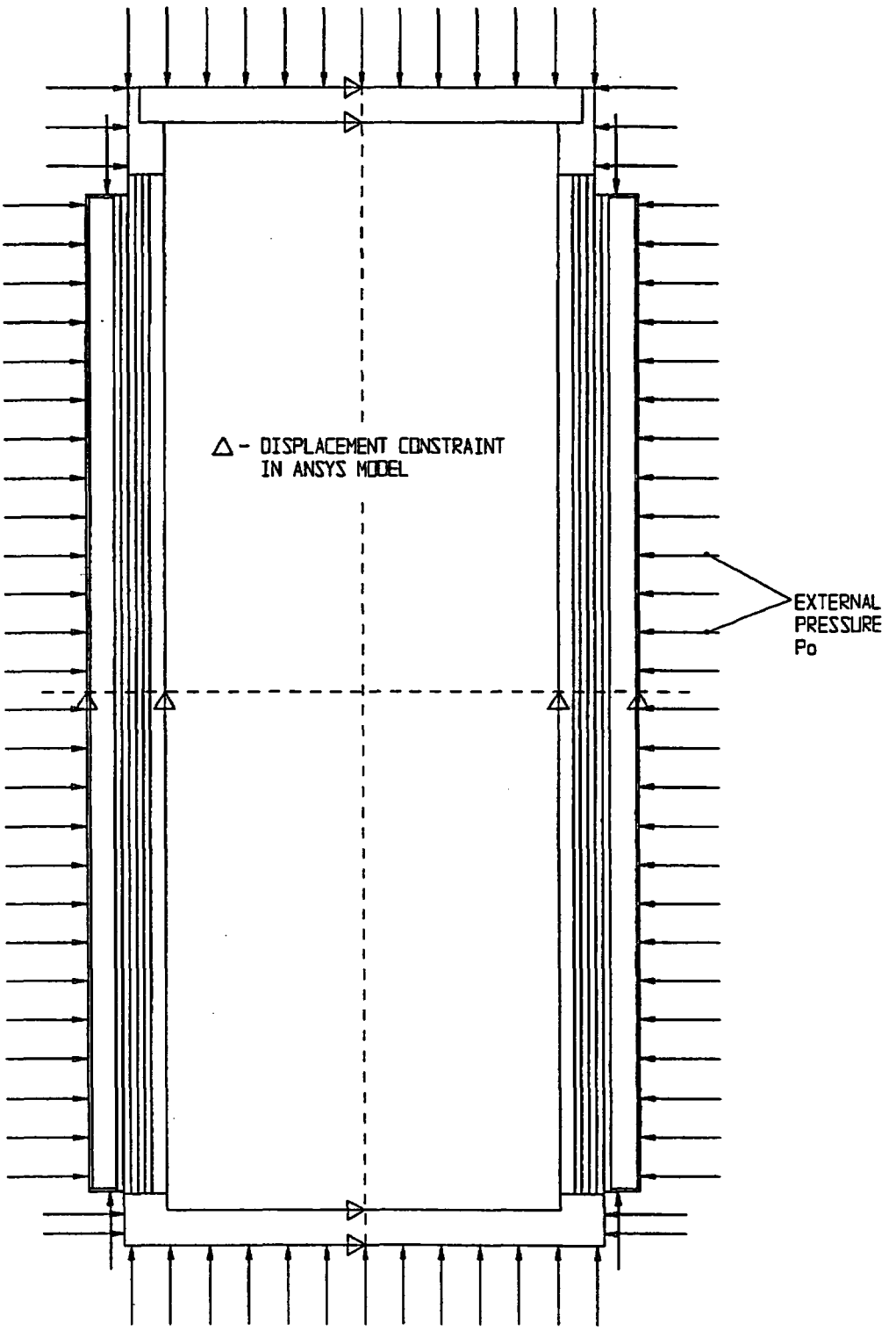

FIGURE 2.1.6; FREE BODY DIAGRAM OF OVERPACK - EXTERNAL PRESSURE

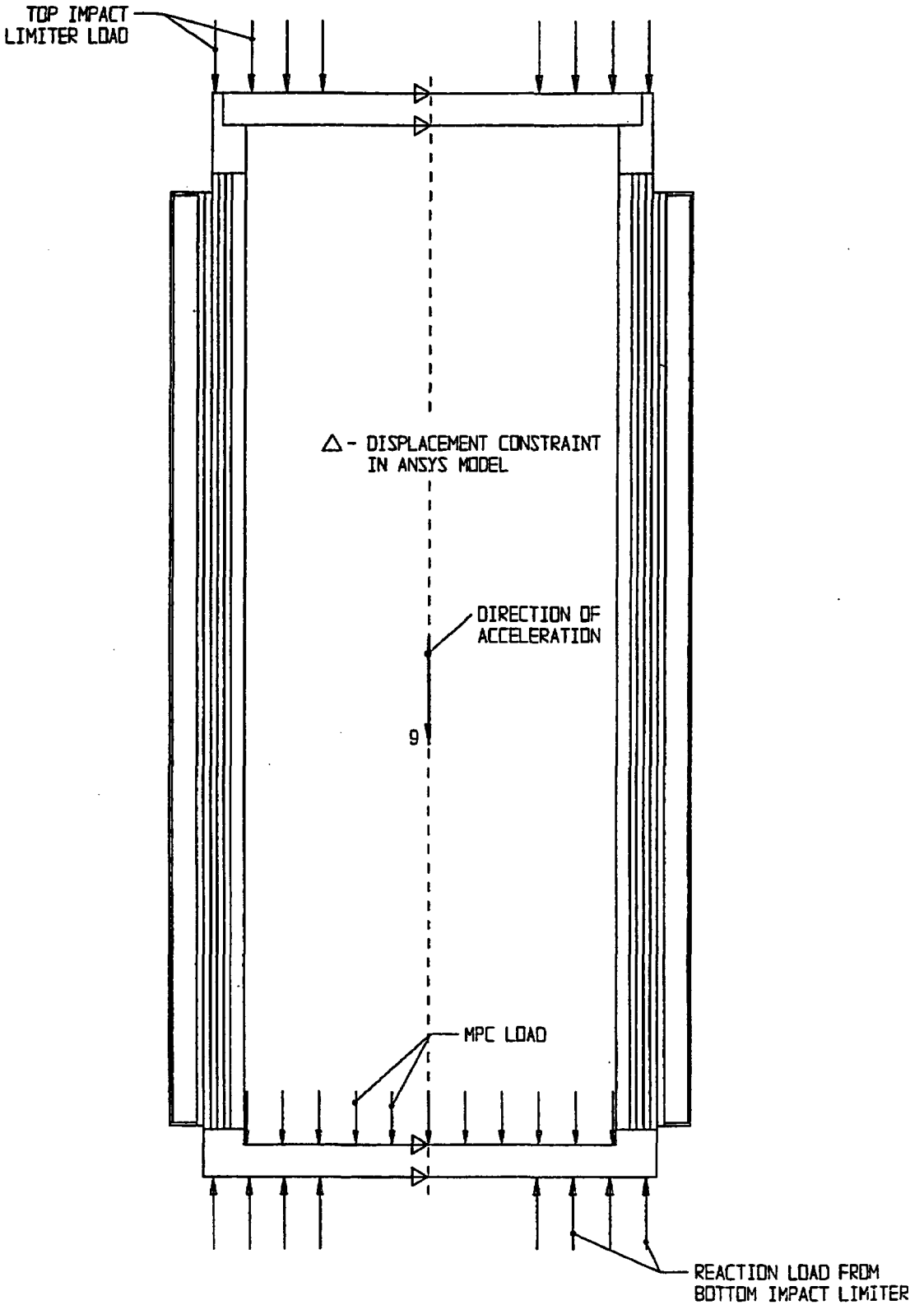

FIGURE 2.1.7; FREE BODY DIAGRAM OF OVERPACK - BOTTOM END DROP

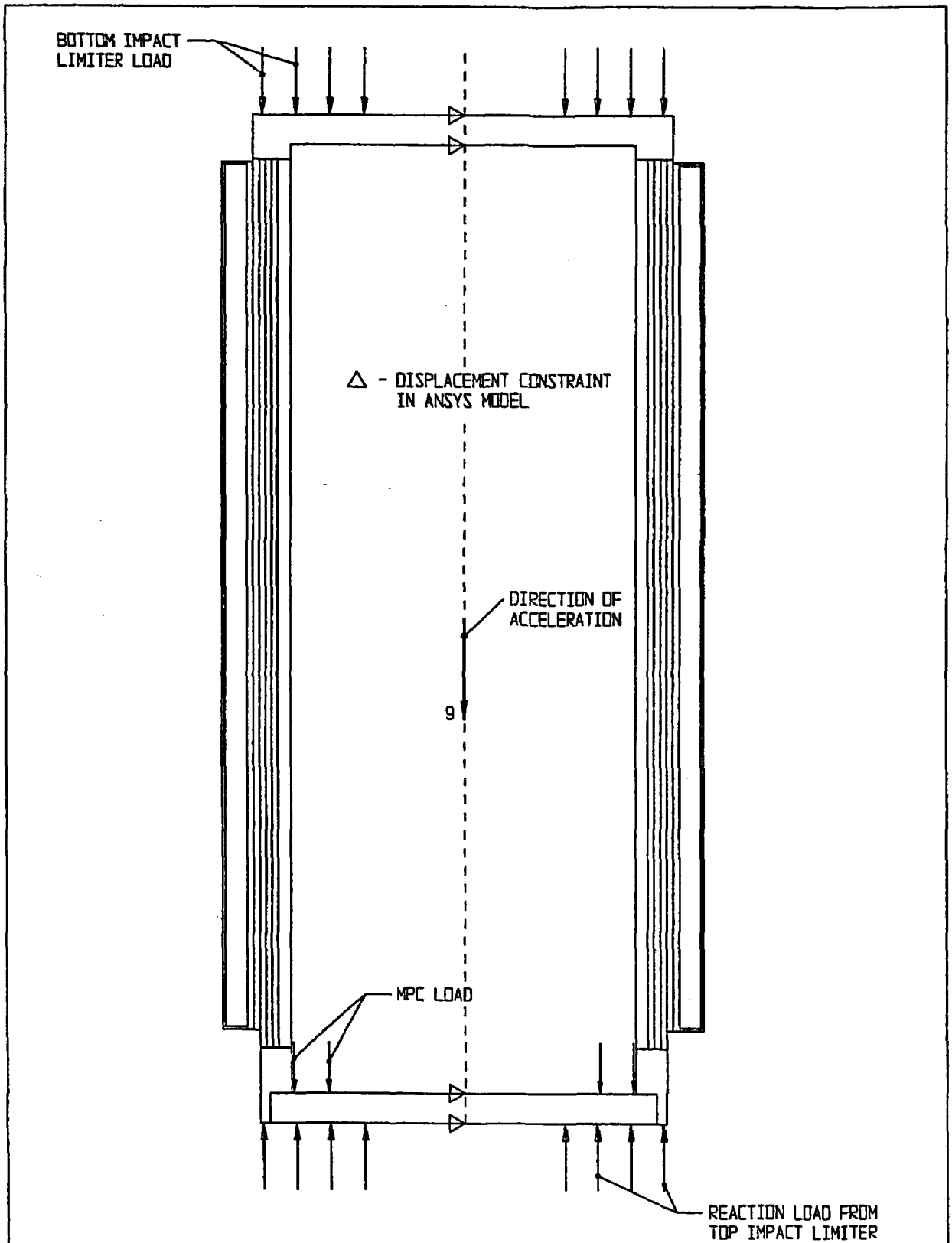

FIGURE 2.1.8; FREE BODY DIAGRAM OF OVERPACK - TOP END DROP

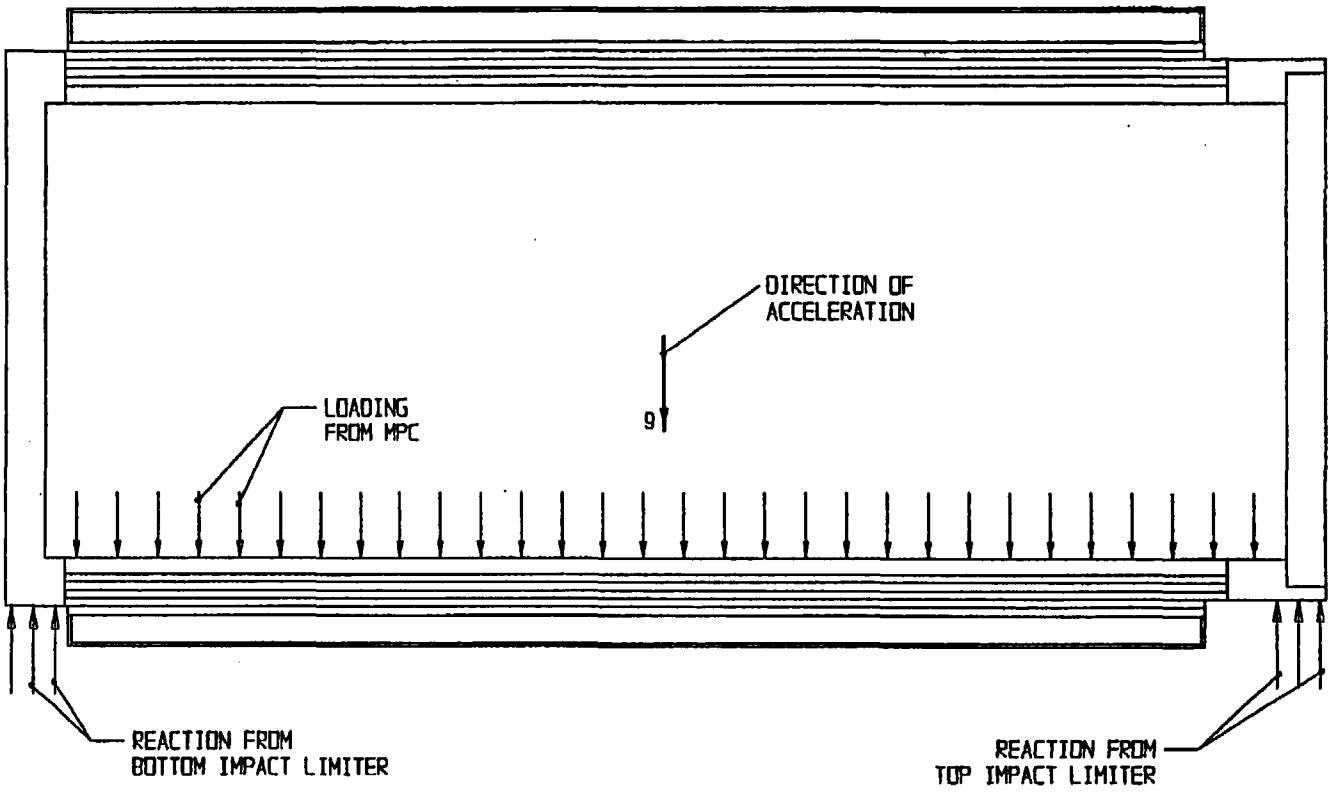

FIGURE 2.1.9; FREE BODY DIAGRAM OF OVERPACK - SIDE DROP

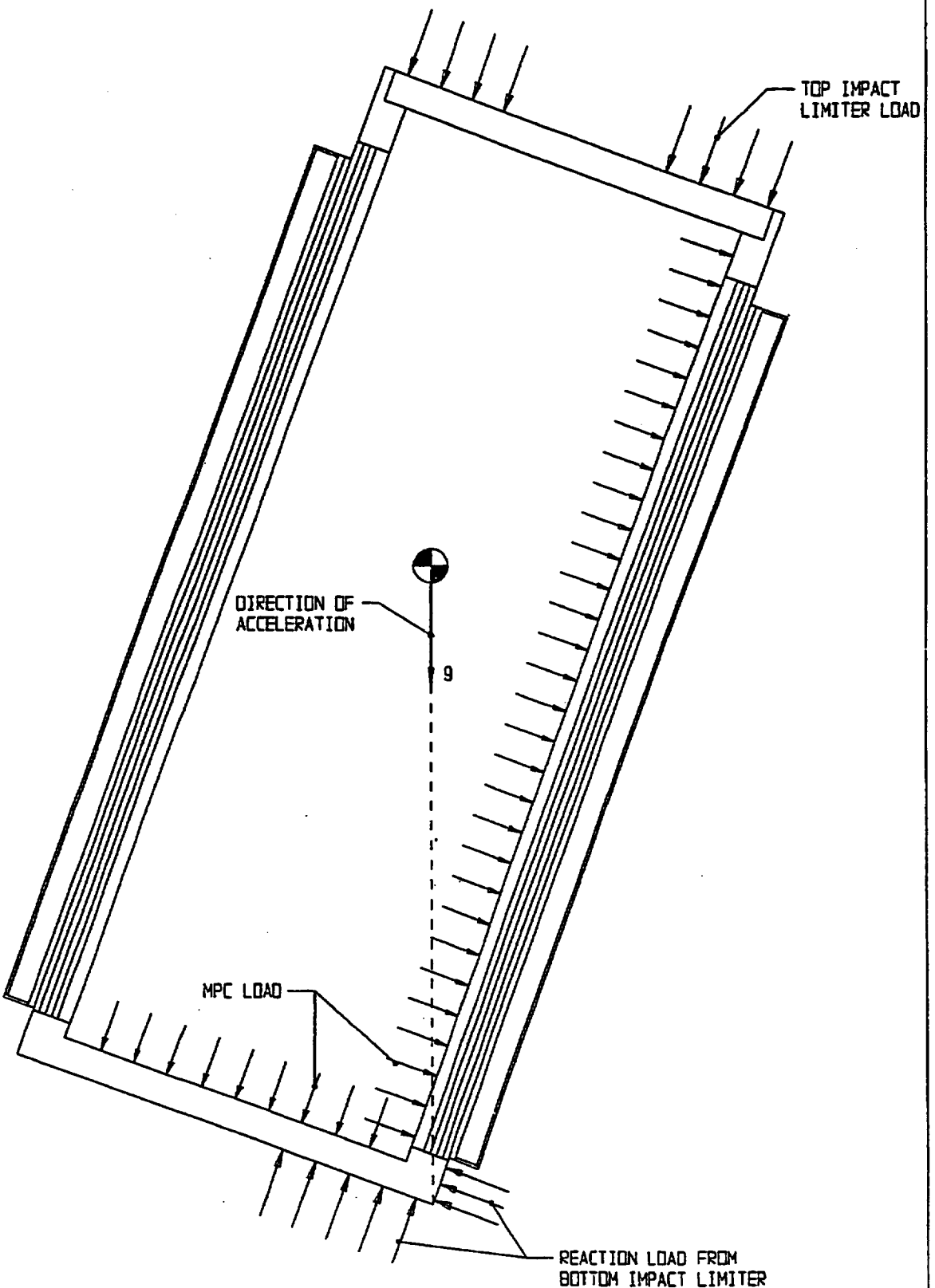

FIGURE 2.1.10 ; FREE BODY DIAGRAM FOR BOTTOM CG - OVER - CORNER DROP

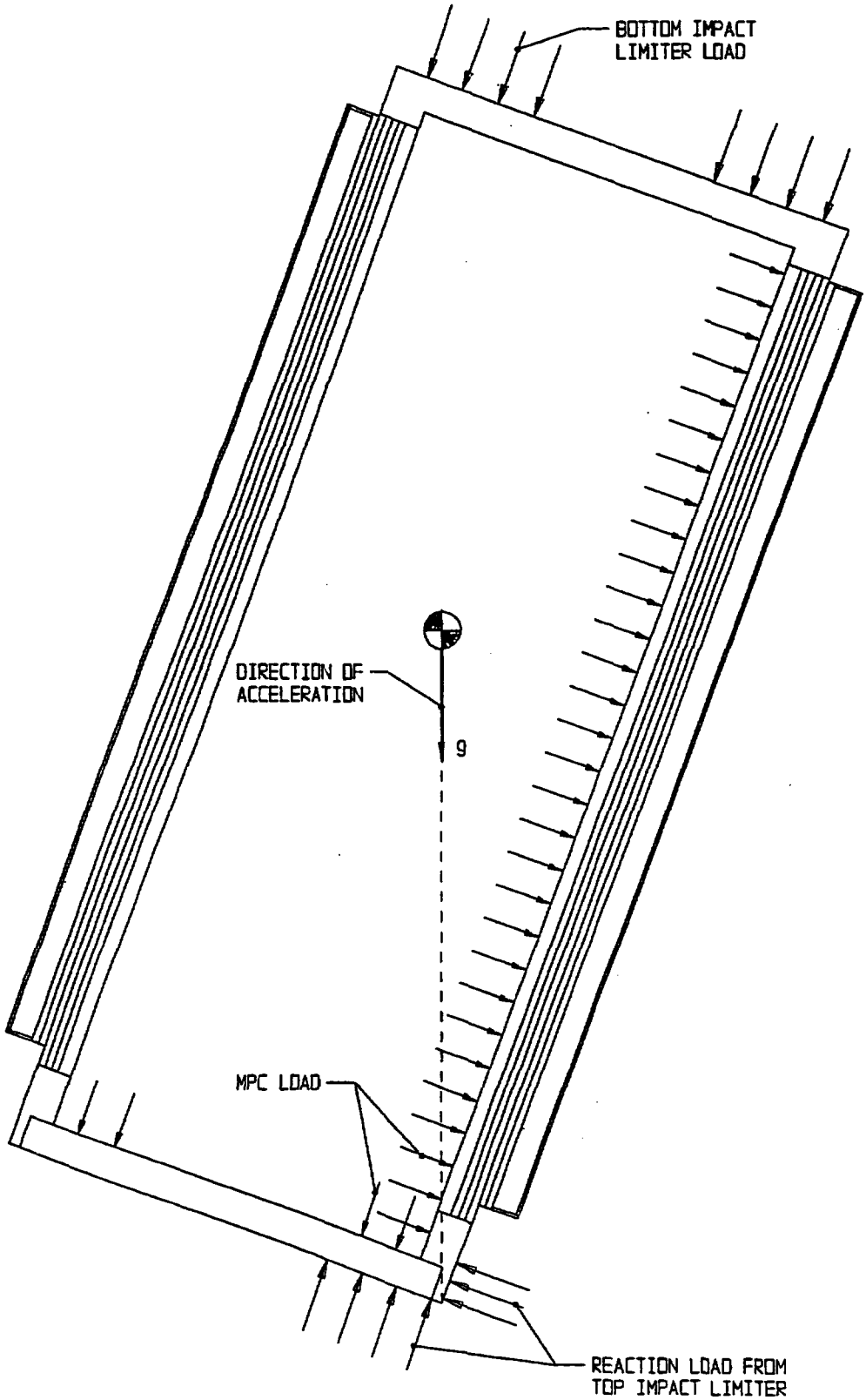

FIGURE 2.1.11; FREE BODY DIAGRAM FOR TOP CG - OVER - CORNER DROP

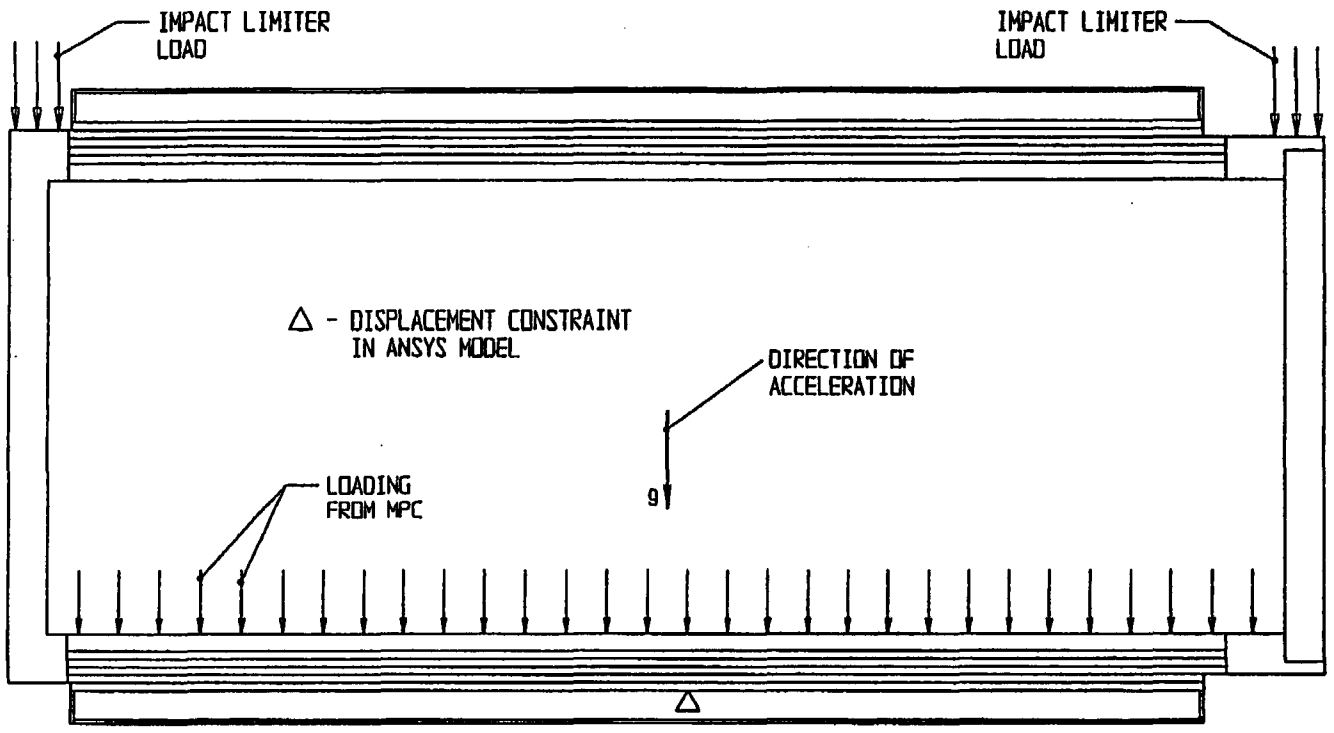

FIGURE 2.1.12; FREE BODY DIAGRAM FOR PUNCTURE DROP ONTO BAR - SIDE

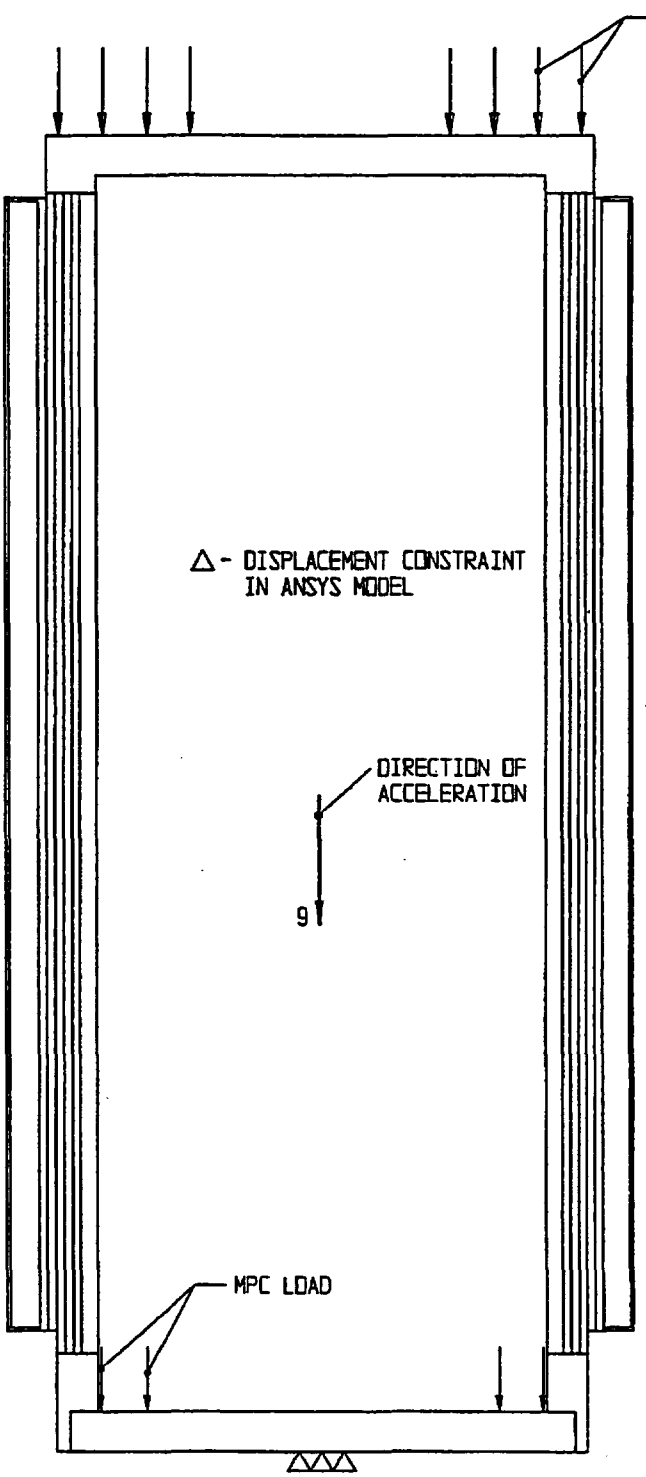

FIGURE 2.1.13; FREE BODY DIAGRAM FOR PUNCTURE DROP ONTO BAR - TOP END

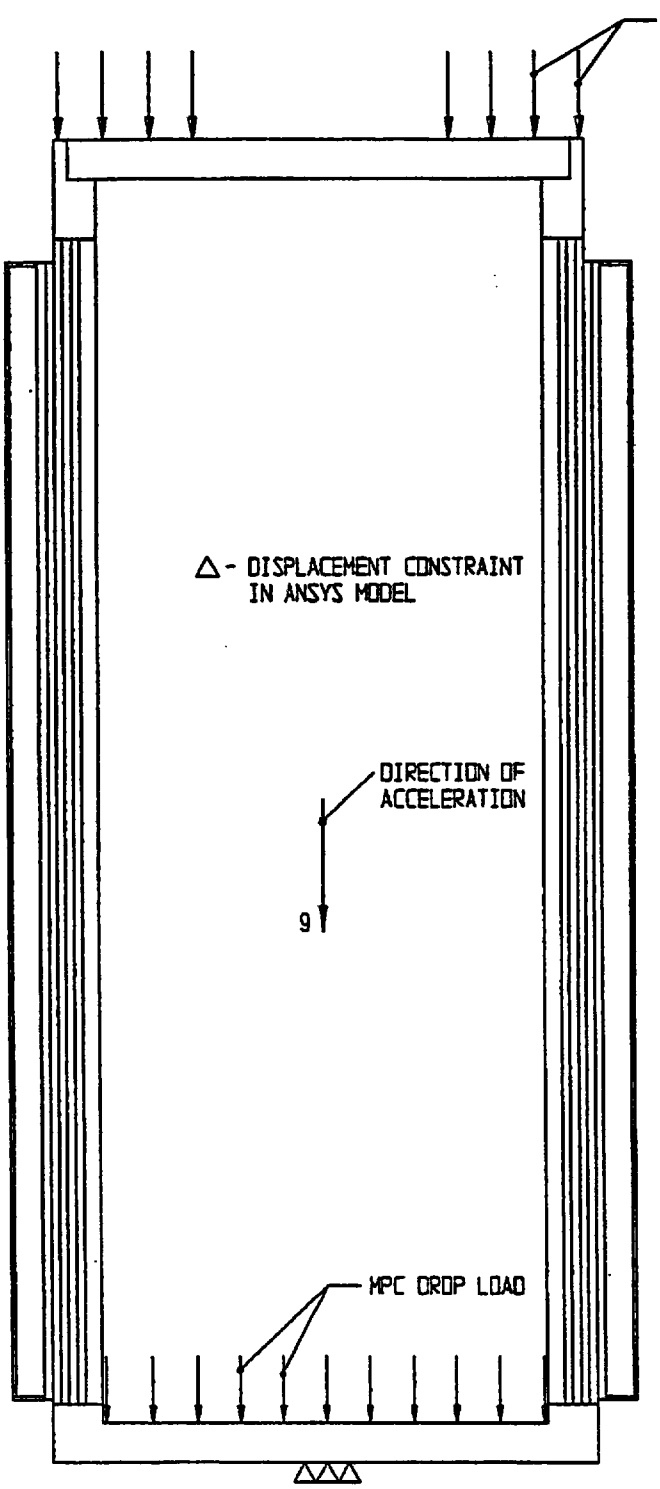

FIGURE 2.1.14; FREE BODY DIAGRAM FOR PUNCTURE DROP ONTO BAR - BOTTOM END

2.2 WEIGHTS AND CENTERS OF GRAVITY

Table 2.2.1 provides the weights of the individual HI-STAR 100 components as well as the total system weights. The weight of the impact limiter is also provided.

The locations of the calculated centers of gravity (CGs) are presented in Table 2.2.2 per the locations described in Figure 2.2.1. All centers of gravity are located on the cask centerline since the non-axisymmetry effects of the cask system plus contents are negligible.

Table 2.2.3 provides the lift weight for the HI-STAR 100 System when the heaviest fully loaded MPC is lifted from the fuel pool. The effect of buoyancy is neglected, and the weight of rigging is set at a conservative value.

Table 2.2.4 provides a table of bounding weights that may be used in calculations where additional conservatism is introduced by increasing the weight.

Table 2.2.1

HI-STAR 100 CALCULATED WEIGHT DATA[†]

Item	Component Weight (lb)	Component Weight (lb)	Total Weight (lb)
Overpack[††] Overpack closure plate	-	7,984	153,710
Bottom impact limiter			17,231
Top impact limiter			19,187
MPC Weights[†††]	**Fuel Basket**	**Basket + Shell Without SNF**	**Fully Loaded with SNF and Fuel Spacers**
MPC-68	16,240	37,591	87,171
MPC-24	20,842	40,868	82,494
MPC-32	12,340	34,507	89,765
MPC-24E/EF	23,535	43,561	85,188
Trojan MPC-24E/EF[††††]	21,284	40,643	80,963
Overpack with loaded MPC-68/68F			240,881
Overpack with loaded MPC-24			236,204
Overpack with loaded MPC-32			243,745
Overpack with loaded MPC-24E/EF			238,898
Overpack with loaded MPC-24E/EF (Trojan)			235,283
Overpack with minimum weight MPC without SNF		187,500	
Total weight of transport package With MPC-68/68F With MPC-24 With MPC-32 With MPC-24E/EF With Trojan MPC-24E/EF	 277,299 272,622 279,893 275,316 271,701		

† All calculated weights are rounded up to the nearest whole number.

†† Including overpack closure plate.

††† MPC vessel (shell, baseplate, and lid)weights include a 4% upward adjustment; fuel weight is design basis, including all non-fuel components and DFC (i.e., 1680 lbs for PWR and 700 lbs for BWR).

†††† MPC vessel weight used is for MPC-24, which bounds shell weight for Trojan MPC-24E/EF due to height difference. Trojan MPC weight includes MPC spacer.

Table 2.2.2

CENTERS OF GRAVITY OF HI-STAR 100 CONFIGURATIONS

Component	Height of CG Above Datum, inches
Overpack empty	99.7
MPC-68 empty	111.5
MPC-24 empty	109.0
MPC-32 empty	113.2
MPC-24E/EF empty	107.8
Trojan MPC-24E/EF	104.2
MPC-68 with fuel in overpack	102.5
MPC-24 with fuel in overpack	102.3
MPC-32 with fuel in overpack	102.1
MPC-24E/EF with fuel in overpack	102.2
Trojan MPC-24E/EF with fuel in overpack	101.0

Note: The datum used for calculations involving the overpack is the bottom of the overpack bottom plate. The datum used for calculations involving the MPC only is the bottom of MPC baseplate (Figure 2.2.1). The location of the loaded Trojan centroid includes top spacer ring above MPC top lid.

Table 2.2.3

CALCULATED MAXIMUM LIFT WEIGHT ON CRANE HOOK ABOVE POOL

Item	Weight (lb)
Total weight of overpack	153,710
Total weight of MPC(upper bound) + fuel	89,765[†]
Overpack closure plate	-7,984
Water in MPC and overpack	16,384
Lift yoke	3,600
Inflatable annulus seal	50
TOTAL	255,525[††]

[†] Includes MPC closure rings.

[††] Trunnions are rated to lift 250,000 lbs. For weight exceeding 250,000 lbs, weight can be reduced by partial draining of the MPC. See Chapter 7 for operational controls.

Table 2.2.4

COMPONENT WEIGHTS AND DIMENSIONS FOR ANALYTIC CALCULATIONS*

Component	Weight (lbs)
MPC baseplate	3,000
MPC closure lid	10,400
MPC shell	5,900
MPC miscellaneous parts	3,700
Fuel basket	24,000/16,400 (PWR/BWR)
Fuel	54,000
Total MPC	90,000
Overpack baseplate	10,000
Overpack closure plate	8,000
Overpack shell	137,000
Total overpack	158,000
Total HI-STAR 100 lift weight	250,000
Impact limiters	37,000
HI-STAR with limiters	282,000
Item	**Dimension (inch)**
Overpack Outer Diameter	96
Overpack Length	203.125
MPC Outer Diameter	68.375
MPC Length	190.5
Overpack Inner Diameter	68.75

Note: Analytical calculations may use weights and dimensions in Table 2.2.4 or actual weights and dimensions for conservatism in calculation of safety factors. Finite element analyses may use weights calculated based on input weight densities.

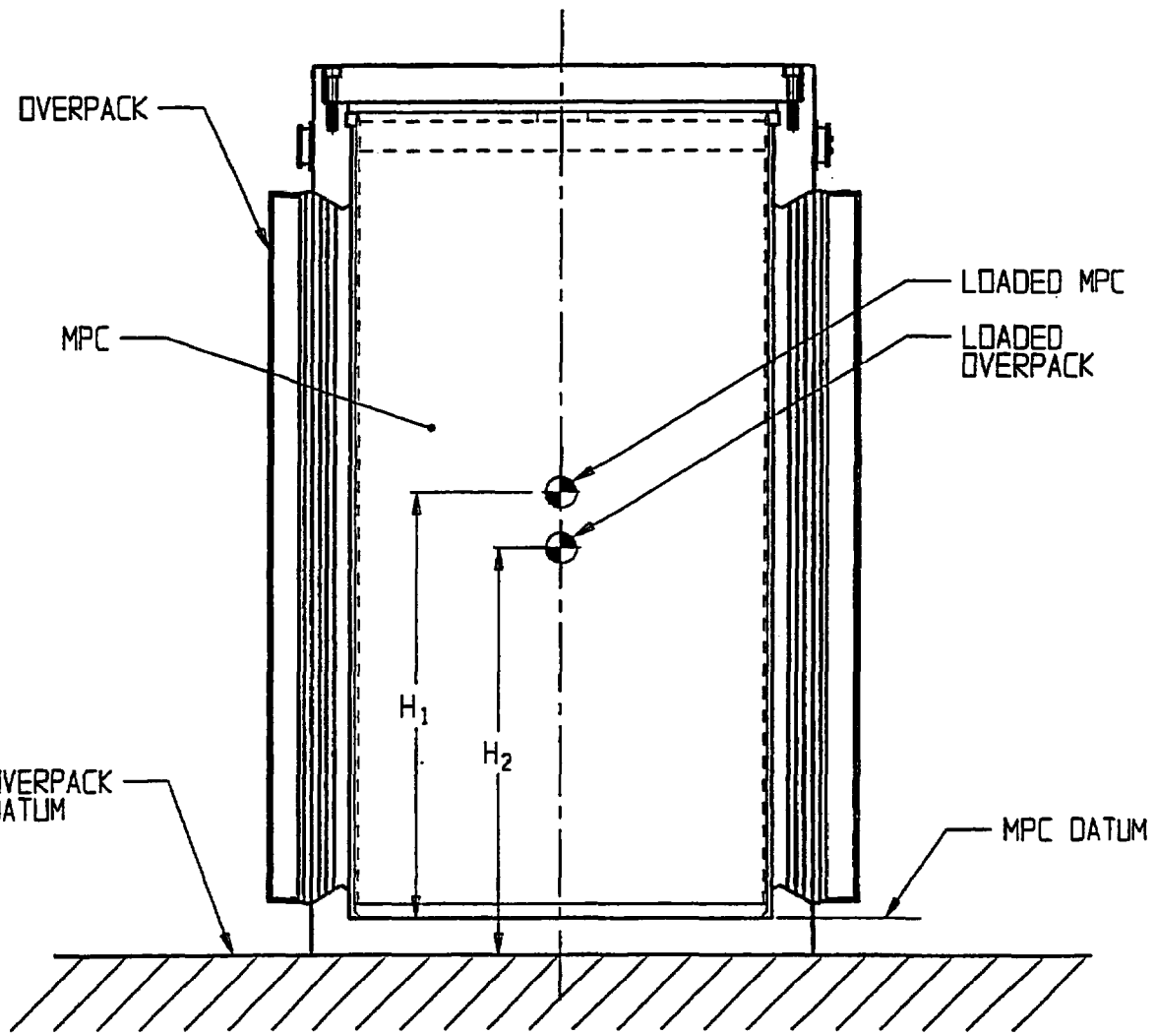

FIGURE 2.2.1; HI-STAR 100 DATUM DEFINITION FOR TABLE 2.2.2

2.3 MECHANICAL PROPERTIES OF MATERIALS

This section provides the mechanical properties used in the structural evaluation. The properties include yield stress, ultimate stress, modulus of elasticity, Poisson's ratio, weight density, and coefficient of thermal expansion. The property values are presented for a range of temperatures for which structural calculations are performed.

The materials selected for use in the HI-STAR 100 MPC and overpack are presented in the Bills-of-Materials in Chapter 1, Section 1.4. In this chapter, the materials are divided into two categories, structural and nonstructural. Structural materials are those that serve a load bearing function. Materials that do not support mechanical loads are considered nonstructural. For example, the overpack inner shell is a structural material, while Holtite-A (neutron shield) is a nonstructural material.

2.3.1 Structural Materials

2.3.1.1 Alloy X

A hypothetical material termed Alloy X is defined for all MPC structural components. The material properties of Alloy X are the least favorable values from the set of candidate stainless alloys. The purpose of a "least favorable" material definition is to ensure that all structural analyses are conservative, regardless of the actual MPC material. For example, when evaluating the stresses in the MPC, it is conservative to work with the minimum values for yield strength and ultimate strength. This guarantees that the material used for fabrication of the MPC is of equal or greater strength than the hypothetical material used in the analysis. In the structural evaluation, the only property for which it is not always conservative to use the minimum values is the coefficient of thermal expansion. Two sets of values for the coefficient of thermal expansion are specified, a minimum set and a maximum set. For each analysis, the set of coefficients, minimum or maximum that causes the more severe load on the cask system is used. Table 2.3.1 lists the numerical values for the material properties of Alloy X versus temperature. These values, taken from the ASME Code, Section II, Part D [2.1.11], are used to complete all structural analyses. The maximum temperatures in MPC components may exceed the allowable limits of temperature during short time duration events. However, under no scenario does the maximum temperature of Alloy X material used in the helium confinement boundary exceed 1000°F. As shown in ASME Code Case N-47-33 (Class 1 Components in Elevated Temperature Service, 1995 Code Cases, Nuclear Components), the strength properties of austenitic stainless steels do not change due to exposure to 1000 °F temperature for up to 10,000 hours. Therefore, there is no significant effect on mechanical properties of the helium confinement boundary or fuel basket material during the short time duration loading. Further description of Alloy X, including the materials from which it is derived, is provided in Appendix 1.A.

Two properties of Alloy X which are not included in Table 2.3.1 are weight density and Poisson's ratio. These properties are assumed constant for all structural analyses, regardless of the temperature. The values used are shown in the table below.

PROPERTY	VALUE
Weight Density (lb./in^3)	0.290
Poisson's Ratio	0.30

2.3.1.2 Carbon Steel, Low-Alloy, and Nickel Alloy Steel

The carbon steels used in the HI-STAR 100 System are SA516 Grade 70, SA515 Grade 70. These steels are not constituents of Alloy X. The material properties of SA516 Grade 70 and SA515 Grade 70 are shown in Tables 2.3.2 and 2.3.3, respectively. The nickel alloy and low-alloy steels are SA203-E and SA350-LF3, respectively. The material properties of SA203-E and SA350-LF3 are given in Table 2.3.4.

Two properties of these steels which are not included in Tables 2.3.2 through 2.3.4 are weight density and Poisson's ratio. These properties are assumed constant for all structural analyses. The values used are shown in the table below.

PROPERTY	VALUE
Weight Density (lb./in^3)	0.283
Poisson's Ratio	0.30

2.3.1.3 Bolting Materials

Material properties of the bolting materials used in the HI-STAR System are given in Table 2.3.5.

2.3.1.4 Weld Material

All weld filler materials utilized in the welding of the Code components will comply with the provisions of the appropriate ASME subsection (e.g., Subsection NB for the overpack and enclosure vessel) and Section IX. All non-Code welds shall also be made using weld procedures that meet Section IX of the ASME Code. All non-code welds shall also be made using weld procedures that meet Section IX of the ASME Code. The minimum tensile strength of the weld wire and filler material (where applicable) will be equal to or greater than the tensile strength of the base metal listed in the ASME Code.

2.3.1.5 Impact Limiter

The Impact Limiter for the HI-STAR 100 System has been named AL-STAR™. AL-STAR is composed of cross core and uni-directional aluminum honeycomb made by layering corrugated sheets of aluminum (Alloy 5052). For the cross core material, alternate layers of corrugated aluminum sheets are laid in orthogonal direction to each other (Figure 2.3.1). The layers are bonded together by a high-temperature epoxy. The Holtec drawing in Section 1.4 illustrates the

arrangement of the cross core and uni-directional honeycomb sectors in AL-STAR to realize adequate crush moduli in all potential impact modes. The external surface of AL-STAR consists of a stainless steel skin to provide long-term protection against weather and environmental conditions.

Rail transport considerations limit the maximum diameter of the impact limiter to 128 inches. The axial dimension of AL-STAR is limited by the considerations of maximum permissible packaging weight for rail transport. Within the limitations of space and weight, AL-STAR must possess sufficient energy absorption capacity so as to meet the design basis rigid body deceleration limits (Table 2.1.10) under all postulated drop orientations. The sizing of the AL-STAR internal structure is principally guided by the above considerations. For example, in order to ensure that a sufficient portion of the honeycomb structure participates in lateral impacts, a thick carbon steel shell buttressed with gussets provides a hard backing surface for the aluminum honeycomb to crush against.

Two properties of the cross core honeycomb germane to its function are the crush strength and the nominal density. The crush strength of AL-STAR is the more important of the two properties; the density is significant in establishing the total weight of the package. The crush strength increases monotonically with density. For example, the cross core honeycomb of 2500 psi crush strength has a nominal density of 27 lb. per cubic foot. At 2,000 psi crush strength, the change in aluminum honeycomb parameters lowers the density to approximately 22 lb. per cubic foot. The crush strength of the honeycomb can be varied within a rather wide range by adjusting the aluminum foil thickness and corrugation size. Drawings in Section 1.4 show the required crush strengths of the honeycomb sectors in the various regions of AL-STAR.

Like all manufactured materials, the crush strength and density of the honeycomb material are subject to slight variation within a manufactured lot. The crush strength will be held to a tolerance of approximately 15% (a nominal crush strength ± 7.5%).

Hexcel Corporation's publication TSB 120, "Mechanical Properties of Hexcel Honeycomb Materials", [2.3.1] provides detailed information on the mechanical characteristics of aluminum honeycomb materials. Hexcel's experimental data shows that the load-deflection curve of aluminum honeycomb simulates the shape of elastic-perfectly plastic materials. The honeycomb crushes at a nearly uniform load (slowly applied) until solidity in the range of 30 to 40% is reached. It is the crushing at constant load characteristic of aluminum honeycomb along with its excellent crush strength-to-weight ratio that makes it an ideal energy absorption material. The cross layered honeycomb (cross-core) has an identical crush strength in two orthogonal directions. In other words, from a load-deflection standpoint, the cross-layered honeycomb is a transversely isotropic material.

A typical honeycomb pressure-strain curve is illustrated in Figure 2.A.2.1 in Appendix 2.A wherein additional discussion on the crush properties of the honeycomb material is provided.

However, three key properties of the honeycomb material which are central to its function as a near-ideal impact limiter crush material are summarized below.

i. The honeycomb material can be used in the "un-crushed" or "pre-crushed" condition. The difference is in the initial "bump" in the pressure-strain curve shown in Figure 2.A.2.1. By pre-crushing the honeycomb, its pressure-strain relationship simulates that of an ideal elastic-perfectly-plastic material, which is most desirable in limiting abrupt peaks in the deceleration of the package under drop events.

ii. Irrespective of the crush strength, under quasi-static loading, all honeycomb materials begin to strain harden at about 60% strain and lock up at about 70%. Thus, a 10-inch thick honeycomb column will crush down to a thickness of 4 inches at near constant force; crushing further will require progressively greater compression force. The six inches of available crush distance is referred to as the available "stroke" in the lexicon of impact limiter design technology.

iii. Because the crush material is made entirely out of one of the most cryogenically competent industrial metals available, aluminum, the pressure-crush behavior of the AL-STAR honeycomb material is insensitive to the environmental temperature range germane to Part 71 transport (-20 degrees F to 100 degrees F). Table Y-1 of the ASME Code [2.1.11] lists the yield strength of the material (Alloy 5052) to be constant in the range -20 degrees F to 350 degrees F.

Independent confirmation of the invariance of the ALSTAR's crush properties with temperature in the range of temperatures applicable to the HI-STAR 100 packaging was provided by experiments conducted by Holtec International in June 1998 [2.3.2] using sample material obtained from Hexcell. The test objective was to evaluate the temperature sensitivity, if any, of the static compression strength of the honeycomb material. To that end, test specimens were cut from the sample material and were subject to static compression testing using a Q.A. validated procedure.

A series of specimens of two different strengths were tested at three different temperatures. The specimens were tested at -29 degrees C, 23 degrees C and 80 degrees C which represent "Cold", "Ambient", and "Heat" environmental conditions. Ten specimens were prepared for each crush strength, to allow for multiple data points at each test temperature. The specimens were not pre-crushed so the static compression-crush curves exhibited an initial peak. After discounting the initial peaks in the static force-crush curve, the constant force range for each specimen could be identified from the test data and a crush pressure for the specimen defined by dividing this constant force by the measured specimen loaded area.

The computed crush pressures showed no significant trending that could be ascribed to environmental effects. Figure 2.3.2 is a plot of the test results and plots the average of the calculated test crush pressures from the series of specimens at each of the three temperatures. The results for individual test samples at any given temperature were within manufacturing tolerance. It is clear from the plotted results that the effect of temperature is well within the data scatter due to manufacturing tolerance. Therefore, within the temperature range germane to the ALSTAR impact limiter, the force-crush characteristic is expected to be essentially unaffected by the coincident honeycomb metal temperature. This leads to the conclusion that environmental temperature effects will not influence impact limiter performance predictions.

Appendix 2.A contains further information on the AL-STAR honeycomb and its performance characteristics. The sensitivity of the package performance to variations in compression strength of the aluminum honeycomb is evaluated in Appendix 2.A.

In summary, the AL-STAR impact limiter is composed of a carbon steel inner shell structure, an assemblage of cross core and uni-directional aluminum honeycombs and a stainless steel external sheathing.

None of the structural materials has a low melting point or is flammable. A Holtite-A layer is situated deep in the honeycomb in such a manner that it does not participate in the crushing process, but provides neutron shielding in the axial direction.

2.3.2 Nonstructural Materials

2.3.2.1 Neutron Shield

The neutron shield in the overpack is not considered as a structural member of the HI-STAR 100 System. Its load carrying capacity is neglected in all structural analyses except where such omission would be nonconservative. The only material property of the neutron shield which is important to the structural evaluation is weight density (1.63 g/cm^2).

2.3.2.2 Boral™ Neutron Absorber

Boral is not a structural member of the HI-STAR 100 System. Its load carrying capacity is neglected in all structural analyses. The only material property of Boral which is important to the structural evaluation is weight density. As the MPC fuel baskets can be constructed with Boral panels of variable areal density, the weight that produces the most severe cask load is assumed in each analysis. (Density 2.644 g/cm^3).

2.3.2.3 Aluminum Heat Conduction Elements

The aluminum heat conduction elements are located between the fuel basket and MPC vessel in several of the early vintage MPC-68s and MPC-68Fs. They have since been removed from the MPC design and none were installed in the PWR MPCs. They are thin, flexible elements whose sole function is to transmit heat from the basket. They are not credited with any structural load capacity and are shaped to provide negligible resistance to basket thermal expansion. The total weight of the aluminum heat conduction elements is less than 1,000 lb. per MPC.

Table 2.3.1

ALLOY X MATERIAL PROPERTIES

Temp. (°F)	Alloy X				
	S_y	S_u[†]	α_{min}	α_{max}	E
-40	30.0	75.0 (70.0)	8.54	8.55	28.82
100	30.0	75.0 (70.0)	8.54	8.55	28.14
150	27.5	73.0 (68.1)	8.64	8.67	27.87
200	25.0	71.0 (66.2)	8.76	8.79	27.6
250	23.75	68.5 (63.85)	8.88	8.9	27.3
300	22.5	66.0 (61.5)	8.97	9.0	27.0
350	21.6	65.2 (60.75)	9.10	9.11	26.75
400	20.7	64.4 (60.0)	9.19	9.21	26.5
450	20.05	64.0 (59.65)	9.28	9.32	26.15
500	19.4	63.5 (59.3)	9.37	9.42	25.8
550	18.8	63.3 (59.1)	9.45	9.50	25.55
600	18.2	63.1 (58.9)	9.53	9.6	25.3
650	17.8	62.8 (58.6)	9.61	9.69	25.05
700	17.3	62.5 (58.4)	9.69	9.76	24.8
750	16.9	62.2 (58.1)	9.76	9.81	24.45
800	16.6	61.7 (57.6)	9.82	9.90	24.1

Definitions:

S_y = Yield Stress (ksi)

α = Mean Coefficient of thermal expansion (in./in. per degree F x 10^{-6})

S_u = Ultimate Stress (ksi)

E = Young's Modulus (psi x 10^6)

Notes:

1. Source for S_y values is Table Y-1 of [2.1.11].
2. Source for S_u values is Table U of [2.1.11].
3. Source for α_{min} and α_{max} values is Table TE-1 of [2.1.11].
4. Source for E values is material group G in Table TM-1 of [2.1.11].

[†] The ultimate stress of Alloy X is dependent on the product form of the material (i.e., forgings vs. plate). Values in parentheses are based on SA-336 forging materials (Type F304, F304LN, F316, and F316LN), which are used solely for the one-piece construction MPC lids. All other values correspond to SA-240 plate material.

Table 2.3.2

SA516, GRADE 70 MATERIAL PROPERTIES

Temp. (°F)	SA516, Grade 70			
	S_y	S_u	α	E
-40	38.0	70.0	5.53	29.34
100	38.0	70.0	5.53	29.34
150	36.3	70.0	5.71	29.1
200	34.6	70.0	5.89	28.8
250	34.15	70.0	6.09	28.6
300	33.7	70.0	6.26	28.3
350	33.15	70.0	6.43	28.0
400	32.6	70.0	6.61	27.7
450	31.65	70.0	6.77	27.5
500	30.7	70.0	6.91	27.3
550	29.4	70.0	7.06	27.0
600	28.1	70.0	7.17	26.7
650	27.6	70.0	7.30	26.1
700	27.4	70.0	7.41	25.5
750	26.5	69.3	7.50	24.85

Definitions:

S_y = Yield Stress (ksi)
α = Mean Coefficient of thermal expansion (in./in. per degree F x 10^{-6})
S_u = Ultimate Stress (ksi)
E = Young's Modulus (psi x 10^6)

Notes:

1. Source for S_y values is Table Y-1 of [2.1.11].
2. Source for S_u values is Table U of [2.1.11].
3. Source for α values is material group C in Table TE-1 of [2.1.11].
4. Source for E values is "Carbon steels with C ≤ 0.30%" in Table TM-1 of [2.1.11].

Table 2.3.3

SA515, GRADE 70 MATERIAL PROPERTIES

Temp. (°F)	SA515, Grade 70			
	S_y	S_u	α	E
-40	38.0	70.0	5.53	29.34
100	38.0	70.0	5.53	29.34
150	36.3	70.0	5.71	29.1
200	34.6	70.0	5.89	28.8
250	34.15	70.0	6.09	28.6
300	33.7	70.0	6.26	28.3
350	33.15	70.0	6.43	28.0
400	32.6	70.0	6.61	27.7
450	31.65	70.0	6.77	27.5
500	30.7	70.0	6.91	27.3
550	29.4	70.0	7.06	27.0
600	28.1	70.0	7.17	26.7
650	27.6	70.0	7.30	26.1
700	27.4	70.0	7.41	25.5
750	26.5	69.3	7.50	24.85

Definitions:

S_y = Yield Stress (ksi)

α = Mean Coefficient of thermal expansion (in./in. per degree F x 10^{-6})

S_u = Ultimate Stress (ksi)

E = Young's Modulus (psi x 10^6)

Notes:

1. Source for S_y values is Table Y-1 of [2.1.11].
2. Source for S_u values is Table U of [2.1.11].
3. Source for α values is material group C in Table TE-1 of [2.1.11].
4. Source for E values is "Carbon steels with C $\leq$ 0.30%" in Table TM-1 of [2.1.11].

Table 2.3.4

SA350-LF3 AND SA203-E MATERIAL PROPERTIES

Temp. (°F)	SA350-LF3			SA350-LF3/SA203-E		SA203-E		
	S_m	S_y	S_u	E	α	S_m	S_y	S_u
-100	23.3	37.5	70.0	28.5	6.20	23.3	40.0	70.0
100	23.3	37.5	70.0	27.6	6.27	23.3	40.0	70.0
200	22.8	34.2	68.5	27.1	6.54	23.3	36.5	70.0
300	22.2	33.2	66.7	26.7	6.78	23.3	35.4	70.0
400	21.5	32.2	64.6	26.1	6.98	22.9	34.3	68.8
500	20.2	30.3	60.7	25.7	7.16	21.6	32.4	64.9
600	18.5	-	-	-	-	-	-	-
700	16.8	-	-	-	-	-	-	-

Definitions:

S_m = Design Stress Intensity (ksi)
S_y = Yield Stress (ksi)
S_u = Ultimate Stress (ksi)
α = Coefficient of Thermal Expansion (in./in. per degree F x 10^{-6})
E = Young's Modulus (psi x 10^6)

Notes:

1. Source for S_m values is Table 2A of [2.1.11].
2. Source for S_y values is Table Y-1 of [2.1.11].
3. Source for S_u values is ratioing S_m values.
4. Source for α values is material group E in Table TE-1 of [2.1.11].
5. Source for E values is material group B in Table TM-1 of [2.1.11].

Table 2.3.5

SB637-N07718, SA564-630, AND SA705-630 MATERIAL PROPERTIES

Temp. (°F)	SB637-N07718				
	S_y	S_u	E	α	S_m
-100	150.0	185.0	29.9	—	50.0
-20	150.0	185.0	—	—	50.0
70	150.0	185.0	29.0	7.05	50.0
100	150.0	185.0	—	7.08	50.0
200	144.0	177.6	28.3	7.22	48.0
300	140.7	173.5	27.8	7.33	46.9
400	138.3	170.6	27.6	7.45	46.1
500	136.8	168.7	27.1	7.57	45.6
600	135.3	166.9	26.8	7.67	45.1
SA705-630/SA564-630 (Age Hardened at 1075°F)					
Temp. (°F)	S_y	S_u	E	α	-
200	115.6	145.0	28.5	5.9	-
300	110.7	145.0	27.9	5.9	-
400	106.7	141	-	-	-
500	103.5	140	-	-	-
SA705-630/SA564-630 (Age Hardened at 1150°F)					
200	97.1	135.0	28.5	5.9	-
300	93.0	135.0	27.9	5.9	-
400	89.8	131.4	-	-	-
500	87	128.5	-	-	-

Definitions:

S_m = Design Stress Intensity (ksi)
S_y = Yield Stress (ksi)
α = Mean Coefficient of thermal expansion (in./in. per degree F x 10^{-6})
S_u = Ultimate Stress (ksi)
E = Young's Modulus (psi x 10^6)

Notes:

1. Source for S_m values is Table 4 of [2.1.11].
2. Source for S_y, S_u values is ratioing design stress intensity values.
3. Source for α values is Tables TE-1 and TE-4 of [2.1.11], as applicable.
4. Source for E values is Table TM-1 of [2.1.11].

Table 2.3.6

YIELD STRENGTH OF SA-193-B8S IMPACT LIMITER ATTACHMENT BOLTS

Yield Stress for Attachment Bolt Calculations[†]	
Item	Yield Stress (psi)
Yield Stress	50,000

† Source for stress is Table 3 of [2.1.11].

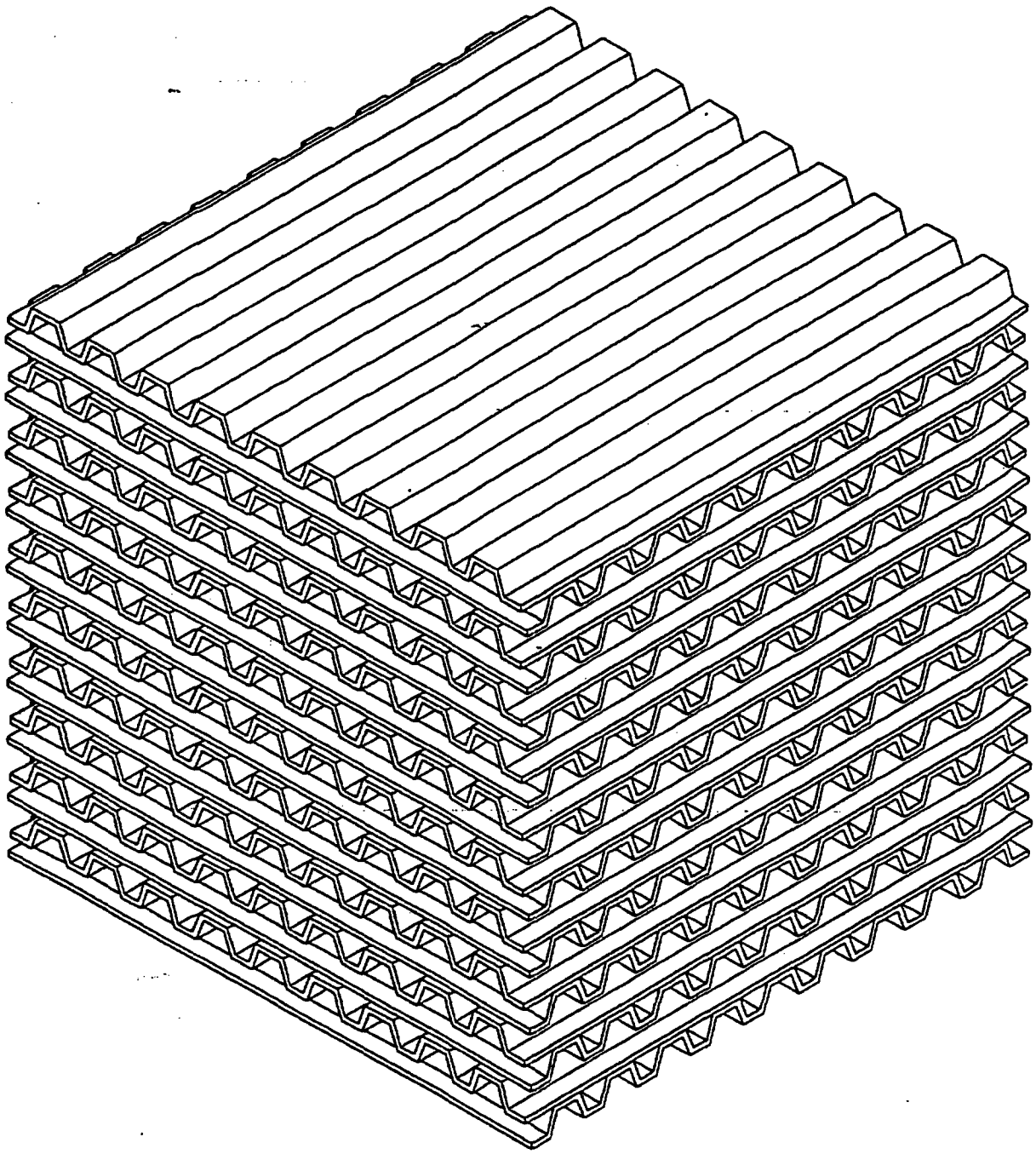

FIGURE 2.3.1; CROSS LAYERED ALUMINUM HONEYCOMB

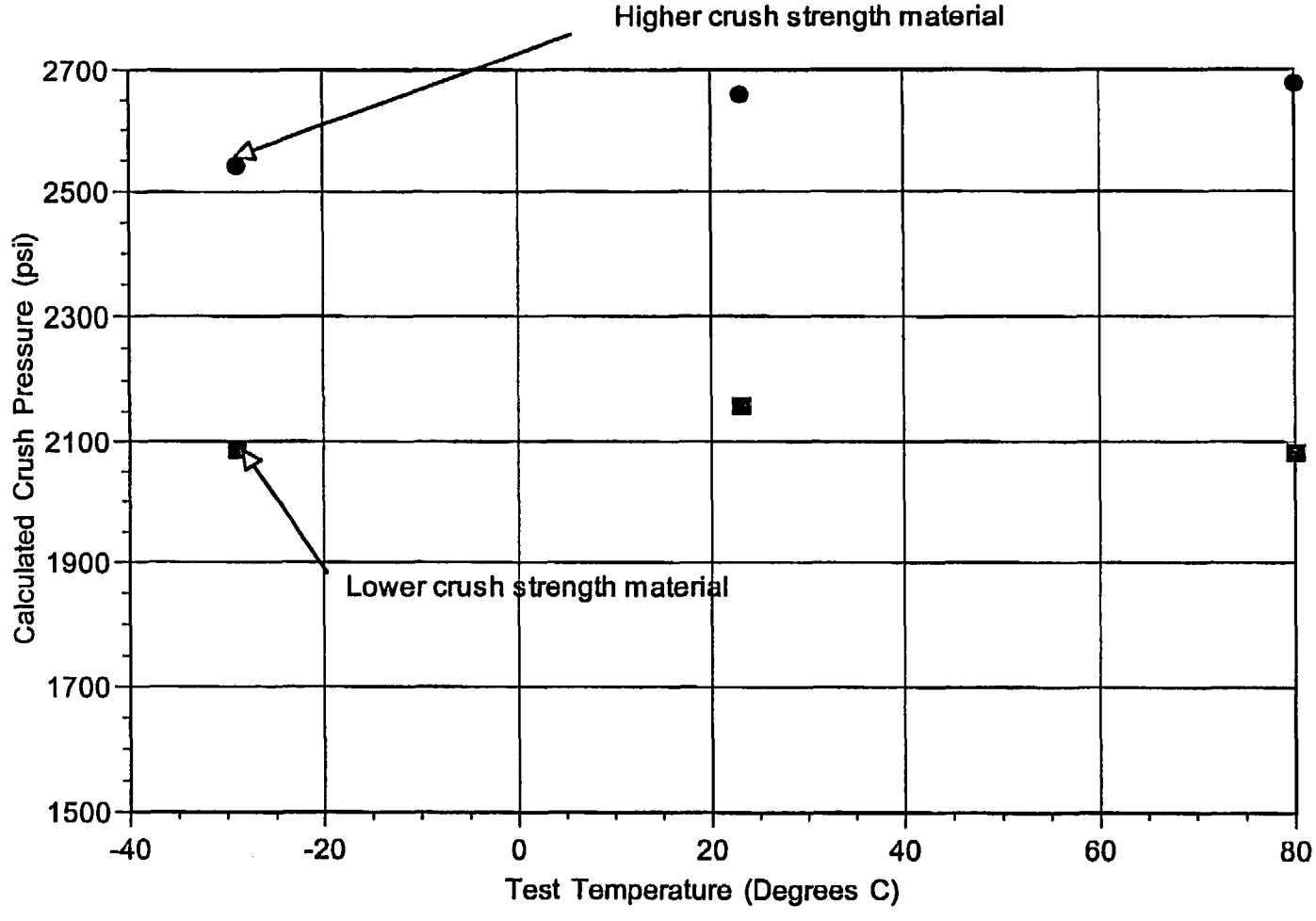

FIGURE 2.3.2 Average Crush Strength of Tested Specimens vs Test Temperature

2.4 GENERAL STANDARDS FOR ALL PACKAGES

The compliance of the HI-STAR 100 System to the general standards for all packaging, specified in 10CFR71.43, is demonstrated in the following paragraphs.

2.4.1 Minimum Package Size

The HI-STAR 100 package meets the requirements of 10CFR71.43(a); the outer diameter of the overpack is approximately 96" and its length is approximately 203".

2.4.2 Tamperproof Feature

During transport operations, a wire tamper seal with a stamped identifier will be attached between the lower base of the upper impact limiter shell and the head of one of the impact limiter attachment bolts for the purpose of indicating possible tampering. In order to access the radioactive contents of the overpack, the upper impact limiter is required to be removed to access the closure plate bolting. This tamper seal satisfies the requirements of 10CFR71.43(b). A second wire tamper seal will be attached between the lower impact limiter and an attachment bolt head to indicate tampering. This seal will prevent access to the drain port. The assembly drawing in Section 1.4 depicts the security seals.

2.4.3 Positive Closure

There are no quick-connect/disconnect valves in the containment boundary of the HI-STAR 100 packaging. The only access to the overpack internals is through the closure plate on the overpack, which weighs over 7000 pounds, and the overpack vent and drain ports which are sealed and protected by bolted cover plates. This closure plate is fastened to the overpack flange with heavy bolts, which are torqued to closure values in Table 7.1.2. Opening of the overpack vent and drain port would require removal of the bolted cover plate and unthreading of the port plug. Inadvertent opening of the overpack is not feasible; opening an overpack requires mobilization of special tools and a source of power. The overpack containment boundary is analyzed for normal and accident condition internal pressure and demonstrates integrity under both conditions.

2.4.4 Chemical and Galvanic Reactions

There is no credible mechanism for significant chemical or galvanic reactions in the HI-STAR 100 System during loading operations.

The MPC, which is filled with helium, provides a nonaqueous and inert environment. Insofar as corrosion is a long-term time-dependent phenomenon, the inert gas environment in the MPC precludes the incidence of corrosion during transport. Furthermore, the only dissimilar material groups in the MPC are: (1) Boral™ and stainless steel and (2) aluminum and stainless steel. Boral and stainless steel have been used in close proximity in wet storage for over 30 years.

Many spent fuel pools at nuclear plants contain fuel racks, which are fabricated from Boral and stainless steel materials, with geometries similar to the HI-STAR 100 MPC. Not one case of chemical or galvanic degradation has been found in fuel racks built by Holtec. This experience provides a sound basis to conclude that corrosion will not occur in these materials. Additionally, the aluminum heat conduction elements and stainless steel basket are very close on the galvanic series chart. Aluminum, like other metals of its genre (e.g., titanium and magnesium) rapidly passivates in an aqueous environment, leading to a thin ceramic (Al2O3) barrier, which renders the material essentially inert and corrosion-free over long periods of application. The physical properties of the material, e.g., thermal expansion coefficient, diffusivity, and thermal conductivity, are essentially unaltered by the exposure of the aluminum metal stock to an aqueous environment.

The aluminum in the optional heat conduction elements will quickly passivate in air and in water to form a protective oxide layer that prevents any significant hydrogen production during MPC cask loading and unloading operations. The aluminum in the Boral, particularly in the core area, will also react with water to generate hydrogen gas. The exact rate of generation and total amount of hydrogen generated is a function of a number of variables (see Section 1.2.1.4.1) and cannot be predicted with any certainty. Therefore, to preclude the potential for hydrogen ignition during lid welding or cutting, the operating procedures in Chapter 7 require monitoring for combustible gas and either exhausting or purging the space beneath the MPC lid with an inert gas during these activities. Once the MPC cavity is drained, dried, and backfilled with helium, the source of hydrogen gas (the aluminum-water reaction) is eliminated.

The HI-STAR 100 overpack combines low-alloy and nickel alloy steels, carbon steels, neutron and gamma shielding, thermal expansion foam, and bolting materials. All of these materials have a long history of nongalvanic behavior within close proximity of each other. The internal and external carbon steel surfaces of the overpack and closure plates are sandblasted and coated to preclude surface oxidation. The coating does not chemically react with borated water. Therefore, chemical or galvanic reactions involving the overpack materials are highly unlikely and are not expected.

The interfacing seating surfaces of the closure plate metallic seals are clad with stainless steel to assure long-term sealing performance and to eliminate the potential for localized corrosion of the seal seating surfaces.

In accordance with NRC Bulletin 96-04, a review of the potential for chemical, galvanic, or other reactions among the materials of the HI-STAR 100 System, its contents and the operating environment, which may produce adverse reactions, has been performed. Table 2.4.1 provides a listing of the materials of fabrication for the HI-STAR 100 System and evaluates the performance of the material in the expected operating environments during short-term loading/unloading operations and transport operations. As a result of this review, no operations were identified which could produce adverse reactions beyond those conditions already analyzed in this SAR.

The HI-STAR 100 System is composed of materials with a long proven history of use in the nuclear industry. The materials are not affected by the radiation levels caused by the spent nuclear fuel. Gamma radiation damage to metals (e.g., aluminum, stainless steel, and carbon steel) does not occur until the dose reaches 1018 rads or more. The gamma dose from the spent nuclear fuel transported in the HI-STAR 100 System is on the order of 1010 rads. Moreover, significant radiation damage due to neutron exposure does not occur for neutron fluences below approximately 1019 n/cm^2 [2.4.1, 2.4.2], which is far greater than the neutron fluence for which components of the HI-STAR 100 System will be exposed.

Table 2.4.1

HI-STAR 100 SYSTEM MATERIAL COMPATIBILITY
WITH OPERATING ENVIRONMENTS

Material/Component	Fuel Pool (Borated and Unborated Water)[1]	Transport (Open to Environment)
Alloy X: -MPC Fuel Basket -MPC Baseplate -MPC Shell -MPC Lid -MPC Fuel Spacers	Stainless steels have been extensively used in spent fuel storage pools with both borated and unborated water with no adverse reactions or interactions with spent fuel.	The MPC internal and external environment will be inert (helium) atmosphere. No adverse interactions identified.
Aluminum -Conduction Inserts	Aluminum and stainless steels form a galvanic couple. However, they are very close on the galvanic series chart and aluminum rapidly passivates in an aqueous environment forming a thin ceramic (Al2O3) barrier. The aluminum will be installed in a passivated condition Therefore, during the short time they are exposed to fuel pool water, corrosion is not expected.	In a non-aqueous atmosphere galvanic corrosion is not expected.
Boral: -Neutron Absorber	Extensive in-pool experience on spent fuel racks with no adverse reactions. See Chapter 7 for additional requirements for combustible gas monitoring and required actions for control of combustible gas accumulation under the MPC lid.	The Boral will be in a helium environment. No adverse reactions identified.

[1] HI-STAR 100 System short-term operating environment during loading and unloading.

Table 2.4.1 (continued)

HI-STAR 100 SYSTEM MATERIAL COMPATIBILITY
WITH OPERATING ENVIRONMENTS

Material/Component	Fuel Pool (Borated and Unborated Water)[2]	Transport (Open to Environment)
Steels: -SA350-LF3 -SA203-E -SA515 Grade 70 -SA516 Grade 70 -SA750 630 17-4 PH -SA564 630 17-4 PH -SA106 -SA193-B7 Overpack Body	All exposed steel surfaces (except seal areas, pocket trunnions, and bolt locations) will be coated with paint specifically selected for performance in the operating environments. Even without coating, no adverse reactions (other than nominal corrosion) have been identified.	Internal surfaces of the overpack will be painted and maintained in an inert atmosphere. Exposed external surfaces (except those listed in fuel pool column) will be painted and will be maintained with a fully painted surface. No adverse reactions identified.
Stainless Steels: -SA240 304 -SA193 Grade B8 -18-8 S/S Miscellaneous Components	Stainless steels have been extensively used in spent fuel storage pools with both borated and unborated water with no adverse reactions.	Stainless steel has a long proven history of corrosion resistance when exposed to the atmosphere. These materials are used for bolts and threaded inserts. No adverse reactions with steel have been identified. No impact on performance.

[2] HI-STAR 100 System short-term operating environment during loading and unloading.

Table 2.4.1 (continued)

HI-STAR 100 SYSTEM MATERIAL COMPATIBILITY
WITH OPERATING ENVIRONMENTS

Material/Component	Fuel Pool (Borated and Unborated Water)[3]	Transport (Open to Environment)
Nickel Alloy: -SB637-NO7718 Bolting	Bolts are not used in pool.	Exposed to weathering effects. No adverse reactions with overpack closure plate. No impact on performance.
Brass: -Rupture Disk	Small surface of rupture disk will be exposed. No significant adverse impact identified.	Exposed to external weathering. No loss of function expected. Disks inspected prior to transport.
Holtite-A: -Neutron Shield	The neutron shield is fully enclosed by the outer enclosure. No adverse reaction identified. No adverse reactions with thermal expansion foam or steel.	The neutron shield is fully enclosed in the outer enclosure. No adverse reaction identified. No adverse reactions with thermal expansion foam or steel.
Silicone Foam: -Thermal Expansion Foam	Fully enclosed in the outer enclosure. No adverse reaction identified. No adverse reactions with neutron shield or steel.	Foam is fully enclosed in outer enclosure. No adverse reaction identified. No adverse reactions with neutron shield or steel.

[3] HI-STAR 100 System short-term operating environment during loading and unloading.

Table 2.4.1 (continued)

HI-STAR 100 SYSTEM MATERIAL COMPATIBILITY
WITH OPERATING ENVIRONMENTS

Material/Component	Fuel Pool (Borated and Unborated Water)[4]	Transport (Open to Environment)
Paint: - Carboline 890 - Thermaline 450	Carboline 890 used fir exterior surfaces. Acceptable performance for short-term exposure in mild borated pool water. Thermaline 450 selected for excellent high temperature resistance properties. Will only be exposed to demineralized water during in-pool operations as annulus is filled prior to placement in the spent fuel pool and the inflatable seal prevents fuel pool water in-leakage. No adverse interation identified which could affect MPC/fuel assembly performance.	Good performance on exterior surfaces. Discoloration is not a concern. During transport, internal overpack surfaces will operate in an inert (helium) atmosphere. No adverse reaction identified.
Metallic Seals: - Alloy X750 - 304 S/S	Not installed or exposed during in-pool handling.	Seals enclosed by closure plate or port cover plates. Closure plate seals seat against stainless steel overlay surfaces. No degradation of seal integrity due to corrosion is expected.

[4] HI-STAR 100 System short-term operating environment during loading and unloading.

2.5 LIFTING AND TIE-DOWN STANDARDS

2.5.1 Lifting Devices

As required by Reg. Guide 7.9, in this subsection, analyses for all lifting operations applicable to the transport of a HI-STAR 100 package are presented to demonstrate compliance with the requirements of paragraph 71.45(a) of 10CFR71.

The HI-STAR 100 System has the following types of lifting devices: lifting trunnions located on the overpack top flange and threaded holes for eye bolts to lift the overpack closure plate. Lifting devices associated with movement of the MPC are not considered here; MPC lifting is addressed in a companion HI-STAR100 document (FSAR, Docket 72-1008), and summarized in Subsection 2.5.1.3.

The evaluation of the adequacy of the lifting devices entails careful consideration of the applied loading and associated stress limits. The load combination D+H, where H is the "handling load", is the generic case for all lifting adequacy assessments. The term D denotes the dead load. Quite obviously, D must be taken as the bounding value of the dead load of the component being lifted. Table 2.2.4 gives bounding weights. In all lifting analyses considered in this document, the handling load H is assumed to be equal to 0.15D. In other words, the inertia amplifier during the lifting operation is assumed to be equal to 0.15g. This value is consistent with the guidelines of the Crane Manufacturer's Association of America (CMAA), Specification No. 70, 1988, Section 3.3, which stipulates a dynamic factor equal to 0.15 for slowly executed lifts. Thus, the "apparent dead load" of the component for stress analysis purposes is $D^* = 1.15D$. Unless otherwise stated, all lifting analyses in this section use the "apparent dead load", D^*, in the lifting analysis.

Analysis methodology to evaluate the adequacy of the lifting device may be analytical or numerical. For the analysis of the trunnion, an accepted conservative technique for computing the bending stress is to assume that the lifting force is applied at the tip of the trunnion "cantilever" and that the stress state is fully developed at the base of the cantilever. This conservative technique, recommended in NUREG-1536 for use in a storage FSAR, is applied to the trunnion analyses presented in this SAR.

The lifting trunnions are designed to meet the requirements of 10CFR71.45(a). The lifting attachments that are part of the HI-STAR 100 package also meet the design requirements of NUREG-0612 [2.1.9], which defines specific additional safety margins to ensure safe handling of heavy loads in critical regions of nuclear power plants. Satisfying the more conservative design requirements of NUREG-0612 ensures that the design requirements of 10CFR71.45(a) are met.

In general, the stress analysis to establish safety in lifting, pursuant to NUREG-0612, 10CFR71.45(a), and the ASME Code, requires evaluation of three discrete zones which may be referred to as (i) the trunnion, (ii) the trunnion/component interface, hereinafter referred to as Region A, and (iii) the rest of the component, specifically the stressed metal zone adjacent to Region A, herein referred to as Region B.

Stress limits germane to each of the above three areas are discussed below:

i. Trunnion: NUREG-0612 requires that under the "apparent dead load", D^*, the maximum primary stress in the trunnion be less than 10% of the trunnion material ultimate strength *and* less than 1/6th of the trunnion material yield strength. In other words, the maximum moment and shear force developed in the trunnion cantilever is less than 1/6 of the moment and shear force corresponding to incipient plasticity, and less than 1/10 of the flexural collapse moment or ultimate shear force for the section.

ii. Region A: Trunnion/Component Interface: Stresses in Region A must meet ASME Code Level A limits under applied load D*. Additionally, paragraph 71.45(a) of 10CFR71 requires that the maximum primary stress under $3D^*$ be less than the yield strength of the weaker of the two materials at the trunnion/component interface. In cases involving section bending, the developed section moment must be compared against the plastic moment at yield. Typically, the stresses in the component in the vicinity of the trunnion/component interface are higher than elsewhere. However, exceptional situations exist. For example, when lifting a loaded MPC, the overpack baseplate, which supports the entire weight of the loaded MPC, is a candidate location for high stress even though it is far removed from the lifting location (which is located in the top lid).

iii. Region B: This region constitutes the remainder of the component where the stress limits under the concurrent action of the apparent dead load D* and other mechanical loads that may be present during handling (e.g. internal pressure) are required to meet Level A Service Limits under normal conditions of transport.

In summary, both Region A and Region B are required to meet the stress limits corresponding to ASME Level A under the load D*. Additionally, portions of the component that may experience high stress during the lift are subject to the stress criterion of paragraph 71.45(a) of 10CFR71, which requires satisfaction of yield strength as the limit when the sole applied load is 3D*. In general, all locations of high stress in the component under D^* must also be checked for compliance with ASME Code Level A stress limits.

Unless explicitly stated otherwise, all analyses of lifting operations presented in this report follow the load definition and allowable stress provisions of the foregoing. Consistent with the practice adopted throughout this chapter, results are presented in dimensionless form, as safety factors, defined as SF, where

SF = (Allowable Stress in the Region Considered)/(Computed Maximum Stress in the Region)

It should be emphasized that the safety factor, SF, defined in the foregoing, represents the additional margin that is over and beyond the margin built into NUREG 0612 (e.g. a factor of 10 on ultimate strength or 6 on yield strength).

In the following subsections, each of the lifting analyses performed to demonstrate compliance with regulations is described. Summary results are presented for each of the analyses.

It is recognized from the discussion in the foregoing that stresses in Region A are subject to two distinct criteria, namely Level A stress limits under D* and any other loading that may be present (such as pressure) and yield strength at 3D*. The "3D*" identifier is used whenever the paragraph 71.45(a) load case (the stresses must be bounded by the yield point at 3D*) is the applied loading.

The HI-STAR 100 System has two types of lifting devices that are used during handling and loading operations. Two lifting trunnions are located on the overpack top flange for vertical package handling operations. There are also four lifting eyeholes for handling of the overpack closure plate. Four lifting eyes are installed in the holes for connection to lifting slings.

The two lifting trunnions on the overpack top flange are spaced at 180-degree intervals. Trunnion analysis results are presented in Subsection 2.5.1.1.

The four threaded holes of the overpack closure plate accommodate lifting eyes that are used only for installation or removal of the overpack closure plate.

2.5.1.1 Overpack Trunnion Analysis

The lifting trunnion for the HI-STAR 100 overpack is presented in the Holtec Drawings (Section 1.4). The two lifting trunnions for HI-STAR 100 are circumferentially spaced at 180 degrees. The trunnions are designed for a two-point lift and are sized to satisfy the aforementioned NUREG-0612 criteria. The trunnion material is SB-637-N07718 bolt material, which is the same high strength material used for the closure plate bolts.

Each trunnion is initially threaded into the outer wall of the overpack top flange and is held in place by a locking pad. During a lifting operation, the moment and shear force are resisted by bearing and shearing stresses in the threaded connection.

The embedded trunnion is analyzed as a cantilever beam subjected to a uniformly distributed load applied over a short span of surface at the outer edge of the trunnion. Calculations demonstrate that the stresses in the trunnions, computed in the manner of the foregoing, comply with NUREG-0612 provisions.

Specifically, the following results are obtained:

Safety Factors from HI-STAR 100 Lifting Trunnion Stress Analysis†			
Item	Value (ksi) or (lb) or (lb-in)	Allowable (ksi) or (lb) or (lb-in)	Safety Factor
Bending stress (Comparison with Yield Stress/6)	17.3	24.5	1.41
Shear stress (Comparison with Yield Stress/6)	7.4	14.7	1.99
Bending Moment (Comparison with Ultimate Moment/10)	323,000	574,600	1.78
Shear Force (Comparison with Ultimate Force/10)	144,000	282,000	1.97

† The bounding lifted load is 250,000 lb. (per Table 2.2.4).

We note from the above that all safety factors are greater than 1.0. A factor of safety of exactly 1.0 means that the maximum stress, under apparent lift load D*, is equal to the yield stress in tension or shear divided by 6, or that the section moment or shear force is equal to the ultimate section moment capacity or section force capacity divided by 10.

It is also important to note that safety factors associated with satisfaction of 10CFR71.45(a) are double those reported in the table since 10CFR71.45 only requires a factor of safety of 3 on the yield strength.

2.5.1.2 Stresses in the Overpack Closure Plate, Main Flange, and Baseplate During Lifting

2.5.1.2.1 Analysis of Closure Plate Lifting Holes and Eyes

The closure plate of the HI-STAR 100 overpack is lifted using four wire rope slings. The slings are attached to the closure plate using clevis eyebolts threaded into four holes in the closure plate.

10CFR71.45(a) requires a safety factor of 3 (based on yield strength) for the stress qualification of the clevis eyebolts. Lid lifting will normally be carried out with a lift angle of 90 degrees. However, to be conservative, the analysis assumes a minimum lift angle of 45 degrees.

The eyebolts are sized for a bounding weight of 9,200 lbs. (a value that includes a 15% dynamic amplifier). The working capacity of standard eyebolts is specified with a safety factor of four. Accordingly, its bolt size is selected such that it has a working capacity of approximately 17,000 lb (vertical). This results in a safety factor of greater than 7.0 calculated against the clevis ultimate load capacity. The tapped holes and specified bolts in the closure plate are analyzed and it is demonstrated that adequate thread strength and engagement length exists using allowable stresses in accordance with NUREG-0612 requirements (which are more severe than 10CFR71.45(a) requirements)

Minimum safety factors are summarized in the table below where we note that a safety factor of 1.0 means that the stress is the lessor of yield stress/6 or ultimate stress/10.

Overpack Top Closure B Minimum Safety Factors			
Item	Value (lb.)	Capacity (lb.)	Minimum Safety Factor
Overpack Top Closure Lifting Bolt Shear	9,200	12,080	1.31
Overpack Top Closure Lifting Bolt Tension	9,200	15,390	1.67

2.5.1.2.2 Top Flange

- ASME Service Condition (Region B)

During lifting of a loaded HI-STAR 100, the top flange of the overpack (in which the lift trunnions are located) is identified as a potential location for high stress levels.

The top flange interface with the trunnion under the lifted load D* is analyzed using simplified strength of materials models that focus on the local stress state in the immediate vicinity of the connection that develops to react the applied trunnion load. The bending moment that is transferred from the trunnion to the top forging is reacted by a shear stress distribution on the threads. Figure 2.5.1 shows a schematic of the distribution used to react the applied moment by thread shear. The top flange is considered a NB component subject to the lifted load and internal pressure. The membrane stress intensity due to both components of load is computed at the interface and compared to the allowable local membrane stress intensity. The interface region is also conservatively considered as subject to the provisions of NUREG-0612 and the thread shear stress and bearing stress are compared to 1/6 of the top forging yield stress in shear or compression. The following table summarizes the results:

Top Flange B Minimum Safety Factors (Interface with Trunnion)			
Item	Value (ksi)	Allowable (ksi)	Safety Factor
Bearing Stress (NUREG-0612 Comparison)	3.808	5.975	1.57
Thread Shear Stress (NUREG-0612 Comparison)	3.376	3.585	1.06
Stress Intensity (NB Comparison)	7.857	34.6	4.4

It is noted from the above that all safety factors are greater than 1.0 and that the safety factors for bearing stress and thread shear stress represent the *additional* margin over the factor of safety inherent in the member by virtue of the load multiplier mandated in NUREG-0612.

- Overpack Top Flange and Baseplate Under 3D*

Analyses are performed for the components of the HI-STAR 100 structure that are considered as Region A (namely, the top flange region and baseplate) and evaluated for safety under three times the apparent lifted load (3D*). A one-quarter symmetry finite element model of the top section of the HI-STAR, without the lid has been constructed. The model is assumed constrained at 36" below the top of the top flange. Contact elements are used to model the interface between the trunnion and the top flange and the material behavior is assumed to be elastic-plastic in nature (i.e. a bi-linear stress strain curve is input into the finite element analysis model). The analysis seeks to demonstrate that under 3 times the lifted load, the maximum primary membrane stress across any section in the immediate vicinity of the trunnion is below the material yield strength and the primary membrane plus primary bending stress across any section does not exceed 1.5 times yield. The overpack baseplate is also analyzed using formulas from classical plate theory, conservatively assuming that the allowable strengths are determined at the component design temperature rather than at the lower normal operating conditions.

The results are summarized in the table below:

Overpack Top Flange and Baseplate Minimum Safety Factors (10CFR71.45(a) Loading)			
Item	Value (ksi)	Allowable (ksi)	Safety Factor
Top Flange Membrane Stress Intensity (3D*)	27.44	32.2	1.17
Top Flange Membrane plus Bending Stress Intensity (3D*)	30.0	48.3	1.61
Baseplate Membrane plus Bending Stress Intensity (3D*)	1.452	32.2	22.2

The safety factors are all greater than 1.0 indicating that the requirements of 10CFR71.45(a) are satisfied in the top flange and baseplate of the HI-STAR 100 overpack.

2.5.1.3 MPC Lifting Analyses

The MPC can be inserted or removed from an overpack by lifting bolts that are designed for installation into threaded holes in the top lid. The HI-STAR 100 FSAR (Docket 72-1008) contains analyses of the components of the MPC that are considered as lifting devices. The strength requirements of the bolts and base metal are examined in based on the requirements of NUREG 0612. For a conservative analysis, we impose the requirements of NUREG-0612 on the closure lid material, which are more severe than the 10CFR71.45(a) requirements. A conservative analysis of the MPC baseplate under the 3D* loading is also performed. The MPC baseplate is modeled as a simply supported plate subject to the load from the fuel basket and the fuel.

The following table summarizes the results from these analyses also performed for the HI-STAR 100 FSAR. As stated earlier, safety factors tabulated in this section represent margins that are over and beyond those implied by the loading magnification mandated in NUREG 0612 or 10CFR71.45(a), as appropriate.

Summary of MPC Lifting Analyses-Minimum Safety Factors			
Item	Value of Stress (ksi) or Load (lb.)	Allowable (ksi) or Capacity (lb.)	Safety Factor
MPC Lifting Bolt Load B NUREG 0612	103,500	111,300	1.08
Baseplate Bending Stress B (3D*)	13.26	20.7	1.56

We note that all factors of safety are greater than 1.0 as required.

2.5.1.4.1 Lifting of Damaged Fuel Canisters

All damaged fuel canisters suitable for deployment in the HI-STAR 100 Package are analyzed for structural integrity during a lifting operation. Appendix 2.B describes the analyses undertaken and summarizes the results obtained.

In conclusion, the synopses of lifting device, device/component interface, and component stresses, under all contemplated lifting operations for the HI-STAR 100 overpack and MPC have been presented in the foregoing, and show that all factors of safety are greater than 1.0.

2.5.2 Tie-Down Devices

2.5.2.1 Discussion

The initial design of the HI-STAR 100 Systems envisioned a shear ring located on the top flange and pocket trunnions located near the bottom of the outer enclosure shell to serve as locations for tie-down. Accordingly, previous issues of the SAR included analyses to qualify the shear ring/pocket trunnion components as tie-down devices complying with the requirements of 10CFR71.45(b).

The pair of semi-obround recesses referred to as pocket trunnions were originally incorporated into the HI-STAR design to permit the cask to be upended (or downended) by using circular shafts inserted in the "pockets" to serve as rotation pivots. Recent handling experience with the seven HI-STAR 100 overpacks manufactured thus far (ca. April 2002) and the HI-TRAC transfer casks (which are similar in overall dimensions and weight) has shown that utilizing an L-shaped cradle, designed as an ancillary under Part 72 regulations for the upending and downending operations, is a more robust method of cask handling. The cradle method of handling Holtec's overpacks and MPCs has garnered considerable experience through ISFSI implementation operations at several sites. Because the cradle method of upending and downending does not require the pocket trunnions, and because

the recesses to incorporate the pocket trunnions lead to increased local dose, the pocket trunnions are being henceforth eliminated from the HI-STAR design. All HI-STAR 100 overpacks (except the first seven units already manufactured) shall be fabricated without the twin pocket trunnions; even in the first seven units that have the shear ring and pocket trunnions, these locations are no longer designated as tie-down locations.

In lieu of relying on the pocket trunnions for tie-down, the revised tie-down arrangement for HI-STAR 100 secures the overpack to the transport vehicles in such a manner that the longitudinal inertia forces (the most frequent mode of motion-induced loading the package during transport) do not exert an overturning moment on the cask (as is the case with a pocket trunnion-based fastening means). In fact, the revised tie-down device seeks to eliminate or minimize all localized loadings on the body of the overpack, thus incorporating an additional element of safety in the transport package.

The new tie-down configuration, pictorially illustrated in Figure 1.2.8, essentially consists of a near-full-length saddle integral to the bed of the transport vehicle to react the lateral and vertical loads, and a pair of End-Restraints, also integral to the transport vehicle, that save for a small calibrated axial clearance to provide for differential thermal expansion, provide a complete axial confinement to the overpack. The details of the design of the tie-down structure are governed by the reaction forces computed using static equilibrium relationships for inertia loads corresponding to §72.45(b) and reported in this SAR.

To comply with the requirements of 10CFR71.45(b), it must be shown by test or analysis that all devices used for package tie-down are acceptable. Therefore, in this section, we present the load analyses of the HI-STAR 100 tie-down system. The HI-STAR 100 System is shown in a transport orientation in Drawing 3930 and in Figure 1.2.8.

To summarize, HI-STAR 100 is secured to the transport vehicle in a horizontal position by the following components (no additional support structure is permanently attached to the cask for transport tie-down):

a. A long saddle support, bearing on the overpack outer enclosure shell and enclosure shell panels, over an angle of approximately 140 degrees. Multiple tie-down straps, sized to support uplift loads, secure the HI-STAR 100 to the saddle. The saddle resists lateral loads and vertical downward oriented loads through its extensive interface with the body of the HI-STAR overpack. Vertical upward directed loads are reacted by the tie-down straps.

b. Longitudinal loads in either direction are transmitted to the End-Restraint by the sacrificial disc on each impact limiter that is specifically designed to resist normal handling decelerations of 17g without impairing the performance of the impact limiters during the mandated Accident Conditions of Transport drop configurations. Because the axial transport loads are bounded by the 10g's in either longitudinal direction, the aluminum honeycomb discs are quite adequate to transmit axial loads without crushing.

In accordance with 10CFR71.45(b), the inertia forces, applied at the center of gravity of the loaded HI-STAR 100, arise from:

a. a horizontal component along the longitudinal axis of ±10g
b. a vertical component of ± 2g
c. a lateral component of ± 5g

These accelerations are referred to as the first set of load amplifiers. These forces are applied simultaneously in the respective directions with their lines of action selected to maximize the reactions. In the following, "load combinations" are identified by assembling the three loads with appropriate plus or minus signs to reflect the fact that the lateral load can be in either direction, the vertical load can be in either direction, and the longitudinal load is uni-directional.

As required by the governing regulations, the components of the cask that are used for tie-down must be capable of withstanding the force combinations without generating stress in the cask components in excess of the material yield strength.

The saddle support under the enclosure shell, the slings, and the front and rear end structures that resist longitudinal load are not part of the HI-STAR 100 package and therefore, are not part of this submittal. The loads used to design these components are determined using the load amplifiers given by the American Association of Railroads (AAR) Field Manual, Rule 88. These amplifiers, henceforth called the second set of load amplifiers, are:

± 7.5g's longitudinal
± 2.0 g's vertical
± 2.0 g's lateral

In what follows, the equations of equilibrium for the packaging subject to three orthogonal inertia loads are set down. Tie-down reactions using either set of load amplifiers are determined from the same equilibrium equations. Numerical results are obtained for both sets of input load amplifiers and presented at the end of this section as Tables 2.5.1 and 2.5.2.

Figure 1.2.8 shows a schematic of the tie-down; Figure 2.5.2 shows a partial free-body diagram of the transport package on the railcar. The following steps to comply with the provisions of 10CFR71.45(b) are carried out:

- Develop the general equilibrium equations to solve for the tie-down forces.

- Apply the equations to develop numerical results for the tie-down forces. Results are provided for the load multipliers specified in 10CFR71.45(b) and for the load multipliers in the AAR Field Manual.

- The tie-down force values with the 10CFR71.45(b) load amplifiers are used to evaluate the structural integrity of the cask components affected by the tie-down devices. Tie-down reactions obtained using the AAR Field Manual amplifiers for are reported for information only (for future use in designing the tie-down members of the railroad car).

2.5.2.2 Equilibrium Equations to Determine the Tie-Down Forces

For longitudinal loading, the applied load, amplified by the imposed deceleration, is reacted directly by either the top or bottom impact limiter. The protruding donut shaped annular portion of the impact limiter is designed to mitigate the results from a 1' free end drop in accordance with regulatory requirements. The impact limiter material crush strength limits the deceleration to 17g's or less (Table 2.1.10), and it is shown in Subsection 2.6 that all components of the HI-STAR 100 package in this load path meet ASME Level A stress limits. Therefore, by suitable choice of support structure on the railcar, the HI-STAR 100 Package is assured of meeting regulatory requirements under the mandated longitudinal transport load of 10g's in either direction.

For vertical loading, the resultant vertical force on the saddle is reacted by a symmetric bearing pressure, or by developing a reacting tension in the tie-down strap. Figure 2.5.12 shows a free body at a saddle support. The vertical load is conservatively assumed resisted by a radial component only, with no credit assumed for any shear stresses arising from friction at the interface. The radial pressure, p_v, is assumed to vary with circumferential location using a cosine function, with peak pressure occurring under the overpack centerline.

For lateral loading, the resultant force is conservatively assumed reacted only by a radial bearing pressure, p_h, distributed on one side of the saddle and varying around the periphery in accordance with a sine function (shear stresses due to frictional effects are conservatively neglected). Figure 2.5.13 shows the appropriate free-body. Since the radial pressure distribution corresponds to both a vertical and lateral force resultant, an opposing vertical force is developed in the tie-down strap. This vertical force is proportional to the applied lateral force, and ensures equilibrium. For the evaluation of lateral force equilibrium, it is also necessary to determine the vertical and horizontal location of the center of pressure of the radial bearing force on the enclosure shell and shell panels. This location is designated by the coordinates y_2 and z_2 in Figure 2.5.2 and in Figure 2.5.13 and ensures that there is no net moment (around the cask centerline longitudinal axis) produced by the bearing pressure.

For the geometry associated with the HI-STAR 100 transport saddles, the induced vertical upward force in the tie-down straps from the application of a lateral load is approximately equal to the magnitude of the lateral load. Thus, for a combination of lateral load and upward vertical load, there are two contributions to the total load in the tie-down sling.

- Equilibrium Equations for Tie-Down

The equilibrium equations necessary to solve for the tie-down forces under the postulated loads will be written using classical vector algebra. There are three loading cases that govern the analysis of the tie-down components: longitudinal (x), vertical (y), and lateral (z). The reaction forces for each loading case are determined by the equations of force and moment equilibrium. The general

equations of force and moment equilibrium are developed following the partial free body diagram shown in Figure 2.5.2. Figure 2.5.2 defines the following force vectors: F_c, F_b, and F_t are the applied loads from the cask, and from the bottom and top impact limiters, respectively. S_i (i=1,2,3) are the three reaction forces at the locations on the saddle support where tie-down straps are located. For all tie-down force calculations to determine the restraint forces, the following bounding values (for a 1g load) are ascribed to the cask and to the overpack (Table 2.2.1).

HI-STAR 100 – 250,000 lb.
Top Impact Limiter – 20,000 lb.
Bottom Impact Limiter – 18,000 lb

Results from numerical computations are summarized in tabular form at the end of this section. In the following sub-sections, discussion of the various loads and the method by which they are reacted, is presented

2.5.2.3 Longitudinal Loading

The longitudinal load is directly resisted by the impact limiters at the top and bottom of the cask. The two impact limiters have an annular region with impact limiting material chosen to resist normal handling loads up to 17g (Table 2.1.10). Therefore, they can resist normal transport longitudinal loads without loss of function in the event of a cask drop accident. The HI-STAR overpack is shown in Subsection 2.6 to meet Level A ASME Code stress limits.

2.5.2.4 Vertical Load

The vertical loads, directed either upwards or downwards, are resisted by the tie-down straps or the saddle support at the three locations shown in Figures 1.2.8 and 2.5.2. Planer equilibrium equations for force and moment equilibrium have the form (refer to Figure 2.5.2):

$$\sum_i S_i = G$$

$$\sum_i x_i S_i = M$$

where $G = F_t+F_c+F_b$ and $M = F_t x_t + F_c x_c - F_b x_b$

These two equations, coupled with the assumption that the cask is rigid, yields the solution for the three tie-down reactions; the magnitude of the three vertical reactions are determined in the form:

$$S_{i(vertical)} = f_i F + g_i M \qquad i = 1,2,3$$

The detailed numerical computations leading to the results reported in tabular form at the end of this subsection conservatively assume that the outermost tie-down straps are located so that their centerlines are approximately 1' from the upper and lower edge of the outer enclosure panels. In the above equation, F is the total vertical applied force and M is the total moment, about a horizontal

axis through the base of the cask, from the vertical components of the applied force. The applied forces are the weights of the cask, and the top and bottom impact limiters, amplified by the appropriate "g" value and located at the centroid of the components (per Figure 2.5.2). When the applied load is directed downward, the reactions at the saddle supports are distributed bearing pressures at the saddle/enclosure shell interface, as shown in Figure 2.5.12; when the applied load is directed upward, the reactions are provided by tensile loads in the tie-down straps, which are distributed to the enclosure shell as a radial pressure.

2.5.2.5 Lateral Load

For this load case, lateral loads, in either direction, are distributed to each saddle support location where tie-down straps are present, and are resisted by a radial bearing pressure distribution at the saddle/enclosure shell interface. The radial pressure distribution has a lateral and vertical resultant force. The lateral component of the reaction load at each saddle/enclosure shell interface is computed from force and moment equilibrium and the same form of solution is achieved as given for the vertical loads. In this case, however, since the resultant resisting force is directed through the cask longitudinal centerline, at each of the support locations, there is an induced vertical force in the tie-down strap that develops to balance the vertical component of the force between the overpack and the support at each location. Figure 2.5.13 shows how the forces are distributed so that at each location, the vertical force from the interface pressure is balanced by the induced load in the tie-down strap, while the horizontal net force from the interface pressure balances the lateral reaction force at that location. The location of the resultant force at the saddle/enclosure shell interface ensures that there is no net moment at the support. That is, the relation between the lateral load, the induced vertical load, and the center of pressure coordinates y_2 and z_2 is:

$$F(\text{lateral}) \times (y_2) = F(\text{induced vertical}) \times (z_2)$$

The saddle support angle is chosen to ensure that the resultant force is inclined approximately 45 degrees to the vertical, so that the applied lateral force induces a vertical force of the same magnitude that is resisted by the tie-down straps.

2.5.2.6 Numerical Results for Tie-Down Reactions

The longitudinal load in either direction is reacted by the impact limiters and does not impose any load on the saddle support or the tie-down straps. The lateral load and vertical load results in a bearing pressure between the saddle support and the enclosure shell and a tensile load in the tie-down strap. The only directional effect leading to different results is the direction of the applied vertical load. Therefore, the load combinations to be considered are:

(1) Longitudinal load, +lateral load, +vertical load upward
(2) Longitudinal load +lateral load, + vertical load downward

The results for the tie-down reactions due to each individual load and due to the defined load combinations are presented in Table 2.5.1.

As noted earlier, the AAR Field Manual, Rule 88 specifies a set of load amplifiers that are appropriate for designing the saddle and the trunnion support but are not part of the packaging qualification effort. For information purposes only, results for the tie-down reactions are provided for the load case combinations using the load amplifiers (defined earlier as the second set) given by the AAR Field Manual, Rule 88. Results are given in Table 2.5.2.

To comply with the governing requirements (10CFR71.45(b)(1)), it should be demonstrated that under the tie-down loads, no part of the cask experience stresses in excess of the material yield strength. It has been noted earlier that the impact limiters are capable of resisting longitudinal loads in excess of the regulatory requirements for transport. Therefore, only transport loads in the vertical and lateral direction need be assessed for their affect on cask stress. The only loads transmitted to the overpack from lateral and vertical loads are radial pressures on the overpack outer enclosure. The enclosure shell is backed by the Holtite-A material, which, in reality, can resist some compression and transfer the load to the intermediate shells. However, since no structural credit is assumed for Holtite-A, it is conservatively considered that the radial loads from the tie-down forces are transmitted only through the radial channel legs connecting the outer enclosure shell to the overpack intermediate shells. The following simplified analysis serves to ensure that the cask components do not exceed their yield stress under the combined action of lateral and vertical tie-down loads.

An examination of the bounding loads from Table 2.5.1 concludes that the most demand on the cask structure occurs when the tie-down strap load, from both lateral and vertical transport forces, is assumed reacted over 180 degrees and therefore, transmitted to the overpack intermediate shells as a compressive direct load in nineteen (19) radial channel legs (see applicable drawing in Section 1.4 showing the radial channels). This enables the determination of a minimum length of contact between the tie-down straps and the enclosure shell to ensure that the direct stress in the radial channels remains below the yield strength. Conservatively evaluating the yield strength of the radial channels at 400 degrees F per Table 2.1.2, Tables 2.3.2 and 2.3.3 give:

Sy = 32,600 psi

The average direct stress, "St", in a channel is computed by first determining the equivalent uniform radial pressure developed at the interface between the tie-down strap and the enclosure shell. From simple equilibrium, this radial pressure is determined by the formula:

$p = 2T/DL$

T is the load in the tie-down strap, D is the outer diameter of the enclosure shell, and L is the length of enclosure shell under pressure.

The pressure, p, is related to the direct compressive load, "G", in one of the channel legs, by the following equation:

$G = p \times (sL)$ where the span between channel legs is approximated as $s = (3.14159 \times (D/2))/19$

Finally, the stress in the channel leg, "St", is given as:

St = G/(tL) where t is the channel leg thickness.

Setting St = Sy and solving for "L", gives: L = (3.14159/19) x (T/t x Sy)

The minimum length L is computed using T = 647,000 lb./2, and t=0.5", to obtain:

L = 3.282"

Since the minimum sling length needed to support the load is 6" (or greater), it is seen that the cask stress developed to resist the lateral and vertical transport loads is much less than the yield stress of the channel legs; therefore, the governing regulatory requirement of 10CFR71.45(b)(1) is satisfied.

2.5.2.7 Structural Integrity of Pocket Trunnions on Applicable HI-STAR 100 Systems

The summary of results provided in tabular form, herein, is applicable only to the units that have been previously manufactured and, therefore, have pocket trunnions. The structural function of the pocket trunnions on applicable HI-STAR 100 Systems is limited to supporting the HI-STAR overpack during upending /downending operations if a separate downending cradle is not employed. If the pocket trunnion recess is utilized as a loaded pivot point during downending, the applied load for this operation is conservatively considered as the loaded weight of the package without impact limiters (250,000 lb.), amplified by a 15% inertia load factor. This load can be applied in any direction as the package is rotated 90 degrees. Results of structural integrity analyses, performed to qualify the rotation trunnion recess on the affected units, are summarized below.

Analyses are performed to evaluate the structural performance of various portions of the pocket trunnion under the stated total load, divided equally between the two trunnions. Since the trunnions are not utilized as tie-down devices, they are not considered as ASME Code items; nevertheless, their performance is evaluated by comparing calculated stresses against yield strengths (to conform to the methodology employed in the HI-STAR 100 FSAR). Analyses for bearing stress levels, primary stress levels in the trunnion recess body, and weld stress in the weld group that attaches the recess forging to the intermediate shells. The methods of analysis include both simple strength of materials evaluation and finite element analysis of the pocket trunnion body. For the bearing stress analysis, the average bearing stress is computed based on the diameter of the male trunnion that would fit the trunnion pocket. For the general primary stress state in the trunnion forging, a finite element model of the trunnion recess is developed. Finally, for the analysis of the weld stress distribution, simple strength of materials equilibrium analysis is used with weld sizes appropriate to the minimum weld configuration in-place on the affected HI-STARs. The maximum weld stress is computed accounting for the weld material between the trunnion recess and the intermediate shells and between the pocket trunnion and the outer enclosure shell.

The results of the pocket trunnion recess analyses for an upending/downending load equal to 125,000 lb. x 1.15, are summarized in the following table:

Structural Integrity Results for HI-STAR Systems Equipped with Pocket Trunnions			
Item	Calculated Stress (ksi)	Allowable Stress (ksi)	Safety Factor = Allowable Value / Calculated Value
Bearing Stress	6.183	97.1	15.71(based on material yield strength)
Pocket Recess Primary Membrane + Primary Bending Stress	14.17	32.33	2.282 (based on 1/3 of trunnion material yield strength)
Maximum Weld Stress	2.399	14.533	4.802 (based on 1/3 of base metal yield strength)

2.5.3 Failure of Lifting and Tie-Down Devices

10CFR71.45 establishes criteria for minimum safety factors for lifting attachments, and provides input design loads for tie-down devices. 10CFR71.45 also requires that the lifting attachments and tie-down devices permanently attached to the cask, be designed in a manner such that a structural failure during lifting or transport will not impair the ability of the transportation package to meet other requirements of Part 10CFR71. In this section of the SAR, the issues concerning a structural failure during lifting or tie-down during transport are addressed. Specifically, the following issues are considered and resolved below:

a. Lifting Attachments:

Analyses are performed, using simple strength of materials concepts and evaluations to demonstrate that the ultimate load carrying capacity of the lifting trunnions is governed by the cross section of the trunnion external to the overpack top forging rather than by any section within the top forging. Detailed calculations that compare the ultimate load capacity of the shank of the lifting trunnion (the external cylindrical portion extending outside of the overpack top forging) to the ultimate load capacity of the top forging are performed. The ultimate load carrying capacity of the trunnion shank is based on an examination of the ultimate capacity of the section in both shear and bending. The ultimate load capacity of the top forging is determined by its capacity to resist moment by thread shear at the trunnion/forging threaded interface and to equilibrate the lifting load by bearing action at the trunnion forging bearing surface interface. It is concluded that the trunnion shank reaches ultimate load capacity limit prior to the top forging reaches its corresponding ultimate load capacity limit. Loss of the external shank of the lifting trunnion will not cause loss of any other structural or shielding function of the HI-STAR 100 overpack; therefore, the requirement imposed by 10CFR71.45(a) is satisfied.

The following safety factors are established:

(Ultimate Bearing Capacity at Trunnion/Top Forging Interface)/(Ultimate Trunnion Load) = 1.16

(Ultimate Moment Capacity at Trunnion/Top Forging Thread Interface)/(Ultimate Trunnion Moment Capacity) = 1.57

b. Tie-Down Devices

There are no tie-down devices that are permanently attached to the cask; therefore, no analyses are required to demonstrate that the requirements of 10CFR71.45(b)(3) are satisfied.

2.5.4 Conclusions

Lifting devices have been considered in Subsection 2.5.1 and Tie-Down devices have been considered in Subsection 2.5.2. It is shown that requirements of 10CFR71.45(a)(lifting devices) and 10CFR71.45(b)(tie-down devices) are satisfied. All safety factors exceed 1.0.

No tie-down device is a permanent part of the cask. All tie-down devices (saddle, tie-down straps, and fore and aft impact limiter targets, are part of the rail car and accordingly are not designed in this SAR. The maximum loads imposed on these items are recorded for subsequent design efforts.

Table 2.5.1

TIE-DOWN REACTIONS[†] - 10CFR71 LOAD RESULTS

Item	Component	Load Combination 1 (kips)	Load Combination 2 (kips)
Impact Limiter Target	Longitudinal	2,880	2,880
Top End Saddle -1	Lateral	420.85	420.85
	Vertical – Saddle	420.85	252.51 + 420.85
	Vertical - Tie-Down Strap	84.17 + 420.85	420.85
Intermediate Saddle-2	Lateral	480.15	480.15
	Vertical - Saddle	480.15	288.09 + 480.15
	Vertical - Tie-Down Strap	96.03 + 480.15	480.15
Bottom End Saddle -3	Lateral	539	539
	Vertical – Saddle	539	323.4 + 539
	Vertical - Tie-Down Strap	107.8 + 539	539

[†] See Figure 2.5.2 for definition of the symbols for the reaction loads.

Table 2.5.2

TIE-DOWN REACTIONS† - AAR RULE 88 LOAD RESULTS

Item	Component	Load Combination 1 (kips)	Load Combination 2 (kips)
Impact Limiter Target	Longitudinal	2,160	2,160
Top End Saddle -1	Lateral	168.34	168.34
	Vertical - Saddle	168.34	252.51 +168.34
	Vertical - Tie-Down Strap	84.17 + 168.34	168.34
Intermediate Saddle-2	Lateral	192.06	192.06
	Vertical - Saddle	192.06	288.09 +192.06
	Vertical - Tie-Down Strap	96.03 +192.06	192.06
Bottom End Saddle -3	Lateral	215.6	215.6
	Vertical - Saddle	215.6	323.4 + 215.6
	Vertical - Tie-Down Strap	107.8 + 215.6	215.6

† See Figure 2.5.2 for definition of the symbols for the reaction loads.

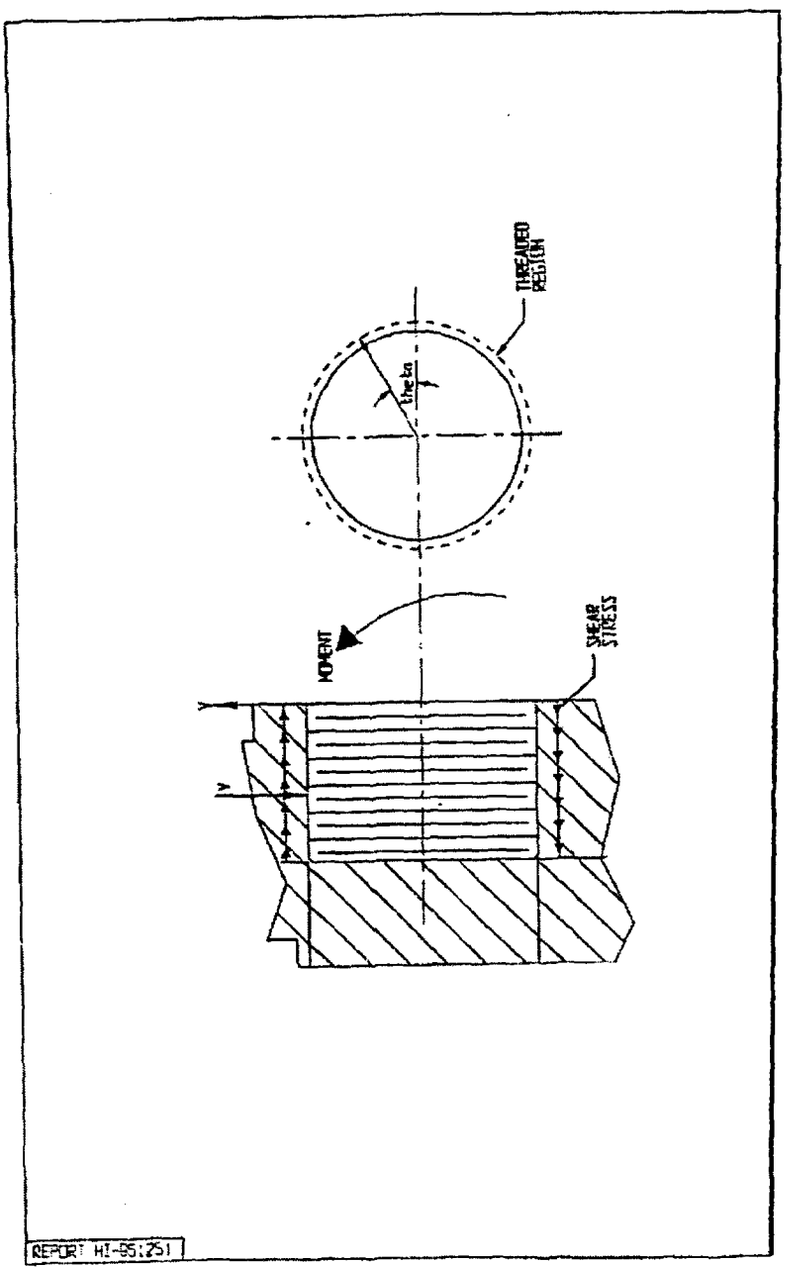

FIGURE 2.5.1; FREE BODY SKETCH OF LIFTING TRUNNION THREADED REGION SHOWING MOMENT BALANCE BY SHEAR STRESS

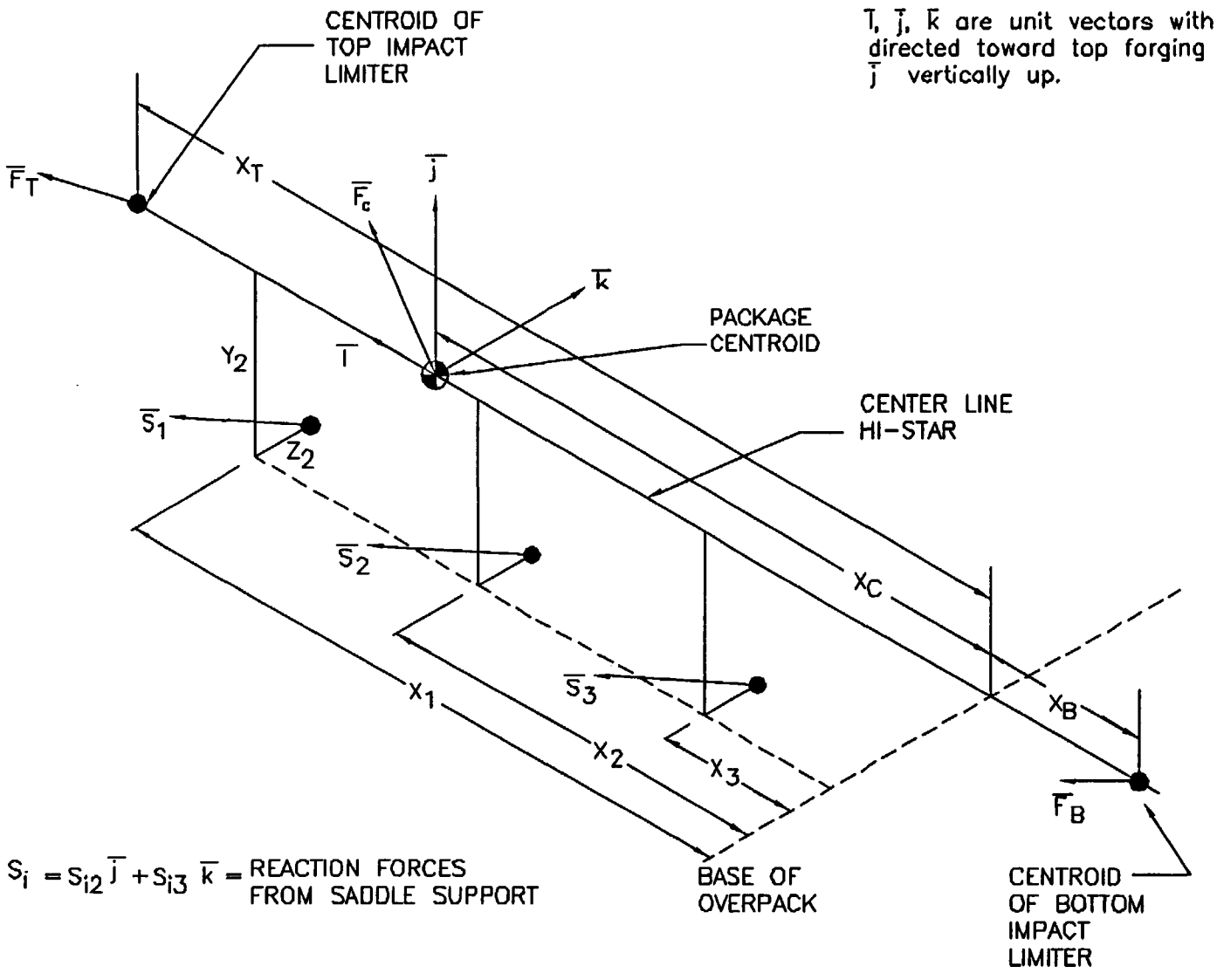

FIGURE 2.5.2; PARTIAL FREE BODY DIAGRAM OF OVERPACK SHOWING APPLIED TRANSPORT LOAD AND TIE-DOWN REACTION VECTORS AT SADDLE SUPPORTS

Figures 2.5.3 through 2.5.11

INTENTIONALLY DELETED

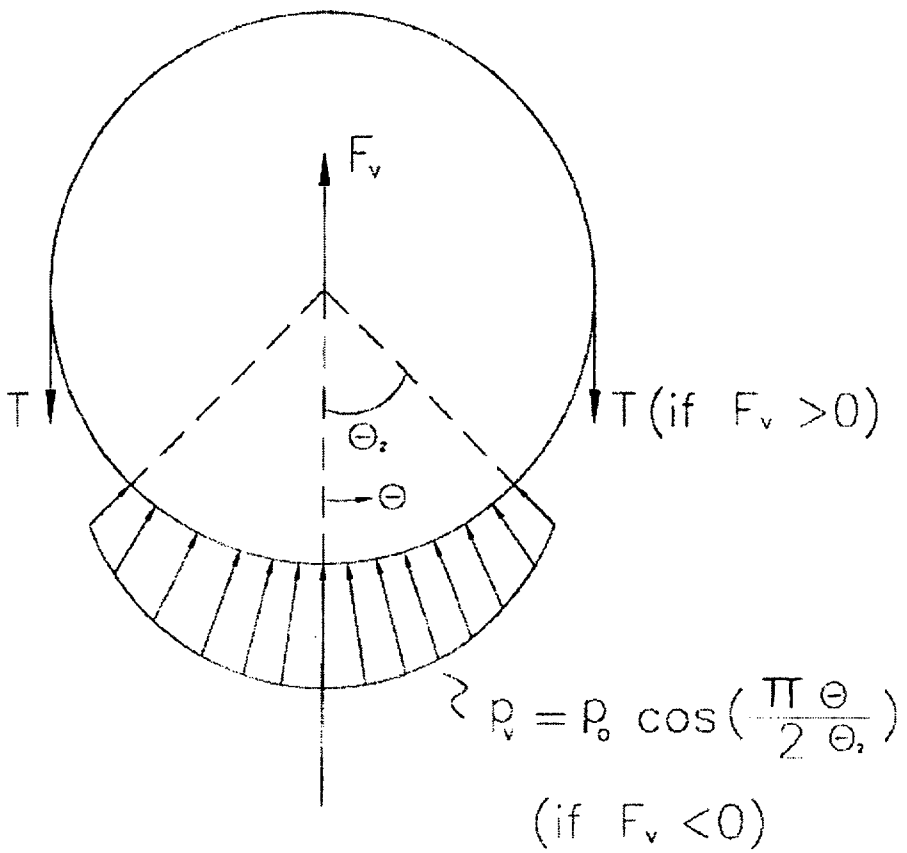

FIGURE 2.5.12; FREE-BODY AT TIE DOWN LOCATION WITH SADDLE SUPPORT AND TIE-DOWN STRAP-VERTICAL REACTION LOAD

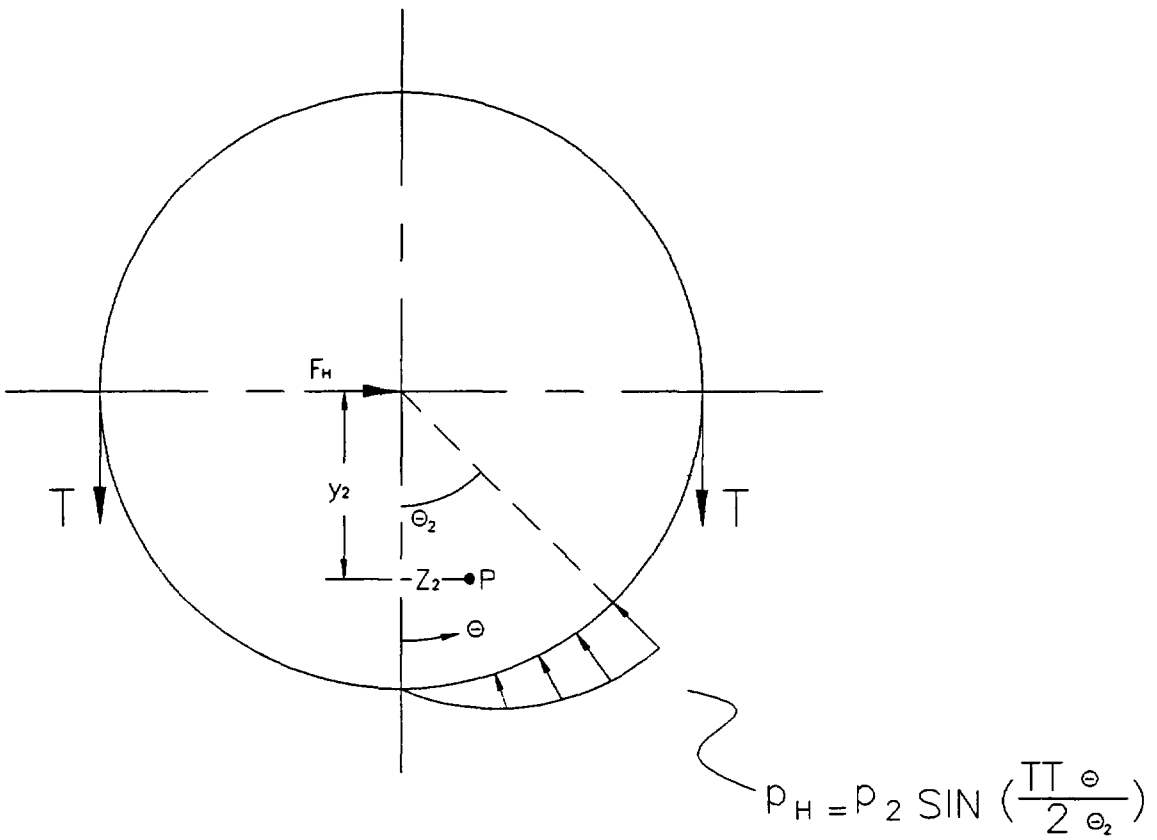

$2T = f(\Theta_2)F_H = F_v$ (VERTICAL RESULTANT ON SADDLE)

PT. P IS LOCATION OF CENTER OF PRESSURE

FIGURE 2.5.13; FREE-BODY AT TIE-DOWN LOCATION WITH SADDLE SUPPORT AND TIE-DOWN STRAP-LATERAL REACTION LOAD

2.6 NORMAL CONDITIONS OF TRANSPORT

The HI-STAR 100 package, when subjected to the normal conditions of transport specified in 10CFR71.71, meets the design criteria in Subsection 2.1.2 (derived from the stipulations in 10CFR71.43 and 10CFR71.51) as demonstrated in the following section.

2.6.1 Heat

Subsection 2.6.1, labeled "Heat" in Regulatory Guide 7.9, is required to contain information on all structural (including thermoelastic) analyses performed on the cask to demonstrate positive safety margins, except for lifting operations that are covered in the preceding Section 2.5. Accordingly, this subsection contains all necessary information on the applied loadings, differential thermal expansion considerations, stress analysis models, and results for all normal conditions of transport. Assessment of potential malfunction under "Cold" conditions is required to be presented in Subsection 2.6.2.

Consistent with Regulatory Guide 7.9, the thermal evaluation of the HI-STAR 100 Package is reported in Chapter 3. The thermal evaluation also establishes the material temperatures, which are used in the structural evaluations discussed in this section and in Section 2.7.

2.6.1.1 Summary of Pressures and Temperatures

Design pressures and design temperatures for all conditions of transport are listed in Tables 2.1.1 and 2.1.2, respectively.

Load cases F1 (Table 2.1.6) and E4 (Table 2.1.7) are defined to study the effect of differential thermal expansion among the constituent components in the HI-STAR 100 Package. Figures 2.6.1 and 2.6.2 provide the defining bounding temperature distributions used for the MPC and overpack finite element thermal stress calculations to maximize stresses that develop due to temperature gradients. The distribution T is applied conservatively to analyze its effect on the fuel basket, the enclosure vessel (helium retention boundary), and the overpack.

2.6.1.2 Differential Thermal Expansion

In addition to the finite element solutions for free expansion stress (due to temperature gradients), simplified closed form calculations are independently performed to demonstrate that a physical interference will not develop between the overpack and the MPC canister, and between the MPC canister and the fuel basket due to unconstrained thermal expansion of each component during normal conditions of transport. To assess this in the most conservative manner, the thermal solutions computed in Chapter 3 are surveyed for the following information.

- The radial temperature distribution in each of the fuel baskets at the location of peak center metal temperature.
- The highest and lowest mean temperatures of the canister shell for the hot environment condition.

- The inner and outer surface temperature of the overpack shell (inner shell, intermediate shells, neutron shield, and outer closure) at the location of highest and lowest surface temperature (which will produce the lowest mean temperature).

The thermal evaluation is performed in Chapter 3. Tables 3.4.17 and 3.4.18 present the resulting temperatures used in the deflection evaluation.

Using the temperature information in the above-mentioned tables, simplified thermoelastic solutions of equivalent axisymmetric problems are used to obtain conservative estimates of gap closures. The following procedure, which conservatively neglects axial variations in temperature distribution, is utilized.

1. Use the surface temperature information for the fuel basket to define a parabolic distribution in the fuel basket that bounds (from above) the actual temperature distribution. Using this result, generate a conservatively high estimate of the radial and axial growth of the different fuel baskets using classical closed form solutions for thermoelastic deformation in cylindrical bodies.

2. Use the temperatures obtained for the canister to predict an estimate of the radial and axial growth of the canister to check the canister-to-basket gaps.

3. Use the temperatures obtained for the canister to predict an estimate of the radial and axial growth of the canister to check the canister-to-overpack gaps.

4. Use the overpack surface temperatures to construct a logarithmic temperature distribution (characteristic of a thick walled cylinder) at the location used for canister thermal growth calculations; and use this distribution to predict an estimate of overpack radial and axial growth.

5. For given initial clearances, compute the operating clearances.

The results are summarized in the tables given below for normal conditions of transport.

THERMOELASTIC DISPLACEMENTS IN THE MPC AND OVERPACK UNDER HOT TEMPERATURE ENVIRONMENT CONDITION				
CANISTER - FUEL BASKET				
	Radial Direction (in.)		Axial Direction (in.)	
Unit	Initial Clearance	Final Gap	Initial Clearance	Final Gap
All PWR MPCs	0.1875	0.101	2.0	1.57
MPC-68	0.1875	0.104	2.0 (min)	1.586 (min)
CANISTER – OVERPACK				
	Radial Direction (in.)		Axial Direction (in.)	
Unit	Initial Clearance	Final Gap	Initial Clearance	Final Gap
All PWR MPCs	0.09375	0.058	0.625	0.422
MPC-68	0.09375	0.059	0.625	0.429

It can be verified by referring to the Design Drawings provided in Section 1.4 of this report, and the foregoing table, that the clearances between the MPC basket and canister structure, as well as those between the MPC shell and overpack inside surface, are sufficient to preclude a temperature induced interference from the thermal expansions listed above.

It is concluded that the HI-STAR 100 package meets the requirement that there be no restraint of free thermal expansion in any of the constituent components (i.e, the fuel basket, the enclosure vessel, and the overpack structure).

2.6.1.3 Stress Calculations

In this subsection, the normal conditions of transport associated with the thermal environment designated as "Heat" are considered. The stresses due to the combined effect of pressure, mechanical loads, and thermal gradient are evaluated. Within this subsection, the effects of fatigue and structure elastic/plastic stability under compression and lateral loading are also considered. Included in the subsection is a complete description of the finite element models developed to assess package performance under various loads. A two-dimensional finite element model of the fuel basket and the MPC enclosure shell is developed to evaluate the effect of pressure, radial temperature gradients and lateral deceleration induced inertia loads. A three-dimensional model of the overpack is also developed in this section to assess performance of the overpack under all load cases. Since both of

these finite element models are used again in Section 2.7, where hypothetical accident conditions of transport are examined, the explanation of the features of the model is presented herein in a general manner. Included in this description of the features of the model is a discussion of the loads applied, how they are chosen, and the methodology used to insure satisfaction of equilibrium. Where the loads, assumptions, geometry, etc. are common to both normal conditions of transport analyses and to hypothetical accident conditions of transport, the detailed description is presented in this section. Where the descriptions and discussions are relevant only for the hypothetical accident condition of transport, the detailed descriptions required for full understanding of the analysis are presented in Section 2.7.

This subsection presents the methodology for calculation of the stresses in the different components of the HI-STAR 100 Package from the load cases assembled in Section 2.1. Where the results are finite element based the methodology and the model is described in detail in this section. Results of finite element stress analyses are used for the comparison with allowable stresses performed in Subsection 2.6.1.4. Loading cases for the MPC fuel basket, the MPC enclosure vessel, and the HI-STAR 100 storage overpack are listed in Tables 2.1.6 through 2.1.8, respectively, for normal conditions of transport. An abbreviated description of each of the analyses is presented in the body of the chapter.

In general, as required by Regulatory Guide 7.9, the comparison of the calculated stresses with their corresponding allowables is presented in Subsection 2.6.1.4. However, for clarity in the narrative in this subsection (2.6.1.3), unnumbered summary tables are presented within the text. The key stress comparisons are subsequently reproduced in numbered tables in Subsection 2.6.1.4 to provide strict compliance with Regulatory Guide 7.9.

For all stress evaluations, the allowable stresses and stress intensities for the various HI-STAR 100 System components are based on bounding high metal temperatures to provide additional conservatism (Table 2.1.21 for the MPC basket and shell, for example). Elastic behavior is assumed for all stress analyses. Elastic analysis is based on the assumption of a linear relationship between stress and strain.

In Section 2.7, the same analytical models described here for normal conditions of transport are used to assess package performance under the hypothetical accident conditions. Therefore, the description of the models provided below is also applicable to the analysis performed in Section 2.7 except as previously noted.

In addition to the loading cases germane to stress evaluations mentioned above, cases pertaining to the elastic stability of the overpack are also considered.

The specific finite element models and component calculations described and reported in this subsection are:

1. MPC stress and stability calculations

2. HI-STAR 100 overpack stress and stability calculations

MPC stress and elastic stability analyses are considered in Subsection 2.6.1.3.1 wherein load cases from Tables 2.1.6 and 2.1.7 appropriate to normal conditions of transport are considered. The following analyses for the MPC are performed:

a. Finite element analysis of the MPC fuel basket and MPC helium retention shell under lateral loads from handling loads during normal transport.
b. Finite element and analytical analysis of the helium retention vessel (enclosure vessel) as an ASME Code pressure vessel.
c. Analysis of the fuel support spacers under longitudinal inertia compression load appropriate to normal conditions of transport.
d. Elastic stability and yielding of the MPC enclosure shell under axial and lateral loads arising from normal handling and external pressure.

Overpack stress and elastic stability analyses are considered in Subsection 2.6.1.3.2. Load cases from Table 2.1.8 are considered. The following analyses are performed to establish the structural adequacy of the overpack:

a. Three-dimensional finite element analysis of the overpack subjected to load cases listed in Table 2.1.8 for normal conditions of transport.
b. Consideration of fabrication stresses.
c. Structural analysis of the closure bolting for normal condition of transport.
d. Stress Analysis of overpack enclosure shell and return.

2.6.1.3.1 MPC Stress Calculations

The structural function of the MPC in the transport mode is stated in Section 2.1. The calculations presented here demonstrate the ability of the MPC to perform its structural function. Analyses are performed for each of the MPC designs. The following subsections describe the model, individual loads, load combinations, and analysis procedures applicable to the MPC.

2.6.1.3.1.1 Analysis of Load Cases F2 (Table 2.1.6) and E2, and E4 (Table 2.1.7)

The load cases considered herein pertain to lateral loading on the MPC components, namely the fuel basket and the enclosure vessel. For this purpose, a finite element model of the MPC is necessary. During normal conditions of transport, a bounding handling load is simulated by applying a deceleration induced inertia load from a 1' drop with impact limiters installed. During hypothetical accident conditions (see Section 2.7), the MPC is subject to the design basis decelerations from a 30' drop. The finite element model used to simulate both load cases is described here and is used for analyses for normal conditions of transport and later in Section 2.7 is used for the hypothetical accident analyses.

- Description of Finite Element Models of the MPCs under Lateral Loading

A finite element model of each MPC is used to assess the effects of normal and accident conditions of transport. The models are constructed using ANSYS [2.6.4], and they are identical to the models used in HI-STAR's 10CFR72 submittal under Docket Number 72-1008. The following model description is common to all MPCs.

The MPC structural model is two-dimensional. It represents a one-inch long cross section of the fuel basket and the MPC canister.

The MPC model includes the fuel basket, the basket support structures, and the MPC shell. A basket support is defined as any structural member that is welded to the inside surface of the MPC shell. A portion of the overpack inner surface is modeled to provide the correct boundary conditions for the MPC. Figures 2.6.3 through 2.6.11 show the MPC models.

The fuel basket support structure shown in the figures here, and in the design drawings in Section 1.4, is a multi-plate structure consisting of solid shims or support members having two separate compressive load supporting members. For conservatism in the finite element model some dual path compression members (i.e., "V" angles) are simulated as single columns. Therefore, the calculated stress intensities in the fuel basket supports from the finite element solution are conservatively overestimated in some locations.

The ANSYS model is not intended to resolve the detailed stress distributions in weld areas. Individual welds are not included in the finite element model.

No credit is taken for any load support offered by the Boral panels, sheathing, and the optional aluminum heat conduction elements. Therefore, these so-called non-structural members are not represented in the model. The bounding MPC weight used, however, does include the mass contributions of these non-structural components.

The model is built using five ANSYS element types: BEAM3, PLANE82, CONTAC12, CONTAC26, and COMBIN14. The fuel basket and MPC shell are modeled entirely with two-dimensional beam elements (BEAM3). Plate-type basket supports are also modeled with BEAM3 elements. Eight-noded plane elements (PLANE82) are used for the solid-type basket supports. The gaps between the fuel basket and the basket supports are represented by two-dimensional point-to-point contact elements (CONTAC12). Contact between the MPC shell and the overpack is modeled using two-dimensional point-to-ground contact elements (CONTAC26) with an appropriate clearance gap.

For each MPC type, three variations of the finite element model were prepared. The basic model includes only the fuel basket and the enclosure shell (Figures 2.6.3 through 2.6.5 show representative configurations) and is used only to study the free thermal expansion due to the temperature field developed in the system. The other two models include a representation of the overpack and are used for the two drop cases considered. Two orientations of the deceleration vector are considered. The 0-degree drop model includes the overpack-MPC interface in the basket orientation illustrated in

Figures 2.6.6 through 2.6.8. The 45-degree drop model represents the overpack interface with the basket oriented in the manner shown in Figures 2.6.9 through 2.6.11. Table 2.6.1 lists the element types and number of elements for all three models for all fuel storage MPC types.

A contact surface is provided in the models used for drop analyses to represent the overpack inner shell. As the MPC makes contact with the overpack, the MPC shell deforms to mate with the inside surface of the inner shell. The nodes that define the elements representing the fuel basket and the MPC shell are located along the centerline of the plate material. As a result, the line of nodes that forms the perimeter of the MPC shell is inset from the real boundary by a distance that is equal to half of the shell thickness. In order to maintain the specified MPC shell/overpack gap dimension, the radius of the overpack inner shell is decreased by an equal amount in the model.

Contact is simulated using two-dimensional point-to-ground elements (CONTAC26). The surface is tangent to the MPC shell at the initial point of impact and extends approximately 135 degrees on both sides. This is sufficient to capture the full extent of contact between the MPC and the overpack.

The three discrete components of the HI-STAR System, namely the fuel basket, the MPC shell, and the overpack, are engineered with small diametral clearances that are large enough to permit unconstrained thermal expansion of the three components under the rated (maximum) heat duty condition. A small diametral gap under ambient conditions is also necessary to assemble the system without physical interference between the contiguous surfaces of the three components. The required gap to ensure unrestricted thermal expansion between the basket and the MPC shell is less than 0.1 inch. This gap, too, will decrease under maximum heat load conditions, but will introduce a physical nonlinearity in the structural events involving lateral loadings (such as side drop of the system) under ambient conditions. It is evident from the system design drawings that the fuel basket, which is non-radially symmetric, is in proximate contact with the MPC shell at a discrete number of locations along the circumferences. At these locations, the MPC shell, backed by the massive overpack weldment, provides a virtually rigid support line to the fuel basket during lateral drop events. Because the fuel basket, the MPC shell, and the overpack are all three-dimensional structural weldments, their inter-body clearances may be somewhat uneven at different azimuthal locations. As the lateral loading is increased, clearances close at the support locations, resulting in the activation of the support from the overpack.

The bending stresses in the basket and the MPC shell at low lateral loading levels, which are too small to close the support location clearances, are secondary stresses since further increase in the loading will activate the overpack's support action, mitigating further increase in the stress. Therefore, to compute primary stresses in the basket and the MPC shell under lateral drop events, the gaps should be assumed to be closed. However, for conservatism, it is assumed that an initial gap of 0.1875" exists, in the direction of the applied deceleration, at all support locations between the basket and the shell, and the diametral gap between the shell and the overpack at the support locations is 3/32". All stresses produced by the applied loading on this configuration are compared with primary stress levels even though the self-limiting stresses should be considered secondary in the strict definition of the ASME Code. Therefore, many of the reported safety factors for conditions of normal transport are conservative in that secondary stress allowables are ignored in the computation of safety factors. Similarly, in Section 2.7, the safety factors reported for the hypothetical accident conditions will also be conservative since the secondary stress is contained in the result.

- Description of Individual Loads and Boundary Conditions Applied to the MPCs

The method of applying each individual load to the MPC model is described in this subsection. The individual loads and the load combinations are shown in Tables 2.1.6 and 2.1.7. As an example, a free-body diagram of the MPC-68 corresponding to each individual load is given in Figures 2.6.12 through 2.6.14. In the following discussion, reference to vertical and horizontal orientations is made. Vertical refers to the direction along the cask axis, and horizontal refers to a radial direction.

Quasi-static structural analysis methods are used. The effect of any dynamic load factors (DLFs) is included in the final evaluation of safety factors. All analyses are carried out using the design basis decelerations in Table 2.1.10.

The MPC models used for side drop evaluations are shown in Figures 2.6.6 through 2.6.11. In each model, the fuel basket and the enclosure vessel are constrained to move only in the direction that is parallel to the acceleration vector. The overpack inner shell, which is defined by three nodes needed to represent the contact surface, is fixed in all degrees of freedom. The fuel basket, enclosure vessel, and overpack inner shell are all connected at one location by linear springs (see Figure 2.6.6, for example).

(a) Accelerations (Load Case F2 (Table 2.1.6) and E2 (Table 2.1.7))

During a side impact event, the stored fuel is directly supported by the cell walls in the fuel basket. Depending on the orientation of the drop, 0 or 45 degrees (see Figures 2.1.3 and 2.1.4), either one or two walls support the fuel. The effect of deceleration on the fuel basket and canister metal structure is accounted for by amplifying the gravity field in the appropriate direction. In the finite element model this load is introduced by applying a uniformly distributed pressure over the full span of the supporting walls. Figure 2.6.15 shows the pressure load on a typical cell for both the 0 degree and the 45 degree drop cases. The magnitude of the pressure is determined by the weight of the fuel assembly (Table 1.2.13), the axial length of the fuel basket support structure, the width of the cell wall, and the impact acceleration. It is assumed that the load is evenly distributed along an axial

length of basket equal to the fuel basket support structure. For example, the pressure applied to an impacted cell wall during a 0-degree side drop event is calculated as follows:

$$p = \frac{a_v W}{L \ell}$$

where:

p = pressure

a_v = ratio of the impact acceleration to the gravitational acceleration

W = weight of a stored fuel assembly

L = axial length of the fuel basket support structure

ℓ = width of a cell wall

For the case of a 45-degree side drop the pressure on any cell wall equals p (defined above) divided by the square root of two. Figures 2.6.13, 2.6.14, and 2.6.15 show the details of the fuel assembly pressure load on the fuel basket.

(b) Internal/External Pressure (Load Case E1 (Table 2.1.7))

Design internal pressure in the MPC model is applied by specifying pressure on the inside surface of the enclosure vessel. The magnitude of the internal pressure applied to the model is taken from Table 2.1.1.

For this load condition, the center of the fuel basket is fixed in all degrees of freedom.

(c) Temperature (Load Cases F1 (Table 2.1.6) and E4 (Table 2.1.7)

Temperature distributions are developed in Chapter 3 and applied as nodal temperatures to the finite element model of the MPC enclosure vessel (confinement boundary). Maximum design heat load has been used to develop the temperature distribution used to demonstrate compliance with ASME Code stress intensity levels. A plot of the applied temperature distribution as a function of radius is shown in Figure 2.6.1. Figure 2.6.12 shows the MPC-68 with the typical boundary conditions for all thermal and pressure load cases.

- Analysis Procedure

The analysis procedure for this set of load cases is as follows:

1. The stress intensity and deformation field due to the combined loads is determined by the finite element solution. Results are then subject to post-processing.

2. The results for each load combination are compared to allowables. The comparison with allowable values is made in Subsection 2.6.1.4.

2.6.1.3.1.2 Analysis of Load Cases E1.a and E1.c (Table 2.1.7)

Load Cases E1.a and E1.c pertain to the performance of the helium retention boundary structure (enclosure vessel) considered as an ASME Section III, Subsection NB pressure vessel.

Since the MPC shell is a pressure vessel, the classical Lame's calculations should be performed to demonstrate the shell's performance as a pressure vessel. Note that dead load has an insignificant effect on this stress state. Calculations for the shell under internal pressure are performed initially. Subsequently, a finite element analysis on the entire helium retention boundary as a pressure vessel subject to both internal pressure and temperature gradients is performed. Finally, confirmatory hand calculations are performed to gain confidence in the finite element predictions,

- Lame's Solution for the MPC Shell

The stress from internal pressure is found using classical formulas:

Define the following quantities:

P = pressure, r = MPC radius, and t = shell thickness.

Using classical thin shell theory, the circumferential stress, $\sigma_1 = Pr/t$, the axial stress $\sigma_2 = Pr/2t$, and the radial stress $\sigma_3 = -P$ are computed for both normal and accident internal pressures. The results are given in the following table:

Classical Shell Theory Results for Normal and Accident Internal Pressures				
Item	σ_1 (psi)	σ_2 (psi)	σ_3 (psi)	$\sigma_1 - \sigma_3$ (psi)
P= 100 psi	6,838	3,419	-100	6,938
P= 200 psi	13,677	6,838	-200	13,877

Table 2.1.21 provides the allowable membrane stress for Load Case E1 for Alloy X under normal conditions of transport. It is seen that a safety factor greater than 1.0 exists

$$FS = \frac{18.1\,ksi}{6.938\,ksi} = 2.6$$

Subsection 2.7.3.3.1 develops the corresponding safety factor for the case of accident pressure.

- Finite Element Analysis (Load Case E1.a and E1.c of Table 2.1.7)

Having performed the classical "thin shell under pressure" evaluation, a finite element analysis is performed where the interaction between the end closures and the MPC shell is rigorously modeled.

The MPC shell, the top lid, and the baseplate together form the helium retention boundary (enclosure vessel) for storage of spent nuclear fuel. In this section, the operating condition consisting of dead weight, internal pressure, and thermal effects for the normal heat condition of transport is evaluated. The top and bottom plates of the MPC enclosure vessel (EV) are modeled using plane axisymmetric elements, while the shell is modeled using the axisymmetric thin shell element. The thickness of the top lid varies in the MPC types and can be either a single thick lid, or two lids, welded around their common periphery; the minimum thickness top lid is modeled in the finite element analysis. As applicable, the results for the MPC top lid are modified to account for the fact that in the dual lid configuration, the two lids act independently under mechanical loading. The temperature distributions for all MPC constructions are nearly identical in magnitude and gradient. Temperature differences across the thickness of both the baseplate and the top lid exist during HI-STAR 100's operations. There is also a thermal gradient from the center of the top lid and baseplate out to the shell wall. The metal temperature profile is essentially parabolic from the centerline of the MPC out to the MPC shell. There is also a parabolic temperature profile along the length of the MPC canister. Figure 2.6.20 shows a sketch of the confinement boundary structure with identifiers A-I (also called locating points) where temperature input data is used to represent a continuous temperature distribution for analysis purposes. The overall dimensions of the confinement boundary are also shown in the figure.

Section 3.4 provides the desired temperatures for thermal stress analysis of the helium retention boundary. From the tables (3.4.22 and 3.4.23), it is seen that the distribution from PWRs provides the largest temperature gradients in the baseplate (from centerline to outer edge) and in the shell (from the joint at the baseplate to the half-height of the cask). It will be shown later that stress intensities are greatest in these components of the vessel. Because of the intimate contact between the two lid plates when the MPC lid is a two-piece unit, there is no significant thermal discontinuity through the thickness; thermal stresses arising in the MPC top lid will be bounding when there is only a single lid. Therefore, for thermal stresses, results from the analysis

that considers the lid as a one-piece unit are used and are amplified to reflect the increase in stress in the dual lid configuration

Figure 2.6.21 shows details of the finite element model of the top lid (considered as a single piece), canister shell, and baseplate. The top lid is modeled with 40 axisymmetric quadrilateral elements; the weld connecting the lid to the shell is modeled by a single element solely to capture the effect of the top lid attachment to the canister offset from the middle surface of the top lid. The MPC canister is modeled by 50 axisymmetric shell elements, with 20 elements concentrated in a short length of shell appropriate to capture the so-called "bending boundary layer" at both the top and bottom ends of the canister. The remaining 10 shell elements model the MPC canister structure away from the shell ends in the region where stress gradients are lower (from the physics of the problem). The baseplate is

modeled by 20 axisymmetric quadrilateral elements. Deformation compatibility at the connections is enforced at the top by the single weld element, and deformation and rotation compatibility at the bottom by additional shell elements between nodes 106-107 and 107-108.

The geometry of the model is listed below (terms are defined in Figure 2.6.21):

H_t = 9.5" (the minimum total thickness lid is assumed)

R_L = 0.5 x 67.25" (Nominal dimension used for calculation)

L_{MPC} = 190.5" (Nominal dimension used for calculation)

t_s = 0.5" (MPC drawing in Section 1.4)

R_S = 0.5 x 68.375" (Nominal radius)

t_{BP} = 2.5" (MPC drawing in Section 1.4)

βL = $2\sqrt{R_s t_s} \approx 12$" (The bending boundary layer)

Stress analyses are carried out for two cases as follows:

a. internal pressure = 100 psi

b. internal pressure = 100 psi, plus applied temperature field

The dead weight of the top lid reduces the stresses due to pressure. For example, the equivalent pressure simulating the effect of the weight of the top lid is an external pressure of 3 psi, which reduces the pressure difference across the top lid to 97 psi. Thus, for conservatism, dead weight of the top lid is neglected to provide additional conservatism in the results. The dead weight of the baseplate, however, adds approximately 0.73 psi to the effective internal pressure acting on the base. The effect of dead weight is still insignificant compared to the 100 psi design pressure, and is therefore neglected. The thermal loading in the confinement vessel is obtained by developing a parabolic temperature profile to the entire length of the MPC canister and to the top lid and baseplate. The temperature data provided at locations A-I in Figures 2.6.20 and 2.6.21 are sufficient to establish the profiles. Through-thickness temperatures are assumed linearly interpolated between top and bottom surfaces of the top lid and baseplate. All material properties and expansion coefficients are considered to be temperature-dependent in the model.

Results for stress intensity are reported for the case of internal pressure alone and for the combined loading of pressure plus temperature (Load Case E1.c in Table 2.1.7). Tables 2.6.6 and 2.6.7 report results at the inside and outside surfaces of the top lid and baseplate at the centerline and at the extreme radius. Canister results are reported in the "bending boundary layer" and at a location near mid-length of the MPC canister. In the tables, the calculated value is the value from the finite element analysis, the categories are P_m = primary membrane; $P_L + P_b$ = local membrane plus primary

bending; and $P_L + P_b + Q$ = primary plus secondary stress intensity. The allowable stress intensity value is obtained from the appropriate table in Section 2.1 for Level A conditions, and the safety factor SF is defined as the allowable strength divided by the calculated value. Allowable stresses for Alloy X are taken at 300° F, which bounds the normal heat condition of transport temperatures everywhere except at the mid-length position of the MPC shell (Location I in Figure 2.6.20) during the normal operation. At Location I, the allowable strength is taken at 400°F. The results given in Tables 2.6.6 and 2.6.7 demonstrate the ruggedness of the MPC as a confinement boundary. Since mechanically induced stresses in the top lid are increased when a dual lid configuration is considered, the stress results obtained from an analysis of a single top lid must be corrected to reflect the maximum stress state when a dual lid configuration is considered. The modifications required are based on the following logic:

Consider the case of a simply supported circular plate of thickness h under uniform lateral pressure "q". Classical strength of materials provides the solution for the maximum stress, which occurs at the center of the plate, in the form:

$\sigma_s = 1.225q(a/h)^2$ where a is the radius of the plate and h is the plate thickness.

Now consider the MPC simply supported top lid as fabricated from two plates "1" and "2", of thickness h_1 and h_2, respectively, where the lower surface of plate 2 is subjected to the internal pressure "q", the upper surface of plate 1 is the outer surface of the helium retention boundary, and the lower surface of plate 1 and the upper surface of plate 2 are in contact. The following sketch shows the dual lid configuration for the purposes of this discussion:

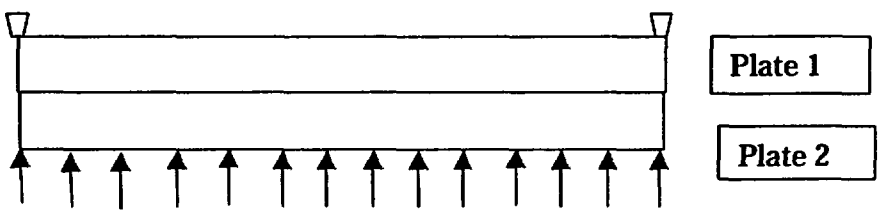

From classical plate theory, if it is assumed that the interface pressure between the two plates is uniform and that both plates deform to the same central deflection, then if

$h_1+h_2 = h$, and if $h_2/h_1 = r$

the following relations exist between the maximum stress in the two individual plates, σ_1, σ_2 and the maximum stress σ_s in the single plate of thickness "h":

$$\frac{\sigma_1}{\sigma_s} = \frac{(1+r)^2}{(1+r^3)} \qquad \frac{\sigma_2}{\sigma_s} = \frac{(1+r)^2}{(1+r^3)}r$$

Since the two lid thicknesses are the same in the dual lid configuration, r = 1.0 so that the stresses in plates 1 and 2 are both two times larger than the maximum stress computed for the single plate lid having the same total thickness. In Tables 2.6.6 and 2.6.7, bounding results for the dual lid configuration are reported by using these ratios at all locations in the top lid.

- Confirmatory Closed Form Solution

The results in Table 2.6.6 and 2.6.7 also show that the baseplate and the shell connection to the baseplate are the most highly stressed regions under the action of internal pressure. To confirm the finite element results, an alternate closed form solution is performed using classical plate and shell theory equations that are listed in or developed from the reference Timoshenko and Woinowsky-Krieger, Theory of Plate and Shells, McGraw Hill, Third Edition.

Assuming that the thick baseplate receives little support against rotation from the thin shell, the bending stress at the centerline is evaluated by considering a simply supported plate of radius a, and thickness h, subjected to lateral pressure p. The maximum bending stress is given by

$$\sigma = \frac{3(3+\nu)}{8} p\left(\frac{a}{h}\right)^2$$

where:

a = .5 x 68.375"

h = 2.5"

ν = 0.3 (Poisson's Ratio)

p = 100 psi

Calculating the stress in the plate gives σ = 23,142 psi.

Now consider the thin MPC shell (t = 0.5") and first assume that the baseplate provides a clamped support to the shell. Under this condition, the bending stress in the thin shell at the connection to the plate is given as:

$$\sigma_{Bp} = 3p\frac{a}{t}\frac{(1-\nu/2)}{\sqrt{3}(1-\nu^2)^{1/2}} = 10{,}553 \text{ psi}$$

In addition to this stress, there is a component of stress in the shell due to the baseplate rotation that causes the shell to rotate. The joint rotation is essentially driven by the behavior of the baseplate as a simply supported plate; the shell offers little resistance because of the disparity in thickness and will essentially follow the rotation of the thick plate.

Using formulas from thin shell theory, the additional axial bending stress in the shell due to this rotation θ can be written in the form

$$\sigma_{B\theta} = 12\,\beta\,D_s\frac{\theta}{t^2}$$

where

$$\theta = pa^3/8D(1+\nu)*\left(1/1+\alpha\right)$$

and

$$D = \frac{Eh^3}{12(1-\nu^2)} \qquad E = \text{plate Young's Modulus}$$

and

$$\alpha = \frac{2\beta a t^3}{h^3(1+\nu)}$$

$$\beta^2 = \sqrt{3(1-\nu^2)}/at$$

$$D_s = \frac{Et^3}{12(1-\nu^2)}$$

Substituting the numerical values gives

$$\sigma_{B\_} = 40{,}563 \text{ psi}$$

Note that the approximate solution is independent of the value chosen for Young's Modulus as long as the material properties for the plate and shell are the same.

Combining the two contributions to the shell bending stress gives the total extreme fiber stress in the longitudinal direction as 51,116 psi. Note that the same confirmatory solution can be obtained from Roark's Formulas for Stress and Strain, McGraw-Hill, 4th Edition, Table XIII. Case 30 in that text contains the solution for the bending moment at the intersection of a long cylinder and a flat plate due to internal pressures. Using the handbook formula, 53,090 psi is obtained.

The baseplate stress value, 23,142 psi, compares well with the finite element result 20,528 psi (Table 2.6.6). The shell joint stress, 51,116 psi, is greater than the finite element result (43,986 psi in Table 2.6.6). This is due to the local effects of the shell-to-baseplate connection offset. That is, the connection between shell and baseplate in the finite element model is at the surface of the baseplate, not at the middle surface of the baseplate. This offset will cause an additional bending moment that will reduce the rotation of the plate and hence, reduce the stress in the shell due to the rotation of the baseplate.

In summary, the approximate closed form solution confirms the accuracy of the finite element analysis in the MPC baseplate region.

2.6.1.3.1.3 Supplementary MPC Calculations

The MPC has been subject to extensive analysis in the companion HI-STAR 100 FSAR (storage) submittal (Docket Number 72-1008). For completeness, certain information from the FSAR has been repeated here and in Section 2.7 where the results are germane to normal conditions of transport and to hypothetical accident conditions of transport, respectively. Because of the different requirements for storage and transport submittals, some of the results presented here may not be directly associated with a load case defined in Tables 2.1.6 and 2.1.7. Nevertheless, their inclusion here is warranted for completeness. In this subsection, results are summarized from these analyses that pertain to normal conditions of transport. In Section 2.7, addition results pertaining to the hypothetical accident conditions of transport are reported.

- Structural Analysis of the Fuel Support Spacers (Load Case F2)

Upper and lower fuel support spacers are utilized to position the active fuel region of the spent nuclear fuel within the poisoned region of the fuel basket. It is necessary to ensure that the spacers will continue to maintain their structural integrity during normal conditions of transport. Ensuring structural integrity implies that the spacer will not buckle under the maximum compressive load, and that the maximum compressive stress will not exceed the compressive strength of the spacer material (Alloy X). Detailed calculations demonstrate that large structural margins in the fuel spacers are available for the entire range of spacer lengths that may be used in HI-STAR 100 applications (for the various acceptable fuel types). The fuel spacers are shown to meet ASME Code Subsection NG stress limits (the spacers are not, however, required to be designed to any ASME Code, however). Standard Code design formulas are used to evaluate elastic stability limits. For normal conditions of transport (Level A Service Condition), a 10g deceleration load is applied and stress and stability issues are considered. The result is summarized below:

Fuel Spacers - Minimum Safety Factors (Load Cases F2)			
Item	Load (lb.)	Capacity (lb.)	Safety Factor
Axial Load - Level A	16,800	46,446	2.76

The safety factor is greater than 1.0, which demonstrates that the fuel spacers meet the requirements of Level A Service Conditions for the normal condition of transport.

The above result also represents a conservative minimum safety factor for the Trojan failed fuel can (FFC) spacer under normal conditions of transport. The reasons are (i) the FFC spacer has the same cross sectional area as the PWR lower fuel spacer and (ii) the FFC spacer supports less weight than the PWR lower fuel spacer. Whereas the PWR lower fuel spacer is designed and licensed to support the design fuel assembly weight of 1680 lb, the maximum weight that the FFC spacer supports is somewhat less than 1680 lb since the total weight of the Trojan FFC plus its contents, which includes the FFC spacer, is restricted to 1680 lb.

- MPC Shell Stability

The MPC shell is examined for elastic/plastic instability due to external pressure or compressive loads introduced as part of the load cases (design external pressure, normal transport). Each load component is examined separately. Design external pressure is applied to the outer surface of the enclosure vessel shell in the MPC model. The magnitude of the external pressure applied to the model is taken from Table 2.1.1. Analysis of the MPC under external pressure is performed using the methodology of ASME Code Case N-284 [2.1.8]. The following stability evaluations are performed for the MPC shell for normal transport conditions:

a. Normal Transport Deceleration Load from 10CFR71.45(b).
b. Design external pressure plus a 1g compressive dead load.

The following table summarizes the limiting result from the calculations:

MPC Shell - Elastic/Plastic Stability (ASME Code Case N-284) - Minimum Safety Factors			
Item	Value	Allowable	Safety Factor
Load Case 10CFR71.45(b) (Yield)	0.193	2.0	10.36
Load Case E1.b - Table 2.1.7 (Stability Interaction Curve)	0.832	1.0	1.20

Note that for the load case associated with the 10CFR71.45(b) requirement, the yield strength criteria in the Code Case N-284 method governs the "allowable" value. In this event, the safety factor 2.0, built into the Code Case, is included in the tabular result in order to obtain the actual safety factor with respect to the yield strength of the material.

The results demonstrate that the MPC shell meets the requirements of Code Case N-284. Note that the stability results presented above are very conservative. The stability analyses carried out for the MPC shell assumed no axial stiffening from the fuel basket supports that run the full length of the shell. An analysis that included the effect of the stiffening (and therefore, recognized the fact that instability will most likely occur between stiffeners) will give increased safety factors for Load Case E1.b.

2.6.1.3.2 Overpack Stress Calculations

The structural functions of the overpack are stated in Section 2.1. The analyses documented here demonstrate the ability of components of the HI-STAR 100 overpack to perform their structural functions under normal conditions of transport. Load cases applicable to the structural evaluation of the HI-STAR 100 overpack under these conditions are compiled in Table 2.1.8.

In this subsection, stresses and stress intensities in the HI-STAR 100 overpack due to the combined effects of thermal gradients, pressure, and mechanical loads are presented. The results are obtained from a series of finite element analyses on the complete overpack and separate analyses on overpack components.

2.6.1.3.2.1 Finite Element Analysis - Load Cases 1 to 4 in Table 2.1.8

Load Case 1 pertains to a demonstration of the containment boundary as an ASME "NB component under Design Pressure and Level A Service Condition thermal loading. Other cases pertain to handling inertia loads imposed during normal conditions of transport and an extreme environmental condition. To analyze these load cases, a suitable finite element model of the complete overpack is required. As noted earlier, since the identical finite element model is used in Section 2.7 to analyze the hypothetical accident conditions of transport, the following discussion refers to both sets of analyses to avoid textual repetition.

- Description of Finite Element Model (Normal Conditions and Hypothetical Accident)

The purpose of the HI-STAR 100 overpack model is to calculate stresses and stress intensities resulting from the loadings defined in Subsection 2.1 and compiled into load cases in Table 2.1.8.

A three-dimensional finite element model of the HI-STAR 100 overpack is used to assess the effects of loads associated with normal conditions of transport. The same finite element model is used in Section 2.7 to evaluate the effects of loading due to hypothetical accident scenarios. The overpack is a large structure subject to a variety of complex loads and boundary conditions. The finite element model developed for this analysis allows efficient determination of the stresses in this complex structure.

The finite element model of the overpack is constructed using ANSYS [2.6.4]. This model is duplicated in the HI-STAR 100 FSAR (10CFR72) submittal for storage.

For structural analysis purposes, the overpack is assumed to be symmetric about a diametral mid-plane. This assumption is reasonable because the purpose of the model is to investigate global stresses in the model. The model is not intended to resolve effects due to small penetrations that produce peak stresses (which are significant only in cyclic fatigue conditions).

Element plots of the model are shown in a series of figures (Figures 2.6.16 through 2.6.19C). Figure 2.6.16 shows an overall view of half of the overpack subject to detailed finite element analysis. The view is directed toward the internal cavity and shows the surface of symmetry. To enforce symmetry,

displacements normal to the plane of symmetry at all nodes on the plane of symmetry are not permitted. Out-of-plane rotations at the nodes on the plane of symmetry are also set to zero. The basic building blocks of the finite element model are 20-node brick (SOLID95), 8-node brick (SOLID45), and 6-node tetrahedron elements (SOLID45). These are 3-D solid elements with 3 degrees of freedom at each node (three linear displacement degrees of freedom). Element densities are increased towards the top and bottom of the model in order to provide increased resolution of the stress fields in those regions.

The top flange/closure plate interface is modeled using linear spring elements (COMBIN14). The concentric seals are not modeled explicitly. The model is not intended to resolve the stress field around the grooves for the seals. The status of joint seal is ascertained by "compression springs" that simulate the O-ring gaskets. Contact between the overpack top flange and closure plate is verified by checking the status of these spring elements. If contact between the closure plate and top flange is maintained under an applied loading (indicated by a compressive load in the "compression springs"), then the integrity of the seal is determined to have been maintained under that load.

The overpack closure bolts are modeled with beam elements (BEAM4). The top of the beam elements represent the bolt head and are connected to the overpack closure plate. The bottom of the elements represents the threaded region of the bolt and is connected to nodes of elements representing the top flange. Torsional displacements of the bolts are suppressed to conform to the degrees of freedom permitted at the nodes of the connecting solid elements.

The inner shell of the overpack is modeled with two solid element layers through the thickness of the shell.

Each of the lifting trunnions is modeled as three rigid beam elements (BEAM4) connected to the top forging. The beams extend from the forging and meet at a single node location. Trunnion stress analysis is documented in Subsection 2.5; the inclusion of the trunnion herein is solely to provide the appropriate offset for handling loads. The beam elements representing the trunnions are not shown on any of the figures describing the finite element model.

The neutron shield material is not a load bearing or supporting component in the finite element model. However, the weight of the neutron shield material must be included in the model in order to obtain the proper inertia loads. The neutron shield material is modeled with SOLID45 elements having a weight density that is specified in Subsection 2.3.2.1. In the model herein, the neutron shield material is included as an element set to ensure that proper accounting of total weight (and accompanying deceleration loads) occurs. Therefore, the neutron shield material must be assigned a Young's Modulus in the model. A value approximately equal to 1% of the Modulus of the steel load carrying components is assigned to the neutron shield material to insure that the neutron shield material serves as a load rather than a structural member in the model.

Figure 2.6.17 shows the finite element grid used for the bottom plate.

Figure 2.6.18 provides the details of the solid element grid for the top forging. Also shown in the figure are the line elements that represent the lid bolts. Since the lid is not shown in this figure, the upper part of the line elements is not attached to any node point.

Figure 2.6.19 shows a view from above of the overpack lid and details the element grid around the 180-degree periphery modeled.

Figure 2.6.19A shows the finite element grid for the inner shell and the five intermediate shells. The inner shell is modeled with two layers of solid elements; each of the five intermediate shells is modeled by a single layer of solid elements to capture a linear stress distribution through the thickness.

Figure 2.6.19B presents the solid element distribution modeling the Holtite-A material. As noted previously, the structural effect of this material is neglected; the elements are included in the model to insure a proper mass distribution for the different analyses.

Finally, Figure 2.6.19C shows the shell element grid used to model the enclosure shell. Thin shell elements are used to simulate all components of the enclosure shell.

It is recognized that the layered shells of the overpack (shown in Figures 2.6.16 and 2.6.19A) are connected to each other and to the inner shell only at their top and bottom extremities. The finite element model must allow for separation between the intermediate shells in the non-connected regions under certain loading. Likewise, the intermediate shells cannot interpenetrate each other or the inner shell structure. To simulate these competing effects without making the model non-linear because of the introduction of contact elements, radial coupling of adjacent intermediate shell nodes is used in appropriate locations of the model. It is necessary to utilize physical reasoning to establish the regions where a nodal coupling is warranted because the shells cannot separate from each other. For example, radial coupling over two 60-degree spans serves to prevent interpenetration where it may occur during an impact simulation. Similarly, where physical reasoning indicates that a separation between the shell layers may occur, the nodes are left uncoupled. For example, when ovalization of the shells may occur under a specified loading, no coupling between shells is assumed. Figure 2.6.22 illustrates the nodal coupling pattern. The intermediate shell nodes that lie in the 60-degree sector between the top and bottom portions of the model remain uncoupled. The intermediate shells, in the uncoupled region, are free to separate from one another as the overpack cross section ovalizes during side impact. This modeling approach ensures that load transfer in a drop with significant lateral deceleration loads is modeled correctly. With respect to the overpack model, "bottom portion" refers to the 60-degree segment of the model closest to the point of impact. Conversely, "top portion" refers to the 60-degree sector farthest from the point of impact. This nodal coupling arrangement conservatively represents the structural behavior of the intermediate shells. In addition, no axial or circumferential nodal coupling has been used between adjacent intermediate shells. Thus, axial bending stiffness of the composite shell structure is conservatively underestimated. This underestimation of stiffness provides additional conservatism to the predicted values for safety factors.

The rotation trunnions present in the first seven HI-STAR 100 units (see Subsection 2.5) are conservatively neglected in the finite element models. Separate calculations, where applicable, are summarized later.

Elements at locations of welds in the modeled components are assumed to have complete connectivity in all directions. Material in the model located at positions where welds exist is assumed to have material properties identical to the base material.

To summarize, the total number of nodes and elements in the overpack model are 11265 and 8642, respectively. The elements used are SOLID45, SOLID95, BEAM4, SHELL63, and COMBIN14.

For all structural analyses, material properties are obtained from the appropriate tables in Section 2.3. Property data for temperatures that are not listed in the material property tables are obtained by linear interpolation. Property values are not extrapolated beyond the limits of the code for any structural analysis.

- Description of Individual Loads and Boundary Conditions

The method of applying each individual load to the overpack model is described in this subsection. The individual loads are defined in Subsection 2.1.2.1 and are listed in Table 2.1.8 for normal conditions of transport. A free-body diagram of the overpack corresponding to each individual load is given in Figures 2.1.5 through 2.1.14. The figures presented in Section 2.1 present a general description of the loading but are lacking in specific details concerning the extent of the area exposed to the load. Therefore, in this subsection, each of the applied loadings for the various cases considered is further discussed and additional details on the specific application of the loads are provided. In the following discussion, reference to vertical and horizontal orientations is made. Vertical refers to the longitudinal direction along the cask axis, and horizontal refers to a lateral direction.

Quasi-static methods of structural analysis are used. The effects of any dynamic load factors (DLF) are discussed in the final evaluation of safety factors. The load combinations are formed from the solution of individual load cases

(a) Accelerations (Used to Form Load Cases 3 and 4 in Table 2.1.8)

Table 2.1.10 provides the bounding values of the accelerations used for design basis structural evaluation. The loading is imposed by amplifying the gravity vector by the design basis deceleration. The proper distribution of the body forces induced by the accelerations is internally consistent based on the mass distribution associated with the different components of the finite element model. How these acceleration induced loadings are put in equilibrium with reaction loads from the impact limiters is discussed in detail in a later section.

In the following, appropriate boundary conditions for analyses for load cases associated with normal conditions of transport (Table 2.1.8) are discussed. However, since the same finite element model is used to evaluate hypothetical accident conditions of transport (Table 2.1.9) in Section 2.7, boundary conditions for Section 2.7 analyses are discussed here, as well, in the ongoing interest of conciseness of the presentation.

Boundary conditions for the model are as follows:

i. End drop - In an end drop, displacement fixities are applied to the model on a cross-section through the top flange that is normal to the drop direction. Figures 2.1.7 and 2.1.8 show the free-body diagram for these load events. No reactions or internal body forces are shown. Further discussion is provided in Section 2.7.

ii. Side drop - In a side drop, the inertia loads are reacted by the impact limiters. The overpack is in equilibrium with essentially end pinned supports. Figure 2.1.9 shows the configuration for this case. Further elaboration is provided in Section 2.7.

(b) Loads on the Overpack from the MPC

Pressures are applied on the inner surfaces of the overpack model to represent loads from the MPC for the drop loads.

i. End drop - For a bottom end drop (Load Case1, Hypothetical Accident, Table 2.1.9), the pressure load on the inside surface of the overpack bottom plate is assumed to be uniform and represents the load from the heaviest MPC (Figure 2.1.7). Note that this analysis conservatively assumes that the drop angle is not exactly 90° from the horizontal; attention is focussed on the overpack baseplate subject to the deceleration load from the heaviest MPC (applied as a uniform pressure) without the ameliorating effect of opposing distributed reaction from the impacted surface.

The magnitude of the pressure is the weight of the heaviest fully loaded MPC divided by the area of the faces of the elements over which the pressure is applied. The weight of the heaviest fully loaded MPC is taken from the tables in Section 2.2, and is amplified by the design basis deceleration. Amplified loads from the MPC (weight times 60g acceleration) are applied as a pressure load to the entire inner surface of the bottom plate or the lid depending on the drop orientation. Note that for a top end drop, the MPC inertia loads act only on an outer annulus of the lid due to the raised surface deliberately introduced to act as a "landing" area for the MPC and reduce lid stress and deformation. By neglecting this raised annular area on the lid and applying the MPC load as a uniform pressure, stresses in the lid and the bolts are maximized. Further discussion is provided in Section 2.7.

ii. Side drop - The shape and extent of the pressure distribution is determined from the results of the structural analysis of the MPC under similar orientations. In the MPC structural analysis, the extent of the support conditions of the MPC shell is determined with contact elements. In the analysis of the MPC under amplified inertia loads, the overpack is represented as a rigid circular surface. Based on results from the MPC evaluations, the loaded region is taken as 72 degrees (measured from the vertical). The MPC load on the overpack model is applied uniformly along the axial length of the inner surface of the model. Further discussion is provided in Section 2.7.

iii. Oblique drop - Figures 2.1.10 and 2.1.11 show the balance loading applied for the oblique drop. A fixed node is defined away from the assumed impact point to insure that the package is in equilibrium under the applied loads. This drop orientation is only considered for the hypothetical accident evaluation. Therefore, a detailed discussion as to the methodology used to apply the loads and insure overall equilibrium is provided in Section 2.7 (specifically 2.7.1.3 and 2.7.1.4).

(c) Temperature (Used to Form Load Case 05 in Table 3.1.5)

Based on the results of the thermal evaluation for the normal hot environment presented in Chapter 3, a temperature distribution with a bounding gradient is applied to the overpack model. The purpose is to determine the stress intensities that develop in the overpack under the applied thermal load. A plot of the applied temperature distribution as a function of radius is shown in Figure 2.6.2.

The temperature distribution is applied to the ANSYS finite element model at discrete nodes using a parabolic curve fit of the computed distribution.

(d) Internal Pressure (Used to Form Load Cases 1 in Table 2.1.8)

Design internal pressure is applied to the overpack model. All interior overpack surfaces, including the inner shell, the bottom of the closure plate, and the top of the bottom plate are loaded with pressure. The magnitude of the internal pressure applied to the model is taken from Table 2.1.1. Figure 2.1.5 shows the displacement constraints for this load case. Figure 2.6.23 is a finite element grid plot showing the surfaces where internal pressure is applied.

(e) External Pressure (Used to Form Load Case 2 in Table 2.1.8)

Design external pressure is applied to the overpack model. External pressure is applied to the model as a uniform pressure on the outer surface of the model. The magnitude of the external pressure applied to the model is taken from Table 2.1.1. Figure 2.1.6 shows the displacement constraints for this load case. External pressures are imposed in the same manner as shown in Figure 2.6.23 except that the surfaces and magnitude are different.

(f) Bolt Pre-load (Used in all load cases in Tables 2.1.8 and 2.1.9)

The overpack closure bolts are torqued to values predicted to preclude separation. This torque generates a pre-load in the bolts and stresses in the closure plate and top flange in the region adjacent to the bolts. The finite element representation of the bolt elements is shown in Figure 2.6.18. The initial preload of the bolts is applied to the overpack model by applying an initial strain to the beam elements representing the bolts. This induces a tensile stress in each of the bolts and a corresponding compression in the seals (represented by spring elements). This load case is present in every load combination.

(g) Fabrication stresses

Fabrication stresses are conservatively computed for the inner shell and all of the intermediate shells. Fabrication effects are not easily introduced into the finite element model unless compression-only contact elements are used. Since the fabrication stresses are circumferential secondary stresses in the shells, the incorporation of this load case is best accomplished outside of the finite element analysis. Therefore, there is no fabrication load case associated with the finite element analyses.

- Finite Element Analysis Solution Procedure

The analysis procedure is as follows:

1. The stress and deformation field due to each individual load is determined.

2. The results from each individual load case are combined in a postprocessor to create each load case. The load cases analyzed are listed in Table 2.1.8 for normal conditions of transport and in Table 2.1.9 for hypothetical accident conditions of transport.

3. The results for each load case are compared to allowables. The calculated values are compared with allowable values in Subsection 2.6.1.4 for normal conditions of transport and in an appropriate subsection of Section 2.7 for hypothetical accident conditions.

2.6.1.3.2.2 Fabrication Stress

The fabrication stresses originate from welding operations to affix the intermediate shells in position. As the molten weld metal solidifies, it shrinks pulling the two parts of the shells together. Adjacent points at the weld location will close together after welding by an amount "δ" which is a complex function of the root opening, shape of the bevel, type of weld process, etc. The residual stresses generated by the welding process are largely confined to the weld metal and the "heat affected zone". The ASME Code recognizes the presence of residual stresses in the welds, but does not require their calculation. The Code also seeks to minimize fabrication stresses in the welds through controlled weld procedures. Nevertheless, fabrication stresses cannot be eliminated completely.

The computation of fabrication stresses is carried out to comply with the provisions of Regulatory Guide 7.8, Article C-1.5. The Regulatory Guide requires that "Fabrication and installation stresses in evaluating transportation loadings should be consistent with the joining, forming, fitting, and aligning processes employed during the construction of casks...the phrase fabrication stresses includes the stresses caused by interference fits and the shrinkage of bonded lead shielding during solidification but does not include the residual stresses due to plate formation, welding, etc.".

A literal interpretation of the above-cited Regulatory Guide text exempts the HI-STAR 100 designer from computing the stresses in the containment and intermediate shells due to welding. However, in the interest of conservatism, an upper bound, on the stresses induced in the containment shell and in the intermediate shells, is computed for the fabrication process.
To calculate the so-called fabrication stresses, it is recalled that in affixing the intermediate shells to the cask body, the design objective does not call for a definite radial surface pressure between the layers. Rather, the objective is to ensure that the shells are not loosely installed. Fortunately, extensive experience in fabricating multi-layer shells has been acquired by the industry over the past half-century. The technology that was developed and has matured for fabrication in older industries (such as oil and chemical) is used in HI-STAR 100 fabrication of the multi-layered shells. Mock-up tests on carbon steel coupons indicate that the total shrinkage after welding can range from 0.010" to 0.0625" for the bevel and fit-up geometry in the HI-STAR 100 design drawings. Therefore, the evaluations are carried out using the upper bound gap of 0.0625". To bound the computed stresses even further, the inter-layer friction coefficient is set equal to zero. It is intuitively apparent that increasing the friction increases the localized stresses near the "point of pull" (i.e., the weld) while mitigating the stresses elsewhere. Since the object is to maximize the distributed (membrane) stress, the friction coefficient is set equal to zero in the analysis.

A two-dimensional finite element analysis of the inner confinement shell and the five intermediate shells is performed to establish the level of fabrication circumferential stress developing during the assembly process. A 180-degree section through the overpack, consisting of six layers of metal, is modeled. The ANSYS finite element code is used to model the fabrication process; each layer is modeled using PLANE42 four node quadrilateral elements. Contact (or lack of contact) is modeled by CONTAC48 point-to-surface elements. Symmetry boundary conditions apply at 90 degrees, and radial movement of the inner node point of the confinement layer is restrained. At -90 degrees, the inner confinement layer is restrained while the remaining layers are subject to a prescribed circumferential displacement d to stretch the layer and to simulate the shrinkage caused by the weld process. Although the actual fabrication process locates the longitudinal weld in each layer at different circumferential orientation, in the analytical simulations all layer welds are located together. This is acceptable for analysis since the stress of interest is the primary membrane component. Figure 2.6.24 shows a partial free body of a small section of one of the layers. Normal pressures p develop between each layer due to the welding process; shear stresses due to friction between the layers also develop since there is relative circumferential movement between the layers. Figure 2.6.25 shows a free body of the forces that develop on each layer.

The fabrication stress distribution is a function of the coefficient-of-friction between the layers. For a large enough coefficient-of-friction the effects of the assembly process are localized near the weld. Localized stresses are not considered as primary stresses. For a coefficient-of-friction = 0.0, the

membrane hoop stress in the component shells is non-local in nature. Therefore, the fabrication stress computation conservatively considers only the case coefficient of friction (COF) = 0.0 since this will develop the largest in-plane primary membrane stress in each layer. The simulation is nonlinear in that each of the contact elements is checked for closure during increments of applied loading (the weld displacement).

The results from the analyses are summarized in the table below:

Fabrication Stresses in Overpack Shells - Minimum Safety Factors (Level A Service Condition at Assembly Temperature)			
Item	Value (ksi)	Allowable (ksi) (Note3)	Safety Factor
First Intermediate Shell (Note 1)	11.22	52.5	4.68
Fourth Intermediate Shell (Note 1)	7.79	52.5	6.74
Inner Shell Mid Plane (Note 2)	10.6	69.9	6.59
Inner Shell Outer Surface (Note 2)	16.27	69.9	4.30

Notes:

1. The fabrication stress is a tensile circumferential stress.
2. The fabrication stress is a compressive circumferential stress
3. Fabrication stresses are self-limiting and are therefore classified as "secondary" and are compared to 3 times the allowable membrane stress or stress intensity.

The above table leads to the conclusion that the maximum possible values for stresses resulting from HI-STAR 100 fabrication process are only a fraction of the relevant ASME Code limit.

2.6.1.3.2.3 Structural Analysis of Overpack Closure Bolting (Load Case1 - Table 2.1.8)

Stresses are developed in the closure bolts due to pre-load, pressure loads, temperature loads, and accident loads. Closure bolts are explored in detail in Reference [2.6.3] prepared for analysis of shipping casks. The analysis herein of the overpack closure bolts under normal conditions of transport and for the hypothetical accident conditions uses the methodology and the procedures defined and explained in Reference [2.6.3]; the sole exception is that some of the formulas in the reference are modified to account for the annulus on the inner surface of the overpack closure lid; this annulus exists for the sole purpose of ensuring that the interface area between the MPC lid and the overpack top closure is a peripheral ring area rather than the entire surface area of the MPC lid. This feature ensures a reduction in the computed bolt stress.

The following combined load case is analyzed for normal conditions of transport.

Normal: Pressure, temperature, and pre-load loads are included (Load Case 1 in Table 2.1.8).

Reference [2.6.3] reports safety factors defined as the calculated stress combination divided by the allowable stress for the load combination. This definition of safety factor is the inverse of the definition consistently used in this SAR. In summarizing the closure bolt analyses performed, results are reported using the safety factor definition of allowable stress divided by calculated stress. The following result for closure lid bolting for normal conditions of transport are obtained:

Overpack Closure Bolt - Safety Factor (Load Case 1 in Table 2.1.8)	
Combined Load Case	Safety Factor on Bolt Tension
Average Tensile Stress	1.44
Combined Tension, Shear, Bending, and Torsion	1.57

It is seen from the above table that the safety factor is greater than 1.0 as required. Note that the magnitude of the safety factors reflect the large preload required for successful performance of the bolts under a hypothetical accident drop event where the demand is more severe.

2.6.1.3.2.4 Stress Analysis of Overpack Enclosure Shell

The overpack enclosure shell and the overpack enclosure return are examined for structural integrity under a bounding internal pressure. Flat beam strips of unit width are employed to simulate the performance of the flat panels and the flat plate return section (see drawings in Subsection 1.4). It is shown that large safety factors exist against overstress due to an internal pressure developing from off-gassing of the neutron absorber material. The minimum safety factors are summarized below:

Location	Calculated Stress (ksi)	Allowable Stress (ksi)	Safety Factor
Enclosure Shell Return (bottom)	2.56	26.3	10.2
Enclosure Shell Return (top)	3.42	26.3	7.68
Enclosure Shell Flat Panels	5.58	26.3	4.71
Weld Shear	0.63	10.52	16.7

2.6.1.3.3 Fatigue Considerations

Regulatory Guide 2.9 requires consideration of fatigue due to cyclic loading during normal conditions of transport. Considerations of fatigue associated with long-term exposure to vibratory motions associated with normal conditions of transport are considered below where individual components of the package are assessed for the potential for fatigue.

- Overpack and MPC Fatigue Considerations

The temperature and pressure cycles within the MPC and the inner shell of the overpack are entirely governed by the mechanical and thermal-hydraulic conditions presented by the fuel. The external surfaces of the overpack, however, are in direct contact with the ambient environment. The considerations of cyclic fatigue due to temperature and pressure cycling of the HI-STAR 100 System, therefore, must focus on different locations depending on the source of the cyclic stress.

As shown in the following, the overpack and the MPCs in the HI-STAR 100 System do not require a detailed fatigue analysis because all applicable loadings are well within the range that permits exemption from fatigue analysis per the provisions of Section III of the ASME Code. Paragraph NB-3222.4 (d) of Section III of the ASME Code provides five criteria that are strictly material and design condition dependent to determine whether a component can be exempted from a detailed fatigue analysis. The sixth criterion is applicable only when dissimilar materials are involved, which is not the case in the HI-STAR 100 System.

The Design Fatigue curves for the overpack and MPC materials are given in Appendix I of Section III of the ASME Code. Each of the five criteria is considered in the following:

i. Atmospheric to Service Pressure Cycle

The number of permissible cycles, n, is bounded by $f(3S_m)$, where f(x) means the number of cycles from the appropriate fatigue curve at stress amplitude of x psi. In other words

$$n < f(3S_m)$$

From Tables 2.1.11 through 2.1.20 for normal conditions, and the fatigue curves, the number of permissible cycles is

n (overpack) $\leq$ 1600 ($3S_m$ = 68,700 psi) (Figure I.9-1 of ASME Appendix I)
n (MPC) $\leq$ 40,000 ($3S_m$ = 46,200 psi) (Figure I.9-2 of ASME Appendix I)

The MPC, which is an all-welded component, is unlikely to undergo more than one cycle, indicating that a huge margin of safety with respect to this criterion exists. The overpack, however, is potentially subject to multiple uses. However, 1000 pressurizations in the 40-year life of the overpack is an upper bound estimate. In conclusion, the projected pressurizations of the HI-STAR components do not warrant a usage factor evaluation.

ii. Normal Service Pressure Fluctuation

Fluctuations in the service pressure during normal operation of a component are considered if the total pressure excursion δ_p exceeds Δ_p.

where

Δ_p = Design pressure * $S/(3S_m)$

S = Value of S_a for one million cycles

Using the above mentioned tables and appropriate fatigue curves,

$$(\Delta p)_{overpack} = \frac{(100)(13000)}{(3)(22,900)} = 18.9\ psi$$

$$(\Delta p)_{MPC} = \frac{(100)(26000)}{(3)(16000)} = 54.2\ psi$$

During normal operation the pressure fields in the MPC and the overpack are steady state. Therefore, normal pressure fluctuations are negligibly small. Normal service pressure oscillations do not warrant a fatigue usage factor evaluation.

iii. Temperature Difference - Startup and Shutdown

Fatigue analysis is not required if the temperature difference ΔT between any two adjacent points on the component during normal service does not exceed $S_a/2E\alpha$, where S_a is the cyclic stress amplitude for the specified number of startup and shutdown cycles. E and α are the Young's Modulus and instantaneous coefficients of thermal expansion (at the service temperature). Assuming 1000 startup and shutdown cycles, Tables 2.3.1 and 2.3.4 and the appropriate ASME fatigue curves in Appendix I or Section III of the ASME Code give:

$$(\Delta T)_{overpack} = \frac{90,000}{(2)(26.1)(6.98)} = 247°F$$

$$(\Delta T)_{MPC} = \frac{130,000}{(2)(25)(9.69)} = 268°F$$

There are no locations on either the overpack or MPC where ΔT between any two adjacent points approach these calculated temperatures. As reported in Tables 3.4.16-18, the maximum ΔT that occurs between two components, the MPC shell and the basket periphery, is only 115 degrees F. Therefore, it is evident this temperature criterion is satisfied for 1,000 startup and shutdown cycles.

iv. Temperature Difference - Normal Service

Significant temperature fluctuations that require consideration in this criterion are those in which the range of temperature difference between any two adjacent points under normal service conditions is less than S/2Eα where S corresponds to 10^6 cycles. Substituting, gives

$$(\Delta T)_{MPC} = \frac{26{,}000}{(2)(25)(9.69)} = 53.7°F$$

$$(\Delta T)_{overpack} = \frac{13{,}000}{(2)(26.1)(6.98)} = 35.7°F$$

During normal operation, the temperature fields in the MPC and the overpack are steady state. Therefore, normal temperature fluctuations are negligibly small. Normal temperature fluctuations do not warrant a fatigue usage factor evaluation.

v. Mechanical Loads

Mechanical loadings of appreciable cycling occur in the HI-STAR 100 System only during transportation. The stress cycling under transportation conditions is considered significant if the stress amplitude is greater than S_a corresponding to 10^6 cycles. It, therefore, follows that the stress limits that exempt the overpack and MPC are 13,000 psi and 26,000 psi, respectively.

From Subsection 2.5.2.1, g-loads typically associated with rail transport will produce stress levels in the MPC and overpack which are a small fraction of the above limits. Therefore, no potential for fatigue expenditure in the MPC and overpack materials is found to exist under transportation conditions.

In conclusion, the overpack and the MPC do not require fatigue evaluation under the exemption criteria of the ASME Code.

- Fatigue Analysis of Closure Bolts:

The maximum tensile stress developed in the overpack closure bolts during normal operating conditions is shown by analyses not to exceed 93.0 ksi. The alternating stress in the bolt is equal to 1/2 of the maximum stress due to normal conditions, or 46.5 ksi. The design service temperature for the bolts per Table 2.1.2 is 350 degrees F. Per Table 2.3.5, the Young's Modulus at 350 degrees F is 27,000 ksi. Therefore, the effective stress intensity amplitude for calculating usage factor using

$$S_a = \frac{(46.5)(4)(30e+06)}{27.7e+06} = 201.4 \text{ ksi}$$

Figure I-9.4 (ASME Code, Appendices) is (ratioing the modulus used in the figure to the modulus used here):

Using Figure I-9.4 (NB, loc. cit), the permissible number of cycles is 200.

This result indicates the main closure bolts should *not be torqued and untorqued more than 200 times. After 200 loading cycles, they must be replaced.*

The total shear area of the overpack closure bolt threads is $A_v = 9.528 \text{ in}^2$. Therefore, the shear stress in the top closure bolt threads is, (use the limiting bolt load for normal operation and the tensile stress area of a bolt = 1.680 in^2).

$$\sigma_v = \frac{93.0 \text{ ksi} \times 1.68 \text{ in}^2}{9.528 \text{ in}^2} = 16.4 \text{ ksi}$$

The shear stress developed in the threads of the overpack closure bolts is significantly less than the stress developed in the bolt. Therefore, fatigue of the overpack closure bolts is not controlled by shear stress in the bolt threads.

- Fatigue Considerations for Top Flange Closure Bolt Threads:

The shear area of the main flange closure bolt threads is 12.371 in.^2. Therefore, the shear stress in the flange threads under the limit load on the bolt is:

$$\sigma_v = \frac{93.0 \text{ ksi} \times 1.68 \text{ in}^2}{12.928 \text{ in}^2} = 12.6 \text{ ksi}$$

The primary membrane stress in the main flange threads is equal to twice the maximum shear stress, or 21.1 ksi. The alternating stress in the threads, S_a, is equal to 1/2 of the total stress range, or 10.56 ksi. At 400 degrees F design temperature (per Table 2.1.2) the Young's Modulus (Table 2.3.4) is 26.1 x 10^6 psi.

The effective stress amplitude accounting for the fatigue strength reduction and Young's Modulus effects is given by

$$S_a = \frac{(12.6)(4)(30)}{26.1} = 57.9 \text{ ksi}$$

Using Figure I-9.4 (of NB, loc. cit), the allowable number of cycles is equal to 1,800.

Therefore, the *maximum service life of the main flange threads is 1,800 cycles* of torquing and untorquing of the overpack closure system.

- MPC Fatigue Analysis

The maximum primary and secondary alternating stress range for normal transport conditions is conservatively assumed to be equal to the allowable alternating stress range of 0.5 x 40,000 psi. Conservatively using a Young's Modulus of 25 x 10^6 psi for the fatigue evaluation, yields

$$S = 20{,}000 \text{ psi} \times \frac{28.3 \times 10^6 \text{ psi}}{25 \times 10^6 \text{ psi}} = 22{,}640 \text{ psi}$$

Cyclic life is in excess of 1 x 10^6 cycles per Figure I-9.2.1 of Appendix I of the ASME Code.

- Satisfaction of Regulatory Guide 7.6 Committment

The minimum alternating stress range, Sa, at 10 cycles from all appropriate fatigue curves is 600 ksi. All primary stresses under any of the analyses performed in this SAR under the required load combinations are shown to lead to stress intensities that are less than the ultimate strength of the containment vessel material (70 ksi). Fabrication stresses are conservatively evaluated and are summarized in Subsection 2.6.1.3.2.2. Maximum fabrication stress intensities are less than 17 ksi. Conservatively assuming a stress concentration of 4 regardless of specific location produces a stress intensity range below 4 x (70 + 17) = 348 ksi (< 600 ksi). Therefore, satisfaction of the Regulatory Guide 7.6 commitment is assured.

2.6.1.4 Comparison with Allowable Stresses

Consistent with the formatting guidelines of Regulatory Guide 7.9, calculated stresses and stress intensities from the finite element analyses are compared with the allowable stresses and stress intensities defined in Subsection 2.1 (Tables 2.1.11 through 2.1.21) as applicable for conditions of normal transport. The results of these comparisons are presented in the form of factors of safety (SF) defined as:

$$SF = \frac{\text{Allowable Stress}}{\text{Calculated Stress}}$$

Safety factors associated components identified as lifting and tie-down devices have been presented in Section 2.5 as required by Regulatory Guide 7.9.

Major conservatisms are inherent in the finite element models for both the MPC fuel basket and the enclosure vessel, and for the HI-STAR 100 overpack. These conservatisms are elucidated here with additional discussion as needed later in the text associated with each particular issue.

Conservative Assumptions in Finite Element Analyses and Evaluation of Safety Factors

1. Comparison with allowable stresses or stress intensities is made using the design temperature of the component rather than the actual operating temperature existing in the metal at that location. As an example, all comparisons with allowables for the Alloy X fuel basket material uses the allowable strength at 725 degrees F (Table 2.1.21). Under the normal heat conditions of transport, temperatures near the periphery of the fuel basket are below 450 degrees F. High stresses in the fuel basket generally occur at the basket periphery. From Table 2.1.19, the allowable stresses for primary membrane plus bending at the two temperatures are compared to evolve the additional margin in the computed safety factor as 27.2/23.1 = 1.18. Therefore, the reported safety factors from the analysis have at least an additional 18% hidden component from this effect. Similar hidden margins from this kind of simplification arise in the various components of the overpack. Depending on the material, these hidden margins, which increase the reported safety factor, may be large or small. From Figures 3.4.17 and 3.4.18 in Chapter 3, it is concluded that the normal heat condition of transport maximum inner shell temperature is less than 300 degrees F. The allowable stresses are uniformly assumed at 400 degrees F per Table 2.1.21. From Table 2.1.11, the additional hidden safety factor multiplier is computed as 35/34.4 = 1.02. In the inner shell of the overpack, the increase in the reported safety factor from this effect is only 2% for normal conditions of transport.

2. Comparisons with primary stress allowables are made with secondary stresses included. This has an adverse effect on the reported safety factor, especially in areas near discontinuities.

3. In the modeling of the HI-STAR 100 overpack, the full structural connectivity of the intermediate shells and the inner containment shell is not included in the finite element model in order to maintain the linear elastic analysis methodology. The neglect of such interaction means that the overall bending stiffness of the overpack is underestimated; this leads to over-prediction of stresses and consequent adverse effects on reported safety factors.

4. In the modeling of the MPC fuel basket, the local reinforcement of the fuel basket panel from the fillet welds is neglected. The increase in the section modulus at the weld location is ignored leading to a decrease in stiffness of the basket panel. Consequently, under mechanical loading, the stress state is overestimated at the basket panel connection.

2.6.1.4.1 MPC Fuel Basket and Enclosure Vessel

It is recalled that the stress analyses have been performed for the load cases applicable to normal conditions of transport as assembled in Tables 2.1.6 and 2.1.7 for the fuel basket and the enclosure vessel, respectively. Detailed analyses, including finite element model details and the necessary explanations to collate and interpret the voluminous numerical results have been archived. A compendium of finite element results for the fuel basket and enclosure vessel for each load case associated with normal conditions of transport has been developed. Tables 2.6.6 and 2.6.7 summarize results obtained from the analyses (for all baskets) of Load Cases E1.a and E1.c defined in Table 2.1.7. Table 2.6.8 contains a synopsis of all safety factors obtained from the results. To further facilitate perusal of results, another level of summarization is performed in Tables 2.6.2 and 2.6.3 where the global minima of safety factor for each load case are presented. Finally, miscellaneous safety factors associated with the fuel basket and the MPC enclosure vessel are reported in Table 2.6.10.

The following element of information is relevant in ascertaining the safety factors under the various load cases presented in the tables.

- In the interest of simplification of presentation and conservatism, the total stress intensities under mechanical loading are considered to be of the primary genre' even though, strictly speaking, a portion can be categorized as secondary (that have much higher stress limits).

A perusal of the results for Tables 2.6.2 and 2.6.3 under different load combinations for the fuel basket and the enclosure vessel reveals that all factors of safety are above 1.0. The relatively modest factor of safety for the fuel basket under side drop events (Load Case F2.a and F2.b) in Table 2.6.2 warrants further explanation.

The wall thickness of the storage cells, which is by far the most significant variable in the fuel basket's structural strength, is significantly greater in the HI-STAR 100 MPCs than in comparable fuel baskets licensed in the past. For example, the cell wall thickness in the TN-32 basket (Docket No. 72-1021, M-56), is 0.1 inch and that in the NAC-STC basket (Docket No. 71-7235) is 0.048 inch. In contrast, the cell wall thickness in the MPC-68 is 0.25 inch. In spite of their relatively high flexural rigidities, computed margins in the HI-STAR 100 fuel baskets are rather modest. This is because of some conservative assumptions in the analysis that lead to an overstatement of the state of stress in the fuel basket. For example:

i. The section properties of longitudinal fillet welds that attach contiguous cell walls to each other are completely neglected in the finite element model (Figure 2.6.15). The fillet welds strengthen the cell wall section modulus at the very locations where maximum stresses develop.

ii. The radial gaps at the fuel basket-MPC shell and at the MPC shell-overpack interface are explicitly modeled. As the applied loading is incrementally increased, the MPC shell and fuel basket deform until a "rigid" backing surface of the overpack is contacted, making further unlimited deformation under lateral loading impossible. Therefore, some portion of the fuel basket and enclosure vessel (EV) stress has the characteristics of secondary stresses (which by definition, are self-limited by deformation in the structure to achieve compatibility). For conservativeness in the incremental analysis, no distinction between deformation controlled (secondary) stress and load controlled (primary) stress in the stress categorization is made. All stresses, regardless of their origin, are considered as primary stresses. Such a conservative interpretation of the Code has a direct (adverse) effect on the computed safety factors.

The above remarks can be illustrated simply by a simple closed-form bounding calculation. If all deformation necessary to close the gaps is eliminated from consideration, then the capacity of the fuel basket cell wall under loads which induce primary bending stress can be ascertained by considering a clamped beam (cell wall) subject to a lateral pressure representing the amplified weight of fuel assembly plus self-weight of the cell wall (e.g., see Figure 2.6.15).

Using the cell wall thickness and an appropriate unsupported length for the MPC-68, for example, the fixed edge bending stress is computed as 238.22 psi (using the actual fuel weights, cell wall weights, cell wall thickness and unsupported length). This implies a safety factor of 5.704 for a Level A event (for a 17g deceleration, SF = 23,100/(238.22 x 17) = 5.704) where the allowable bending stress intensity for Alloy X at 725 degrees F (Table 2.1.21) has been used. The above simple calculation demonstrates that the inherent safety margin under accident loading is considerably greater than is implied by the result in Table 2.6.8 (SF=2.42) for the MPC-68 and 0-degree drop orientation. Similar conclusions can be reached for other MPCs by performing scoping calculations in a similar manner.

iii. The SNF inertia loading on the cell panels is simulated by a uniform pressure, which is a most conservative approach for incorporating the SNF/cell wall structure interaction.

The above assumptions all act to depress the computed values of factors of safety in the fuel basket finite element analysis and render conservative results.

The reported values do not include the effect of dynamic load amplification. Calculations show that, for the duration of impact and the predominant natural frequency of the basket panels under lateral hypothetical accident conditions, the dynamic load factors (DLF) are bounded by 1.05. It is expected that for the normal condition of transport 1' drop, the amplification would be reduced further.

Table 2.6.8 does not report the safety factors associated with Load Case F1 in Table 2.1.6 where it is shown that secondary stresses due to the thermal gradients are below the allowable secondary stress

intensity limits. A representative stress intensity level arising from fuel basket thermal gradients is 15.07 ksi. Using the allowable stress intensity limit for primary plus secondary components per Table 2.1.21, the following representative fuel basket safety factor appropriate to Load Case F1 is obtained as "SF", where:

SF = 46.2 ksi/15.07 ksi = 3.06 (Load Case F1 from Table 2.1.6)

It is concluded that since all reported factors of safety for the fuel basket panels (based on stress analysis) are greater than the DLF, the MPC fuel basket is structurally adequate for its intended functions during and after a postulated lateral drop event associated with the normal conditions of transport.

Tables 2.6.6 and 2.6.7 report stress intensities and safety factors for the helium retention boundary (enclosure vessel) subject to internal pressure alone and to internal pressure plus the normal operating condition temperature with the most severe thermal gradient (Load Cases E1.a and E1.c in Table 2.1.7). Table 2.6.8 reports safety factors from the finite element analyses of the 1' free drop simulating a normal handling condition of transport. The final values for safety factors in the various locations of the helium retention boundary provide assurance that the MPC enclosure vessel is a robust pressure vessel.

2.6.1.4.2 Overpack

2.6.1.4.2.1 Discussion

The overpack is subject to the load cases listed in Table 2.1.8 for normal conditions of transport. Results from the series of finite element analyses are tabulated for normal heat and cold conditions of transport. The tabular results include contributions from mechanical and thermal loading and are needed to insure satisfaction of primary plus secondary stress limits for normal conditions of transport. Results are also tabulated from analyses that neglect thermal stresses. These tables are used to check primary stress limits.
The following text is a brief description of how the results are presented for evaluation and how the evaluation is organized in final form:

- The stress intensity results are sorted by safety factor in ascending order for each component making up the overpack. In particular, results are sorted separately for locations in the lid, the inner shell, and the bottom plate that together make up the containment boundary.

- The extensive body of results is initially summarized in Table 2.6.9 wherein the minimum safety factor for different components of the overpack for each of the load cases is presented. This table lists minimum safety factors for the load cases associated with the normal heat conditions of transport. All safety factors are conservatively computed using allowable stresses based on the maximum normal operating temperatures (see Tables 2.1.2 and 2.1.21 for temperatures and for allowable stresses).

- The finite element analyses include the stress state induced by bolt preload but do not include the effect of secondary fabrication stresses. Table 2.6.5 presents results of re-calculation of the safety factors for the inner containment shell and for the intermediate shells to include the "fabrication stresses" reported in Subsection 2.6.1.3.2.2. Table 2.6.5 summarizes these recomputed safety factors, based on limits for primary plus secondary stresses, and reports the limiting safety factors for the overpack shells for events subject to normal conditions of transport (Level A Service Conditions). The incorporation of the fabrication stress and the computation of revised safety factors begins with the individual principal stress components for the shells, conservatively adds the circumferential fabrication stress in the inner and intermediate shells to the principal stress having the same sign as the fabrication stress, and then re-computes the stress intensity and the safety factor. For the inner shell, the safety factors including fabrication stress are computed from principal stress data including mechanical and thermal loading. For the intermediate shell, however, the recomputed safety factors are based on principal stresses that only include mechanical loading (no thermal stresses need be evaluated for a component designed in accordance with ASME Code Section III, Subsection NF regardless of Class 1 or Class 3 designation (see paragraph NF-3121.11)).

- Finally, Table 2.6.4 summarizes the minimum values of safety factors (global minima) for the overpack components for the normal conditions of transport.

The modifications summarized in Table 2.6.5 are briefly discussed below for the normal heat conditions of transport. The same series of modifications are also performed for the normal cold conditions of transport.

Case 1 (Pressure) - Safety factors are summarized in Table 2.6.9 prior to inclusion of fabrication stress. Table 2.6.5 shows the modified safety factor resulting from "adding" the fabrication stress for the inner containment shell to the appropriate principal stress that includes the combination of mechanical plus thermal loads. The same conservative methodology is applied to modify the safety factor for the intermediate shell to include fabrication stress. However, since the intermediate shells are designed to ASME Code Section III, Subsection NF, no thermal stresses need be included in the strength evaluation.

Case 3 (1 foot drop): Results are tabulated including both thermal and mechanical loading. Safety factors for the inner containment shell are summarized in Table.2.6.9 prior to inclusion of fabrication stress. Table 2.6.5 shows modified safety factors that are computed in the same manner as reported for Case 1. For the intermediate shell, principal stress results that do not include thermal stress effects are conservatively modified to include fabrication effects.

2.6.1.4.3 Result Summary for the Normal Heat Condition of Transport

- Stress Results from Overall Finite Element Models of the MPC and Overpack

Tables 2.6.6 through 2.6.9 summarize minimum safety factors from load cases analyzed using the finite element models of the MPC fuel basket plus canister and the overpack described in Subsections 2.6.1.3.1 and 2.6.1.3.2. All safety factors are greater than 1.0 and are greater than any credible dynamic amplifier for the location. Table 2.6.5 provides a summary table that includes the effect of fabrication stress on safety factors for the intermediate and inner shells of the overpack. Table 2.6.5 reports safety factors based on primary plus secondary allowable strengths.

- Status of Lid Bolts and Seals on the Overpack

The finite element analysis for the overpack provides results at the lid-to-top flange interface. In particular, tabulated results for seals and lid bolts are examined. The output results for each load combination indicate that all seal springs remain closed (i.e. the loading in the elements representing the seal remains compressive) indicating that the sealworthiness of the bolted joint will not be breached during normal heat conditions of transport.

Each load combination results in a report of the total compressive force on the closure plate-overpack interface as well as the total tangential force ("friction force"). If the ratio "total friction force/total compressive force" is formed for each set of results, the maximum value of the ratio is 0.219. There will be no slip of the closure plate relative to the overpack if the interface coefficient of friction is greater than the value given above. Mark's Handbook for Mechanical Engineers [3.4.9] in Table 3.2.1 shows $\mu = 0.74\text{-}0.79$ for clean and dry steel on steel surfaces. Therefore, it is concluded that there is no propensity for relative movement.

Based on the results of the finite element analysis for normal heat conditions of transport, the following conclusions are reached.

No bolt overstress is indicated under any loading event associated with normal conditions of transport. This confirms the results of alternate closure bolt analyses, performed in accordance with NUREG/CR-6007 UCRL-ID-110637, "Stress Analysis of Closure Bolts for Shipping Casks", by Mok, Fischer, and Hsu, LLL, 1993.

The closure plate seals do not unload under any load combination; therefore, the seals continue to perform their function.

- Stress and Stability Results from Miscellaneous Component Analyses in Subsection 2.6.1.3

Tables 2.6.10 and 2.6.11 repeat summary results from additional analyses described and reported on in Subsection 2.6.1.3 for components of the MPC and the overpack. The safety factors are summarized in this subsection in accordance with the requirements of Regulatory Guide 7.9. The tables report comparisons of calculated values with allowable values for both stress and stability and represent a compilation of miscellaneous analyses.

- Overpack Internal Pressure Test

The overpack is considered as an ASME pressure vessel. A hydrostatic test of the overpack under 1.5 times internal pressure must result in no stresses in excess of the material yield strength at room temperature to meet the requirement of 10CFR71.85(b). In the following, the necessary results to support the conclusion that the HI-STAR 100 transport containment boundary meets the requirement are presented. Table 2.3.4 gives the material yield strengths of SA350 LF3 and SA 203-E as 37.5 ksi and 40.0 ksi, respectively, at 100 degrees F. A survey of the safety factors for the containment boundary reported in Table 2.6.9 gives the following minimum safety factors:

CONTAINMENT BOUNDARY SAFETY FACTORS - Internal Pressure	
Item	Safety Factor
Lid	2.87
Inner Shell	12.1
Baseplate	11.2

These safety factors are determined using allowable stress intensities at the reference temperatures listed in Table 2.1.21 that are less than the yield stress for the corresponding material at room temperature. From the large safety factors in the above table, it is concluded, without further analysis, that an increase in the internal pressure by 50% will not cause stresses in the containment boundary to exceed the material yield stress.

- Summary of Minimum Safety Factors for Normal Heat Conditions of Transport

Tables 2.6.2 through 2.6.4 present a concise summary of safety factors for the fuel basket, the enclosure vessel, and the overpack, respectively. Locations within this SAR from which the summary results are culled are also indicated in the above tables.

Based on the results of all analyses, with results presented or summarized in the text and in tables, it is concluded that:

i. All safety factors reported in the text and in the summary tables are greater than 1.0.

ii. There is no restraint of free thermal expansion between component parts of the HI-STAR 100 System.

Therefore, the HI-STAR 100 System, under the normal heat conditions of transport, has adequate structural integrity to satisfy the subcriticality, containment, shielding, and temperature requirements of 10CFR71.

2.6.2 Cold

The Normal Cold Condition of Transport assumes an ambient environmental temperature of -20 degrees Farenheit and maximum decay heat. A special condition of extreme cold is also defined where the system and environmental temperature is at -40 degrees F and the system is exposed to increased external pressure with minimum internal pressure. A discussion of the resistance to failure due to brittle fracture is provided in Subsection 2.1.2.3.

The value of the ambient temperature has two principal effects on the HI-STAR 100 storage system, namely:

i. The steady-state temperature of all material points in the cask system will go up or down by the amount of change in the ambient temperature.

ii. As the ambient temperature drops, the absolute temperature of the contained helium will drop accordingly, producing a proportional reduction in the internal pressure in accordance with the Ideal Gas Law.

In other words, the temperature gradients in the cask system under steady-state conditions, will remain the same regardless of the value of the ambient temperature. The internal pressure, on the other hand, will decline with the lowering of the ambient temperature. Since the stresses under normal transport condition arise principally from pressure and thermal gradients, it follows that the stress field in the MPC under a bounding "cold" ambient would be smaller than the "heat" condition of normal transport, treated in the preceding subsection. Therefore, the stress margins computed in Section 2.6.1 can be conservatively assumed to apply to the "cold" condition as well. Calculations using the methodology outlined in NUREG/CR-6007 UCRL-ID-110637, "Stress Analysis of Closure

Bolts for Shipping Casks", by Mok, Fischer, and Hsu, LLL, 1993 demonstrate that the overpack closure bolts will retain the helium seal under the cold ambient conditions.

In addition, allowable stresses generally increase with decreasing temperatures. Safety factors, therefore, will be greater for an analysis at cold temperatures than at hot temperatures. Therefore, the safety factors reported for the hot conditions in Subsection 2.6.1 provide the limiting margins. The overpack, however, is analyzed under cold conditions to ensure that the integrity of the seals is maintained.

As no liquids are included in the HI-STAR 100 System design, loads due to expansion of freezing liquids are not considered.

2.6.2.1 Differential Thermal Expansion

The methodology for determination of the effects of differential thermal expansion in the normal heat condition of transport has been presented in Subsection 2.6.1.2. The same methodology is applied to evaluate the normal cold condition of transport.

The results are summarized in the tables given below for normal cold condition of transport.

THERMOELASTIC DISPLACEMENTS IN THE MPC AND OVERPACK UNDER COLD TEMPERATURE ENVIRONMENT CONDITION				
CANISTER - FUEL BASKET				
	Radial Direction (in.)		Axial Direction (in.)	
Unit	Initial Clearance	Final Gap	Initial Clearance	Final Gap
All PWRs	0.1875	0.095	2.0	1.524
BWR	0.1875	0.101	2.0(min)	1.554 (min)
CANISTER - OVERPACK				
	Radial Direction (in.)		Axial Direction (in.)	
Unit	Initial Clearance	Final Gap	Initial Clearance	Final Gap
All PWRs	0.09375	0.069	0.625	0.487
BWR	0.09375	0.071	0.625	0.497

It can be verified by referring to the Design Drawings, and the foregoing table, that the clearances between the MPC basket and canister structure, as well as those between the MPC shell and overpack inside surface, are sufficient to preclude a temperature induced interference from the thermal expansions listed above.

It is concluded that the HI-STAR 100 package meets the requirement that there be no restraint of free thermal expansion that would lead to development of primary stresses under normal cold conditions of transport.

2.6.2.2 MPC Stress Analysis

The only significant load on the MPCs under cold conditions arises from the postulated 1-foot side drop. Since the allowable stress intensities are higher under the extreme cold condition, results for the MPCs are bounded by the analysis for heat; no additional solutions need to be considered. Since the MPCs are constructed of austenitic stainless steel, there is no possibility of a brittle fracture occurring in any of the MPCs

2.6.2.3 Overpack Stress Analysis

Table 1 of NRC Regulatory Guide 7.8 [2.1.2] mandates load cases at the extreme cold temperature. The overpack may not be bounded by the results of the heat condition load cases for these following conditions:

- increased external pressure with minimum internal pressure, and extreme cold at - 40 degrees F.
- minimal internal pressure plus 1 foot drop with extreme cold condition at - 20 degrees F.
- rapid ambient temperature change during normal condition of transport (note that this case is not explicitly listed as a load case in Regulatory Guide 7.8).

The first two bulleted items are presented in Table 2.1.8; the results of those analyses are presented here. Structural evaluation for the last bulleted item is performed in this subsection. The structural evaluation uses inputs from thermal transient analyses performed and reported in Chapter 3 subsection 3.4.3.1.

Results of finite element analyses for increased external pressure with minimum internal pressure, and for minimum internal pressure plus 1 foot drop (Load Cases 2 and 4 in Table 2.1.8)

Safety factors for Load Cases 2 and 4 in Table 2.1.8 are computed from the results tabulated from the archived finite element analyses Table 2.6.12 summarizes the safety factors obtained. The finite element analysis does not clearly elucidate the effect of temperature on bolt preload. Separate calculations, using the methodology outlined in NUREG/CR-6007 UCRL-ID-110637, "Stress Analysis of Closure Bolts for Shipping Casks", by Mok, Fischer, and Hsu, LLL, 1993 analyze the closure bolts under extreme cold ambient condition plus pressure and provides the appropriate

change in bolt preload expected from operation at the extreme low temperature. A small decrease from the initial preload stress in the bolt results from this operating condition.

The computed change in stress due to the assumption of a severe local low temperature condition is insignificant compared to the initial bolt stress and to the change in the allowable bolt stress because of the lowered temperature. It is concluded that the small change in bolt preload stress has no effect on structural calculations and safety factors.

The overpack load cases for normal conditions of transport described for the hot condition are re-analyzed for the cold condition in accordance with the requirements of Regulatory Guide 7.9. Since higher allowable stresses apply to the overpack components, it is not expected that the re-analyses will result in lower safety factors than have been already reported for the heat condition. The purpose of the analyses is to demonstrate that the overpack seals remain intact under the cold condition. The results of the analyses for normal cold conditions of transport are summarized in Tables 2.6.12 and 2.6.13.

Stress Analysis for Rapid Lowering of Ambient Temperature from 100 degrees F to –40 degrees F (Load Case 5 in Table 2.1.8)

During transportation, the HI-STAR 100 packaging may experience changes in the ambient temperature. Since the HI-STAR 100 packaging is a passive heat rejection device, a change in the ambient temperature has a direct influence on the temperature of its metal parts. In the preceding sub-sections, all structural integrity evaluations have focused on the steady state thermal conditions using 100°F and -40°F as the limiting upper and lower ambient steady state values. In this sub-section, the structural consequences of a rapid change from the hot (100°F) to cold (-40°F) ambient condition is considered. This scenario is labelled as ASME Code Service Condition A, which requires that the range of primary plus secondary stress intensity must be less than 3 S_m (S_m = allowable stress intensity at the mean metal temperature). The loadings assumed to exist coincidentally with the thermal stresses from the transient event are: (i) overpack internal design pressure, P_i and (ii) the inertial deceleration load during transport (10g's). The primary plus secondary stress intensity range from the simultaneous action of internal pressure, axial g-load (10 g's), and thermal transient must be shown to be less than $3S_m$.

It should be noted that the reverse transient (i.e. rapid change from cold to hot will produce a less severe thermal stress gradient. Therefore, the magnitudes of the results of a "rapid cooldown" event bound the corresponding results for the "rapid heat up" event.

To perform a bounding evaluation, it is necessary to identify the material locations on the overpack where the thermal stresses are apt to be most adverse. The thick top forging, which is directly exposed to the ambient air during transport is clearly a candidate location. The other location is the planar cross section of the overpack at approximately mid-height where the heat emission rate from the SNF is at its maximum. These locations are identified in Figure 3.4.24 and further explained in sub-section 3.4.3.

To evolve thermal gradient results for the postulated rapid ambient temperature change, a transient temperature problem is formulated and solved in Chapter 3. The thermal problem and finite element model are fully articulated in Chapter 3 (Subsection 3.4.3.1) where a three-dimensional thermal transient analysis of the HI-STAR 100 Package is performed under a postulated rapid drop in ambient temperature (100 degree F to –40 degree F in one hour). The design basis decay heat load is imposed throughout the time span of the transient solution. The temperature profiles through the wall of the overpack and the top forging are determined as functions of time and the change in thermal gradient through the wall of the sections are documented in Chapter 3, Figures 3.4.25-3.4.27. These locations are limiting since there is direct exposure to the ambient temperature on the outer surface of these components. It is shown in the figures that the top forging experiences a change in through-wall thermal gradient of less than 2.5 degrees K (4.5 degrees F) and that other sections of the overpack experience an even weaker change in thermal gradient. The finite element analyses for normal conditions of transport report results and safety factors for all locations for the normal heat and cold conditions of storage (under assumed steady state thermal conditions). The following additional calculation provides the stress state due to the maximum through-wall thermal gradient in the top forging. This stress state is then combined with the stresses from other load cases and stress intensities formed.

Based on the results from the thermal solutions, the material properties for this calculation are obtained for a metal temperature of 150 degrees F. For the top forging material, the Young's Modulus, E, and the coefficient of linear thermal expansion, α, are (at 150 degrees F):

$E = 27{,}400{,}000$ psi

$\alpha = 6.405 \times 10^{-6}$ inch/inch-degree F

As reported in sub-section 3.4.3.1, the maximum change in temperature difference in the top forging material is bounded by 4.5°F. The ASME Code, (paragraph NB-3222.4(a)(4)) defines a significant temperature change ΔT_s as

$\Delta T_s = S/2E\alpha$

Where S is the value of S_a from the applicable design fatigue curve for 1 million cycles. For the forging material, S = 18,900 psi, which yields

$\Delta T_s = 18{,}900/(2 \times 27{,}400{,}000 \times 0.00000641) = 53.9$ °F

It therefore follows that the metal temperature gradient change produced by the rapid cooldown (or heat up event) does not lead to a significant stress adder. Nevertheless, the factor of safety under this loading condition is quantified.

The linear temperature profile gives a linear stress distribution through the wall thickness with compressive stresses at the inside surface of the top forging. The magnitude of the stress due to the maximum thermal gradient is:

$\Delta\sigma = E\alpha(\Delta T)/(2(1-\nu))$

For ΔT=(4.5 degrees F (change) +1.5 degrees F (initial)) and $\nu = 0.3$, the stress intensity is computed as:

$\Delta\sigma = 752$ psi

This stress is now combined with transport longitudinal stress from a 10g deceleration plus longitudinal stress from the normal condition internal pressure. These stresses are computed below:

Pressure stress:

p = 100 psi (internal pressure per Table 2.1.1)
inside radius of top forging = a = 34.375"
outside radius of top forging = b = 41.625"

The magnitude of the longitudinal and circumferential stresses at the inside surface is

$\sigma_x = (a^2/(b^2-a^2))p = 2.14 \times p = 214$ psi

$\sigma_h = ((a^2 + b^2)/(b^2-a^2))p = 5.289 \times p = 529$ psi

Axial stress from deceleration:

The package weight = 282,000 lb. (Table 2.2.4)

The direct stress due to the axial deceleration is

σ_d = 10g x 282,000 lb/Area where the cross-section area is Area= 1731 sq. inch

Therefore,

$\sigma_d = 1{,}629$ psi

Adding the absolute values of the stresses (for conservation), the maximum surface stress intensity is

$SI = (\sigma_d + \sigma_x + \Delta\sigma) + p = 2{,}695$ psi

This value is compared against 3 x the allowable stress intensity since it involves a secondary thermal stress. From Table 2.1.13, the allowable primary plus secondary stress intensity is

SI(allowable) 3 x allowable membrane stress intensity = 69,100 psi

The safety factor is 69,100/2,695 = 25.64

Therefore, the HI-STAR 100 overpack is shown to meet the Level A stress intensity limits under the rapid ambient temperature change event with a large margin of safety.

Conclusions

Based on the results of the finite element analysis and the calculations carried out within this subsection, the following conclusions are reached for normal cold conditions of transport:

- No bolt yielding is indicated under any loading event.
- The closure plate seal springs do not unload under any load combination; therefore, the seals continue to perform their function.
- The postulated rapid drop in the ambient temperature from hot (100 degrees F) to cold (-40 degrees F) conditions of transport has no appreciable effect on the stress intensities in the transport overpack. The top forging will experience a small increase in through-wall thermal gradient. Calculations show that the change in thermal stress induced by this through-wall thermal gradient is small; large safety factors are calculated when the secondary thermal stress is combined with the pressure stress and the longitudinal transport stress.

Relative movement between the top flange and the top closure lid has been examined for the normal cold condition of transport. Each load combination reported provides the total compressive force on the lands as well as the total tangential force on the lands ("friction force"). If the ratio "total friction force/total compressive force" is formed for each set of results appropriate to the cold condition of normal transport, the maximum value of the ratio is 0.138. There will be no slip of the closure plate relative to the overpack if the coefficient of friction is greater than the value given above. Mark's Handbook for Mechanical Engineers [2.6.2] shows μ = 0.74-0.79 for clean and dry steel on steel surfaces. Therefore, it is concluded that there is no propensity for relative movement.

Since the results show that all safety factors are greater than 1.0, it is concluded that the HI-STAR 100 System under the normal cold conditions of transport has adequate structural integrity to satisfy the subcriticality, containment, shielding, and temperature requirements of 10CFR71.

2.6.3 Reduced External Pressure

The effects of a reduced external pressure equal to 3.5 psia, which is required by USNRC Regulatory Guide 7.8 [2.1.2], are bounded by the effects of the accident internal pressure for the overpack (Table 2.1.1). This is considered in Subsection 2.7 for the overpack inner shell. This case does not provide any bounding loads for other components of the overpack containment boundary. Therefore, the only additional analysis performed here to demonstrate package performance for this condition is an analysis of the outer enclosure shell panels.

Under this load condition, the outer enclosure shell panels (see Section 1.4, Drawing) deform as long plates under the 3.5 psi pressure that tends to deform the panels away from the neutron absorber material. The stress developed in this situation can be determined by considering the panel as a clamped beam subject to lateral pressure. The appropriate dimensions are:

L = unsupported width of panel = 7.875"

t = panel thickness = 0.5"

p = differential pressure = 3.5 psi

The stress is computed from classical strength of materials beam theory as:

$$\sigma = 0.5p\left(\frac{L}{t}\right)^2$$

Substituting the numerical values gives the stress as 434 psi. From Table 2.1.15, the allowable stress is 26.3 ksi for this condition. Therefore, the safety factor is

$$SF = 60.6$$

Clearly, this event is not a safety concern for package performance.

2.6.4 Increased External Pressure

The effects of an external pressure equal to 20 psia on the package, which is required by USNRC Regulatory Guide 7.8 [2.1.2], are bounded by the effects of the large value for the design external pressure specified for the hypothetical accident (Table 2.1.1). Instability of the overpack shells is examined in Section 2.7. Therefore, no additional analyses need be performed here to demonstrate package performance.

2.6.5 Vibration

During transport, vibratory motions occur which could cause low-level stress cycles in the system due to beam-like deformations. If any of the package components have natural frequencies in the flexible range (i.e., below 33 Hz), or near the flexible range, then resonance may amplify the low level input into a significant stress response.

As discussed in Section 2.1, there are no "flexible" beam-like members in the HI-STAR 100 MPC. The MPC is a fully welded, braced construction over its entire length and it is fully supported by the overpack during transport. Since the MPC is supported by the overpack, and is itself a rigid structure, any vibration problems would manifest themselves in the fuel basket walls.

It is shown below that the lowest frequency of the fuel basket walls and the overpack, acting as a beam, are well above 33 Hz. Therefore, additional stresses from vibration are not expected.

The lowest frequency of vibration during normal transport conditions will occur due to vibrations of a fuel basket cell wall. It is demonstrated that the lowest frequency of the component, computed based on the assumption that there is support sufficient to limit vibration to that representative of a clamped beam, is 658 Hz for a PWR basket and 1,200 Hz for a BWR basket.

These frequencies are significantly higher than the 33 Hz transition frequency for rigidity.

When in a horizontal position, the overpack is supported over a considerable length of the enclosure shell. Conservatively considering the HI-STAR as a supported beam at only the two ends of the enclosure shell, and assuming the total mass of the MPC moves with the overpack, an estimate of the lowest material frequency of the structure during transport is in excess of 469 Hz

Based on these frequency calculations, it is concluded that vibration effects are minimal and no new calculations are required.

2.6.6 Water Spray

The condition is not applicable to the HI-STAR 100 System per Reg. Guide 7.8 [2.1.2].

2.6.7 Free Drop

The structural analysis of a 1-foot side drop under heat and cold conditions has been performed in Subsections 2.6.1 and 2.6.2 for heat and cold conditions of normal transport. As demonstrated in Subsections 2.6.1 and 2.6.2, safety factors are well over 1.0.

2.6.8 Corner Drop

This condition is not applicable to the HI-STAR 100 System per [2.1.2].

2.6.9 Compression

The condition is not applicable to the HI-STAR 100 System per [2.1.2].

2.6.10 Penetration

The condition is not applicable to the HI-STAR 100 System per [2.1.2].

Table 2.6.1

FINITE ELEMENTS IN THE MPC STRUCTURAL MODELS

MPC Type	Model Type		
Element Type	Basic	0 Degree Drop	45 Degree Drop
MPC-24	1068	1179	1178
BEAM3	1028	1028	1028
CONTAC12	40	38	38
CONTAC26	0	110	110
COMBIN14	0	3	2
MPC-32	766	873	872
BEAM3	738	738	738
CONTAC12	28	27	24
CONTAC26	0	106	105
COMBIN14	0	2	5
MPC-68	1234	1347	1344
BEAM3	1174	1174	1174
PLANE82	16	16	16
CONTAC12	44	43	40
CONTAC26	0	112	111
COMBIN14	0	2	3

Table 2.6.1 Continued

FINITE ELEMENTS IN THE MPC STRUCTURAL MODELS

MPC Type	Model Type		
Element Type	Basic	0 Degree Drop	45 Degree Drop
MPC-24E/24EF	1070	1183	1182
BEAM3	1030	1030	1030
CONTAC12	40	38	38
CONTAC26	0	112	112
COMBIN14	0	3	2

Table 2.6.2

MINIMUM SAFETY FACTORS FOR THE MPC FUEL BASKET - NORMAL CONDITIONS OF TRANSPORT

Case Number	Load[1] Combination	Safety Factor	Location in SAR where Details are Provided
F1	T or T'	3.06	2.6.1.4.1
F2			
F2.a	D+H, 1 ft side drop 0°	1.57	Table 2.6.8
F2.b	D+H, 1 ft side drop 45°	1.29	Table 2.6.8

1 The symbols used for loads are defined in Subsection 2.1.2.1.

Table 2.6.3

MINIMUM SAFETY FACTORS FOR THE MPC ENCLOSURE VESSEL - NORMAL CONDITIONS OF TRANSPORT

Case Number	Load Combination[1]	Safety Factor	Location in SAR where Details are Provided or Safety Factors Extracted
E1			
E1.a	Design internal pressure, P_i	5.06 1.5 1.36	Lid Table 2.6.6 Baseplate Table 2.6.6 Shell Table 2.6.6
E1.b	Design external pressure, P_o	NA NA 1.2	Lid P_i bounds Baseplate P_i bounds Shell Table 2.6.10
E1.c	Design internal pressure plus temperature	8.50 2.67 1.5	Lid Table 2.6.7 Base Table 2.6.7 Shell Table 2.6.7
E2			
E2.a	(P_i, P_o) + D + H, 1 ft side drop, 0 deg.	1.41	Table 2.6.8
E2.b	(P_i, P_o) + D + H, 1 ft. side drop, 45 deg.	1.63	Table 2.6.8
E4	T or T'	Sections show expansion does not result in restraint of free thermal expansion	2.6.1.2

1 The symbols used for loads are defined in Subsection 2.1.2.1.

Table 2.6.4

MINIMUM SAFETY FACTORS FOR OVERPACK FOR NORMAL CONDITION OF TRANSPORT

Case Number	Load Combination[1]	Safety Factor	Location in SAR where Details are Provided
1	$T_h + P_i + F + W_s$	1.65	Table 2.6.5
2	$T_s + P_o + F + W_s$	3.38	Table 2.6.13
3	$T_h + D_{sn} + P_i + F + W_s$	1.68	Table 2.6.9
4	$T_c + D_{sn} + P_o + F + W_s$	2.41	Table 2.6.13

1 The symbols used here are defined in Subsection 2.1.2.1.

Table 2.6.5

MINIMUM SAFETY FACTORS INCLUDING FABRICATION STRESSES –
PRIMARY PLUS SECONDARY STRESS INTENSITY, NORMAL HEAT CONDITIONS OF TRANSPORT

Case	Inner Shell Exterior Surface	Intermediate Shell
1 - Internal pressure	1.65	4.12
3 - 1 ft. Side Drop	1.70	2.42

Note: Thermal stresses are included for inner containment shell per ASME Section III, Subsection NB, but excluded in intermediate shell per ASME Code, Section III, Subsection NF.

Table 2.6.6

STRESS INTENSITY RESULTS FOR CONFINEMENT BOUNDARY - INTERNAL PRESSURE ONLY (Load Case E1.a in Table 2.1.7)

Component Locations (Per Fig. 2.6.20)	Calculated Value of Stress Intensity (psi)	Category	Table 2.1.19 Allowable Value (psi)†	Safety Factor (Allowable/Calculated)
Top Lid††				
A	3,282	$P_L + P_b$	30,000	9.14
Neutral Axis	40.4	P_m	20,000	495
B	3,210	$P_L + P_b$	30,000	9.34
C	1,374	$P_L + P_b$	30,000	21.8
Neutral Axis	1,462	P_m	20,000	13.6
D	5,920	$P_L + P_b$	30,000	5.06
Baseplate				
E	19,683	$P_L + P_b$	30,000	1.5
Neutral Axis	412	P_m	20,000	48.5
F	20,528	$P_L + P_b$	30,000	1.5
G	9,695	$P_L + P_b$	30,000	3.1
Neutral Axis	2,278	P_m	20,000	8.8
H	8,340	$P_L + P_b$	30,000	3.5

† Stress intensity taken at 300 degrees F in this comparison.

†† The stresses in the top lid are reported for the dual lid configuration. The stresses for the single lid configuration are 50% less (see Subsection 2.6.1.3.1.2 for further details).

Table 2.6.6 Continued

STRESS INTENSITY RESULTS FOR CONFINEMENT BOUNDARY -
INTERNAL PRESSURE ONLY (Load Case E1.a in Table 2.1.7)

Component Locations (Per Fig.2.6.20)	Calculated Value of Stress Intensity (psi)	Category	Table 2.1.19 Allowable Value (psi)†	Safety Factor (Allowable/Calculated)
Canister				
I	6,860	P_m	18,700	2.72
Upper Bending	7,189	$P_L + P_b + Q$	30,000	4.2
Boundary Layer	7,044	$P_L + P_b$	20,000	2.8
Region				
Lower Bending	43,986	$P_L + P_b + Q$	60,000	1.36
Boundary Layer	10,621	$P_L + P_b$	30,000	2.82
Region				

† Allowable stress intensity based at 300 degrees F except for Location I where allowable stress intensity values are based on 400 degree F.

Table 2.6.7

PRIMARY AND SECONDARY STRESS INTENSITY RESULTS FOR
HELIUM RETENTION BOUNDARY - PRESSURE PLUS THERMAL LOADING (Load Case E1.c in Table 2.1.7)

Component Locations (Per Fig. 2.6.20)	Calculated Value of Stress Intensity (psi)	Category	Table 2.1.19 Allowable Value (psi)†	Safety Factor (Allowable/Calculated)
Top Lid††				
A	4,634	$P_L + P_b + Q$	60,000	12.9
Neutral Axis	1,464	P_L	30,000	20.4
B	2,140	$P_L + P_b + Q$	60,000	28.0
C	1,942	$P_L + P_b + Q$	60,000	30.8
Neutral Axis	3,528	P_L	30,000	8.50
D	7,048	$P_L + P_b + Q$	60,000	8.51
Baseplate				
E	22,434	$P_L + P_b + Q$	60,000	2.67
Neutral Axis	1,743	P_L	30,000	17.2
F	18,988	$P_L + P_b + Q$	60,000	3.16
G	5,621	$P_m + P_L$	60,000	10.7
Neutral Axis	5,410	P_L	30,000	5.55
H	12,128	$P_L + P_b + Q$	60,000	4.95

† Allowable stresses based on temperature of 300 degrees F.

†† The stresses in the top lid are reported for the dual lid configuration. The stresses for the single lid configuration are 50% less (see Subsection 2.6.1.3.1.2 for further details).

Table 2.6.7 Continued

PRIMARY AND SECONDARY STRESS INTENSITY RESULTS FOR
HELIUM RETENTION BOUNDARY - PRESSURE PLUS THERMAL LOADING (Load Case E1.c in Table 2.1.7)

Component Locations (Per Fig.2.6.20)	Calculated Value of Stress Intensity (psi)	Category	Table 2.1.19 Allowable Value (psi)[1]	Safety Factor (Allowable/Calculated)
Canister				
I	6,897	P_L	28,100	4.07
Upper Bending	6,525	$P_L + P_b + Q$	60,000	9.2
Boundary Layer Region	3,351	P_L	30,000	8.95
Lower Bending	40,070	$P_L + P_b + Q$	60,000	1.5
Boundary Layer Region	6,665	P_L	30,000	4.5

[1] Allowable stresses based on temperature of 300 degree F except at Location I where the temperatures are based on 400 degrees F.

Table 2.6.8 - FINITE ELEMENT ANALYSIS RESULTS
MINIMUM SAFETY FACTORS FOR MPC COMPONENTS UNDER NORMAL CONDITIONS

Component - Stress Result	MPC-24		MPC-68	
	1 Ft. Side Drop, 0 deg Orientation Load Case F2.a or E2.a	1 Ft. Side Drop, 45 deg Orientation Load Case F2.b or E2.b	1 Ft. Side Drop, 0 deg Orientation Load Case F2.a or E2.a	1 Ft. Side Drop, 45 deg Orientation Load Case F2.b or E2.b
Fuel Basket – Primary Membrane (P_m)	4.12	5.64	4.42	6.16
Fuel Basket - Local Membrane Plus Primary Bending ($P_L + P_b$)	1.73	1.87	2.42	1.50
Enclosure Vessel - Primary Membrane (P_m)	2.71	2.71	2.67	2.72
Enclosure Vessel - Local Membrane Plus Primary Bending ($P_L + P_b$)	3.30	3.29	2.17	1.80
Basket Supports - Primary Membrane (P_m)	N/A	N/A	5.33	5.34
Basket Supports - Local Membrane Plus Primary Bending ($P_L + P_b$)	N/A	N/A	1.67	2.16

Table 2.6.8 (Continued) - FINITE ELEMENT ANALYSIS RESULTS
MINIMUM SAFETY FACTORS FOR MPC COMPONENTS UNDER NORMAL CONDITIONS

Component - Stress Result	MPC-32		MPC-24E/EF	
	1 Ft. Side Drop, 0 deg Orientation Load Case F2.a or E2.a	1 Ft. Side Drop, 45 deg Orientation Load Case F2.b or E2.b	1 Ft. Side Drop, 0 deg Orientation Load Case F2.a or E2.a	1 Ft. Side Drop, 45 deg Orientation Load Case F2.b or E2.b
Fuel Basket - Primary Membrane (P_m)	4.05	5.65	4.05	5.56
Fuel Basket - Local Membrane Plus Primary Bending ($P_L + P_b$)	1.57	1.29	1.69	1.83
Enclosure Vessel - Primary Membrane (P_m)	2.55	2.69	2.71	2.71
Enclosure Vessel - Local Membrane Plus Primary Bending ($P_L + P_b$)	1.41	1.63	3.05	3.14
Basket Supports - Primary Membrane (P_m)	3.96	5.33	N/A	N/A
Basket Supports - Local Membrane Plus Primary Bending ($P_L + P_b$)	3.49	3.12	N/A	N/A

Table 2.6.9 - FINITE ELEMENT ANALYSIS RESULTS
MINIMUM SAFETY FACTORS FOR OVERPACK COMPONENTS UNDER NORMAL CONDITIONS (Hot Environment)

Component – Stress Result	Hot Environment Load Case 1	1 Ft. Side Drop Load Case 3
Lid - Local Membrane Plus Primary Bending ($P_L + P_b$)	2.87	2.14
Inner Shell - Local Membrane Plus Primary Bending ($P_L + P_b$)	12.1	3.24
Inner Shell - Primary Membrane (P_m)	13.7	3.53
Intermediate Shells - Local Membrane Plus Primary Bending ($P_L + P_b$)	17.3	2.51
Baseplate - Local Membrane Plus Primary Bending ($P_L + P_b$)	11.2	6.28
Enclosure Shell - Primary Membrane (P_m)	35.2	3.24

Table 2.6.9 (Continued) - FINITE ELEMENT ANALYSIS RESULTS

MINIMUM SAFETY FACTORS FOR OVERPACK COMPONENTS UNDER NORMAL CONDITIONS (Hot Environment)

Component - Stress Result	Hot Environment Load Case 1	1 Ft. Side Drop Load Case 3
Lid - Local Membrane Plus Primary Bending Plus Secondary ($P_L + P_b + Q$)	2.14	1.90
Inner Shell - Local Membrane Plus Primary Bending Plus Secondary ($P_L + P_b + Q$)	2.69	2.84
Intermediate Shells - Local Membrane Plus Primary Bending Plus Secondary ($P_L + P_b + Q$ excluding thermal stress)	34.5	5.01
Baseplate - Local Membrane Plus Primary Bending Plus Secondary ($P_L + P_b + Q$)	1.81	1.68
Enclosure Shell - Local Membrane Plus Primary Bending Plus Secondary ($P_L + P_b + Q$)	1.97	1.88

Table 2.6.10

SAFETY FACTORS FROM MISCELLANEOUS MPC CALCULATIONS -
NORMAL CONDITIONS OF TRANSPORT - HOT ENVIRONMENT

Item	Loading	Safety Factor	Location in SAR Where Details are Provided
Fuel Support Spacers	1' Drop (Load Case F2 in Table 2.1.6)	2.76	Subsection 2.6.1.3.1.3
MPC Stability	Code Case N-284 (Load Case E1.b in Table 2.1.7)	1.2	Subsection 2.6.1.3.1.3

Table 2.6.11

MINIMUM SAFETY FACTORS FROM MISCELLANEOUS OVERPACK CALCULATIONS
NORMAL HOT CONDITIONS OF TRANSPORT

Item	Loading	Safety Factor	Location in SAR Where Details are Provided
Fabrication Stress in Inner Shell	Fabrication	4.3	Subsection 2.6.1.3.2.2
Closure Bolt	Average Tensile Stress Including Pre-Load	1.44	Subsection 2.6.1.3.2.3

Table 2.6.12 - FINITE ELEMENT ANALYSIS RESULTS
MINIMUM SAFETY FACTORS FOR OVERPACK COMPONENTS UNDER NORMAL CONDITIONS (Cold Environment)

Component - Stress Result	Super-Cold Environment Load Case 2	1 Ft. Side Drop Load Case 4
Lid - Local Membrane Plus Primary Bending ($P_L + P_b$)	4.55	2.97
Inner Shell - Local Membrane Plus Primary Bending ($P_L + P_b$)	14.4	3.37
Inner Shell - Primary Membrane (P_m)	16.5	3.53
Intermediate Shells - Local Membrane Plus Primary Bending ($P_L + P_b$)	21.7	2.48
Baseplate - Local Membrane Plus Primary Bending ($P_L + P_b$)	722.8	7.84
Enclosure Shell - Primary Membrane (P_m)	50.2	3.21

Table 2.6.12 (Continued)

FINITE ELEMENT ANALYSIS RESULTS
MINIMUM SAFETY FACTORS FOR OVERPACK COMPONENTS UNDER NORMAL CONDITIONS (Cold Environment)

Component - Stress Result	Super-Cold Environment Load Case 2	1 Ft. Side Drop Load Case 4
Lid - Local Membrane Plus Primary Bending Plus Secondary ($P_L + P_b + Q$)	8.79	5.79
Inner Shell - Local Membrane Plus Primary Bending Plus Secondary ($P_L + P_b + Q$)	15.5	6.36
Intermediate Shells - Local Membrane Plus Primary Bending Plus Secondary ($P_L + P_b + Q$ excluding thermal stress)	43.24	4.95
Baseplate - Local Membrane Plus Primary Bending Plus Secondary ($P_L + P_b + Q$)	83.8	15.1
Enclosure Shell - Local Membrane Plus Primary Bending Plus Secondary ($P_L + P_b + Q$)	21.4	7.67

Table 2.6.13

MINIMUM SAFETY FACTORS INCLUDING FABRICATION STRESS - PRIMARY PLUS SECONDARY STRESS INTENSITY, NORMAL COLD CONDITIONS OF TRANSPORT

Case	Inner Shell Exterior Surface	Intermediate Shell
2 Pressure (Secondary Stress)	3.38	4.22
4 1 ft. Side Drop (Secondary Stress)	2.58	2.41

Note: Thermal stresses are included for inner containment shell per ASME Section III, Subsection NB, but excluded in intermediate shell per ASME Code, Section III, Subsection NF.

Table 2.6.14

MISCELLANEOUS SAFETY FACTOR FOR OVERPACK			
Item	**Loading**	**Safety Factor**	**Location in SAR Where Details are Provided**
Outer Enclosure Panels	Reduced External Pressure	60.6	Subsection 2.6.3

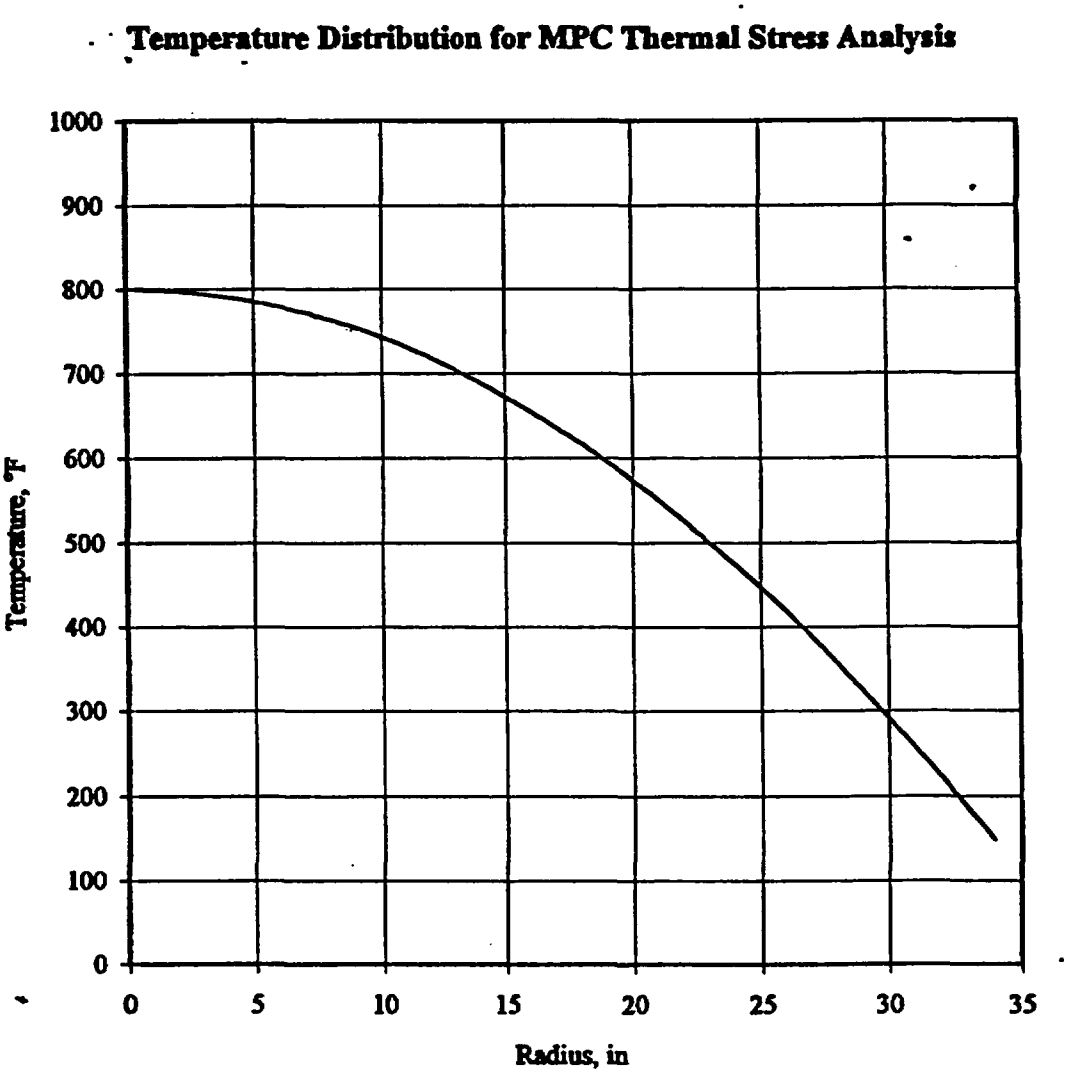

FIGURE 2.6.1; TEMPERATURE DISTRIBUTION FOR MPC THERMAL STRESS ANALYSIS

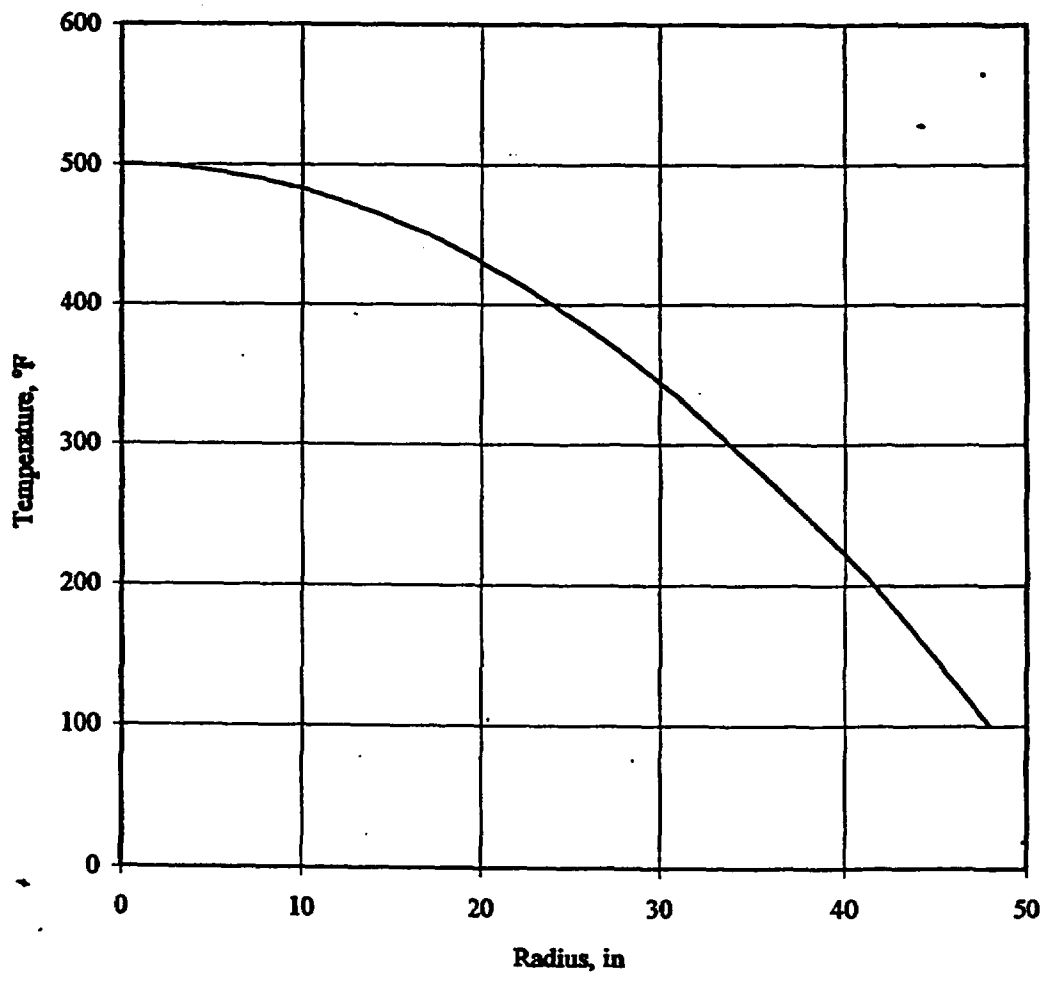

FIGURE 2.6.2; TEMPERATURE DISTRIBUTION FOR OVERPACK THERMAL STRESS ANALYSIS

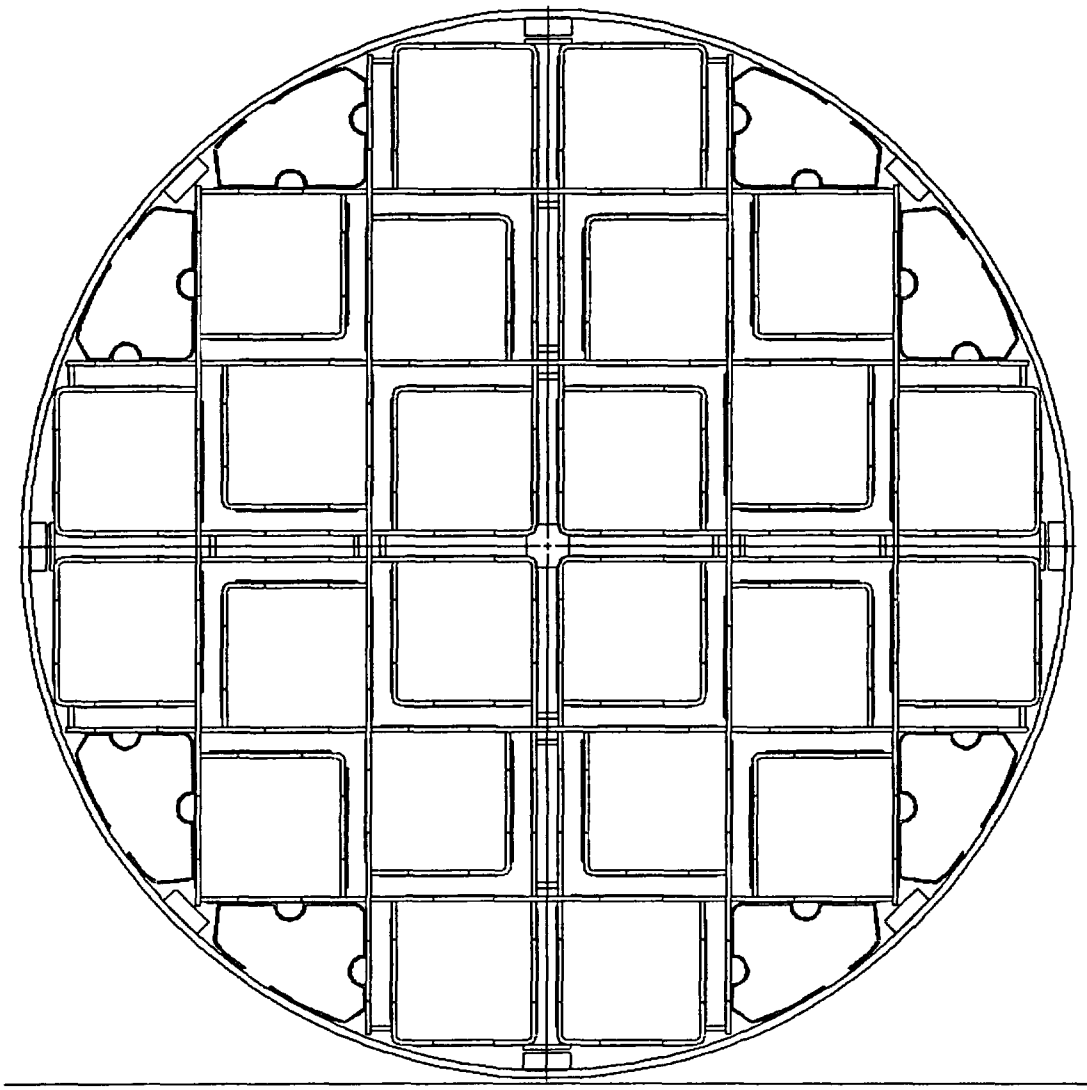

Note: Heat conduction elements shown in-place for clarity, but they are not considered in the analysis.

FIGURE 2.6.3; FINITE ELEMENT MODEL OF MPC24/24E/24EF (BASIC MODEL)

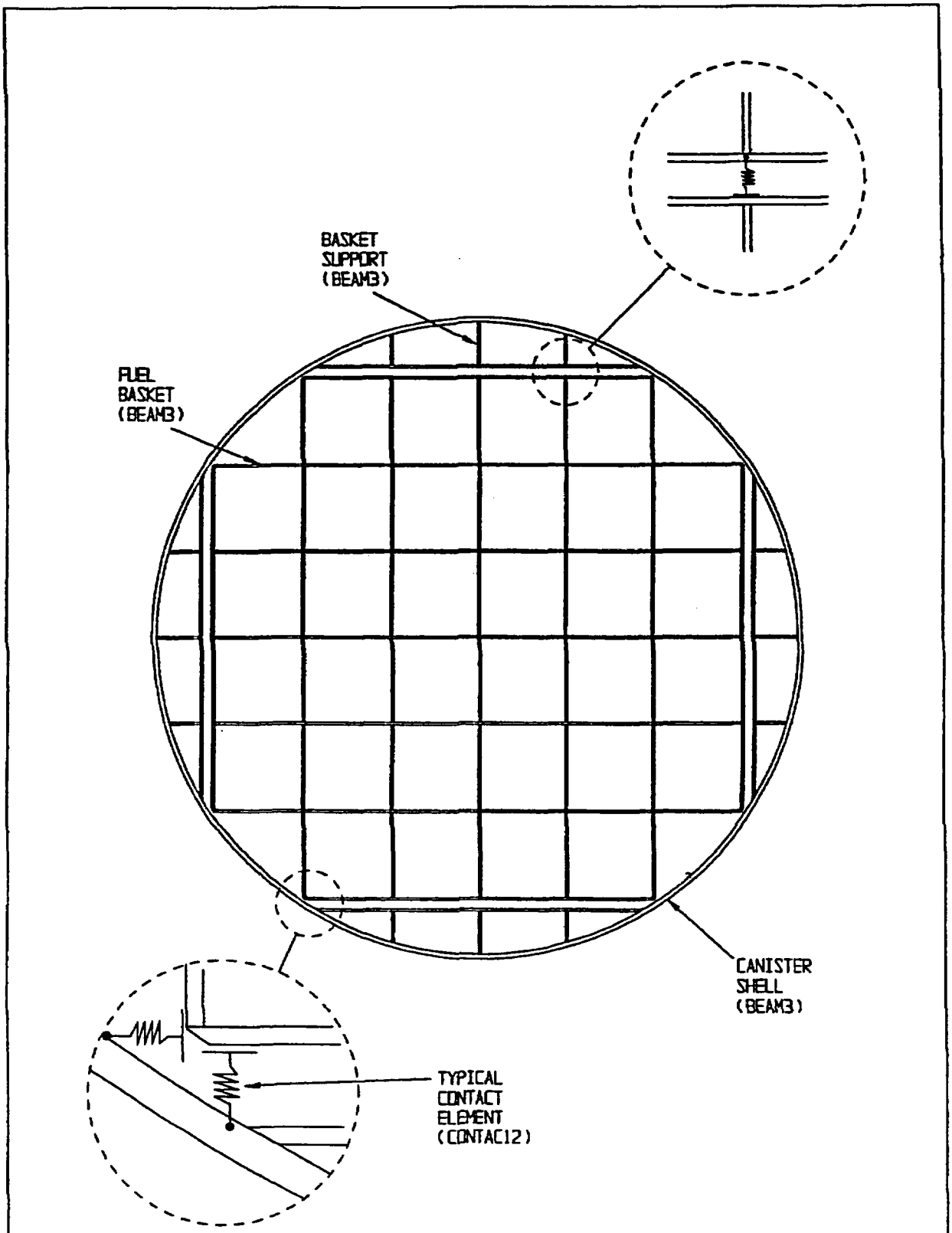

FIGURE 2.6.4; FINITE ELEMENT MODEL FOR MPC-32
(BASIC MODEL)

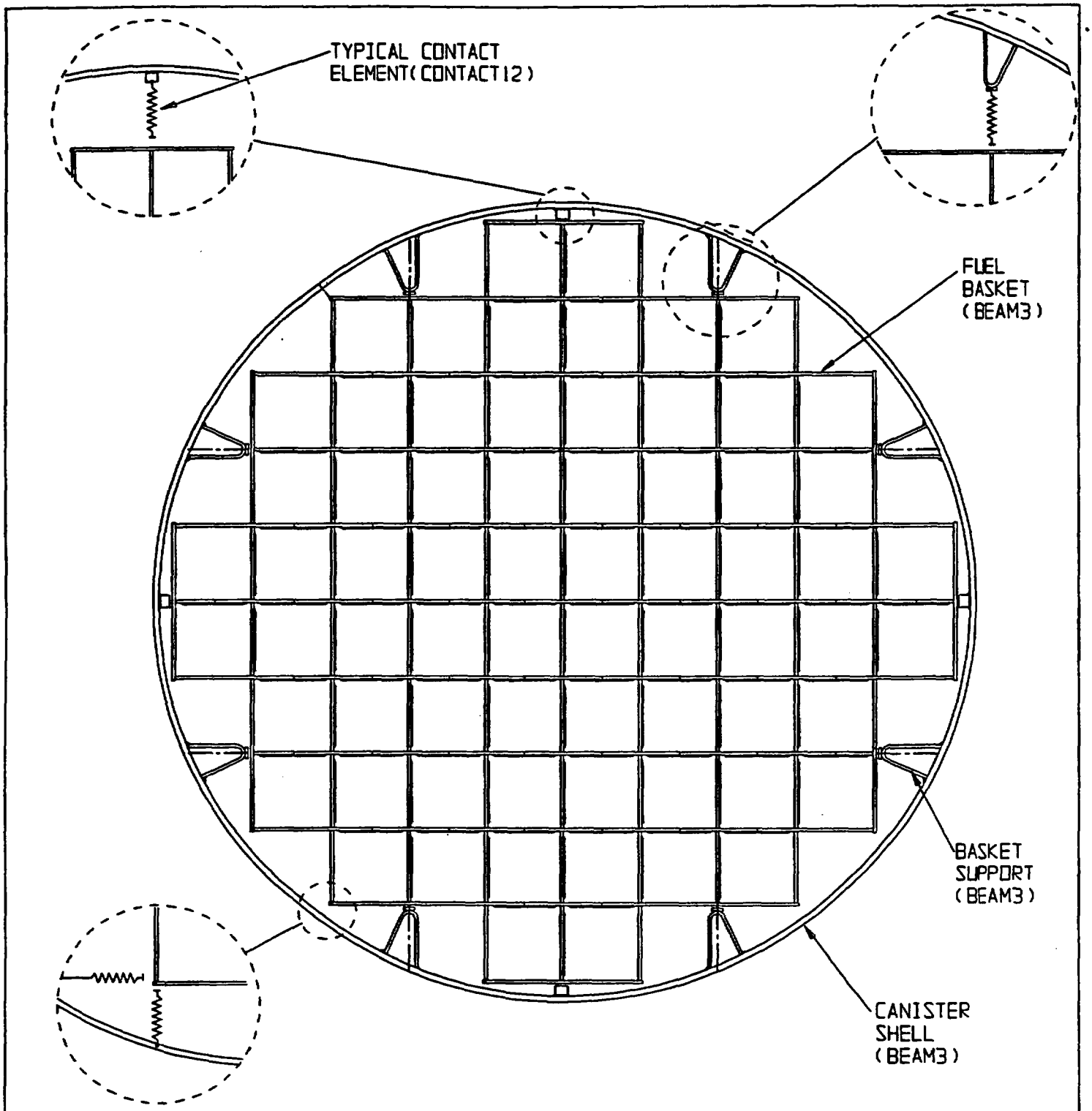

FIGURE 2.6.5; FINITE ELEMENT MODEL OF MPC-68

(BASIC MODEL)

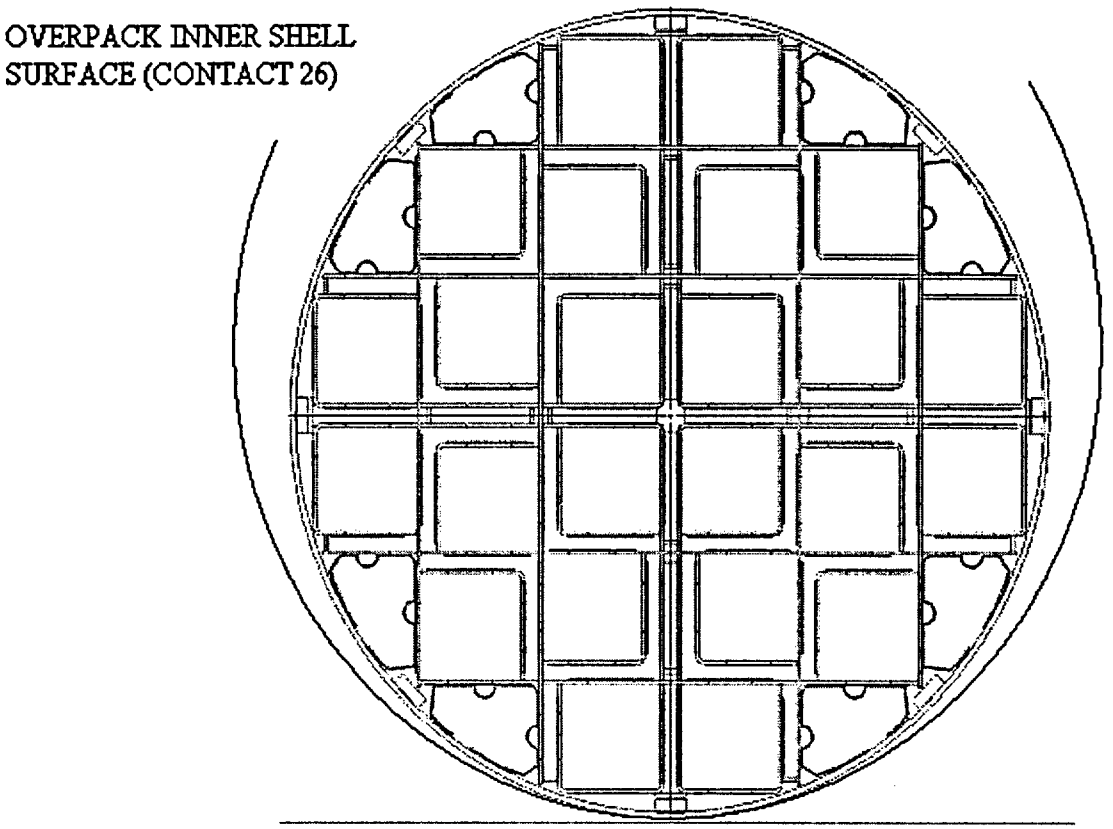

Note: Heat conduction elements shown in-place for clarity, but they are not considered in the analysis.

FIGURE 2.6.6; FINITE ELEMENT MODEL OF MPC-24/24E/24EF (0 DEGREE DROP MODEL)

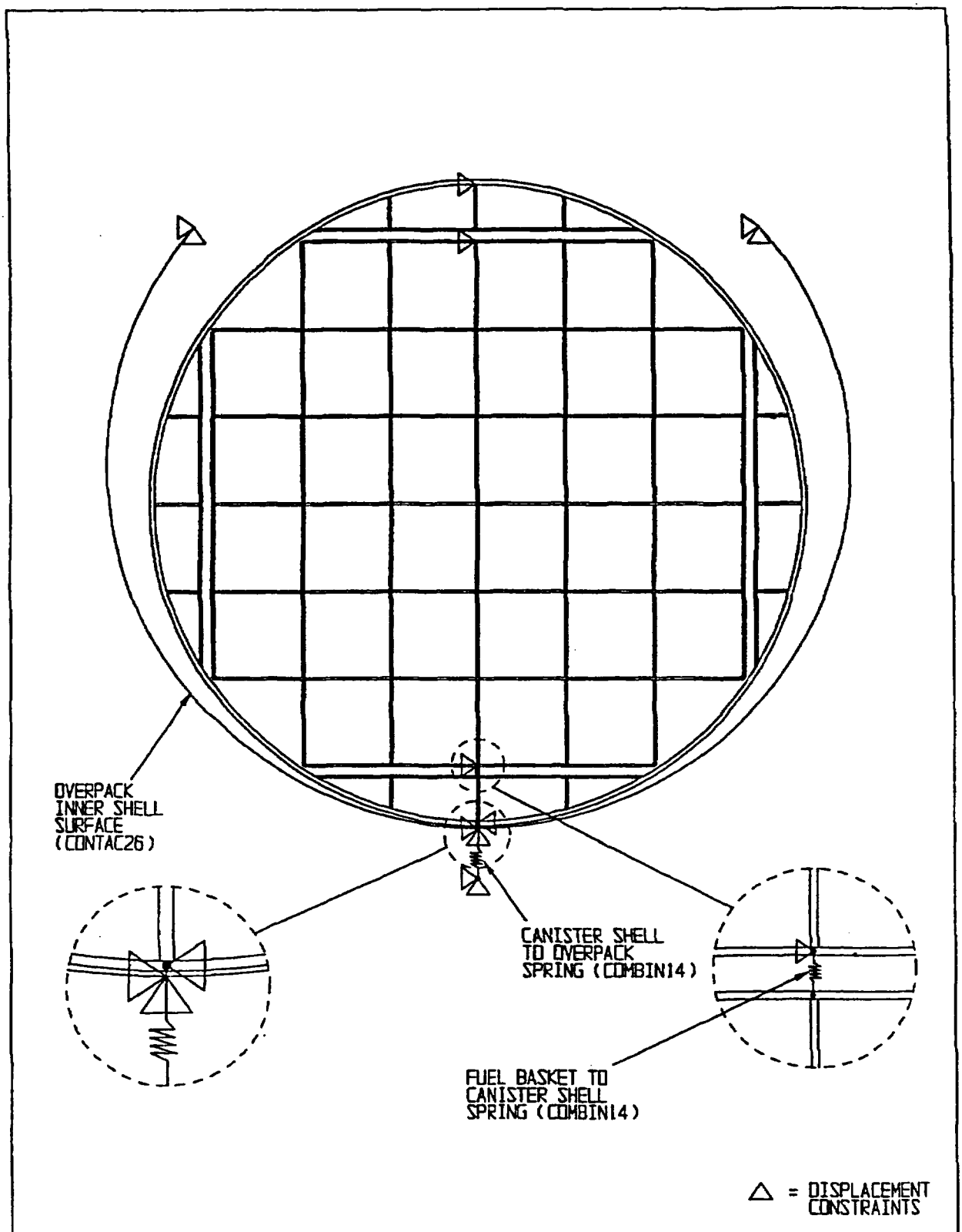

FIGURE 2.6.7; FINITE ELEMENT MODEL FOR MPC-32

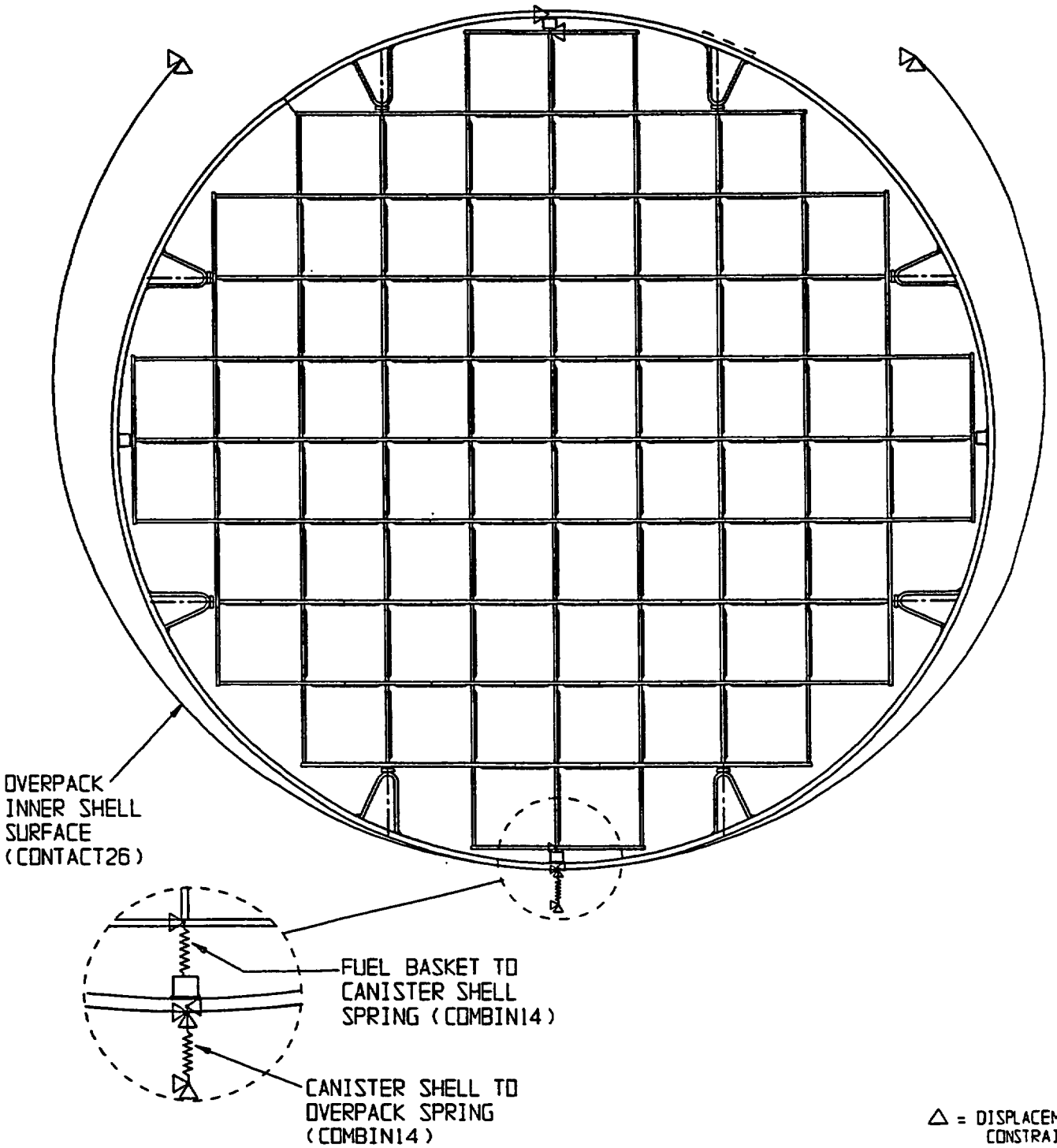

FIGURE 2.6.8; FINITE ELEMENT MODEL OF MPC-68

(0 DEGREE DROP MODEL)

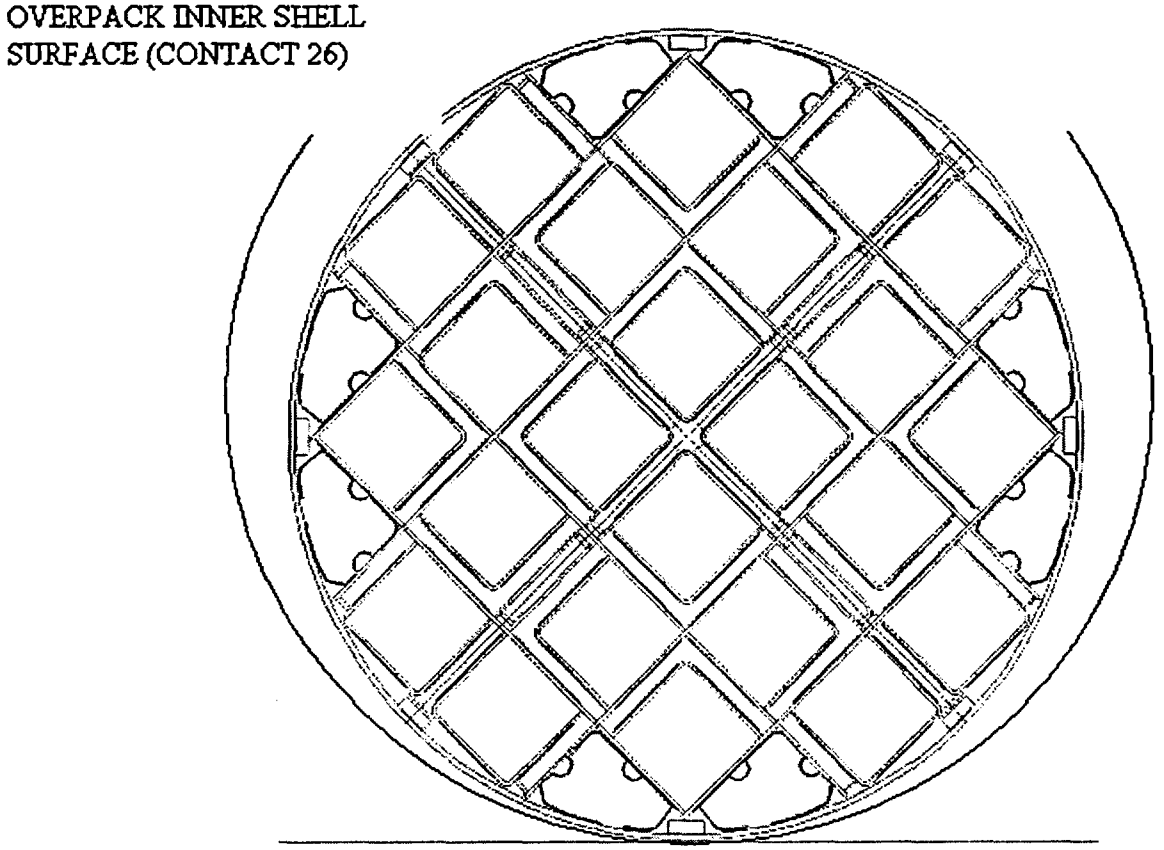

Note: Heat conduction elements shown in-place for clarity, but they are not considered in the analysis.

FIGURE 2.6.9; FINITE ELEMENT MODEL OF MPC-24/24E/24EF (45 DEGREE DROP MODEL)

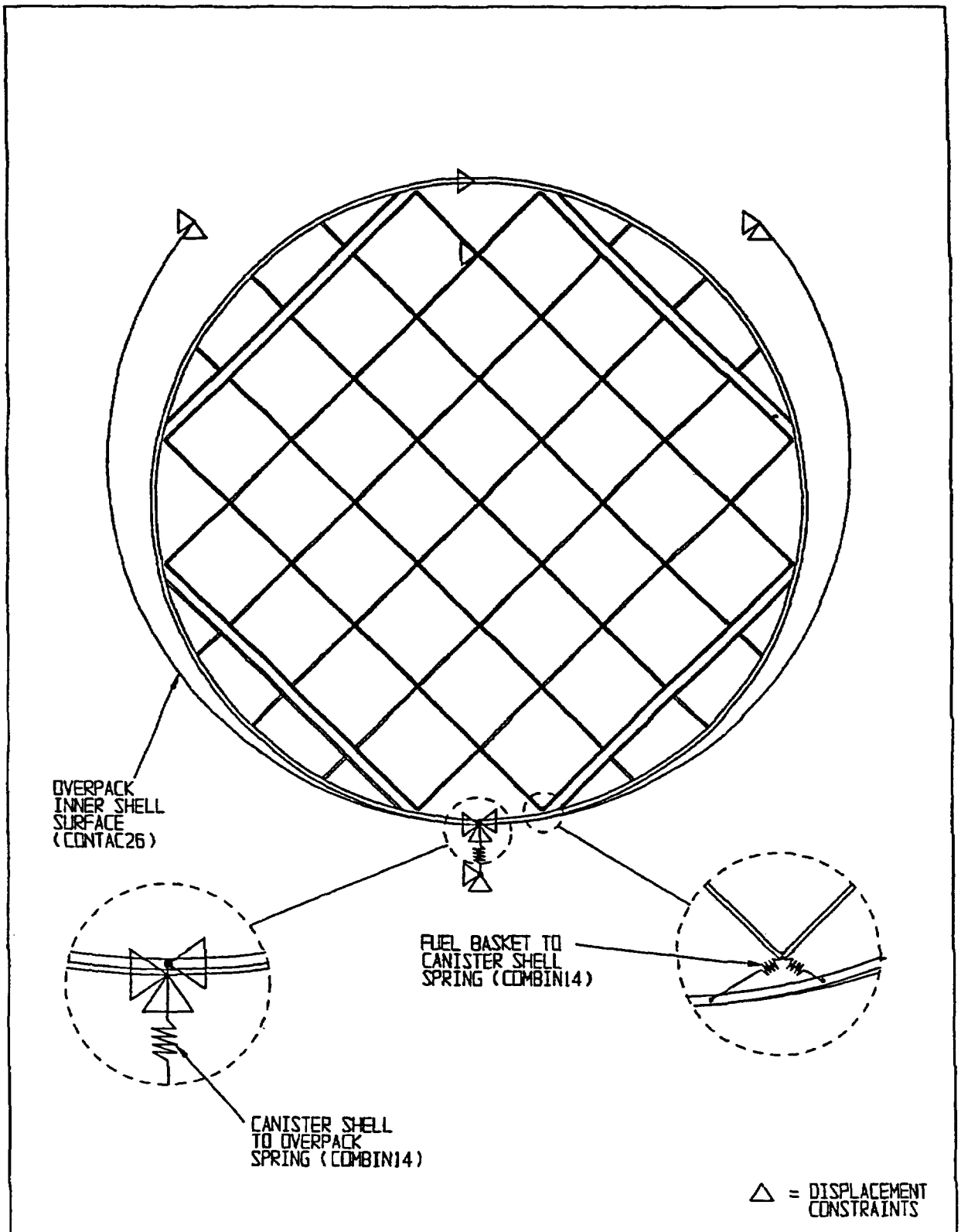

FIGURE 2.6.10; FINITE ELEMENT MODEL FOR MPC-32

(45 DEGREE DROP MODEL)

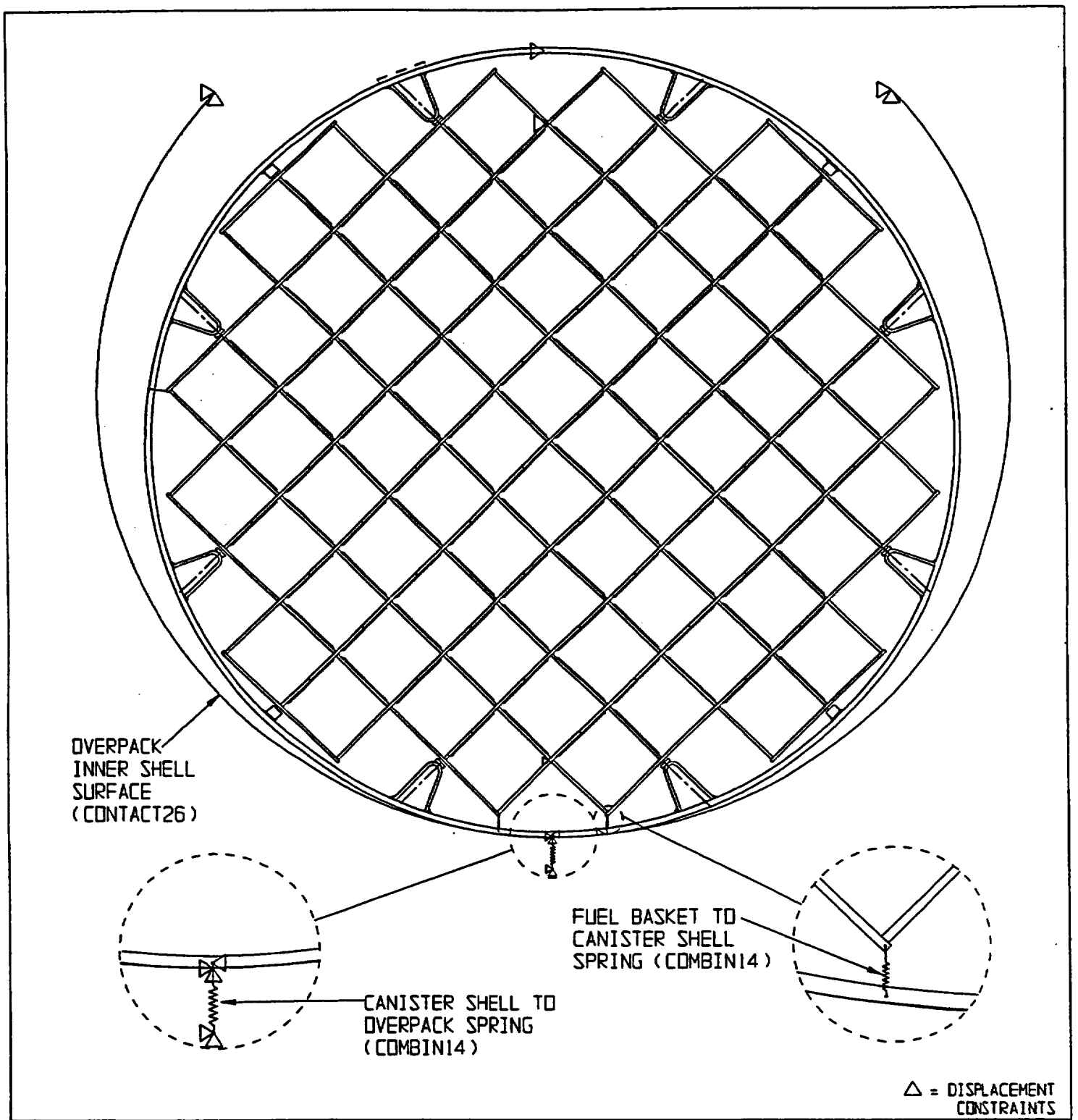

FIGURE 2.6.11; FINITE ELEMENT MODEL OF MPC-68

(45 DEGREE DROP MODEL)

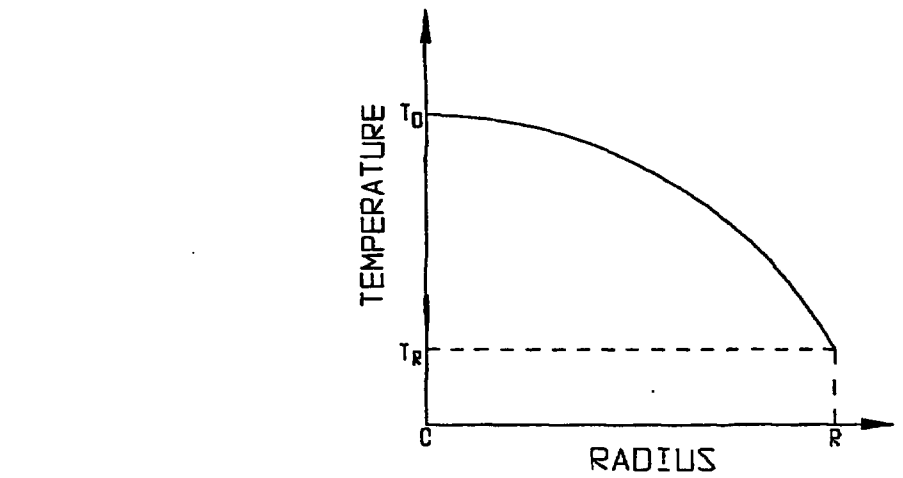

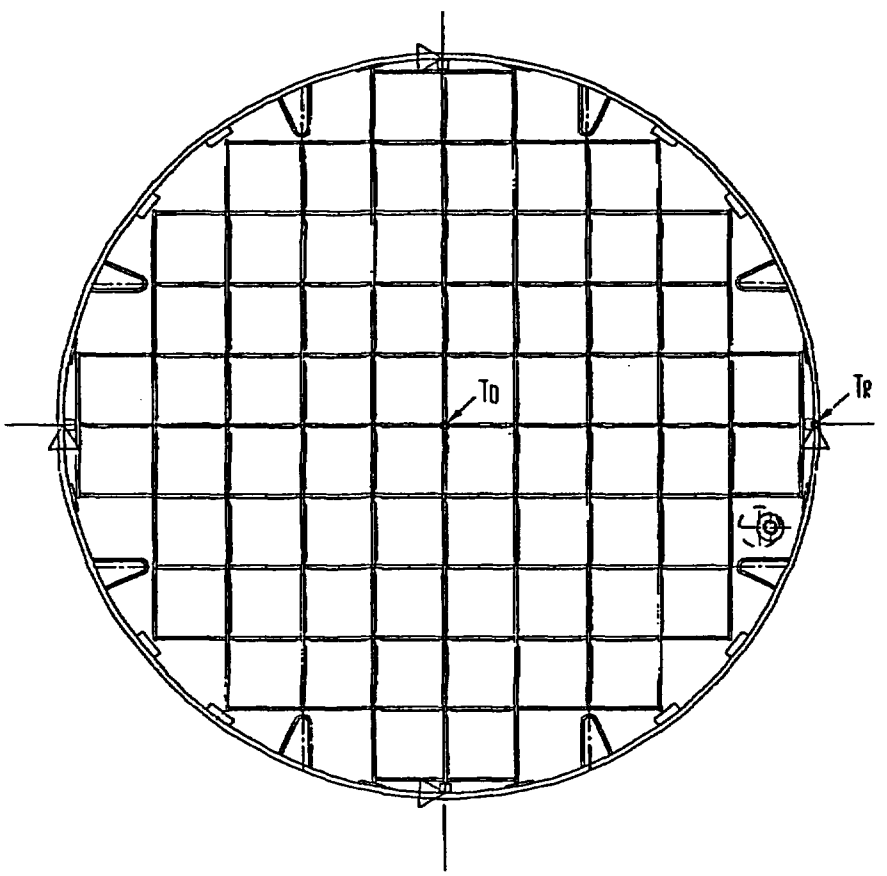

△ = DISPLACEMENT CONSTRAINTS

FIGURE 2.6.12; MPC THERMAL LOAD

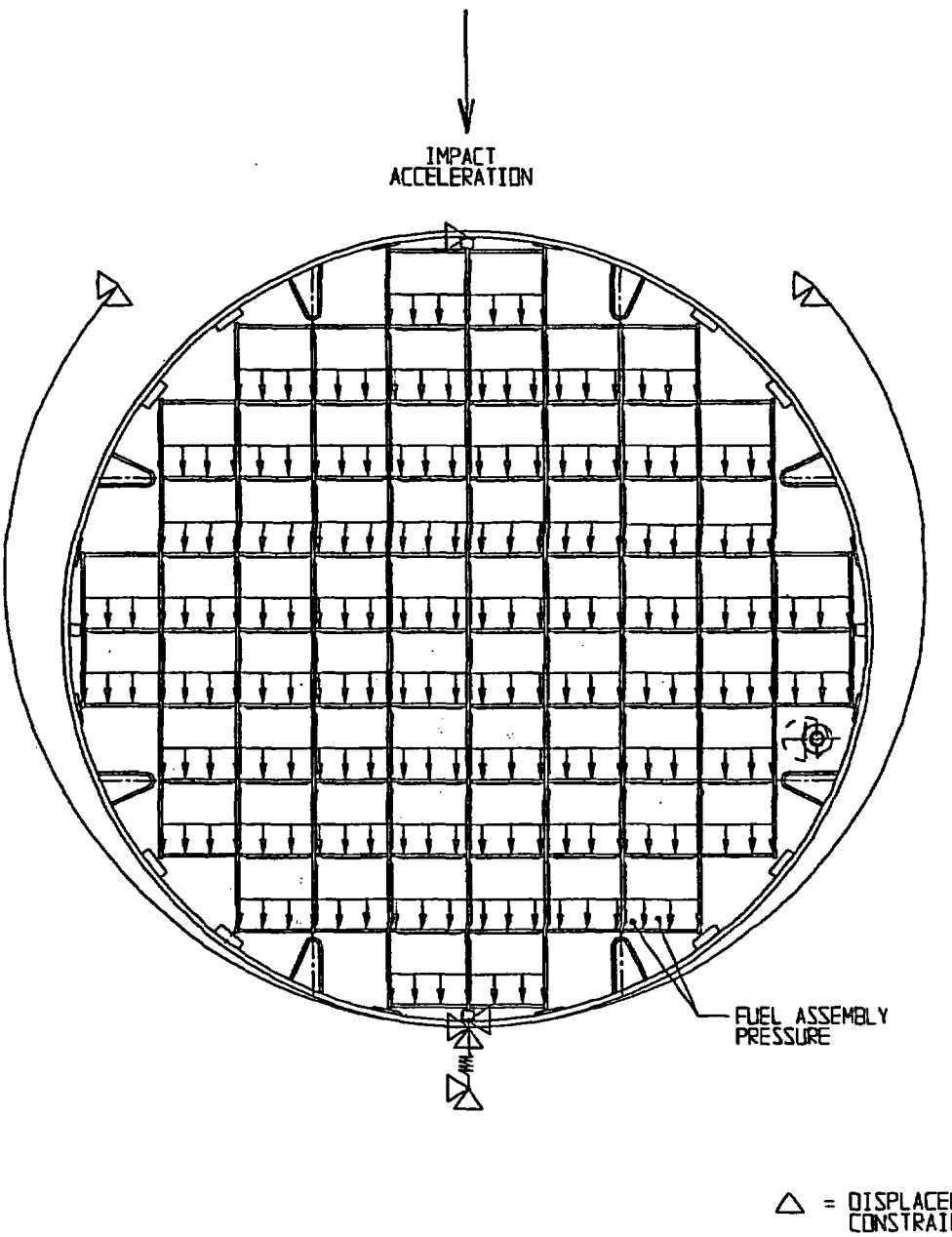

FIGURE 2.6.13; 0 DEGREE SIDE DROP OF MPC

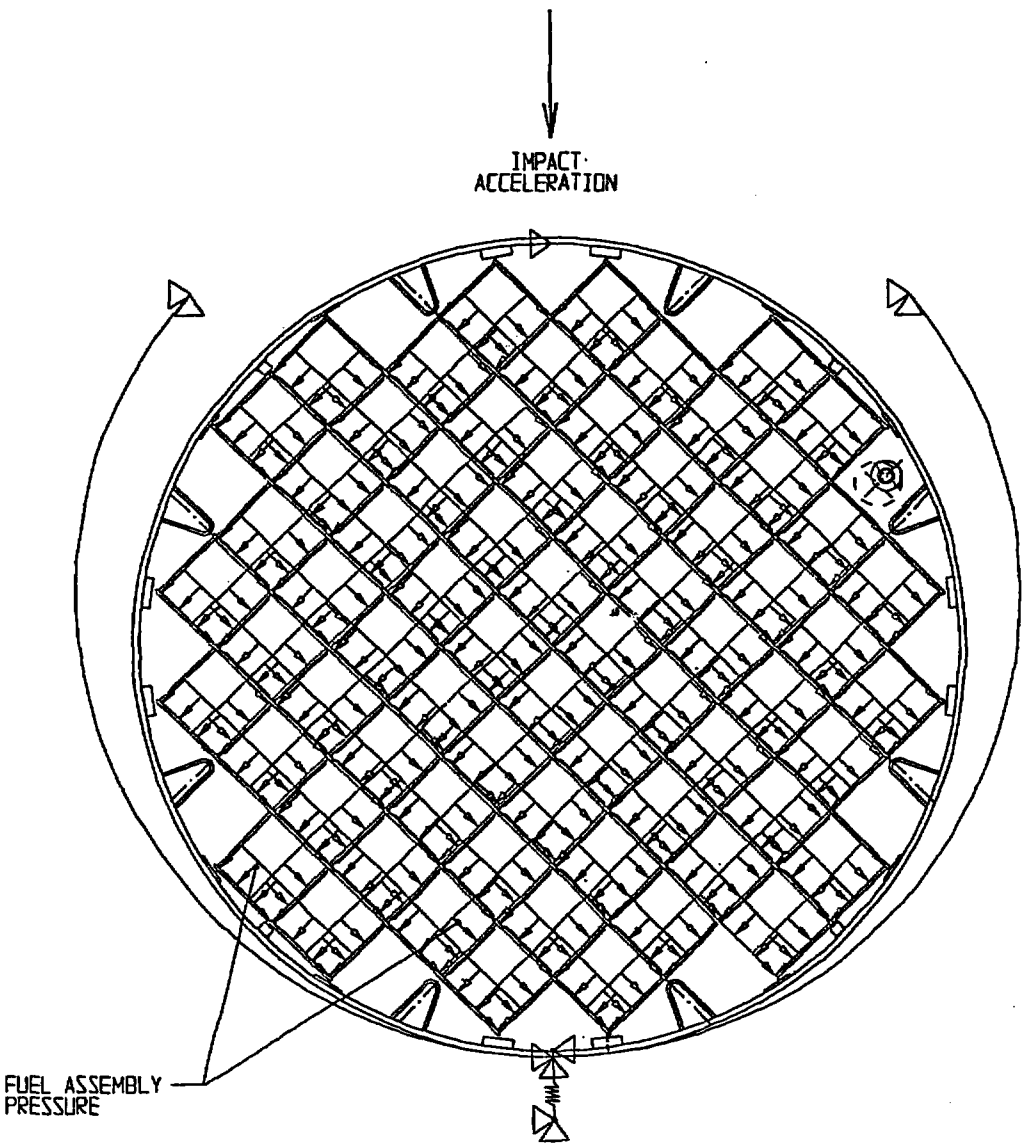

FIGURE 2.6.14; 45 DEGREE SIDE DROP OF MPC

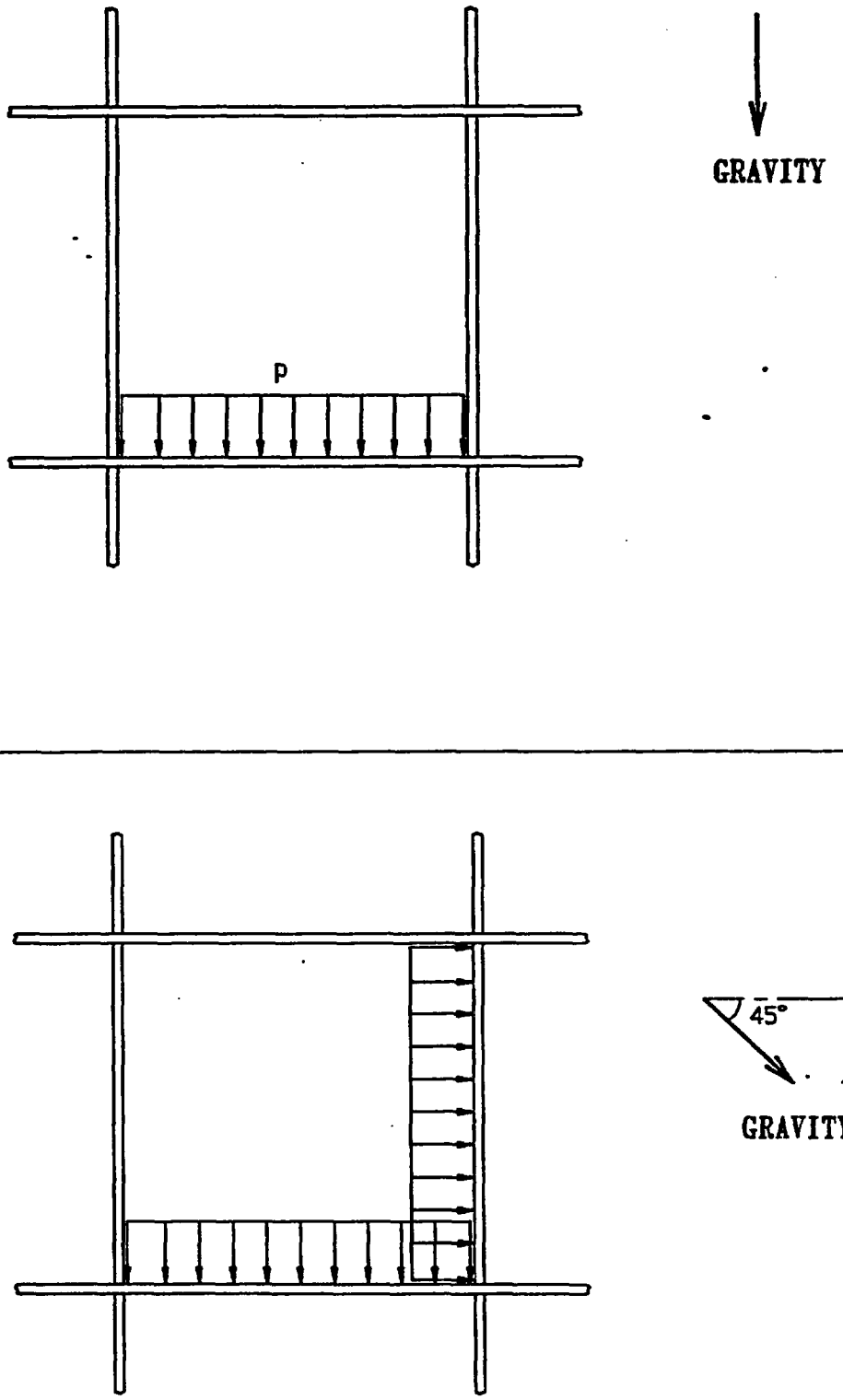

FIGURE 2.6.15; DETAIL OF FUEL ASSEMBLY PRESSURE LOAD ON MPC BASKET

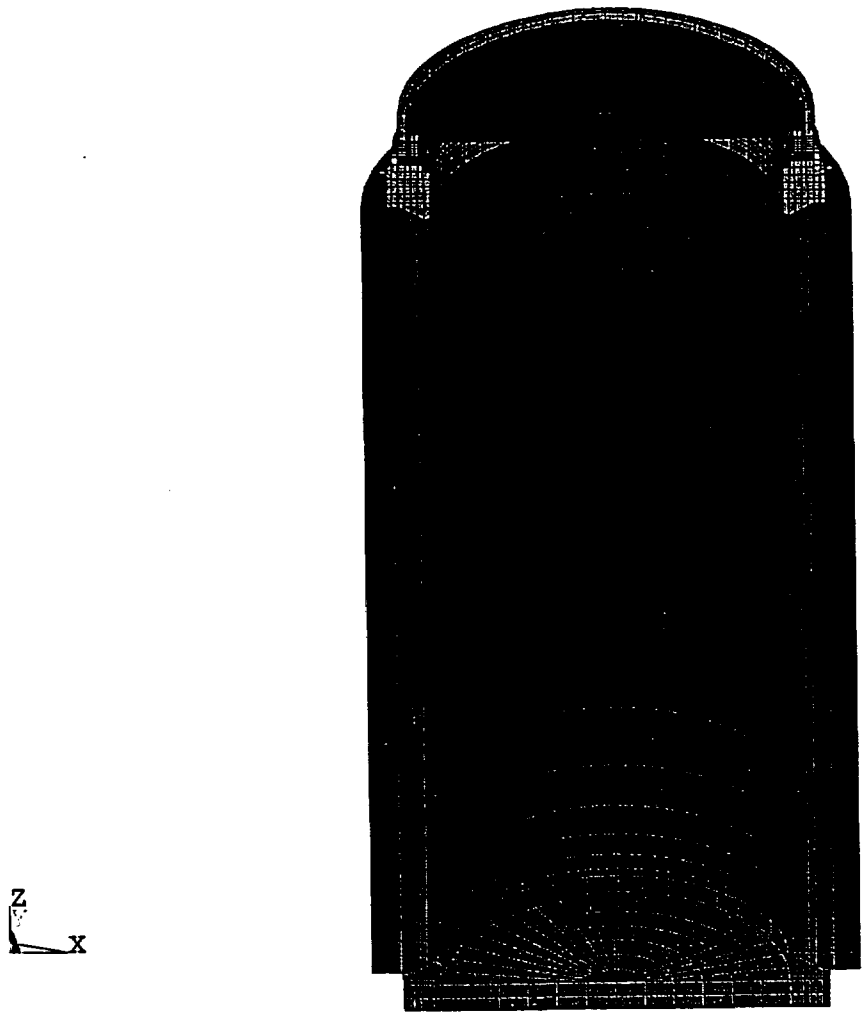

FIGURE 2.6.16 OVERPACK FINITE ELEMENT MODEL

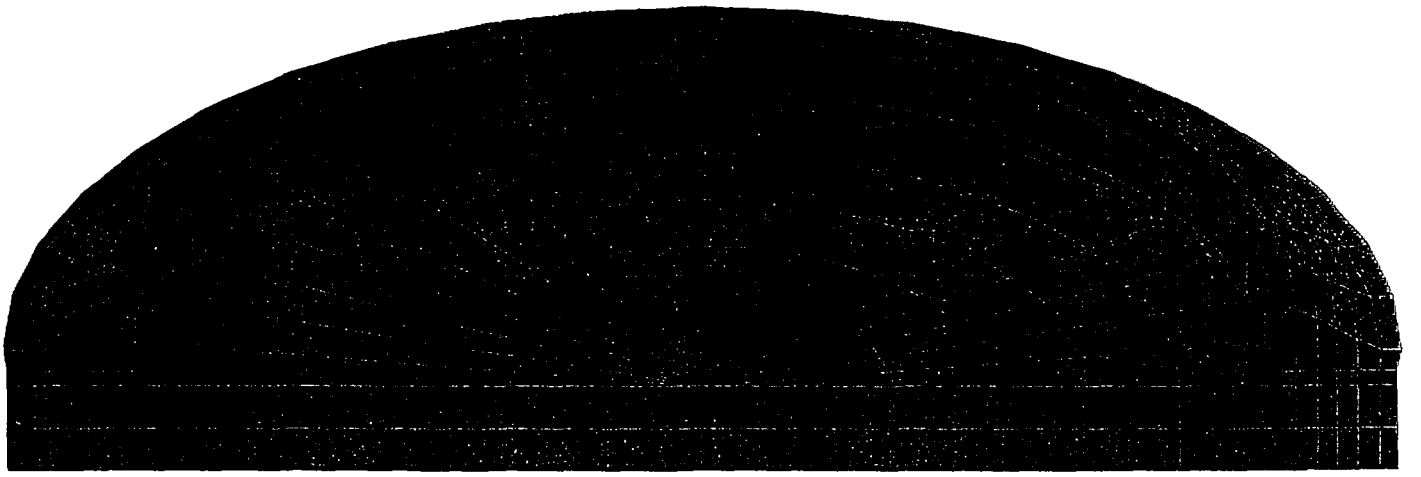

FIGURE 2.6.17 OVERPACK BOTTOM PLATE

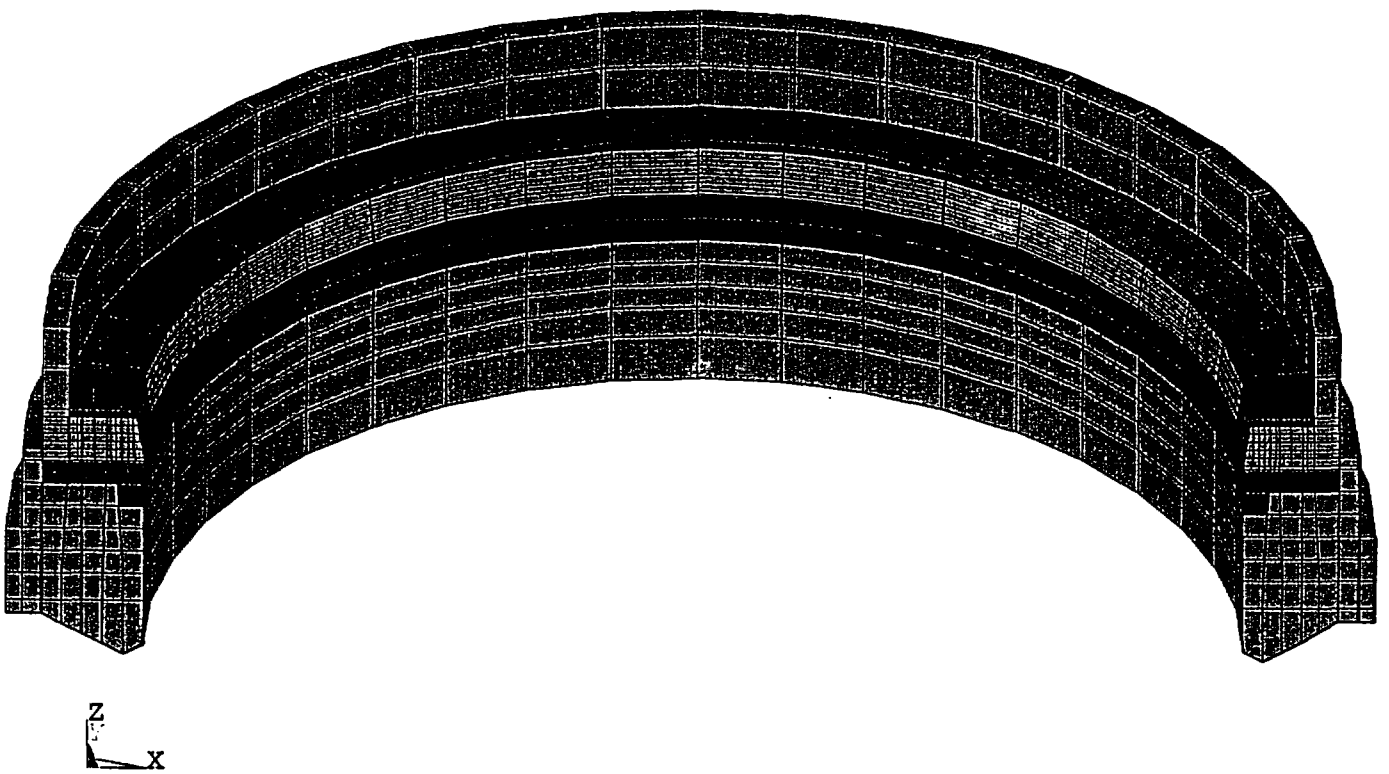

FIGURE 2.6.18 OVERPACK TOP FORGING

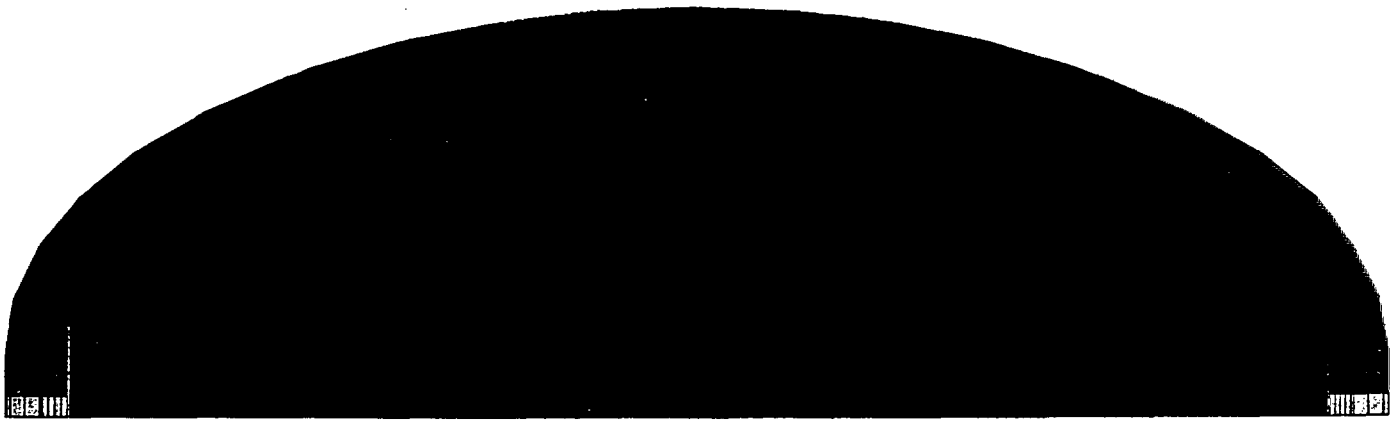

FIGURE 2.6.19 OVERPACK LID

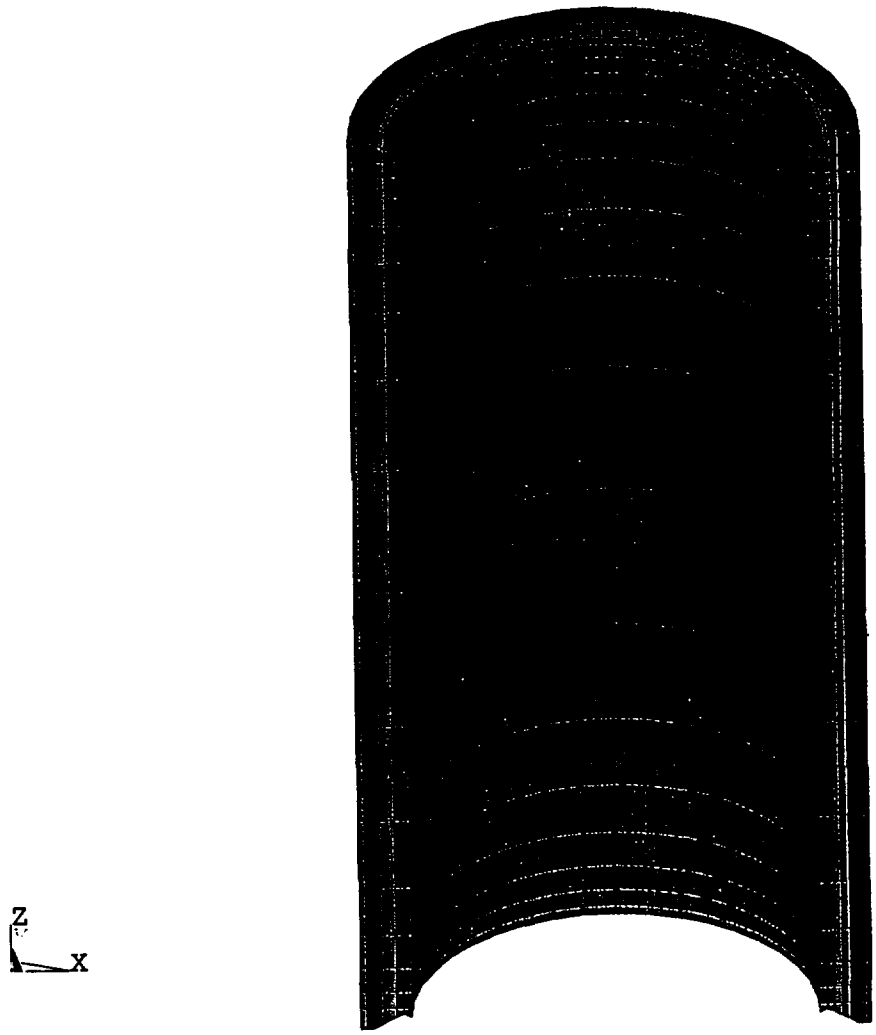

FIGURE 2.6.19A OVERPACK INNER AND INTERMEDIATE SHELLS

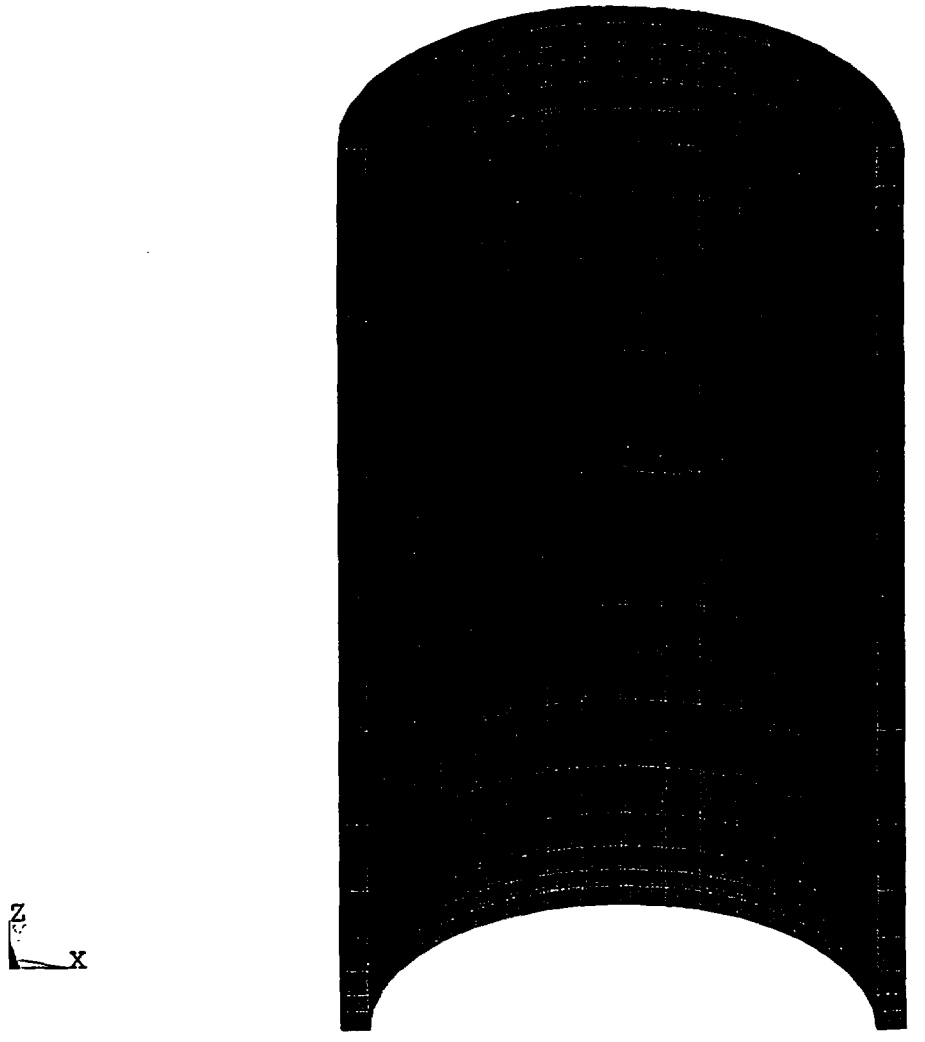

FIGURE 2.6.19B OVERPACK HOLTITE A ELEMENTS

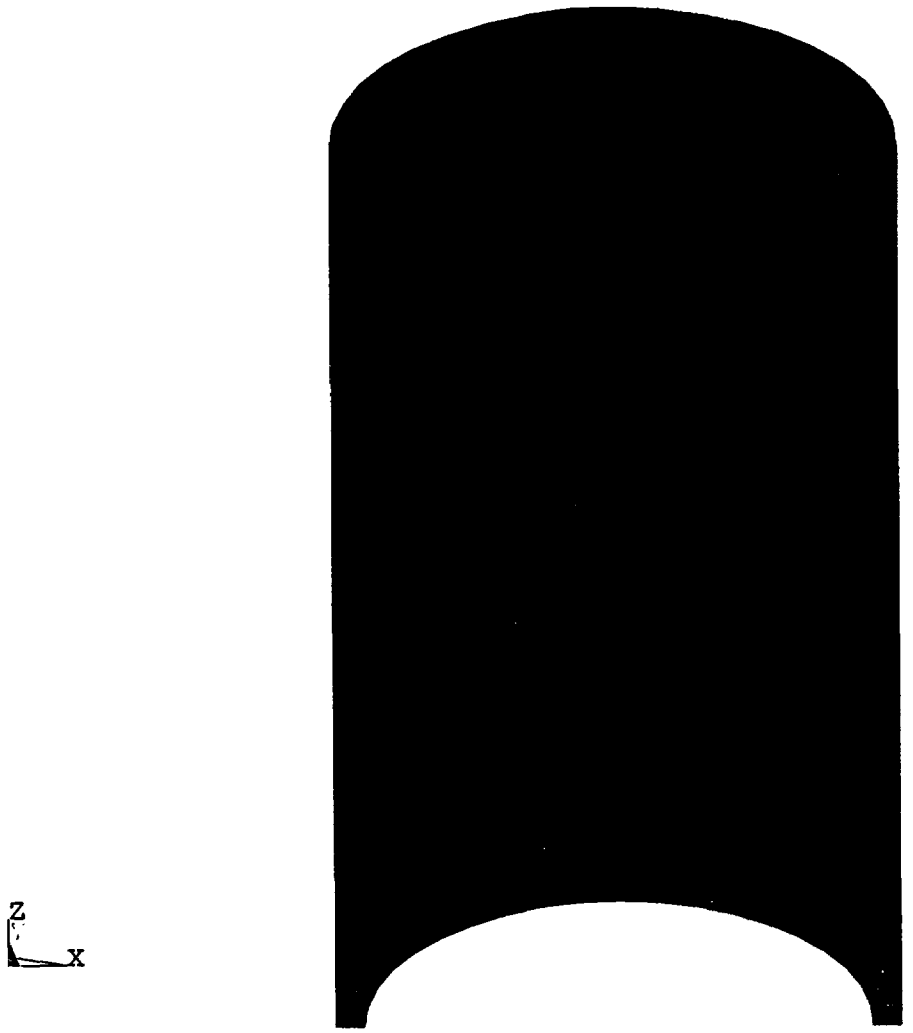

FIGURE 2.6.19C OVERPACK OUTER ENCLOSURE

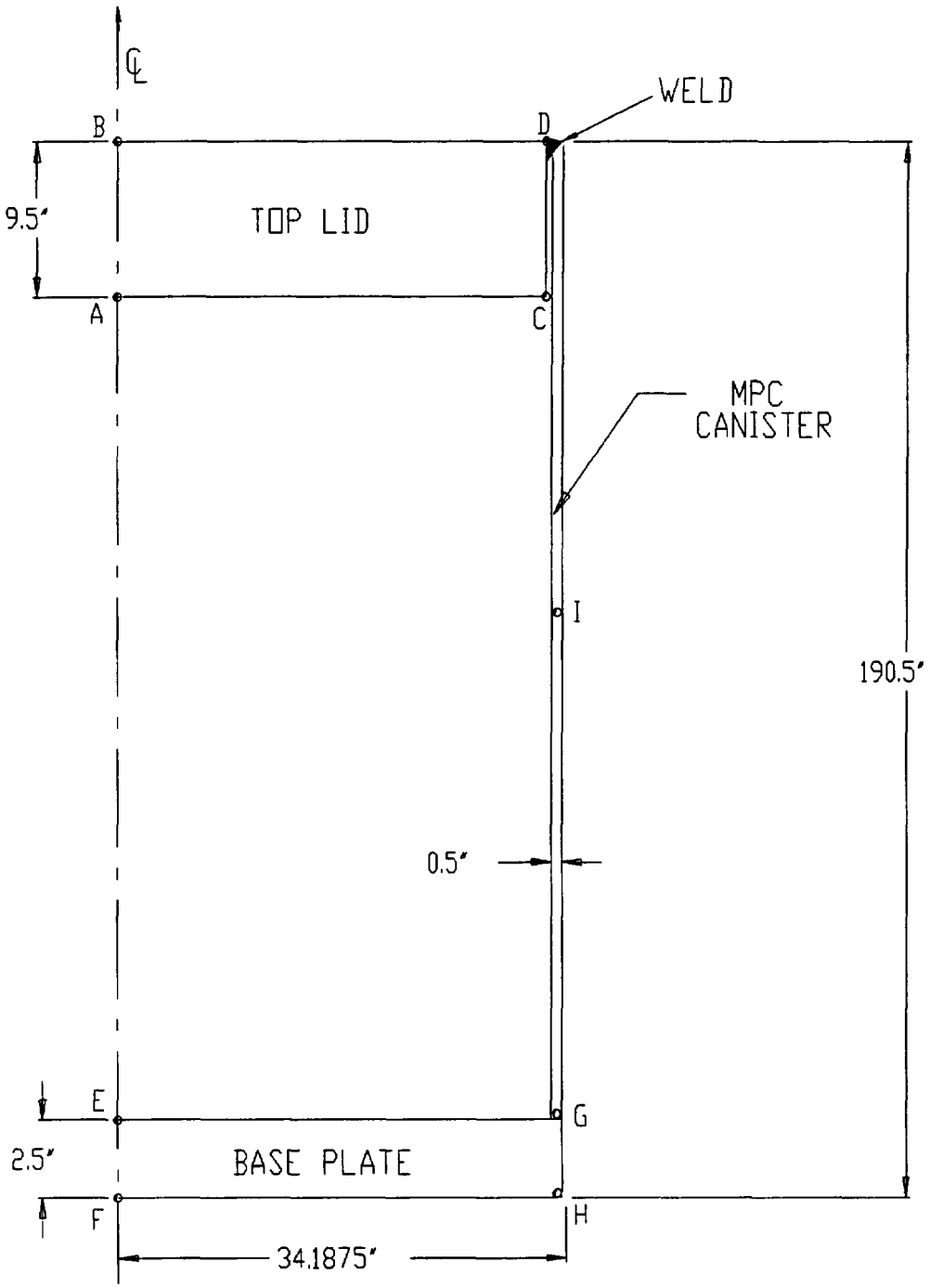

NOTE: SEE SECTION 2.6.1.3.1.2 FOR VARIOUS LENGTH/THICKNESS SYMBOLS.

FIGURE 2.6.20 CONFINEMENT BOUNDARY MODEL SHOWING TEMPERATURE DATA POINTS

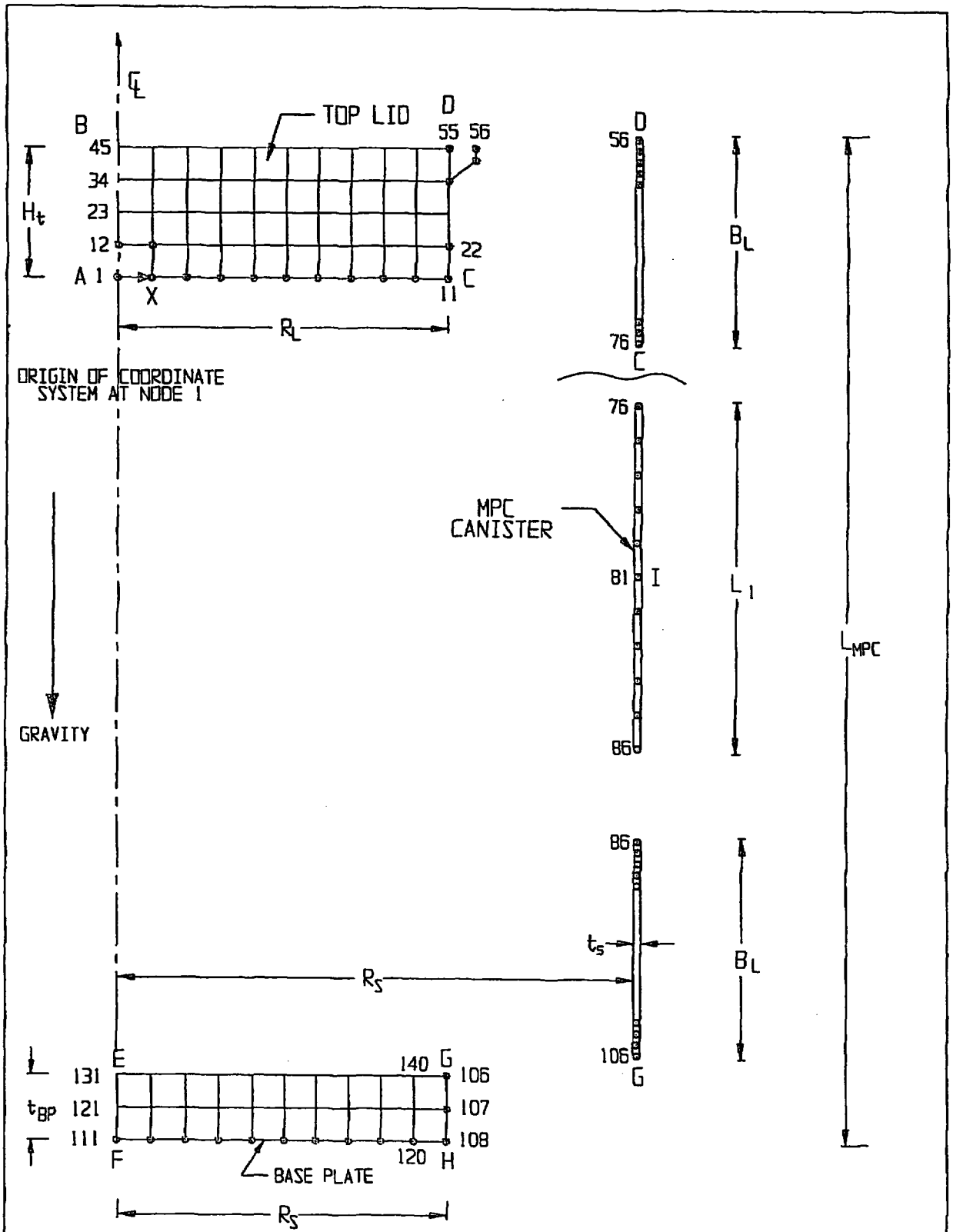

FIGURE 2.6.21 MPC - CONFINEMENT BOUNDARY FINITE ELEMENT GRID (EXPLODED VIEW)

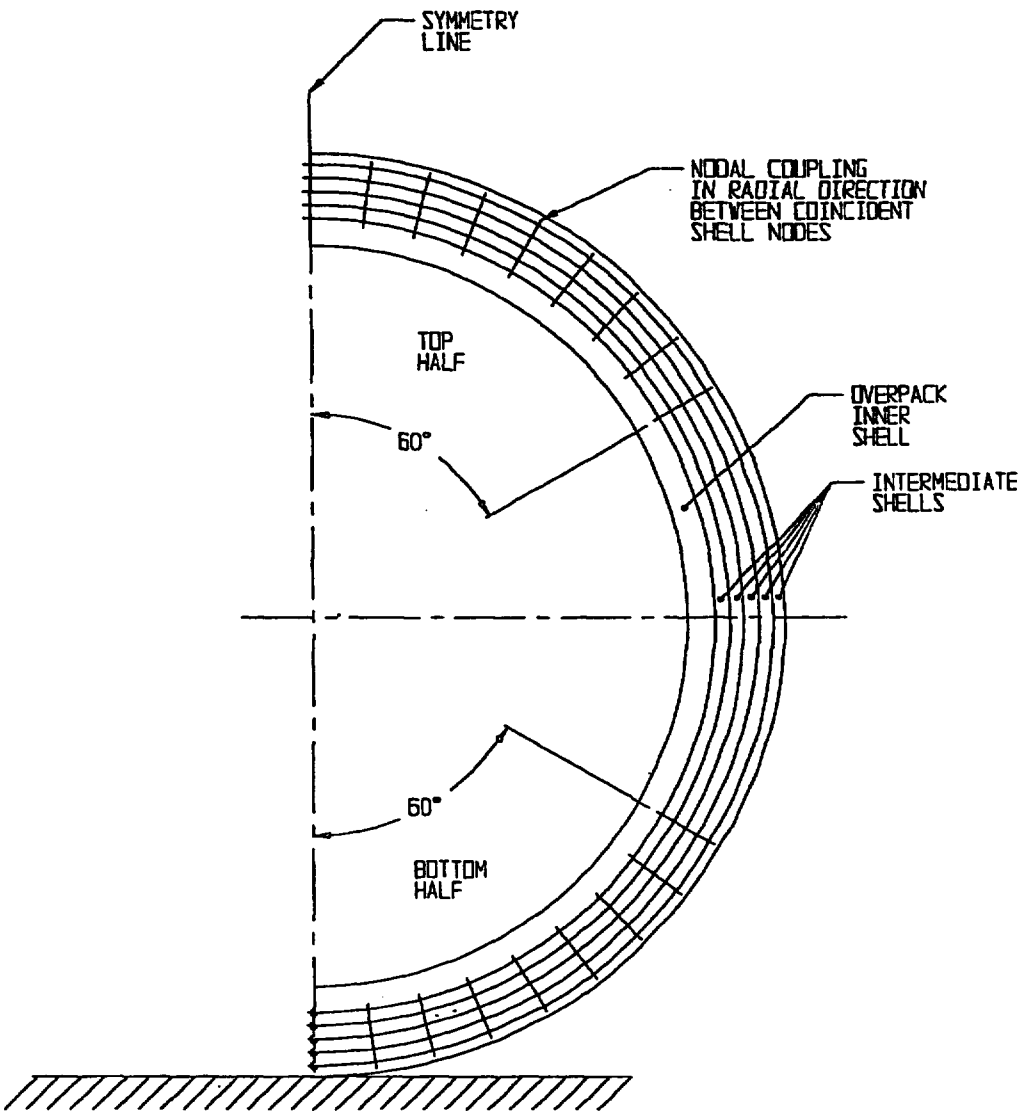

FIGURE 2.6.22; NODAL COUPLING IN OVERPACK
FINITE ELEMENT MODEL

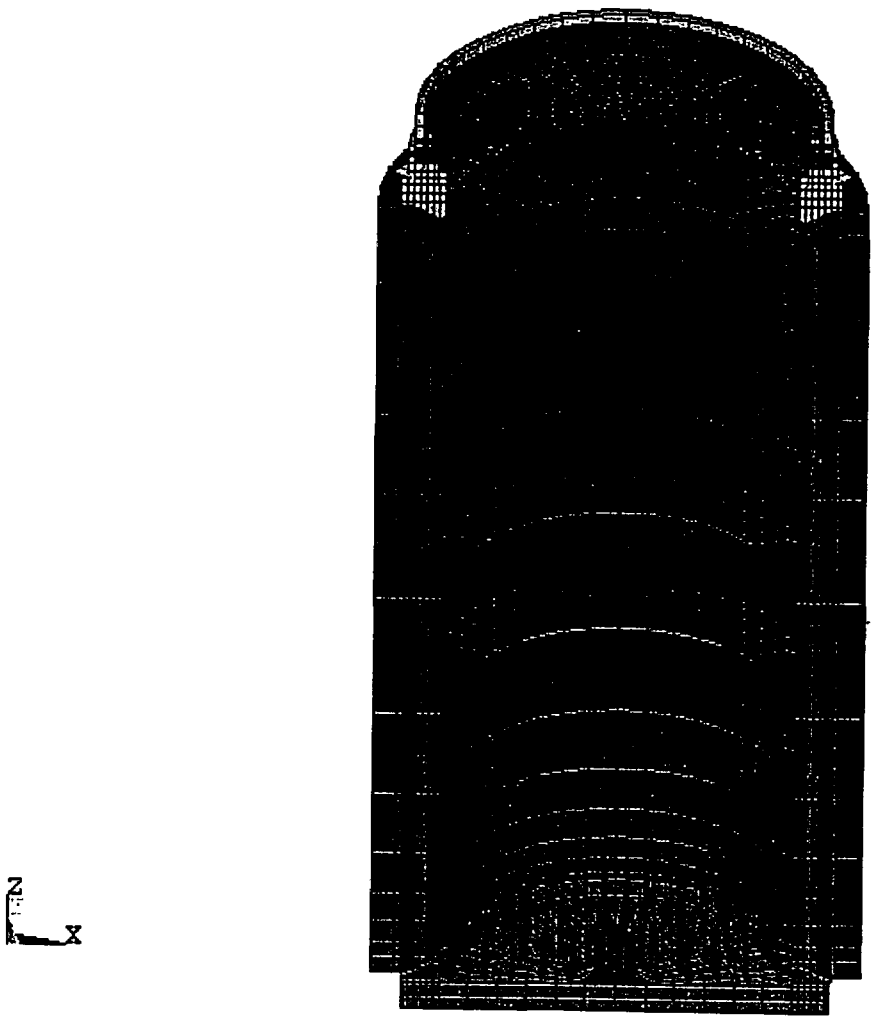

FIGURE 2.6.23 OVERPACK INTERNAL PRESSURE LOADING

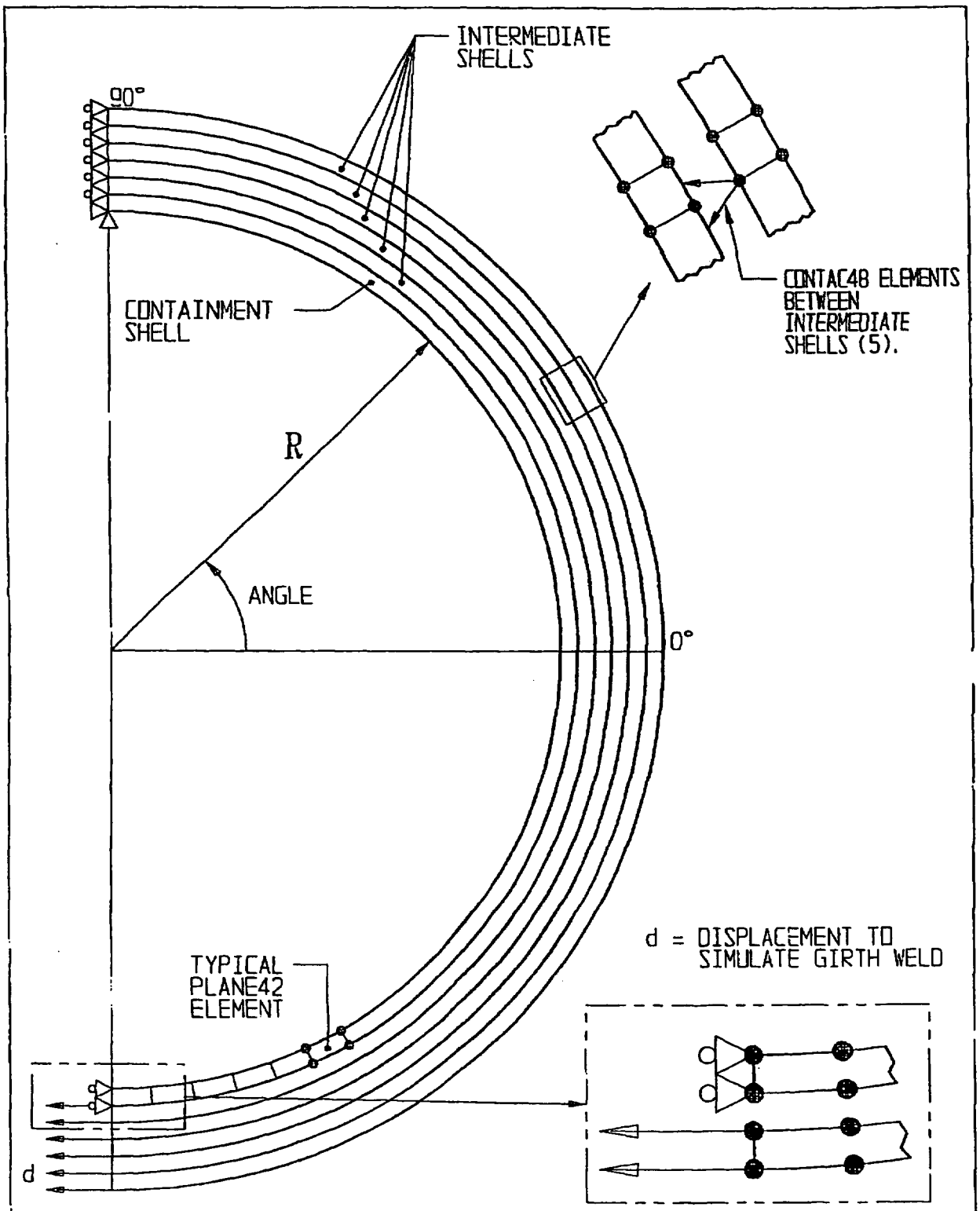

FIGURE 2.6.24; SIMULATION MODEL FOR FABRICATION STRESSES IN THE OVERPACK

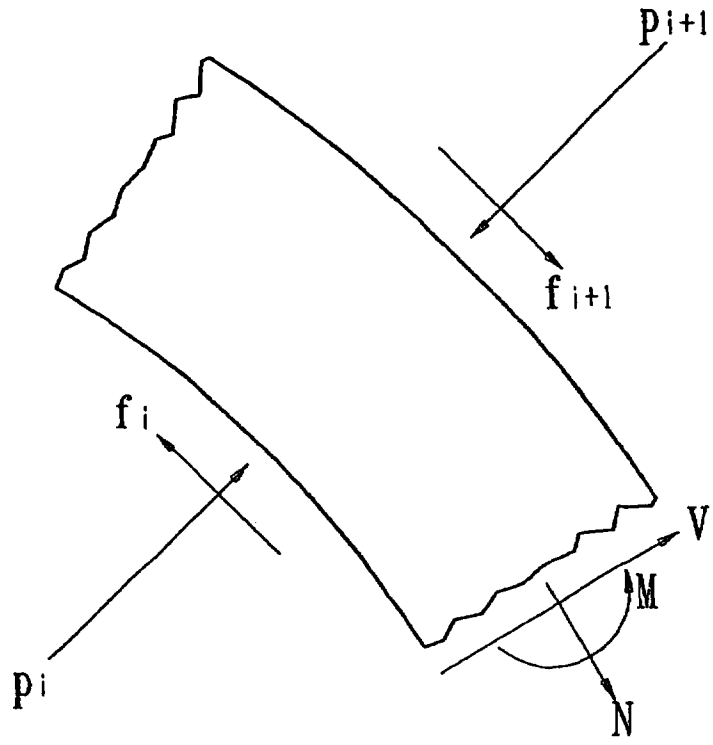

$$|f_i| \leq COF * |p_i|$$

COF = COEFFICIENT OF FRICTION

FIGURE 2.6.25; PARTIAL FREE BODY DIAGRAM OF A SHELL SECTION

2.7 HYPOTHETICAL ACCIDENT CONDITIONS

It was shown in the preceding section that the load combinations for normal conditions of transport do not induce stresses or stress intensities in excess of allowables. Therefore, it is concluded that the effectiveness of the HI-STAR 100 System is not reduced under normal conditions of transport.

The hypothetical accident conditions, as defined in 10CFR71.73 and Regulatory Guide 7.9, are applied to the HI-STAR 100 System in the required sequence. The system is first subjected to a 9 meter (30 foot) drop in the most damaging orientation, then subject to a 1 meter (40 inch) drop onto a 6 inch diameter mild steel pin (of length sufficient to cause damage to the steel structure), followed by a 1475^{o}F temperature fire environment for 30 minutes, and finally to a water immersion test.

The overpack containment boundary is also subjected to deep immersion in accordance with 10CFR71.61.

It is shown in the following subsections that the HI-STAR 100 System meets the standards set forth in 10CFR71, when it is subjected to the hypothetical accident conditions specified in 10CFR71.73. In particular, sufficient analytical and experimental evidence is presented herein to support the conclusion that HI-STAR 100 packaging, when subjected to hypothetical accident conditions, has adequate structural integrity to satisfy the subcriticality, containment, shielding, and temperature requirements of 10CFR71.

2.7.1 Free Drop

In this section the performance and structural integrity of the HI-STAR 100 System is evaluated for the most severe drop events. The drop events that are potentially most damaging are the end drops (top or bottom), the side drop, the orientation for which the center of gravity is directly over the point of impact, an oblique drop where the angle of impact is somewhere between center of gravity over corner and a near side drop, and an orientation where package rotation after an impact at one end induces a larger impact deceleration when the other end impacts the target (e.g., slapdown).

The structural assessment of the package is performed in two parts. In the first part, a numerical model to simulate the drop events is prepared and benchmarked against 1/8 scale static tests of the HI-STAR 100 impact limiters, and ¼-scale dynamic drop tests of the HI-STAR 100 Package. This numerical/experimental effort is carried out to confirm that the maximum rigid body decelerations experienced by the package are less than the design basis values set forth in Table 2.1.10. In the second part, the structural integrity of components under the inertia loads due to design basis deceleration levels is evaluated. The deceleration sustained by the internals, such as the fuel basket, are further amplified in recognition of the elasticity of the internal structures. The dynamic amplifier is considered as an added multiplier on the rigid body deceleration in the structural assessments. Dynamic amplifiers applicable to components of the package have been developed from evaluating the behavior of simplified models.

Part One: Maximum Rigid Body Deceleration Under 10CFR71.73 Free Drop Event

The determination of the AL-STAR impact limiter performance under postulated 10CFR71.73 free drop events was carried out in six phases as summarized below and further elaborated in Appendix 2.A.

i. Characterize honeycomb material crush behavior: Coupons of both unidirectional and cross-core honeycomb materials at different nominal crush strength values were prepared and tested. A typical pressure vs. deflection curve is shown in Figure 2.A.2.1 in Appendix 2.A. The pressure in the flat portion of the curve denotes the crush pressure.

Mathematical correlation of the data from the population of coupons tested showed that the pressure/crush curve for a honeycomb stock can be represented by one equation wherein the crush pressure, p_c, is the sole variable. This commonality in the deformation characteristic of the AL-STAR honeycomb materials of different crush strength is extremely helpful in simplifying the dynamic model for the impact limiter.

ii. AL-STAR Force-Crush Relationship: The AL-STAR impact limiter is a radially symmetric structure whose external and internal diameters are fixed: the I.D. is set by the overpack diameter at its extremities and the O.D. is limited by rail transport considerations to 128". Within this annular space, the arrangement of the aluminum honeycomb material is specified so that the impact limiter can absorb the kinetic energy from a 30' drop event in *any* orientation. The axial dimension of the impact limiter is also limited by considerations of the overall weight of the packaging. To design the impact limiter within the above-mentioned constraints called for a method to predict the force required to crush the impact limiter by a given amount in any given orientation. The mathematical model to define the force-crush (F-d) curve is described in Appendix 2.A. The F-d model was used to establish the nominal crush strengths of the honeycomb sectors used in the various locations of the AL-STAR honeycomb volume to obtain the desired energy absorption characteristics in the equipment.

iii. Static Scale Model Tests: The static 1/8 scale model tests consisted of preparing 1/8 scale models of the AL-STAR impact limiter and subjecting them to static crush tests in various orientations under normal and abnormal temperature conditions. One object of these tests was to confirm the validity of the theoretical F-d model. Confirming the structural adequacy of the AL-STAR backing structure (which is a thick carbon steel weldment) and the external skin were also objectives of the scale model test. The 1/8 scale static tests, as described in Appendix 2.A, met all project goals: a weakness in the AL-STAR backing structure was identified and corrected in a redesign of the backing structure. The test data also showed that Holtec's F-d model provided a reasonably accurate analytical tool to predict the static crushing behavior of AL-STAR in the various potential crushing orientations. The adequacy of the F-d model to predict static crush behavior was an essential prerequisite for the dynamic test correlation effort that followed.

iv. Dynamic Scale Model Tests: A 1/4 scale model of the HI-STAR 100 Package, including AL-STAR impact limiters, was used for drop testing. The drawings for the 1/4 scale impact limiters are provided in Section 1.4. Appendix 2.A herein provides a complete synopsis of the AL-STAR impact limiter design development program, including the 1/4 scale model drop tests which demonstrated the performance of the package. The objectives of the drop tests may be stated as follows:

i. Select a sufficient number of drop orientations to ensure that under the worst-case orientations, the structural adequacy of the package is demonstrated by testing.

ii. Prove that the peak rigid body decelerations experienced by the package in any of the tests is below the Table 2.1.10 design basis value.

iii. Demonstrate that the impact limiters prevent the cask from direct contact with the unyielding surface and remain attached through the end of the drop event.

Four drop configurations, namely, vertical (top end), horizontal (side), center-of-gravity-over-corner (CGOC), and slap-down (fully described in Appendix 2.A) were identified as a complete set capable of realizing the aforementioned objectives. The tests were performed in two distinct series as described below.

The first test series, conducted in August 1997, indicated the need to modify the honeycomb material crush strength utilized. The first dynamic test series also helped quantify the dynamic multiplier applicable to the statically determined honeycomb crush strength under impact conditions.

The second test series showed that the peak deceleration in all four drop orientations tested met the Table 2.1.10 limits. Despite meeting deceleration limits, the attachment bolts between the bottom impact limiter and the overpack failed in the side drop test. This required an additional design improvement to the bottom impact limiter-to-overpack attachment design, and re-performance of the side drop test. For the final four tests used for evaluation in Appendix 2.A, no attachment bolts sustained a failure.

v. AL-STAR Dynamic Response Model: The 1/4 scale tests provided valuable information on the package response which was used to confirm the veracity of Holtec's dynamic simulation model developed for predicting the package response under the other drop conditions. Like all orthotropic materials, the crushing of the honeycomb requires greater force under an impact load than the load necessary to achieve the same extent of crush under static conditions. The conversion of the static "force (F) - crush (d)" model to dynamic conditions simply means applying a dynamic factor to the formula. In other words, under dynamic conditions, the relation between crush force "F" and crush "d" is given as:

$$F = Z\, f(d)$$

where f(d) is the crush force corresponding to the compression "d" under static conditions and Z is the dynamic multiplier function. The value of Z was quantified by the first series of 1/4 scale dynamic scale model test, such that a dynamic response simulation model could be developed that satisfied all equilibrium expectations.

In addition to comparing the predicted peak decelerations with the measured value, the duration of crushing and crush depth predicted by the dynamic model were also compared with the measured test data. The comparisons, presented in Appendix 2.A, confirm the ability of the dynamic model to simulate the behavior of the package under a drop event.

vi. Sensitivity Studies: A significant result from the 1/4 scale model dynamic tests was a complete validation of the dynamic model. For every test performed, the AL-STAR dynamic model was able to simulate the peak accelerations, total crush, *and* crush duration with reasonable agreement. The experimentally benchmarked mathematical model could now be used to simulate drop events for a variety of HI-STAR 100 package weights and honeycomb crush strengths. Results of the simulations to determine the effects of variations in aluminum honeycomb crush strengths and package weights are presented in Appendix 2.A.

The results summarized in Table 2.A.5 of Appendix 2.A demonstrates that the maximum rigid body deceleration experienced by the HI-STAR 100 package equipped with the AL-STAR impact limiter (see the applicable drawing in Section 1.4 herein) will be less than 60g's regardless of the orientation of impact. Therefore, in the balance of analyses performed to evaluate the consequences of "free drop" under the provisions of 10CFR71.73, the package will be assumed to be subject to a rigid body deceleration equal to 60 g's. It is clear from inspection of the geometry of the package that the most vulnerable direction of inertia loading for the HI-STAR fuel basket is the transverse direction wherein the flat panels of the basket are subjected to lateral inertia loading from the contained SNF. As mentioned earlier, the flexibility of basket panel acts to further amplify the package deceleration, which must be considered in the evaluation of results from the stress analysis model. In summary, the net result of the work effort described in the foregoing and further elaborated in Appendix 2.A was to confirm the validity of 60g as the *design basis* rigid body deceleration for the 10CFR71.73 drop event.

In Appendix 2.A, additional supporting technical information requested in Paragraph 2.7 of Reg. Guide 7.9 is provided. Information provided includes free-body diagrams, sketches, governing equations, test method for model testing, scaling factors, discussion of the law of similitude, measurements of crush, impact duration, deceleration histograms, effect of tolerances on package response, and demonstration that the model test will give conservative results for peak g-force and maximum deformation.

Additionally, Reg. Guide 7.9 calls for evaluation of the response of the package in terms of stress and strain to components and structural members, including investigation of structural stability as well as the consequences of the combined effects of temperature gradients, pressure, and other loads. Part Two of the work effort, described in the following, fulfills the above Reg. Guide 7.9 stipulations.

Part Two: Stress Analysis

The second part of the analysis is performed using the ANSYS finite element software [2.6.4]. The MPC and overpack models used here are identical to those presented in Section 2.6. The loads are applied to the models in accordance with the load combinations defined in Table 2.1.6 (Load Cases F3), Table 2.1.7 (Load Cases E3), and Table 2.1.9 (Load Cases 1-16) for hypothetical accident conditions of transport. The detailed application of each load case is described in the subsections that follow. The presentation and content follows the formatting requirements of Regulatory Guide 7.9. The results from conditions of "Heat" and "Cold" are considered together in the following presentation.

The analysis of the different hypothetical accident conditions of transport are carried out using general finite element models of the MPC and the overpack as well as calculations based on simplified models amenable to strength of materials solutions. The analyses using strength of materials solutions focus on specific loading conditions applied to component parts of the MPC and/or the overpack. The finite element analysis of the overpack involves a complex 3-D model of the overpack to which a series of loads are applied. The results from the solutions are then combined in a post-processing phase to make up the different accident load combination. Given the complexity of the overpack finite element analysis model, some discussion of the stress report is presented to facilitate an understanding of the conclusions. For each of the load combinations, the following components are identified for reporting purposes:

1. Seal
2. Bolts
3. Lid
4. Inner Shell (including the top flange)
5. Intermediate Shells
6. Baseplate
7. Enclosure

The postprocessor collects the nodal stresses from the finite element solution, for each of the components in turn, and reports the principal stresses and the stress intensity at selected locations where physical reasoning suggests that high stresses may occur under the different postulated load combinations. In order to identify the minimum safety factor for each of the above components after the load cases are combined, the collection of nodes is sorted by stress intensity magnitude in descending order. Therefore, since the hypothetical accident condition load combinations involve a comparison of primary stress intensities, a minimum safety factor for each of the defined components in the model may be identified as occurring at the node point with the largest calculated stress intensity. Safety factors are computed using the allowable stress intensities for the material at the reference temperature identified for the component and reported under one of the seven groups identified above. The post-processor collects, sorts, and reports the necessary information to enable documentation of the satisfaction of the applicable requirements. The following items are collected and evaluated for each load combination:

Seals: The normal force in each of the springs representing the seal is reported and shown to remain in compression under the load. Maintaining a compressive load in the seal springs assures that there is no separation at the component interfaces.

Bolts: The bolts are initially preloaded by applying an initial strain sufficient to result in the desired pre-stress. Subsequent to the application of the different loads to form a specified load combination, the bolts are shown not to unload.

Lid: For each load combination, the lid primary membrane plus primary bending stress intensities are compared to the allowable values at the designated reference temperature.

Inner Shell: Primary membrane and primary membrane plus bending stress intensity distributions are examined and compared to allowable stress intensity values

Intermediate Shells: The five intermediate shells are examined at stress location points and compared to allowable stress intensities at the appropriate reference temperature. Since accident conditions of transport represent a Level D condition (where the comparison of calculated value vs. allowable value is always based on stress intensity), there is no differentiation between intermediate shells considered as Class 1 or Class 3 components.

Baseplate: Primary membrane plus bending stress intensities are compared to allowable values at the component reference temperature.

Enclosure: The plate and shell elements making up the enclosure for the Holtite-A material are compared to primary membrane stress intensity allowable values.

In the finite element analysis of all load combinations associated with hypothetical accident events, the initial preload case of the bolts and the internal pressure case are included in the final combination. Since no secondary stresses need be evaluated per the ASME Code requirements for an accident level event, the thermal stress load case for the "Heat" condition is not included as a specific load case. However, the allowable stress intensities used for the safety factor evaluation are obtained at the appropriate "Heat" condition reference temperature. In the reporting of safety factors, the variation in allowable stress intensity with temperature is ignored; this introduces an additional measure of conservatism in the reported safety factors since the reference temperatures (Table 2.1.21) are higher than the actual calculated temperatures. For the "Cold" condition, there are no temperature gradients developed. The interaction stresses developed to maintain compatibility under the uniform ambient temperature change are included in the analysis and are treated as primary stresses in the evaluation of the safety factor.

2.7.1.1 End Drop

- Overpack Stress (Load Cases 1,2,9, and 10 in Table 2.1.9)

The overpack is evaluated under both a top end drop and a bottom end drop. In both cases, the impact limiter reaction is assumed to act over the entire area that is backed by structural metal. Given that the total dropped weight is W and that the maximum acceleration is A, the impact

$$|R| = \frac{WA}{g}$$

limiter total reaction load follows from force equilibrium.
This reaction load R is imposed on the appropriate region of the overpack (either lid outer surface or bottom plate outer surface as a uniform pressure load to maximize the bending of the lid or bottom plate.

Since the same finite element model described and used in Section 2.6 for evaluation of loading associated with normal conditions of transport is used here with different applied loads, no further discussion of the model or the analysis methodology is required. Figures 2.1.7 and 2.1.8 show the loading on the overpack in the bottom down and the top down configurations, respectively. The results of the analyses for the top end and bottom end drops are collected and safety factors from the limiting locations in the model are reported in Tables 2.7.5 and 2.7.6 for both heat and cold environments. Table 2.7.5 presents the minimum safety factors for each of the components identified above for the "Heat" condition and Table 2.7.6 presents the safety factors for the "Cold" condition. Within each table, the component is identified, and the minimum safety factor reported.

- Overpack Stability

Structural stability of the overpack containment inner shell under the end drop is assessed. The case of the accident end drop is evaluated for elastic and plastic stability in accordance with the methodology of ASME Code Case N-284 [2.1.8]. All required interaction equation requirements set by [2.1.8] are met. For this event, yield strength limits rather than instability limits govern the minimum safety factor. The minimum safety factor for this case is summarized below:

Code Case N-284 Minimum Safety Factors - (Load Case 1 and 2 in Table 2.1.9)			
Item	Calculated Interaction Value	Allowable Interaction Value†	Safety Factor against Yield†
Load Case 1 and 2 in Table 2.1.9	0.62	1.34	2.16

† Note that in computing the safety factor against yield for this table, the safety factor implicit in the Code Case N-284 allowable interaction equation is included. Note also that the safety factors given above from the Code Case analysis are all safety factors against the circumferential or longitudinal stresses reaching the material yield stress. The actual safety factors against instability are larger than

the factors reported in the table. In other words, yield strength rather than stability is the limiting condition. Finally, note that fabrication stresses have been included in the stability calculations even though these stresses are self-limiting. Therefore, all results corresponding to the calculated stability interaction equations are very conservative.

The result for the heat environment bound the similar result for the cold environment since yield strengths and elastic modulus are higher. Therefore, no analysis is performed for stability under cold conditions.

- Closure Bolt Analysis

Stresses are developed in the closure bolts due to pre-load, pressure loads, temperature loads, and accident loads. Closure bolts are explored in detail in Reference [2.6.3], which deals with the analysis of shipping casks. The analysis of the overpack closure bolts under normal conditions of transport has been reported in Section 2.6. This subsection presents the results for the analysis for the hypothetical accident end drop. The analysis follows the procedures defined in Reference [2.6.3]. The allowable stresses used for the closure bolts follows that reference. Note that the analyses provide alternative confirmation of the results from the finite element analysis; namely, under any of the identified load combinations, the bolts do not unload.

The following combined load case is for the hypothetical top end drop accident condition of transport. This drop conservatively assumes a nearly vertical orientation with the impact limiter reaction load applied at the outermost location of the lid. This results in the closure bolts resisting the inertial load from the MPC plus contents in addition to the inertia load from the closure lid itself. In reality, the load from the MPC would not load the bolts.

Top End Drop: Pressure, temperature, and pre-load loads are included.

Reference [2.6.3] reports safety factors defined as the calculated stress divided by the allowable stress for the load combination. This definition of safety factor is the inverse of the definition consistently used in this SAR. In summarizing the closure bolt analyses, results are reported using the safety factor definition of allowable stress divided by calculated stress. The following result for closure lid bolting for the top end drop hypothetical accident condition of transport is obtained.

Overpack Closure Bolt - Safety Factor (Load Case 2 in Table 2.1.9)	
Combined Load Case	Safety Factor on Bolt Tension
Average Tensile Stress	1.30

It is seen from the above table that the safety factor is greater than 1.0 as required. Note that the average tensile stress reflects the preload stress required for successful performance of the bolts as well as the applied load from the hypothetical accident drop event.

- MPC Fuel Basket Stability and Stress (Load Case F3.a in Table 2.1.6)

Under top or bottom end drop in a hypothetical accident condition of transport, the MPC is subject to its own amplified self-weight, causing compressive longitudinal stress in the fuel basket cell walls. The following analysis demonstrates that stability or yield is not a credible safety concern in the fuel basket walls under a hypothetical end drop accident condition of transport.

- MPC Fuel Basket Stability

Stability of the basket panels, under longitudinal deceleration loading (Load Cases F3.a in Table 2.1.6), is demonstrated in the following manner. Table 2.2.1 provides the weight of each fuel basket (including sheathing and Boral). The corresponding metal areas of the basket bearing on the MPC baseplate or top lid can be computed for each MPC basket by direct calculation from the appropriate drawings. Dividing weight by bearing area and multiplying by the design basis deceleration for the hypothetical accident from Table 2.1.10 gives the axial stress in the load bearing walls. The results for each basket are compared and the bounding result (maximum weight/area) reported below:

Fuel Basket Compressive Stress For End Drop (Load Case F3.a)			
Item	Weight (lb.)	Bearing Area (sq. inch)	Stress (psi)
Bounding Basket (at 60g's deceleration)	23,535	346.61	4,074

To demonstrate that elastic instability in the basket panels is not credible, the flat panel buckling stress, σ_{cr}, (critical stress level at which elastic buckling may occur) is computed using the formula in reference [2.6.1].

For conservatism, the MPC fuel basket is modeled as a rectangular plate simply supported along two sides and uniformly compressed in the parallel direction. The width of the plate is equal to the maximum unsupported width of a panel from all fuel basket types. Reference [2.6.1] provides the critical stress formula for these conditions as

$$\sigma_{cr} = \frac{2.3\pi^2 E}{12(1-\nu^2)}\left(\frac{T}{W}\right)^2$$

where T is the panel thickness and W is the width of the panel, E is the Young's Modulus at the metal temperature and ν is the metal Poisson's Ratio. The following table summarizes the calculation for the critical buckling stress using the formula given above:

Elastic Stability Result for a Flat Panel	
Reference Temperature	725 degrees F
T (bounding thickness)	9/32 inch
W (bounding width)	11.0 inch
E	24,600,000 psi
Critical Axial Stress	33,430 psi

It is noted that the critical axial stress is an order of magnitude greater than the computed basket axial stress reported in the foregoing. Therefore, it is demonstrated that elastic stability under hypothetical accident condition of transport longitudinal deceleration inertia load is not a concern.

- MPC Fuel Basket Stress

The safety factor against yielding of the basket under longitudinal compressive stress from a design basis inertial loading is given by

$$SF = 17,100/4,074 = 4.198$$

where the yield stress of Alloy X has been taken from Table 2.3.1 at 725 degrees F.

Therefore, plastic deformation of the fuel basket under design basis deceleration is not credible.

Analyses of the Damaged Fuel canisters to be transported in the HI-STAR 100 Package are performed to demonstrate structural integrity under an end drop condition. A summary of the methodology and the results for all canisters is provided in Appendix 2.B.

- MPC Enclosure Shell Stability

Structural stability of the MPC enclosure shell under the end drop is evaluated for elastic and plastic/stability in accordance with the ASME Code Case N-284 [2.1.8]. All required interaction equation requirements set by [2.1.8] are met. It is shown that yield strength limits rather than instability limits govern the minimum safety factor. The minimum safety factor for this case is summarized below:

MPC Shell Elastic/Plastic Stability (Load Case E3.a Table 2.1.7)			
Item	Value	Allowable*	Safety Factor
Yield	0.698	1.34	1.92

* For Load Case E3.a, the yield strength criteria in the Code Case N-284 method govern. In this event, the safety factor 1.34, built into the Code Case, is included in the tabular result in order to obtain the actual safety factor with respect to the yield strength of the material.

- MPC Closure Lid Stress (Load Case E3.a)

The closure lid, the closure lid peripheral weld, and the closure ring are examined for maximum stresses developed during the hypothetical end drop accident event.

The closure lid is modeled as a single simply supported plate and is subject to deceleration from an end drop plus appropriate design pressures. Results are presented for both the single and dual lid configurations (in parentheses) for top end and bottom end drops. For the dual lid configuration, the two plates each support their own amplified weight as simply supported plates under a bottom end drop. The inner lid transfers the total load to the outer plate through the peripheral weld between the two lids. Under a top end drop scenario, the inner lid is partially supported by the outer lid and the amplified load is transmitted by a combination of peripheral support and interface contact pressure. The results for minimum safety factor are reported in the table below:

MPC Top Closure Lid - Minimum Safety Factors - Load Case E3.a in Table 2.1.7			
Item	Stress(ksi) or Load(lb.)	Allowable Stress (ksi) or Load Capacity (lb.)	Safety Factor
Lid Bending Stress - Load Case E3.a (bottom end drop)	3.35/(7.94)	60.7	18.1/(7.65)
Lid Bending Stress* - Load Case E3.a (top end drop)	21.9/(43.8)	60.7	2.77/(1.39)
Lid-to-Shell Peripheral Weld Load - Load Case E3.a	624,000	1,477,000**	2.37
Lid-to-Lid Peripheral Weld Load - Load Case E3.a (bottom end drop)	312,000	443,200***	1.42

* Stress computation is conservatively based on peripheral support at the outer diameter of the MPC lid. For a top end drop, the actual support diameter is .77 of the outer diameter. Therefore, an analysis based on an overhung plate would provide stresses reduced by a multiplier of 0.59. Consequently, the safety factors would be amplified by the factor 1.69.

** Based on a 0.625" single groove weld and conservatively includes a quality factor of 0.45.

*** This is a non-Code weld; limit is based on a 0.1875 groove weld and includes a quality factor of 0.45 for additional conservatism

Safety factors are greater than 1.0 as required. The limiting condition for the lid bending evaluation is a top end hypothetical accident end drop because the lid supports the amplified fuel weight as well as the lid amplified self-weight.

- MPC Baseplate and Canister Stress (Load Case E3.a)

Load Case E3.a provides the limiting accident loading on the baseplate wherein the combined effect of a 60g deceleration plus external pressure is considered. The top end hypothetical accident condition is limiting in transport, and here it is conservatively assumed that accident external pressure acts simultaneously, which exceeds the requirements of Table 2.1.7. The results are summarized below:

MPC Baseplate Minimum Safety Factors – Load Cases E3, Table 2.1.7			
Item	Value (ksi)	Allowable (ksi)	Safety Factor
Center of Baseplate - Primary Bending (Load Case E3)	22.12	67.32	3.04
Shell Bending Stress at Connection to Baseplate	31.47	67.32	2.14

Note that all safety factors are greater than 1.0. Also, note that the calculated stress conservatively includes both primary and secondary self-limiting stress components. For the hypothetical transport drop accident, the safety factor computed for the shell bending stress intensity need only consider the effect of primary membrane plus bending stresses that are to be compared against the ultimate stress at temperature for this ASME Code Service Level D event. Since secondary stresses have been included in the evaluation, the reported result for safety factor is conservatively low.

- Trojan MPC Spacer

The Trojan MPC-24E/EF enclosure vessel is 9 inches shorter in length than the generic MPC-24E/EF enclosure vessel. Thus, when the Trojan MPC-24E/EF is transported inside the HI-STAR 100, the axial clearance between the MPC lid and the HI-STAR 100 closure plate is greater than 10 inches. In order to prevent the Trojan MPC from thrusting forward and impacting the closure plate during a top-end drop or a tip-over event (i.e., slapdown), a spacer device is positioned on top of the MPC lid. The Trojan MPC spacer, depicted in Figure 1.1.5, is fabricated from SA240-304 stainless steel in the shape of a circular I-beam. The web of the spacer measures 1-inch thick and has a mean diameter of 60 inches. The total height of the MPC spacer is 9 inches.

During a top end drop, the MPC spacer must support the amplified weight of a fully loaded Trojan MPC-24E/EF. Based on a bounding MPC weight of 90,000 lb (Table 2.2.4) and a bounding deceleration of 60g (Table 2.1.10), the maximum compressive stress in the web is computed as follows.

Cross-sectional area of web (A) = $\pi \times D \times t = \pi\ (60)\ (1) = 188.5\ in^2$

Amplified weight of MPC (P) = $G \times W = (60)\ (90{,}000) = 5.4 \times 10^6$ lb

Compressive stress in web = $P/A = (5.4 \times 10^6) / 188.5 = 28{,}647$ psi

From Table 2.1.18, the primary membrane stress intensity limit for Alloy X (of which SA240-304 is a member) under Level D conditions is 44.9 ksi at 400°F. Therefore, the safety factor against compressive failure of the Trojan MPC spacer, per ASME Code Subsection NB stress limits, is

SF = 44,900 / 28,647 = 1.56

2.7.1.2 Side Drop (Load Cases F3 in Table 2.1.6, E3 in Table 2.1.7, and 3 and 11 in Table 2.1.9)

- MPC Fuel Basket and Canister Finite Element Analysis (Load Cases E3.b, E3.c in Table 2.1.7 and Load Cases F3.b, F3.c in Table 2.1.6)

The MPC configurations are assessed for a hypothetical accident condition of transport side drop. All fuel cells are loaded with design basis spent nuclear fuel (SNF). Evaluations are performed for the 0 degree and the 45 degree circumferential orientations of the fuel basket as defined in Figures 2.1.3 and 2.1.4 and are obtained using the finite element model described in Section 2.6.

The results for each MPC configuration for the two different drop orientations are evaluated for each appropriate load case listed in Tables 2.1.6 and 2.1.7. Analyses are performed only for the hot ambient temperature condition since this is the bounding case for the MPC; as noted in Section 2.6, allowable stresses are lower for the "heat" environmental condition.

- Elastic/Plastic Stability of the MPC Fuel Basket

Following the provisions of Appendix F of the ASME Code [2.1.12] for stability analysis of Subsection NG structures, (F1331.5(a)(1)), a comprehensive buckling analysis is performed using ANSYS. For this analysis, ANSYS's large deformation capabilities are used. This feature allows ANSYS to account for large nodal rotations in the fuel basket, which are characteristic of column buckling. The large deflection option is "turned on" so that equilibrium equations for each load increment are computed based on the current deformed shape. The interaction between compressive and lateral loading, caused by the deformation, is included in a rigorous manner. Subsequent to the large deformation analysis, the basket panel that is most susceptible to buckling failure is identified by a review of the results. The lateral displacement of a node located at the mid-span of the panel is measured for the range of impact decelerations. The buckling or collapse load is defined as the impact deceleration for which a slight increase in its magnitude results in a disproportionate increase in the lateral displacement.

The stability requirement for the MPC fuel basket under lateral loading is satisfied if two-thirds of the collapse deceleration load is greater than the design basis horizontal acceleration (Table 2.1.10). Figures 2.7.1, through 2.7.6 are plots of lateral displacement versus impact deceleration for representative fuel baskets. It should be noted that the displacements in Figures 2.7.1, 2.7.2, 2.73, 2.74, and 2.7.5 are expressed in $1x10^{-1}$ inch and Figure 2.7.6 is expressed in $1x10^{-2}$ inch. The plots clearly show that the large deflection collapse load of the MPC fuel basket is greater than 1.5 times the inertia load corresponding to the design basis deceleration for all baskets in all orientations. Thus, the requirements of Appendix F are met for lateral deceleration loading under Subsection NG

stress limits for faulted conditions. Therefore, it is concluded that stability of the spent fuel basket cell walls is assured under the hypothetical accident side drop (from 30') condition of transport.

An alternative solution for the stability of the fuel basket panel is obtained using the methodology espoused in NUREG/CR-6322 [2.7.3]. In particular, the fuel basket panels are considered as wide plates in accordance with Section 5 of NUREG/CR-6322. Eq.(19) in that section is utilized with the "K" factor set to the value appropriate to a clamped panel. Material properties are selected corresponding to a metal temperature of 500 degrees F which bounds computed metal temperatures at the periphery of the basket. The critical buckling stress is:

$$\sigma_{cr} = \left(\frac{\pi}{K}\right)^2 \frac{E}{12(1-\nu^2)}\left(\frac{h}{a}\right)^2$$

where h is the panel thickness, a is the unsupported panel length, E is the Young's Modulus of Alloy X at 500 degrees F (Table 2.3.1), v is Poisson's Ratio, and K=0.65 (per Figure 6 of NUREG/CR-6322).

Parameters appropriate to a MPC-24E basket are used; the following table shows the results from the finite element stress analysis and from the stability calculation.

Panel Buckling Results From NUREG/CR-6322			
Item	Finite Element Stress (ksi)	Critical Buckling Stress (ksi)	Factor of Safety
Stress	13.339	49.826	3.74

For a stainless steel member under an accident condition load, the recommended safety factor is 2.12. It is seen that the calculated safety factor exceeds this value; therefore, an independent confirmation of the stability predictions of the large deflection analysis is obtained based on classical plate stability analysis.

- Overpack Stress Analysis (Load Cases 3 and 11 in Table 2.1.9)

The overpack is assumed to be subject to a 60g side drop in the manner of the load combinations of Table 2.1.9 for both heat and cold environmental conditions as prescribed by Regulatory Guide 7.9. Reaction loads provided by the impact limiters are imposed as vertical pressures at each end of the overpack on areas of the structure that serve as backing. The applied mechanical loading is internal pressure, inertia load from the MPC and inertia load from the overpack self-weight. Figure 2.1.9 shows the assumed loading for this simulation. Figures 2.7.7, and Figures 2.7.11-2.7.13 are useful to aid in understanding the methodology used to apply the MPC loads and the balancing impact limiter reactions. Figure 2.7.7 shows a view of the overpack looking along the longitudinal axis for the general case of an oblique drop. While the intent of the figure is to describe the reaction loads from the impact limiter under a general oblique drop orientation, only the features necessary to elaborate on the side drop reaction load are discussed here. A region defined by the angle θ supports the applied loading in a side drop.

This angle is 18 degrees for the side drop and is chosen based on two considerations. First, the predictions from the theoretical model at the time of maximum "g" loading are examined and a projected loaded area on the top forging and bottom plate estimated. Second, the post-drop evaluation of the tested impact limiters from the one-eighth scale static test and the one-quarter scale dynamic test were visually examined and provided insight into the extent of the loaded region of the overpack at the impact limiter-hard surface interface. From these two evaluations, a conservatively low angle estimate is made for the finite element analysis. Figure 2.7.12 shows the extent around the periphery of the loading imposed by the MPC. From Section 2.6, the angle over which the MPC load is applied to the inner shell of the overpack is 72 degrees from the vertical on each half of the overpack. This angle is determined from the detailed analysis of the MPC enclosure shell and the fuel basket under 60g loading. The inertia load from overpack self-weight is applied by imposing an amplified value for the gravitational constant. Details of the finite element model have been discussed in Section 2.6. The results of the finite element analyses for load cases 3 and 11 in Table 2.1.9, for the overpack, are post-processed as previously discussed; Tables 2.7.5 and 2.7.6 summarize the results for each overpack component and identify the minimum safety factors.

2.7.1.3 Corner Drop

Figures 2.1.10 and 2.1.11 show the assumed loading for the bottom center of gravity over corner (CGOC) drop and the top CGOC drop, respectively. The impact limiter reaction load is applied as a pressure loading acting on two surfaces. From the geometry of the cask, with impact limiters in place, the angle of impact is 67.5 degrees from the horizontal plane. Although the theoretical and tested deceleration levels are below 60g's, the design basis 60g-deceleration load is used as the input loading and applied vertically. Therefore, a 55g load is applied along the longitudinal axis of the cask, and a 23g load is applied perpendicular to the cask longitudinal axis.

The lateral inertia load from the MPC, amplified by the appropriate multiplier corresponding to 23g's, is applied in the manner shown in Figures 2.7.11 and 2.7.12. The longitudinal component of the load from the MPC, amplified by 55g, is applied as a pressure over the inside surface of the lid as shown in Figure 2.7.8. In reality, the load would be applied over a narrow annulus near the outside radius of the lid because of the raised "landing region". To maximize lid and bolt stress, however, the load is applied as a uniform pressure in the finite element model. The corresponding lateral and longitudinal loads from the overpack self-weight are applied by imposing amplified gravitational accelerations in the appropriate directions.

The loading from the impact limiter at the other end of the overpack, not involved in the impact, is applied as a uniform pressure over the surface of the backed area at the other impact limiter. Figure 2.7.10 shows the loading on the outside surface of the bottom plate that arises from the bottom end impact limiter during simulation of a top end drop. The total bottom impact limiter weight is amplified by 55g's and applied as a pressure load. At the top end, where the impact limiter provides the distributed crush force to balance the inertia forces, the balancing reaction loads from the impact limiter are applied as a distributed side pressure loading and a distributed end surface pressure. The extent of the loaded region for this drop orientation is defined by the angle θ in Figure 2.7.7. For this

case, the angle is approximately 68 degrees since a large "backed" area of the impact limiter is involved in resisting the crush. The angle is consistent with the predictions from the intersection geometry analysis used to develop the force-deformation data used in Appendix 2.A. That force-crush model has been successfully used to predict maximum decelerations and extent of crush. Static finite element models require setting a fixed origin to insure satisfaction of all equilibrium equations. The center of gravity-over-corner orientation, in theory, provides automatic satisfaction of moment equilibrium so that all forces and moments at such a fixed origin location should be zero.

In this analysis and in the general oblique drop analysis, the fixed point is assumed at a location at the end of the overpack not impacted. The results from the finite element simulation confirm that the computed reactions are negligibly small compared to the applied loads. The loads from internal pressure are self-balancing and do not alter the calculation of equilibrium reactions. Tables 2.7.5 and 2.7.6 summarize the results from these analyses.

Results for the MPC and its internals have been discussed in Subsections 2.7.1.1 and 2.7.1.2 for the end and side drops, respectively, under the action of 60g deceleration and appropriate pressure loading. Under an oblique drop at an angle θ with respect to the target plane ($\theta = 0$ degrees equals the side drop), the MPC and its internals experience deceleration loads parallel and perpendicular to the MPC longitudinal axis. Each of these deceleration components, however, is less than the 60g design basis deceleration used in the end and side drop analyses. For the pure end drop, all stresses in the fuel basket and in the MPC canister (enclosure vessel) are axial. For the pure side drop, the conservative analysis of a 2-D section of the fuel basket and enclosure vessel gives rise to stresses in a plane perpendicular to the longitudinal axis of the MPC/fuel basket.

The results for any oblique drop can be obtained by a linear combination of the results for pure end drop and pure side drop. That is, the combined stress intensity is formed from the results of the two individual cases, after adjustment for the actual lateral and longitudinal "g" levels experienced by the components.

The MPC lid and baseplate are thick plate components; as such, the stress intensities experienced in the end drop orientation (which loads the lid and/or the baseplate in flexure) bound all other cases. Therefore, in what follows; only the enclosure vessel and the fuel basket need be considered. For each of these structures, the result "R_θ", at a general oblique drop angle θ, is expressed in terms of the result for an end drop "R_{90}" and the result obtained for a pure side drop "R_0" as:

$$R_\Theta = R_{90}\left(\frac{g_E}{60}\right) + R_0\left(\frac{g_S}{60}\right)$$

where g_E and g_S are the axial and lateral decelerations imposed on the MPC canister and fuel basket during the oblique drop at angle θ.

Since $g_E = 60 \sin\theta$, and $g_S = 60 \cos\theta$,

for a design basis oblique drop where the vertical deceleration is 60 g's, the result for the oblique drop is always expressed in the form,

$R_\theta = R_{90} \sin \theta + R_0 \cos \theta$

The following results are obtained for the end drop and side drop analyses:

End Drop:

Fuel Basket – maximum longitudinal membrane stress = 4,074 psi

Enclosure Vessel – maximum longitudinal compressive stress = 11,260 psi

The enclosure vessel result is obtained from the Code Case N-284 evaluation for a bottom end drop and conservatively bounds the result for a top end drop. The longitudinal compressive stress in the enclosure vessel includes the effect of external pressure.

Side Drop:

Stress intensity results for the fuel basket and enclosure vessel are summarized in Table 2.7.4. From Table 2.7.4, for the pure side drop, the minimum safety factor for the fuel basket is 1.17 (primary membrane plus primary bending). The corresponding minimum safety factor for the enclosure vessel is 2.64 (again, for primary membrane plus primary bending). The preceding results are obtained by surveying the summary of minimum safety factors in Table 2.7.4 for all MPC's and both fuel basket orientations within the MPC.

For the pure side drop orientation, the stress intensities (SI) associated with the minimum safety factors are:

Fuel Basket SI = 47,060 psi
Enclosure Vessel SI = 24,650 psi

The stress intensities at the most limiting location for the general oblique drop orientation are then computed as:

Fuel Basket SI = $4{,}074 \sin \theta + 47{,}060 \cos \theta$

Enclosure Vessel SI = $11{,}260 \sin \theta + 24{,}650 \cos \theta$

For the corner drop, $\theta = 67.5°$ leading to the following final results:

C.G. OVER CORNER DROP MPC SAFETY FACTORS			
Item	Calculated S.I.	Allowable S.I.	Safety Factor
Fuel Basket	21,773 psi	55,450 psi†	2.55
Enclosure Vessel	19,836 psi	65,200 psi ††	3.29

† at 725°F
†† at 450°F

As expected, the safety factors obtained for the corner drop are larger than the corresponding values obtained for the side drop.

Results for general oblique drop angles are now considered for the overpack. In particular, a 30-degree oblique drop is deemed to be most representative of a scenario where only a primary impact is involved. The general formula utilized in the preceding for the specific case of center-of-gravity-over-corner can also be used for a 30-degree drop angle. The following results are reported for the fuel basket and enclosure vessel.

30 DEGREE OBLIQUE DROP MPC SAFETY FACTORS			
Item	Calculated S.I. (psi)	Allowable S.I. (psi)	Safety Factor
Fuel Basket	42,792	55,450†	1.30
Enclosure Vessel	26,978	65,200††	2.42

† at 725°F
†† at 450°F

2.7.1.3.1 MPC "F Class" Enclosure Vessel Lid-to-Shell Weld

The Holtec MPCs labeled with the suffix "F" (designated as "F Class" in this subsection) are intended to store non-intact fuel (defined as damaged fuel in the latest revision of ISG-1 and "failed fuel and fuel debris" in this SAR).

To be certified to store loose fuel debris, the MPC must fulfill the function of the "secondary containment" required by 10CFR71.63(b). To qualify as a "secondary containment", the MPC Enclosure Vessel must be able to withstand the accident condition loading without releasing its contents. The accident condition mechanical loading for the secondary containment is identical to those for the primary containment, namely the inertia forces produced by a 60g deceleration. From Table 2.1.7, the pressure loads applicable to the MPC Enclosure Vessel during a hypothetical vertical end drop (Load Case E3.a) are the normal condition pressures. Therefore, per Table 2.1.1, the maximum pressure differential that exists across the MPC shell when a drop occurs is 60 psig. For conservatism, however, the accident condition internal pressure of 200 psig is used to qualify the MPC Enclosure Vessel as a secondary containment. All candidate

vulnerable locations in the MPC Enclosure Vessel must be analyzed to ensure that a thru-wall breach in the pressure-retaining boundary does not occur under the loading combination defined above. In the case of the primary containment (the HI-STAR 100 overpack), the location of containment vulnerability is the cask lid-to-body forging bolted joint; the evaluation of the lid-to-body closure bolt has been analyzed to demonstrate containment integrity and the results of the evaluation summarized in Subsection 2.7.1.1 of the SAR. For the MPC "F Class", considered as secondary containment, the corresponding locations of vulnerability are the two extremities of the Enclosure Vessel where the vessel shell is joined to flat (plate-like) members.

The top lid-to-shell joint, a J-groove (partial penetration) joint made at the plant after fuel loading, is one candidate location, as this weld cannot be volumetrically examined even though the top lid is relatively thick. The MPC baseplate to the shell weld, on the other hand, is a shop-fabricated and volumetrically examined junction. However, because the baseplate is thinner than the top lid, it may experience greater flexural action under the accident condition mechanical loading, resulting in somewhat greater junction region stresses. Therefore, the weld joints at both extremities of the MPC Enclosure Vessel are denoted as candidate locations whose structural integrity under the load combination appropriate to the MPC's secondary containment function must be demonstrated.

a. Top lid-to-shell joint

For MPCs with the "F" designation, this joint has been buttressed with a thick tapered shell and deeper J-groove weld than that utilized in the standard MPC Enclosure Vessel. A Holtec proprietary position paper, DS-213, "Acceptable Flaw Size in MPC Lid-to-Shell Welds", submitted to the NRC in support of the original certification of HI-STAR 100 in 1999 demonstrates that the largest postulated flaw in the most adverse orientation in the lid-to-shell joint in the "F" canister will not propagate under the impulsive inertia loading arising from a 60g axial deceleration of the MPC's contents.

An elastic stress analysis in the spirit of the ASME Code documented below likewise shows a large margin of safety against joint failure. For conservatism, the following assumptions are made.

i. The closure ring (the structural member present to provide a second welded barrier against leakage of the contents) is assumed to be absent.

ii. Even though a thru-wall failure of the joint is the appropriate failure criterion for the joint, non-exceedance of the ASME Code Section III Subsection NB stress intensity limits appropriate to Level D limits, which will occur at a much lower loading level, is set down as the acceptance limit. However, no weld efficiency factor is applied to the lid-to-shell weld since it is not required by Subsection NB.

iii. The MPC model with the heaviest contents (MPC-32) is used in the analysis to bound the results for all "Type F" MPC models.

The MPC top lid may be fabricated as a single thick circular plate, or may by fabricated as a dual lid with the outer lid attached to the shell with the "J" groove weld, and the inner lid attached to the outer lid around the common periphery. The dual lid configuration has been analyzed for both Normal Conditions of Transport and Hypothetical Accident Conditions of Transport for MPC's carrying intact fuel; the results are documented in Subsection 2.6.1.3.1.2, and 2.7.1.1, respectively. The evaluation for the "F Class" MPC to provide secondary containment capability utilizes the same analytical model but introduces additional assumptions into the analysis to direct load to the lid-to-shell weld. In particular, a top end drop is postulated with the dual lids subjected to a 60g deceleration loading from the fuel, fuel basket, and lid weight, together with the accident internal pressure of the MPC. During a top end drop, the MPC cannot rotate relative to the HI-STAR overpack because of close clearances between the vessel shell and the inner surface of the overpack cavity. Therefore, regardless of the angle of impact, the reaction load from the HI-STAR to equilibrate the applied loads on the lid is uniformly distributed around the circumference. A bounding condition for this analysis for secondary containment is presumed to be a top end drop where the Enclosure Vessel shell is assumed to contact the support (the HI-STAR lid) before the Enclosure Vessel lid; with this conservative assumption, the peripheral weld is subject to the entire applied load. The key results from the analyses (the case of dual lids bounds the analysis assuming a single thick lid) to support qualification of the MPC "F Class" as secondary containment are summarized in the table below:

KEY RESULTS FOR SECONDARY CONTAINMENT QUALIFICATION OF F CLASS MPC's – Load Case E3.a in Table 2.1.7 (Top End Drop)

Item	Stress Intensity (ksi) or Load (lb)	Allowable Stress Intensity @ 550 Degrees F (ksi) or Load Capacity (lb)	Safety Factor
Structural Lid Bending Stress Intensity	46.05	60.7	1.32
Shield Plug Bending Stress Intensity	46.65	60.7	1.30
Lid-to-Shell Weld Load	5,268,000	6,627,000	1.26
Primary Local Axial Membrane Stress Intensity at Shell Contact Interface	24.53	40.45	1.65

b. Baseplate-to-Shell Joint

Because the baseplate-to-shell connection is a volumetrically examined, full penetration joint, flaw propagation under the accident condition inertia loads is not a concern for this location. As in the case of the top lid-to-shell junction, the baseplate-to-shell joint is established to be sufficiently robust if the stress intensity limits under the above load combination (appropriate for §71.63(b)) are below their corresponding limits for level D condition for Section III Class 1 (NB) components. Since the baseplate-to-shell joint in the MPC "F Class" units is identical to the joint in the MPC's used for intact fuel, no new analyses are required. The results of evaluation of this joint are reported in Subsection 2.7.1.1 and demonstrate substantial safety factors.

The above analyses demonstrate that the Enclosure Vessel for "Type F" MPCs is capable of serving as a "secondary containment" as required by §71.63(b).

2.7.1.4 Oblique Drops

Appendix 2.A contains results of analytical simulations for various orientations of the cask at impact. In Appendix 2.A, it is shown that lateral decelerations are large for the near side drop (slapdown) and decrease as the angle of orientation, with respect to the horizontal plane, increases. Therefore, it is likely that results presented in Subsections 2.7.1.1 through 2.7.1.3 are bounding for all orientations other than the near side drop (slapdown) in that at any other angle, the resulting g-loads in each direction (longitudinal and lateral) are smaller than the bounding deceleration loads applied in the end, side, and corner drops. Nevertheless, based on the results obtained in Appendix 2.A, the case of an oblique drop with primary impact at 30 degrees from the horizontal is analyzed in detail. This case covers all orientations where the maximum deceleration load occurs and is reacted by the primary impact limiter. For this case, moment equilibrium includes inertia loads from overpack rotation as well as linear deceleration. For the 30-degree drop orientation at the primary impact location, the design basis deceleration load is applied with 52g lateral component and 30g longitudinal component. The loads are applied in the same manner as discussed in Subsection 2.7.1.3 with one additional complication. In contrast to the center of gravity over corner orientation where moment equilibrium is automatically satisfied when the loads are correctly applied, the applied loads and the reaction loads from the impact limiter are not initially in moment equilibrium. No inertial loading due to overpack rotational motion at the instant being considered is included. Without an additional inertial moment loading component, a large reaction force would develop at the far-removed arbitrary fixed reference point because the impact limiter reaction loads are offset from the overpack and MPC inertia loads from the linear decelerations. Figure 2.7.14 shows the overpack in a general oblique orientation. Appropriate arrows show the impact limiter reaction forces and the components of the applied linear decelerations. The loads from the MPC are not shown on the figure but they are applied as previously described for the corner drop. It is clear that moment equilibrium is not satisfied unless reaction loads develop at the arbitrarily chosen fixed support location far removed from the impact point. In the real drop scenario, since there is only a primary impact reaction, the cask must have angular accelerations imposed to insure moment equilibrium since the fixed point is an artifact to meet the requirements of the finite element analysis. To zero this reaction

load at the point far-removed from the impact location, an additional load case with a unit angular velocity imposed at the mass center of the system and no other loads is developed. An angular acceleration is internally generated by ANSYS for this load case. The solution to this load case provides a reaction at the hypothetical fixed point assumed at the end of the overpack far removed from the impact location to balance the imposed inertial moment. The addition of this load case, with proper magnitude and sign ascribed to the input angular velocity, serves to eliminate all reactions at the far-removed fixed point. By adding this inertia moment load case, both force and moment equilibrium equations are satisfied for the oblique drop case where there is only a single impact limiter providing external forces to react the cask motion. With reference to Figure 2.7.7, the extent of the impact limiter loaded region on the overpack for this case is $\theta = 63$ degrees. This angle is estimated from the projected geometry from the theoretical analysis in Appendix 2.A. Figure 2.7.9 shows a side view of the top forging with the end loading from the impact limiter applied as a pressure over the loaded region.

The finite element solution provides stress intensity results for the hot and cold conditions. The safety factors are summarized in Tables 2.7.5 and 2.7.6 (identified as Load Cases 20 and 21 corresponding to the "heat" and "cold" environmental conditions).

The near side drop with impact at the secondary impact limiter (slapdown) is a special case that also merits detailed analysis. For this case, the angle of the cask with the target is near zero degrees, similar to that used for the side drop analysis. The nature of the equilibrium equations is quite different, however. For the side drop, Figure 2.7.17 shows that equilibrium is satisfied by impact limiter reaction pressures at both impact locations. The reaction lateral pressure distribution at each impact limiter is distributed in the manner described by Figure 2.7.7. For the side drop evaluation, no introduction of a rotational component to the overpack is required to insure moment equilibrium. For the analysis of the near side drop secondary impact case, all of the reaction force required to insure that force equilibrium is maintained under the inertia induced loads, is imposed at the location of the secondary impact limiter. Figure 2.7.18 shows a side view of the overpack with the reaction load applied over a specified arc in the same manner as described by Figure 2.7.7. At the time of peak secondary impact deceleration, the theoretical analysis predicted minimal axial deceleration. Therefore, to perform the stress analysis using the finite element model, no axial deceleration is imposed. Referring to Figure 2.7.7, the angle θ for this evaluation is chosen on the basis of observed experimental results and theoretical prediction. The angle is related to the angle associated with the observed crush depth of the impact limiter itself. For a near side drop, the outer diameter of the impact limiter is known, and if the crush depth is observed, calculated, or measured, the angular extent of impact limiter crushed material is easily determined. The outer radius, "Ri" of the impact limiter, and the observed and calculated crush depth (see results in Appendix 2.A for a full scale impact limiter), "d", are:

$Ri = 64"$; $d = 15"$

Therefore, the angle "φ" (on either side of a vertical diameter through the impact limiter) that is associated with the extent of loaded crushed surface of the impact limiter is obtained from simple geometry as:

$Cos(\varphi) = 1\text{-}d/Ri$

The angle over which the load is applied at the crushed surface of the impact limiter is calculated to be:

$\varphi = 40$ degrees (measured from the vertical, on both sides of the vertical centerline).

The angle of significant reaction loads on the interface surface of the top forging, is greater than this angle. However, it is conservative to perform the finite element analysis of the "slapdown" secondary impact event, using the load angle

$\theta = \varphi = 40$ degrees.

Note that this angle used for the "slapdown" evaluation is larger than the conservative value used to evaluate the side drop. This reflects the increased crush imparted to the impact limiter since the entire amplified load is reacted at the top end. The load from the MPC is imposed on the appropriate inside surface of the inner shell as a uniform load in the same manner as for the side drop analysis. Moment equilibrium is provided by imposing the additional pure rotation on the overpack sufficient to generate opposite reaction forces that zero out the combined reactions at the "balance point" from the applied inertia decelerations plus the pure rotation case. Because the MPC is constrained within the overpack, no departure from a uniform load transfer to the overpack is anticipated. Therefore, the enforcement of moment equilibrium for this condition is ensured solely by the determination of a proper balancing moment by determining an appropriate angular acceleration for the overpack. This assumption has little effect on the computation of the primary stress intensity distribution that results from the impact.

The results of the analysis are tabulated and combined with other load conditions, and the combined load case is designated as "Load Case 22". Bolt preload, internal pressure, and the inertia loads are combined to form this "slapdown" simulation. The top-end secondary impact analysis reported herein bounds a similar analysis of the bottom end secondary impact case. Summary results for minimum safety factors are reported in Table 2.7.5 only for the "Heat" environmental condition as previous results have demonstrated that this case produces the minimum safety factors. Only primary stress intensities are surveyed and reported in accordance with ASME requirements. Also evaluated is the bolt stress, the net friction force, and the state of the seals and lands. From the post-processed results, it is concluded that no bolts are overstressed, no portion of the seals suffer unloading, and that there is sufficient frictional force to insure that the lid is maintained in position.

The preceding discussion focussed on the transport overpack analyses. The minimum safety factors for the MPC fuel basket and enclosure vessel, for arbitrary drop orientation, are obtained from the general formulation in the preceding subsection 2.7.1.3. The angle that provides the maximum combined stress intensity (S.I.) can be determined by classical means, and the minimum safety factor established. The results are summarized in the table below:

GENERAL OBLIQUE DROP ORIENTATION MPC – SAFETY FACTORS				
Item	Drop Orientation Angle (Degrees)	Calculated S.I. (psi)	Allowable S.I. (psi)	Safety Factor
Fuel Basket	4.54	47,208	55,450	1.17
Enclosure Vessel	24.55	27,100	65,200	2.41

2.7.1.5 Comparison with Allowable Stresses

Tables 2.7.4 through 2.7.8 summarize the limiting safety factor obtained for each hypothetical free drop accident condition of transport defined by the requirements of Regulatory Guide 7.9. In particular, Table 2.7.4 is a summary of safety factors from the analyses of the MPC fuel basket and enclosure vessel, and Tables 2.7.5 and 2.7.6 report safety factors from the overpack analyses. Finally, Tables 2.7.7 and 2.7.8 contain safety factor summary results from miscellaneous evaluations reported within the text. From these results, tables are constructed that summarize limiting safety factors for all of the hypothetical accident conditions of transport that are associated with drop events. Tables 2.7.1 through Tables 2.7.3 present the overall summary of the most limiting safety factor for each of the components of interest for all hypothetical accident conditions of transport. It is concluded from these tables that large factors of safety exist in the fuel basket, in the MPC shell, and in the various components of the overpack under all hypothetical accident conditions of transport associated with free drop events.

It is noted that the overpack finite element results are developed using a 3-D model of the overpack. Even though symmetry conditions reduce the size of the model, there are over 8000 elements and 11000 nodes.

The postulated accident conditions all tend to load localized regions of the overpack. As an illustration, consider Load Case 20, the 30-degree oblique top-end impact with the target. The limiting results for safety factors are reported in Table 2.7.5. Figures 2.7.15 and 2.7.16 show stress intensity distributions for the inner shell and for the assemblage of intermediate shells, respectively. As expected, the regions of highest stress intensity are naturally concentrated near the impacted region.

2.7.2 Puncture

- Overpack Structural Components

10CFR71 mandates that a puncture event be considered as a hypothetical accident condition. For this event, it is postulated that the package falls freely through a distance of 1 meter and impacts a 6 inch diameter mild steel bar. The effects of the puncture drop are most severe when the steel bar is perpendicular to the impact surface. Therefore, all puncture analyses assume that the bar is perpendicular to the impact surface. It is assumed that the steel bar has a flow stress equal to 48,000 psi, which is representative of mild steel. The maximum resisting force can then be calculated as

$$F_R = \frac{\pi D^2}{4} \times 48{,}000\ psi = 1.357 \times 10^6\ lb$$

where D equals the diameter of the steel bar.

$$|A_p| = \frac{F_R\, g}{W}$$

Since the maximum force applied to the cask is limited to the above value, the average deceleration of the cask can be computed assuming it to be rigid. The average deceleration of the cask (plus contents) (weight = W) is determined as:

For a bounding (low) weight of 230,000 lb. (Table 2.2.1), for example, the rigid body average deceleration over the time duration of impact, is 5.9g.

Candidate locations for impact that have the potential to cause the most severe damage are near the center of the closure plate (top-end puncture), the center of the bottom plate (bottom puncture), and the center height of the overpack shells (side puncture). In accordance with Regulatory Guide 7.9, local damage near the point of impact and the overall effect on the package must be assessed.

An estimate of local puncture resistance is obtained by using Nelms' equation [2.7.1] that is generally applicable only for lead backed shells. Nevertheless, it is useful to obtain an indication as to whether a potential problem exists in the HI-STAR 100 System. The equation is applied using an ultimate strength of 70,000 psi that is appropriate for the selected impact regions. Nelms' equation predicts a minimum thickness of material necessary to preclude significant puncture damage. For the HI-STAR 100 System,

$$t_m = \left(W/S_u\right)^{0.71} = 2.65 \quad inch$$

Inasmuch as the HI-STAR 100 overpack has substantially more material thickness in the baseplate, the closure plate, the top flange and the inner plus the initial intermediate shell, the overpack meets local puncture requirements as required by Nelms' equation.

The global effects of puncture are calculated using the overpack model described in Section 2.6, which is the same model that is used for the drop assessments. Figures 2.1.12 through 2.1.14 show free body diagrams of the overpack for the side, top, and bottom puncture events, respectively. In each case, the nodes on the surface of the overpack that directly impact the steel bar are fixed in all degrees of freedom. By then applying acceleration, A_p, a reaction force develops at those nodes equal in magnitude with F_R. Tables 2.7.5 and 2.7.6 summarize the safety factors for the overpack components obtained for the puncture acceleration computed above for both heat and cold environmental conditions. Note that for the stress intensities in the lid and baseplate, the highest stresses are exactly under the impact point. The results include the effect of the interface contact stress between the puncture pin and the plate surface. This local effect is not required to be included in the stress intensity comparison with allowable values for the hypothetical accident. Therefore, in the reporting of safety factors, the effect of local surface pressure is not included; rather, the radial and tangential stresses at the load point are used to form the stress intensity and set the lateral surface stress to zero. Tables 2.7.5 and 2.7.6 specifically identify this item by a note. Figure 2.7.17 shows the stress intensity distribution in the lid resulting from a top-end puncture analysis. The localized nature of the stress intensity distribution is clearly evident. The reported safety factors in the summary tables are adjusted to eliminate the effect of non-primary stress components.

- Closure Bolts

The methodology to analyze closure bolts is provided in reference [2.6.3] prepared for analysis of shipping casks. The analysis of the overpack closure bolts under normal conditions of transport, in accordance with the provisions of [2.6.3], has been reported in Section 2.6. In this subsection, the similar analysis for the hypothetical puncture accident is summarized. The analysis follows the procedures defined in Reference [2.6.3] and uses the allowable stresses for the closure bolts in that reference.

The following combined load case is analyzed for the hypothetical pin puncture accident condition of transport.

Puncture: Pressure, temperature, and pre-load loads are included.

Reference [2.6.3] reports safety factors defined as the calculated stress combination divided by the allowable stress for the load combination. This definition of safety factor is the inverse of the definition consistently used in this SAR. In summarizing the closure bolt analysis, results are reported using the SAR safety factor definition of allowable stress divided by calculated stress. The following result for closure lid bolting for the top end drop hypothetical accident condition of transport is obtained.

Overpack Closure Bolt - Safety Factor (Load Case 7 in Table 2.1.9)	
Item	Safety Factor on Bolt Tension
Average Tensile Stress in Bolt	1.86

2.7.3 Thermal

In this subsection, the structural consequences of the thirty-minute fire event are evaluated using the metal temperature data from Section 3.5 where a detailed analysis of the fire and post-fire condition is presented. Specifically, it desired to establish that:

1. The metal temperature, averaged across any section of the containment boundary, remains below the maximum permissible temperature for the Level A condition in the ASME Code for NB components. Strictly speaking, the fire event is a Level D condition for which Subsection NB of the ASME Code, Section III does not prescribe a specific metal temperature limit. The Level A limit is imposed herein for convenience because it obviates the need for creep considerations to ascertain post-fire containment integrity.

2. The external skin of the overpack, directly exposed to the fire will not slump (i.e., suffer rapid primary creep). This condition is readily ruled out for steel components if the metal temperature remains below 50% of the metal melting point.

3. Internal interferences among the constituents of the HI-STAR 100 System do not develop due to their differential thermal expansion during and after the fire transient.

4. Overpack closure bolts will not unload during a transport fire.

5. The helium retention boundary and the containment boundary both continue to perform their function as ASME "NB" pressure vessels.

2.7.3.1 Summary of Pressures and Temperatures

The following peak temperatures (per Tables 3.5.4 and 3.4.11) and pressures are used in Subsections 2.7.3.2, 2.7.3.3, and 2.7.3.4.

Overpack closure plate/bolts	514 degrees F (post-fire)
Overpack bottom plate	662 degrees F (post-fire)
Overpack outer closure	226 degrees F (initial pre-fire cold temperature); 1348 degrees F (maximum)
Overpack containment shell	395 degrees F (MPC –Shell post-fire temp. - increment of 24 degrees F (from data in Table 3.4.11))
MPC-Shell	419 degrees F (post-fire)
Basket (center)	751 degrees F (post-fire)
Basket (periphery)	478 degrees F (MPC-Shell post fire + 59 degrees F - (from data in Table 3.4.11))

It should be noted that the overpack containment shell, closure plate, and bottom plate temperatures are not specifically reported in Table 3.5.4. The temperatures listed above are based on the closest temperature report location. The overpack containment shell temperature is the lowest temperature

that occurs prior to the fire accident and is used for the differential thermal expansion analysis. The overpack containment shell temperature falls (post-fire) below the outside basket temperature and subsequently lags the basket temperature by 24 degrees F. The 24 degree F lag is the same lag that occurs in the normal heat condition listed in Table 3.4.11 (i.e., 306 degrees F for the MPC outer shell surface - 282 degrees F for the overpack inner surface). This will maximize the potential for interference between the overpack and the MPC. Similarly, the temperature difference between the MPC shell and the fuel basket periphery will be essentially the same exists in the normal heat conditions of transport. Therefore, from Table 3.4.11, the basket peripheral temperature for the fire event analyses is set as the MPC shell temperature plus the maximum difference (365-306) degrees F from the table.

Subsection 3.5.3 contains a discussion of the peak bulk temperatures occurring during and after the fire transient. It is concluded in that section that:

1. The containment boundary protected by the intermediate shells remains below 500 degrees F (SA-203-E material).
2. The containment boundary that is within the confines of the impact limiters remains below 700 degrees F (SA-350 LF3 material).
3. The portion of the containment boundary directly exposed to the fire may have local outer surface temperatures in excess of 700 degrees F, but the bulk metal temperature of the material volume remains under 700 degrees F (SA-350 LF3 material).

The conclusions in Subsection 3.5.3 enable the statement that the containment boundary metal bulk temperatures remain at or below the upper limits permitted by the ASME Code. Therefore, stress evaluations that make comparisons to allowable stresses to demonstrate that the containment boundary continues to perform as a viable pressure vessel use allowable stresses that are given in the ASME Code (i.e., there is no extrapolation of allowable stresses beyond the recognized code limits). For the helium retention boundary stress calculations, however, allowable stresses for a conservatively high temperature (see Table 2.1.2 and 2.1.21) are used when pressure vessel code compliance is demonstrated.

From Table 3.5.4 in Subsection 3.5.4 of Chapter 3, it is concluded that:

> The maximum temperature of the ferritic steel material in the body of the HI-STAR 100 overpack (the outer enclosure and the intermediate shells outside of the containment boundary is well below 50% of the material melting point. (The melting point of carbon and low alloy steels is approximately 2750 degrees F, per Mark's Standard Handbook, Ninth Edition, pp 6-11.)
>
> The shielding experiences temperatures above its stated limit for effectiveness. This means that a limited loss of shielding effectiveness may occur. The shielding analysis in Chapter 5 (Subsection 5.1.2) recognizes this and conservatively assumes that all shielding is lost in post-fire shielding analyses.

Pressures during the fire transient are bounded by the internal and the external design pressures for accident conditions for the MPC shell as stated in Section 2.1. For internal pressure, Table 3.5.3 supports this conclusion. The following calculation is presented to support the conclusion for MPC external pressure.

The overpack annulus initial fill pressure is 14 psig (max.) per the specification in Chapter 7. The overpack annulus lower bound fill temperature is 70 degrees F. The fire condition MPC shell peak temperature is 419 degrees F per Table 3.5.4 and the use of this as the average gas temperature in the annulus is conservative.

Using the above data, the fire condition peak pressure in the annulus between the overpack and the MPC shell is calculated by using the ideal gas law with constant volume assumed in the gap as:

p_{fire}= (14+14.7) x (419 + 460)/(70 + 460) = 47.6 psia = 32.9 psig.

2.7.3.2 Differential Thermal Expansion

The methodology for establishing that there will be no restraint of free thermal expansion has been presented in Subsection 2.6.1.2 for normal conditions of transport. The same methodology is applied in this subsection to evaluate the potential for component interference during and after the postulated hypothetical fire. For conservatism, use the temperatures in the overpack and the MPC temperatures that will maximize the potential for interference between the overpack and the MPC regardless of at what point in time the temperatures occurred. It is shown that there is no structural restraint of free-end expansion in the axial or radial directions under the most limiting temperature difference between the hot basket and the colder overpack/enclosure vessel. Thus, the ability to remove fuel by normal means is not inhibited by structural constraint of free-end expansion. The table below summarizes the results obtained for the limiting MPC temperature distributions assumed.

THERMOELASTIC DISPLACEMENTS IN THE MPC AND OVERPACK UNDER FIRE CONDITION				
CANISTER - FUEL BASKET				
	Radial Direction(in.)		Axial Direction (in.)	
Worst Case Unit	Initial Clearance	Final Gap	Initial Clearance	Final Gap
Bounding MPC	0.1875	0.117	2.0	1.672
CANISTER – OVERPACK				
	Radial Direction (in.)		Axial Direction (in.)	
Worst Case Unit	Initial Clearance	Final Gap	Initial Clearance	Final Gap
Bounding MPC	0.09375	0.004	0.625	0.291

Using the most conservative assumptions (i.e., do not consider a real "snapshot" in time during and after the fire, but rather assume the most detrimental temperature distribution occurs at the same instant in time) that maximize the potential for interference, it is demonstrated that no restraint of free thermal expansion in either the radial or axial directions occurs.

2.7.3.3 Stress Calculations

Under the fire accident, pressures in the MPC and overpack increase simultaneously, while the allowable strengths of the material may decrease from their values under normal conditions of transport. The MPC and overpack stresses are shown below (allowables are taken from Tables 2.1.21). It is required that both the helium retention boundary and the containment boundary meet Level D Service Limits of the ASME Code and continue to function as pressure vessels.

2.7.3.3.1 MPC

- Top Closure

The MPC Top Closure analysis for the fire condition is Load Case E5 in Table 2.1.7. The top closure is conservatively modeled as a simply supported plate considered to be loaded by the accident internal pressure plus self-weight acting in the same direction. For determination of the safety factor, the value of allowable stress from Table 2.1.20 appropriate to the fire temperature is used. The table below summarizes the result (where a multiplier of 2.0 has been incorporated to reflect the bounding dual lid design):

MPC Top Closure Safety Factor for Load Case E5 in Table 2.1.7			
Item	Value (ksi)	Allowable (ksi)	Safety Factor
Bending Stress	3.158 x 2	54.23	8.59

- Baseplate

Under the fire accident condition, the baseplate is subject to accident internal pressure (200 psi). If the HI-STAR 100 is assumed to be in the vertical position, then the baseplate also may support the weight of the fuel basket and the fuel loading. If the HI-STAR 100 is assumed to be oriented in the horizontal position, then the baseplate supports only internal pressure. For a conservative analysis, it is assumed that the internal pressure stress and the stress from basket weight and from fuel weight add. This Load Case E5 is summarized below. The second row is the result that is obtained if the basket and fuel weight is neglected.

MPC Baseplate Safety Factor under Hypothetical Fire Accident			
Item	Value (ksi)	Allowable (ksi)	Safety Factor
Baseplate Bending Stress (Including Basket and Fuel Weight)	46.32	54.23	1.17
Baseplate Bending Stress (Neglecting Basket, Fuel, and Self Weight)	42.28	54.23	1.28

- Shell

The MPC shell is examined for elastic/plastic stability under the fire accident external pressure using the ASME Code Case N-284 analysis method. The result from the stability analysis for Load Case E5 in Table 2.1.7 is summarized below:

MPC Canister Safety Factor - Stability under External Accident Pressure			
Item	Calculated Interaction Factor	Allowable Interaction Factor	Safety Factor
Elastic Stability	0.845	1.00	1.18

The shell is also analyzed for stress under the accident internal pressure by using the Lame' solution previously used in Section 2.6. The stress due to the internal accident pressure of 200 psi is (P = pressure, r = MPC radius, t = shell thickness):

$$\sigma_1 = \frac{Pr}{t} = \frac{(200\,\text{psi})(68.375\,\text{in}/2)}{0.5\,\text{in}} = 13{,}675\,\text{psi}$$

$$\sigma_2 = \frac{Pr}{2t} = 6{,}838\,\text{psi}$$

$$\sigma_3 = -P = -200\,\text{psi}$$

The maximum stress intensity is $\sigma_1 - \sigma_3 = 13{,}875$ psi

The safety factor is,

$$SF = \frac{36.15\,\text{ksi}}{13.875\,\text{ksi}} = 2.61$$

2.7.3.3.2 Overpack

The overpack stresses for normal heat conditions of transport are reported in Section 2.6. Since these stress solutions are based on linear elasticity, the stresses reported can be scaled up to account for the accident internal pressure and the safety factor computed based on the allowable stress for the fire temperature.

Generally, in the fire accident case, only primary stresses are of interest to demonstrate continued containment. Secondary stresses may be included in the evaluation, but they merely demonstrate additional levels of conservatism. Table 2.6.4 gives the minimum safety factor for the primary stress case of $T_h + P_i + F + W_s$.

The highest stress occurs in the inner shell, and has the value 2,832 psi.

The ratio of the accident pressure to normal pressure is (see Table 2.1.1) $\frac{200}{100} = 2.00$.

Using this factor, the safety factor is computed as follows:

For the inner shell at 500 degree F fire temperature per Table 2.1.21, the allowable membrane stress intensity under the fire condition is compared to the amplified mean stress and the safety factor computed as

$$SF = \frac{45.4\,\text{ksi}}{(5.664 + 0.200)\,\text{ksi}} = 7.74$$

2.7.3.3.3 Closure Bolts

Under the fire transient, it is required to demonstrate that the stresses in the closure bolts do not exceed allowable limits and the bolted joint does not unload to the extent that the pressure boundary is breached. To that end, an analysis of the fire condition is carried out with the purpose of determining the bolt stresses under the applied loading. The methodology employed for this analysis is that presented in the report, "Stress Analysis for Closure Bolts for Shipping Casks" [2.6.3]. The loadings applied are fire temperature, bolt preload, and accident internal pressure. The following result for closure lid bolting for the hypothetical fire accident is obtained.

Overpack Closure Bolt - Safety Factor (Load Case 19 in Table 2.1.9)	
Combined Load Case	Safety Factor on Bolt Tension
Average Tensile Stress	1.69

The average bolt tensile stress under the conditions of pressure, preload, and thermal effects appropriate to the hypothetical fire accident condition of transport is 8.5% greater than the average bolt tensile stress computed under the normal heat condition of transport. Therefore, it is concluded that there will be only minor unloading of the bolted joint and no breach of containment.

2.7.3.3.4 Bounding Thermal Stresses During the Fire Transient

Regulatory Guide 7.6, Section C.7 states that the extreme total stress intensity range between the initial state and accident conditions should be less than twice the adjusted value of the alternating stress intensity at 10 cycles given by the appropriate fatigue curves. It is demonstrated here that under very conservative assumptions on the calculation of thermal stresses, this regulatory requirement is met by the HI-STAR 100 System.

Under the fire transient, thermal gradients can lead to secondary or peak stresses due to local constraint by adjacent material that is at a lower temperature. The ASME Code does not require that secondary stresses be held to any limit for Level D Service Conditions. Nevertheless, bounding calculations are performed here to estimate the magnitude of the thermal stress. The most limiting secondary stress intensity state arises by conservatively assuming complete restraint of material by surrounding cooler material and has the solution:

$$|\sigma| = E \alpha \Delta T$$

where

E = Young's Modulus at temperature
α = coefficient of linear thermal expansion
ΔT = temperature change from 70 degrees F, the assumed assembly temperature

For the fuel basket, $\Delta T = 775 - 70 = 705$ degrees F. The use of 775 degrees F is justified as follows:

The peak temperature of the fuel basket is 950 degrees F during the fire per Table 2.1.2. For a conservative estimate of the temperature between *two adjacent points* on the fuel basket, use the bounding hypothetical accident temperature limit for the enclosure vessel lid or baseplate from Table 2.1.2 as representative of the change between *two adjacent points* on the fuel basket. Therefore, no extrapolation of data is required for the calculations to follow.

From the material property table for Alloy X,

$$E = 24.282 \times 10^{6} \text{ psi}$$
$$\alpha = 9.853 \times 10^{-6} \text{ inch/inch- degree F}$$

Therefore,

$$\sigma = 24.282 \times 9.853 \times 705 = 168{,}672 \text{ psi}$$

The conservative assumption is made that the maximum peak stress intensity due to mechanical loading plus thermal constraint occur at the same point at the same instant in time and reaches the value of S_u at room temperature. Thus, the total stress intensity range from assembly to this hypothetical conservative state is

$$S_R = 168{,}672 + 75{,}000 = 243{,}672 \text{ psi}$$

The alternating stress intensity range, after accounting for temperature effects of Young's Modulus, is

$$S_a = \frac{S_R}{2} x \frac{\text{Young's Modulus (70° F)}}{\text{Young's Modulus (775° F)}}$$

$$= 121{,}836 \text{ psi } x \frac{28.14}{24.282} = 141{,}194 \text{ psi}$$

For the overpack, the most severely constrained material is at the bottom plate. Material properties for this calculation are the values available at 700 degrees F and the peak temperature is conservatively set at 700 degrees F.

Young's Modulus = $E = 24.9 \times 10^{6}$ psi (at 700 degrees F)

Coefficient of linear thermal expansion = $\alpha = 7.52 \times 10^{-6}$ inch/inch-degrees F (Estimated)

Therefore, the secondary stress intensity due to fully constrained thermal growth is

$$\sigma = 24.9 \times 7.52 \times (700\text{-}70) = 117{,}966 \text{ psi}$$

Conservatively, assuming that the membrane plus primary bending stress intensity achieves the ultimate strength at room temperature, at the same location in space and at the same instant in time, gives the total stress intensity range at this hypothetical location as

$$S_R = 117{,}966 + 75{,}000 = 192{,}966 \text{ psi}$$

The alternating stress intensity range, after accounting for temperature effects of Young's Modulus, is

$$S_a = \frac{192,966}{2} x \frac{28.14}{24.9} = 109,037 \text{ psi}$$

These computed values for bounding alternating stress intensities are used in the next subsection for comparisons with allowable values.

2.7.3.4 Comparison of Fire Accident Results with Allowable Stresses

Stress

The safety factors for the MPC and overpack during a fire are addressed in Section 2.7.3.3. The lowest safety factors are 1.18 and 7.74 for the MPC and overpack, respectively.

Bounding Fire Transient

In accordance with Regulatory Position C.7 of the Regulatory Guide 7.6, Figure I-9.2.1 of ASME, Section III, Appendix I, gives the 10-cycle alternating stress intensity range as

S_{ALT} (Alloy X) = 700,000 psi

Using the calculated stress intensity range from Subsection 2.7.3.3, the safety factor for the MPC basket is

$$SF = \frac{700,000}{141,194} = 4.96$$

Figure I-9.1 of ASME Section III, Appendix I is used for the overpack even though the temperature is limited to below 700 degrees F. It is conservative to use this curve for this short time event since increased temperatures will improve the material ductility. From that table, the 10-cycle alternating stress intensity range is given as 400,000 psi. Therefore using the aforementioned calculated results for stress intensity range from Subsection 2.7.3.3, the safety factor is computed as:

$$SF = \frac{400,000}{109,037} = 3.67$$

An analysis of the threaded holes in the top closure has been performed to assess the length of engagement and stress requirements imposed on the connection by the transport loads. The methodology used to evaluate the connection is that set forth in Machinery's Handbook and uses the specific characteristics of the threaded joint. As part of the calculation, it is demonstrated that the bolt force required to maintain the seal (seal seating load plus pressure force) is only 27% of the total bolt preload force that must be applied to ensure bolt performance under the various drop scenarios.

That is, there is 73% excess capacity. Therefore, the momentary joint decompression due to the hypothetical fire accident is not sufficient to unload the seal.

The above calculations demonstrate that the requirements of Paragraph C.7 of Regulatory Guide 7.6 are satisfied.

2.7.4 Immersion - Fissile Material

In order for the spent nuclear fuel in the HI-STAR 100 System to become flooded with water, a leak must develop in both the overpack containment structure and the MPC enclosure vessel. The analysis provided demonstrates that both the overpack containment boundary and the MPC enclosure vessel meet the applicable stress and stress intensity allowables for normal conditions of transport and hypothetical accident conditions. Therefore, no leak will develop.

10CFR71.73(c)(5) specifies that fissile material packages, in those cases where water inleakage has not been assumed for criticality analysis, must be evaluated for immersion under a head of water of at least 0.9 m (3 ft.) in the attitude for which maximum leakage is expected. The criticality analyses presented in Chapter 6 conservatively assumes flooding with water at optimum moderation. Therefore, this paragraph is not applicable. However, analysis is presented to demonstrate that there is no water inleakage and verify that the flooded assumption made in the criticality analysis is conservative.

A head of water at a depth of 0.9 m (3 ft.) is equal to 1.3 psi. This pressure is bounded by the MPC enclosure vessel normal condition of transport and hypothetical accident condition external pressures listed in Table 2.1.1. The head of water (1.3 psi) is also bounded by the hypothetical accident condition external pressure for the overpack. Analysis provided in this chapter demonstrates that both the overpack containment boundary and the MPC enclosure vessel meet the applicable stress and stress intensity allowables for normal conditions of transport and hypothetical accident conditions. Therefore, there is no in-leakage of water into the overpack or MPC under a head of water at a depth of 0.9 m (3 ft.).

2.7.5 Immersion - All Packages

Deep submergence of the HI-STAR 100 System in 200 meters (656 ft.) of water creates an external pressure load equal to 284 psi, which is less than the external design pressure of 300 psi. This condition is established as Load Case 18 in Table 2.1.9. Since the containment boundary is not punctured, stability of the package can be evaluated considering an undamaged package. The results for an external pressure of 300 psi bound the results for 21.7 psi gauge pressure that is established in 10CFR71.73(c)(6) as the applicable external pressure for this evaluation. The elastic/plastic stability of the overpack has been examined using the methodology of ASME Code Case N-284. In the analysis, all structural resistance to the external pressure is conservatively concentrated in the inner containment shell. No credit is given to any structural support by the intermediate shells. The external pressure is assumed to act directly on the outer surface of the inner containment shell and the secondary fabrication stress is assumed to add to the stress due to the deep submergence pressure. The results for this case are summarized below:

Overpack Stability using ASME Code Case N-284 - Load Case 18 in Table 2.1.9			
Item	Value from Interaction Curve	Allowable Interaction Curve Value	Safety Factor
Yield Stress Limit	0.577	1.34	2.32
Elastic Stability	0.253	1.0	3.95

It is noted that Code Case N-284 imposes limits on both stress and stability and includes a built-in safety factor of 1.34 for the Level D Service Limit. Therefore, the first row in the table above reports the true safety factor existing against exceeding the yield stress in the inner containment shell; the second row in the table provides the safety factor against elastic instability of the inner shell. The large values for the safety factors that are obtained, even with the conservative assumptions, attests to the ruggedness of the inner containment shell.

The analysis performed above for a 300 psi external pressure also confirms that the package meets the requirements of 10CFR71.61 that a 290 psi external pressure can be supported without any instability.

2.7.6 Summary of Damage

The results presented in Subsections 2.7.1 through 2.7.5 show that the HI-STAR 100 System meets the requirements of 10CFR71.61 and 10CFR71.73. All safety factors are greater than 1.0 for the hypothetical accident conditions of transport. Therefore, the HI-STAR 100 package, under the hypothetical accident conditions of transport, has adequate structural integrity to satisfy the subcriticality, containment, shielding, and temperature requirements of 10CFR71.

Table 2.7.1

MINIMUM SAFETY FACTORS FOR THE MPC FUEL BASKET UNDER HYPOTHETICAL ACCIDENT CONDITIONS OF TRANSPORT

Load Case Number	Load Combination†	Safety Factor	Location in SAR where Calculations or Results are Presented
F3			
F3.a	D + H', end drop	4.19	Subsection 2.7.1.1; Table 2.7.7
F3.b	D + H', 0° side drop	1.16	Table 2.7.4
F3.c	D + H', 45° side drop	1.28	Table 2.7.4

† The symbols used for loads are defined in Subsection 2.1.2.1.

Table 2.7.2

MINIMUM SAFETY FACTORS FOR THE MPC ENCLOSURE VESSEL
FOR HYPOTHETICAL CONDITIONS OF TRANSPORT

Load Case Number	Load Combination†	Safety Factor	Location in SAR where Calculations or Results are Presented	
E3				
E3.a	D + H' + P_o, end drop	1.4 3.04 1.92	Lid Baseplate Shell	Table 2.7.7 Table 2.7.7 Table 2.7.7
E3.b	D + H' + P_i, 0 deg. side drop	2.14 1.16	Shell Supports	Table 2.7.4 Table 2.7.4
E3.c	D + H' + P_i, 45 deg. side drop	2.74 1.51	Shell Supports	Table 2.7.4 Table 2.7.4
E5	P_i^* or P_o^*	8.59 1.17 1.18 (buckling) 4.16 (mean stress)	Lid Baseplate Shell	Table 2.7.7 Table 2.7.7 Table 2.7.7 Subsection 2.7.3.3.1

† The symbols used for loads are defined in Subsection 2.1.2.1.

Table 2.7.3

MINIMUM SAFETY FACTORS FOR THE OVERPACK
FOR HYPOTHETICAL ACCIDENT CONDITIONS OF TRANSPORT

Load Case Number	Load Combination†	Safety Factor	Location in SAR where Calculations or Results are Presented
1	$T_h + D_{ba} + P_i + F + W_s$	2.16	Table 2.7.8
2	$T_h + D_{tn} + P_i + F + W_s$	1.75	Table 2.7.5
3	$T_h + D_{sa} + P_i + F + W_s$	2.19	Table 2.7.5
4	$T_h + D_{ca} + P_i + F + W_s$	1.49	Table 2.7.5
5	$T_h + D_{ga} + P_i + F + W_s$	2.60	Table 2.7.5
6	$T_h + P_s + P_i + F + W_s$	2.80	Table 2.7.5
7	$T_h + P_t + P_i + F + W_s$	2.03 (see note 1)	Table 2.7.5
8	$T_h + P_b + P_i + F + W_s$	1.46	Table 2.7.5
9	$T_c + D_{ba} + P_o + F + W_s$	4.17	Table 2.7.6
10	$T_c + D_{tn} + P_o + F + W_s$	1.87	Table 2.7.6
11	$T_c + D_{sa} + P_o + F + W_s$	2.19	Table 2.7.6
12	$T_c + D_{ca} + P_o + F + W_s$	1.73	Table 2.7.6
13	$T_c + D_{ga} + P_o + F + W_s$	2.65	Table 2.7.6
14	$T_c + P_s + P_o + F + W_s$	3.05	Table 2.7.6
15	$T_c + P_t + P_o + F + W_s$	2.09 (see note 1)	Table 2.7.6
16	$T_c + P_b + P_o + F + W_s$	1.46	Table 2.76
17	$T_f + P_i + F + W_s$	pre-load maintained	Subsection 2.7.3.4
18	P_o^*	2.32	Table 2.7.8
19	$P_i^* + T_f + F + W_s$	7.74	Subsection 2.7.3.3.2
20	$T_h + D_{ga} + P_i + F + W_s$	1.77	Table 2.7.5
21	$T_c + D_{ga} + P_i + F + W_s$	1.84	Table 2.7.6
22	$T_c + D_{ga} + P_i + F + W_s$	2.14	Table 2.7.5

Note: 1. This reported stress is directly under the point of impact. Therefore, the calculated value does not represent a primary stress; however, primary stress levels are met by this peak stress intensity.

† The symbols used here are defined in Subsection 2.1.2.1.

Table 2.7.4 - FINITE ELEMENT ANALYSIS RESULTS
MINIMUM SAFETY FACTORS FOR MPC COMPONENTS UNDER ACCIDENT CONDITIONS

Component - Stress Result	MPC-24		MPC-32		MPC-68	
	30 Ft. Side Drop, 0° Orientation Load Case F3.b or E3.b	30 Ft. Side Drop, 45° Orientation Load Case F3.c or E3.c	30 Ft. Side Drop, 0° Orientation Load Case F3.b or E3.b	30 Ft. Side Drop, 45° Orientation Load Case F3.c or E3.c	30 Ft. Side Drop, 0° Orientation Load Case F3.b or E3.b	30 Ft. Side Drop, 45° Orientation Load Case F3.c or E3.c
Fuel Basket – Primary Membrane (P_m)	2.80	3.85	2.78	3.90	3.07	4.30
Fuel Basket - Local Membrane Plus Primary Bending ($P_L + P_b$)	1.19	1.29	1.19	1.28	2.64	1.56
Enclosure Vessel - Primary Membrane (P_m)	6.43	6.88	5.77	6.95	5.65	7.13
Enclosure Vessel - Local Membrane Plus Primary Bending ($P_L + P_b$)	4.24	4.28	2.14	3.56	3.07	2.74
Basket Supports - Primary Membrane (P_m)	N/A	N/A	2.72	3.83	6.68	8.68
Basket Supports - Local Membrane Plus Primary Bending ($P_L + P_b$)	N/A	N/A	3.89	4.75	1.16	1.51

Table 2.7.4 (Continued) - FINITE ELEMENT ANALYSIS RESULTS
MINIMUM SAFETY FACTORS FOR MPC COMPONENTS UNDER ACCIDENT CONDITIONS

Component - Stress Result	MPC-24E/EF	
	30 Ft. Side Drop, 0 deg Orientation Load Case F3.b or E3.b	30 Ft. Side Drop, 45 deg Orientation Load Case F3.c or E3.c
Fuel Basket – Primary Membrane (P_m)	2.75	3.80
Fuel Basket - Local Membrane Plus Primary Bending ($P_L + P_b$)	1.16	1.28
Enclosure Vessel - Primary Membrane (P_m)	6.41	6.88
Enclosure Vessel - Local Membrane Plus Primary Bending ($P_L + P_b$)	3.15	4.14

Table 2.7.5 - FINITE ELEMENT ANALYSIS RESULTS
MINIMUM SAFETY FACTORS FOR OVERPACK COMPONENTS UNDER ACCIDENT CONDITIONS (Hot Environment)

Component – Stress Result	30 Ft. Bottom End Drop Load Case 1	30 Ft. Top End Drop Load Case 2	30 Ft. Side Drop Load Case 3	30 Ft. C.G. Over-the-Bottom-Corner Drop Load Case 4
Lid – Local Membrane Plus Primary Bending ($P_L + P_b$)	34.04	1.75	2.60	7.76
Inner Shell – Local Membrane Plus Primary Bending ($P_L + P_b$)	4.35	10.02	2.19	2.93
Inner Shell – Primary Membrane (P_m)	4.48	7.39	2.45	2.33
Intermediate Shells - Local Membrane Plus Primary Bending ($P_L + P_b$)	6.63	7.95	2.33	1.49
Baseplate - Local Membrane Plus Primary Bending ($P_L + P_b$)	7.05	21.6	4.71	2.78
Enclosure Shell - Primary Membrane (P_m)	16.44	12.23	2.19	5.48

Notes: 1. Load cases are defined in Table 2.1.9.

Table 2.7.5 (Continued) - FINITE ELEMENT ANALYSIS RESULTS
MINIMUM SAFETY FACTORS FOR OVERPACK COMPONENTS UNDER ACCIDENT CONDITIONS (Hot Environment)

Component - Stress Result	30 Ft. C.G. Over-the-Top-Corner Drop Load Case 5	Side Puncture Load Case 6	Top End Puncture Load Case 7	Bottom End Puncture Load Case 8	30 Ft. – 30 degree Drop Load Case 20	30 Ft. – Slapdown Load Case 22
Lid – Local Membrane Plus Primary Bending ($P_L + P_b$)	3.69	5.70	2.03 (See Note 2)	6.29	1.77	2.22
Inner Shell – Local Membrane Plus Primary Bending ($P_L + P_b$)	3.16	2.80	29.29	9.52	2.78	2.73
Inner Shell – Primary Membrane (P_m)	2.60	5.95	26.5	10.61	2.45	2.14
Intermediate Shells - Local Membrane Plus Primary Bending ($P_L + P_b$)	3.52	6.19	32.52	15.12	3.28	2.88
Baseplate - Local Membrane Plus Primary Bending ($P_L + P_b$)	6.95	21.62	28.62	1.46	27.32	17.9
Enclosure Shell - Primary Membrane (P_m)	3.56	4.53	51.32	29.9	8.02	2.40

Notes: 1. Load cases are defined in Table 2.1.9.
2. Stress Intensity computed just outboard of the loaded area since surface stress is not a primary stress component.

Table 2.7.6 - FINITE ELEMENT ANALYSIS RESULTS
MINIMUM SAFETY FACTORS FOR OVERPACK COMPONENTS UNDER ACCIDENT CONDITIONS (Cold Environment)

Component – Stress Result	30 Ft. Bottom End Drop Load Case 9	30 Ft. Top End Drop Load Case 10	30 Ft. Side Drop Load Case 11	30 Ft. C.G. Over-the-Bottom-Corner Drop Load Case 12
Lid – Local Membrane Plus Primary Bending ($P_L + P_b$)	30.29	1.87	2.73	8.00
Inner Shell – Local Membrane Plus Primary Bending ($P_L + P_b$)	4.17	9.69	2.19	2.94
Inner Shell – Primary Membrane (P_m)	4.37	7.33	2.47	2.36
Intermediate Shells - Local Membrane Plus Primary Bending ($P_L + P_b$)	4.95	8.66	2.61	1.73
Baseplate - Local Membrane Plus Primary Bending ($P_L + P_b$)	7.73	17.07	4.80	2.73
Enclosure Shell - Primary Membrane (P_m)	20.08	18.4	2.45	5.71

Notes: 1. Load cases are defined in Table 2.1.9.

Table 2.7.6 (Continued) - FINITE ELEMENT ANALYSIS RESULTS
MINIMUM SAFETY FACTORS FOR OVERPACK COMPONENTS UNDER ACCIDENT CONDITIONS (Cold Environment)

Component – Stress Result	30 Ft. C.G. Over-the-Top-Corner Drop Load Case 13	Side Puncture Load Case 14	Top End Puncture Load Case 15	Bottom End Puncture Load Case 16	30 Ft.. – 30 degree Drop Load Case 21
Lid – Local Membrane Plus Primary Bending ($P_L + P_b$)	3.91	5.91	2.09 (See Note 2)	6.64	1.84
Inner Shell – Local Membrane Plus Primary Bending ($P_L + P_b$)	3.21	3.05	24.97	8.54	2.78
Inner Shell – Primary Membrane (P_m)	2.65	7.60	17.03	9.59	2.48
Intermediate Shells - Local Membrane Plus Primary Bending ($P_L + P_b$)	4.10	7.06	27.55	14.9	3.81
Baseplate - Local Membrane Plus Primary Bending ($P_L + P_b$)	7.08	29.69	47.25	1.46	21.91
Enclosure Shell - Primary Membrane (P_m)	4.13	5.17	57.21	76.5	9.64

Notes: 1. Load cases are defined in Table 2.1.9.
2. Surface pressure not included in safety factor evaluation since it is not a primary stress.

Table 2.7.7

MINIMUM SAFETY FACTORS FOR MISCELLANEOUS ITEMS - MPC FUEL BASKET/CANISTER - HYPOTHETICAL ACCIDENT CONDITIONS OF TRANSFER

Item	Loading	Safety Factor	Location in SAR Where Calculations or Results are Presented
Fuel Basket Axial Stress	End Drop	4.19	Subsection 2.7.1.1
Fuel Basket Axial Stress	Fire Transient (Regulatory Position C.7 of Regulatory Guide 7.6)	4.96	Subsection 2.7.3.4
MPC Canister Stability	30' End Drop (Load Case E3.a, Table 2.1.7)	1.92	Subsection 2.7.1.1
MPC Top Closure Lid Bending Stress	30' End Drop (Load Case E3.a in Table 2.1.7)	2.8 (single lid) 1.4 (dual lid)	Subsection 2.7.1.1
MPC Top Closure Lid – Loading in Peripheral Weld	30' End Drop (Load Case E3.a in Table 2.1.7)	2.37	Subsection 2.7.1.1
MPC Baseplate Bending Stress	30' End Drop (Load Case E3.a in Table 2.1.7)	3.04	Subsection 2.7.1.1
MPC Canister at Connection to Baseplate	30' End Drop (Load Case E3.a in Table 2.1.7)	2.14	Subsection 2.7.1.1
MPC Top Closure Lid Bending Stress	Fire accident (Load Case E5 in Table 2.1.7)	8.59	Subsection 2.7.3.3.1
MPC Baseplate Bending Stress	Fire accident (Load Case E5 in Table 2.1.7)	1.17	Subsection 2.7.3.3.1
MPC Canister Stability	Fire accident (Load Case E5 in Table 2.1.7)	1.18	Subsection 2.7.3.3.1
MPC Shell Mean Stress	Fire accident (Load Case E5 in Table 2.1.7)	4.16	Subsection 2.7.3.3.1

Table 2.7.8

MINIMUM SAFETY FACTORS FOR MISCELLANEOUS ITEMS - OVERPACK - HYPOTHETICAL ACCIDENT CONDITIONS OF TRANSPORT

Item	Loading	Safety Factor	Location in SAR Where Calculations or Results are Presented
Overpack Stability	30' End Drop (Load Cases 1 and 2 in Table 2.1.9)	2.16	Subsection 2.7.1.1
Closure Bolts	30' End Drop (Load Case 2 in Table 2.1.9)	1.30	Subsection 2.7.1.1
Closure Bolts	Top End Puncture	1.86	Subsection 2.7.2
Overpack Inner Shell Mean Stress	Fire Transient	7.74	Subsection 2.7.3.3.2
Closure Bolts	Fire Transient	1.69	Subsection 2.7.3.3.3
Overpack Stress	Fire Transient (Regulatory Position C.7 of Regulatory Guide 7.6)	3.67	Subsection 2.7.3.4
Overpack Stability (Yield Stress Criteria)	Immersion (Load Case 18 in Table 2.1.9)	2.32	Subsection 2.7.5
Overpack Stability (Stability Criteria)	Immersion (Load Case 18 in Table 2.1.9)	3.95	Subsection 2.7.5

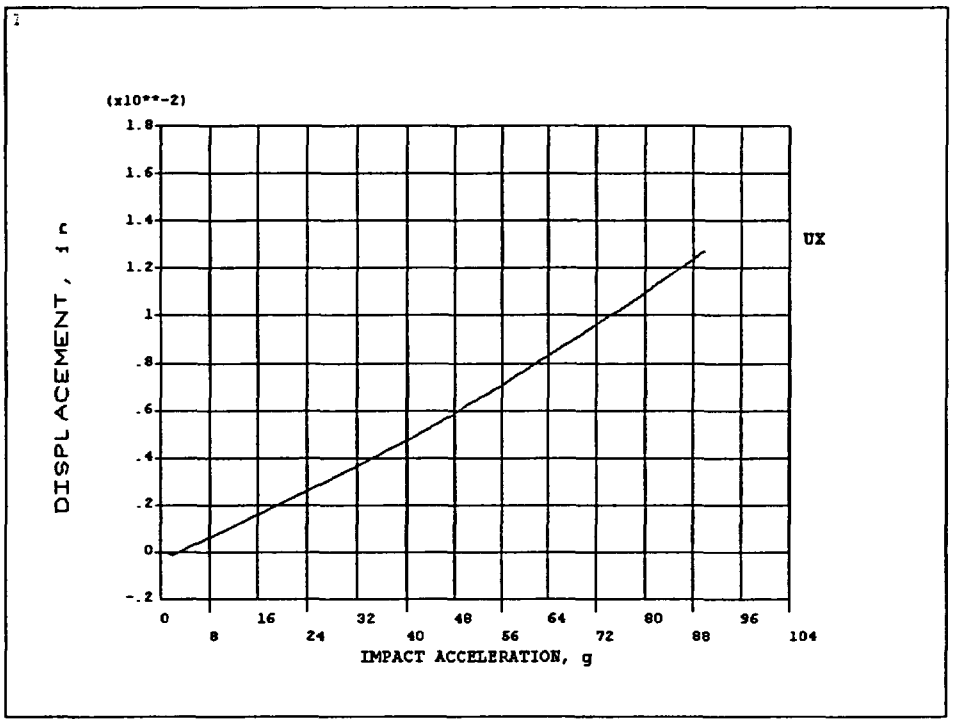

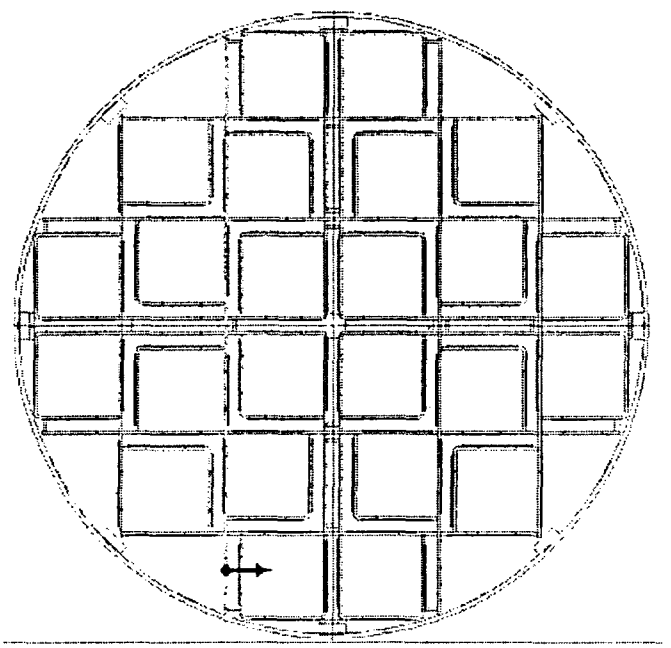

FIGURE 2.7.1; NON-LINEAR BUCKLING ANALYSIS FOR MPC-24
DISPLACEMENT vs. IMPACT ACCELERATION (0° DROP)

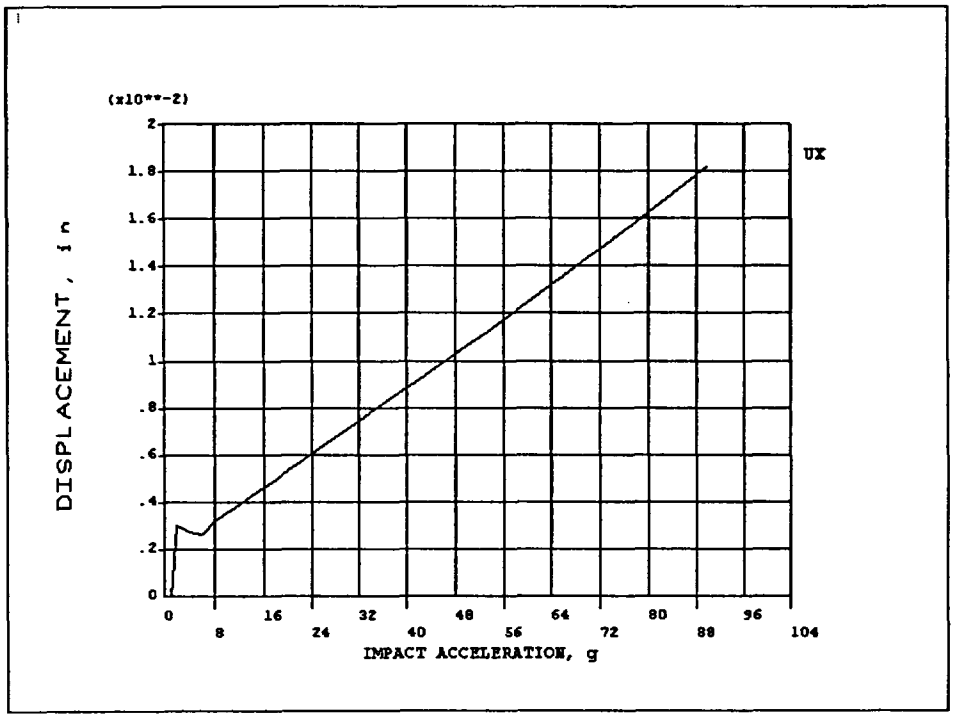

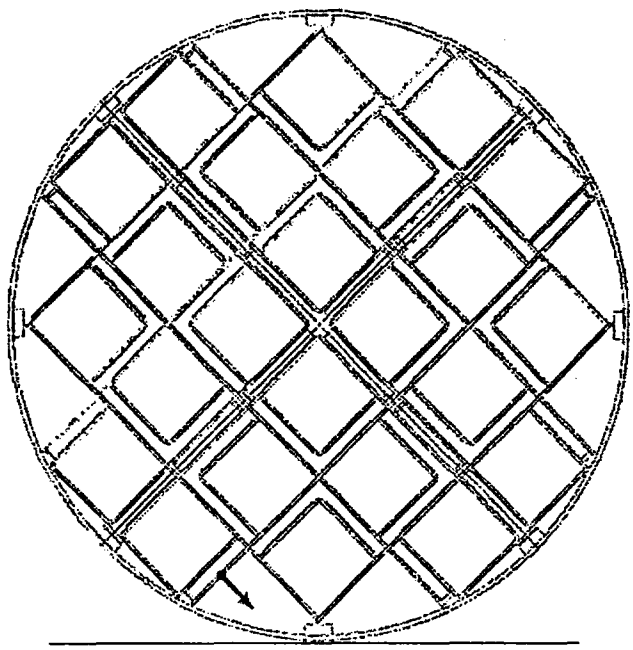

FIGURE 2.7.2; NON-LINEAR BUCKLING ANALYSIS FOR MPC-24
DISPLACEMENT vs. IMPACT ACCELERATION (45° DROP)

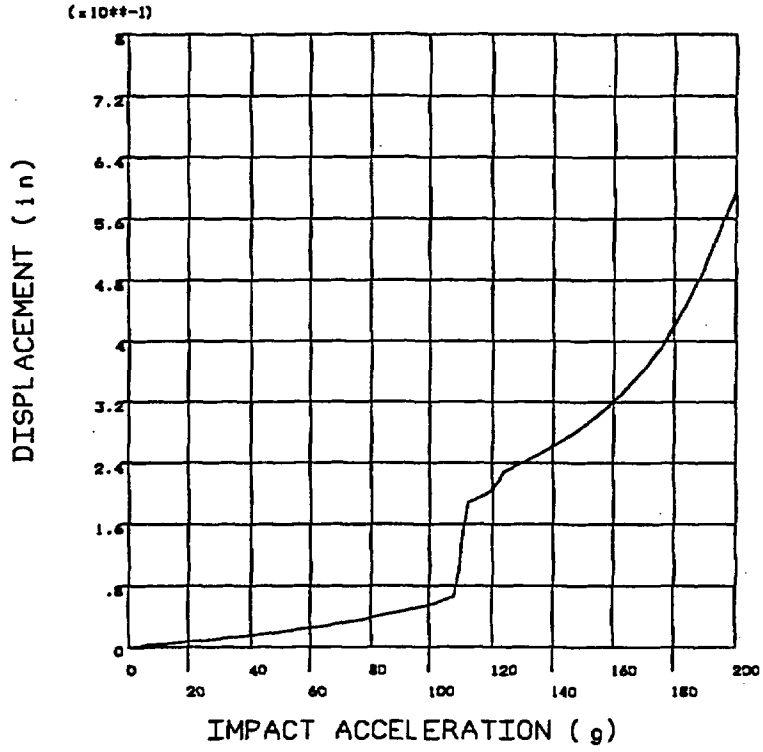

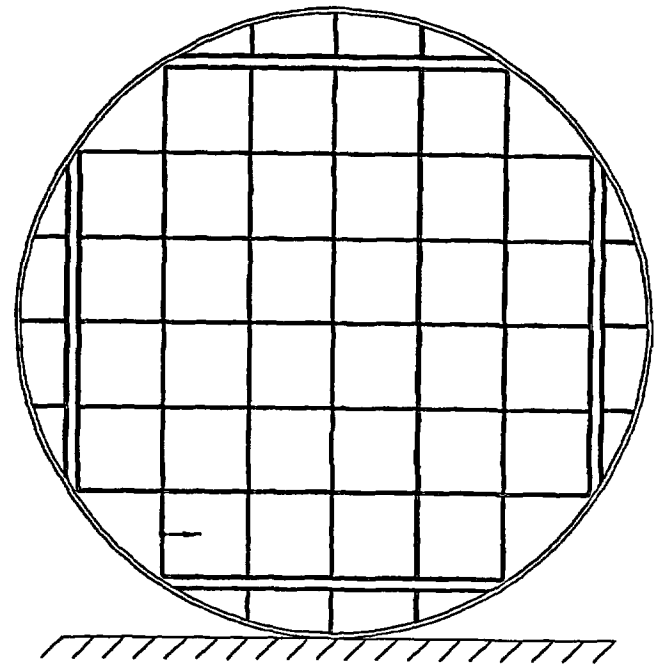

FIGURE 2.7.3 ; NON-LINEAR BUCKLING ANALYSIS FOR MPC-32
DISPLACEMENT Vs. IMPACT ACCELERATION (0° DROP)

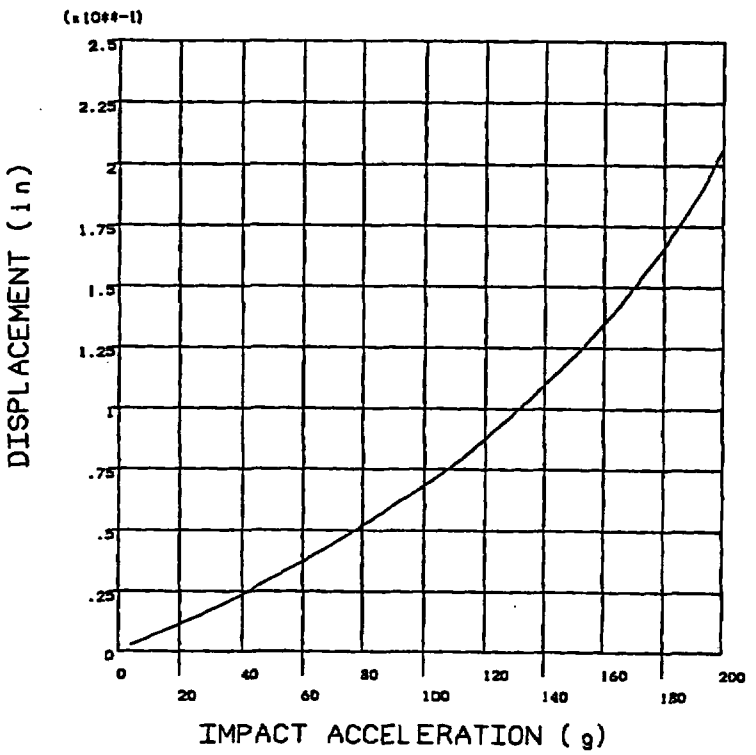

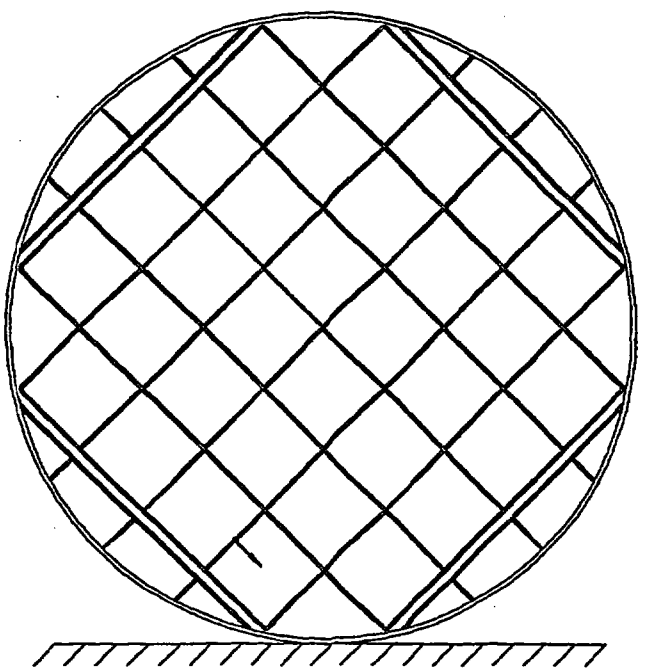

FIGURE 2.7.4 ; NON-LINEAR BUCKLING ANALYSIS FOR MPC-32
DISPLACEMENT Vs. IMPACT ACCELERATION (45° DROP)

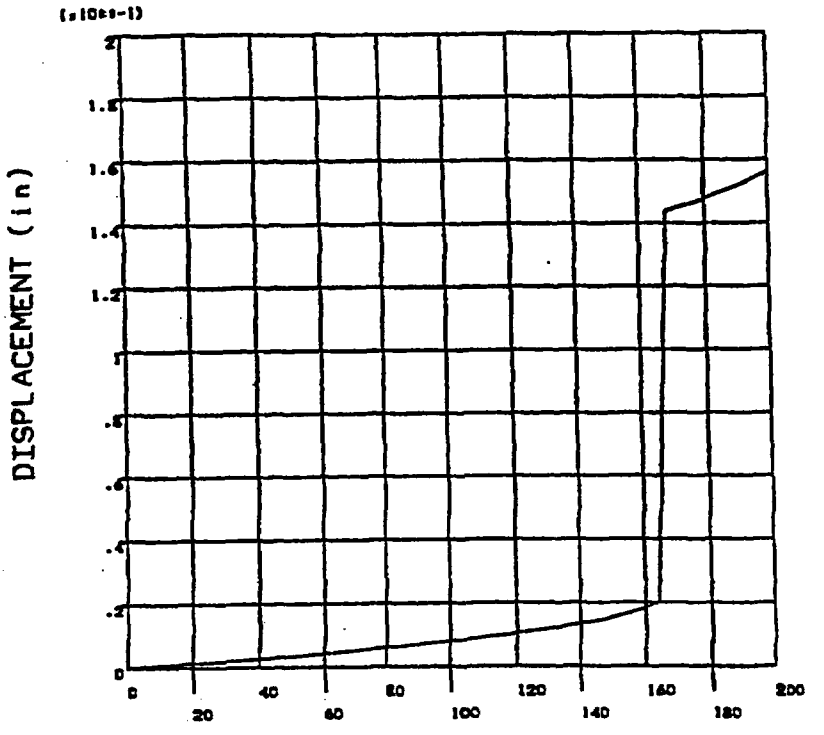

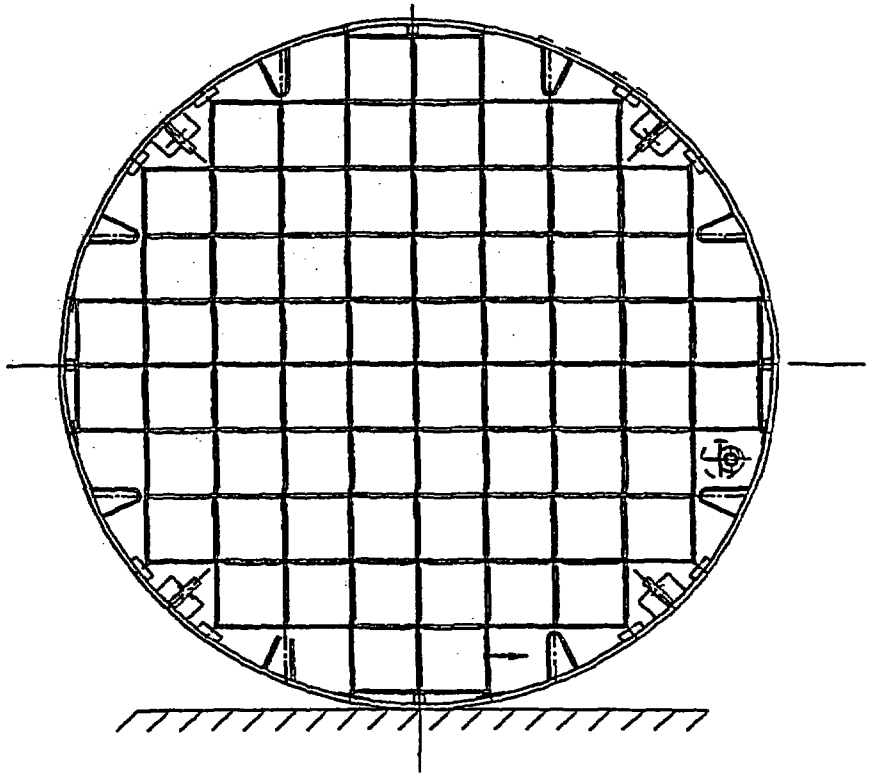

FIGURE 2.7.5: NON-LINEAR BUCKLING ANALYSIS FOR MPC-68
DISPLACEMENT Vs. IMPACT ACCELERATION (0° DROP)

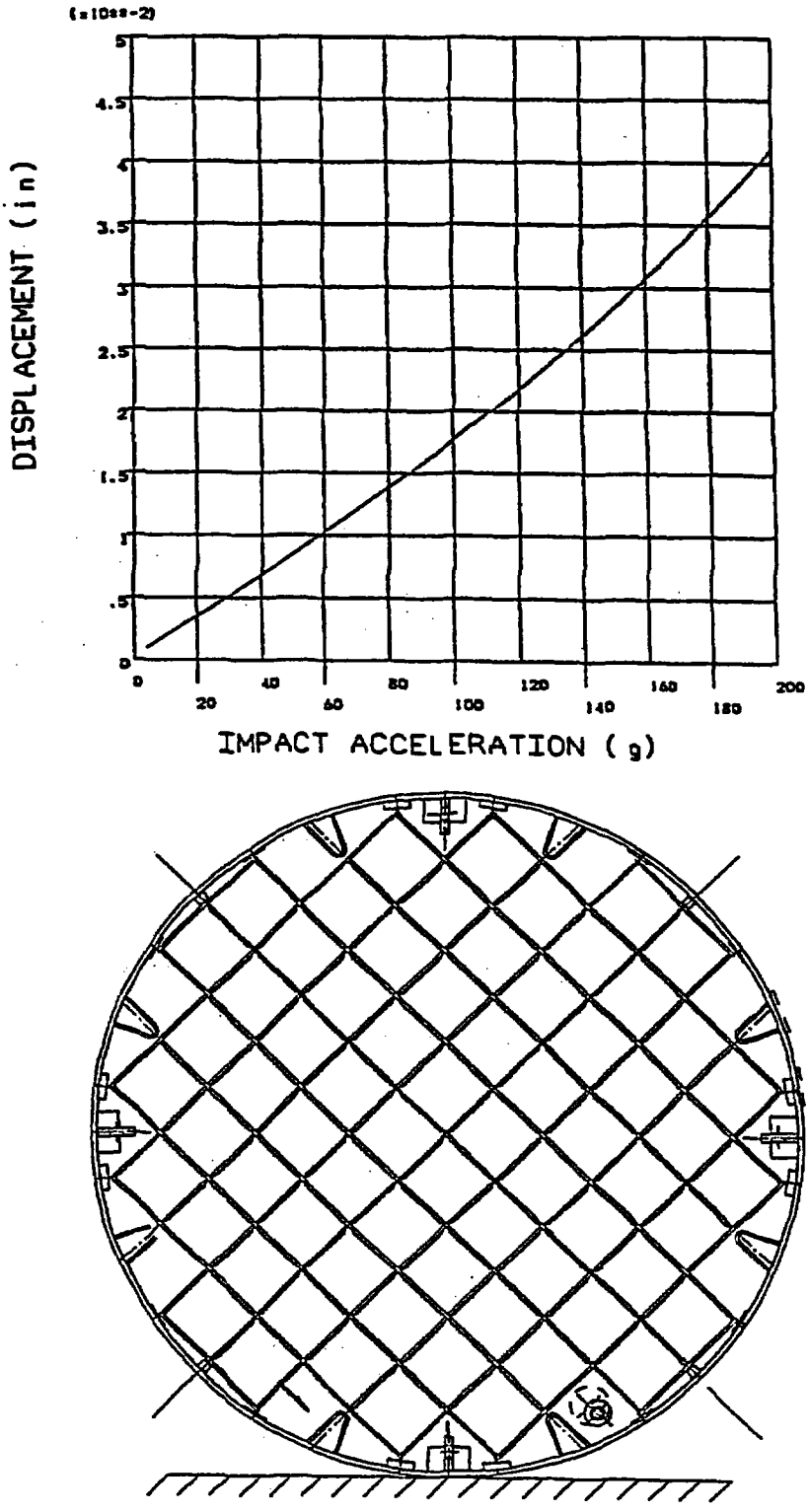

FIGURE 2.7.6: NON-LINEAR BUCKLING ANALYSIS FOR MPC-68
DISPLACEMENT Vs. IMPACT ACCELERATION (45° DROP)

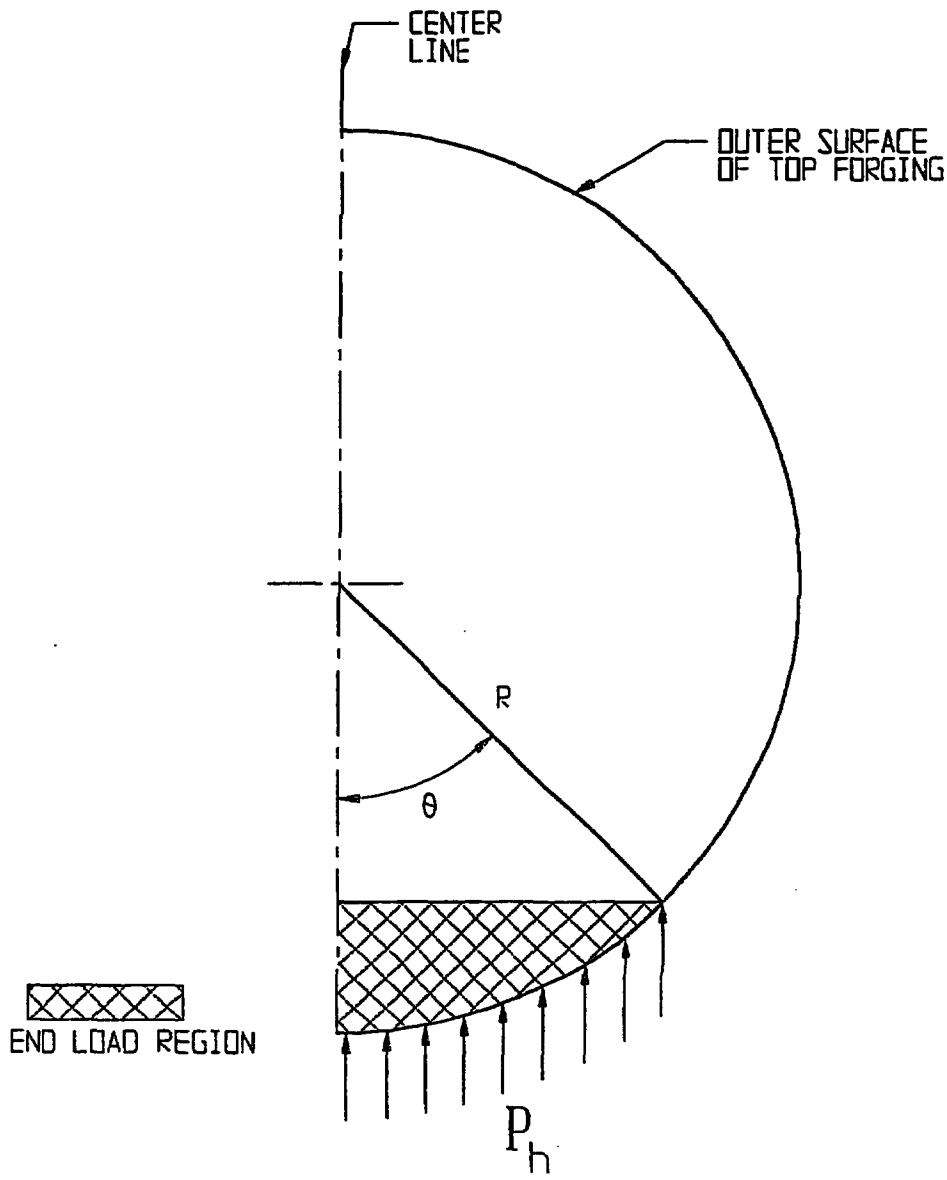

FIGURE 2.7.7; IMPACT LIMITER LOADED AREAS ON THE OVERPACK

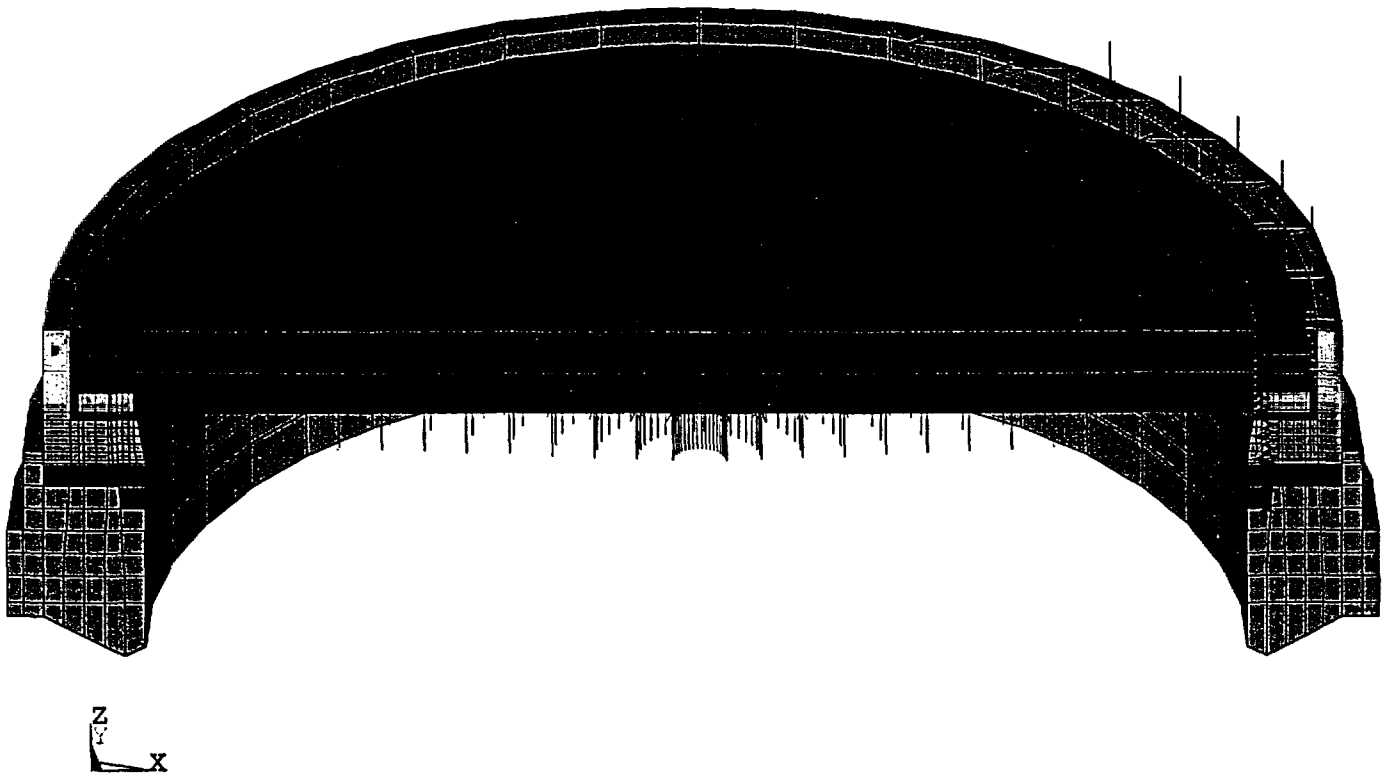

FIGURE 2.7.8 TOP LID LOADING – DROP ANALYSIS

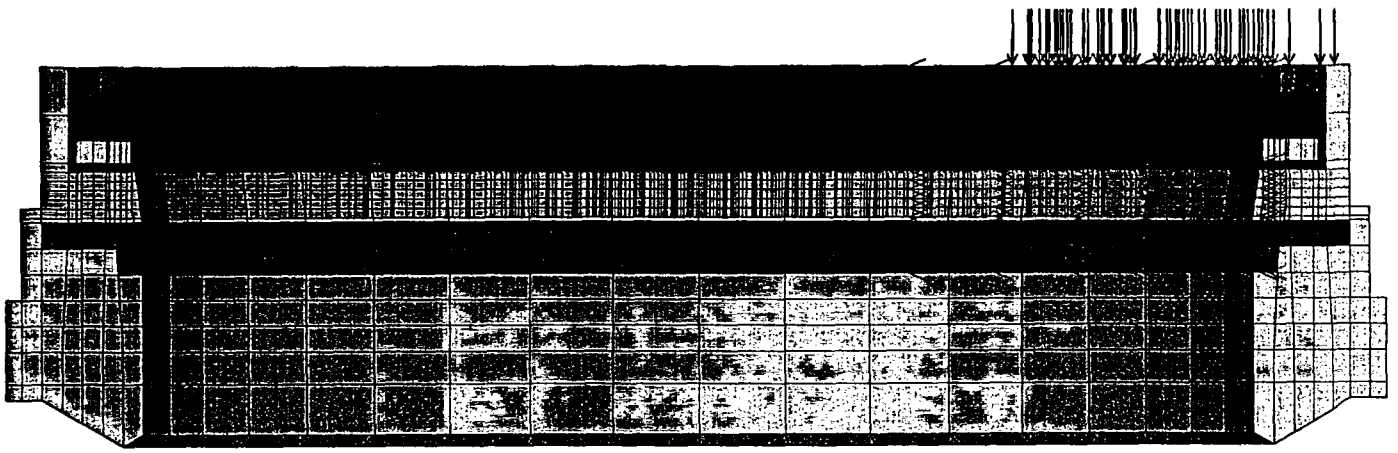

FIGURE 2.7.9 SIDE VIEW OF TOP FORGING SHOWING END LOADS

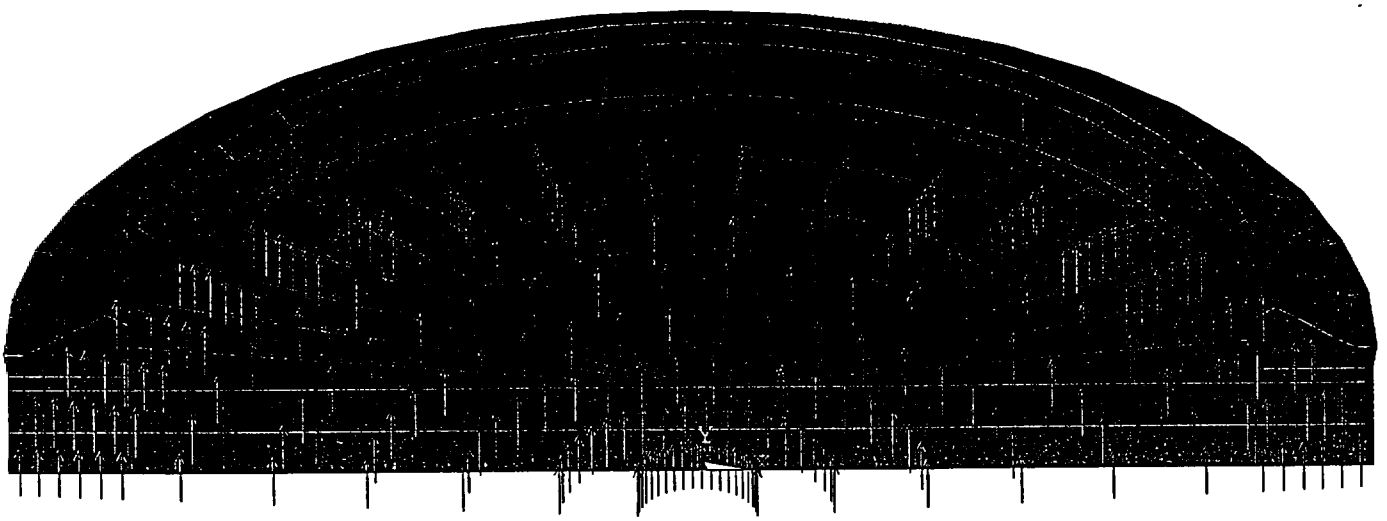

FIGURE 2.7.10 BASEPLATE LOADING FROM IMPACT LIMITER – TOP END DROP

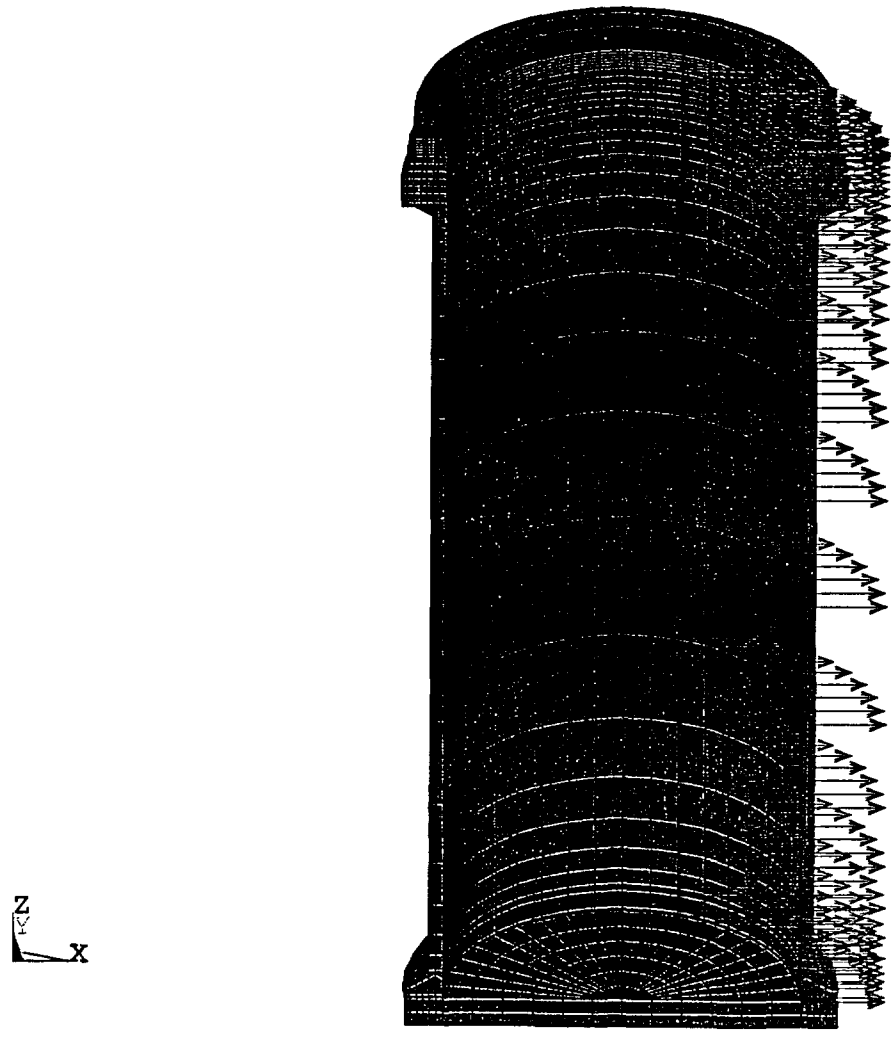

FIGURE 2.7.11 LOADING FROM MPC ON INNER SHELL

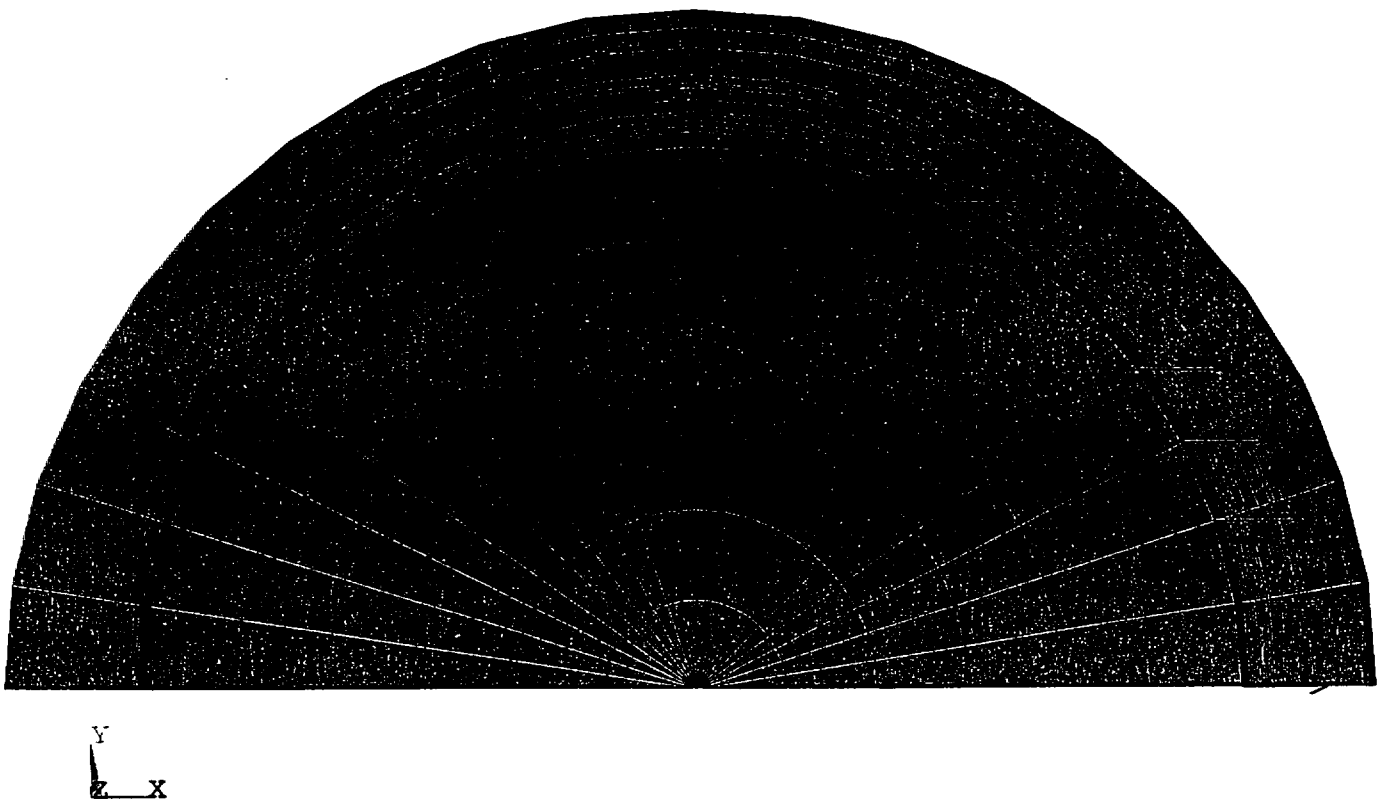

FIGURE 2.7.12 END VIEW SHOWING MPC LOADING ON INNER SHELL

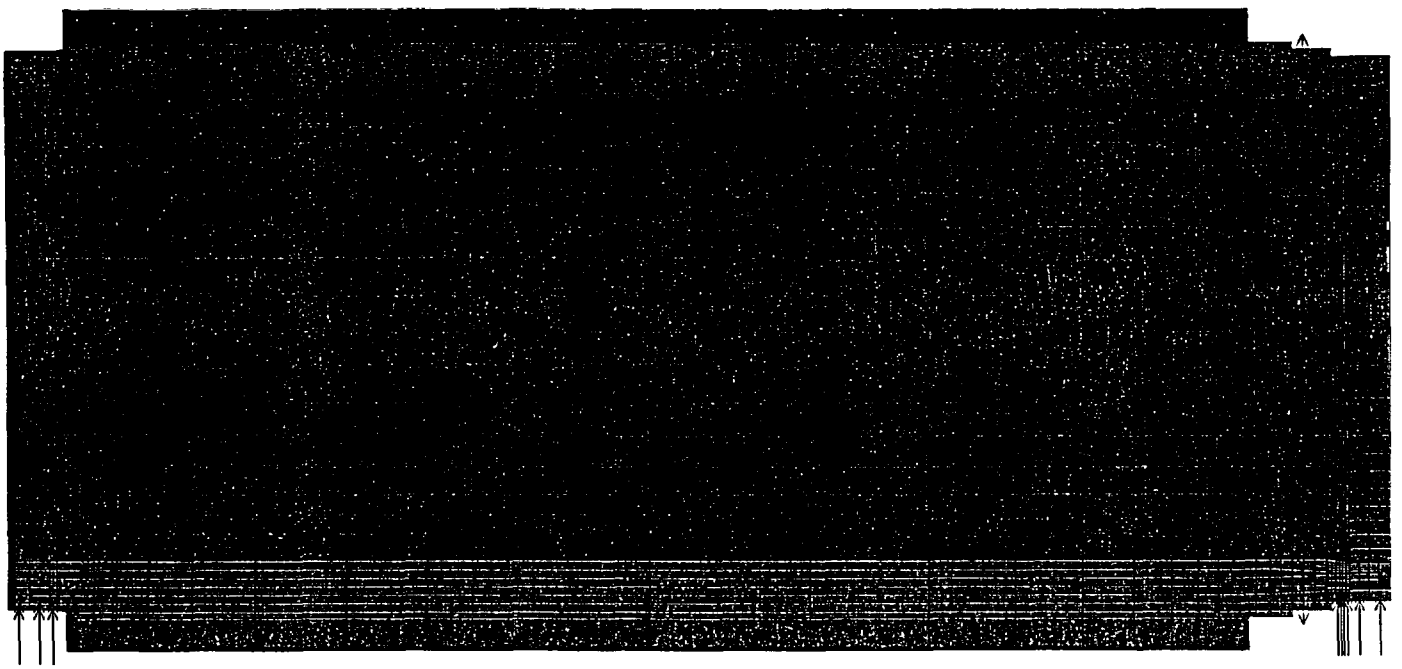

FIGURE 2.7.13 LOAD FROM IMPACT LIMITER AT SUPPORT LOCATIONS – SIDE DROP

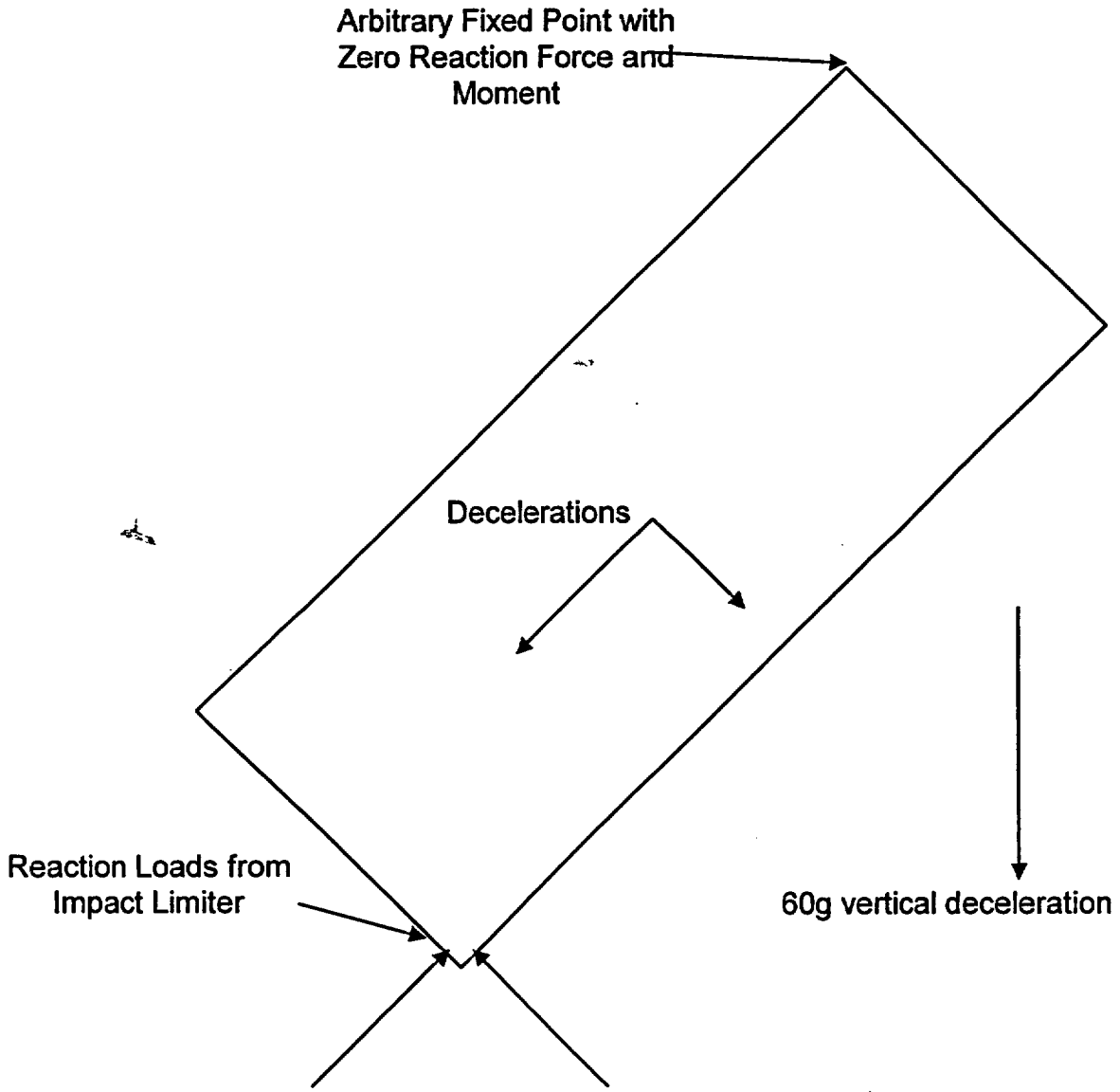

FIGURE 2.7.14 OBLIQUE DROP SHOWING OFFSET OF IMPACT LIMITER REACTION LOAD FROM APPLIED INERTIA LOADS

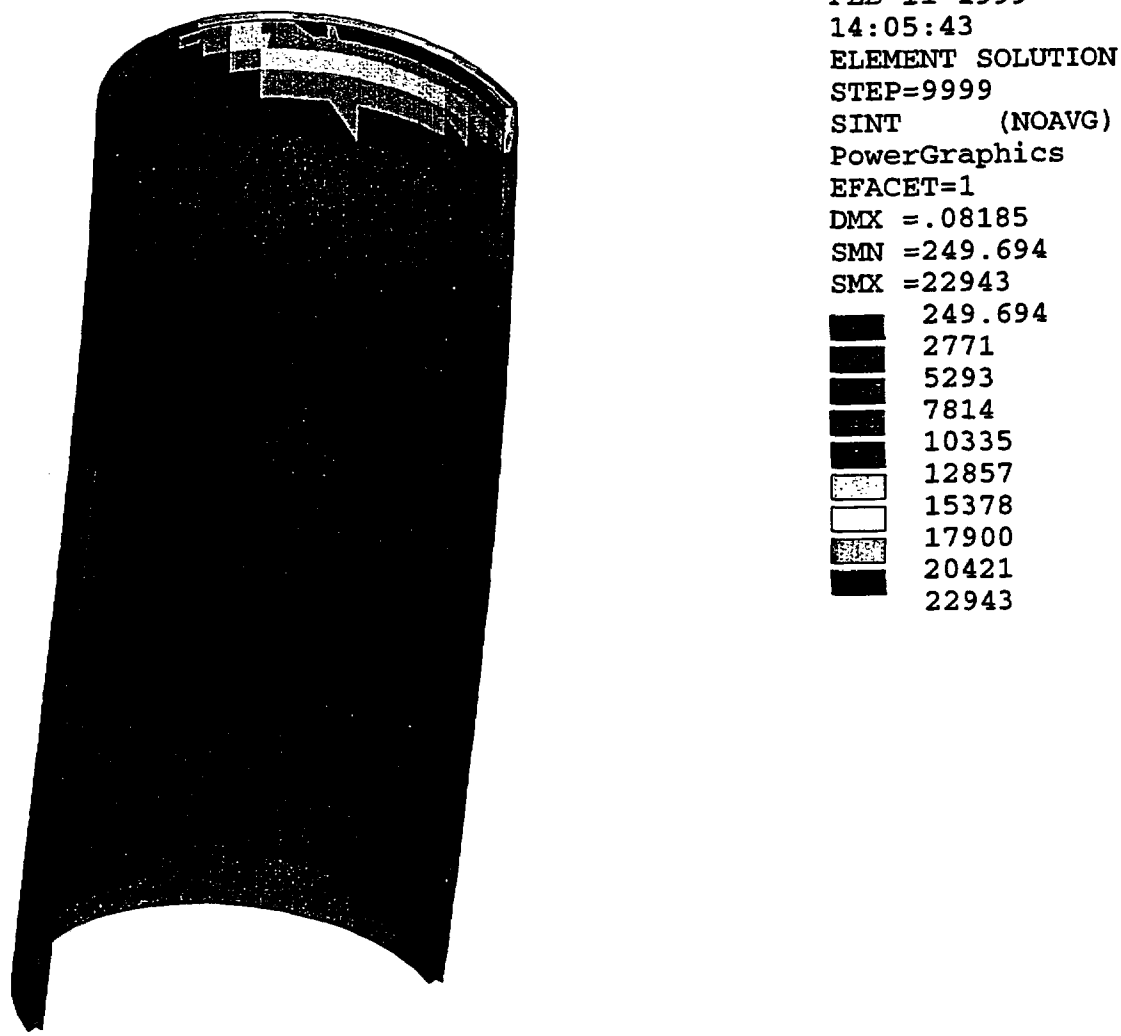

FIGURE 2.7.15 – INNER SHELL STRESS INTENSITY DISTRIBUTION – "HEAT" CONDITION – 30 DEGREE – TOP END IMPACT

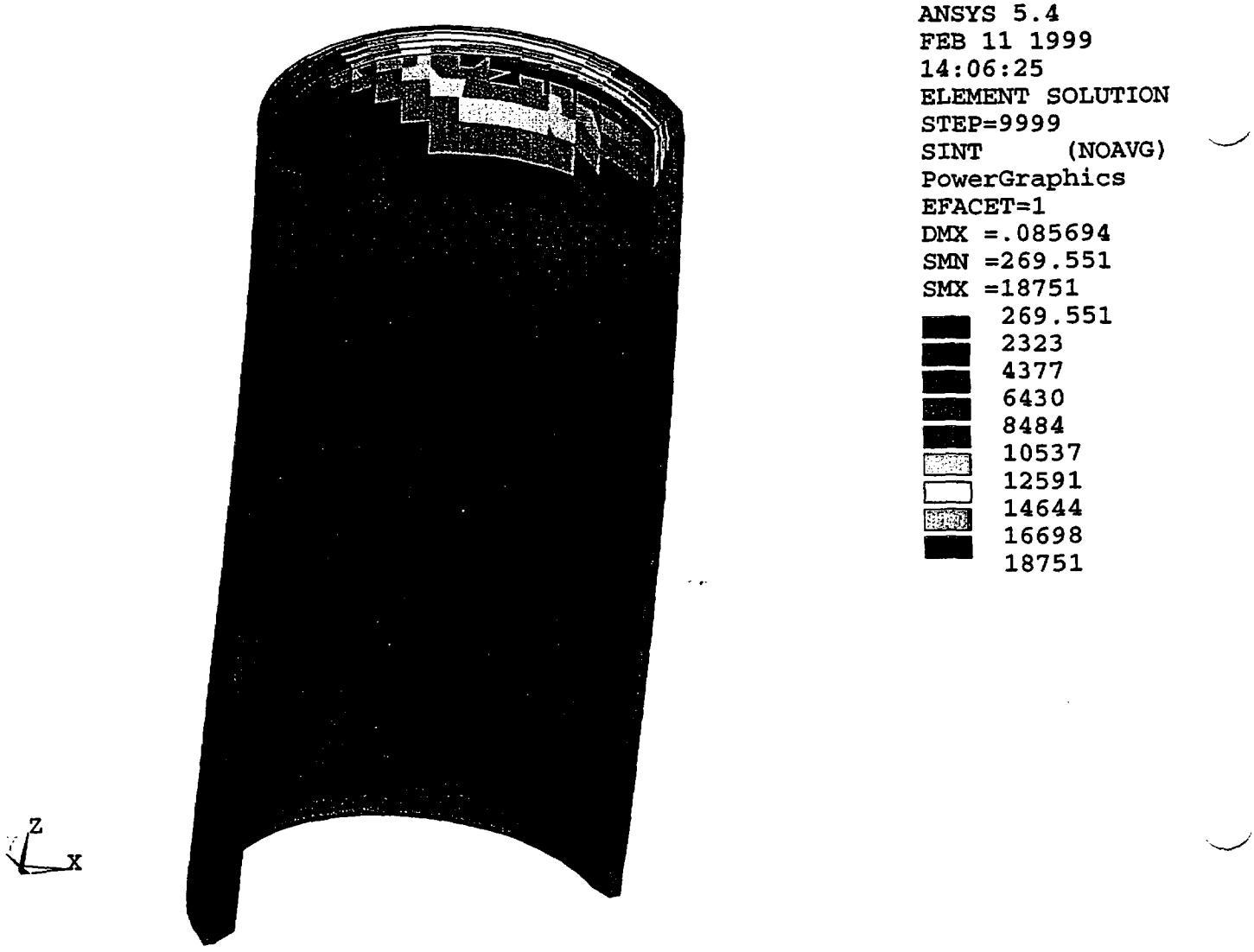

FIGURE 2.7.16 - INTERMEDIATE SHELL-STRESS INTENSITY DISTRIBUTION - "HEAT" CONDITION - 30 DEGREE - TOP - END IMPACT

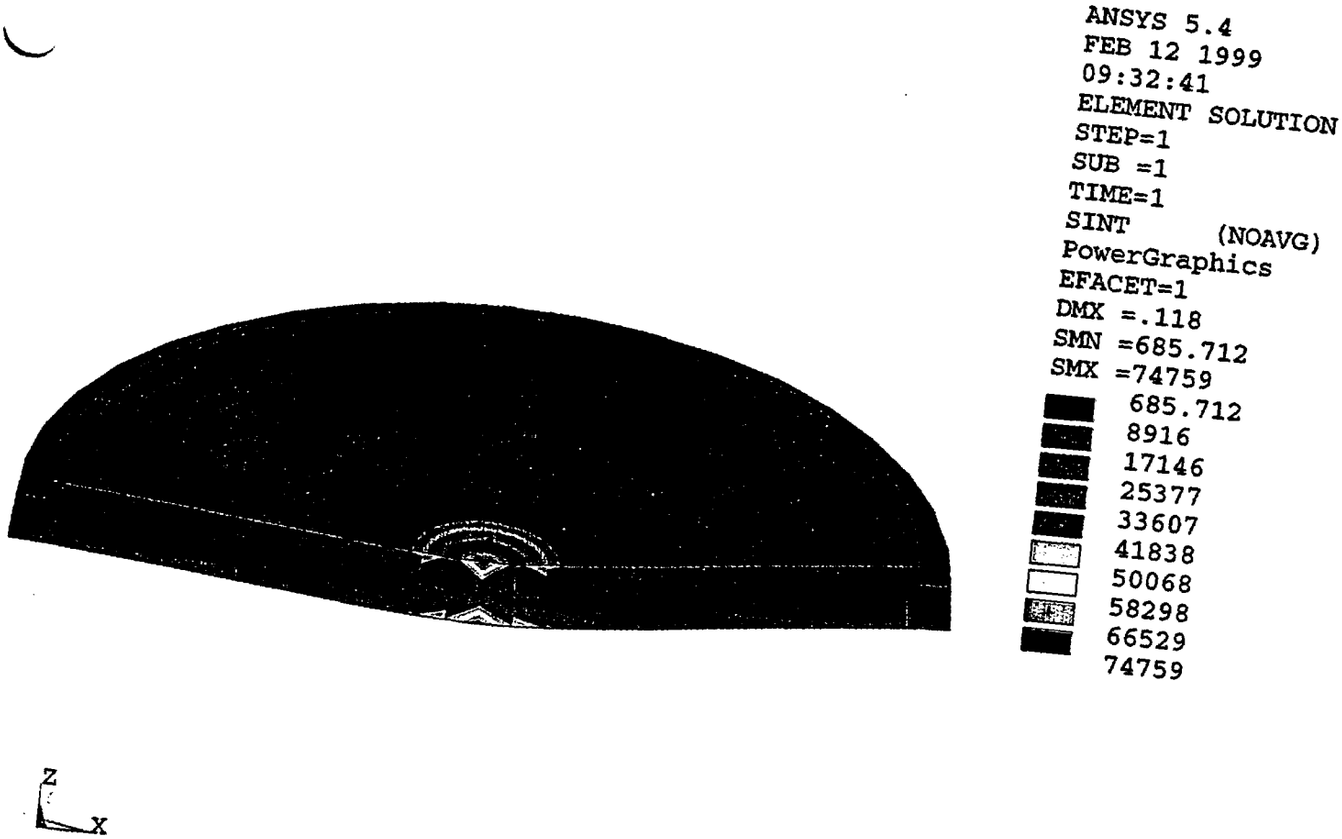

FIGURE 2.7.17 - LOCALIZED STRESS INTENSITY DISTRIBUTION IN LID - TOP END PUNCTURE (DEFORMED SHAPE EXPANDED FOR CLARITY)

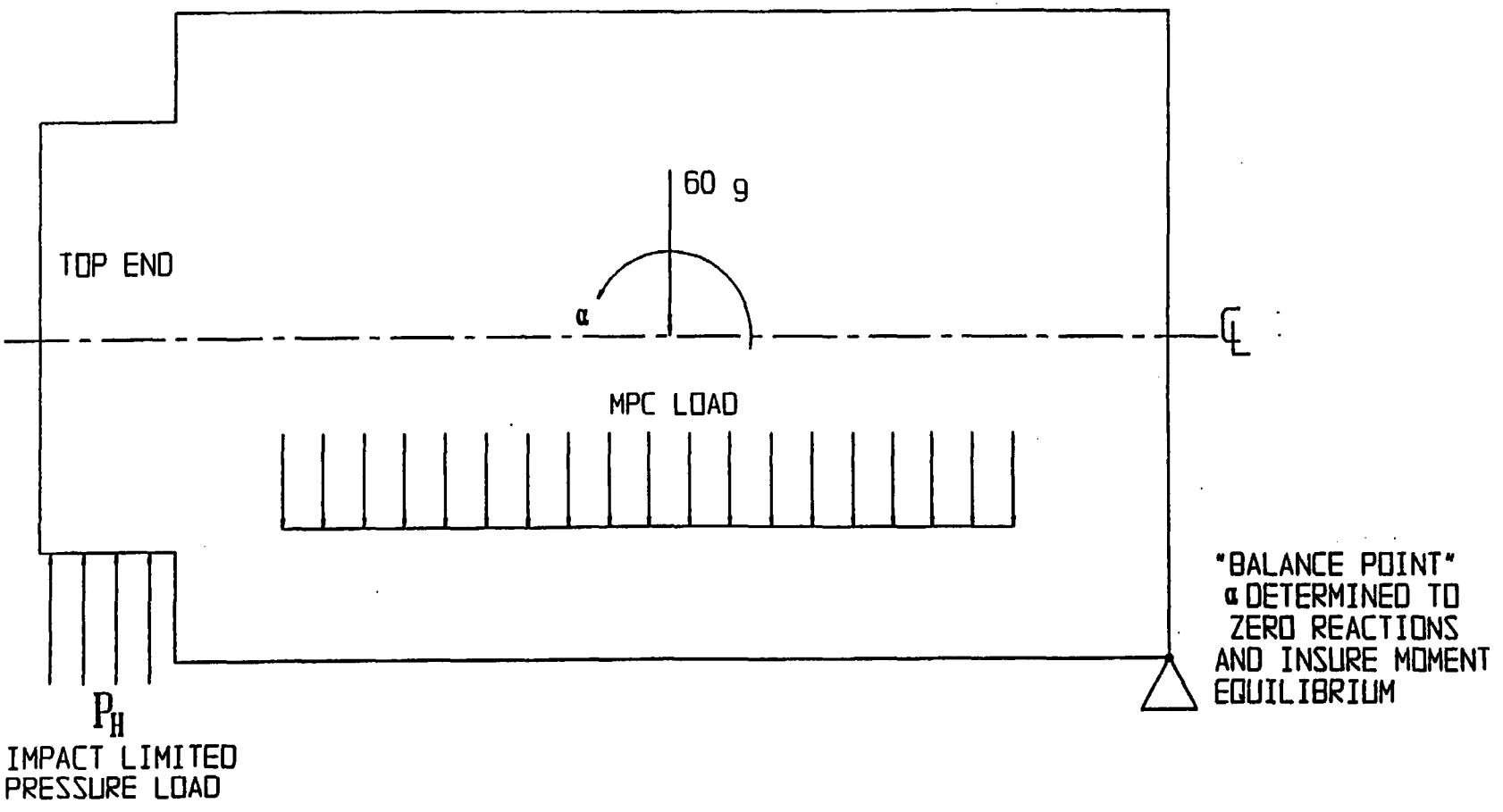

FIGURE 2.7.18; IMPACT LOADS FOR SLAPDOWN FINITE ELEMENT ANALYSIS

Figures 2.7.19 through 2.7.22

INTENTIONALLY DELETED

2.8 SPECIAL FORM

This section is not applicable to the HI-STAR 100 System. This application does not seek approval for transport of special form radioactive material as defined in 10CFR71.4.

2.9 FUEL RODS

The cladding of the fuel rods is the initial confinement boundary in the HI-STAR 100 System. Analyses have been performed in Chapter 3 to ensure that the maximum temperature of the fuel cladding is below the Pacific Northwest Laboratory's threshold values for various cooling times. These temperature limits ensure that the fuel cladding will not degrade in an inert helium environment. Additional details on the fuel rod cladding temperature analyses for the spent fuel to be loaded into the HI-STAR 100 System are provided in Chapter 3.

The dimensions of the storage cell openings in the MPC are equal to or greater than those used in spent fuel racks supplied by Holtec International. Thousands of fuel assemblies have been shuffled in and out of these cells over the years without a single instance of cladding failure. The vast body of physical evidence from prior spent fuel handling operations provides confirmation that the fuel handling and loading operations with the HI-STAR 100 MPC will not endanger or compromise the integrity of the cladding or the structural integrity of the assembly.

The HI-STAR 100 System is designed and evaluated for a maximum deceleration of 60g's. Studies of the capability of spent fuel rods to resist impact loads [2.9.1] indicate that the most vulnerable fuel can withstand greater than 60 g's in the side impact orientation. Therefore, limiting the HI-STAR 100 System to a maximum deceleration of 60 g's (perpendicular to the longitudinal axis of the overpack during all normal and hypothetical accident conditions) ensures that fuel rod cladding integrity is maintained. In [2.9.1], it is assumed that the fuel rod cladding provides the only structural resistance to bending and buckling of the rod. For accidents where the predominate deceleration is directed along the longitudinal axis of the overpack, [2.9.1] also demonstrates that no elastic instability or yielding of the cladding will occur until the deceleration level is well above the HI-STAR 100 limit of 60g's. The solutions presented in [2.9.1], however, assume that the fuel pellets are not intimately attached to the cladding when subjected to an axial deceleration load that may cause an elastic instability of the fuel rod cladding.

The limit based on classical Euler buckling analyses performed by Lawrence Livermore National Laboratory in [2.9.1] is 82 g's. In the LLNL report, the limiting axial load to ensure fuel rod stability is obtained by modeling the fuel rod as a simply supported beam with unsupported length equal to the grid strap spacing. The limiting load under this condition is:

$$F = \pi^2 EI/L^2$$

In the preceding formula, E = Young's Modulus of the cladding, I = area moment of inertia of the cladding, and L = spacing of the grid straps.

Assuming that F = WxA/g with W being the weight of a fuel rod, and A = the deceleration, the Euler buckling formula can be expressed as

$$A/g = \pi^2 (ER^3tn/W_{fa}L^2) = \pi^2\beta$$

In the preceding formula, g = gravity, n = number of fuel rods in the fuel assembly, W_{fa} = the total weight of the fuel assembly, t = cladding wall thickness, and R = cladding mean radius.

Using the preceding formula, a survey of a large variety of fuel assembly types in [2.9.1] concluded that a 17 x 17 PWR assembly resulted in the minimum value for deceleration and results in the lower bound limit of:

A/g = 82

The fuel pellet weight was omitted from the analysis in [2.9.1] by virtue of the assumption that under axial load, the cladding did not support the fuel pellet mass. Since the results may not be conservative because of the assumption concerning the behavior of the fuel pellet mass, a new analysis of the structural response of the fuel cladding is presented here... It is demonstrated that the maximum axially oriented deceleration that can be applied to the fuel cladding is in excess of the design basis deceleration specified in this SAR. Therefore, the initial confinement boundary remains intact during a hypothetical accident of transport where large axially directed decelerations are experienced by the HI-STAR 100 package.

The analysis reported here considers the most limiting fuel rod in the fuel assembly. Most limiting is defined as the fuel rod that may undergo the largest bending (lateral) deformations in the event of a loss of elastic stability. The fuel rod is modeled as a thin-walled elastic tube capable of undergoing large lateral displacements in the event that high axial loads cause a loss of stability (i.e., the non-linear interaction of axial and bending behavior of the elastic tube is included in the problem formulation). The fuel rod and the fuel pellet mass is included in the analysis with the fuel pellet mass assumed to contribute only its mass to the analysis. In the HI-STAR 100 spent fuel basket, continuous support to limit lateral movement is provided to the fuel assembly along its entire length. The extent of lateral movement of any fuel rod in a fuel assembly is limited to: (1) the clearance gap between the grid straps and the fuel basket cell wall at the grid strap locations; and, (2) the maximum available gap between the fuel basket cell wall and the fuel rod in the region between the grid straps. Note that the grid straps act as fuel rod spacers at the strap locations; away from the grid straps, however, there is no restraint against fuel rod –to-rod contact under a loading giving rise to large lateral motion of the individual rods. Under the incremental application of axial deceleration to the fuel rod, the fuel rod compresses and displaces from the axially oriented inertial loads experienced. The non-linear numerical analysis proceeds to track the behavior of the fuel rod up to and beyond contact with the rigid confining walls of the HI-STAR 100 fuel basket.

The analysis is carried out for the "most limiting" spent fuel assembly. The "most limiting" criteria used herein is based on the simple elastic stability formula assuming buckling occurs only between grid straps. This is identical to the methodology employed in [2.9.1] to identify the fuel assembly that limits design basis axial deceleration loading. Table 2.9.1 presents tabular data for a wide variety of fuel assemblies. Considerable data was obtained using the tables in [2.9.2]. The configuration with the lowest value of "Beta" is the most limiting for simple elastic Euler buckling between grid straps; the Westinghouse 14x14 Vantage,"W14V", PWR configuration is used to obtain results.

The material properties used in the non-linear analysis are those for irradiated Zircalloy and are obtained from [2.9.1]. The Young's Modulus and the cladding dynamic yield stress are set as:

$E = 10{,}400{,}000$ psi

$\sigma_y = 80{,}500$ psi

The fuel cladding material is assumed to have no tensile or compressive stress capacity beyond the material yield strength.

Calculations are performed for two limiting assumptions on the magnitude of resisting moment at the grid straps. Figures 2.9.1 through 2.9.9 aid in understanding the calculation. It is shown in the detailed calculations that the maximum stress in the fuel rod cladding occurs subsequent to the cladding deflecting and contacting the fuel basket cell wall. Two limiting analyses are carried out. The initial analysis assumes that the large deflection of the cladding between two grid straps occurs without any resisting moment at the grid strap supports. This maximizes the stress in the free span of the cladding, but eliminates all cladding stress at the grid strap supports. It is shown that this analysis provides a conservative lower bound on the limiting deceleration. The second analysis assumes a reasonable level of moment resistance to develop at the grid straps; the level developed is based on an assumed deflection shape for the cladding spans adjacent to the span subject to detailed analysis. For this second analysis, the limiting decelerations are much larger with the limit stress level occurring in the free span and at the grid strap support locations.

It is concluded that the most conservative set of assumptions on structural response still lead to the conclusion that the fuel rod cladding remains intact under the design basis deceleration levels set for the HI-STAR 100.

Table 2.9.1 FUEL ASSEMBLY DIMENSIONAL DATA

Array ID	Array Name	Rod O.D. (in.)	Clad Thk. (in.)	R_{mean} (in.)	# of Rods	Assy Wt. (lb.)	Rod Length (in.)	# of Spans	Average Span (in.)	Material Modulus	BETA
						PWR					
14x14A01	W14OFA	0.4000	0.0243	0.20608	179	1177	151.85	6	25.30833	10400000	0.525127806
14x14A02	W14OFA	0.4000	0.0243	0.20608	179	1177	151.85	6	25.30833	10400000	0.525127806
14x14A03	W14V	0.4000	0.0243	0.20608	179	1177	151.85	6	25.30833	10400000	0.525127806
14x14B01	W14STD	0.4220	0.0243	0.21708	179	1302	152.4	6	25.4	10400000	0.550863067
14x14B02	XX14TR	0.4170	0.0295	0.21588	179	1215	152	6	25.33333	10400000	0.708523868
14x14B03	XX14STD	0.4240	0.0300	0.21950	179	1271.2	149.1	8	18.6375	10400000	1.337586884
14x14C01	CE14	0.4400	0.0280	0.22700	176	1270	147	8	18.375	10400000	1.398051576
14x14C02	CE14	0.4400	0.0280	0.22700	176	1220	137	8	17.125	10400000	1.67556245
14x14D01	W14SS	0.4220	0.0165	0.21513	180	1247	126.68	6	21.11333	24700000	1.31385062
15x15A01	CE15P	0.4180	0.0260	0.21550	204	1360	140	9	15.55556	10400000	1.677523904
15x15B01	W15OFA	0.4220	0.0245	0.21713	204	1459	151.85	6	25.30833	10400000	0.569346561
15x15B02	W15V5H	0.4220	0.0245	0.21713	204	1459	151.85	6	25.30833	10400000	0.569346561
15x15B03	W15	0.4220	0.0243	0.21708	204	1440	151.83	6	25.305	10400000	0.571905185
15x15B04	W15	0.4220	0.0243	0.21708	204	1443	151.83	6	25.305	10400000	0.570716193
15x15B05	15(2a-319)	0.4220	0.0242	0.21705	204	1472	151.88	6	25.31333	10400000	0.556610964
15x15C01	SPC15	0.4240	0.0300	0.21950	204	1425	152	6	25.33333	10400000	0.73601861
15x15C02	SPC15	0.4240	0.0300	0.21950	204	1425	152	6	25.33333	10400000	0.73601861
15x15C03	XX15	0.4240	0.0300	0.21950	204	1432.8	152.065	6	25.34417	10400000	0.731386148
15x15C04	XX15	0.4170	0.0300	0.21600	204	1338.6	139.423	9	15.49144	10400000	1.996693327
15x15D01	BW15	0.4300	0.0265	0.22163	208	1515	153.68	7	21.95429	10400000	0.854569793
15x15D02	BW15	0.4300	0.0265	0.22163	208	1515	153.68	7	21.95429	10400000	0.854569793
15x15D03	BW15	0.4300	0.0265	0.22163	208	1515	153.68	7	21.95429	10400000	0.854569793
15x15G01	HN15SS	0.4220	0.0165	0.21513	204	1421	126.72	6	21.12	24700000	1.305875606
16x16A01	CE16	0.3820	0.0250	0.19725	236	1430	161	10	16.1	10400000	1.270423729

Table 2.9.1 FUEL ASSEMBLY DIMENSIONAL DATA (continued)

Array ID	Array Name	Rod O.D. (in.)	Clad Thk. (in.)	R_{mean} (in.)	# of Rods	Assy Wt. (lb)	Rod Length (in.)	# of Spans	Average Span (in.)	Material Modulus	BETA
16x16A02	CE16	0.3820	0.0250	0.19725	236	1300	146.499	9	16.27767	10400000	1.367126598
17x17A01	W17OFA	0.3600	0.0225	0.18563	264	1373	151.635	7	21.66214	10400000	0.613275783
17x17A02	W17OFA	0.3600	0.0225	0.18563	264	1365	152.3	7	21.75714	10400000	0.611494853
17x17B01	W17STD	0.3740	0.0225	0.19263	264	1482	151.635	7	21.66214	10400000	0.634902014
17x17B02	W17P+	0.3740	0.0225	0.19263	264	1482	151.635	7	21.66214	10400000	0.634902014
17x17C01	BW17	0.3790	0.0240	0.19550	264	1505	152.688	7	21.81257	10400000	0.687604262
						BWR					
6x6A02	XX/ANF6	0.5645	0.0360	0.29125	36	328.4	116.65	4	29.1625	10400000	1.192294364
6x6C01	HB6	0.5630	0.0320	0.28950	36	270	83	3	20.75	10400000	2.500527046
7x7A01	HB7	0.4860	0.0330	0.25125	49	276	83.2	3	20.8	10400000	2.233705011
7x7B01	GE-7	0.5630	0.0320	0.28950	49	682.5	159	7	19.875	10400000	1.467601583
7x7B02	GE-7	0.5630	0.0370	0.29075	49	681	164	7	20.5	10400000	1.619330439
7x7B03	GE-7	0.5630	0.0370	0.29075	49	674.4	164	7	20.5	10400000	1.635177979
7x7B04	GE-7	0.5700	0.0355	0.29388	49	600	161.1	7	20.1375	10400000	1.887049713
7x7B05	GE-7	0.5630	0.0340	0.29000	49	600	161.1	7	20.1375	10400000	1.736760659
8x8B03	GE-8	0.4930	0.0340	0.25500	63	681	164	7	20.5	10400000	1.2906798
8x8C02	GE-8R	0.4830	0.0320	0.24950	62	600	159	7	19.875	10400000	1.352138354
8x8C03	GE-8R	0.4830	0.0320	0.24950	62	600	163.71	7	20.46375	10400000	1.27545448
9x9D01	XX/ANF9	0.4240	0.0300	0.21950	79	575.3	163.84	8	18.20444	10400000	1.367212516
10x10E01	XX10SS	0.3940	0.0220	0.20250	96	376.6	89.98	4	17.996	24700000	3.551678654

Array ID, Rod OD, Clad Thk and # of Rods from Tables 6.2.1 and 6.2.2.

Rmean, Average Span and THETA are Calculated.

Zircaloy Modulus from LLNL Report [2.9.1].

Stainless Steel (348H) Modulus from ASME Code, Section III, Part D.

Table 2.9.1 FUEL ASSEMBLY DIMENSIONAL DATA (continued)

PWR Assy. Wt., Rod Len. and # of Spans (exc. as noted below) from DOE/RW-0184, Vol. 3, UC-70, -71 and -85, Dec. 1987.
Assy. Wt., Rod Len. and # of Spans for 15x15B03, 15x15B04, 15x15C01 and 15x15C02 from ORNL/TM-9591/V1-R1.
BWR Assy. Wt., Rod Len. and # of Spans (exc. as noted below) from ORNL/TM-10902.
Assy. Wt., Rod Len. and # of Spans for 6x6A02, 9x9D01 and 10x10E01 from DOE/RW-0184, Vol. 3, UC-70, -71 and -85, Dec. 1987.
Assy. Wt., Rod Len. and # of Spans for 7x7B04 and 7x7B05 from ORNL/TM-9591/V1-R1.
Assy. Wt. for 8x8C02 and 8x8C03 from ORNL/TM-9591/V1-R1.

In the following, a physical description of the structural instability problem is provided with the aid of Figures 2.9.1 to 2.9.9. A stored fuel assembly consists of a square grid of fuel rods. Each fuel rod consists of a thin-walled cylinder surrounding and containing the fuel pellets. The majority of the total weight of a fuel rod is in the fuel pellets; however, the entire structural resistance of the fuel rod to lateral and longitudinal loads is provided by the cladding. Hereinafter, the use of the words "fuel rod", "fuel rod cladding", or just "cladding" means the structural thin cylinder. The weight of the fuel pellets is conservatively assumed to be attached to the cladding for all discussions and evaluations.

Figure 2.9.1 shows a typical fuel rod in a fuel assembly. Also shown in Figure 2.9.1 are the grid straps and the surrounding walls of the spent fuel basket cell walls. The grid straps serve to maintain the fuel rods in a square array at a certain number of locations along the length of the fuel assembly. When the fuel rod is subject to a loading causing a lateral deformation, the grid strap locations are the first locations along the length of the rod where contact with the fuel basket cell walls occurs. The fuel basket cell walls are assumed to be rigid surfaces. The fuel rod is assumed to be subjected to some axial load and has some slightly initially deformed shape. For the purposes of the analysis, it is assumed that displacement under load occurs in a 2-D plane and that the ends of the fuel rod cladding have a specified boundary condition to restrain lateral deflection. The ends of the fuel rod cladding are assumed to be simply supported and the grid straps along the length of the fuel assembly are assumed to have gap "g_1" relative to the cell walls of the fuel basket. The figure shows a typical fuel rod in the assembly that is located by gaps "g_2" and "g_3" with respect to the fuel basket walls. Because the individual fuel rod is long and slender and is not perfectly straight, it will deform under a small axial load into the position shown in Figure 2.9.2. The actual axial load is due to the distributed weight subject to a deceleration from a hypothetical accident of transport. For the purposes of this discussion, it is assumed that some equivalent axial load is applied to one end of the fuel rod cladding. Because of the distributed weight and the fact that a deceleration load is not likely to be exactly axially oriented, the predominately axial load will induce a lateral displacement of the fuel rod cladding between the two end supports. The displacement will not be symmetric but will be larger toward the end of the cladding where support against the axial deceleration is provided. Depending on the number of grid straps, either one or two grid straps will initially make contact with the fuel basket cell wall and the contact will not be exactly centered along the length of the cell. Figure 2.9.3 illustrates the position of the fuel rod after the axial load has increased beyond the value when initial contact occurred and additional grid straps are now in contact with the cell wall. The maximum stress in the fuel rod will occur at the location of maximum curvature and will be a function of the bending moment ($F_2 \times (g_2 - g_1)$).

At some load $F_3 > F_2$, either the limiting stress in the fuel rod cladding is achieved or the rod begins to experience large lateral movements between grid plates because of the coupling between axial and lateral load and deformation. Figure 2.9.4 shows the deformation mode experienced by the fuel rod cladding caused by the onset of an instability between two grid straps that are in contact with the fuel basket cell wall.

Once the lateral displacement initiates, the rod displaces until contact with the cell wall occurs at the mid point "A" (see Figure 2.9.5) or the cladding stress exceeds the cladding material yield strength.

Depending on the particular location of the fuel rod in the fuel assembly, the highest stressed portion of the fuel rod will occur in the segment with the larger of the two gaps "g_2" and "g_3". For the discussion to follow, assume that $g_2 > g_3$. The boundary condition at the grid strap is conservatively assumed as simply-supported so that the analysis need not consider what happens in adjacent spans between grid straps. At this point in the loading process, the maximum bending moment occurs at the contact point and has the value $F_4 \times (g_2-g_1)$. Figure 2.9.5 shows the displaced configuration at the load level where initial contact occurs with the fuel cell wall. If the maximum fuel rod stress (from the bending moment and from the axial load) equals the yield stress of the fuel rod cladding, it is assumed that $F_3 = F_4$ is the maximum axial load that can be supported. The maximum stress in the fuel rod cladding occurs at point "A" in Figure 2.9.5 since that location has the maximum bending moment. If the cladding stress is still below yield, additional load can be supported. As the load is further increased, the bending moment is decreased and replaced by reaction loads, "V", at the grid strap and the contact point. These reaction loads V are shown in Figure 2.9.7 and are normal to the cell wall surface. Figure 2.9.6 shows the configuration after the load has been further increased from the value at initial contact. There are two distinct regions that need to be considered subsequent to initial contact with the fuel basket cell wall. During the additional loading phase, the point "A" becomes two "traveling" points, A, and A'. Since the bending moment at A' and A is zero, the moment $F_5 \times (g_2-g_1)$ is balanced by forces V at the grid strap and at point A or A'. This is shown in Figure 2.9.7 where the unsupported length current "a" is shown with the balancing load. At this point in the process, two "failure" modes are possible for the fuel rod cladding.

The axial load that develops in the unsupported region between the grid strap and point A' causes increased deformation and stress in that segment, or,

The straight region of the rod, between A and A', begins to experience a lateral deformation away from the cell wall.

Note that in this latter scenario, the slope at A or A' remains zero so this should never govern unless the flat region becomes large. The final limiting load occurs when the maximum stress in either portion of the rod exceeds the yield stress of the tube. In what follows, the most limiting fuel assembly from the array of fuel types considered is subject to detailed analysis and the limiting load established. This limit axial load is considered as the product of the fuel rod weight times the deceleration. Therefore, establishing the limiting load to reach cladding material yield establishes the limiting axial deceleration that can be imposed.

The preceding discussion has assumed end conditions of simple support for conservatism. The location of the fuel rod determines the actual free gap between grid straps. For example, a fuel rod furthest from the cell wall that resists lateral movement of the assembly moves to close up all of the clearances that exist between it and the resisting cell wall. The clearance between rods is the rod pitch minus the rod diameter. In a 14 x 14 assembly, there are 13 clearance gaps plus an additional clearance g_3 between the nearest rod and the cell wall. Therefore, the gap g_2 is given as

$$g_2 = 13(\text{pitch-diameter}) + g_3$$

Figure 2.9.9 provides an illustration of the fuel rod deformation for a case of 5 fuel rods in a column. Clearly for this case, the available lateral movement can be considerable for the "furthest" fuel rod. On the other hand, for this fuel rod, there will be considerable moment resistance at the grid strap from the adjacent section of the fuel rod. The situation is different when the rod being analyzed is assumed to be the closest to the cell wall. In this case, the clearance gap is much smaller, but the moment resistance provided by adjacent sections of the rod is reduced. For calculation purposes, we assume that a moment resistance is provided as M = f x K for the fuel rod under analysis where

K = 3EI/L , L= span between grid straps, and "f" is an assumed fraction of K

The preceding result for the rotational spring constant assumes a simple support at each end of the span with an end moment "M" applied. Classical strength of materials gives the result for the spring constant. The arbitrary assumption of a constant reduction in the spring constant is to account for undetermined interactions between axial force in the rod and the calculated spring constant. As the compressive force in the adjacent members increases, the spring constant will be reduced. On the other hand, as the adjacent span contacts its near cell wall, the spring constant increases. On balance, it should be conservative to assume a considerable reduction in the spring constant available to the span being analyzed in detail. As a further conservatism, the angle defined by the geometry is used without including any additional elastic displacement shape. This will further reduce the value of the resisting moment at any stage of the solution. In the detailed calculations, two limiting cases are examined. To limit the analysis to a single rod, it is assumed that after "stack-up" of the rods (see Figure 2.9.9), the lateral support provided by the cell wall supports all of the rods. That is, the rods are considered to have non-deforming cross-section.

Numerical Analysis - Based on the tabular results in Table 2.9.1, the fuel assembly with the smallest value for the deceleration based on the classical Euler buckling formula is analyzed in detail. The following input data is specified for the limiting 14 x 14 assembly [2.9.2]:

Inside dimension of a HI-STAR 100 fuel basket cell
$s := 8.75 \cdot in$

Outside envelope dimension of grid plate
$gp := 7.763 \cdot in$

Outer diameter of fuel rod cladding
$D := .4 \cdot in$

Wall thickness of cladding
$t := .0243 \cdot in$

Weight of fuel assembly (including end fittings)
$W := 1177 \cdot lbf$

Number of fuel rods + guide/instrument
tubes in a column or row

$n := 14$

Overall length of fuel rod between assumed end support

$L_t := 151 \cdot in$

Length of fuel rod between grid straps

$L_s := 25.3 \cdot in$

Average clearance to cell wall at a grid strap location
assuming a straight and centered fuel assembly

$g_1 := .5 \cdot (s - gp)$

$g_1 = 0.494\,in$

Rod pitch

$pitch := 0.556 \cdot in$

$Clearance := (n - 1) \cdot (pitch - D)$

$Clearance = 2.028\,in$

Minimum available clearance for lateral movement of a fuel
rod between grid straps

$g_3 := g_1 + .5 \cdot [gp - (n \cdot D + Clearance)]$

$g_3 = 0.561\,in$

Maximum available clearances for lateral movement of a
fuel rod between grid straps

$g_2 := g_3 + Clearance$

$g_2 = 2.589\,in$

Young's Modulus of Zircalloy [2.9.1]

$E := 10400000 \cdot psi$

Dynamic Yield Strength of Zircalloy [2.9.1]

$\sigma_y := 80500 \cdot psi$

Geometry Calculations:

Compute the metal cross section area A, the metal area moment of inertia I, and the total weight of a single fuel rod (conservatively assume that end fittings are only supported by fuel rods in the loading scenario of interest).

$$A := \frac{\pi}{4}\cdot\left[D^2 - (D - 2\cdot t)^2\right]$$

$$I := \frac{\pi}{64}\cdot\left[D^4 - (D - 2\cdot t)^4\right]$$

$$A = 0.029\,in^2$$

$$I = 5.082\times 10^{-4}\,in^4$$

$$W_r := \frac{W}{n^2}$$

$$W_r = 6.005\,lbf$$

As an initial lower bound calculation, assume no rotational support from adjacent spans and define a multiplying factor

$f := 0.0$

Compute the rotational spring constant available from adjacent sections of the rod.

$$K := 3\cdot E\cdot\frac{I}{L_s}\cdot f$$

$$K = 0\,lbf\cdot in$$

Now compute the limiting load, if applied at one end of the fuel rod cladding, which causes an overall elastic instability and contact with the cell wall. Assume buckling in a symmetric mode for a conservatively low result. The purpose of this calculation is solely to demonstrate the flexibility of the single fuel rod. No resisting moment capacity is assumed to be present at the fittings.

$$P_0 := \pi^2\cdot E\cdot\frac{I}{L_t^2}$$

$$P_0 = 2.288\,lbf$$

Note that this is less than the weight of the rod itself. This demonstrates that in the absence of any additional axial support, the fuel rod will bow and be supported by the cell walls under a very small axial load. In reality, however, there is additional axial support that would increase this initial buckling load. The stress induced in the rod by this overall deflected shape is small.

$$Stress_1 := \frac{P_0 \cdot g_1 \cdot D}{2 \cdot I}$$

$Stress_1 = 444.32\,psi$

$$Stress_d := \frac{P_0}{A}$$

$Stress_d = 79.76\,psi$

The conclusion of this initial calculation is that grid straps come in contact; consideration of what happens between a grid strap is the only region that requires further investigation. First calculate the classical Euler buckling load based on a pin-ended rod and assume conservatively that the entire weight of the rod is providing the axial driving force. This gives a conservatively low estimate of the limiting deceleration that can be resisted before a perfectly straight rod buckles.

$$a_{lim1} := \pi^2 \cdot E \cdot \frac{I}{L_s^2 \cdot W_r}$$

$a_{lim1} = 13.57$

The rigid body angle of rotation at the grid strap under this load that causes contact is:

$$\theta_1 := \text{atan}\left[2 \cdot \frac{(g_2 - g_1)}{L_s}\right]$$

$\theta_1 = 9.406\,deg$

Conservatively assume resisting moment at the grid is proportional to this "rigid body" angle:

$M_r := K \cdot \theta_1$

$M_r = 0\,in{\cdot}lbf$

(in this first analysis, no resisting moment is assumed)

The total stress at the grid strap due to the axial force and the resisting moment is

$$\sigma_{gs} := \frac{W_r \cdot a_{lim1}}{A} + \frac{M_r \cdot D}{2 \cdot I}$$

$\sigma_{gs} = 2841.172\,psi$

The total stress at the contact location is

$$Stress_2 := \frac{\left[W_r \cdot a_{lim1} \cdot (g_2 - g_1) - M_r\right] \cdot D}{2 \cdot I}$$

$Stress_2 = 6.721 \times 10^4\,psi$

$$Stress_{2d} := \frac{W_r \cdot a_{lim1}}{A}$$

$$Stress_{2d} = 2841.172\,psi$$

$$Stress_{2t} := Stress_2 + Stress_{2d}$$

$$Stress_{2t} = 7.005 \times 10^4\,psi$$

This is the maximum value of the stress at this location since, for further increase in axial load, the moment will decrease with consequent large decrease in the total stress.

The safety factor is

$$\frac{\sigma_y}{Stress_{2t}} = 1.149$$

The axial load in the unsupported portion of the beam at this instant is

$$P_{ax} := \frac{(W_r \cdot a_{lim1})}{\cos(\theta_1)}$$

$$P_{ax} = 82.599\,lbf$$

At this point in the load process, a certain axial load exists in the unsupported span on either side of the contact point. However, since the unsupported span is approximately 50% of the original span, the allowable deceleration limit is larger. As the axial load is incrementally increased, the moment at the contact point is reduced to zero with consequent increases in the lateral force V at the grid strap and at the contact points A and A'. Figure 2.9.8 provides the necessary information to determine the elastic deformation that occurs in the unsupported span as the axial load increases and the contact points separate (and, therefore, decreasing the free span).

From geometry, coupled with the assumption that the deflected shape is a half "sin" function with peak value δ, the following relations are developed:

Assume "a" is a fraction of 50% of the span (the following calculations show only the final iterated assumption for the fraction

$$\varepsilon := .9$$

$$a := \varepsilon \cdot \left(\frac{L_s}{2}\right)$$

$$a = 11.385\,in$$

Calculate "b" in Figure 2.9.8

$$b := \left[(a)^2 + (g_2 - g_1)^2 \right]^{.5}$$

$b = 11.576\,in$

An equation for δ can be developed from the geometric relation

$$\frac{(g_2 - g_1)}{a} := \frac{b}{2(R - \delta)}$$

(please note that the above equation is imported from the electronic spreadsheet program MathCad. The solid rectangle appearing after the equation is a MathCad symbol designating that no computations are performed on that line)

The inverse of the radius of curvature, R, at the point of peak elastic deflection of the free span, is computed as the second derivative of the assumed sin wave deflection shape. Based on the geometry in Figure 2.9.8, the peak deflection is:

$$\delta := .5 \cdot \left[\left[a \cdot \frac{b}{2 \cdot (g_2 - g_1)} \right]^2 + 4 \cdot \left(\frac{b}{\pi} \right)^2 \right]^{.5} - a \cdot \frac{b}{4 \cdot (g_2 - g_1)}$$

$\delta = 0.426\,in$

For the assumed "a", the limiting axial load capacity in the unsupported region is conservatively estimated as:

$$a_{lim2} := \pi^2 \cdot E \cdot \frac{I}{(b)^2 \cdot W_r}$$

$a_{lim2} = 64.816$

The corresponding rigid body angle is:

$$\theta_2 := \operatorname{atan}\left[1 \cdot \frac{(g_2 - g_1)}{a} \right]$$

$\theta_2 = 10.429\,deg$

The axial load in the unsupported portion of the beam at this instant is

$$P_{ax} := \frac{(W_r \cdot a_{lim2})}{\cos(\theta_2)}$$

$P_{ax} = 395.763\,lbf$

The resisting moment is

$M_r := K \cdot \theta_2$

$M_r = 0\,in{\cdot}lbf$

The total stress in the middle of the unsupported section of free span "b" is

$$stress_3 := \frac{\left(P_{ax} \cdot \delta - M_r\right) \cdot D}{2 \cdot I}$$

$stress_3 = 6.635 \times 10^4\,psi$

$$stress_{3d} := \frac{P_{ax}}{A}$$

$stress_{3d} = 1.38 \times 10^4\,psi$

$stress_{3t} := stress_3 + stress_{3d}$

$stress_{3t} = 8.015 \times 10^4\,psi$

The safety factor is

$$\frac{\sigma_y}{stress_{3t}} = 1.004$$

The total stress at the grid strap due to the axial force and the resisting moment is

$$\sigma_{gs} := \frac{W_r \cdot a_{lim2}}{A} + \frac{M_r \cdot D}{2 \cdot I}$$

$\sigma_{gs} = 1.357 \times 10^4\,psi$

The safety factor is

$$\frac{\sigma_y}{\sigma_{gs}} = 5.932$$

For this set of assumptions, the stress capacity of the rod cladding has been achieved, so that the limiting deceleration is:

$A_{limit} := a_{lim2}$

$A_{limit} = 64.816$

This exceeds the design basis for the HI-STAR 100 package.

If there is any restraining moment from the adjacent span, there is a possibility of exceeding the rod structural limits at that location due to the induced stress. Therefore, the above calculations are repeated for an assumed moment capacity at the grid strap.

$f := 1.$

$$K := 3 \cdot E \cdot \frac{I}{L_s} \cdot f$$

The rigid body angle of rotation at the grid strap under this load that causes contact is:

$$\theta_1 := \operatorname{atan}\left[2 \cdot \frac{(g_2 - g_1)}{L_s} \right]$$

$\theta_1 = 9.406\,\text{deg}$

Conservatively assume resisting moment at the grid is a function of this angle,

$M_r := K \cdot \theta_1$

$M_r = 102.875\,\text{in·lbf}$

The total stress at the grid strap due to the axial force and the resisting moment is

$$\sigma_{gs} := \frac{W_r \cdot a_{lim1}}{A} + \frac{M_r \cdot D}{2 \cdot I}$$

$\sigma_{gs} = 4.333 \times 10^4\,\text{psi}$

The total stress at the contact location is

$$\text{Stress}_2 := \frac{\left[W_r \cdot a_{lim1} \cdot (g_2 - g_1) - M_r\right] \cdot D}{2 \cdot I}$$

$\text{Stress}_2 = 2.672 \times 10^4\,\text{psi}$

$$\text{Stress}_{2d} := \frac{W_r \cdot a_{lim1}}{A}$$

$\text{Stress}_{2d} = 2841.172\,\text{psi}$

$\text{Stress}_{2t} := \text{Stress}_2 + \text{Stress}_{2d}$

$\text{Stress}_{2t} = 2.956 \times 10^4\,\text{psi}$

This is the maximum value of the stress at this location since, for further increase in axial load, the moment will decrease with consequent large decrease in the total stress.

The axial load in the unsupported portion of the beam at this instant is

$$P_{ax} := \frac{(W_r \cdot a_{lim1})}{\cos(\theta_1)}$$

$P_{ax} = 82.599\,\text{lbf}$

At this point in the load process, a certain axial load exists in the unsupported span on either side of the contact point. However, since the unsupported span is approximately 50% of the original span, the allowable deceleration limit is larger. As the axial load is incrementally increased, the moment at the contact point is reduced to zero with consequent increases in the lateral force V at the grid strap and at the contact points A and A'. Figure 2.9.8 provides the necessary information to determine the elastic deformation that occurs in the unsupported span as the axial load increases and the contact points separate (and, therefore, decreasing the free span).

From geometry, coupled with the assumption that the deflected shape is a half "sine" function with peak value "δ", the following relations are developed:

Assume "a" is a fraction of 50% of the span (the following calculations show only the final iterated assumption for the fraction

$\varepsilon := .7$

$$a := \varepsilon \cdot \left(\frac{L_s}{2}\right)$$

$a = 8.855\,\text{in}$

Calculate "b" in Figure 2.9.8

$$b := \left[(a)^2 + (g_2 - g_1)^2\right]^{.5}$$

$b = 9.1\,\text{in}$

The inverse of the radius of curvature, R, at the point of peak elastic deflection of the free span, is computed as the second derivative of the assumed sin wave deflection shape. Based on the geometry in Figure 2.9.8, the peak deflection is:

$$\delta := .5 \cdot \left[\left[a \cdot \frac{b}{2 \cdot (g_2 - g_1)}\right]^2 + 4 \cdot \left(\frac{b}{\pi}\right)^2\right]^{.5} - a \cdot \frac{b}{4 \cdot (g_2 - g_1)}$$

$\delta = 0.427\,\text{in}$

For the assumed "a", the limiting axial load capacity in the unsupported region is conservatively estimated as:

$$a_{lim2} := \pi^2 \cdot E \cdot \frac{I}{(b)^2 \cdot W_r}$$

$$a_{lim2} = 104.9$$

The corresponding rigid body angle is:

$$\theta_2 := \operatorname{atan}\left[1 \cdot \frac{(g_2 - g_1)}{a}\right]$$

$$\theta_2 = 13.314\,\text{deg}$$

The axial load in the unsupported portion of the beam at this instant is

$$P_{ax} := \frac{(W_r \cdot a_{lim2})}{\cos(\theta_2)}$$

$$P_{ax} = 647.331\,\text{lbf}$$

The resisting moment is

$$M_r := K \cdot \theta_2$$

$$M_r = 145.619\,\text{in·lbf}$$

The total stress in the middle of the unsupported section of free span "b" is

$$\text{stress}_3 := \frac{(P_{ax} \cdot \delta - M_r) \cdot D}{2 \cdot I}$$

$$\text{stress}_3 = 5.145 \times 10^4\,\text{psi}$$

$$\text{stress}_{3d} := \frac{P_{ax}}{A}$$

$$\text{stress}_{3d} = 2.257 \times 10^4\,\text{psi}$$

$$\text{stress}_{3t} := \text{stress}_3 + \text{stress}_{3d}$$

$$\text{stress}_{3t} = 7.402 \times 10^4\,\text{psi}$$

The safety factor is

$$\frac{\sigma_y}{\text{stress}_{3t}} = 1.088$$

The total stress at the grid strap due to the axial force and the resisting moment is

$$\sigma_{gs} := \frac{W_r \cdot a_{lim2}}{A} + \frac{M_r \cdot D}{2 \cdot I}$$

$$\sigma_{gs} = 7.928 \times 10^4 \text{ psi}$$

The safety factor is

$$\frac{\sigma_y}{\sigma_{gs}} = 1.015$$

For this set of assumptions, the stress capacity of the rod cladding has been achieved, so that the limit deceleration is:

$A_{limit} := a_{lim2}$

$A_{limit} = 104.9$

Conclusions

An analysis has demonstrated that for the most limiting PWR fuel assembly stored in the HI-STAR 100 fuel basket, a conservative lower bound limit on acceptable axial decelerations exceeds the 60g design basis of the cask. For a reasonable assumption of moment resisting capacity at the grid straps, the axial deceleration limit exceeds the design basis by a large margin.

It is concluded that fuel rod integrity is maintained in the event of a hypothetical accident condition leading to a 60g design basis deceleration in the direction normal to the target.

FUEL ROD DEFORMATION PHASES

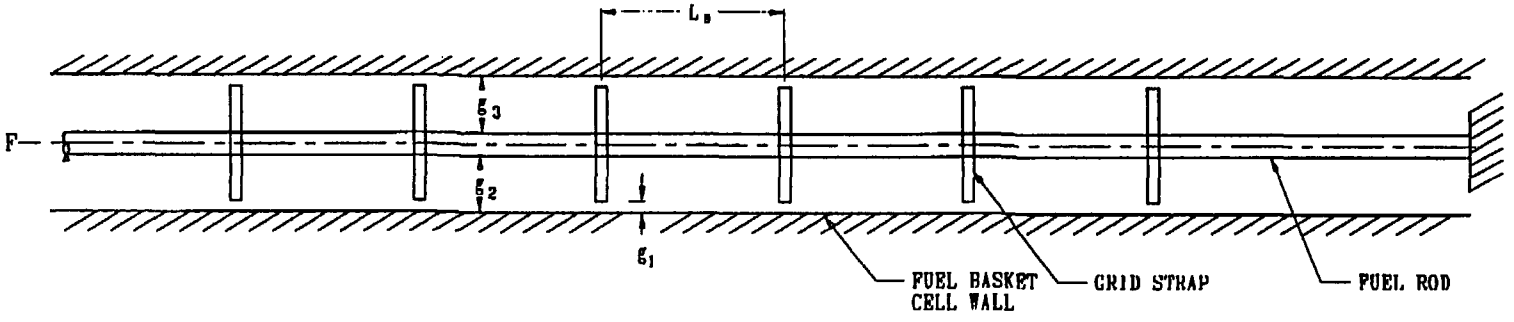

FIGURE 2.9.1: $g_1 > 0$

FUEL ROD DEFORMATION PHASES

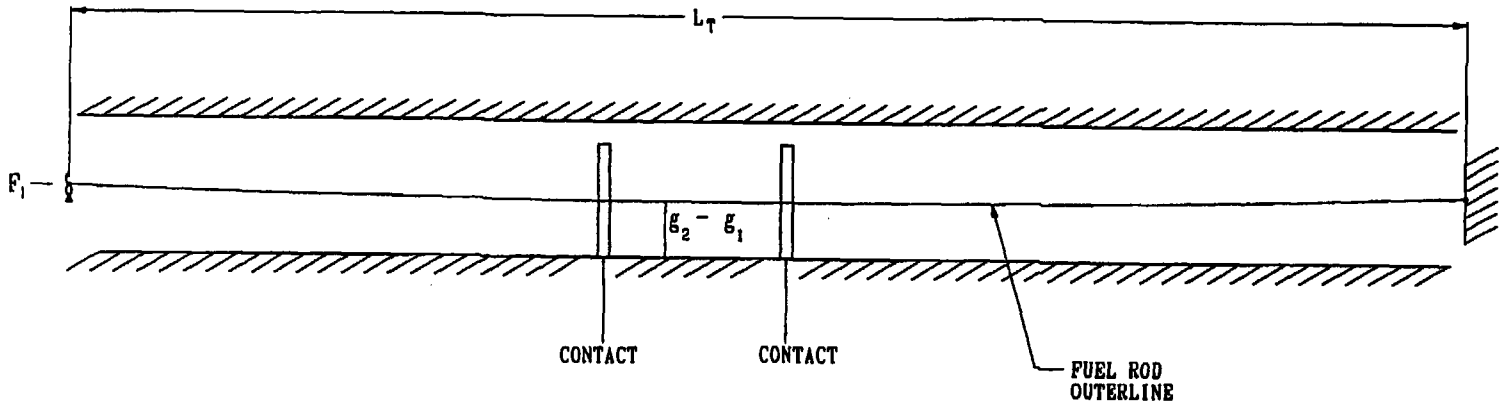

FIGURE 2.9.2; $g_1 = 0$

FUEL ROD DEFORMATION PHASES

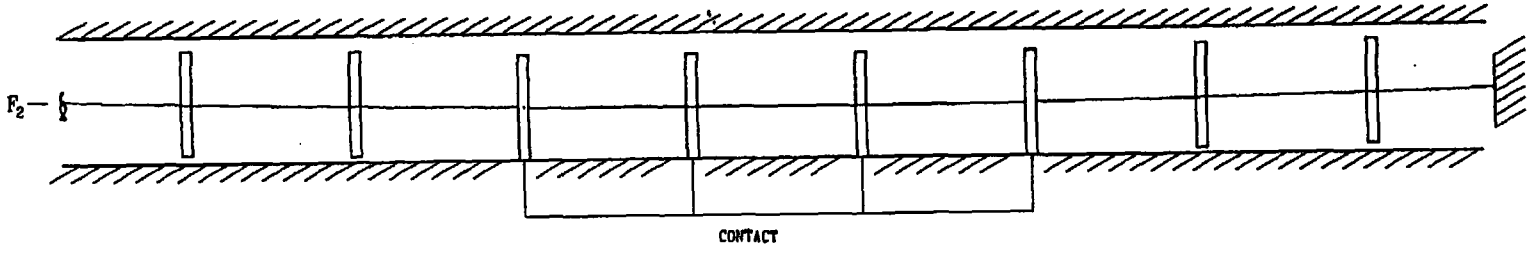

FIGURE 2.9.3; $g_1 = 0$, $F_2 > F_1$

FUEL ROD DEFORMATION PHASES

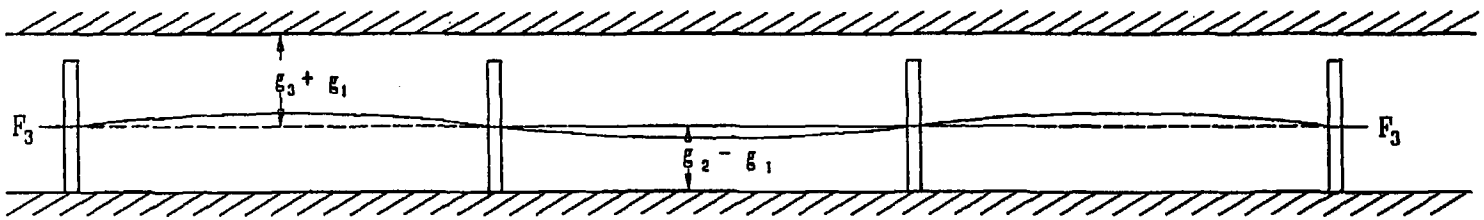

FIGURE 2.9.4; INTER-GRID STRAP DEFORMATION $F_3 > F_2$

FUEL ROD DEFORMATION PHASES

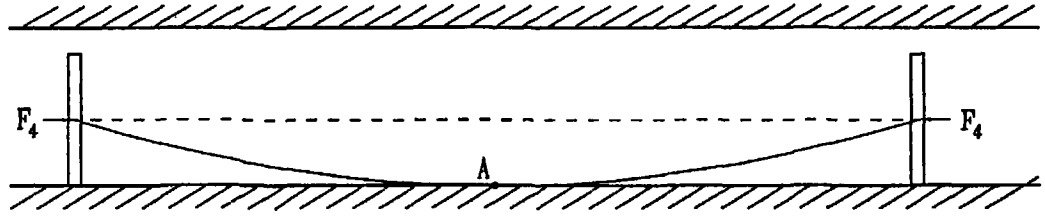

FIGURE 2.9.5; POINT CONTACT AT LOAD F_4
MAXIMUM BENDING MOMENT AT A

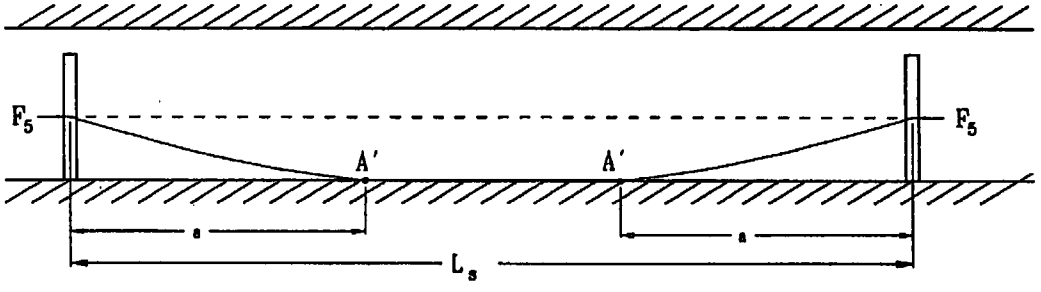

FIGURE 2.9.6; EXTENDED REGION OF CONTACT
$F_5 > F_4$, ZERO BENDING MOMENT AT A'

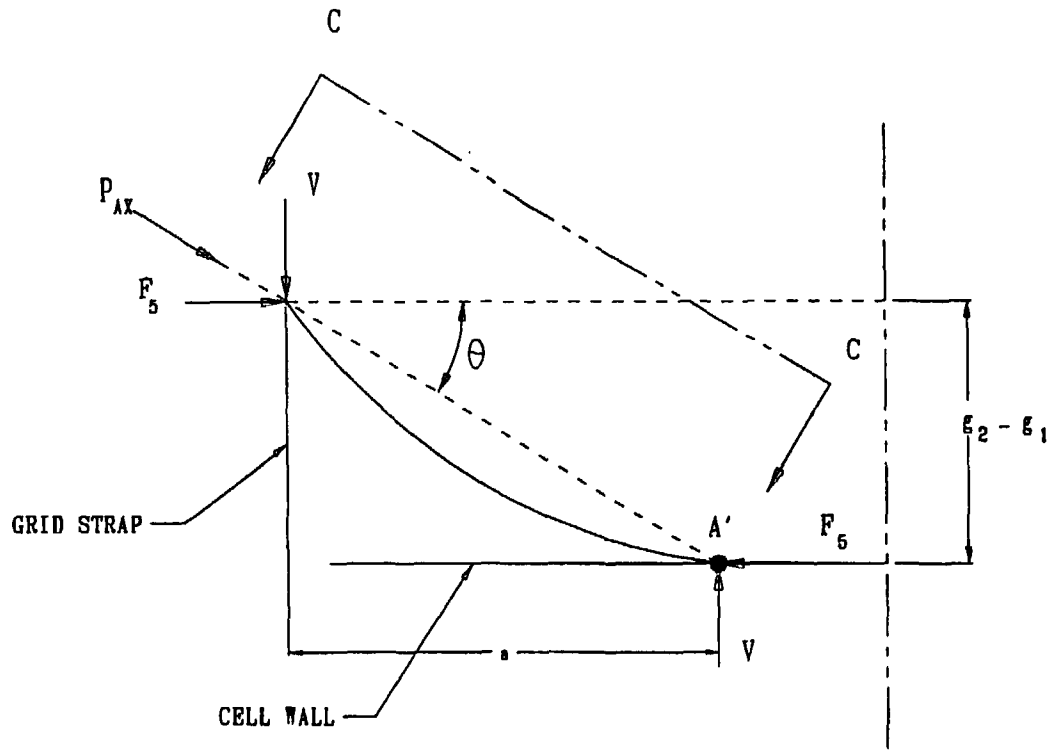

FIGURE 2.9.7; FREE BODY DIAGRAM WHEN MOMENT AT A' = 0
$P_{AX} = F_5/\cos(\theta)$. RESISTING MOMENT M_R
AT GRID STRAP NOT SHOWN

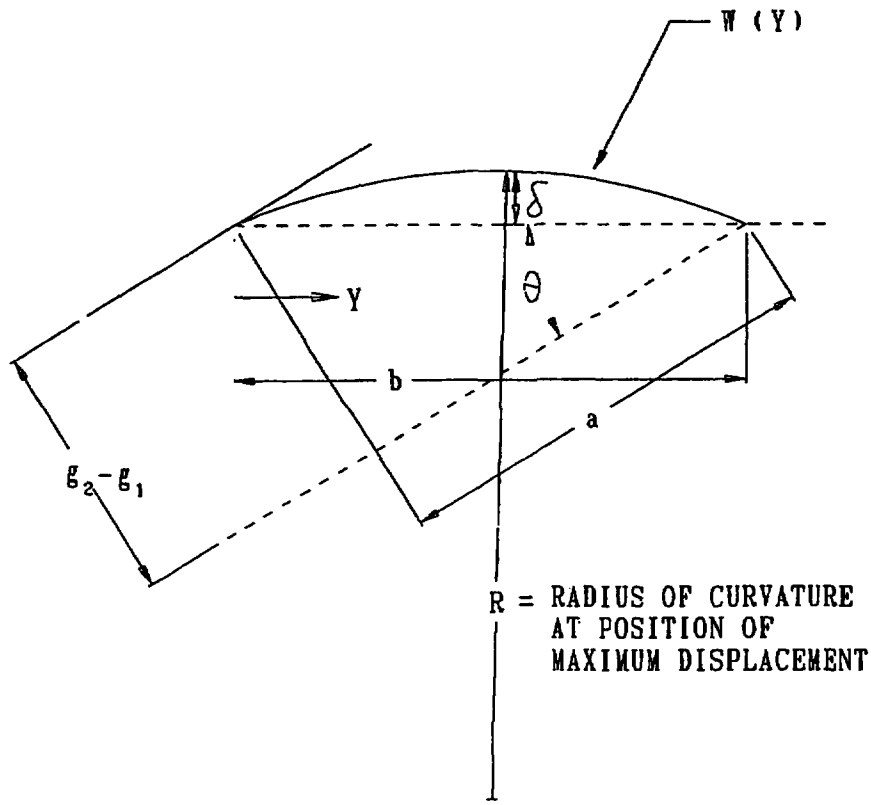

$$Z = R - \delta$$

$$W(Y) = \delta \sin(\pi Y/b)$$

FIGURE 2.9.8; VIEW C - C

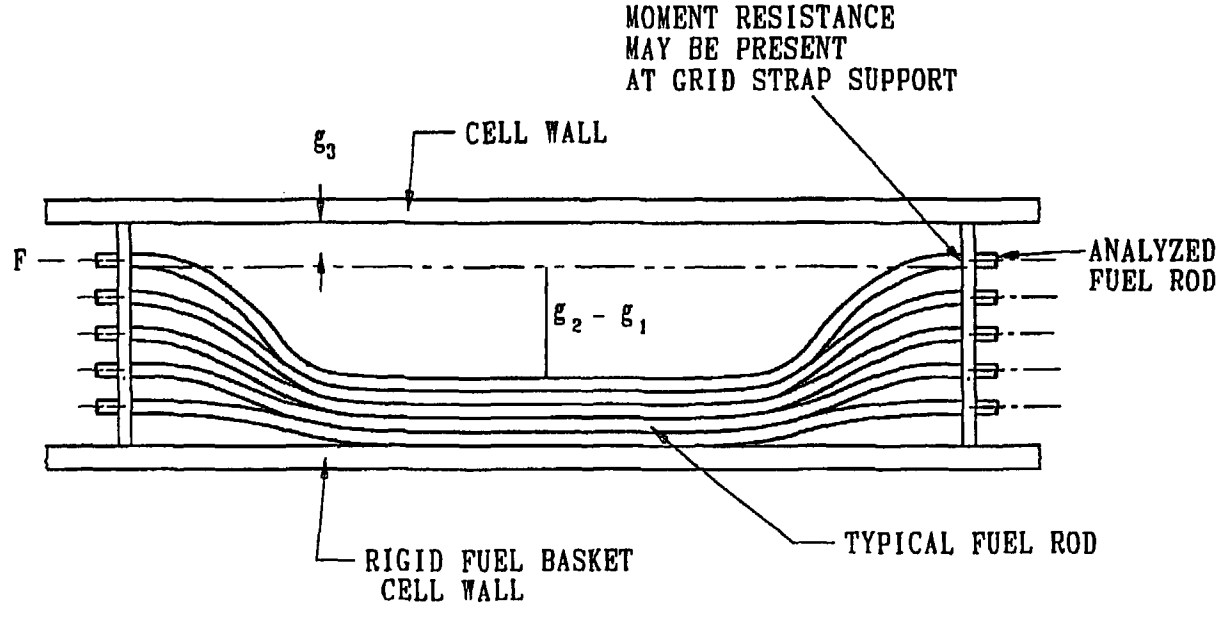

FIGURE 2.9.9; EXAGGERATED DETAIL SHOWING MULTIPLE FUEL RODS SUBJECT TO LATERAL DEFLECTION WITH FINAL STACKING OF ROD COLUMN

2.10 MISCELLANEOUS ITEMS

2.10.1 Appendices

The following appendices are included as supplementary material for Chapter 2 of the SAR.

APPENDIX 2.A: IMPACT LIMITER CHARACTERISTICS, DYNAMIC SIMULATION OF HYPOTHETICAL ACCIDENT EVENT, AND SCALE MODEL TESTS

(This appendix was 2.H in previous SAR revisions; it has been renumbered reflecting the removal of other appendices from the SAR)

APPENDIX 2.B: SUMMARY OF RESULTS FOR STRUCTURAL INTEGRITY OF DAMAGED FUEL CANISTERS

ALL OTHER APPENDICES (2.C through 2.AO) - DELETED

2.10.2 Summary of NUREG -1617/10CFR71 Compliance

This subsection provides a "road map" of technical information to demonstrate that the SAR in compliance with the provisions of NUREG-1617 and associated referenced sections of 10CFR71 necessary to certify the HI-STAR 100 package for transport.

Description of Structural Design

The package structural design description and the contents of the application meet the requirements of 10CFR 71.31 and Regulatory Guide 7.9. Applicable sections where this is demonstrated are 1.2.1; 1.3; 1.4; and 2.1.

The codes and standards used in the package design are listed in 1.3. The use of the ASME Boiler and Pressure Vessel Code is in compliance with NUREG/CR-6407, "Classification of Transportation Packaging and Dry Spent Fuel Storage Components".

Material Properties

There are no significant chemical, galvanic or other reactions among the packaging components, among package contents, or between the packaging components and the contents in dry or wet environment conditions. The applicable subsection where this is demonstrated is 2.4.4.

The effects of radiation on materials are considered and package containment is constructed from materials that meet the requirements of Reg. Guides 7.11 and 7.12. Applicable subsections where this is demonstrated are: 1.2.1; 2.1.2; and, 2.4.4.

Lifting and Tie-Down Standards for All Packages

Lifting and Tie-Down systems meet 10CFR 71.45 standards. The applicable section where this is demonstrated is 2.5.

General Considerations for Structural Evaluation of Packaging

The packaging structural evaluation meets the requirements of 10CFR 71.35. Applicable chapters and/or sections where this is demonstrated are: 2.5; 2.6; 2.7

Normal Conditions of Transport

The packaging structural performance under normal conditions of transport demonstrate that there will be no substantial reduction in the effectiveness of the packaging. The applicable section where this is demonstrated is 2.6.

Hypothetical Accident Conditions

The packaging structural performance under the hypothetical accident conditions demonstrates that the packaging has adequate structural integrity to satisfy the subcriticality, containment, shielding, and temperature requirements of 10CFR Part 71. The applicable section where this is demonstrated is 2.7.

Special Requirement for Irradiated Nuclear Fuel Shipments

The containment structure meets the 10CFR 71.61 requirements for irradiated nuclear fuel shipments. The applicable section where this is demonstrated is 2.7.

Internal Pressure Test

The containment structure meets the 10CFR 71.85(b) requirements for pressure test without yielding. The applicable subsection where this is demonstrated is 2.6.1.4.3.

2.11 REFERENCES

[2.1.1] 10CFR Part 71, "Packaging and Transportation of Radioactive Materials", Title 10 of the Code of Federal Regulations, Office of the Federal Register, Washington, D.C.

[2.1.2] Regulatory Guide 7.8, "Load Combinations for the Structural Analysis of Shipping Casks for Radioactive Material", Revision 1, March, 1989, U.S. Nuclear Regulatory Commission.

[2.1.3] 10CFR Part 72, "Licensing Requirements for the Storage of Spent Fuel in an Independent Spent Fuel Storage Installation", Title 10 of the Code of Federal Regulations, Office of the Federal Register, Washington, D.C.

[2.1.4] Regulatory Guide 7.6, "Design Criteria for the Structural Analysis of Shipping Cask Containment Vessels", Revision 1, March, 1978, U.S. Nuclear Regulatory Commission.

[2.1.5] ASME Boiler & Pressure Vessel Code, Section III, Subsection NB, American Society of Mechanical Engineers, 1995.

[2.1.6] ASME Boiler & Pressure Vessel Code, Section III, Subsection NG, American Society of Mechanical Engineers, 1995.

[2.1.7] ASME Boiler & Pressure Vessel Code, Section III, Subsection NF, American Society of Mechanical Engineers, 1995.

[2.1.8] Code Case N-284, "Metal Containment Shell Buckling Design Methods", Section III, Division 1, Class MC, Approval Date 8/25/80.

[2.1.9] NUREG-0612, "Control of Heavy Loads at Nuclear Power Plants," United States Nuclear Regulatory Commission, July, 1980.

[2.1.10] ANSI N14.6-1993, "American National Standard for Special Lifting Devices for Shipping Containers Weighing 10,000 Pounds (4,500 kg) or More for Nuclear Materials," American National Standards Institute, Inc.

[2.1.11] ASME Boiler & Pressure Vessel Code, Section II, Part D, American Society of Mechanical Engineers, 1995.

[2.1.12] ASME Boiler & Pressure Vessel Code, Section III, Appendices, American Society of Mechanical Engineers, 1995.

[2.1.13] Regulatory Guide 7.11, "Fracture Toughness Criteria of Base Material for Ferritic Steel Shipping Cask Containment Vessels with a Maximum Wall Thickness of 4 Inches", United States Nuclear Regulatory Commission, June, 1991.

[2.1.14] Regulatory Guide 7.12, "Fracture Toughness Criteria of Base Material for Ferritic Steel Shipping Cask Containment Vessels with a Wall Thickness Greater Than 4 Inches But Not Exceeding 12 Inches", United States Regulatory Commission, June, 1991.

[2.1.15] NUREG/CR-1815, "Recommendations for Protecting Against Failure by Brittle Fracture in Ferritic Steel Shipping Containers Up to Four Inches Thick."

[2.1.16] Aerospace Structural Metals Handbook, Manson.

[2.1.17] ARMCO Product Data Bulletin S-22

[2.1.18] NUREG-1617 Standard Review Plan for Transportation Packages for Spent Nuclear Fuel (Draft Report, March 1998).

[2.3.1] Hexcel Corporation Publication TSB 120, "Mechanical Properties of Hexcel Honeycomb Materials".

[2.3.2] Test Report For Aluminum Honeycomb Static Compression Testing Under Different Temperatures, Holtec Proprietary Report HI-981979, June 1998.

[2.4.1] NRC Bulletin 96-04: Chemical, Galvanic or Other Reactions in Spent Fuel Storage and Transportation Casks, July 5, 1996.

[2.4.2] L.W. Ricketts, Fundamentals of Nuclear Hardening of Electronic Equipment, Robert E. Krieger Publishing Company, Malabar, FL, 1986.

[2.4.3] D.R. Olander, "Fundamental Aspects of Nuclear Reactor Fuel Elements," TID-26711-P1, 1976.

[2.6.1] Theory of Elastic Stability, S.P. Timoshenko and J. Gere, McGraw Hill.

[2.6.2] Mark's Standard Handbook for Mechanical Engineering, 9th ed.

[2.6.3] Mok, Fischer, and Hsu, "Stress Analysis of Closure Bolts for Shipping Casks" (NUREG/CR-6007-UCRL-ID-110637), Lawrence Livermore National Laboratory/Kaiser Engineering, 1993.

[2.6.4] ANSYS Finite Element Code, Version 5.2, ANSYS Inc., 1995.

[2.7.1] Shappert, L.B., "Cask Designer's Guide: A Guide for Design, Fabrication, and Operation of Shipping Casks for Nuclear Applications," ORNL-RSIC-68, Oak Ridge National Laboratories, Feb. 1970.

[2.7.2] American Society of Civil Engineers, Structural Analysis and Design of Nuclear Power Plants, ASCE No. 58.

[2.7.3] NUREG/CR-6322, "Buckling Analysis of Spent Fuel Basket", Lawrence Livermore National Laboratory, May, 1995.

[2.9.1] Chun, Witte, Schwartz, "Dynamic Impact Effects on Spent Fuel Assemblies", UCID-21246, Lawrence Livermore National Laboratory, October 20, 1987.

[2.9.2] Physical and Decay Characteristics of Commercial LWR Spent Fuel, Oak Ridge National Laboratory Report, J. Roddy, H. Claiborne, R. Ashline, P. Johnson, and B. Rhyne, ORNL/TM-9591/V1-R1, 1/86.

APPENDIX 2.A:
DESIGN, TESTING, AND COMPUTER SIMULATION OF THE AL-STAR™ IMPACT LIMITER

2.A.1 INTRODUCTION

As stated in Subsection 2.7, the central purpose of the AL-STAR™ impact limiter is to limit the package maximum deceleration, α_{max}, under a postulated drop event to a specified design value. For the regulatory 9-meter hypothetical free drop event, the AL-STAR design is engineered to limit the maximum rigid body deceleration to 60 times the acceleration due to gravity (Table 2.1.10). The HI-STAR packaging, consisting of the loaded overpack and top and bottom impact limiters (illustrated in Figure 2.A.1.1) is essentially a cylindrical body with a rigid interior (namely, the overpack) surrounded by a pair of relatively soft crushable structures. The crushable structure (impact limiter) must deform and absorb the kinetic energy of impact without detaching itself from the overpack, disintegrating, or otherwise malfunctioning. A falling cylindrical body may theoretically impact the target surface in an infinite number of orientations; the impact limiter must limit decelerations to below 60g's and preserve the limiter-to-overpack connection regardless of the impact orientation. Figure 2.A.1.2 presents the side drop event. In general, a drop event orientation is defined by the angle of the HI-STAR 100 longitudinal axis, θ, with the impact surface. In this notation, $\theta = 0$ means a side drop and $\theta = 90°$ implies a vertical or end drop scenario. Inasmuch as the top and bottom impact limiter are made of identical crush material, the top or bottom vertical drop events are mathematically and physically equivalent as far as the impact limiter design is concerned. In any orientation, the drop height is measured from the lowest point on the package.

An intermediate value of θ, $\theta = 67.5°$, warrants special mention. At $\theta = 67.5$ degrees, the point of impact is directly below the center of gravity (C.G.) of the HI-STAR 100 package. This drop orientation is traditionally called the C.G.-over-corner (CGOC) configuration. The CGOC orientation is the demarcation line between single and dual impact events. At $90° > \theta > 67.5°$, the leading end of the packaging (denoted as the "primary" impact limiter) is the sole participant in absorbing the incident kinetic energy. At $\theta < 67.5°$ drop orientations, the initial impact and crush of the leading (primary) impact limiter is followed by the downward rotation of the system with the initial impact surface acting as the pivot, culminating in the impact of the opposite (secondary) impact limiter on the target surface. In the dual impact scenarios, the first and second impact limiter crush events are referred to as the "primary" and "secondary" impacts, respectively. It is reasonable to speculate that for certain values of θ, the secondary impact may be the more severe of the two. As stated earlier, the design of AL-STAR must ensure that $\alpha_{max} \leq 60$, regardless of the value of θ.

The AL-STAR attachment design must ensure that both impact limiters remain attached to the cask during and after the impact event. The impact limiters are also required to prevent cask body-to-unyielding target contact.

Finally, the package design must satisfy all criteria in ambient temperature conditions ranging from -20° to 100°F, and with humidity ranging from 0 to 100%. Therefore, the impact limiter design must be functionally insensitive to temperature and environmental conditions.

An aluminum honeycomb-based impact limiter design was selected as the preferred material for development. The detailed design of the AL-STAR impact limiters is presented in Holtec Drawing 1765 located in Section 1.4. A pictorial view of AL-STAR is presented in Figure 2.A.1.3.

Figure 2.A.1.3 indicates that in addition to the crushable honeycomb, the AL-STAR contains two internal cylindrical shells (also denoted as "rings"), which are stiffened with radial gussets. These carbon steel shells are sized to behave as undeformable surfaces during impact events. They are essentially the "backbone" of the impact limiter, lending a predictability to the impact limiter crush behavior and forcing the energy absorption to occur in the honeycomb metal mass. The design of this backbone structure was a subject of in-depth computer and experimental 1/8 scale static testing, as documented in Holtec Report HI-962501 [2.A.4] and summarized in Section 2.A.4 herein.

Another noteworthy aspect of the AL-STAR impact limiter design is the arrangement of uniaxial and cross core (biaxial) honeycombs. Regions of the honeycomb space that experience impact loading in only one direction are equipped with unidirectional honeycomb sectors. The regions where the direction of the impact loads can vary have cross-core (bi-directional) honeycomb material, as detailed in Subsection 2.3.1.5.

To summarize, the design objectives of the AL-STAR impact limiter are set down as five discrete items, namely:

i. Limit peak deceleration (α_{max}) to 60g's under all potential drop orientations.

ii. Impact limiter must not detach from the cask under a 9-meter drop event, under any impact orientation.

iii. The impact limiters must bring the cask body to a complete stop, such that the overpack does not come in physical contact with the target surface.

iv. Crush material must be equally effective at -20° and 100°F, with humidity ranging from 0 to 100%.

v. All external surfaces must be corrosion-resistant.

The last two objectives are realized by utilizing aluminum honeycomb (Type 5052) as crush material and stainless steel (Type 304), for the external skin enclosure. As shown in the ASME Code (Section II, Part D, Table Y-1), the essential property of the constituent material for the honeycomb and the external skin, namely the yield strength remains constant in the -20° F to

100° F range. The surface of the carbon steel impact limiter backbone is painted to limit corrosion.

The remaining design objectives, namely, limiting of the maximum rigid body deceleration, α_{max}, to 60 g's under a 9-meter drop event, maintaining positive attachment of the AL-STAR impact limiters to the overpack, and preventing contact of the overpack with the unyielding surface, are demonstrated by a combination of numerical simulations and scale model static and dynamic testing. This was accomplished through a research and development effort that is broadly subdivided into six phases, as follows:

Phase 1: Characterize the honeycomb pressure-deflection relationship.

Phase 2: Propose a force (static) vs. crush (F vs. d) model for AL-STAR.

Phase 3: Perform 1/8 scale model static compression tests to validate the force-crush model and to establish the adequacy of the AL-STAR backbone structure.

Phase 4: Conduct 9-meter quarter-scale model dynamic drop tests in selected limiting drop configurations and obtain test data.

Phase 5: Simulate the experimental drop tests with a suitable "dynamic model" and establish that the dynamic model predictions of deceleration, crush and event time duration reasonably match the experimentally measured values. A reasonable prediction of the peak decelerations of each drop event is the minimum for the dynamic model to be acceptable.

Phase 6: Utilize the experimentally confirmed dynamic model to evaluate the effects of tolerances on crush properties and on package weight, and to confirm the adequacy of the full-scale impact limiter design.

It is of crucial importance that the dynamic model benchmarked in Phase 5 be of high reliability, since it becomes the analytical model for the accident-event response prediction of the packaging when tolerances on material behavior and package mass are considered (Phase 6).

In this appendix, a description of the overall program and results for each of the six phases is presented.

2.A.2 Phase 1: Material Pressure-Crush Relationship

The extent of deflection, Δ, sustained by a honeycomb material when subjected to a uniform pressure, p, is an essential element of information in the impact limiter design. Towards this end, coupon specimens of uniaxial and cross-core honeycomb of various nominal crush strengths and

densities were compression-tested by the material manufacturer. The results showed that all honeycomb coupons shared some common load-deflection characteristics, namely:

The initial pressure-deflection curve resembled an elastic material (pressure roughly proportional to deflection).

Upon reaching a limiting pressure, the material crushed at near constant pressure until the crush reached approximately 60-70 percent of the initial thickness. The required crush force had to increase rapidly to achieve small incremental crushing for strains beyond approximately 60-70 percent.

Figure 2.A.2.1 shows a typical static pressure-deflection curve for a 1"-thick honeycomb specimen. The curve with the initial peak is that of an un-precrushed honeycomb specimen; the curve without the peak (shown as a dashed line only where a difference occurs) corresponds to a pre-crushed specimen. Dynamic testing subsequently showed that removal of the initial peak by pre-crushing the material was a desired feature whenever a large flat area of honeycomb material experienced a crush force (such as in a 90 degree end drop).

Curve fitting of data from all tested coupons indicated that a single mathematical relationship between the applied pressure and compression strain could be developed. The mathematical relationship can provide a reasonable fit for coupons of all crush strengths (crush strength defined as the pressure corresponding to the flat portion of the curve in Figure 2.A.2.1; i.e., it is the constant pressure at which the honeycomb undergoes near-perfect plastic deformation). In other words, the pressure, p, for a given strain, ε, is represented by a unique function of the crush pressure, p_c, i.e.

$$p = f(p_c, \varepsilon)$$

The relationship between p and compression strain was used in the subsequent mathematical efforts to simulate AL-STAR crush behavior. The above mathematical relation was developed to simulate material behavior for a honeycomb material under both non-pre-crushed and pre-crushed conditions.

2.A.3 Phase 2: Static Force-Crush Prediction Model

An essential step towards the development of a reliable dynamic model to simulate the impact of a dropped HI-STAR 100 package is to develop a static force-crush model that can subsequently be validated by scale model tests. The force-crush model should reliably duplicate the resistance provided by an impact limiter for a range of crush orientations for the full range of crush depths.

The required force-crush model for AL-STAR is developed using the concept of interpenetration, which is explained using the case of the side drop ($\theta = 0$) as an example (Figure 2.A.3.1(a)).

The condition existing in all impact limiter drop scenarios is that the relatively soft honeycomb material lies between two "hard" surfaces that are advancing towards each other during the impact. One of these two rigid surfaces is the essentially unyielding target (Rigid Body 1) and the other is the structural backbone of the impact limiter (Rigid Body 2). While the target surface is flat, the backbone structure is cylindrical in profile. When squeezed between the two surfaces, the honeycomb material (at each instant in time) will crush at one or both interface locations. To determine which interface surface will undergo crushing at a given point during the impact event, the concept of interpenetration area is utilized as explained below.

In this concept, two separate crush scenarios, one assuming that the crush occurs at the external interface (target-to-impact limiter), and the other assuming that the crushing is at the internal interface (structural backbone/overpack-to-impact limiter), are compared at each instant during a simulated compression of the impact limiter. A metal honeycomb impact limiter, in general, may have multiple honeycomb material sections crushing at each interface. For simplicity in explaining the concept of interpenetration, we assume that each of the interfaces is characterized by a uniform distribution of honeycomb having crush pressures p_1 and p_2, respectively. To determine the resistive force developed to crush the impact limiter by a small amount, d, against the external target, the impact limiter is assumed to penetrate the target by the amount "d" without deformation. The resulting area A_1 for the case of side drop, illustrated in Figure 2.A.3.1(b), can be computed as an algebraic expression in the amount of approach, d. (For oblique drop events, ANSYS [2.A.1] or CADKEY [2.A.2] are used to compute interpenetration area as a function of incremental interpenetration.) The pressure-compression relationship for the honeycomb stock at the external interface provides the crush pressure p_1 that develops due to deformation "d". The total force required for crush "d", at the external interface, is therefore equal to p_1A_1.

In the second (independent) scenario, the impact limiter external surface is assumed to undergo no movement; rather, the backbone structure (along with the overpack) advances towards the target by an amount d (Figure 2.A.3.1(c)). Once again, assuming that the cylindrical rigid body moves through an amount "d", the resistance pressure developed in the honeycomb material lying in the path of penetration is available from the appropriate material pressure-compression curve. If the pressure corresponding to the deformation is p_2 and the projected area at the internal interface is A_2, then the total resistive force encountered in realizing an approach equal to "d" between the overpack-backbone assemblage and the target under this latter scenario is p_2A_2. In an actual drop event, at each instant during the event, incremental crush occurs at one of the two interfaces. If $p_1A_1 < p_2A_2$ at a given instant then crushing will occur at the external interface. Likewise, $p_1A_1 > p_2A_2$ will imply that crushing will occur internal to the impact limiter. The smaller of p_1A_1 and $p_2 A_2$ is the required crush force and the corresponding location of crush is where the honeycomb material will compress to realize the approach equal to d. This "inequality test" to determine where crushing occurs is performed at every increment of crush during the simulation of the event. The appropriate value of the crush force is used in the equilibrium equations at that instant. The concept of interpenetration at two interfaces has been confirmed during testing of the impact limiters; the total crush is observed to be a sum of compression at each of the two interfaces.

To construct a mathematical force-deformation relationship for AL-STAR in any given orientation, the above process is repeated as the crush "d" is increased in small increments starting with the beginning of compression (d = 0). It is quite clear that the development of the force-deflection model (F-d model) for AL-STAR in any orientation is a straightforward analysis in 3-D geometry. The F-d curve for AL-STAR for any given value of θ can be developed where, other than the geometry of the impact limiter, the crush strengths p of the honeycomb materials utilized in the impact limiter are the only other required inputs.

The force (F) vs. crush (d) relationship developed using the foregoing method is referred to as the F-d model that is subject to validation by appropriate 1/8 scale model compression tests described in the following section.

2.A.4 Phase 3: One-Eighth Scale Model Static Compression Tests

The 1/8 scale model tests consist of subjecting scaled replicas of the full-size AL-STAR to static compression tests in an engineered fixture such that the force-compression curve for the scaled model can be obtained in various orientations of compression. The scale model is made by making the diameters and length of the model one-eighth of the full-size AL-STAR. The thicknesses of the backbone components (i.e., the inner and outer shells and gussets), and the external skin (see Figure 2.A.1.3) are also scaled to one-eighth times the corresponding dimensions (to the nearest sheet metal gage, where applicable) in the full-size AL-STAR. In the one-eighth model, the performance of the attachment system is not assessed nor is the cask body modeled. However, the interface between overpack and impact limiter where the compression load is resisted is properly simulated. The crush pressure is a material property of the energy absorbing material; therefore, the material (and its density) is not scaled. The 1/8 scale model, therefore, has approximately $(1/8)^3$, or 1/512 the volume and weight of the full-size unit. Holtec documents [2.A.3, 2.A.4] provide complete details on the 1/8 scale model geometry and fabrication. The static compression behavior of such a 1/8-scale model is correlated with that of a full-size unit using the geometric scaling information. For example, under an axial compression test the area under crush in the scale model will be 1/64 of the full-size AL-STAR (recall that the diameter is scaled down by a factor of 8). Therefore, the crush force (which is crush force pressure times the area under crush) will be 1/64 of the full-size unit. On the other hand, the crush stroke (extent of deformation before "lock up") will be 1/8 of the full-size AL-STAR because the axial length of the scale model (which corresponds to the height of the crush column in axial compression) is one-eighth of the full-size hardware. Thus, the total energy absorbed (force times compression) will be $(1/8)^3$ of the full-size unit. The same scaling factor can be shown to apply in all directions of crush.

In summary, the 1/8 scale model scales the geometric dimensions of AL-STAR. The previously discussed F-d model is required to translate the force-crush relationship from the 1/8 scale replica to the full-size unit. In order to use the analytical F-d model as a valid vehicle for predicting the force-crush of the full-size (or quarter-scale) AL-STAR, it is necessary to check its prediction ability against actual test data from 1/8-scale model static compression tests.

The objectives of static scale model tests are twofold:

i. Determine whether the static force-crush relationship predicted by the F-d model appropriately simulates the actual relationship determined by test;

ii. Determine whether the backbone structure of the AL-STAR impact limiter is sufficiently rigid to withstand and transmit the large loads associated with the postulated accident scenarios.

2.A.4.1 Static Compression Tests on Initial Candidate Crush Material

To assess compression performance, a QA validated AL-STAR static test procedure was prepared [2.A.3] for the one-eighth scale model static compression tests and a series of cold and hot static compression tests performed on an impact limiter configuration with the initial candidate crush material. Holtec calculation package HI-961501 [2.A.4] contains a comprehensive documentation of the 1/8 scale static test program and results for the impact limiter configuration. A summary of the complete test program and test results is presented below.

Four 1/8-scale models were fabricated with details of the impact limiter carefully scaled, including the stiffening cylinders and the stainless steel skin. No impact limiter attachment bolts were incorporated in the model.

Aluminum honeycomb segments provided for the 1/8-scale models were manufactured utilizing the same procedures and processes as for the full-scale impact limiter. As stated earlier, the crush strengths were not scaled because they are considered as material properties.

An adjustable 1/8 scale static test fixture was designed, analyzed, and fabricated. The test fixture interfaced with the impact limiter and simulated the overpack hard surface. The test fixture could be adjusted to simulate any crush orientation. Figure 2.A.4.1 shows the test fixture and the 1/8 scale impact limiter being loaded in the heavy-load testing machine.

The following static one-eighth scale test series were carried out:

Test No.	Orientation, degrees	Temperature
1	0 (side)	+120°F
2	30 (oblique)	Ambient
3	60 (oblique)	Ambient
4	90 (end)	-30°F

For all tests except the end compression (where the orientation is immaterial), the circumferential orientation of the impact limiter was selected so that the initial point of contact between the impact limiter and the test machine was at the interface of two aluminum honeycomb secttions. After each test, the impact limiters were cut open and examined.

Observations Based on 1/8 Scale Model Testing

- Effect of Ambient Temperature:

  The end compression test was performed with the impact limiter cold (-30°F), the side compression test was performed with the impact limiter hot (+120°F), and the two oblique tests performed at ambient temperature. The material behavior showed no influence of test temperature. This confirms the expected result since the aluminum honeycomb and stainless steel skin yield strengths are insensitive to temperature in the range of interest (-20° F to 100° F) as prescribed in Table Y-1 of the ASME Code.

- Side compression orientation - 0 degree:

  The inner stiffening cylinder experienced considerable permanent deformation. The gussets which buttress the inner cylinder buckled. The outer stiffening cylinder performed elastically.

- Oblique compression orientation:

  Two oblique orientation static tests were performed. The 30-degree oblique test again showed the need to thicken the inner stiffening cylinder and to rearrange the stiffening gussets.

  The 60-degree oblique test was a complete success; no plastic deformation of the backbone structure was indicated.

  As would be expected, in those cases where the hard region (backbone structure) of the impact limiter sustained deformations, the scale model exhibited greater flexibility in the physical testing than the analytical prediction (the flexibility of the backbone structure added to the crush of the honeycomb resulting in a greater total measured deflection).

- End compression orientation - 90 degree:

  The end-compression orientation is, structurally speaking, the least complicated of the four test configurations. The loading of the AL-STAR scale model in this test is purely axisymmetric. The initial peak in the pressure/deformation curve seen in the coupon tests (Figure 2.A.2.1) was clearly evident in the axial (end) compression test (Figure 2.A.4.3). The backbone structure performed without sustaining plastic deformation.

- Comparison of experimental and analytical predictions

  Out of the four static 1/8-scale model tests, two tests (side compression and 30-degree oblique) were unsatisfactory because the backbone structure of the impact limiter did not remain elastic. These tests served to identify the need to reinforce the AL-STAR backbone structure. The other tests, namely end-compression (90 degree) and 60-degree oblique, wherein the backbone structure performed as designed, showed close agreement with the numerical model. Figures 2.A.4.3 and 2.A.4.4, respectively, show the static test results for 90-degree (end-compression) and 60 degree (oblique) cases, along with the prediction of the F-d model. There is good agreement between the computer model and the test data.

In summary, the 1/8 scale model static test program identified the required design changes to the internal structure of the impact limiters. The 1/8 scale model tests showed that the load-compliance characteristics of AL-STAR are insensitive to the changes in the ambient environment. A comparison of the test results with the mathematical model predictions from the F-d model indicated that the mathematical model was in good agreement with 1/8-scale static crush tests whenever the backbone structure performed as required (i.e. remained elastic). Since the crush geometry of the scale model was *not altered* by the strengthening of the backbone, any subsequent reinforcing of the backbone did not alter the F-d relationship for the impact limiter. The two successful static tests that showed excellent agreement with the computer F-d model, therefore, continued to serve as a valid benchmark of the numerical model after the backbone is stiffened. The reinforced backbone structure is incorporated into the final design drawings for the AL-STAR, and was confirmed as acceptable during the dynamic (1/4-scale) model drop tests. Subsequent to the one-quarter scale dynamic tests and the analytical correlation (Phases 4-6), three additional $1/8^{th}$ scale confirmatory static tests were performed on impact limiters that included the internal backbone structure and the final crush material orientations used in the quarter-scale drop tests and in the analytical correlation. These additional confirmatory static tests were performed at room temperature. The tests simulated the crush orientation corresponding to the side drop, the "center-of-gravity-over corner" drop, and the end drop, respectively. Force-deflection results from the static test are compared with the predictions from the theory for the $1/8^{th}$-scale impact limiters. Subsection 2.A.10 discusses the results obtained from these three additional static tests.

2.A.5 Phase 4: 9 Meter Quarter-Scale Model Drop Tests

The one-quarter scale model dynamic tests provide physical confirmation of the HI-STAR impact limiter design and the performance of the attachment system. The quarter-scale and full-scale design of the impact limiter is presented in drawings in Section 1.4.

In the 1/4 scale model drop test program, an instrumented scale model of the HI-STAR 100 dual-purpose cask was assembled with the top and bottom AL-STAR impact limiters, raised to a height of 9 meters (measured from the lowest point on the package), and then released to free fall onto an unyielding concrete and steel armor target (unyielding target). The impact limiter attachment system is reproduced in the model using the appropriate scale for bolt diameters, etc.

A detailed description of the quarter-scale model, instrumentation, data acquisition, and data processing is presented in a proprietary Holtec document [2.A.7]; a concise self-contained summary is provided in the following.

2.A.5.1 Test Plan:

The drop test program was performed at the drop testing facilities at the Oak Ridge National Laboratory. The target at the ORNL facility complies with guidance of IAEA Safety Series 37, Article A-618.

The quarter-scale model testing of the package required the design and fabrication of scale models of AL-STAR, the HI-STAR overpack, and the multi-purpose canister. The quarter-scale replicas of AL-STAR were prepared using the scaling procedure described previously in the context of the 1/8 scale model. In the scale model for the MPC and the overpack, the emphasis is in scaling the weight and moment of inertia, because it is these properties (translational as well as rotational) which are key to the response in the drop event. A schematic of the MPC design used in the scale model is shown in Figure 2.A.5.1. The weight of the MPC replica was set at 1,380 lbs (to simulate an 88,320 lb loaded multi-purpose canister).

The overpack scale model likewise is a cylindrical body whose length and outside diameter are 1/4, whose weight is 1/64, and whose mass moment of inertia is 1/1024 of the respective design parameters in the full-size hardware, as summarized below:

Key Quarter Scale HI-STAR Overpack Model Data			
Length (inch)	O.D. (nominal) (inch)	Overpack Plus MPC Weight (lb.)	Mass Moment of Inertia About a Transverse Centroidal Axis (Overpack Plus MPC) (lb.-in^2)
50.7813	21	3,733	1.351E+06

Figures 2.A.5.2 through 2.A.5.4 illustrate the principal geometric data of the quarter-scale overpack model. These figures are adapted from the design drawing 1546 (proprietary) provided in Section 1.4 of this report. It is evident from the above description that the quarter-scale model is, from a geometrical and inertia standpoint, a quarter-scale emulation of a 84" diameter x 203.125" long, 238,900 lb. (approximate) HI-STAR system (overpack and loaded MPC). Finally, the attachment bolts which join the impact limiter to the overpack are also scaled down to 25% of their size in the full-size hardware (in both diameter and thread engagement length), as can be seen from Figures 2.A.5.3 and 2.A.5.4 or the applicable drawing in Section 1.4.

The one-quarter scale drop tests were performed with four discrete orientations of the cask longitudinal axis with respect to the impact surface, as defined below.

Test A – Vertical Drop (Top End): The cask is dropped such that the deceleration of the cask upon impact is essentially vertical.

Test B: Center of Gravity-Over-Corner (CGOC): For HI-STAR 100, C.G.-over-corner means an orientation wherein the axis of the cask is at 67.5° from the horizontal at the instant of release at the 9-meter height. This test seeks to establish the adequacy of the impact limiter under non-symmetric impact loading.

Test C – Side Drop: The cask is held horizontal with the lowest point on the package 9 meters above the target surface when released for free fall. In this test, both impact limiters participate, and the impact impulse is essentially equally divided between them.

Test D – Slapdown: In this test, the cask axis is held at 15° from the horizontal with the lowest point of the cask assembly at 9 meters from the impact surface. The orientation is such that the top end impact limiter impacts the surface first and the bottom end impact limiter experiences the secondary impact.

Each of the four tests has distinct impact characteristics. For example, in the "side drop" test both impact limiters will strike the target simultaneously; only one impact limiter sustains impact in the "end drop" test. The CGOC test involves a primary impact on one impact limiter at an angle such that the gravity vector is oriented with a line passing through the cask center of gravity and the lowest corner of the limiter. Finally, the slapdown test involves impact at both impact limiters with a very slight time separation. These four tests are deemed to adequately represent the limiting impact scenarios under the hypothetical accident conditions of 10CFR71.73.

The torque values used to secure the attachment bolts in the scale model package warrant special mention. The impact limiter attachment bolts serve two major functions during transportation:

1. During normal transport, the attachment bolts ensure that the impact limiters remain attached to the HI-STAR 100 overpack during a 10g axial deceleration as mandated by 10CFR71.45, and during exposure to normal vibratory loading that may reasonably be expected during the course of a normal transport operation. To ensure against loss of attachment due to vibratory loading during normal transport, an initial bolt pre-stress of 30,000 psi has been set, based on common engineering practice. For the bolt diameters specified for the HI-STAR 100 package, the pre-load torque is 245 ft-lb and 1,500 ft-lb for the top and bottom impact limiter attachment bolts, respectively.

2. During the hypothetical accident, the attachment bolts ensure that the impact limiters remain attached to the HI-STAR 100 overpack during and after the impact with the unyielding surface.

The bottom impact limiter is attached to the overpack by 16 bolts aligned with the longitudinal axis of the overpack and arranged in a circular pattern (Figure 2.A.5.4 shows the bottom view of the one-quarter scale replica). These bolts perform their function by developing tensile stress to

resist loading during the hypothetical accident. Because of close clearances with the overpack shielding, the bottom impact limiter also has a set of eight circumferentially arranged alignment pins that fit into mating holes in the overpack bottom plate. These mating holes are plugged when the impact limiter is not in place.

The top impact limiter is attached to the overpack using twenty radial bolts that are designed to resist relative motion and transfer loads by shear (Figure 2.A.5.3 shows the top view of the one-quarter scale replica).

Although the attachment analyses do not require pre-load (by application of an initial bolt torque) to demonstrate that the required performance during normal transport conditions is achieved, the presence of pre-load serves only to enhance the performance of bolting which resists loads by developing tensile bolt forces (bottom impact limiter attachment bolts). Pre-stress in the bottom impact limiter attachment bolts serves to develop an interfacial pressure between the two components being joined together. This interfacial pressure acts as a reserve against separation at the interface of the impact limiter and the overpack when the external force or moment act to separate them during the drop event. The actual tensile stress bolt will rise significantly over the initial pre-stress if and only if the external load acting to break apart the interface is large enough to cancel out the interfacial pressure.

The effect of pre-load on the performance of bolting that resists loads by shear (top impact limiter attachment bolts) is different. The presence of both tensile stress (due to bolt pre-load) and shear stress in the bolt (due to the impact loads in a drop event) will increase the maximum principal stress in the bolt, which will consequently reduce the shear capacity of the bolts. Applying a pre-load in excess of the required amount in the 1/4 scale HI-STAR 100 drop tests will therefore result in a conservative evaluation of the top impact limiter attachment bolts.

Based on the initial torque values set in the full-scale package, the appropriate bolt pre-load torque for the 1/4-scale impact limiter attachment bolts is (to the nearest foot-pound):

Top impact limiter (radial) bolts: 4 ft-lb. (full scale equivalent = 245 ft.-lb)
Bottom impact limiter (axial) bolts: 23 ft-lb. (full scale equivalent =1500 ft.-lb.)

Since a bolt pre-load will enhance the performance of bolts (located at the bottom impact limiter interface) that resist loading by developing tensile stress, the bolt torque was conservatively set at 20 ft-lb. or below for the bottom impact limiter bolts. Since a bolt pre-load will degrade the performance of bolts (located at the top impact limiter interface) that resist loading by developing shear stress, the bolt torque was conservatively set at 4 ft-lb. or above for the top impact limiter bolts.

The end drop onto the top impact limiter tests the resistance of the twenty radial attachment bolts against failure from shear. The use of an initial torque value (15 ft-lb.), in excess of 4 ft-lb., is conservative for evaluation of the performance of the bolts to resist shearing strains (i.e., as noted

earlier, due to an interaction relation between tension and shear, the presence of any tensile strain will reduce the allowable shear strain prior to failure).

The C.G. over corner drop used an initial torque of 15 ft-lb., a value below the mandated value of 20 ft-lb. on the bottom impact limiter. This is again conservative for the evaluation of the performance of the bottom impact limiter attachment bolts, since the presence of additional prestress would enhance the ability of the bolts to retain the impact limiter in position.

The slapdown test was performed using low initial bolt torque values for both impact limiters that simulated "hand-tight" values. Thus, there is almost no contribution from pre-load on the bolts on either impact limiter. In the slapdown drop, the bottom impact limiter experienced the largest deceleration. This test demonstrated that the use of a lower pre-load on the most highly loaded attachment bolt does not affect the ability of the bolts to perform their required function.

Finally, the final side drop used the bolt pre-loads that correlate with the final bolt pre-loads specified (top impact limiter - 4 ft-lb.; bottom impact limiter - 20 ft-lb.) for the one-quarter scale tests.

A minimum of five calibrated unidirectional accelerometers was installed on the test package for each test. Schematics of the accelerometer locations and numbering system for all four tests are presented in Figures 2.A.5.5 and 2.A.5.6.

The accelerometers are placed at three axial locations along the height of the overpack model and at different circumferential locations at each axial location. The placement of the accelerometers axially reflects locations consistent with the detailed 2-D finite element analyses of the MPC that conservatively neglected the effect of stiffening provided to the MPC shell by the MPC baseplate. Figure 2.A.5..2 shows the three cutouts of the outer 5/8" thick cylinder that are machined flat to position the accelerometers. The following table provides the locations of the accelerometers.

ACCELEROMETER LOCATIONS FOR ONE-QUARTER SCALE DROP TESTS								
NUMBER	TOP END DROP		SIDE DROP		SLAPDOWN		CG-OVER-CORNER	
	Axial (inch)	Peripheral (degrees)	Axial (inch)	Peripheral (degrees)	Axial (inch)	Peripheral (degrees)	Axial (inch)	Peripheral (degrees)
1	44.781	0	5	0	44.781 25	0	5	0
2	25	0	25	0	25	0	5	+120
3	5	0	44.781	0	5	0	5	-120
4	44.781	+120	25	+90	44.781	+120	44.781	0
5	44.781	-120	25	-90	44.781	-120	44.781	+120
6	5	+120	–	–	5	+120	44.781	-120

Notes:

1. All accelerometer axial distances measured from top end surface of overpack model (without impact limiters in place).
2. Peripheral locations measured from plane containing accelerometer #1; clockwise direction, viewed from Section A-A in Figures 2.A.5.5 and 2.A.5.6, is positive.

In addition to recording the deceleration during impact, a high-speed camera and a video camera were used to record the test events. The high-speed camera was used to confirm orientation angles just prior to impact and to aid in the evaluation of extent of crush subsequent to the test. The tests were conducted by attaching the ¼ scale package to a 15-ton mobile crane through appropriate rigging and lifting the package to the required height. An electronically activated guillotine-type cable cutter device was used for releasing the package for free fall. An array of photographs labelled Figures 2.A.5.7 through 2.A.5.13 provide pre-test and post-test visuals of the package. These photographs show quite clearly that the post-crush impact limiters maintained their own physical integrity and the attachments to the overpack scale model suffered no failures.

The following acceptance criteria for the scale model dynamic drop tests were identified in the Test Plan [2.A.11]:

- Filtered decelerations limited to a maximum of 60g's (after scaling to full-scale geometry) for all drop orientations.
- No impact of the cask body on the target surface.
- No separation of impact limiters from the cask body through the entire drop event.

2.A.5.2 Results of First Series of Drop Tests

The first series of three one-quarter scale drop tests (types A, B, and C denoted above) were performed in August 1997 and produced significant information [2.A.5]. Table 2.A.1 shows the maximum filtered decelerations registered in the three one-quarter scale tests after the test results are scaled up to the full-scale AL-STAR (by dividing test results by four).

Table 2.A.1: Peak Decelerations from August 1997 Tests

Test I.D.	Orientation	Deceleration (g)
A.	End Drop	134
B.	C.G.-Over-Corner	37.84
C.	Side Drop	51.3

The peak filtered deceleration in the first end-drop test was clearly above the 60g-design limit established for the HI-STAR 100 design. The reasons for this discrepancy were determined to be the use of a low value of the dynamic multiplier assumed in designing the impact limiter, and the lack of pre-crush of the honeycomb material. Numerical analyses also indicated that the honeycomb compression modulus was dependent on the impact limiter velocity during the drops. This confirms laboratory data available in the historical literature [2.A.9]. The velocity and deceleration information obtained from the first round dynamic drop tests enabled development of a simple dynamic correlation multiplier to be applied to the honeycomb material's static F-d behavior. This multiplier is an additional "experimentally based" input term in the computer prediction model for simulation of dynamic drop events [2.A.6]. Data from the initial test series shows that this multiplier is independent of test orientation and is a function of the ratio of crush velocity during the crushing process divided by the impact velocity at the initiation of crush. Based on the numerical analysis of the August 1997 tests, the honeycomb material was appropriately revised with new crush strengths and new sets of ¼ scale model impact limiters were manufactured. The correlation of the August 1997 quarter-scale tests with the numerical results from the computer model is presented in section 2.A.6.

In summary, the chief contribution of the August tests, therefore, lay in providing the database to quantify the crushing characteristic of the honeycomb material under dynamic conditions [2.A.6]. Since none of these tests is ascribed to confirmation of the final performance of the AL-STAR impact limiters, no accelerometer raw or filtered results are included herein. The full set of acceleration data (both raw and filtered) is provided in [2.A.5].

2.A.5.3 Results of the Second Series of Drop Tests

The second round of one-quarter scale dynamic drop tests, conducted in December 1997 and February 1998, using the new (lower crush strength) impact limiter materials, occurred in three phases. The first phase consisted of the top end drop, CGOC drop, and side drop tests. While the decelerations in all cases were within the design limit, the attachment system for the bottom impact limiter did not survive the side drop test. The attachment system was redesigned prior to the remaining (slapdown) test. The slapdown test is considered to be the most definitive test of the cask/impact limiter attachment integrity. The slapdown test was successfully completed, with the bottom impact limiter remaining in place during and after the secondary impact, on December 29, 1997 in Phase 2 of the second test series. In order to confirm the adequacy of the attachment system under side drop conditions, the side drop test was repeated in February 1998 during Phase 3. This test reconfirmed the attachment system integrity.

The results from the second round test series demonstrates that the HI-STAR 100 package meets all test acceptance criteria, namely:

- Appropriately filtered decelerations of less than 60g's (after appropriate scaling to reflect the full-size mass and geometry) for all tested orientations;
- All attachment bolts remained intact, ensuring that the impact limiters do not separate from the cask body through and after the drop event;
- No impact of the cask body on the target surface.

Figures 2.A.5.14 through 2.A.5.21, drawn from reference 2.A.7, provide the raw (unfiltered) and filtered deceleration time-histories for each of the four drop scenarios for the key accelerometers used to assess package performance. The accelerometer station numbers indicated in these accelerograms are located by referring to Figures 2.A.5.5 or 2.A.5.6, as applicable. The test report [2.A.7] provides the necessary background to justify the use of this data to evaluate package performance. The following remarks are pertinent concerning the results presented in Figures 2.A.5.14 through 2.A.5.21.

End Drop Decelerations (Figures 2.A.5.14, 2.A.5.15, and 2.A.5.15a-c)

All accelerometers for this test recorded decelerations in the direction of crush. Two accelerometers were subsequently determined to be defective (documented in [2.A.7]). The figures show the raw, the filtered response at 450Hz cut-off frequency, and a combined plot of the raw and filtered data covering a reduced time period. All of these results are obtained from the records from the working accelerometers. All working accelerometers gave essentially identical response; the final evaluation of performance presented herein is the average of the response from the accelerometers deemed to be recording correctly. Figures 2.A.5.15b and 2.A.5.15c demonstrate that the sensitivity to cut-off filter frequency is small even up to 1250Hz.

Center of Gravity Over Corner Decelerations (Figures 2.A.5.16, 2.A.5.17, and 2.A5.17a)

The CGOC test was performed immediately after the end drop using the same set of accelerometers. The evaluation of the data after this test clearly determined that the same two accelerometers deemed suspect in the end drop test was also providing erroneous date here. Subsequent independent plate impact tests that definitively showed that these accelerometers were indeed faulty are documented in [2.A.7]. The acceleration data in the figures represents the vertical acceleration obtained by appropriate combination of the raw time data from the longitudinal and lateral mounted accelerometers on the inclined scale model cask. The raw vertical accelerations were then subject to filtering to remove non-rigid body behavior. Raw, filtered, and combined raw and filtered data over the strong response time period are presented.

Slap Down Decelerations (Figures 2.A.5.18, 2.A.5.19, and 2.A.5.19a)

Although the initial release of the package was at an angle of 15 degrees from the horizontal, the high-speed camera showed that impact occurred with the overpack longitudinal axis at an angle of 7.2 degrees from the horizontal. The numerical simulation of this test reflected the actual angle of impact rather than the initial setting at nine meters. The results for all accelerometers (raw data and filtered) are provided in [2.A.7]. The raw and filtered data presented in the figures here represent the deceleration at the bottom end of the package that experiences the larger magnitude secondary impact. Numerical analysis demonstrated that the peak deceleration from secondary impact is insensitive to impact angles between 5 and 12 degrees from the horizontal and decreases as the angle increases above 12 degrees. Raw, filtered, and combined raw and filtered data over the strong response time period are presented.

Side Drop Decelerations (Figures 2.A.5.20, 2.A.5.21, and 2.A.5.21a)

Both impact limiters are supposed to impact the target simultaneously in this test. An evaluation of the individual accelerometer data and an examination of the high-speed camera film clearly indicated that there was a small angle existing between the overpack longitudinal axis and the target horizontal surface at the moment of impact. This caused the expected result that accelerometer readings at one end of the package were slightly higher than readings at the other end. The results for raw and filtered data represent results obtained by averaging the data from the accelerometers at the ends of the package. Raw, filtered, and combined raw and filtered data over the strong response time period are presented.

The filter frequency used for the End Drop and CGOC Drop is 450 Hz. The filter frequency used for the Slap Down and Side Drops was 350 Hz. These filter frequencies were established by examination of the power spectral density function for each raw data trace that clearly showed that the majority of the energy occurred at frequencies well below the cut-off frequency. Independent confirmation of the appropriateness of the cut-off frequencies was made by determining the lowest frequency of elastic vibration of the package acting as either a bar or a simply supported beam. As described above, the sensitivity to cut-off frequency was examined for the end drop case by re-analyzing the data for three cut-off frequencies.

Table 2.A.2 provides the peak deceleration data culled from the above-mentioned accelograms for the four drop scenarios after filtering to remove high frequency effects. The table contains the results from the actual 1/4-scale experiments scaled up to the full-size packaging. The test report [2.A.7] provides the detailed information on this final one-quarter scale dynamic drop test series with raw and filtered outputs from all accelerometers. The test report also includes details on the filtering methodology, on the data reduction, and on the evaluation of the performance of the various accelerometers used in each of the tests.

In all of the four final one-quarter scale dynamic drop tests, the impact limiter attachments successfully performed without a single attachment bolt failure (ensuring that the impact limiters did not separate from the overpack), rigid body decelerations were below 60 g's, and the cask body did not contact the unyielding target surface. Also, additional crush margin remained in the aluminum honeycomb material.

Table 2.A.2: Peak Decelerations from AL-STAR™ Drop Tests (Second Series)

Test Case	Orientation	Peak Decelerations (g)
A	End-Drop	53.9
B	C.G.-over-Corner	38.8
C	Side Drop	45.7
D	Slap-Down	59

2.A.6 Phase 5: Numerical Prediction Model for Dynamic Analysis

The numerical prediction model for dynamic drop events utilizes the previously discussed force-crush (F-d) model and incorporates the information into the dynamic equations of equilibrium. Using the procedure discussed previously, the static F-d curves for the AL-STAR impact limiter under the four drop scenarios are readily constructed. Figures 2.A.6.1 to 2.A.6.4, respectively, provide the static force vs. crush plots for the full scale impact limiter with test orientations for drop cases A, B, C, and D (primary impact). An appropriate analytical fit for each curve is developed using the commercial graphing package Deltagraph [2.A.8]. Figures 2.A.6.1 through 2.A.6.4 also provide curves for upper and lower bound material strengths.

We now discuss the application of the F-d model to the prediction of impact limiter performance in a dynamic drop environment. In symbolic form, we can write the static resistive (crush) force, F, as a function of the crush depth, Δ, where a zero value for Δ represents an uncrushed condition.

$$F = f(\Delta)$$

The above symbolic formula represents the data on Figures 2.A.6.1 to 2.A.6.4 in analytical form. We have previously explicitly discussed the mathematical concepts underlying the above formulation by referencing the particular case of a side drop. In general, the static F-d curve can be expressed as a sum of local crush pressures multiplied by interface areas where the interface areas may be a function of the current crush. That is, the mathematical relation for static compression (which is validated by comparison to static testing) is also expressible in the form

$$f(\Delta) = \sum_i p_i A_i$$

where p_i are the crush pressures of the materials participating in the crush and A_i are the interface areas associated with the different crush strengths. The determination of the areas A_i as a function of crush depth, Δ, has previously been discussed within the context of interpenetration.

The dynamic model for simulating a packaging drop event consists of solving the classical Newtonian equations of motion. In the case of a unidirectional impact such as an end drop (θ=90°), side drop (θ=0), or CGOC drop, the equation of motion simply reduces to:

$$M\frac{d^2\Delta}{dt^2} = Force + Mg$$

where: M = mass of system undergoing deceleration

$d^2\Delta/dt^2$ = second derivative of package movement (which is equal to the impact limiter crush because the target is immovable and rigid).

The resistive "Force" opposes the downward movement and is given by the static force-crush functional relationship (appropriate for the drop orientation) multiplied by a dynamic multiplier Z. As noted earlier, there is historical evidence that metal honeycomb crush pressure is a linear function of velocity [2.A.9]. The Holtec correlation of the August 1997 test data by numerical simulation [2.A.6] also confirmed that the best correlation is achieved if the dynamic multiplier is represented by a linear function of local crush velocity ($d\Delta/dt$). Introducing the dynamic multiplier, the dynamic equation of force equilibrium for a case involving only primary impacts becomes

$$M\frac{d^2\Delta}{dt^2} = ZF + Mg = Zf(\Delta) + Mg$$

The above equation is a second order non-linear differential equation in the time coordinate t, which can be solved for the post-contact event using any standard equation solver package. The initial condition is: @ t = 0, Δ = 0, $d\Delta/dt = V_o$ (approach velocity at impact). We note that since the acceleration is an explicit function of both deformation and velocity, maximum acceleration will not, in general, occur at the instant when the velocity of the package is zero.

If the impact event involves both primary and secondary impacts, as is the case for the slapdown event (indeed any event wherein θ<67.5°), then both the mass M and rotational moment of inertia I are involved. The modeling of a dual impact event is only slightly more involved than

the single variable modeling of the single impact case discussed above. Figure 2.A.6.5 pictorially illustrates the sequence of events leading to an appropriate mathematical model. Figure 2.A.6.6 provides the appropriate free-body diagrams associated with each portion of the event.

In the first step, the inertia force of the falling package is resisted by the crush force developed at the primary impact location. While the downward momentum of the package is dissipated by the resistive force, the package also experiences the overturning couple produced by the non-co-linearity of the inertia force (which acts at the centroid) and the resistive force which acts at the primary impact zone (Figure 2.A.6.5(a)). The dynamic equation of force equilibrium is given above in terms of the downward movement of the package centroid and the resistive force static compression curve, modified by the dynamic factor Z, appropriate to the initial orientation at primary impact. The package decelerates and then begins to overturn, in effect pivoting about the initial point of contact in the primary impact region, gathering angular momentum as the second impact limiter (mounted at the far end) approaches the target surface. Referring to Figure 2.A.6.5(b), the dynamic equation insuring moment equilibrium during the overturning (before the initiation of the secondary impact) phase can be written as

$$I_p \frac{d^2\phi}{dt^2} = -MgR\cos(\phi)$$

where I_p: moment of inertia of the package about the pivot point

ϕ: angular acceleration with respect to the horizontal plane

R: radial distance of the package C.G. with respect to the pivot point.

The initial conditions for this phase are: $t = 0$, $\phi = \theta$, $d\phi/dt = 0$ where t is now redefined at the initiation of rotational motion.

Finally, the secondary impact commences wherein the angular momentum of the package plus any linear momentum not dissipated by the primary impact is dissipated by the crushing of the second impact limiter. During the secondary impact phase, the equation of dynamic moment equilibrium can be written by inspection of Figure 2.A.6.5(c):

$$I_p \frac{d^2\phi}{dt^2} = -MgR\cos(\phi) + Zf(D\phi)D$$

where $f(D\phi)$ is the static resistive force at the secondary impact location under compression $D\phi$, Z is the current dynamic multiplier appropriate to the secondary impact location, D is the moment arm, and I_p is the moment of inertia of the package about the pivot point. During this phase of the motion, the equation of dynamic force equilibrium is modified to reflect dynamic resistive forces from both impact limiters since the entire package may continue to move toward

the target surface with both impact limiters providing a dynamic resistive force. Therefore, during the final phase of the impact event, the dynamic force equilibrium equation can be written as

$$M\frac{d^2\Delta}{dt^2} = Z_1F_1 + Z_2F_2 + Mg$$

where Z_i and F_I (i=1,2) represent the dynamic multiplier and static compression force appropriate to the primary and secondary impact limiter behavior during the final phase of the event. The dynamic multipliers Z_i (i =1,2) reflect the current value of the local crush velocities at each of the limiters.

The above formulation assumes, for simplicity, that the pivot point does not slide during the overturning or secondary impact phases.

It is evident from the foregoing that the impact limiter is essentially simulated by a non-linear spring whose static force-deformation curve is known a' priori (from the F-d model) as a function of the drop orientation. The solution of this rigid body dynamics problem featuring up to two non-linear springs can be determined using any one of several standard software packages available in the public domain. Holtec International utilizes the commercial package WORKING MODEL [2.A.10], which has been validated in the company's QA system for this purpose.

The dynamic simulation model, constructed in the manner of the foregoing, was utilized to simulate all seven one-quarter scale drop events (three in the first series, four in the second series). In order to develop a high level of confidence, it was decided that the model should be validated at all three levels, namely, a comparison of acceleration, crush, and duration of impact. In other words, to be acceptable, the numerical prediction model must predict α_{max}, maximum crush sustained d_{max}, and the duration of impact, with reasonable accuracy. Since the actual crush d_{max} could be measured, and the duration of impact and α_{max} were available from accelerometer data, comparison between theory and experiment with respect to all three key indicators was possible. Tables 2.A.3 and 2.A.4 provide the results in a concise form for all of the one-quarter scale dynamic drop tests for the first and second series, respectively.

Note that in the tables, the comparison is made after scaling up the model results to reflect a full-scale package.

Table 2.A.3: Comparison Between Test Data and Prediction Model Results (First Test Series)

Case I.D.	Deceleration (g's)		Total Crush Depth (inch)		Impact Duration (milli-seconds)	
	Predicted	Measured	Predicted	Measured	Predicted	Measured
A. End-Drop	134.2	134.0	2.42	2.42	3.5	Not measured
B. C.G.O.C.	37.8	37.84	16	16	13.25	16.6
C. Side Drop	50.5	51.3	9.1	9.51	8.25	10.74

Table 2.A.4: Comparison Between Test Data and Prediction Model Results (Second Test Series)

Case I.D.	Deceleration (g's)		Total Crush Depth (inch)			Impact Duration (milli-seconds)	
	Predicted	Measured	Predicted	Measured	Max. Available	Predicted	Measured
A. End Drop	53.0	53.9	11.3	10.6	17.659	38.8	37.2
B. C.G.-Over-Corner	38.7	38.8	12*	9.82*	25.06	51.0	61/45.2
C. Side Drop	43.5	45.7	10.9	12.5	16	38.5	53.1 (averaged value)
D. Slap-Down							
Primary	46.4	49.0	9.50	10.7	16	48.5	44.4
Secondary	59.9	59.0	12.8	13.5	16	35.8	41.2

* For C.G.-Over-Corner, only crush at the external interface is measured.

It is evident from both Tables 2.A.3 and 2.A.4 that the numerical prediction model is robust in predicting all seven impact tests. Not only are peak values of α_{max} for each test predicted with good agreement, but also the crush depth and impact duration is also reliably simulated.

A perusal of the numerical results in Table 2.A.4 yields two additional insights into the behavior of AL-STAR which are most helpful in the "fine tuning" of the full-scale AL-STAR design:

i. The maximum deceleration, α_{max}, predicted as well as measured, under the most limiting scenario (slapdown), is close to the permissible limit of 60g's.

ii. The maximum crush, predicted as well as measured, in all drop scenarios, is well below the available limit (i.e., the value at which the crush material will "lock up").

The state-of-the-art manufacturing technology for aluminum honeycombs permits the material to be manufactured within a total tolerance range of 12 to 13% (between the maximum and minimum values). The above observations suggest that the upper and lower bound range of crush pressures for the honeycomb material in the AL-STAR impact limiter should be set at 95% and 82% of the values of honeycomb material used in the second series quarter-scale tests.

Finally, the agreement between the predictions and measured data in the above correlation effort fosters a high level of confidence in the numerical model, which can now be used to conduct sensitivity studies.

2.A.7 Phase 6: Simulation of the Effects of Material Crush Strength Variation, Package Mass Tolerances, and Oblique Drop Orientations

Having ensured the technical reliability of the numerical prediction model, it is now necessary to evaluate the system behavior under all "limiting conditions". As noted earlier, the impact limiter materials are insensitive to environmental temperature changes within the limits of –20° F and 100° F. Therefore, limiting conditions are broadly defined here as arising from two sources:

i. Variation in the impact limiter honeycomb crush strength due to material manufacturing tolerance.

ii. Variation in the package weight (due to different MPC types that may be transported in the HI-STAR 100 overpack, and manufacturing tolerances in fabrication of the overpack and impact limiters).

iii Variation in package angle of impact with the target.

To examine all limiting scenarios, additional simulations using the mathematical model were performed. The crush strength of the honeycomb material was varied within the range permitted in the Holtec Drawing 1765. The packaging weight was set at its upper bound and lower bound value (upper bound weight is 280,000 lb., and lower bound weight is 270,000 lb. based on values listed in Table 2.2.1). Three additional drop orientations (30 degree, 45 degree, and 60 degree orientation angle, measured from the horizontal) that were not the subject of tests were also analyzed numerically using input crush strength data that would maximize the decelerations with an average weight. The purpose of these additional simulations with varied drop angle is to ascertain which, if any, oblique drop orientation merits detailed finite element stress analysis to meet the requirements of the Regulatory Guide. Figures 2.A.7.1-2.A.7.3 provide the static crush force vs. crush depth information used in the dynamic simulation of these accident events. Table 2.A.5 provides key output data, peak decelerations and maximum crush, as obtained from these numerical simulations.

Table 2.A.5: Sensitivity of Package Response to Package Weight, Crush Material Strength Variations, and Package Orientation at Impact

Orientation	Case	Deceleration (g's)	Maximum Total Crush (2-interfaces) (inch)	Available Crush Stroke (inch)
End Drop	Max. Strength, Min. Weight	52.85	11.4	17.659
	Min. Strength, Max. Weight	46.3	12.8	17.659
C.G. Over Corner	Max. Strength, Min. Weight	38.25	17.0	25.06
	Min. Strength, Max. Weight	35.6	18.5	25.06
Side Drop	Max. Strength, Min. Weight	42.5	11.2	16
	Min. Strength, Max. Weight	37.5	12.7	16
Slap Down (secondary impact bounds)	Max. Strength, Min. Weight	58.5	13.2	16
	Min. Strength, Max. Weight	52.6	15.1	16
Oblique Drop – 30 degrees	Max. Strength, Min. Weight	36.44	19.57	24.1
Oblique Drop – 45 degrees	Max. Strength, Min. Weight	35.62	22.39	25.72
Oblique Drop – 60 degrees	Max. Strength, Min. Weight	38.01	19.2	25.65

The following conclusions are readily derived from Table 2.A.5 results:

i. The maximum value of α_{max} is less than 60g's in all cases.

ii. The total crush of the impact limiter is below the available "stroke", i.e., the overpack body will not contact the unyielding target surface nor will any "lock-up" of the crush material occur.

iii. The three oblique drop simulations considered all produce approximately the same vertical deceleration from the primary impact. The decelerations resulting from the subsequent secondary impact, after rotation of the HI-STAR 100, are all below the value obtained from the simulation of the "slapdown" at low angles of impact. If the "limiting" oblique drop is considered as the simulation providing

maximum deceleration perpendicular to the longitudinal axis of the cask, then the drop most likely to develop the largest bending of the overpack in the oblique orientation is at 30 degree orientation (from the horizontal axis). Therefore, this case is subjected to detailed stress analysis in Section 2.7 with the applied impact loading (along and perpendicular to the cask axis) balanced solely by the cask inertia forces and moments.

In conclusion, the above work provides full confidence that the HI-STAR 100 packaging will perform in the manner set forth in the NRC regulations (10CFR71.73) under all conceivable hypothetical accident conditions of transport.

2.A.8 One-Foot Drop

Paragraph 2.6 of Reg. Guide 7.8 requires evaluation of the package response under a one-foot drop onto a flat unyielding surface in a position that is expected to inflict maximum damage.

Using the prediction model, the maximum deceleration sustained by the package under the one-foot end and side drop scenarios, the latter expected to produce maximum stress in the fuel basket, was computed. Table 2.A.6 provides summary results for the limiting case of minimum package weight and upper bound material crush strength (so as to maximize the decelerations).

Table 2.A.6: Peak Decelerations Under One-Foot Drop Event

Scenario	Max. Deceleration in g's	Crush (inch)	Duration of Impact (milli-seconds)
90° End Drop	17.25	0.85	20.0
0° Side Drop	11.45	1.33	26.0

2.A.9 Equivalent Dynamic Factor (EDF)

It is instructive to compute an effective equivalent dynamic factor on the predicted static crush force corresponding to the instant of maximum deceleration during the drop event. Table 2.A.7 presents the pseudo-deceleration (obtained by dividing the static force by the mass of the package) and the predicted deceleration; the ratio of the two is the "equivalent dynamic factor" (EDF). The EDF is also equal to the peak dynamic crush force divided by the static resistance force at the coincident instance of crush when the dynamic crush force is maximized. Note that the differences in package weight used in the table below reflect the actual weight of the impact limiters used in each one-quarter scale drop test (after increasing to full-scale equivalent values).

Table 2.A.7: Equivalent Dynamic Factor (EDF) for Different Drop Scenarios

	Predicted Force (lbs) x 10^{-7}			Predicted Max. Deceleration		
Scenario	Static	Dynamic	Participating Package Weight (lbs)	Pseudo-Accn (static)	Dynamic (from Table 2.A.4)	EDF
End Drop	1.0785	1.454	274,336	39.313	53	1.348
CGOC Drop	0.8	1.059	273,680	29.231	38.7	1.324
Side Drop	0.4	0.597	137,270*	29.14	43.5	1.493
Slapdown	0.345	0.6607	†	†	59.9	1.915

* Only half of the total package weight participates at each impact limiter.
† Indeterminate for this drop configuration.

The last column of the above table demonstrates that the EDF, as defined above, is not a constant value independent of drop orientation.

2.A.10 Additional 1/8th Scale Static Tests

Three additional static crush tests on 1/8th scale impact limiters have been performed subsequent to the completion of all quarter-scale dynamic testing and theoretical correlation. The F-d test results for each of three impact limiter orientations are compared with the analytical F-d predictions in Figures 2.A.10.1-2.A.10.3. Figure 2.A.10.1 compares test results with theoretical prediction for the crush orientation corresponding to a side impact, Figure 2.A.10.2 presents the results for the Center-of-Gravity-Over-Corner impact orientation, and Figure 2.A.10.3 presents results for the end impact orientation. In all tests, the crush material orientation and location duplicated the final configurations subjected to quarter-scale tests. The internal backbone structure was also faithfully reproduced. The welds were also scaled to the extent practical given the thin material gages used for the one-eighth-scale model. In the three figures, the solid line without symbols represents the predictions of the theory developed for the F-d curves, while filled circles represent test results. Within the range tested for each orientation, good agreement is observed between theory and test for the side and CGOC crush orientation. For the end drop orientation, however, the tested results suggest that inclusion of some elastic behavior at the cask-impact limiter interface into the theory might improve the static correlation. The dynamic test results presented in Table 2.A.4, however, demonstrate conclusively that the prediction of peak deceleration, extent of crush, and impact duration would not be affected by these elastic effects that "smooth" the abrupt "staircase" shape of the F-d curve.

2.A.11 Conclusions

The AL-STAR impact limiter design was subjected to a series of static and dynamic tests to validate its functional performance. The 1/8 model static tests conducted under cold and hot, as well as ambient conditions, confirmed that AL-STAR's functional characteristics are independent of the environmental temperature conditions in the range specified in 10CFR71.73. The successful static tests on the 1/8 scale model (namely, end test and 60° oblique test) also correlated well with the theoretical force-crush model developed by Holtec. Subsequent static tests, performed after the final successful one-quarter scale dynamic tests, provided additional confirmation of the validity of the fundamental F-d model.

The static compression tests were followed by quarter-scale drop tests. The first series, in August 1997, consisting of three tests, provided the necessary test data to determine the dynamic multiplier applicable to the honeycomb materials. The numerical model for simulating the dynamic crushing of AL-STAR showed good agreement with the first test series data when the correct dynamic factor was incorporated in the computer model (Table 2.A.3).

While the prediction model for simulating AL-STAR crushing under 9-meter drop conditions was extremely well correlated, the peak deceleration under the end- drop condition in the August 1997 tests exceeded the acceptance criteria.

The second series of tests wherein the crush strength of the honeycomb was lowered (as selected by the prediction model), performed as expected. The agreement between the test data and the prediction model is high (Table 2.A.4).

The prediction model for AL-STAR therefore stands correlated with seven (7) quarter-scale drop events. The first three tests used different honeycomb crush strength materials than the last four, proving the ability of the prediction model to predict the AL-STAR crush performance for a wide range of crush material properties. The backbone structure of AL-STAR, enhanced after the 1/8-model static compression tests, performed as designed in all seven quarter-scale drop tests.

Finally, the AL-STAR-to-overpack attachment system remained intact and the cask did not contact the unyielding target during all four final dynamic tests.

2.A.12 References

[2.A.1] ANSYS 5.3 Ansys Inc., 1996.

[2.A.2] CADKEY, Version 7, 1996.

[2.A.3] Project Procedure No. HPP-5014-5, HI-STAR Aluminum Honeycomb 1/8 Scale Impact Limiter Static Test Procedure.

[2.A.4] HI-STAR 1/8 Scale Impact Limiter Test Report, HI-961501, Holtec International, June 1996.

[2.A.5] Holtec Report HI-971774, Impact Limiter Test Results – 30' Drop Tests – August 1997

[2.A.6] Holtec Report HI-971783, Improved Correlation of ORNL 30' Drop Tests – August 1997

[2.A.7] Holtec Report HI-981891, "Impact Limiter Test Report - Second Series", (Rev. 1), 1998.

[2.A.8] Deltagraph Pro 3.5, Deltapoint Software, 1995.

[2.A.9] J.M. Lewallen and E.A. Ripperger, Energy Dissipating Characteristics of Trussgrid Aluminum Honeycomb, SMRL RM-5, University of Texas Structural Mechanics Research Laboratory, 1962.

[2.A.10] Working Model 3.0, Knowledge Revolution, 1995.

[2.A.11] HI-STAR 100 Impact Limiter Test Program, Holtec Report No. HI-951278.

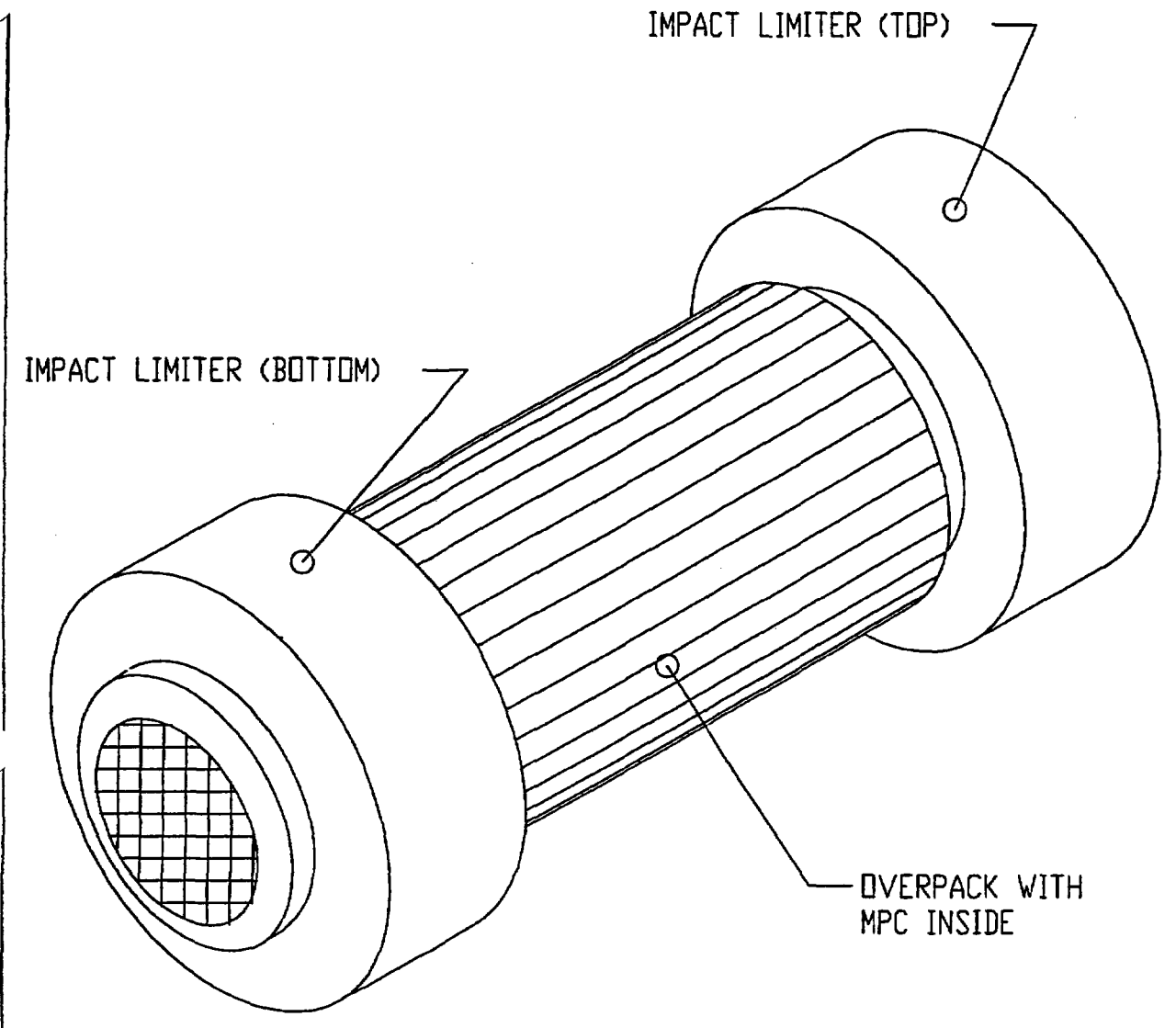

FIGURE 2.A.1.1; HI-STAR 100 PACKAGE WITH TOP AND BOTTOM IMPACT LIMITERS

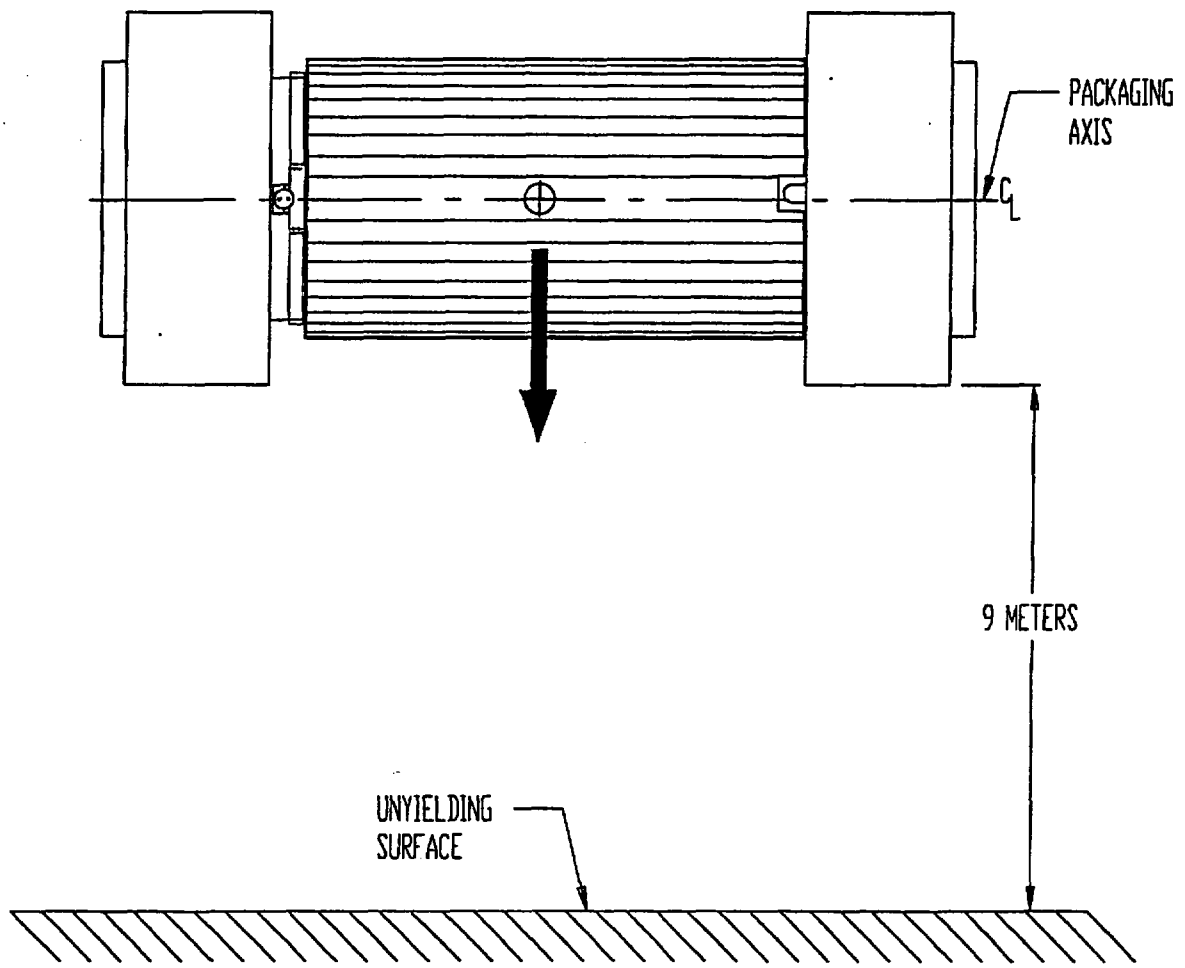

FIGURE 2.A.1.2; DROP FROM 9 METERS ON TO AN ESSENTIALLY UNYIELDING SURFACE (HYPOTHETICAL ACCIDENT CONDITION)

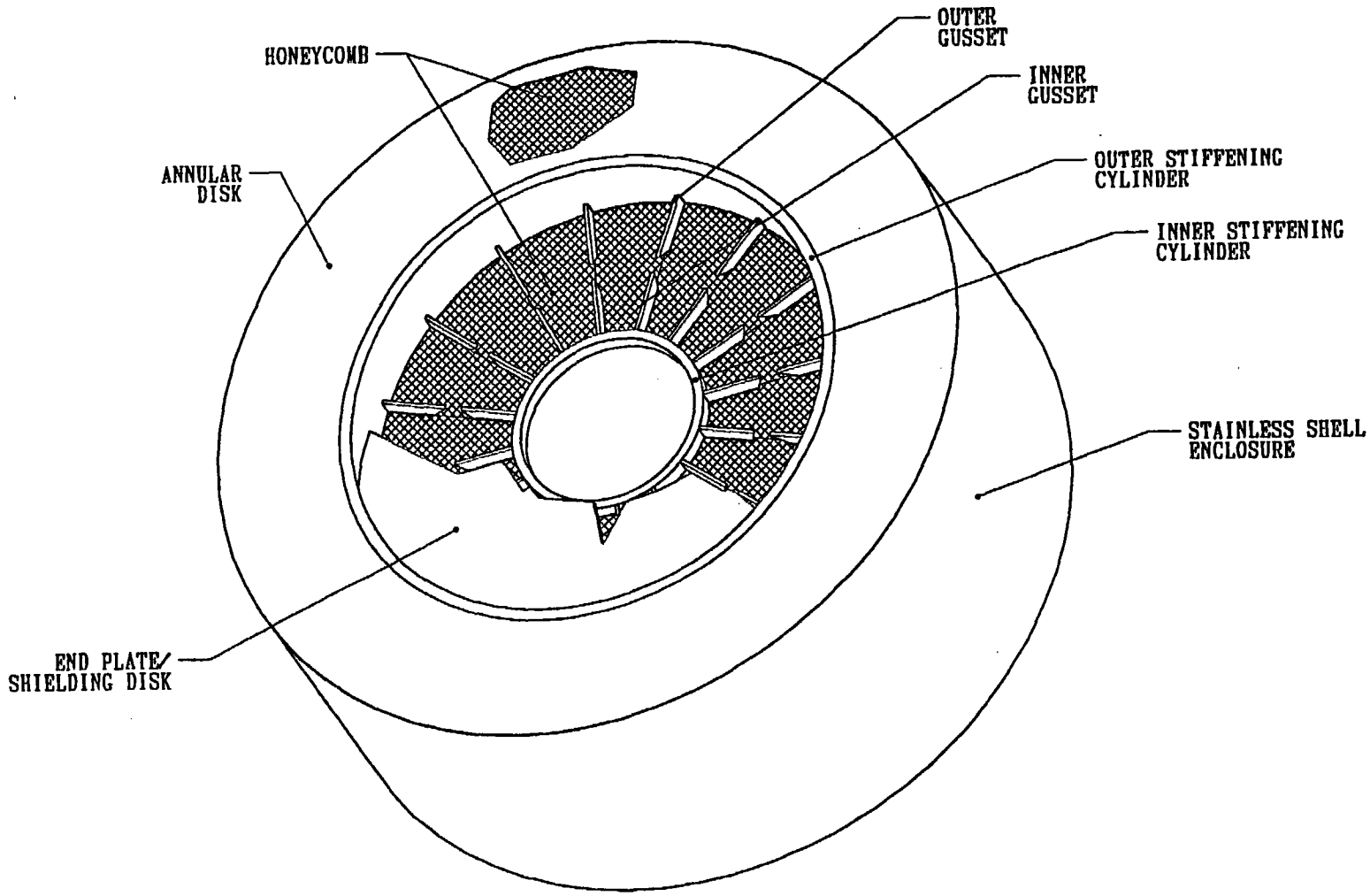

FIGURE 2.A.1.3; PICTORIAL VIEW OF AL-STAR (WITH A PORTION REMOVED)

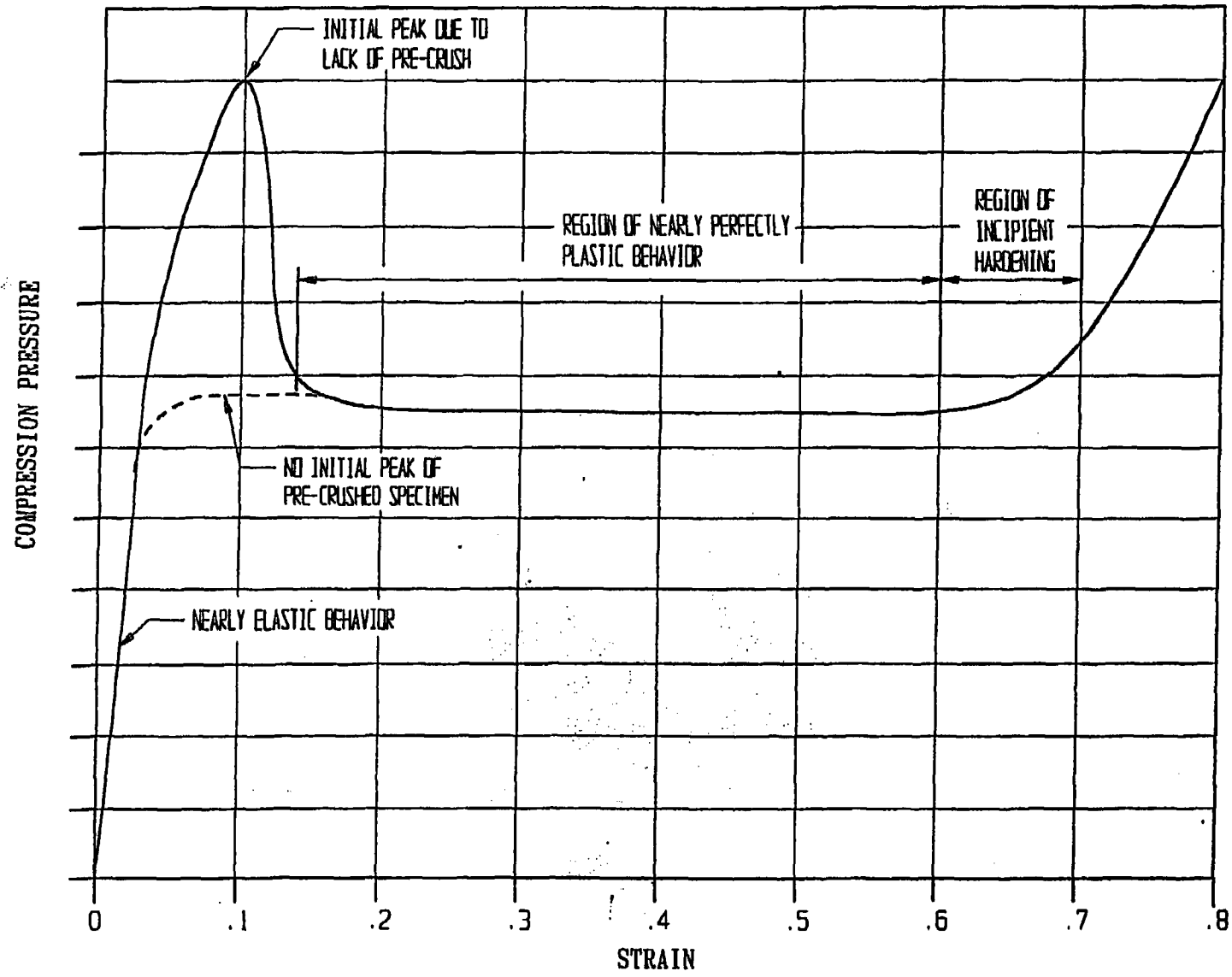

FIGURE 2.A.2.1; PRESSURE-CRUSH STRAIN CURVE (STATIC TESTING)

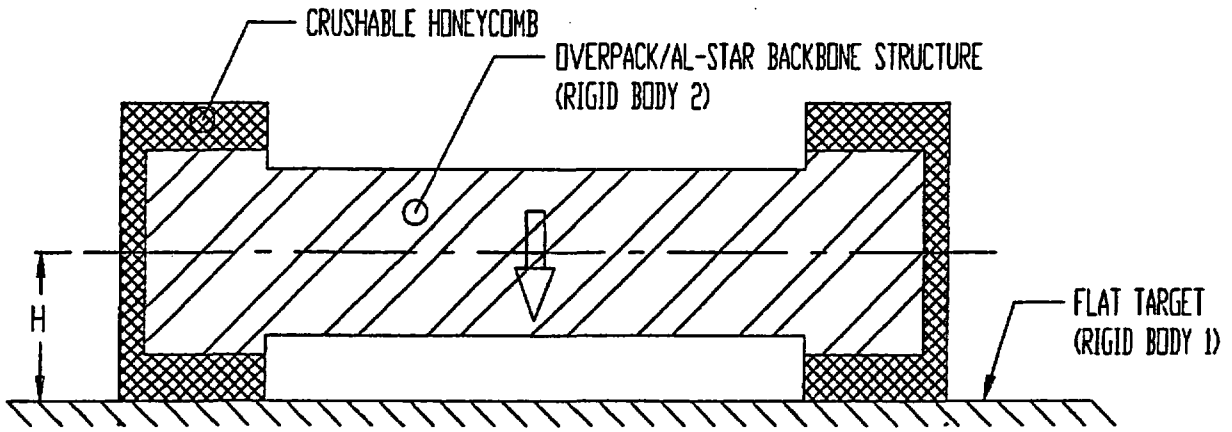

(a) TWO RIGID BODIES APPROACH EACH OTHER WITH A SOFT CRUSHABLE METAL MASS BETWEEN THEM (INITIATION OF CRUSHING)

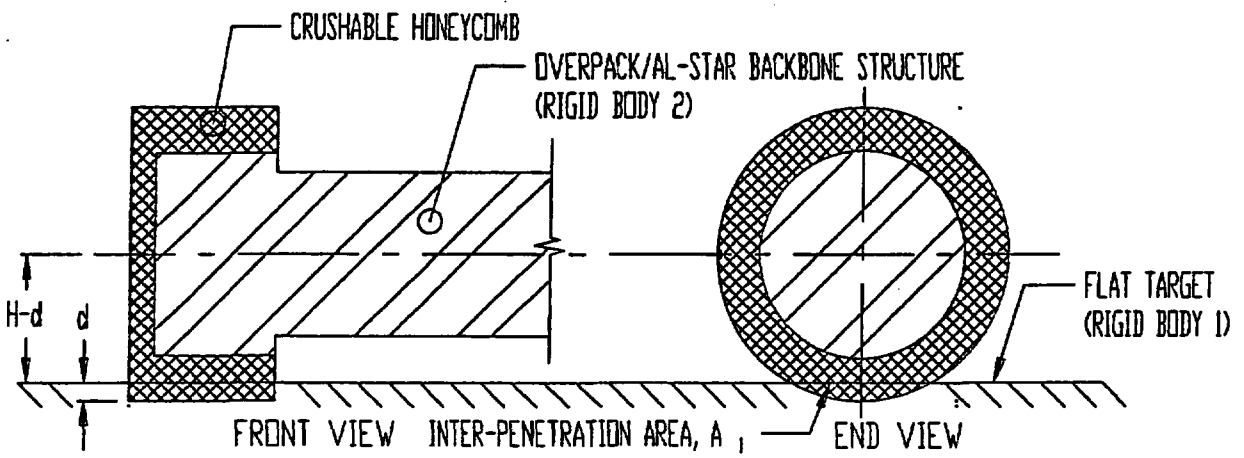

(b) SCENARIO ONE: CRUSHING OCCURS AT THE AL-STAR/TARGET INTERFACE; DEFORMATION = d; NO CRUSH AT AL-STAR BACKBONE/HONEYCOMB INTERFACE

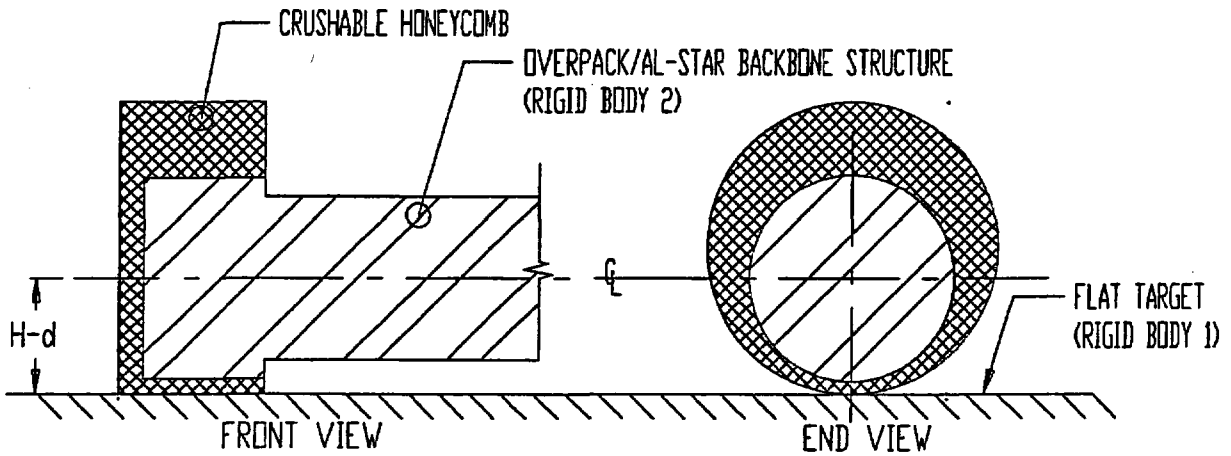

(c) SCENARIO TWO: CRUSHING OCCURS AT THE AL-STAR BACKBONE/HONEYCOMB INTERFACE.; NO CRUSH AT THE AL-STAR/TARGET INTERFACE

FIGURE 2.A.3.1; ILLUSTRATION OF THE FORCE-CRUSH MODEL CONSTRUCTION USING THE EXAMPLE OF THE SIDE DROP EVENT.

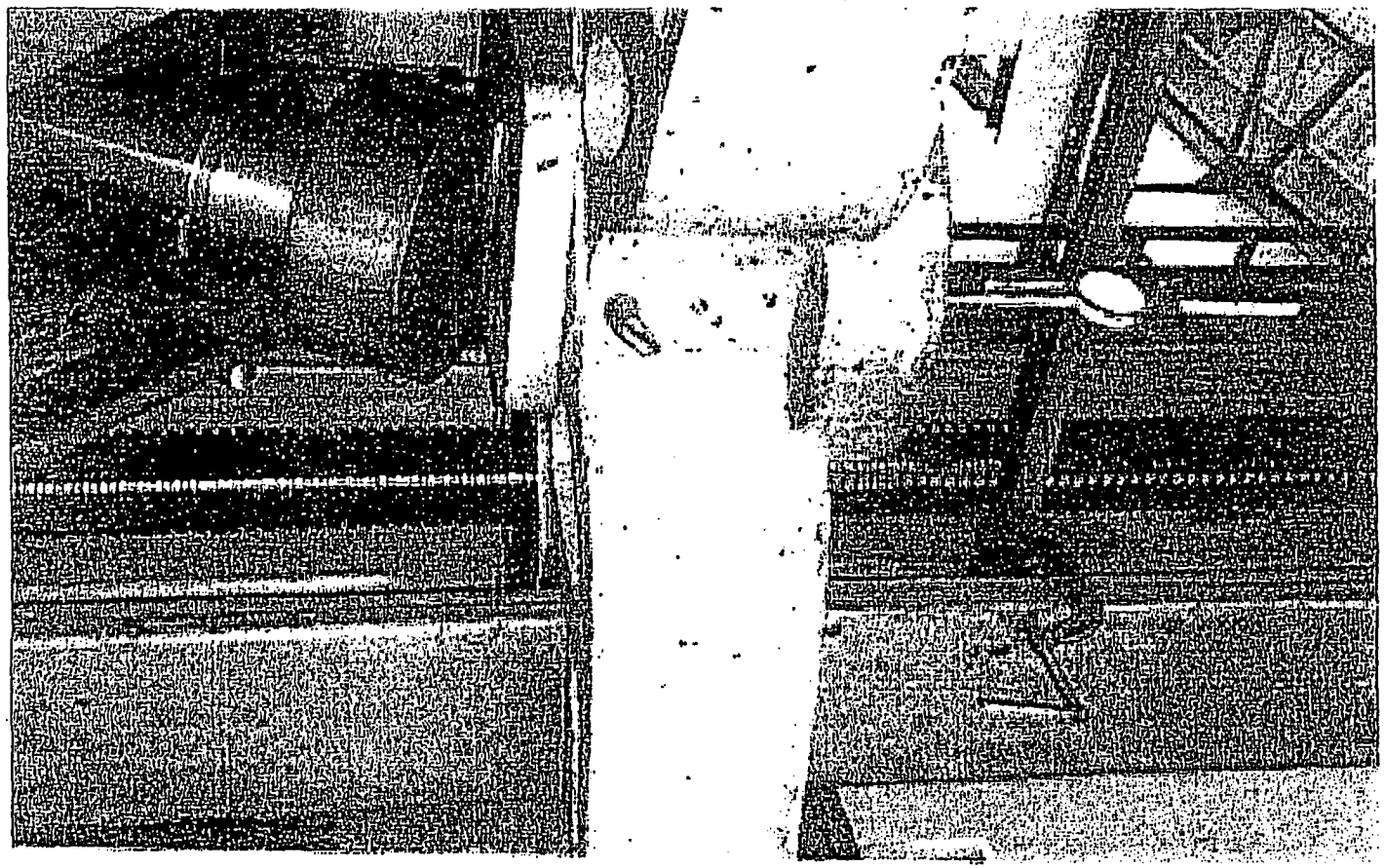

FIGURE 2.A.4.1 ; **TEST FIXTURE**

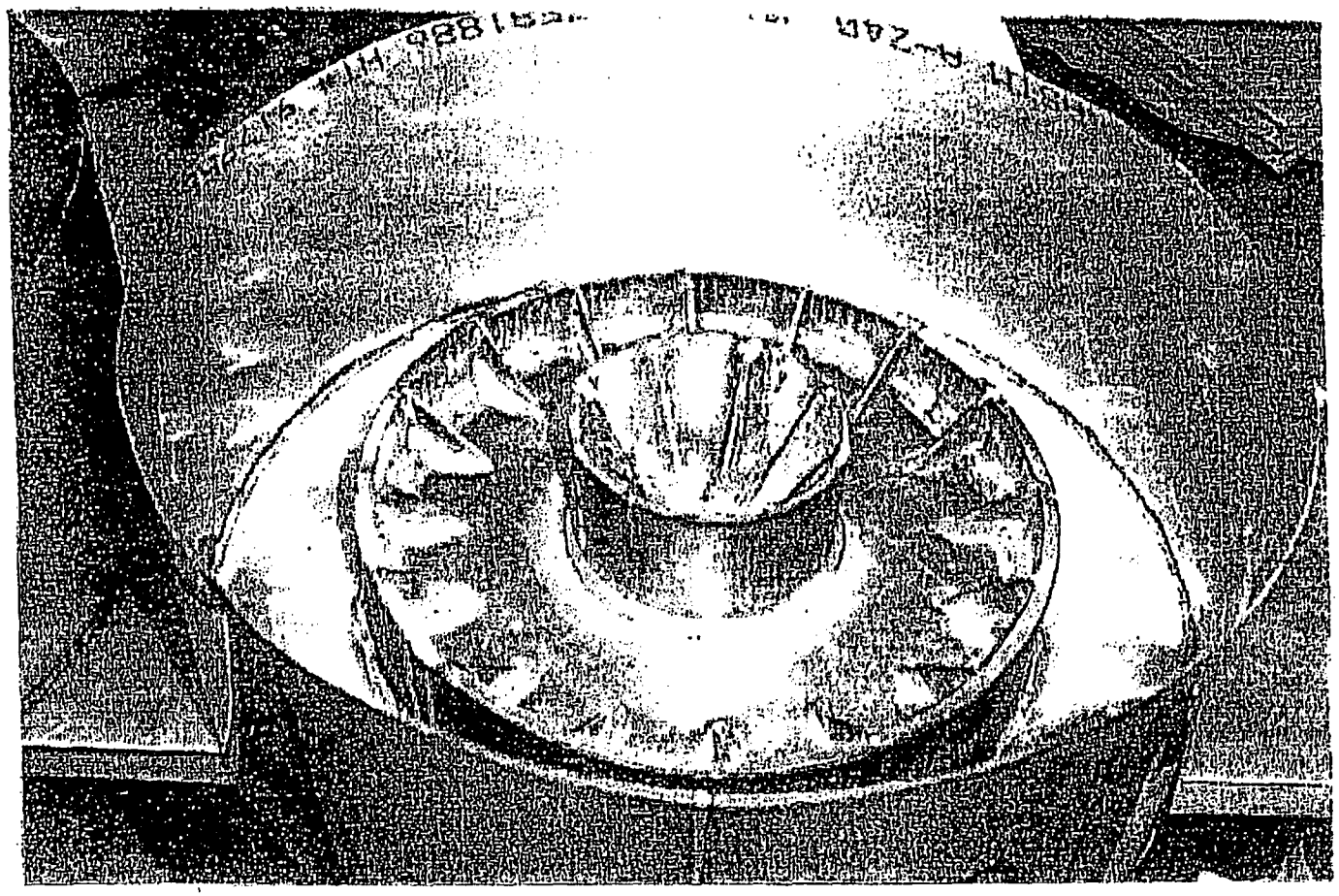

FIGURE 2.A.4.2 ; INTERNAL STIFFENING STRUCTURE IN 1/8 SCALE MODEL

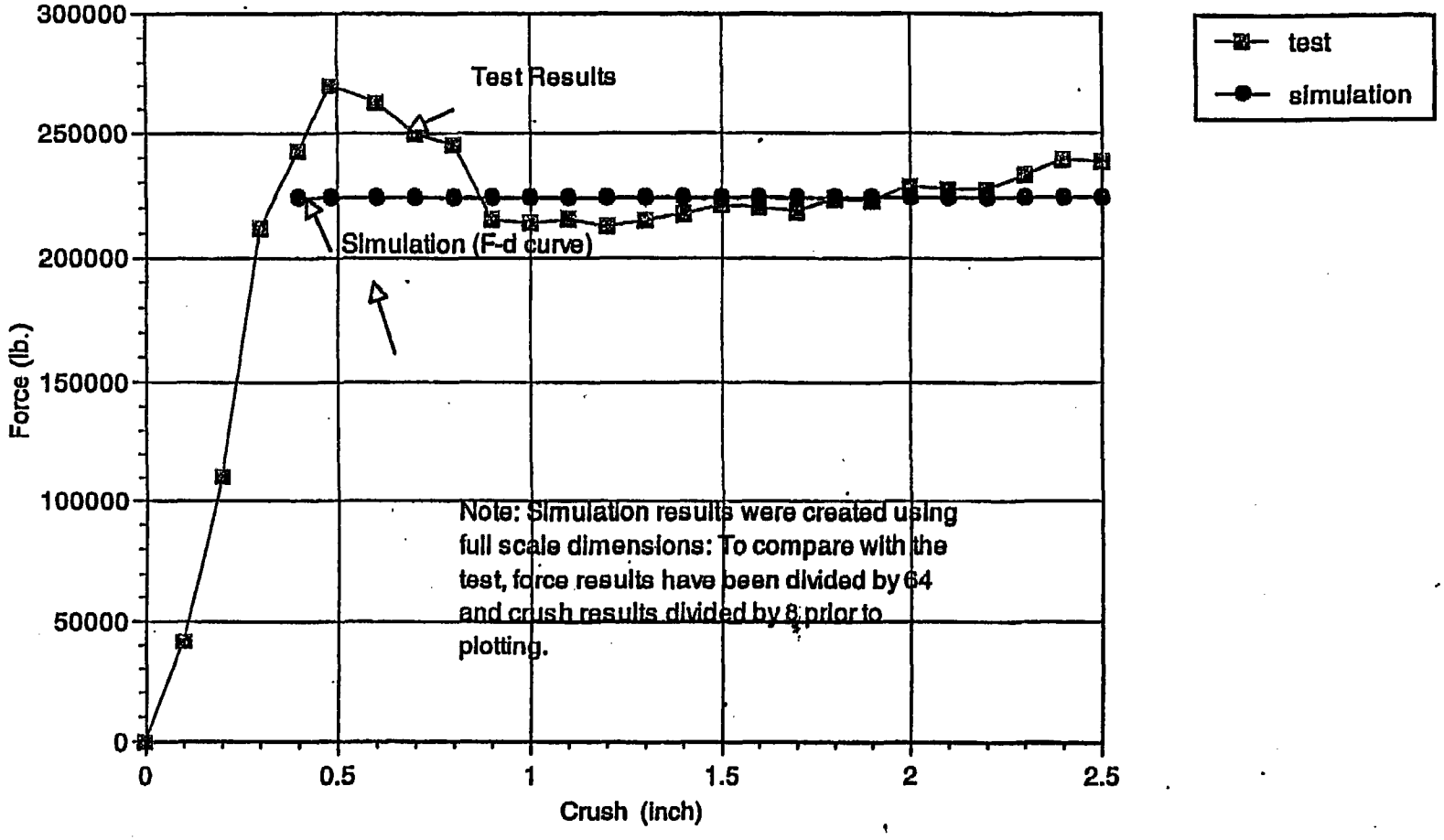

FIGURE 2.A.4.3 - 1/8th Scale Initial Impact Limiter Configuration - Comparison of Static Force-Crush Data from Test and Simulation - END DROP

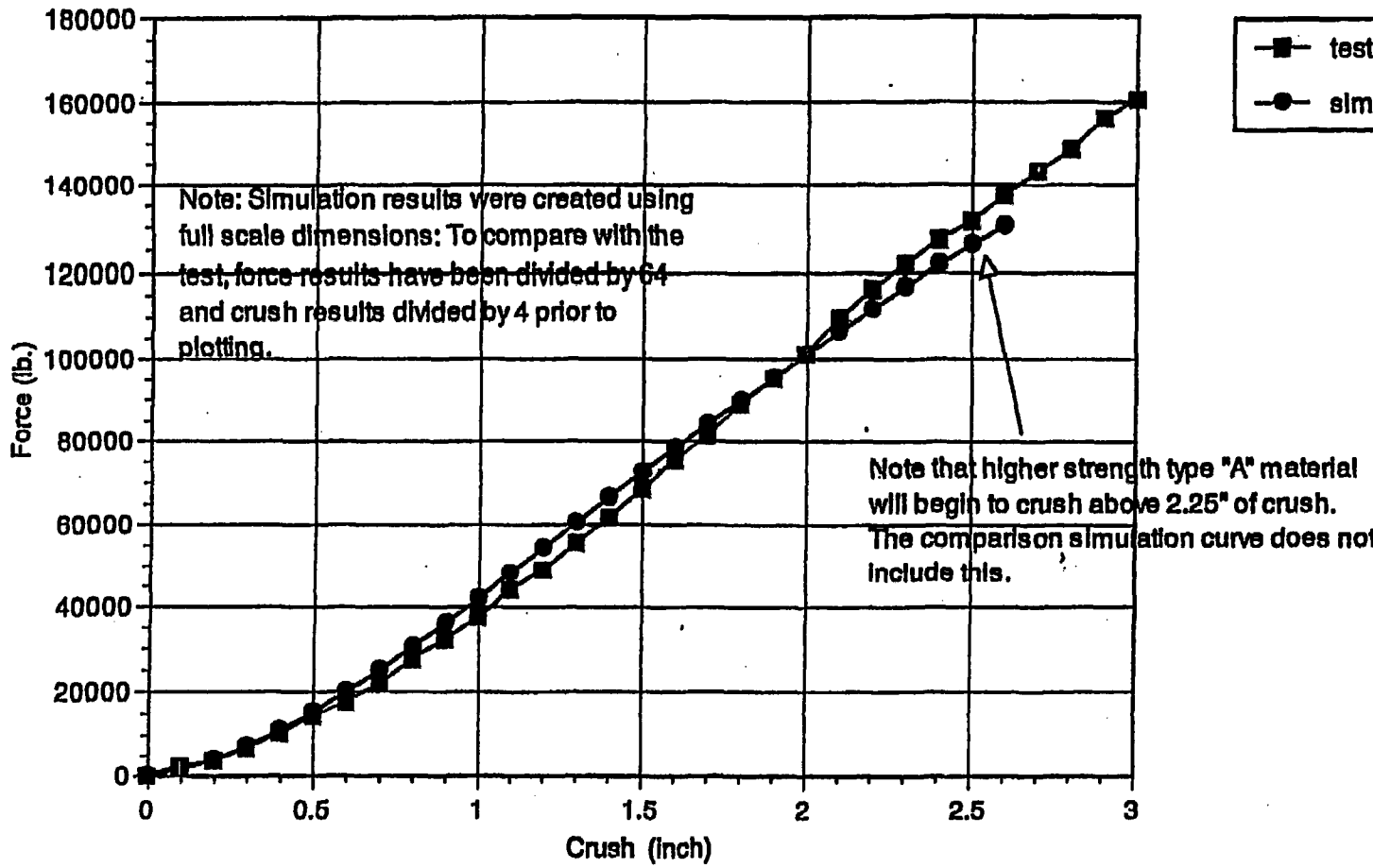

FIGURE 2A.4.4 : 1/8th Scale Initial Impact Limiter Configuration - Comparison of Static Force-Crush Data from Test and Simulation - 60 DEGREE CRUSH

FIGURE WITHHELD UNDER 10 CFR 2.390

FIGURE WITHHELD UNDER 10 CFR 2.390

FIGURE WITHHELD UNDER 10 CFR 2.390

FIGURE WITHHELD UNDER 10 CFR 2.390

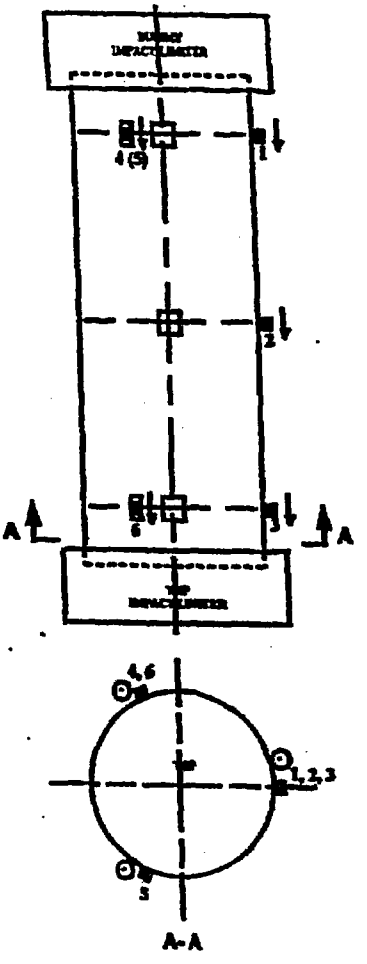

(a) Accelerometer Location - Top End Drop

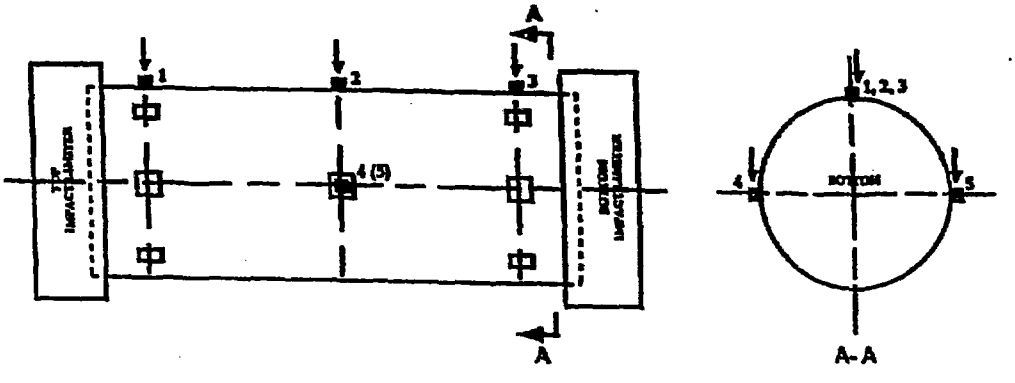

FIGURE 2.A.5.5 ; ACCELEROMETER LOCATIONS FOR END AND SIDE DROPS

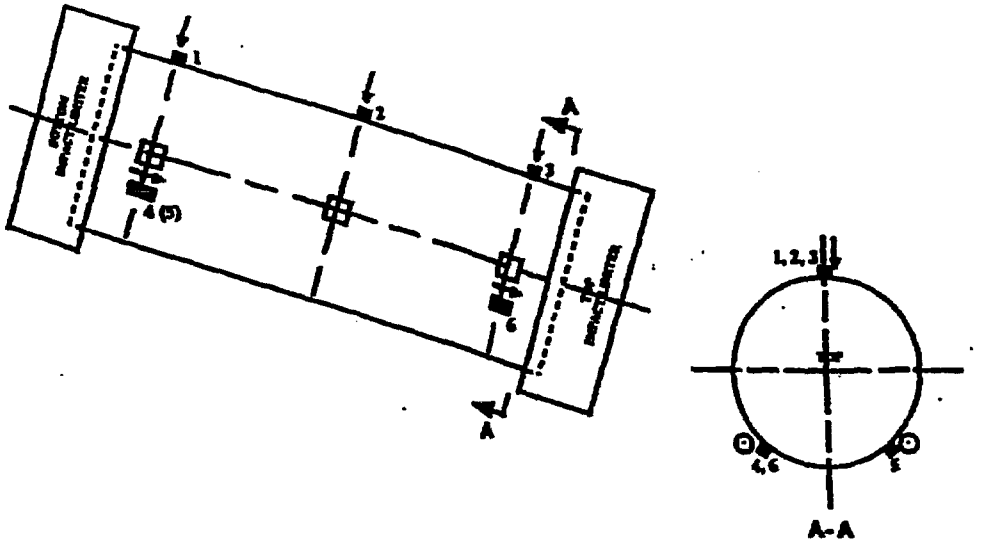

(c) Accelerometer Location - Slap Down Drop

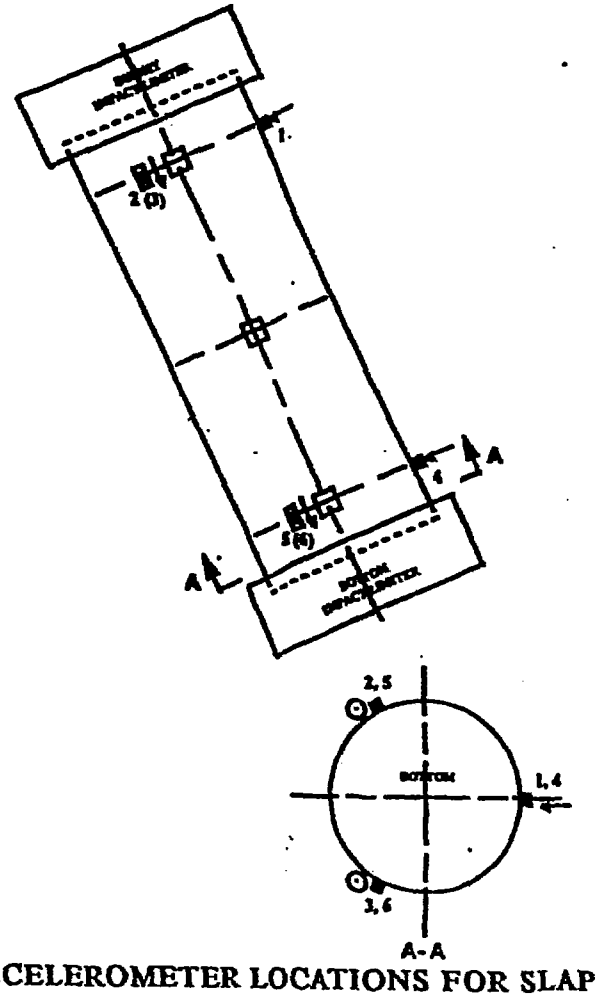

FIGURE 2A5.6 : ACCELEROMETER LOCATIONS FOR SLAP DOWN AND CGOC DROPS

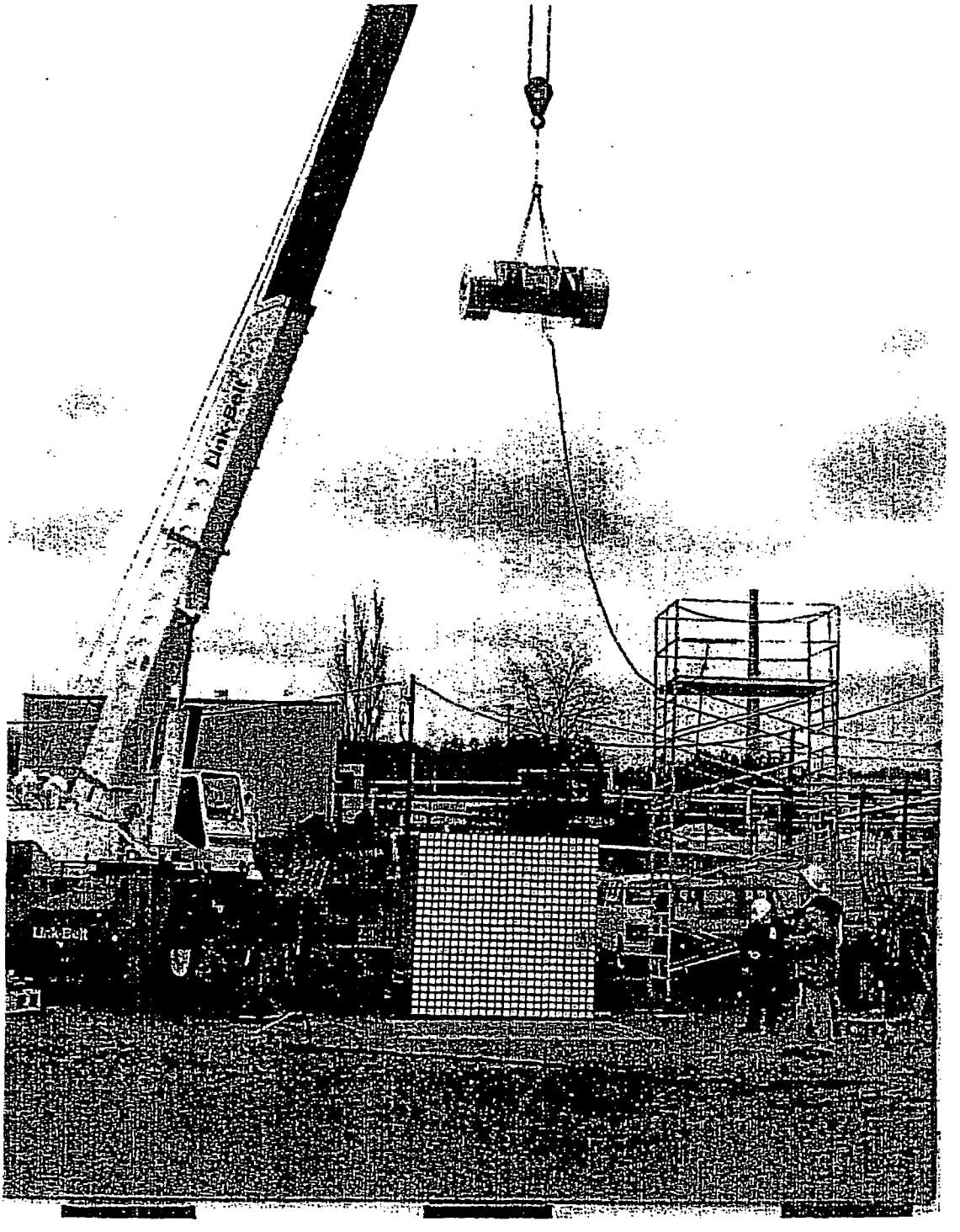

FIGURE 2.A.5.7 : ¼ SCALE HI-STAR 100 PACKAGING AT 30 FT (9 M) PRIOR TO SIDE DROP

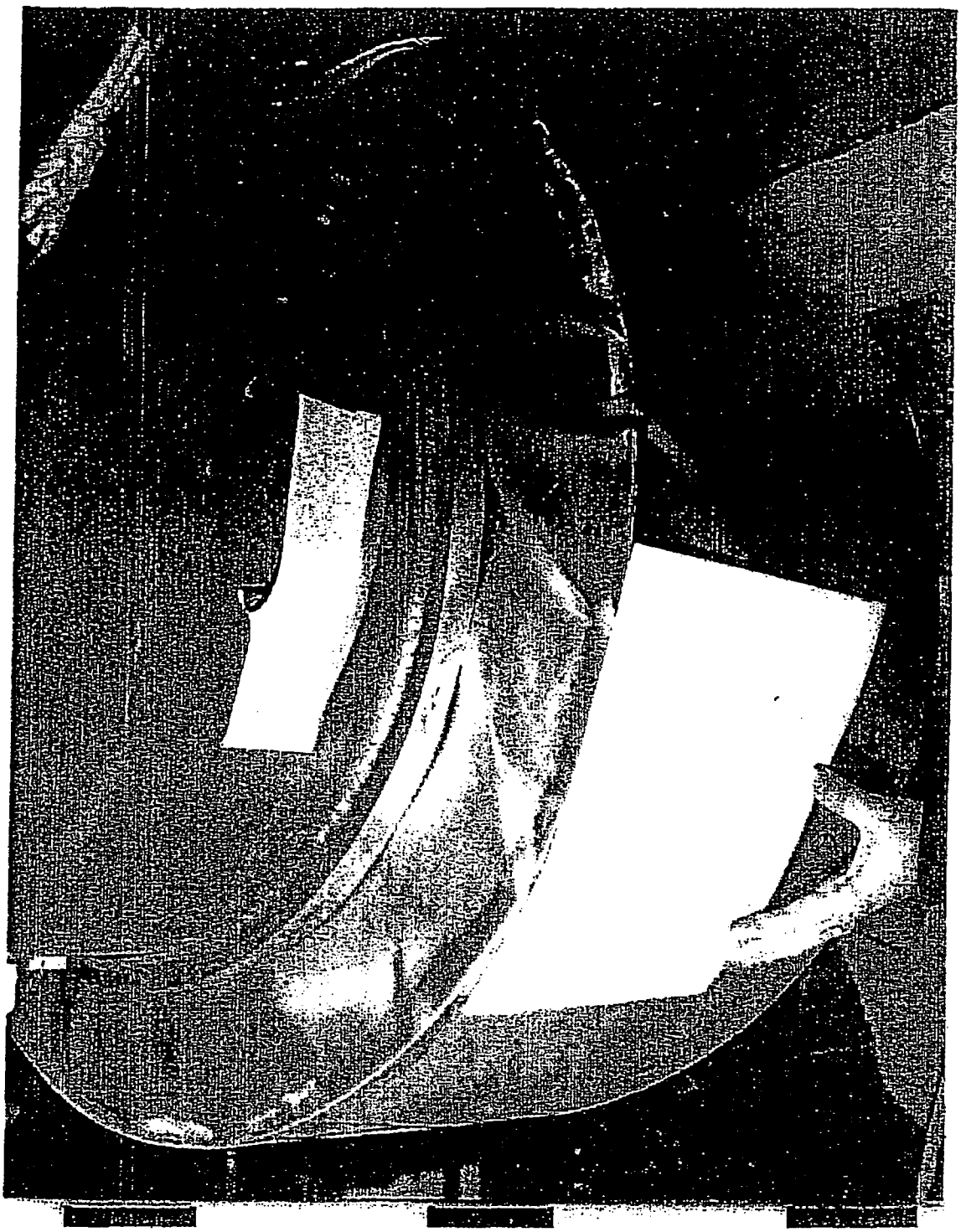

FIGURE 2.A.5.8 ; ¼ SCALE BOTTOM IMPACT LIMITER AFTER SIDE DROP

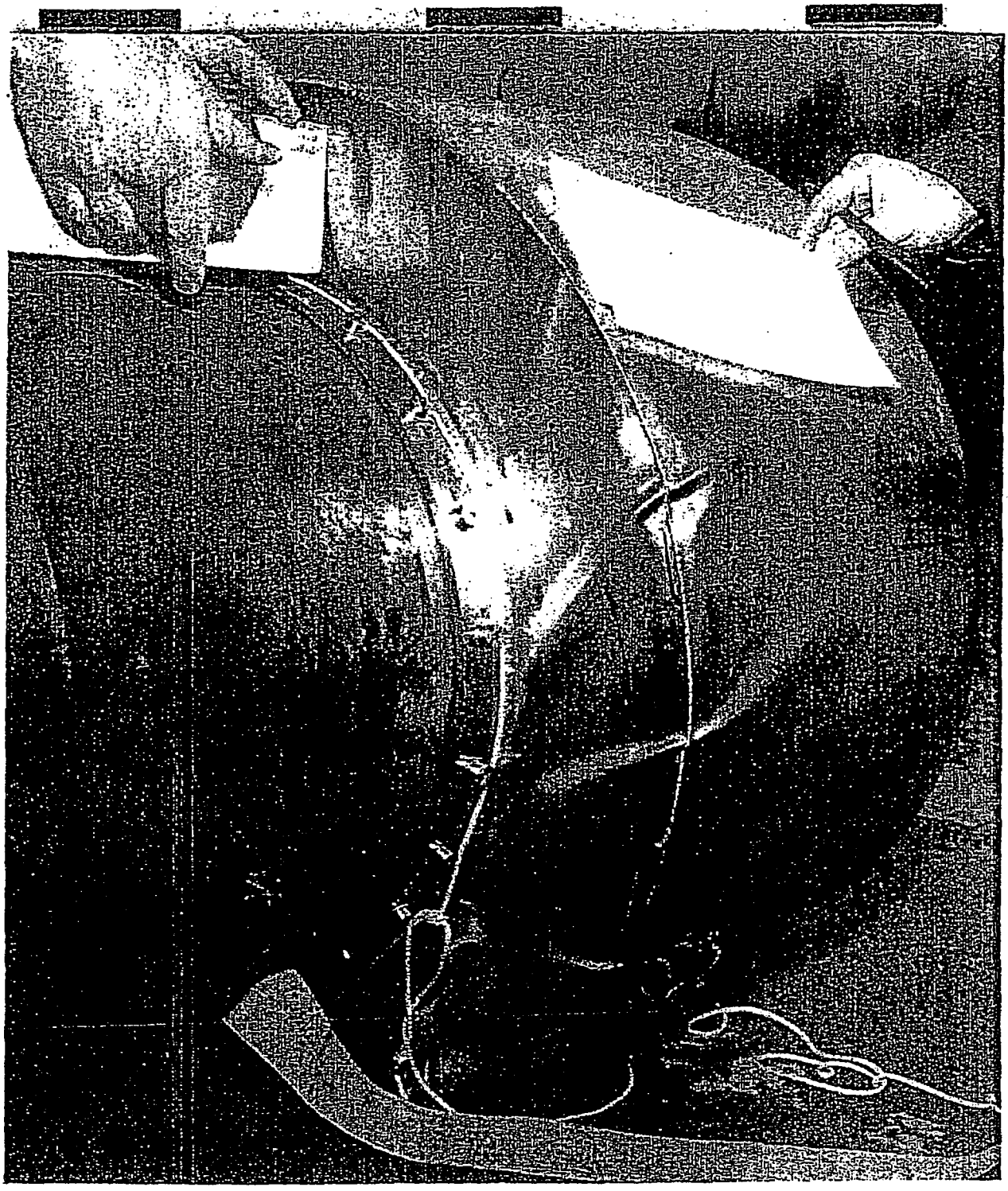

FIGURE 2.A.5.9 : 1/4 SCALE TOP IMPACT LIMITER AFTER SIDE DROP

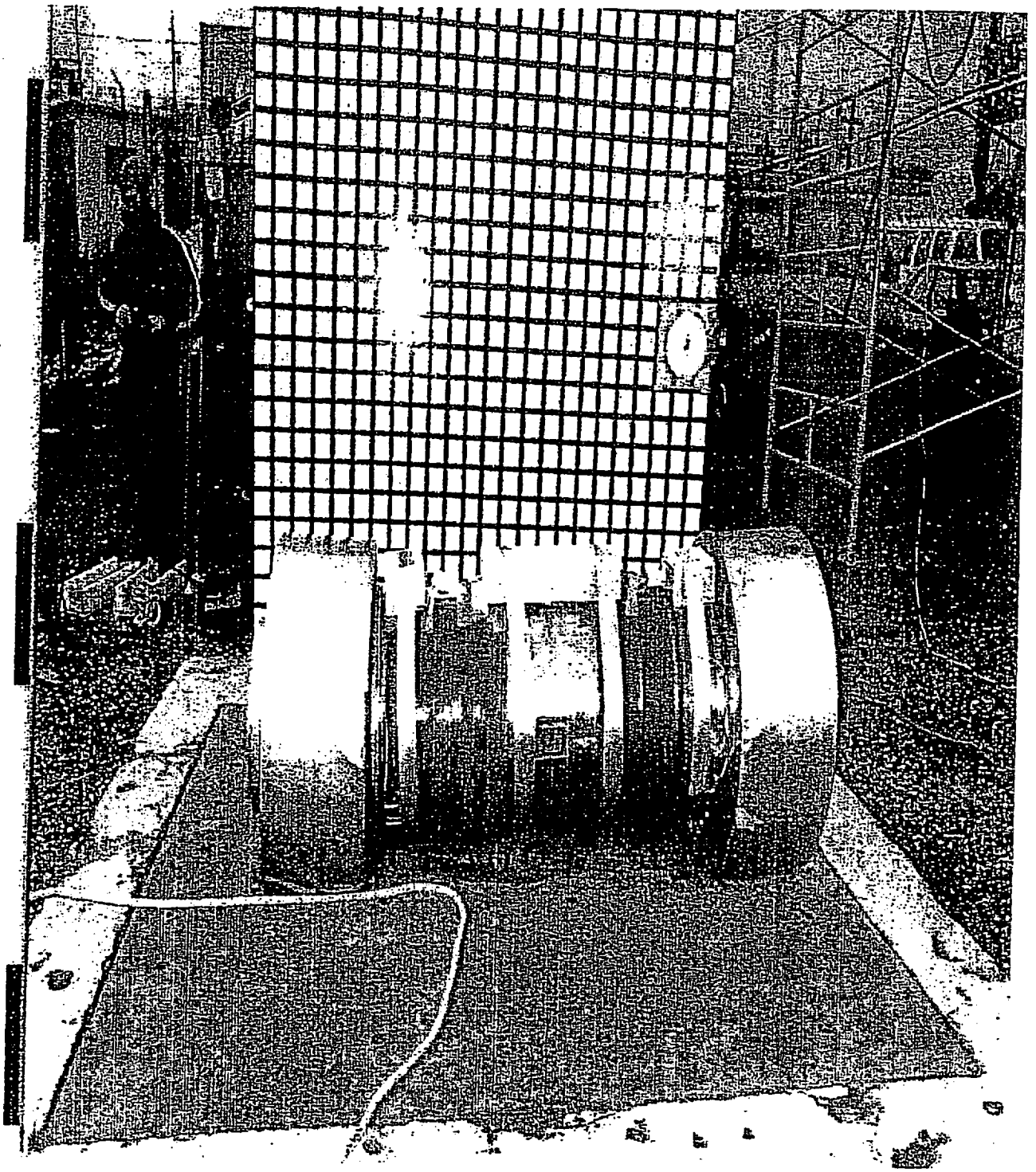

FIGURE 2.A.5.10 : 1/4 SCALE HI-STAR 100 PACKAGING AFTER SLAP DOWN DROP

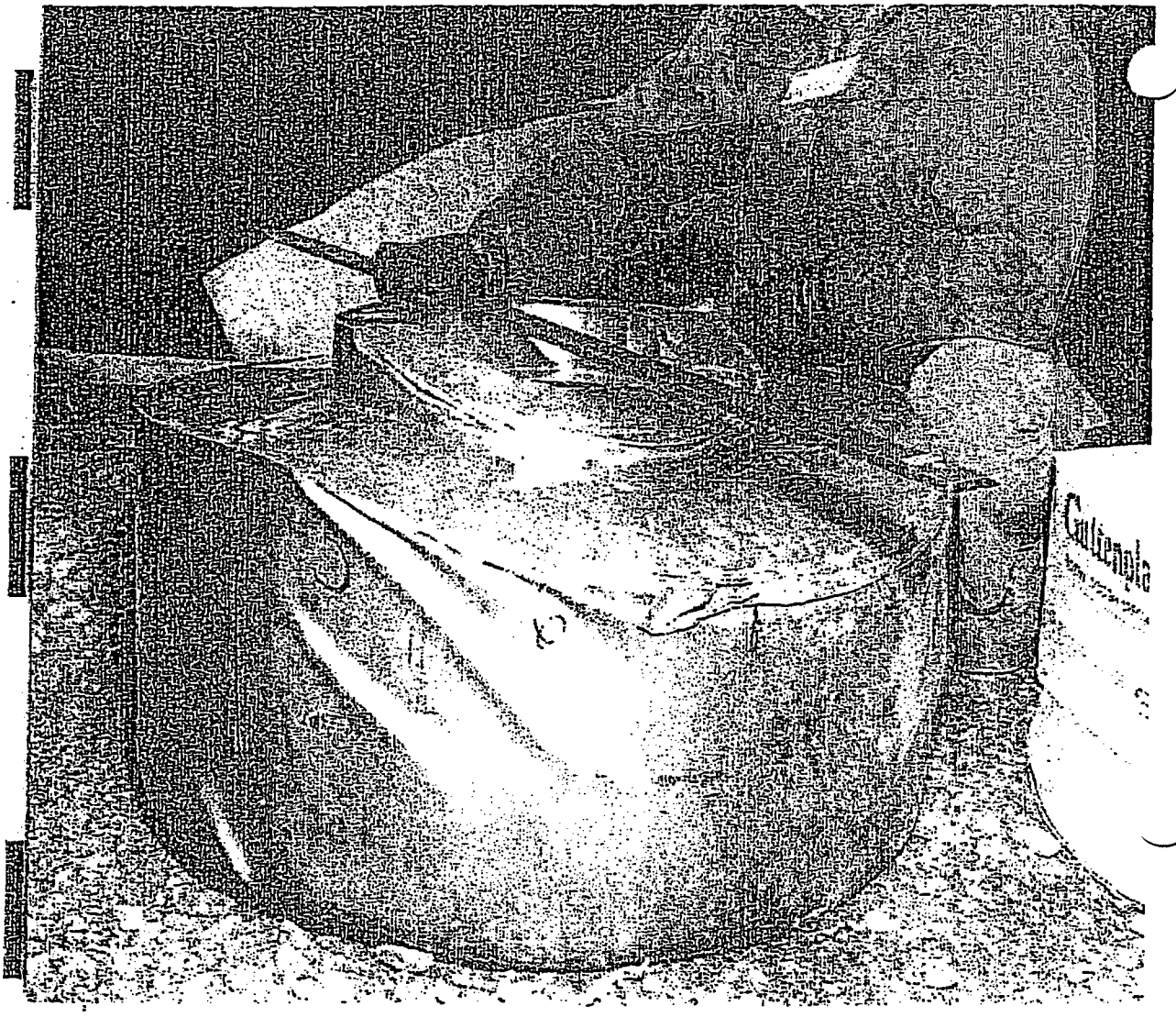

FIGURE 2.A.5.11 ; 1/4 SCALE IMPACT LIMITER AFTER C.G. OVER CORNER DROP

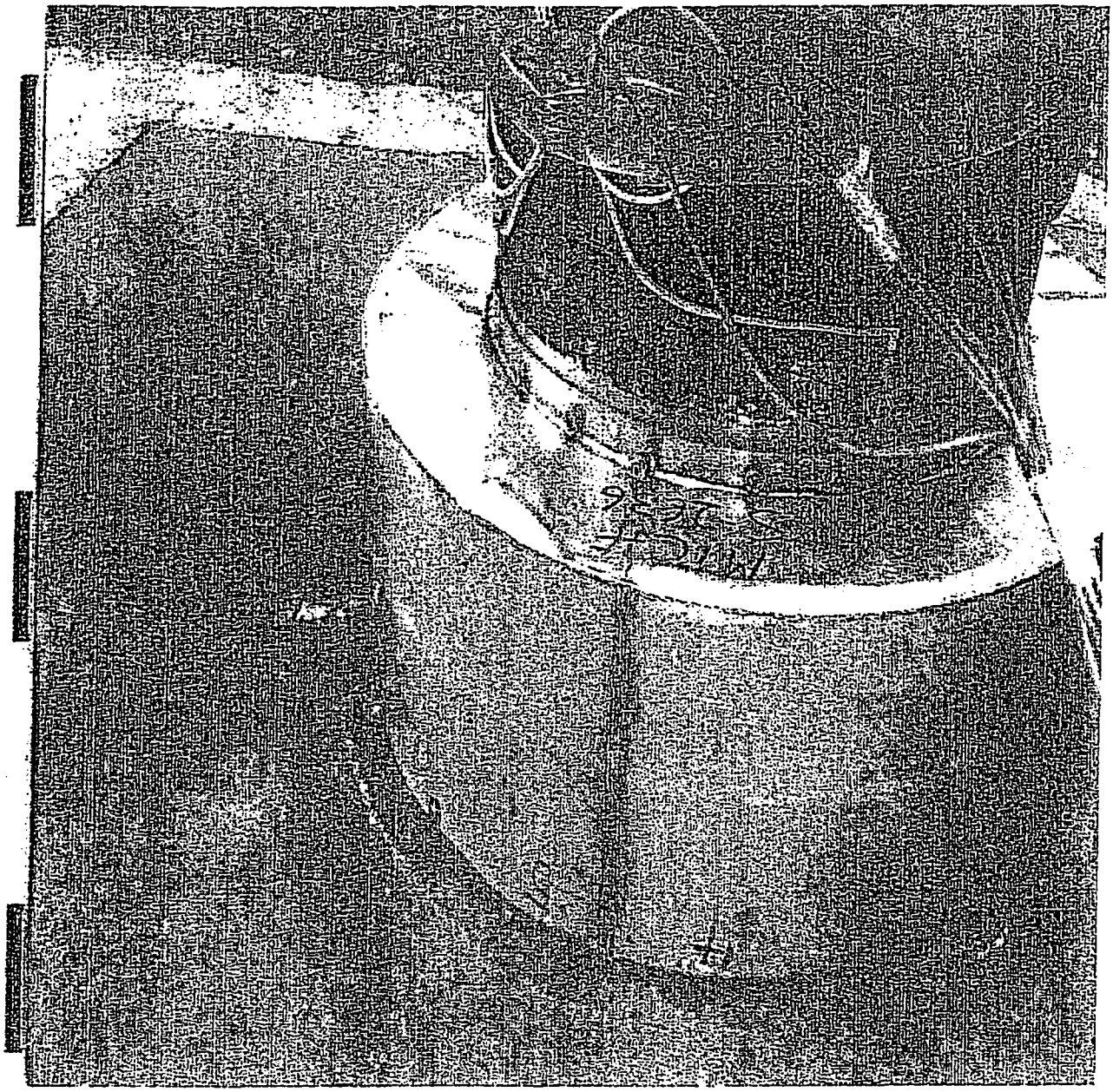

FIGURE 2.A.5.12 : 1/4 SCALE HI-STAR 100 PACKAGING AFTER TOP END DROP

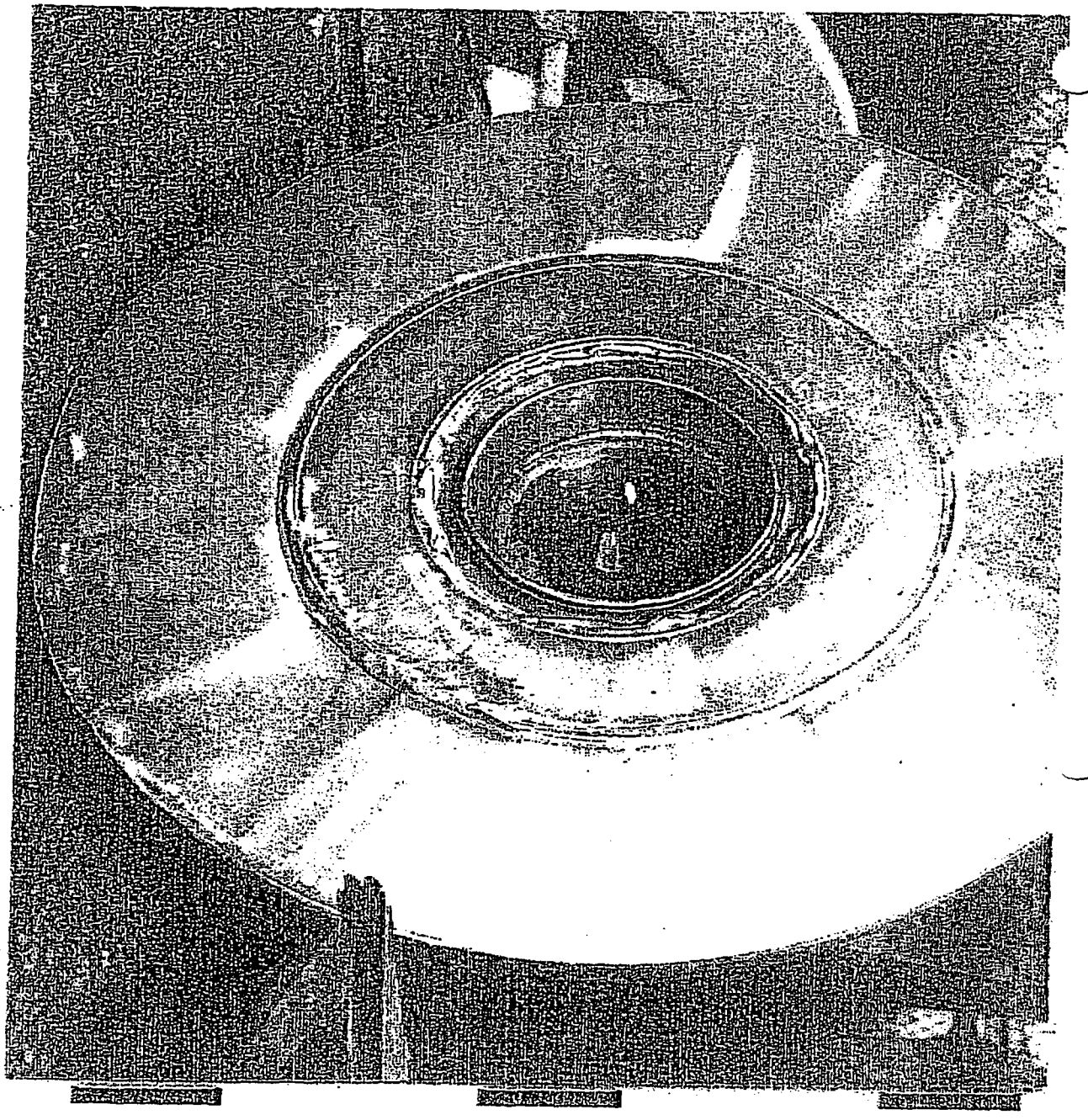

FIGURE 2.A.5.13 : 1/4 SCALE IMPACT LIMITER TOP END DROP

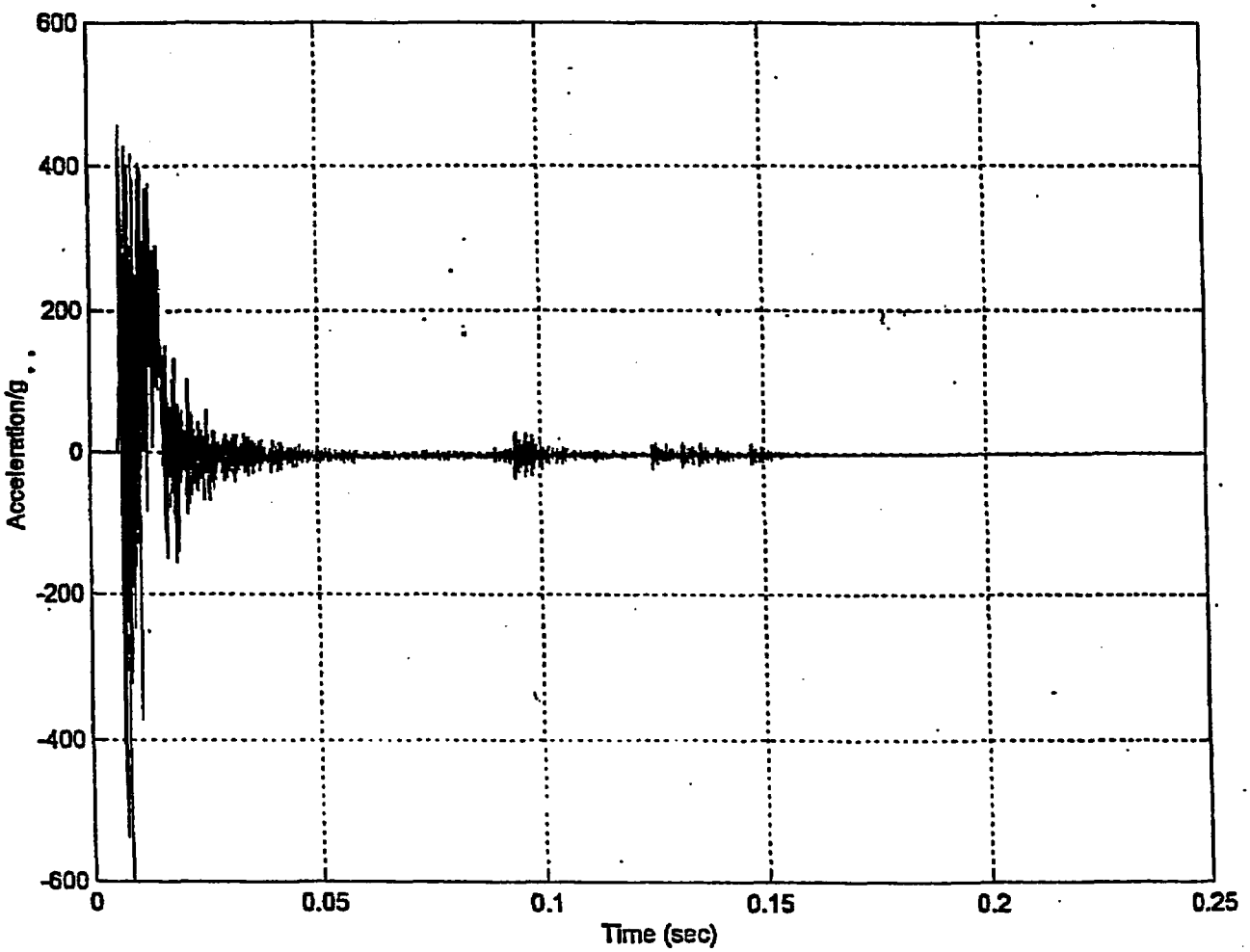

FIGURE 2.A.5.14 ; ACCELERATION RAW DATA FOR TOP END DROP

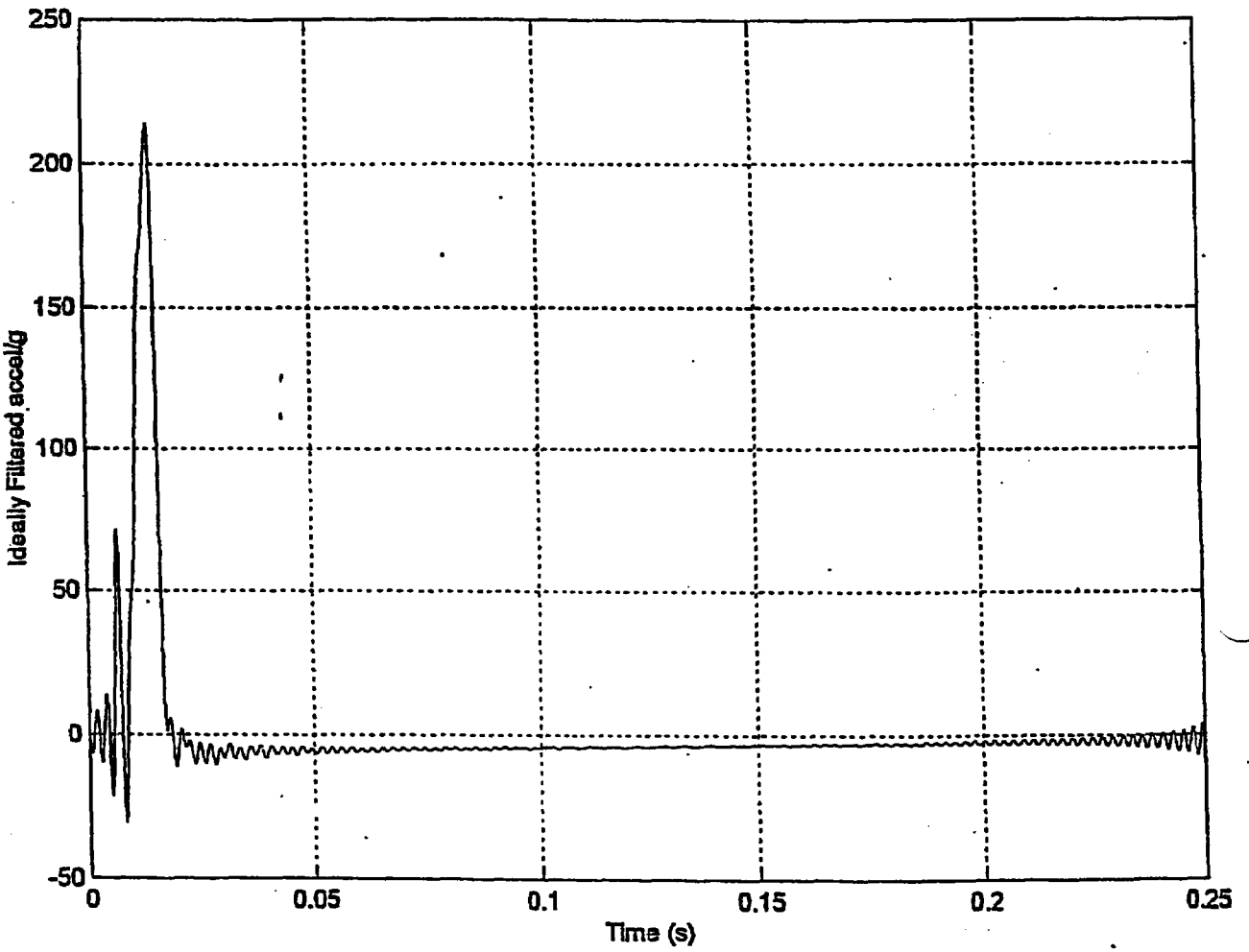

FIGURE 2.A.5.15 ; ACCELERATION DATA FILTERED AT 450 Hz FOR TOP END DROP

FIGURE 2.A.5.15A ; TOP END DROP

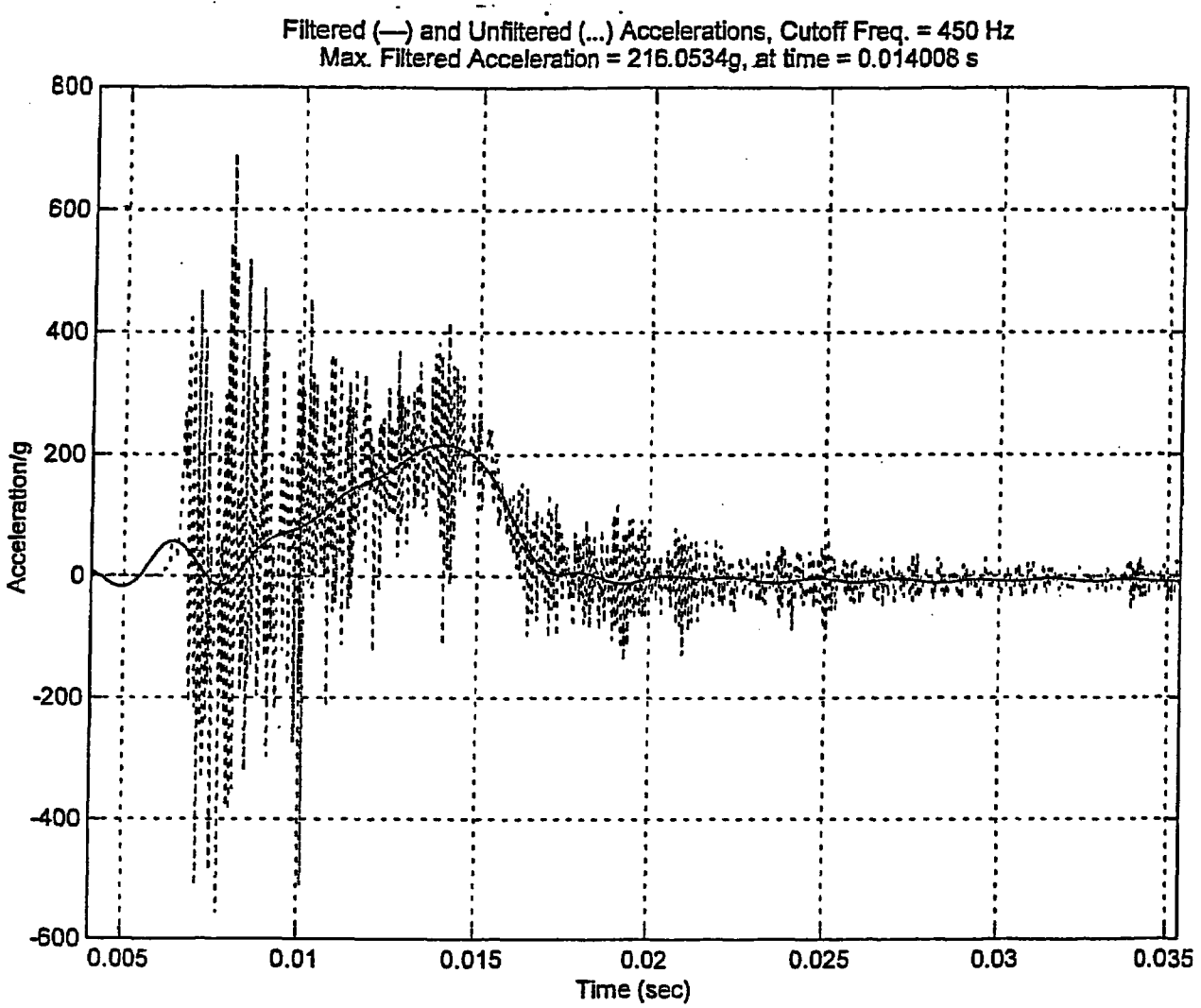

FIGURE 2.A.5.15B ; TOP END DROP

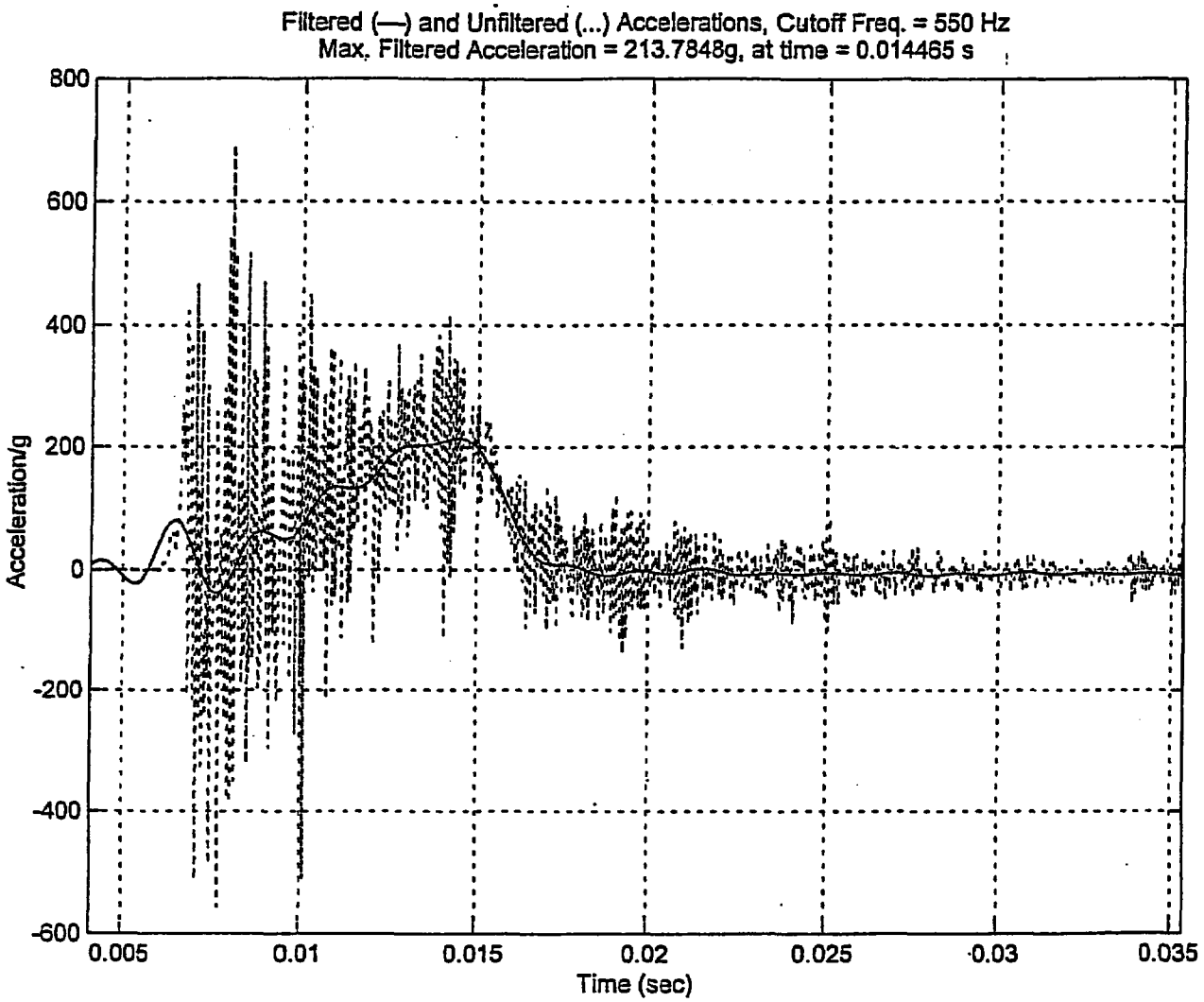

FIGURE 2.A.5.15C ; TOP END DROP

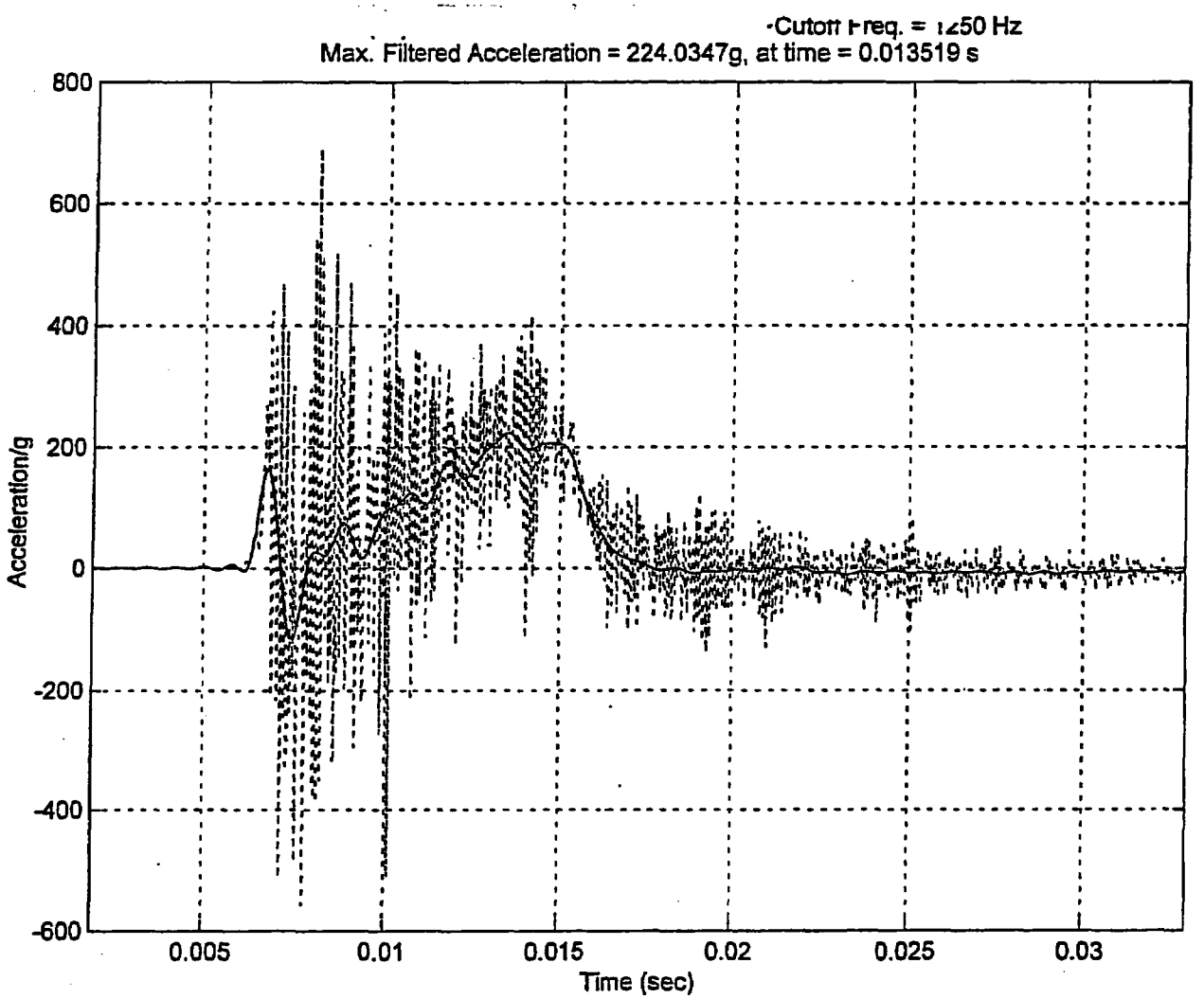

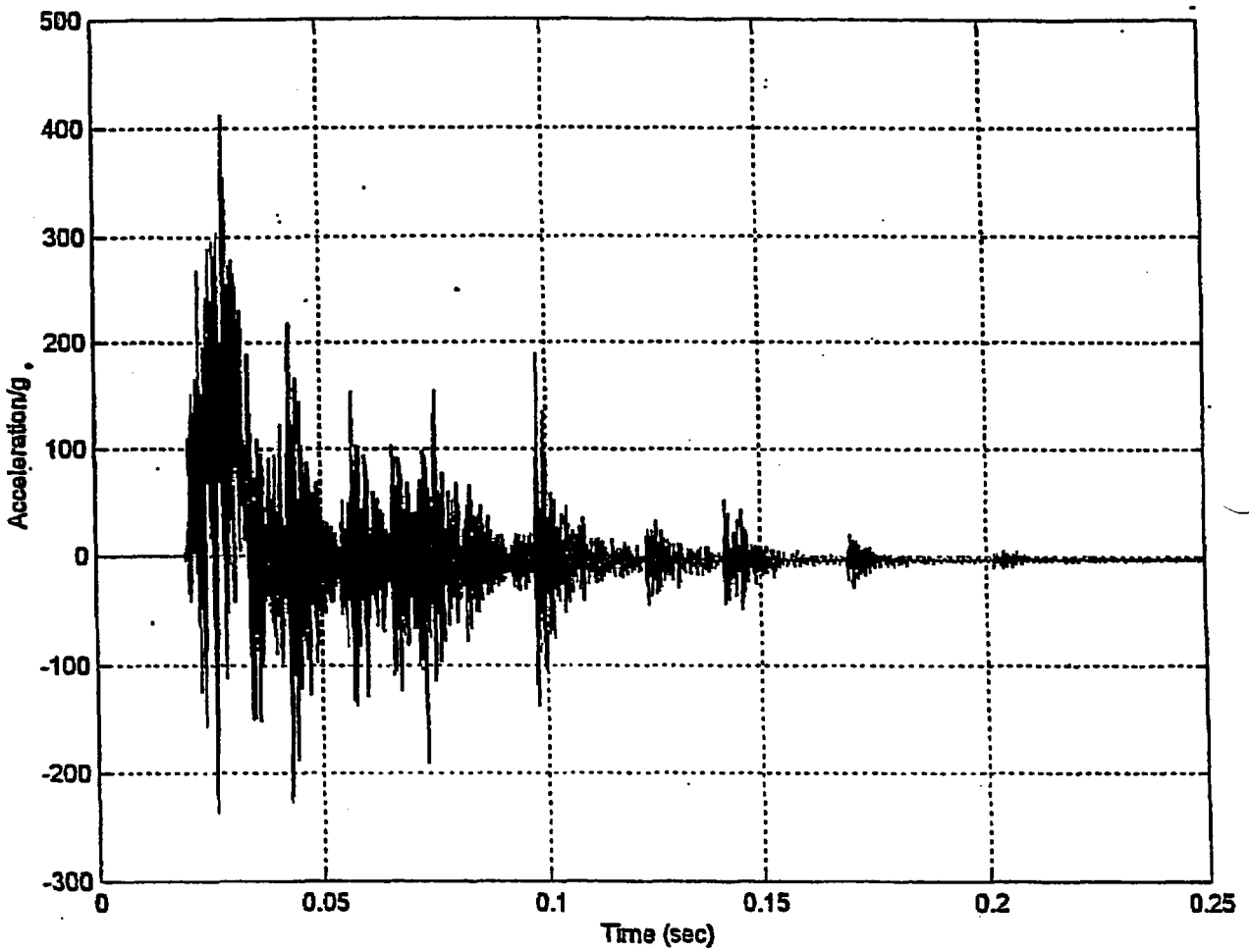

FIGURE 2.A.5.16 : ACCELERATION RAW DATA FOR C.G. OVER CORNER DROP

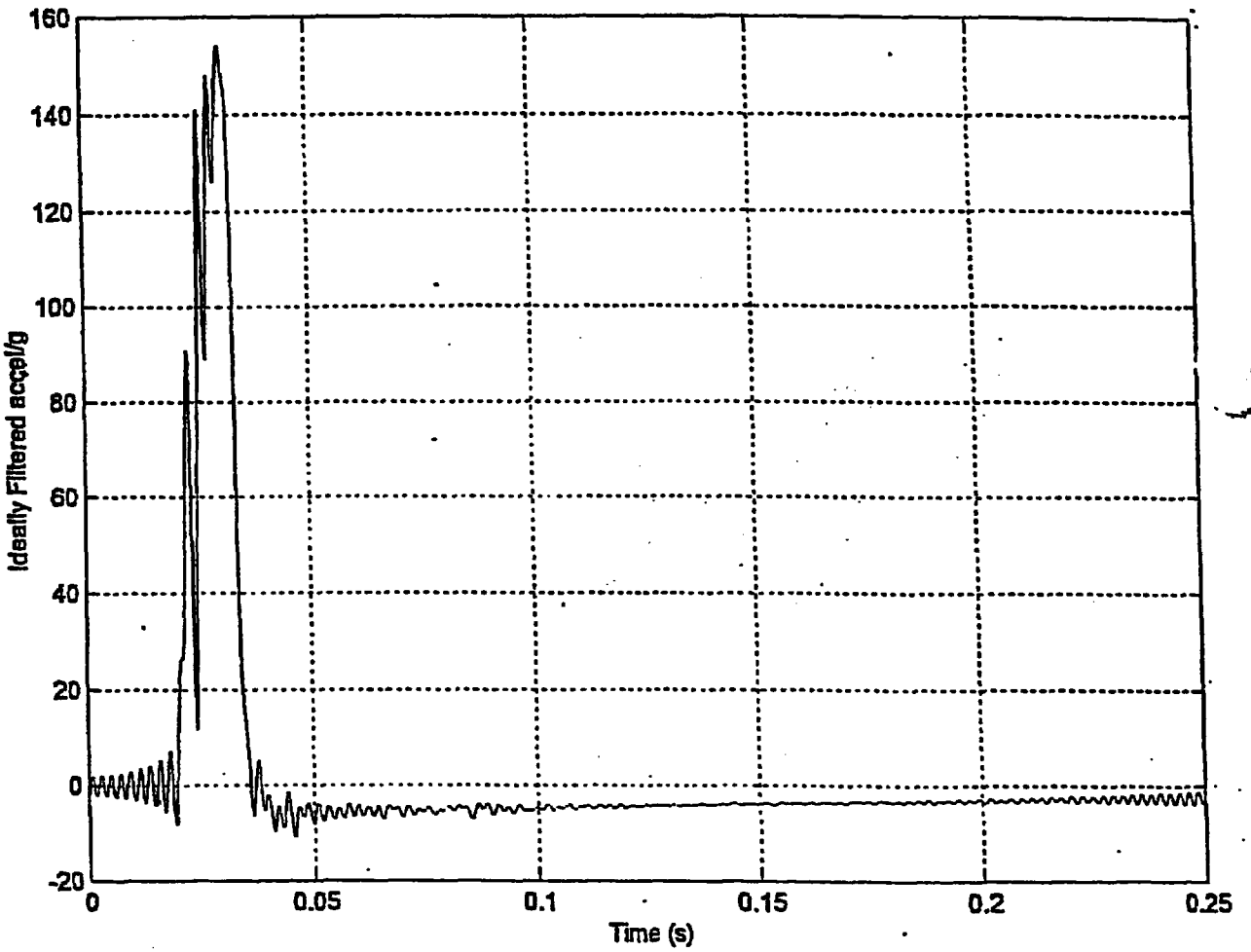

FIGURE 2.A.5.17 ; ACCELERATION DATA FILTERED AT 450 Hz FOR C.G. OVER CORNER

FIGURE 2.A.5.17A : CG OVER CORNER

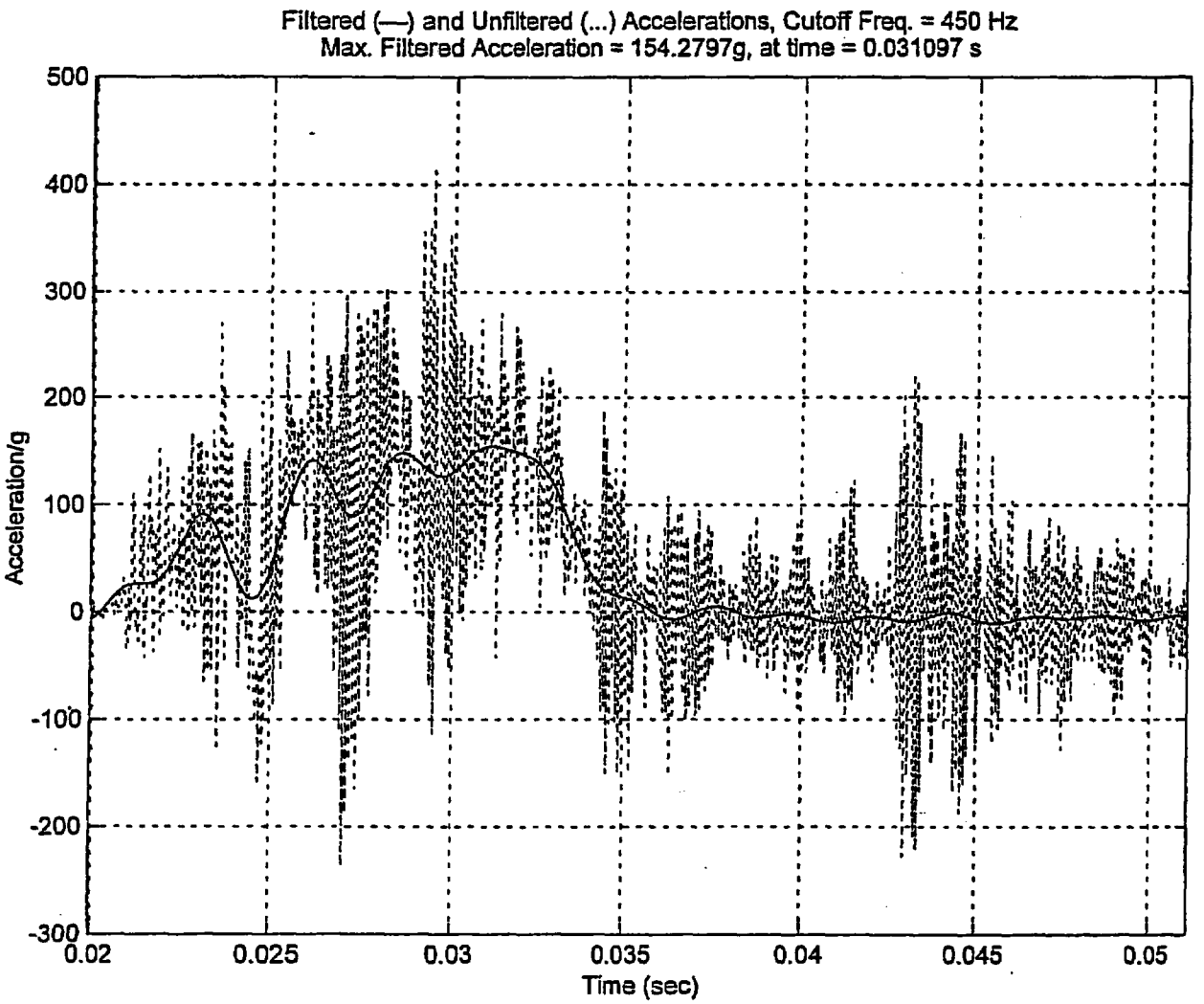

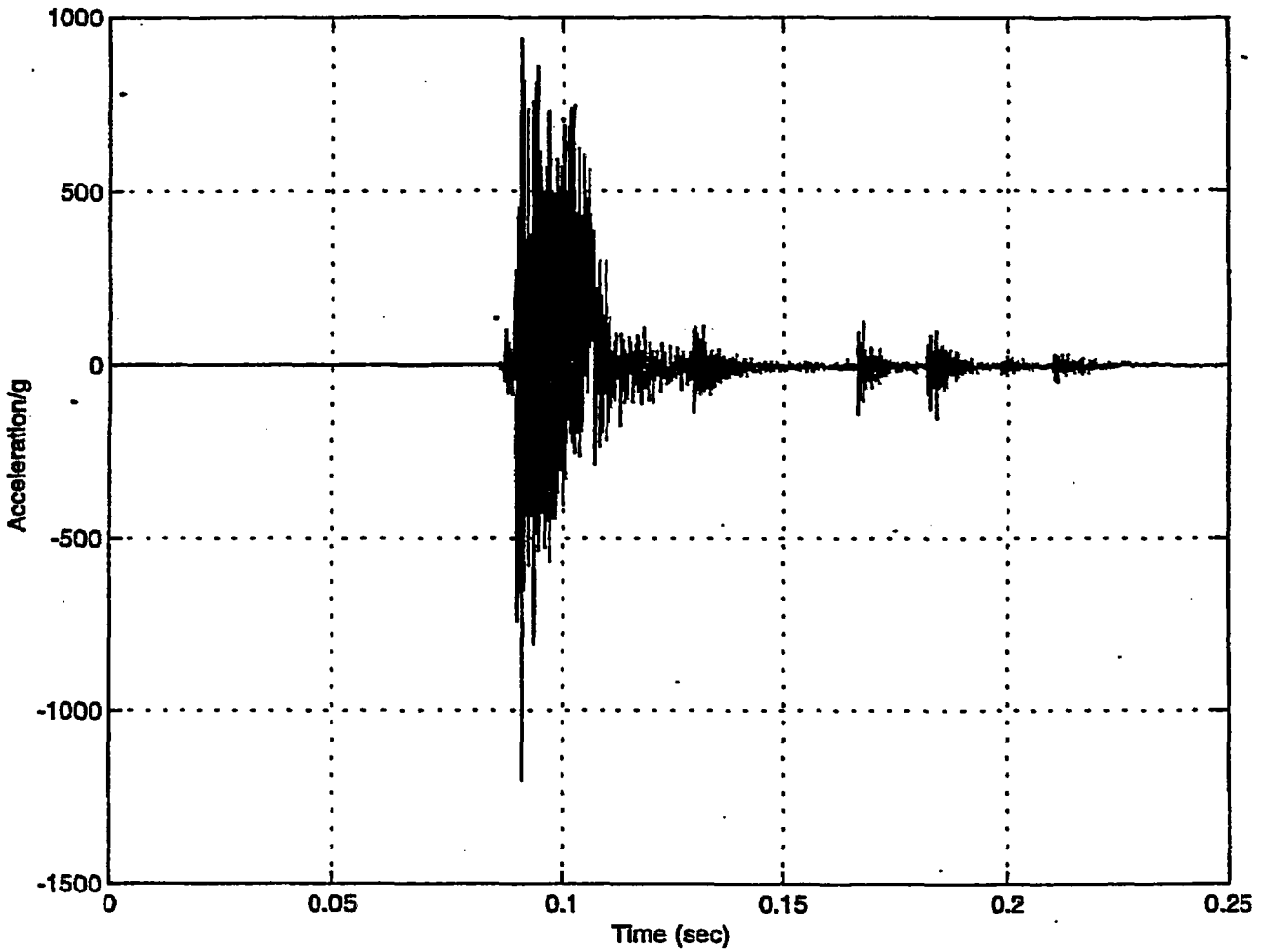

FIGURE 2.A.5.18 : ACCELERATION RAW DATA AT BOTTOM END DURING SLAPDOWN DROP

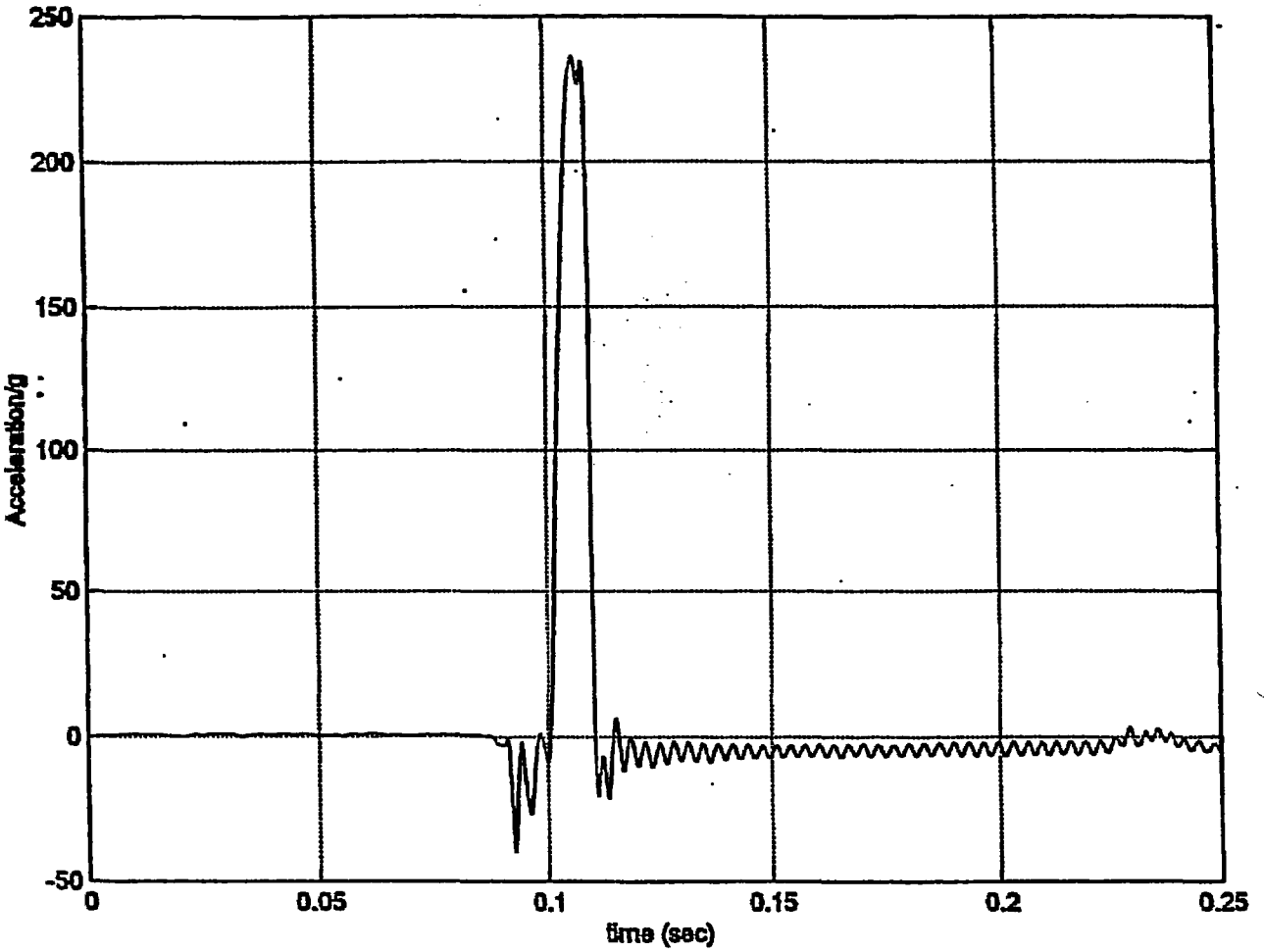

FIGURE 2.A.5.19 ; ACCELERATION DATA FILTERED AT 350 Hz FOR SLAPDOWN DROP

FIGURE 2.A.5.19A ; : SLAP DOWN

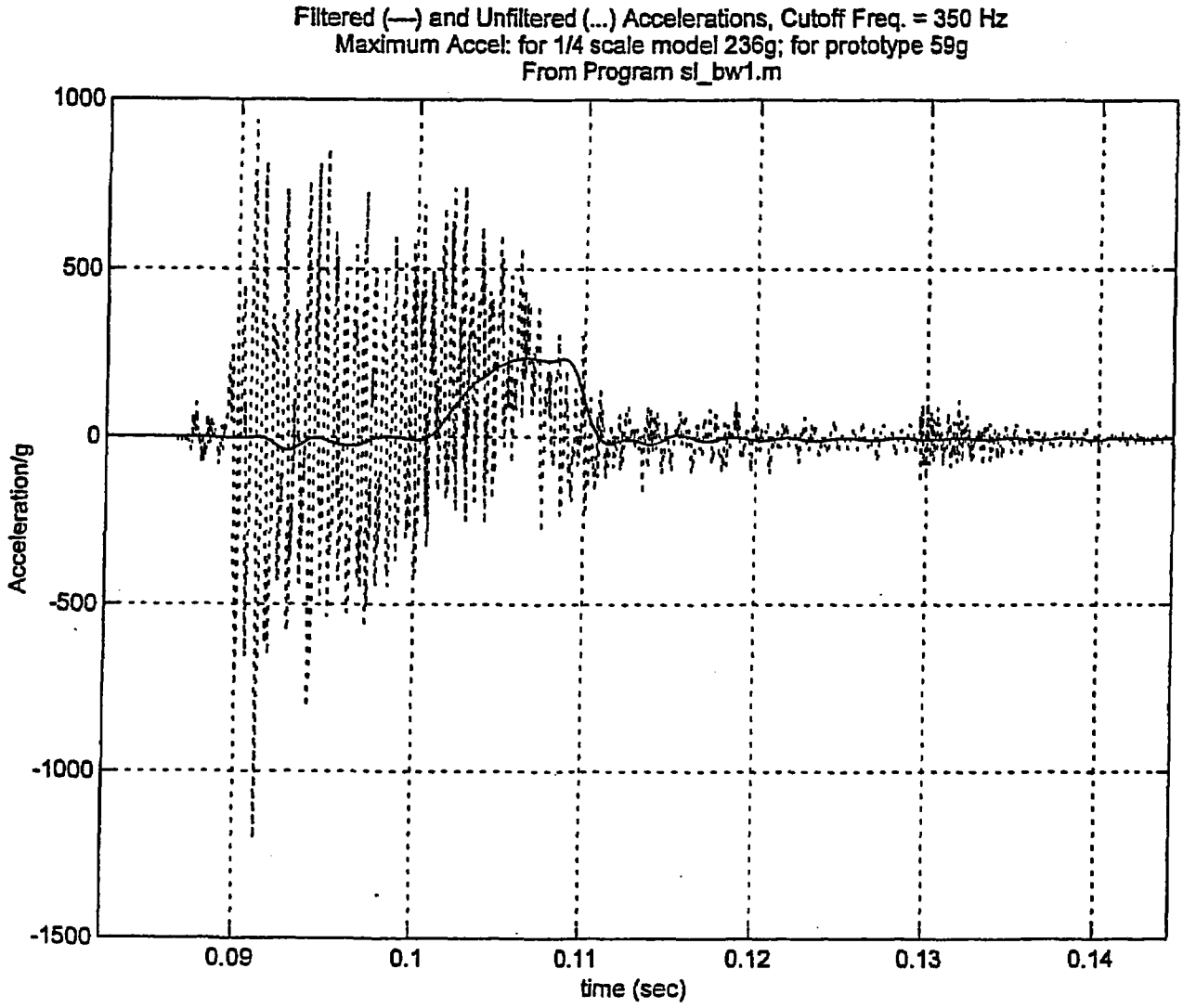

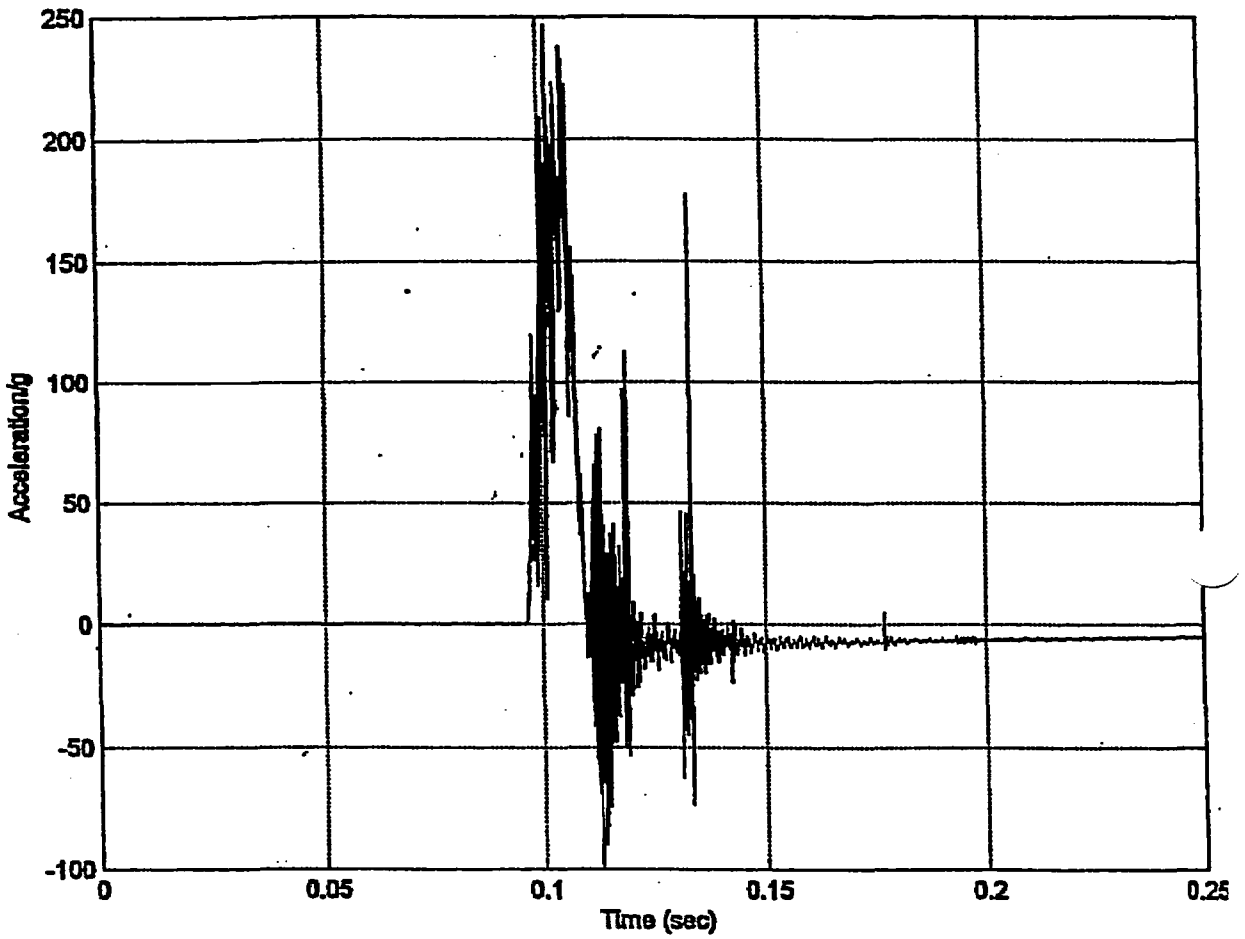

FIGURE 2.A.5.20 : ACCELERATION RAW DATA FOR SIDE DROP

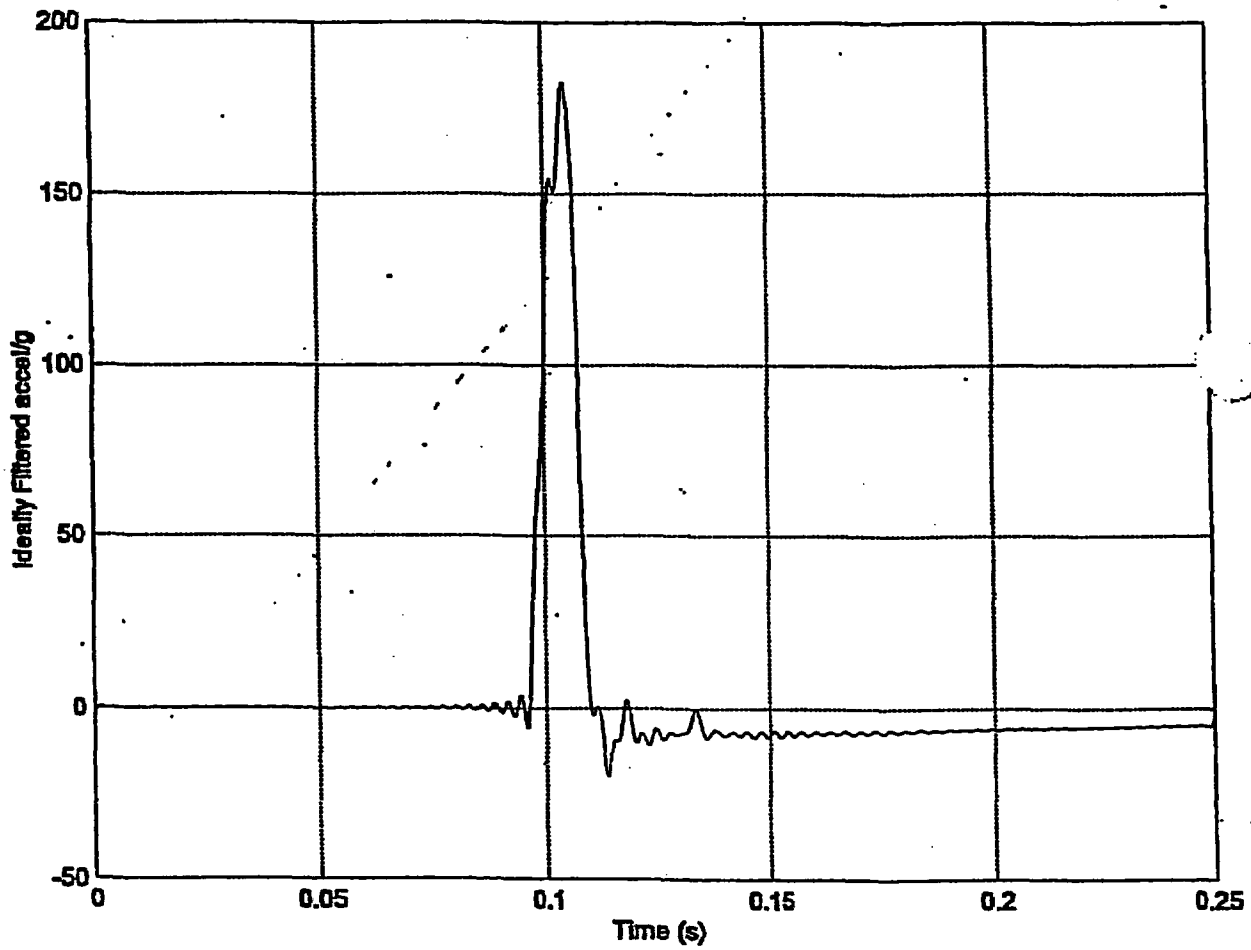

FIGURE 2.A.5.21 ; ACCELERATION DATA FILTERED AT 350 Hz FOR SIDE DROP

FIGURE 2.A.5.21A

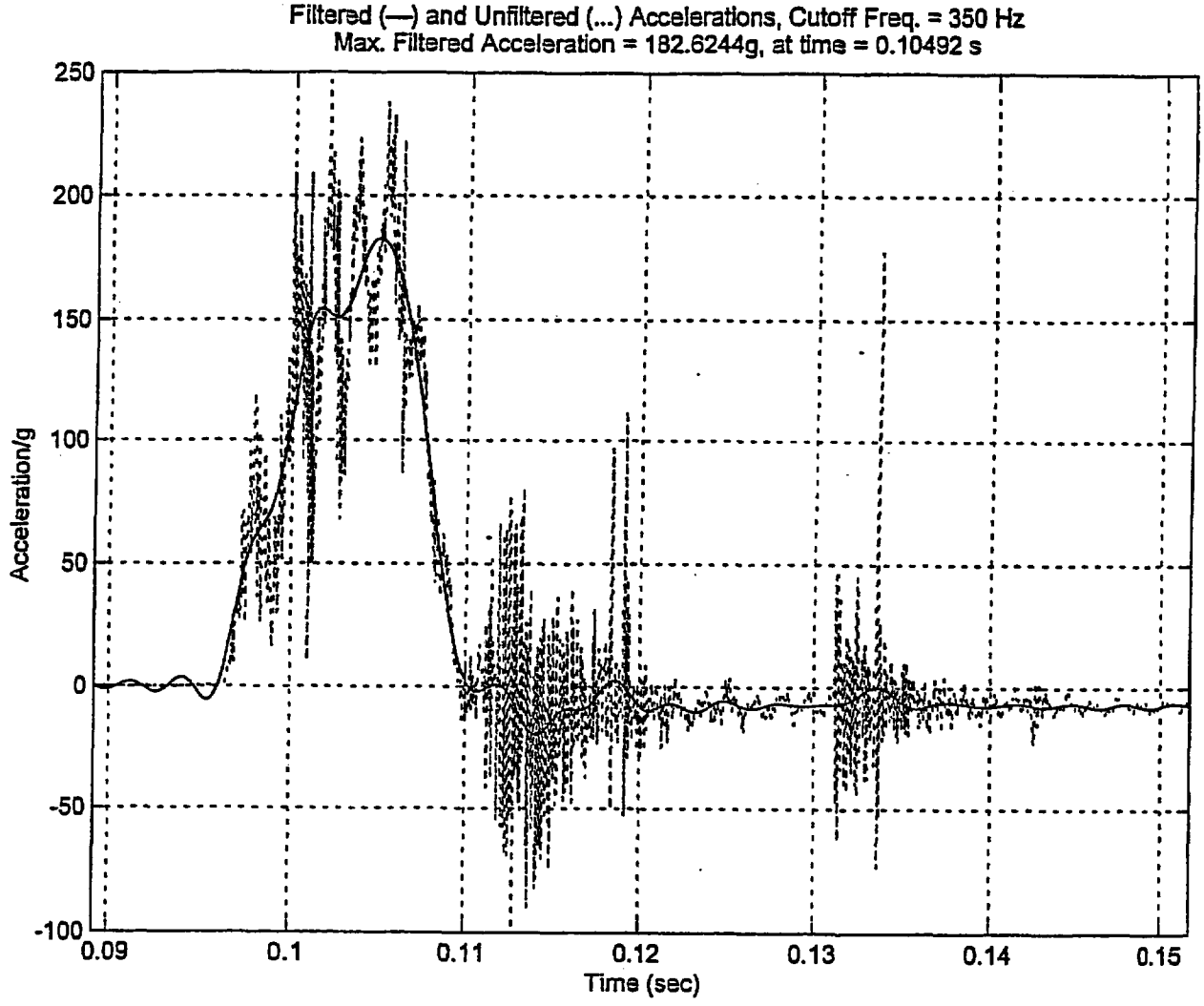

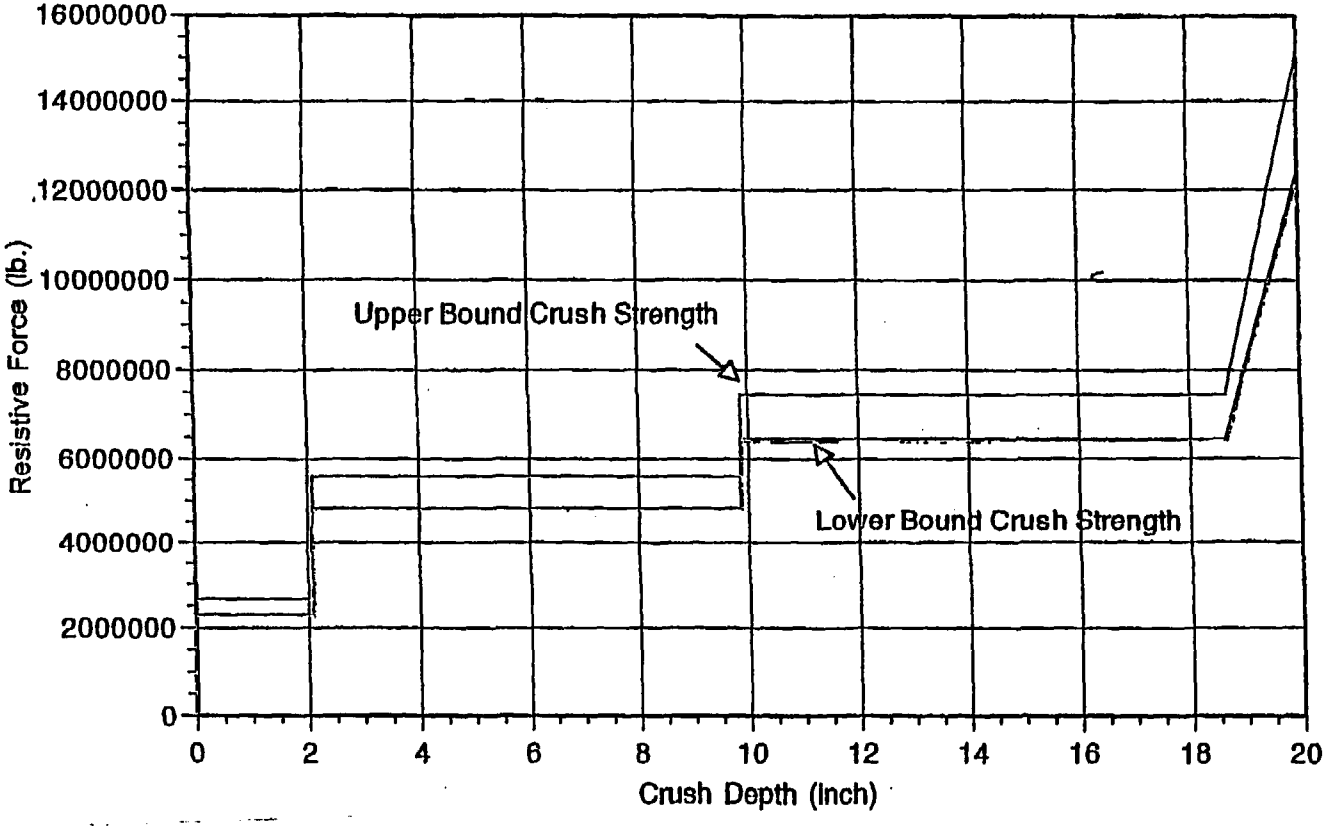

FIGURE 2.A.6.1 : - Impact Limiter Force vs. Crush Depth ($\theta = 90$ degrees)

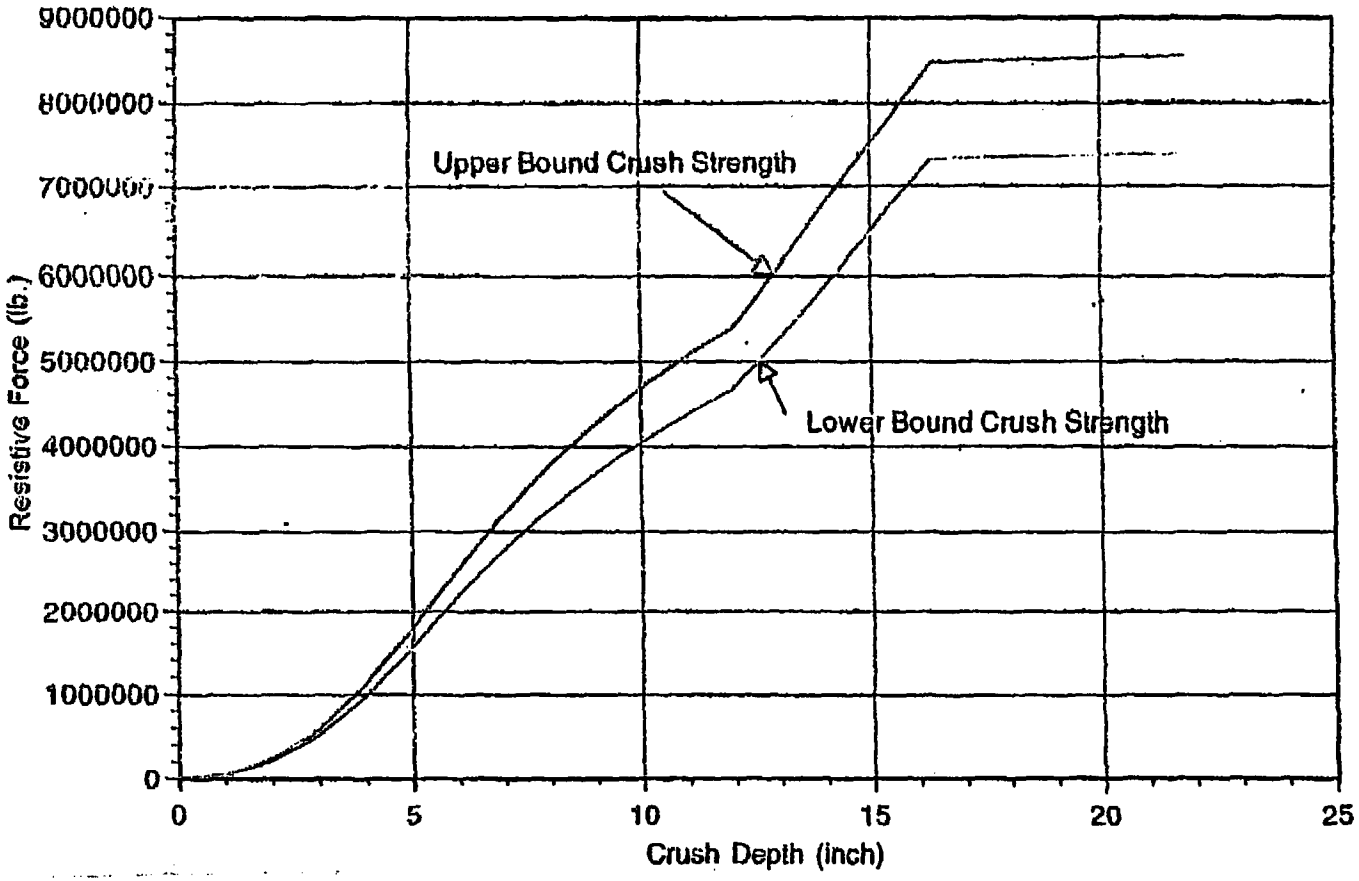

FIGURE 2.A.6.2 ; Impact Limiter Force vs. Crush Depth ($\theta = 67.5$ degrees)

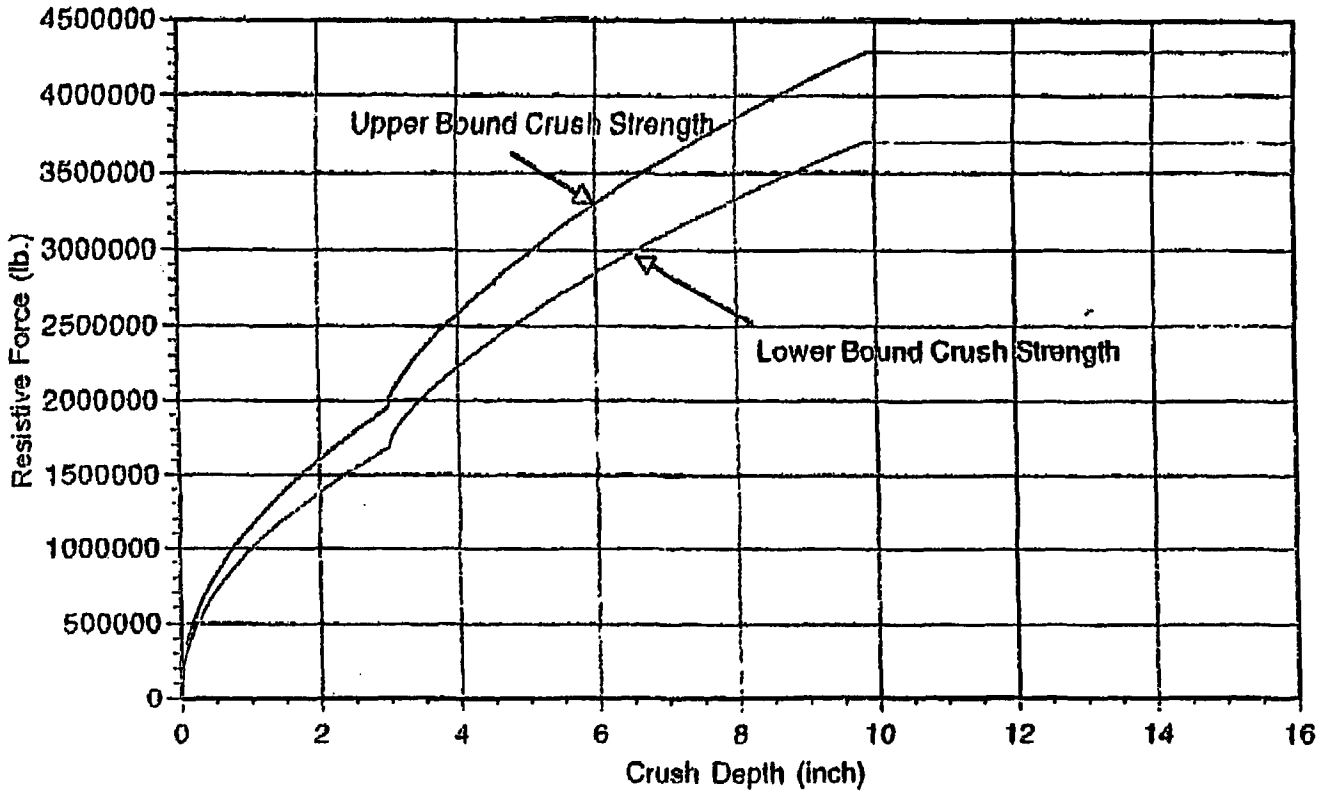

FIGURE 2.A.6.3 ; - Impact Limiter Force vs. Crush Depth (θ = 0 degrees)

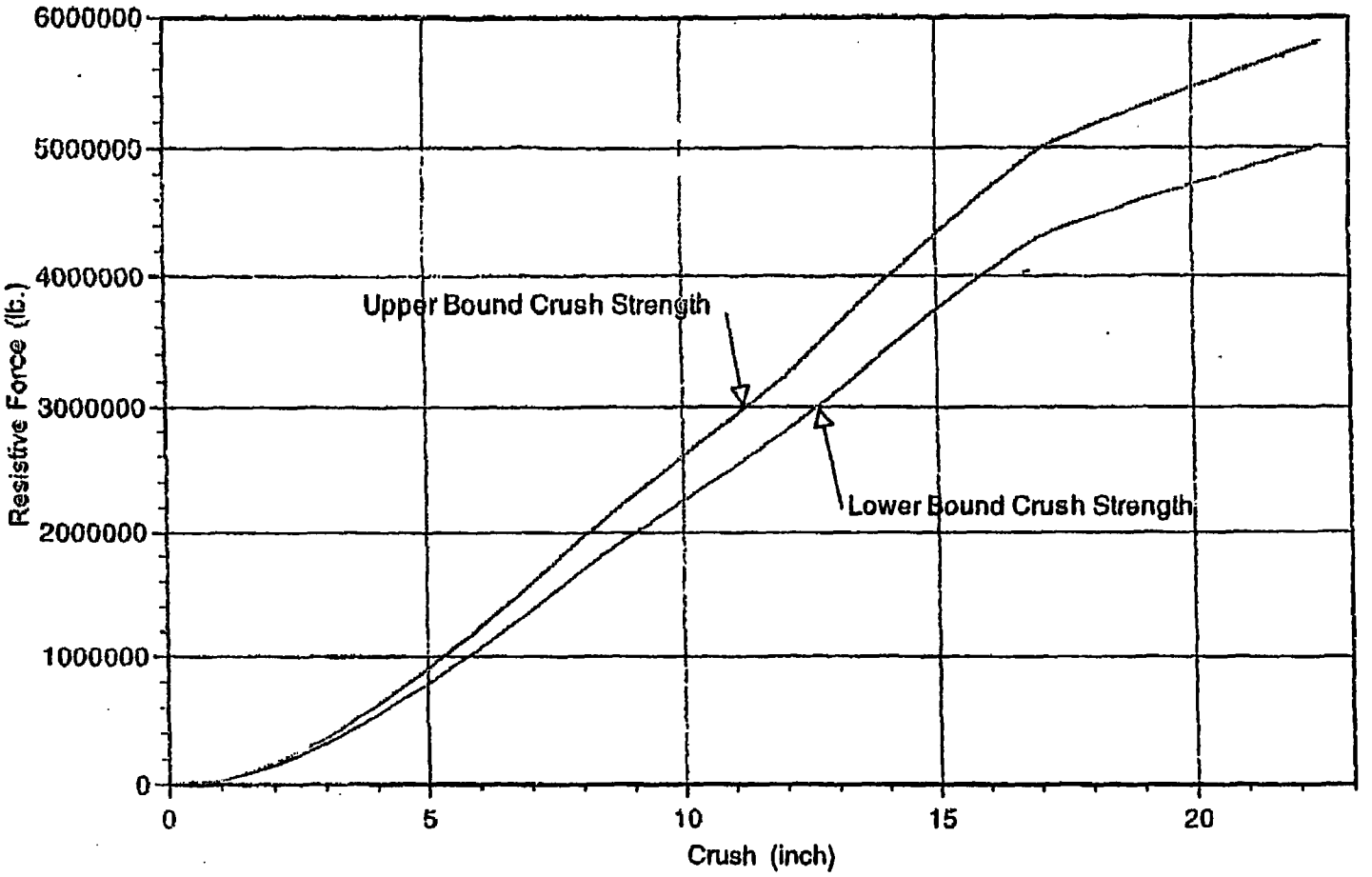

FIGURE 2.A.6.4 ; - Impact Limiter Force vs. Crush Depth ($\theta = 15$ degrees)

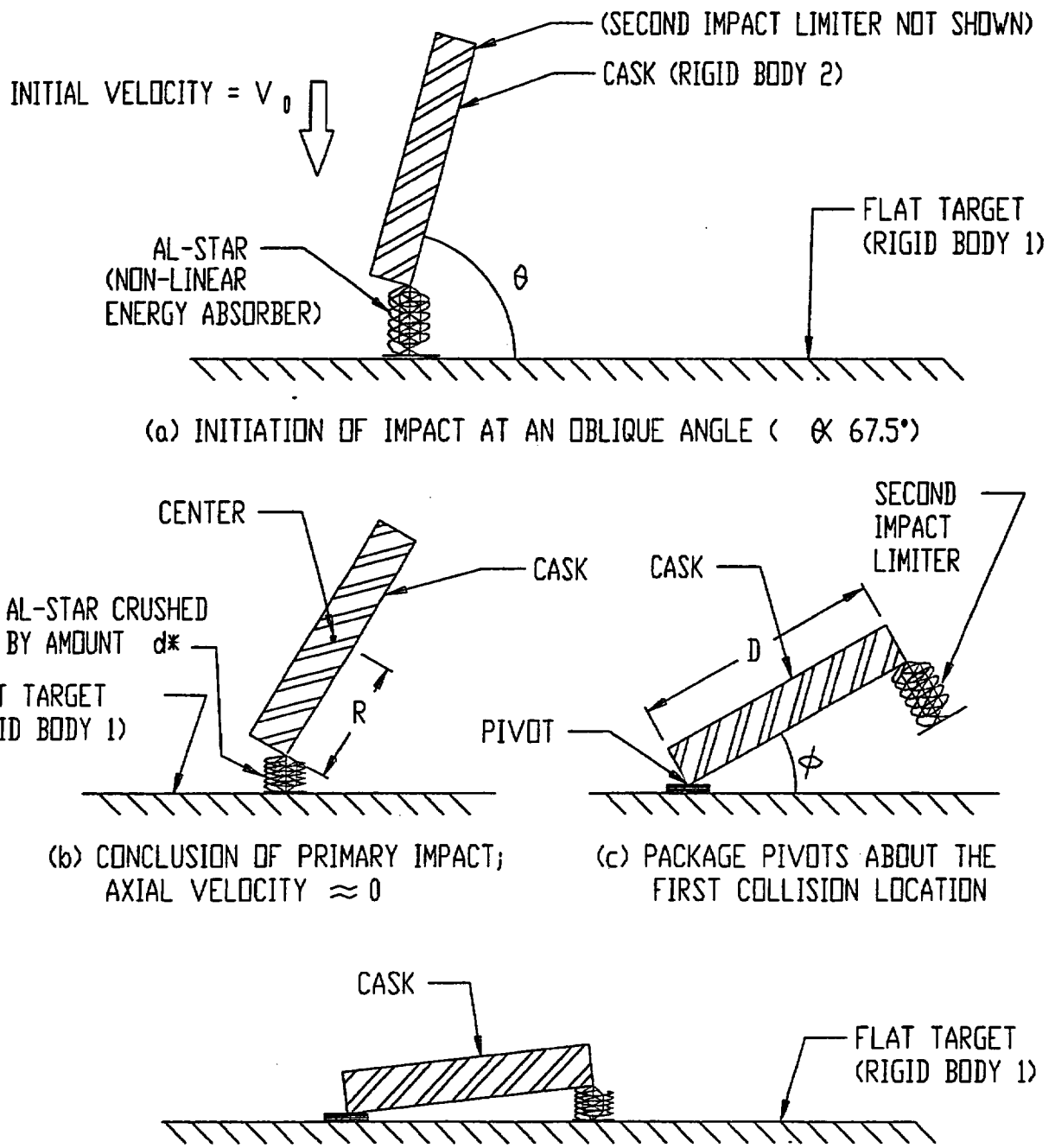

FIGURE 2.A.6.5; DYNAMIC MODEL FOR DUAL IMPACT SCENARIOS

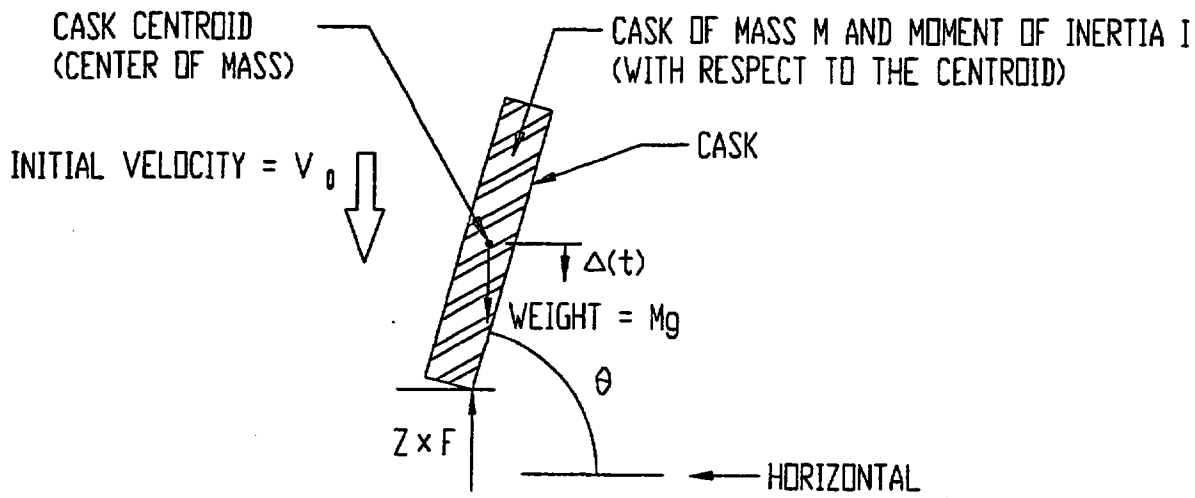

(a) INITIATION OF IMPACT AT AN OBLIQUE ANGLE ($\theta \leq 67.5°$)

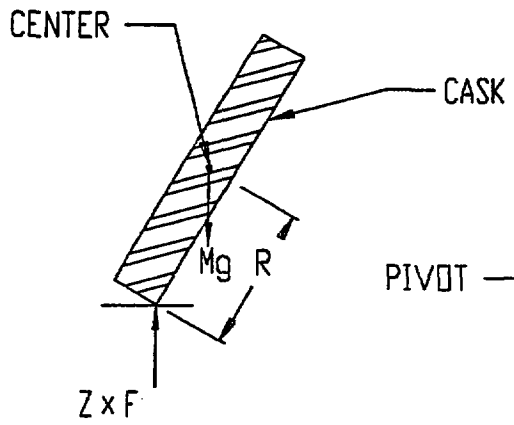

(b) CONCLUSION OF PRIMARY IMPACT; AXIAL VELOCITY ≈ 0

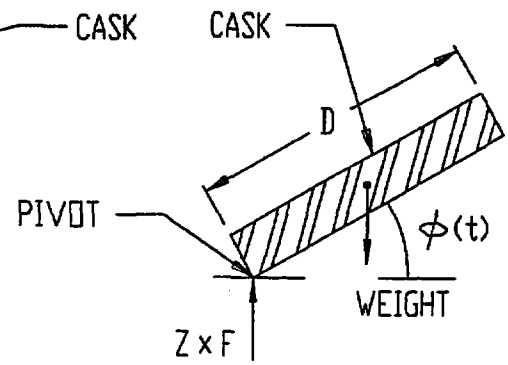

(c) PACKAGE PIVOTS ABOUT THE FIRST COLLISION LOCATION

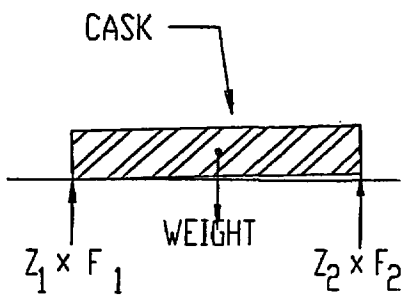

(c) SECONDARY IMPACT AT THE SECOND IMPACT LIMITER

FIGURE 2.A.6.6; FREE-BODY DIAGRAM FOR IMPACT SCENARIOS

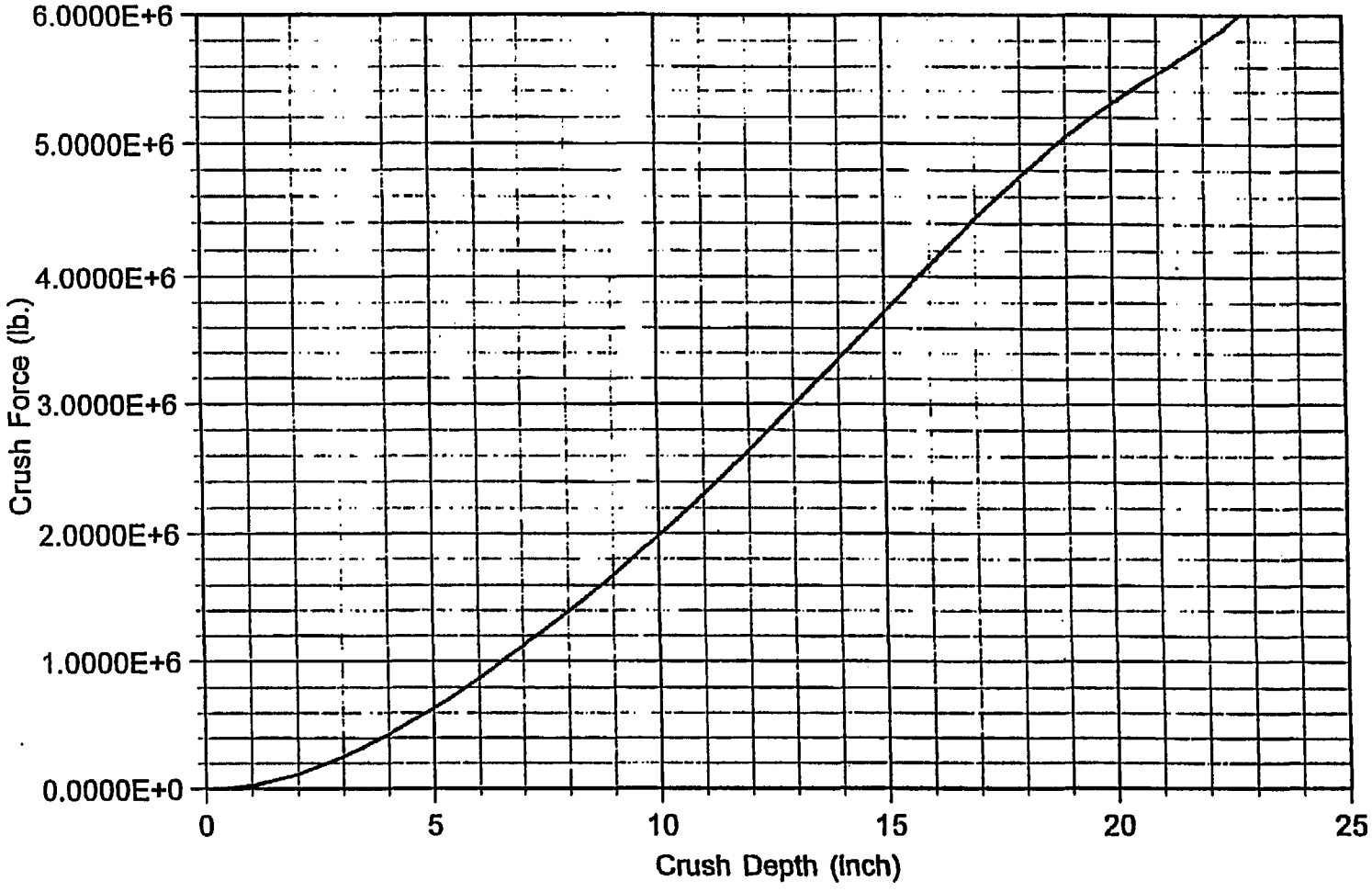

FIGURE 2.A.7.1 ; Static Crush Force vs Crush Depth - Impact at 30 Degrees with Horizontal Target

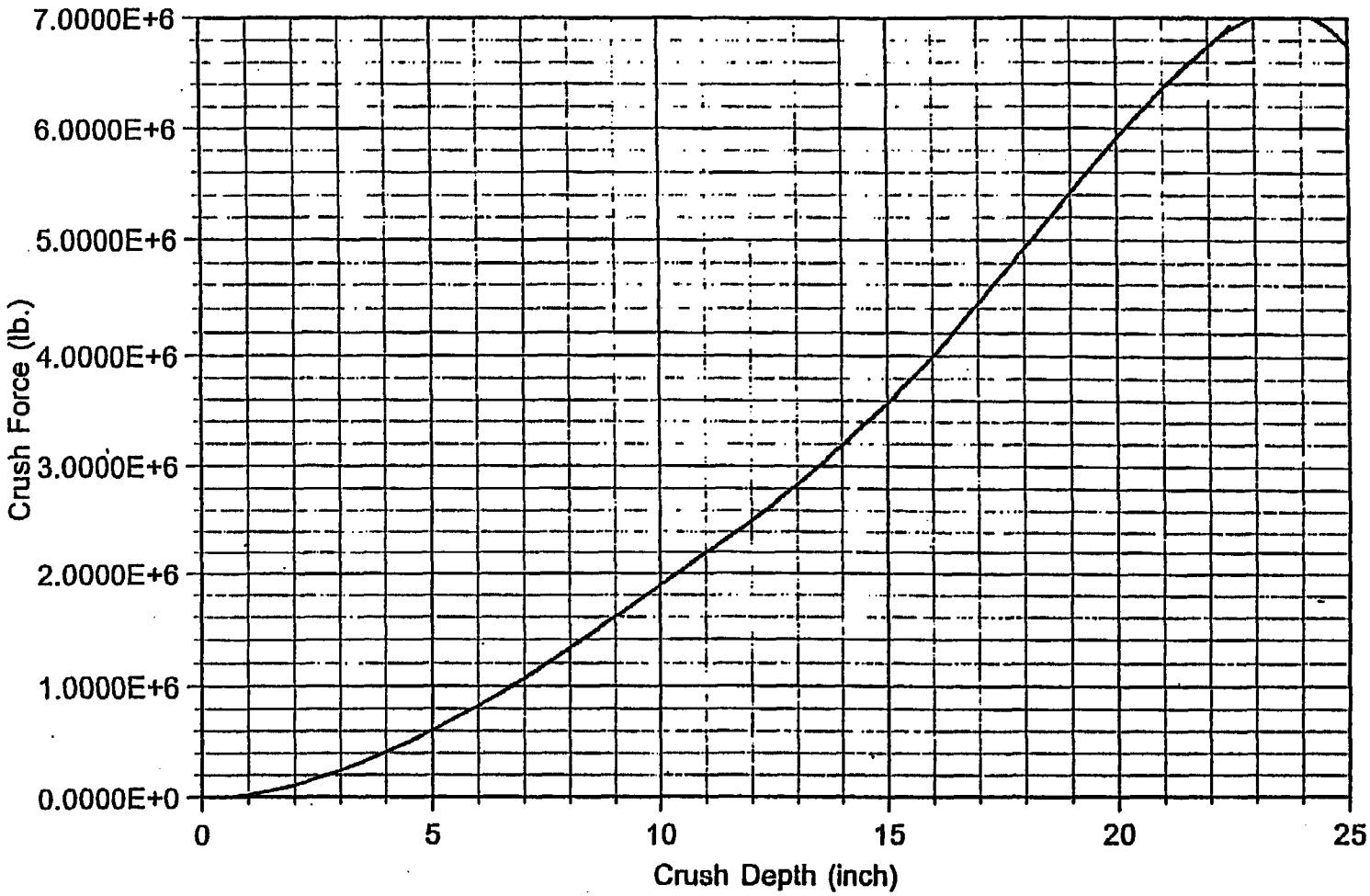

FIGURE 2.A.7.2 : Static Crush Force vs Crush Depth - Impact at 45 Degrees with Horizontal Target

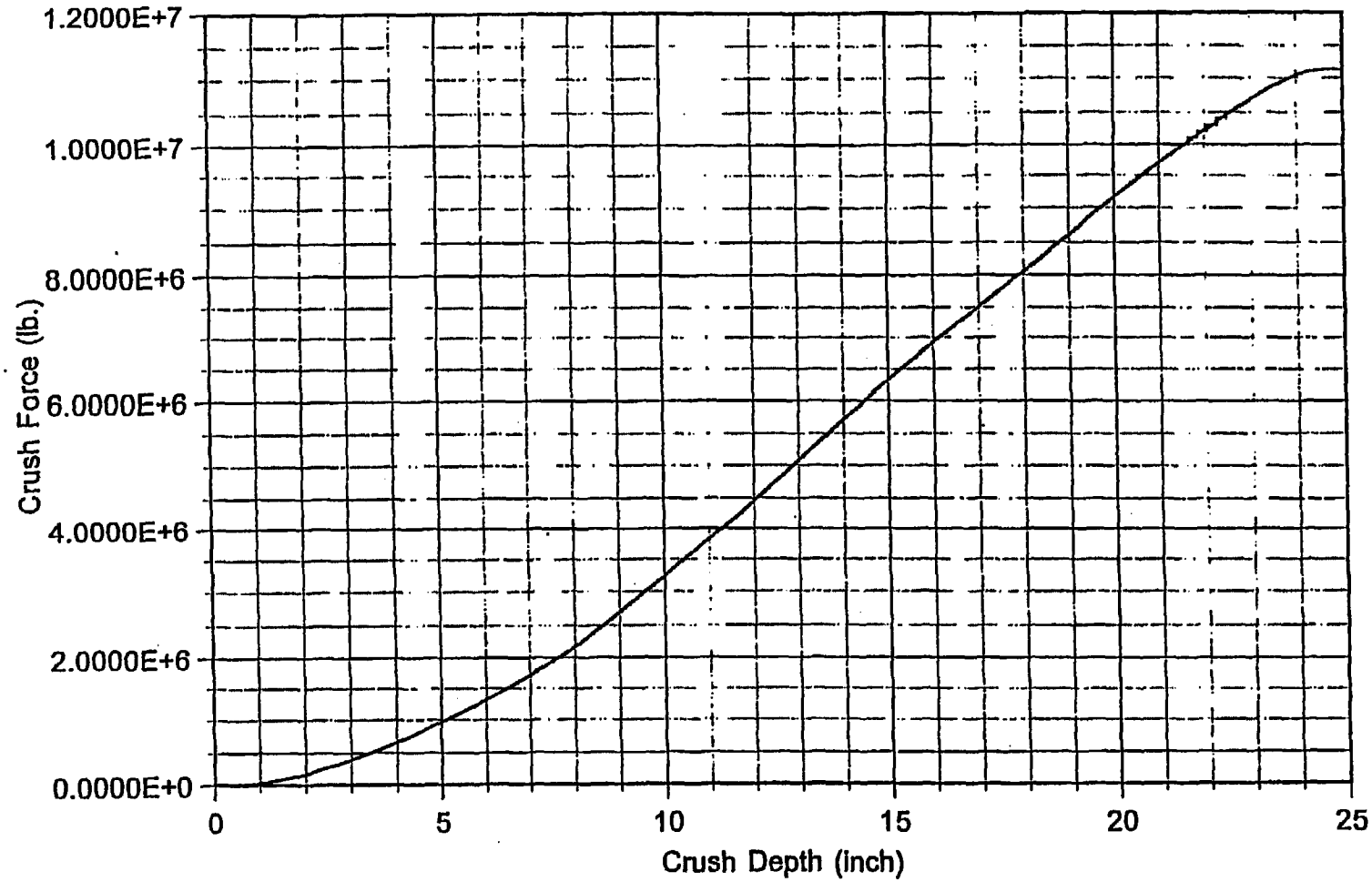

FIGURE 2.A.7.3 ; Static Crush Force vs Crush Depth - Impact at 60 Degrees with Horizontal Target

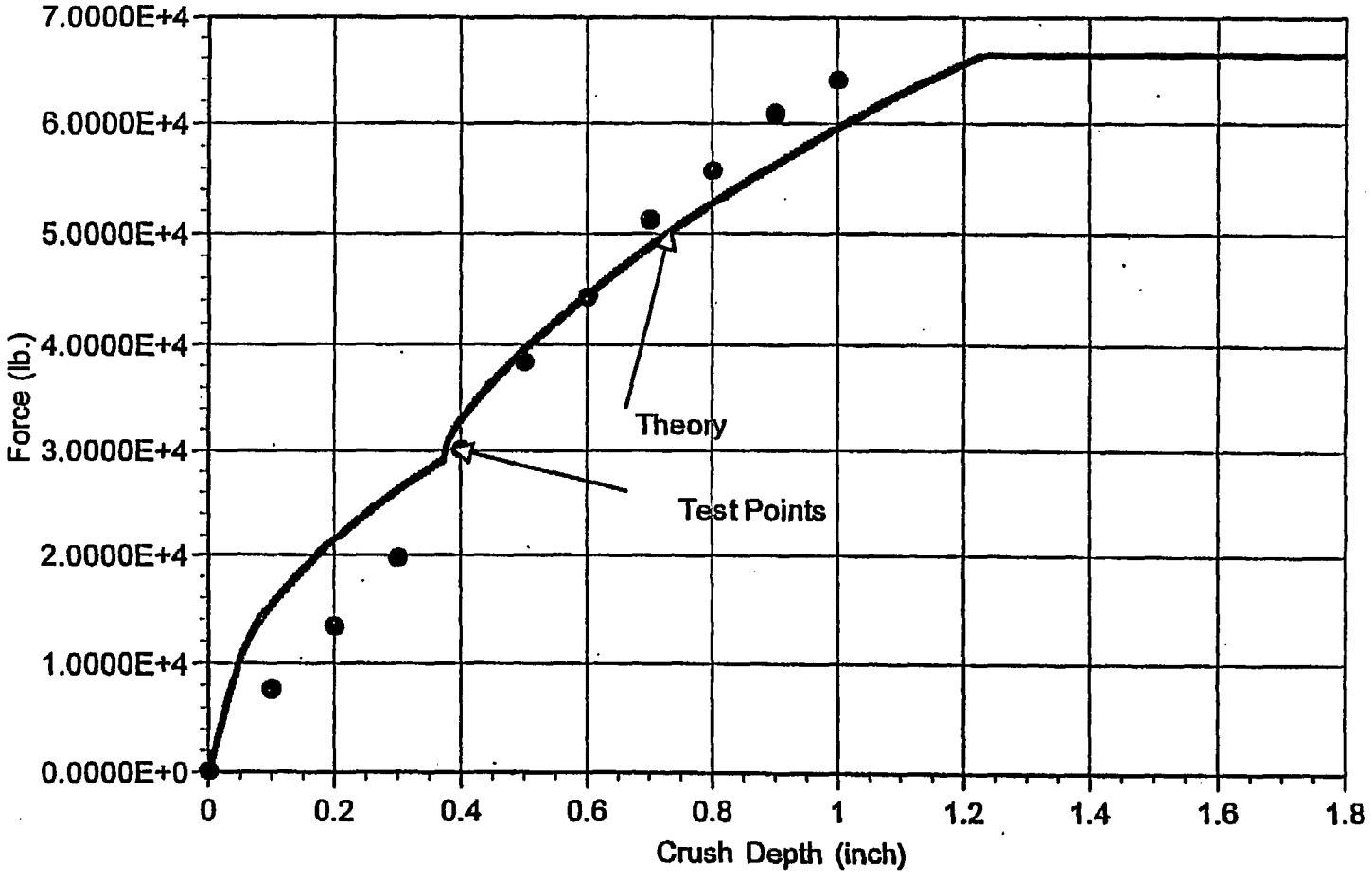

FIGURE 2.A.10.1 ; 1/8th Scale Impact Limiter - Crush Force vs. Crush Depth - Side Orientation -

HI-951251 REV. 10

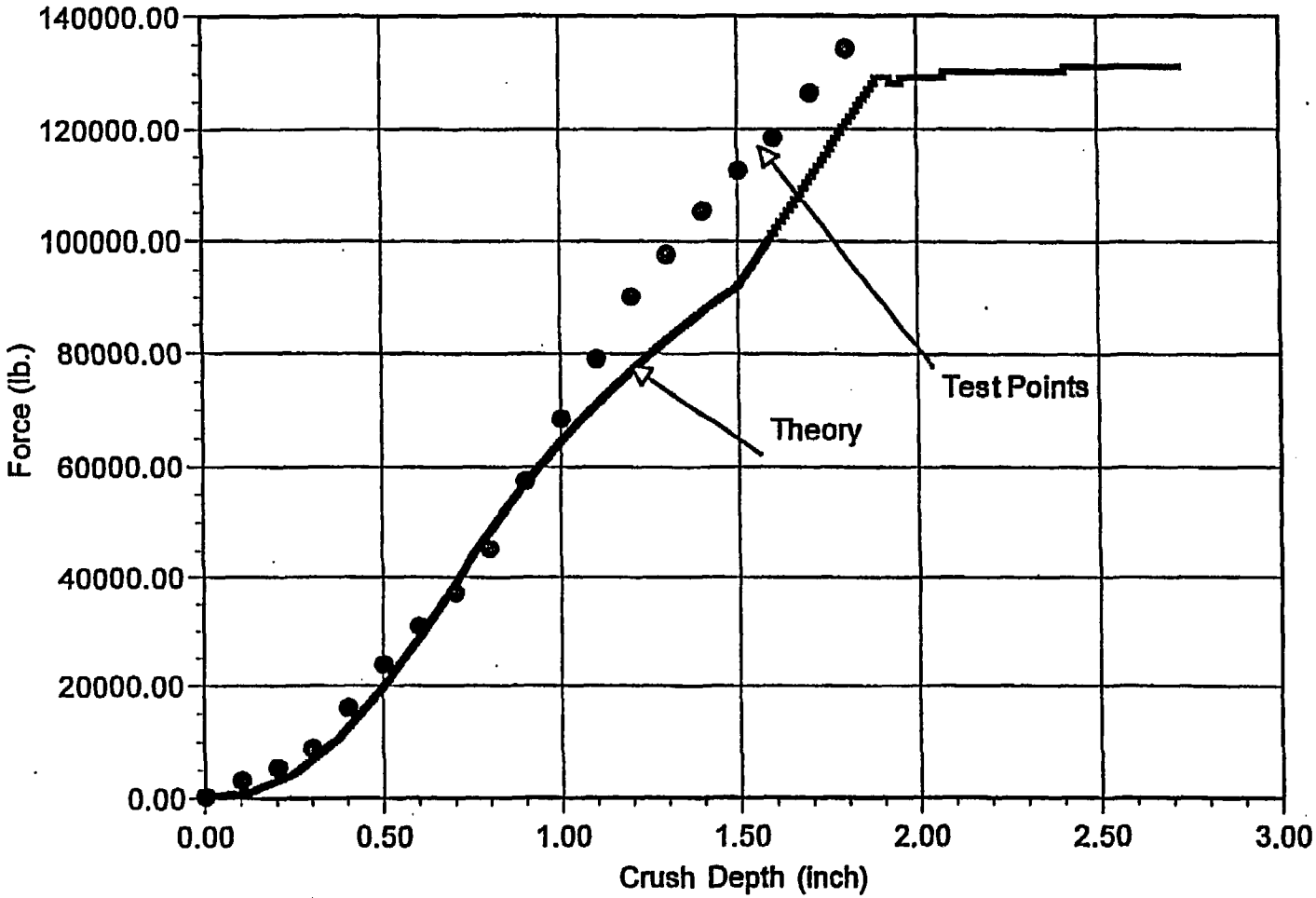

FIGURE 2A.10.2 : 1/8th Scale Impact Limiter - Crush Force vs. Crush Depth - Center of Gravity Over Corner Orientation HI-951251 REV. 10

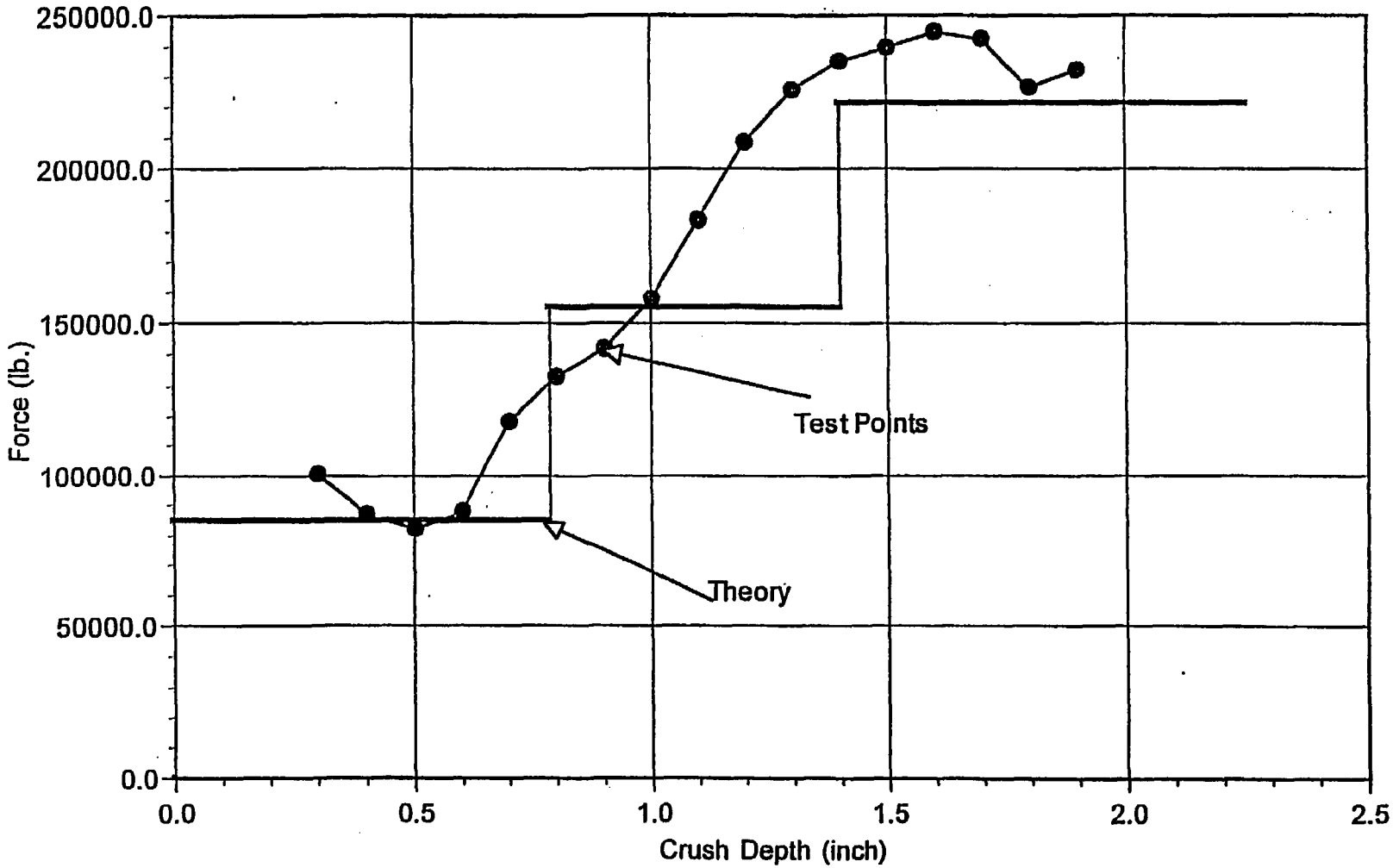

FIGURE 2.A.10.3 ; 1/8th Scale Impact Limiter - Crush Force vs. Crush Depth - End Orientation

HI-951251 REV. 10

Appendix 2.B

SUMMARY OF RESULTS FOR STRUCTURAL INTEGRITY OF DAMAGED FUEL CANISTERS

2.B.1 Introduction

Damaged Fuel Canisters or Containers (DFCs) to be deployed in the HI-STAR 100 System transport package have been evaluated to demonstrate that the canisters are structurally adequate to support the mechanical loads postulated during normal lifting operations while in long-term storage, and during a hypothetical end drop accident condition. The evaluations address the following damaged/failed fuel canisters for transportation in the Hi-STAR 100 System:

- Holtec-designed DFC for Dresden Unit 1 and Humboldt Bay fuel
- Transnuclear designed DFC for Dresden Unit 1 fuel
- Dresden Unit 1 Thoria Rod Canister
- Holtec-designed DFC for Trojan plant fuel
- Sierra Nuclear Corporation (SNC)-designed Failed Fuel Can for Trojan plant fuel

2.B.2 Methodology

The structural load path in each of the analyzed canisters was evaluated using basic strength of materials formulations. The various structural components were modeled as axial or bending members and stresses computed. Depending on the particular DFC, the load path includes components such as the container sleeve and collar, various weld configurations, load tabs, closure components and lifting bolts. Axial plus bending stresses were computed, together with applicable bearing stresses and weld stresses. Comparison with appropriate allowable strengths at temperature was performed. Input data for all applicable DFC's came from the drawings. The design temperature for lifting evaluation was 150°F (since the DFC is in the spent fuel pool). The design temperature for accident conditions is 725°F.

For the SNC-designed Trojan Failed Fuel Can, the existing calculations prepared by SNC were reviewed by Holtec and determined to bound the loadings applicable to the HI-STAR 100 System. Therefore, no new calculations were prepared for the Trojan Failed Fuel Can.

2.B.3 Acceptance Criteria

The upper closure assembly must meet the requirements set forth for special lifting devices used in nuclear applications [1]. The remaining components of the damaged fuel canister are governed by the stress limits of the ASME Code Section III, Subsection NG and Section III, Appendix F, as applicable [2].

2.B.4 Assumptions

Buckling is not a concern during an accident since during a drop, the canister will be supported by the walls of the fuel basket.

The strength of welds is assumed to decrease the same as the base metal as temperatures increase.

An inertia load factor 1.15 is applied to all loads during a lifting analysis, except for the lifting analysis of the Trojan failed fuel can which assumes a 10% dynamic load factor.

2.B.5 Summary of Results

Table 2.B.1 presents minimum safety factors for each DFC from among all of the computations and evaluations performed on the different damaged fuel canisters to be certified for transport in the HI-STAR 100 System.

2.B.6 References

[1] ANSI N14-6-1993, "American National Standard for Special Lifting Devices for Shipping Containers Weighing 10,000 Pounds (4,500 kg) or More for Nuclear Materials", ANSI, Inc.

[2] ASME Boiler and Pressure Vessel Code, Section III, Subsection NG and Appendix F, 1995.

Table 2.B.1

SUMMARY OF SAFETY FACTORS FOR DAMAGED FUELCONTAINERS

Unit – (Maximum weight including contents -lbs)	Component	Calculated Stress (ksi)	Allowable Stress (ksi)	Safety Factor = (Allowable Value)/(Calculated Value)	Remarks
Holtec-designed Dresden/HB BWR DFC	Lifting – Upper Closure Assembly	1.687	1.9251	1.141	Allowable weld stress includes a 0.35 quality factor
	60g end drop	10.667	37.920	3.6	Level D stress limits
Transnuclear DFC (550 lb.)	Lifting – Lid Frame Assembly	0.526	4.583	8.7	Bearing Stress
	60g end drop	12.316	37.920	3.1	Level D stress limits
Dresden Thoria Rod Canister (390 lb.)	Lifting – Lid Frame Assembly	0.3735	4.583	12.27	Bearing Stress
	60g end drop	8.733	37.920	4.3	Level D stress limits
Holtec-designed Trojan DFC (1680 lb.)	Lifting – Lifting Bolt	13.702	25.000	1.825	
	60g end drop	11.618	26.586	2.3	Spot welds
Trojan Failed Fuel Can	Lifting – Lifting Bar	6.2	6.37†	1.03	Bending Stress
	124g end drop	8.25	11.7	1.42††	Level D stress limits

† Allowable stress is equal to 1/3 of yield stress per [1].

†† Conservatively based on bounding 124g vertical end drop used in SNC calculations. Per Table 2.1.10, the design basis deceleration for the HI-STAR 100 is 60g.

Appendices 2.C through 2.AO

INTENTIONALLY DELETED

CHAPTER 3: THERMAL EVALUATION

3.0 INTRODUCTION

In this chapter, compliance of the HI-STAR System thermal performance to 10CFR71 requirements is established for normal transport and hypothetical accident conditions of transport. The analysis considers passive rejection of decay heat from the spent nuclear fuel (SNF) to an environment under the most severe 10CFR71 mandated design basis ambient conditions.

10CFR71 defines the requirements and acceptance criteria that must be fulfilled by the cask thermal design. The requirements and acceptance criteria applicable to the thermal analysis presented in this chapter are summarized here as follows:

1. The applicant must include a description of the proposed package in sufficient detail to identify the package accurately and provide a sufficient basis for the evaluation of the package. [71.33].

   The description must include, with respect to the packaging, specific materials of construction, weights, dimensions, and fabrication methods of materials specifically used as nonfissile neutron absorbers or moderators [71.33(a)(5)(ii)]; and structural and mechanical means for the transfer and dissipation of heat [71.33(a)(5)(v)].

   The description must include, with respect to the contents of the package, chemical and physical form [71.33(b)(3)]; maximum normal operating pressure [71.33(b)(5)]; maximum amount of decay heat [71.33(b)(7)]; and identification and volumes of any coolants [71.33(b)(8)].

2. A package must be designed, constructed, and prepared for shipment so that under normal conditions of transport there would be no substantial reduction in the effectiveness of the packaging [71.43(f) and 71.51(a)(1)].

3. A package must be designed, constructed, and prepared for shipment so that in still air at 100°F and in the shade, no accessible surface of the package would have a temperature exceeding 185°F in an exclusive use shipment [71.43(g)].

4. Compliance with the permitted activity release limits for a Type B package may not depend on filters or on a mechanical cooling system [71.51(c)].

5. With respect to the initial conditions for the events of normal conditions of transport and hypothetical accident conditions, the demonstration of compliance with the requirements of 10CFR71 must be based on the ambient temperature preceding and following the event remaining constant at that value between -20°F and 100°F which is most unfavorable for the feature

under consideration. The initial internal pressure within the containment system must be considered to be the maximum normal operating pressure, unless a lower internal pressure consistent with the ambient temperature considered to precede and follow the event is more unfavorable [71.71(b) and 71.73(b)].

6. For normal conditions of transport, a heat event consisting of an ambient temperature of 100°F in still air and prescribed insolation must be evaluated [71.71(c)(1)].

7. For normal conditions of transport, a cold event consisting of an ambient temperature of -40°F in still air and shade must be evaluated [71.71(c)(2)].

8. Evaluation for hypothetical accident conditions is to be based on sequential application of the specified events, in the prescribed order, to determine their cumulative effect on a package [71.73(a)].

9. For hypothetical accident conditions, a thermal event consisting of a fully engulfing hydrocarbon fuel/air fire with an average emissivity coefficient of at least 0.9, with an average flame temperature of at least 1475°F for a period of 30 minutes [71.73(c)(4)].

As demonstrated in this chapter, the HI-STAR System design and thermal analyses comply with all nine requirements and acceptance criteria listed above. Subsection 3.2 lists the material properties data required to perform the thermal analyses and Subsection 3.3 provides the applicable temperature limits criteria required to demonstrate the adequacy of the HI-STAR System design under all conditions. All thermal analyses to evaluate the normal conditions of transport performance of a HI-STAR System are described in Subsection 3.4. All thermal analyses for hypothetical accident conditions are described in Subsection 3.5. A summary discussion of regulatory compliance is included in Subsection 3.6.

This revision to the HI-STAR transport Safety Analysis Report incorporates certain conforming changes to the multi purpose canisters (MPCs) that are engineered to be transported in the HI-STAR overpack and adoption of ISG-11, Rev. 2 requirements. The principal changes are:

- The Aluminum Heat Conduction Elements (AHCE) in the MPC, required under CoCs 9261-1 and 9261-2, are rendered optional hardware.

- Include a higher capacity PWR basket configuration (MPC-32).

- Include an enhanced 24-cell PWR basket layout (MPC-24E), an enlarged cell opening for the MPC-24 and a shortened-height MPC-24E for Trojan fuel.

- Raise the nominal helium fill pressure to 42.8 psig.

- Relax certain elements of excessive conservatism in the mathematical models to retain a moderate level of conservatism.

- The thermal evaluation is revised to comply with the ISG-11, Rev. 2 temperature limits [3.1.5].

- Define a "load-and-go" operation wherein only the preferred method of MPC demoisturization - Forced Helium Dehydration (FHD) – is permitted.

Aside from the above-mentioned changes, this revision of this chapter is essentially identical to its predecessor.

3.1 DISCUSSION

Sectional views of the HI-STAR System have been presented earlier (see Figures 1.1.3 and 1.1.4). The system essentially consists of a loaded MPC situated inside an overpack equipped with a bolted closure. The fuel assemblies reside inside the MPC that has two redundant welded closures. The MPC contains a stainless steel honeycomb fuel basket that provides square-shaped fuel compartments of appropriate dimensions to facilitate insertion of fuel assemblies prior to welding of the MPC lid. Each fuel cell wall (except outer periphery MPC-32 and MPC-68 cell walls) is provided with Boral (thermal neutron absorber) sandwiched between a stainless steel sheathing plate and the cell wall along the entire length of the active fuel region. Prior to sealing the MPC lid, the MPC is backfilled with helium to the levels specified in Table 1.2.3. This provides a stable and inert environment for the transport of the SNF. Additionally, the annular gap between the MPC and the overpack is backfilled with helium before the overpack vent and drain port plug plugs are installed. Heat is transferred from the SNF in the HI-STAR to the environment by passive heat transport mechanisms only.

The helium backfill gas is an integral part of the MPC and overpack thermal designs. The helium fills all the spaces between solid components and provides an improved conduction medium (compared to air) for dissipating decay heat in the MPC. Additionally, helium in the spaces between the fuel basket and the MPC shell is heated differentially and, therefore, subject to the "Rayleigh" effect which is discussed in detail later (Subsection 3.4.1.1.5). To ensure that the helium gas is retained and is not diluted by lower conductivity air, the MPC helium retention boundary is designed to comply with the provisions of the ASME B&PV Code Section III, Subsection NB, as an all-seal-welded pressure vessel with redundant closures. Similarly, the overpack containment boundary is designed as an ASME B&PV Code Section III, Subsection NB pressure vessel. Both the MPC helium retention boundary and the overpack containment boundary are required to meet maximum leakage rate requirements included in Section 7.4 of this SAR. These leakage rate criteria ensure the presence of helium during transport. The helium gas is therefore retained and undiluted, and may be credited in the thermal analyses.

An important thermal design criterion imposed on the HI-STAR System is to limit the maximum fuel cladding temperature during normal transport to below design basis limits (Table 1.2.3). An equally important design criterion is to reduce temperature gradients within the MPC to minimize thermal stresses. In order to meet these design objectives, the HI-STAR MPC basket is designed to possess certain distinctive characteristics, which are summarized in the following.

The MPC design minimizes resistance to heat transfer within the basket and basket periphery regions. This is ensured by a high structural integrity all-welded honeycomb structure. The MPC design incorporates top and bottom plenums with interconnected downcomer paths. The top plenum is formed between the MPC lid and the top of the honeycomb fuel basket with additional semicircular holes in the top of each fuel cell wall. The bottom plenum is formed by large elongated semicircular holes at the base of all cell walls. The MPC basket is designed to eliminate structural discontinuities (i.e., gaps) which introduce large thermal resistances to heat flow. Consequently, temperature gradients are minimized in this design, which results in lower thermal stresses within the basket. Low thermal stresses are also ensured by an MPC design that

permits unrestrained axial and radial growth of the basket to eliminate the possibility of thermally induced stresses due to restraint of free-end expansion.

The HI-STAR System is designed for transport of PWR and BWR spent fuel assemblies and features two distinct MPC fuel basket geometries. For intact PWR fuel, a 24-assembly design(depicted in Figure 1.2.5) and a higher capacity canister (MPC-32) are available. A 68-assembly design for the transport of intact or specified damaged BWR fuel is shown in Figure 1.2.3. Damaged BWR fuel must be placed in a damaged fuel container for transport in the MPC-68. Extensively damaged BWR fuel assemblies (e.g. severed rods) classified as fuel debris shall be transported in the MPC-68F. The MPC-68F is identical to the MPC-68, except for the ^{10}B loading of the Boral panels for criticality control. Each basket design must comply with the required temperature limits under the imposed heat generation loads from the fuel assembly contents. For normal transport conditions, the maximum decay heat loads for the PWR and BWR MPCs are summarized in Table 1.2.3. The complete HI-STAR System consisting of the overpack and MPC under transport conditions is conservatively analyzed for the imposed design heat loads.

Thermal analysis of the HI-STAR System is based on including all three fundamental modes of heat transfer: conduction, natural convection and thermal radiation. Different combinations of these modes are active in different parts of the system. These modes are properly identified and conservatively analyzed within each region of the MPC and overpack, to enable bounding calculations of the temperature distribution within the HI-STAR System for both PWR and BWR MPC basket designs.

On the outside surface of the overpack, heat is dissipated to the environment by buoyancy induced convective air flow (natural convection) and thermal radiation. In the overpack internal metal structure, only conductive heat transport is possible. Between metal surfaces (e.g., between neighboring fuel rod surfaces) heat transport is due to a combination of conduction through a gaseous medium (helium) and thermal radiation. Finally, buoyancy-induced convective heat transport occurs within the open spaces of the MPC, aided by the MPC design which provides low pressure drop helium flow recirculation loops formed by the fuel cells, top plenum, downcomers, and bottom plenum. However, in the interest of conservatism, no credit for buoyancy-induced heat transport in the HI-STAR MPC basket is taken to satisfy either temperature or stress intensity limits. Heat transfer between the fuel basket external surface and MPC enclosure shell inside wall is further influenced by the so-called "Rayleigh" effect in differentially heated vertical cavities and "Rayleigh-Benard" effect in horizontal channels heated from below. A discussion on these effects is provided in Subsection 3.4.1.1.5.

The total heat generation in each assembly is non-uniformly distributed over the active fuel to account for design basis-fuel burnup distribution listed in Chapter 1 (Table 1.2.15 and Figures 1.2.13 and 1.2.14). As discussed later in this chapter (Subsection 3.4.6), an array of conservative assumptions bias the results of the thermal analysis towards much reduced computed margins than would be obtained by a rigorous analysis of the problem.

The complete thermal analysis is performed using the industry standard ANSYS finite element modeling package [3.1.1] and the finite volume Computational Fluid Dynamics (CFD) code FLUENT [3.1.2]. ANSYS has been previously used and accepted by the NRC on numerous dockets. The FLUENT CFD program is independently benchmarked and validated with a wide class of theoretical and experimental studies reported in the technical journals. Additionally, Holtec has confirmed the code's capability to reliably predict temperature fields in dry storage applications using independent full-scale test data from a loaded cask [3.1.3]. This study concluded that FLUENT can be used to model all modes of heat transfer, namely, conduction, convection, and radiation in dry cask systems.

3.2 SUMMARY OF THERMAL PROPERTIES OF MATERIALS

Materials present in the HI-STAR System include stainless steels, carbon steels, aluminum, neutron shield, Boral neutron absorber and helium. In Table 3.2.1, a summary of references used to obtain cask material properties for performing all thermal analyses is presented.

Tables 3.2.2, 3.2.3 and 3.2.9 provide numerical thermal conductivity data for all materials at several representative temperatures. Table 3.2.8 lists the thermal properties of Boral components (i.e., B_4C core and aluminum cladding materials).

Surface emissivity data for key materials of construction are provided in Table 3.2.4. The emissivity properties of painted surfaces are generally excellent. Kern [3.2.5] reports an emissivity range of 0.8 to 0.98 for a wide variety of paints. In the HI-STAR thermal analysis, an emissivity of 0.85[†] is applied to exterior painted surfaces. A conservative solar absorbtivity coefficient of 1.0 is applied to all exposed cask surfaces.

In Table 3.2.5, the heat capacity and density data of different cask materials is presented. These properties are used in performing transient (hypothetical fire accident condition, for example) analyses. MPC Rayleigh effect calculations use helium density, heat capacity, and gas viscosity properties data which are listed in Tables 3.2.5 and 3.2.6.

The HI-STAR System's outside surface heat transfer coefficient is calculated by accounting for both natural convection heat transfer and radiation. The natural convection coefficient of a heated horizontal cylinder depends upon the product of the Grashof (Gr) and Prandtl (Pr) numbers. Following the approach developed by Jakob and Hawkins [3.2.9], GrPr is expressed as $L^3\Delta T\ Z$, where L is the diameter of the cask, ΔT is the HI-STAR System overpack surface-to-ambient temperature differential and Z is a parameter which depends upon air properties, which are known functions of temperature, evaluated at the average film temperature. The temperature dependence of Z for air is provided in Table 3.2.7.

---

† This is conservative with respect to prior cask industry practice, which has historically accepted higher emissivities. For example, the emissivity for painted surfaces (ε=0.95) is used in the TN-32 cask TSAR (Docket 72-1021).

Table 3.2.1

SUMMARY OF HI-STAR SYSTEM MATERIALS
THERMAL PROPERTY REFERENCES

Material	Emissivity	Conductivity	Density	Heat Capacity
Helium	NA	Handbook [3.2.2]	Ideal Gas Law	Handbook [3.2.2]
Air	NA	Handbook [3.2.2]	Ideal Gas Law	Handbook [3.2.2]
Zircaloy Cladding	EPRI [3.2.3]	NUREG [3.2.6], [3.2.7]	Rust [3.2.4]	Rust [3.2.4]
UO_2	Not Used	NUREG [3.2.6], [3.2.7]	Rust [3.2.4]	Rust [3.2.4]
Stainless Steel	Kern [3.2.5]	ASME [3.2.8]	Marks [3.2.1]	Marks [3.2.1]
Carbon Steel	Kern [3.2.5]	ASME [3.2.8]	Marks [3.2.1]	Marks [3.2.1]
Aluminum Alloy 5052 (Impact Limiters)	Not Used	ASME [3.2.8]	ASME [3.2.8]	ASME [3.2.8]
Aluminum Alloy 1100 (Heat Conduction Elements)	Handbook [3.2.2]	ASME [3.2.8]	ASME [3.2.8]	ASME [3.2.8]
Boral†	Marks [3.2.1]	Test Data	Test Data	Test Data
Holtite-A††	Not Used	Test Data	Test Data	Test Data

† AAR Structures' Boral thermophysical test data.

†† From Holtite-A test data (Appendix 1.B).

Table 3.2.2

SUMMARY OF HI-STAR SYSTEM MATERIALS
THERMAL CONDUCTIVITY DATA

Material	@ 200°F (Btu/ft-hr-°F)	@ 450°F (Btu/ft-hr-°F)	@ 700°F (Btu/ft-hr-°F)
Helium	0.0976	0.1289	0.1575
Air	0.0173	0.0225	0.0272
Alloy X	8.4	9.8	11.0
Carbon Steel Radial Connectors	29.2	27.1	24.6
Carbon Steel Gamma Shield Layers	24.4	23.9	22.4
Impact Limiter Aluminum Alloy 5052	84.4	90.9	97.4
Holtite-A†			
Cryogenic Steel	23.8	23.7	22.3

† No credit taken for conduction through radial Holtite for the steady-state analysis, and before and after fire conditions for fire accident analysis. A conservative upper bound conductivity (1.0 Btu/ft-hr-°F) is applied during the fire condition to the radial neutron shield (between intermediate shells and overpack enclosure shell).

Table 3.2.3

SUMMARY OF FUEL ELEMENT COMPONENTS
THERMAL CONDUCTIVITY DATA

Fuel Cladding		**Fuel (UO_2)**	
Temperature (°F)	**Conductivity (Btu/ft-hr-°F)**	**Temperature (°F)**	**Conductivity (Btu/ft-hr-°F)**
392	8.28†	100	3.48
572	8.76	448	3.48
752	9.60	570	3.24
932	10.44	793	2.28†

† Lowest value of conductivity is used in the thermal analysis for conservatism.

Table 3.2.4

SUMMARY OF MATERIALS SURFACE EMISSIVITY DATA

Material	Emissivity
Fuel cladding	0.80
Painted exterior surface	0.85
Rolled carbon steel	0.66
Stainless steel	0.36
Sandblasted aluminum	0.40
Boral	0.26†

† From Marks' Handbook (Oxidized Aluminum Surface)

Table 3.2.5

MATERIALS DENSITY AND HEAT CAPACITY PROPERTIES SUMMARY

Materials	Density (lbm/ft^3)	Heat Capacity (Btu/lbm-°F)
Helium	(Ideal Gas Law)	1.24
Zircaloy Cladding	409	0.0728
Fuel (UO_2)	684	0.056
Carbon Steel	489	0.1
Stainless Steel	501	0.12
Boral	154.7	0.13
Impact Limiter Alloy 5052	167.6	0.23
Aluminum Alloy 1100	169.3	0.23
Holtite-A†	105.0	0.39

† Conservatively postulated to underestimate thermal inertia for fire accident analysis.

Table 3.2.6

HELIUM GAS VISCOSITY† VARIATION WITH TEMPERATURE

Temperature (°F)	Viscosity (Micropoise)
167.4	220.5
200.3	228.2
297.4	250.6
346.9	261.8
463.0	288.7
537.8	299.8
737.6	338.8

† Obtained from Rohsenow and Hartnett [3.2.2].

Table 3.2.7

VARIATION OF NATURAL CONVECTION PROPERTIES
PARAMETER "Z" FOR AIR WITH TEMPERATURE

Temperature (°F)	Z (ft^{-3} $°F^{-1}$)†
40	2.1×10^{6}
140	9.0×10^{5}
240	4.6×10^{5}
340	2.6×10^{5}
440	1.5×10^{5}

† Obtained from Jakob and Hawkins [3.2.9].

Table 3.2.8

BORAL COMPONENT MATERIALS[†]
THERMAL CONDUCTIVITY DATA

Temperature (°F)	B_4C Core Conductivity (Btu/ft-hr-°F)	Aluminum Cladding Conductivity (Btu/ft-hr-°F)
212	48.09	100.00
392	48.03	104.51
572	47.28	108.04
752	46.35	109.43

† Both B_4C and aluminum cladding conductivity values are obtained from AAR Structures Boral thermophysical test data.

Table 3.2.9

HEAT CONDUCTION ELEMENTS (ALUMINUM ALLOY 1100)
THERMAL CONDUCTIVITY DATA

Temperature (°F)	Conductivity (Btu/ft×hr×°F)
100	131.8
200	128.5
300	126.2
400	124.5

3.3 TECHNICAL SPECIFICATIONS FOR COMPONENTS

HI-STAR System materials and components which are required to be maintained within their safe operating temperature ranges to ensure their intended function are summarized in Table 3.3.1. Long-term stability and continued neutron shielding ability of the Holtite-A neutron shield material under normal transport conditions are ensured when material exposure temperatures are maintained below the maximum allowable limit. The overpack metallic seals will continue to ensure leak tightness of the closure plate, and drain and vent ports if the manufacturer's recommended design temperature limits are not exceeded. Integrity of SNF during transport requires demonstration of HI-STAR System thermal performance to maintain fuel cladding temperatures below design basis limits. Boral used in MPC baskets for criticality control (a composite material composed of B_4C and aluminum) is stable up to 1000°F for short-term and 850°F for long term dry storage[†]. However, for conservatism, a lower maximum temperature limit is imposed.

Compliance to 10CFR71 requires evaluation of hypothetical accident conditions. The inherent mechanical stability characteristics of the HI-STAR System materials and components ensure that no significant functional degradation is possible due to exposure to short-term temperature excursions outside the normal long-term temperature limits. For evaluation of the HI-STAR System's thermal performance under hypothetical accident conditions, material temperature limits for short-duration events are also provided in Table 3.3.1. In this Table, the cladding temperature limits of ISG-11, Rev. 2 [3.1.5] are adopted for Commercial Spent Fuel (CSF). These limits are applicable to all fuel types, burnup levels and cladding materials approved by the NRC for power generation. Subsections 3.3.1 through 3.3.3 and their associated tables and figures are no longer needed and are deleted.

[†] AAR Structures Boral thermophysical test data.

Table 3.3.1

HI-STAR SYSTEM MATERIAL TEMPERATURE LIMITS

Material	Normal Condition Temperature Limits	Accident Condition Temperature Limits
CSF Cladding	752°F	1058°F
Boral†	800°F	950°F
Overpack Closure Plate Mechanical Seals	See Table 4.1.1	See Table 4.1.1
Overpack Vent and Drain Port Plug Seals	See Table 4.1.1	See Table 4.1.1
Aluminum Alloy 5052	176°F††	1105°F†††
Holtite-A	300°F††††	N/A†††††
Aluminum Heat Conduction Elements (Alloy 1100)	725°F	950°F

† Based on AAR Structures Boral thermophysical test data.

†† AL-STAR impact limiter aluminum honeycomb test data.

††† Melting range of alloy is 1105°F-1200°F [3.3.1].

†††† Neutron shield manufacturer's test data (Appendix 1.B).

††††† For shielding analysis (Chapter 5), Holtite-A is conservatively assumed to be lost during the fire accident.

Tables 3.3.2 through 3.3.8

[INTENTIONALLY DELETED]

3.4 THERMAL EVALUATION FOR NORMAL CONDITIONS OF TRANSPORT

3.4.1 Thermal Model

The HI-STAR MPC basket designs consist of four distinct geometries engineered to hold 24 and 32 PWR (MPC-24, MPC-24E and MPC-32) or 68 BWR (MPC-68) fuel assemblies. The fuel basket forms a honeycomb matrix of square-shaped fuel compartments to retain the fuel assemblies during transport (refer to Figures 1.2.3 and 1.2.5 for an illustration of PWR and BWR baskets). The basket is formed by an interlocking honeycomb structure of steel plates and full-length edge welding of the cell corners to form an integral basket configuration. Individual cell walls (except outer periphery MPC-68 and MPC-32 cell walls) are provided with Boral neutron absorber panels, which consists of a Boral plate sandwiched between the cell wall and a stainless steel sheathing plate, for the full length of the active fuel region.

The design basis decay heat generation per PWR or BWR assembly for normal transport for each MPC type is specified in Table 1.2.13. The decay heat is considered to be nonuniformly distributed over the active fuel length based on the design basis axial burnup distribution specified in Chapter 1 (see Table 1.2.15 and Figures 1.2.13 and 1.2.14).

Transport of heat from the MPC basket interior to the basket periphery is accomplished by conduction through the MPC basket metal grid structure and the narrow helium gaps between the fuel assemblies and fuel cell walls. Heat dissipation in the MPC basket periphery-to-MPC shell gap is by a combination of helium conduction, natural convection (by means of the "Rayleigh" effect) and radiation across the gap. Between the MPC shell and the overpack inner shell is a small clearance which is evacuated and backfilled with helium. Helium, besides being inert, is a better conductor of heat than air. Thus, heat conduction through the helium gap between the MPC and the overpack will minimize temperature differentials across this region.

The overpack, under normal transport conditions, passively rejects heat to the environment. Cooling of the exterior system surfaces is by natural convection and radiation. During transport, the HI-STAR System is placed in a horizontal position with stainless steel encased aluminum honeycomb impact limiters installed at both ends of the overpack. To conservatively maximize the calculated internal temperatures, the thermal conductivity of the impact limiters is set essentially equal to zero. Under normal transport conditions, the MPC shell rests on the overpack internal cavity surface forming an eccentric gap. Direct contact between the MPC and overpack surfaces is expected to minimize heat transfer resistance in this region of intimate contact. Significantly improved conductive heat transport due to reduction in the helium gap near the contact region is accounted for in the thermal analysis of the HI-STAR System. The HI-STAR System is conservatively analyzed assuming a minimum 0.02-inch gap at the line of metal-to-metal contact. Analytical modeling details of the various thermal transport mechanisms are provided in the following.

3.4.1.1 Analytical Model - General Remarks

Transport of heat from the heat generation region (fuel assemblies) to the outside environment is analyzed broadly in terms of three interdependent thermal models.

i. The first model considers transport of heat from the fuel assembly to the basket cell walls. This model recognizes the combined effects of conduction (through helium) and radiation, and is essentially a finite element technology-based update of the classical Wooton & Epstein [3.4.1] formulation (which considers radiative heat exchange between fuel rod surfaces).

ii. The second model considers heat transport within an MPC cross section by conduction and radiation. The effective cross sectional thermal conductivity of the basket region obtained from the combined fuel assembly/basket heat conduction radiation model is applied to an axisymmetric thermal model of the HI-STAR System on the FLUENT [3.1.2] code.

iii. The third model deals with the transmission of heat from the MPC exterior surface to the external environment (heat sink). From the MPC shell to the cask exterior surface, heat is conducted through an array of concentric shells representing the MPC-to-overpack helium gap, the overpack inner shell, the intermediate shells, the Holtite-A neutron shielding and finally the overpack outer shell. Heat rejection from the outside cask surfaces to ambient air is considered by accounting for natural convection and thermal radiation heat transfer mechanisms from the exposed cask surfaces. Insolation on exposed cask surfaces is based on 12-hour levels prescribed in 10CFR71, averaged over a 24-hour period.

The following subsections contain a systematic description of the mathematical models devised to articulate the temperature field in the HI-STAR System. Table 3.4.2 shows the relationship between the mathematical models and the corresponding regions (i.e., fuel, MPC, overpack, etc.) of the HI-STAR System. The description begins with the method to characterize the heat transfer behavior of the prismatic (square) opening referred to as the "fuel space" containing a heat emitting fuel assembly. The methodology utilizes a finite-volume procedure to replace the heterogeneous SNF/fuel space region with an equivalent solid body having a well-defined temperature-dependent conductivity. In the following subsection, the method to replace the composite walls of the fuel basket cells with equivalent "solid" walls is presented. Having created the mathematical equivalents for the SNF/fuel spaces and the fuel basket walls, the method to represent the MPC cylinder containing the fuel basket by an equivalent cylinder whose thermal conductivity is a function of the spatial location and coincident temperature is presented.

Following the approach of presenting descriptions starting from the inside and moving to the outer region of a cask, the next subsections present the mathematical model to simulate the overpack. Subsection 3.4.1.1.12 concludes the presentation with a description of how the different models for the specific regions within the HI-STAR System are assembled into the final finite element model.

3.4.1.1.1 Overview of the Thermal Model

Thermal analysis of the HI-STAR System is performed by assuming that the system is subject to its maximum heat duty with each storage location occupied and with the heat generation rate in each stored fuel assembly equal to the design basis maximum value. While the assumption of equal heat generation imputes a certain symmetry to the cask thermal problem, the thermal model must incorporate three attributes of the physical problem to perform a rigorous analysis:

i. While the rate of heat conduction through metals is a relatively weak function of temperature, radiation heat exchange is a nonlinear function of surface temperatures.

ii. Heat generation in the MPC is axially non-uniform due to a non-uniform axial burnup profile in the fuel assemblies.

iii. Inasmuch as the transfer of heat occurs from the inside of the basket region to the outside, the temperature field in the MPC is spatially distributed with the maximum values reached in the central region.

It is clearly impractical to explicitly model every fuel rod in every stored fuel assembly explicitly. Instead, the cross section bounded by the inside of the storage cell, which surrounds the assemblage of fuel rods and the interstitial helium gas, is replaced with an "equivalent" square (solid) section characterized by an effective thermal conductivity. Figure 3.4.1 pictorially illustrates the homogenization concept. Further details on this process for determining the effective conductivity is presented in Subsection 3.4.1.1.2. It suffices to state here that the effective conductivity of the cell space will be a function of temperature, because radiation heat transfer (a major component of the heat transport mechanism between the fuel rods to the basket metal square) is a strong function of the absolute temperatures of the participating bodies. Therefore, in effect, every storage cell location will have a different value of effective conductivity in the homogenized model. The process of determining the temperature-dependent effective conductivity is carried out using a finite volume procedure.

In the next step of homogenization, a planar section of MPC is considered. With each storage cell inside space replaced with an equivalent solid square, the MPC cross section consists of a metallic gridwork (basket cell walls with each cell space containing a solid fuel square with an effective thermal conductivity) circumscribed by a circular ring (MPC shell). There are four principal materials in this section that are included in all MPCs, namely the homogenized fuel cell squares, the Alloy X MPC structural materials in the MPC (including Boral sheathing material), Boral and helium gas. Aluminum heat conduction elements (AHCEs), included optionally in the MPC design, are appropriately ignored in the heat dissipation calculations. Each of the four constituent materials in this section has a different conductivity. As discussed earlier, the conductivity of the homogenized fuel cell is a strong function of temperature.

In order to replace this thermally heterogeneous MPC section with an equivalent conduction-only lamina, resort to the finite-element procedure is necessary. Because the rate of transport of heat within the MPC is influenced by radiation, which is a temperature-dependent effect, the equivalent

conductivity of the MPC lamina must be computed as a function of temperature. Finally, it is recognized that the MPC section consists of two discrete regions, namely, the basket region and the periphery region. The periphery region is the space between the peripheral storage cells and the MPC enclosure shell. This space is essentially full of helium gas surrounded by Alloy X plates and optionally aluminum heat conduction elements. Accordingly, as illustrated in Figure 3.4.2 for MPC-68, the MPC cross section is replaced with two homogenized regions with temperature-dependent conductivities. In particular, the effective conductivity of the fuel cells is subsumed into the equivalent conductivity of the basket cross section using a finite element procedure. The ANSYS finite-element code is the vehicle for all modeling efforts described in the foregoing.

In summary, appropriate finite element models are used to replace the MPC cross section with an equivalent two-region homogeneous conduction lamina whose local conductivity is a known function of coincident absolute temperature. Thus, the MPC cylinder containing discrete fuel assemblies, helium, Boral, Alloy X and optionally AHCEs* is replaced with a right circular cylinder whose material conductivity will vary with radial and axial position as a function of the coincident temperature.

The MPC-to-overpack gap is simply an annular space that is readily modeled with an equivalent conductivity that reflects the conduction and radiation modes of heat transfer. The overpack is a radially symmetric structure except for the neutron absorber region which is built from radial connectors and Holtite. Using the classical equivalence procedure as described in Section 3.4.1.1.9, this region is replaced with an equivalent radially symmetric annular cylinder.

The thermal analysis procedure described above makes frequent use of equivalent thermal properties to ease the geometric modeling of the cask components. These equivalent properties are rigorously calculated values based on detailed evaluations of actual cask system geometries. All these calculations are performed conservatively to ensure a bounding representation of the cask system. This process, commonly referred to as submodeling, yields accurate (not approximate) results. Given the detailed nature of the submodeling process, experimental validation of the individual submodels is not necessary.

In this manner, a HI-STAR System overpack containing a loaded MPC is replaced with a right circular cylinder with spatially varying temperature-dependent conductivity. Heat is generated within the basket space in this cylinder in the manner of the prescribed axial distribution. In addition, heat is deposited from insolation on its external surface. Natural convection and thermal radiation to ambient air dissipate heat. Details of the elements of mathematical modeling are provided in the following sections.

* In the thermal model, AHCEs are appropriately ignored.

3.4.1.1.2 Fuel Region Effective Thermal Conductivity Calculation

Thermal properties of a large number of PWR and BWR fuel assembly configurations manufactured by the major fuel suppliers (i.e., Westinghouse, CE, B&W, and GE) have been evaluated for inclusion in the HI-STAR System thermal analysis. Bounding PWR and BWR fuel assembly configurations are determined using the simplified procedure described below. This is followed by the determination of temperature-dependent properties of the bounding PWR and BWR fuel assembly configurations to be used for cask thermal analysis using a finite-volume (FLUENT) approach.

To determine which of the numerous PWR assembly types listed in Table 3.4.4 should be used in the thermal model for the PWR fuel baskets, we must establish which assembly has the maximum thermal resistance. The same determination must be made for the MPC-68, out of the menu of SNF types listed in Table 3.4.5. For this purpose, we utilize a simplified procedure that we describe below.

Each fuel assembly consists of a large array of fuel rods typically arranged on a square layout. Every fuel rod in this array is generating heat due to radioactive decay in the enclosed fuel pellets. There is a finite temperature difference required to transport heat from the innermost fuel rods to the storage cell walls. Heat transport within the fuel assembly is based on principles of conduction heat transfer combined with the highly conservative analytical model proposed by Wooton and Epstein [3.4.1]. The Wooton-Epstein model considers radiative heat exchange between individual fuel rod surfaces as a means to bound the hottest fuel rod cladding temperature.

Transport of heat energy within any cross section of a fuel assembly is due to a combination of radiative energy exchange and conduction through the helium gas that fills the interstices between the fuel rods in the array. With the assumption of uniform heat generation within any given horizontal cross section of a fuel assembly, the combined radiation and conduction heat transport effects result in the following heat flow equation:

$$Q = \sigma C_o F_\varepsilon A [T_C^4 - T_B^4] + 13.5740 L K_{cs} [T_C - T_B]$$

where,

$$F_\varepsilon = Emissivity\ Factor = \frac{1}{\left(\frac{1}{\varepsilon_C} + \frac{1}{\varepsilon_B} - 1\right)}$$

ε_C, ε_B = emissivities of fuel cladding, fuel basket (see Table 3.2.4)

C_o = *Assembly Geometry Factor*

$$= \frac{4N}{(N+1)^2} \text{ (when N is odd)}$$

$$= \frac{4}{N+2} \text{ (when N is even)}$$

N = Number of rows or columns of rods arranged in a square array

A = fuel assembly "box" heat transfer area
= 4 × width × length (ft^2)

L = fuel assembly length (ft)

K_{cs} = fuel assembly constituent materials volume fraction weighted mixture conductivity (Btu/ft-hr-°F)

T_C = hottest fuel cladding temperature (°R)

T_B = box temperature (°R)

Q = net radial heat transport from the assembly interior (Btu/hr)

σ = Stefan-Boltzman Constant (0.1714×10^{-8} Btu/ft^2-hr-°R^4)

In the above heat flow equation, the first term is the Wooten-Epstein radiative heat flow contribution while the second term is the conduction heat transport contribution based on the classical solution to the temperature distribution problem inside a square shaped block with uniform heat generation [3.4.3]. The 13.574 factor in the conduction term of the equation is the shape factor for two-dimensional heat transfer in a square section. Planar fuel assembly heat transport by conduction occurs through a series of resistances formed by the interstitial helium fill gas, fuel cladding and enclosed fuel. An effective planar mixture conductivity is determined by a volume fraction weighted sum of the individual constituent materials resistances. For BWR assemblies, this formulation is applied to the region inside the fuel channel. A second conduction and radiation model is applied between the channel and the fuel basket gap. These two models are combined, in series, to yield a total effective conductivity.

The effective thermal conductivities of several representative intact PWR and BWR assemblies are presented in Tables 3.4.4 and 3.4.5. At higher temperatures (greater than 450°F), the zircaloy clad fuel assemblies with the lowest effective thermal conductivities are the Westinghouse 17×17 OFA (PWR) and the General Electric GE-11 9×9 (BWR). A discussion of fuel assembly conductivities for some of the newer 10×10 array and plant specific BWR fuel designs is presented near the end of this subsection. Based on this simplified analysis, the Westinghouse 17×17 OFA PWR and GE-11 9×9 BWR fuel assemblies are determined to be the bounding configurations for analysis at design basis

maximum heat loads. As discussed in Section 3.3.2, stainless clad fuel assemblies with significantly lower decay heat emission characteristics are not deemed to be bounding.

Several of the assemblies listed in Tables 3.4.5 were excluded from consideration when determining the bounding assembly because of their extremely low decay heat loads. The excluded assemblies, which were each used at a single reactor only, are physically small and have extremely low burnups and long cooling times. These factors combine to result in decay heat loads that are much lower than the design basis maximum. The excluded assemblies are:

Dresden Unit 1 8×8
Dresden Unit 1 6×6
Allis-Chalmers 10×10 Stainless
Exxon Nuclear 10×10 Stainless
Humboldt Bay 7x7
Quad^{+} 8x8

The Allis-Chalmers and Exxon assemblies are used only in the LaCrosse reactor of the Dairyland Power Cooperative. The design basis assembly decay heat loads for Dresden Unit 1 and LaCrosse SNF (Tables 1.2.14 and 1.2.19) are approximately 58% lower and 69% lower, respectively, than the MPC-68 design basis assembly maximum heat load (Table 1.2.13). Examining Table 3.4.5, the effective thermal conductivity of damaged Dresden Unit 1 fuel assemblies inside DFCs (the lowest of any Dresden Unit 1 assembly) and LaCrosse fuel assemblies are approximately 40% lower and 30% lower, respectively, than that of the bounding (GE-11 9×9) fuel assembly. Consequently, the fuel cladding temperatures in the HI-STAR System with Dresden Unit 1 and LaCrosse fuel assemblies (intact or damaged) will be bounded by design basis fuel cladding temperatures.

To accommodate Trojan Nuclear Plant (TNP) SNF in a HI-STAR System's MPC-24E canister*, the discharged fuel characteristics at this permanently shutdown site are evaluated herein. To permit TNP fuel in the HI-STAR System, it is necessary to confirm that certain key fuel parameters, viz. burnup (B) and cask decay heat (D) are bounded by the thermal design limits (42,500 MWD/MTU and 20 kW for PWR MPCs). The TNP SNF is a member of the 17x17 class of fuel types. The bulk of the fuel inventory is from Westinghouse and balance from B&W. The B&W SNF configuration and cladding dimensions are same as that of the Westinghouse 17x17 SNF. The fuel is more than nine years old and the burnups are in the range of 5073 MWD/MTU to 41889 MWD/MTU. The TNP SNF burnups are bounded by the design maximum for PWR class of fuel (i.e. $B < 42500$ MWD/MTU). Because the fuel decay heat is exponentially attenuating with time, it is conservative to evaluate decay heat on a date that precedes fuel loading. For this purpose, a reference date (RD) of 11/9/2001 is employed herein. The decay heat from the most emissive Trojan fuel is bounded by 725 W on RD. Postulating every cell location in an MPC-24E is occupied by this most heat emissive fuel assembly, a conservatively bounding $D = 17.4$ kW† is computed. The Trojan MPC-24E heat loads are below the HI-STAR System design heat load (i.e. $D < 20$ kW) by a significant margin.

* The height of MPC-24E for Trojan SNF is shorter than the height of generic HI-STAR MPCs.
† Projected MPC heat loads are much lower (in the range of 6 kW to 14.5 kW in circa 2003).

A limited number of Trojan assemblies have poison inserts (RCCAs and BPRAs) and other non-fuel hardware (Thimble Plugs). The inclusion of PWR non-fuel hardware influences the MPC thermal response in two ways: (i) The presence of non-fuel hardware increases the effective basket conductivity, thus enhancing heat dissipation and lowering fuel temperatures and (ii) Volume displaced by the mass of non-fuel hardware lowers the available cavity free volume for accommodating gas released in hypothetical rod rupture scenarios. For a conservatively bounding evaluation, the thermal modeling ignores the presence of non-fuel hardware and the MPC cavity volume is computed based on volume displacement by the heaviest fuel (bounding weight) with non-fuel hardware included.

Having established the governing (most resistive) PWR and BWR SNF types, a finite-volume code is used to determine the effective conductivities in a conservative manner. Detailed conduction-radiation finite-volume models of the bounding PWR and BWR fuel assemblies are developed in the FLUENT code as shown in Figures 3.4.7 and 3.4.8, respectively. The PWR model was originally developed on the ANSYS code which enables individual rod-to-rod and rod-to-basket wall view factor calculations to be performed using that code's AUX12 processor. Limitations of radiation modeling techniques implemented in ANSYS make it difficult to take advantage of the symmetry of the fuel assembly geometry. Unacceptably long CPU time and large workspace requirements necessary for performing gray body radiation calculations for a complete fuel assembly geometry on ANSYS prompted the development of an alternate simplified model on the FLUENT code. The FLUENT model was benchmarked with the ANSYS model results for a Westinghouse 17×17 OFA fuel assembly geometry for the case of black body radiation (emissivities = 1). The FLUENT model was found to yield conservative results in comparison to the ANSYS model for the "black" surface case. The FLUENT model benchmarked in this manner is used to solve the gray body radiation problem to provide the necessary results for determining the effective thermal conductivity of the governing PWR fuel assembly. The same modeling approach using FLUENT is then applied to the governing BWR fuel assembly and the effective conductivity of GE-11 9×9 fuel is determined.

An equivalent homogeneous material that fills the basket opening replaces the combined fuel rods-helium matrix by the following two-step procedure. In the first step, the FLUENT-based fuel assembly model is solved by applying equal heat generation per unit length to the individual fuel rods and a uniform boundary temperature along the basket cell opening inside periphery. The temperature difference between the peak cladding and boundary temperatures is used to determine an effective conductivity as described in the next step. For this purpose, we consider a two-dimensional cross section of a square shaped block of size equal to 2L and a uniform volumetric heat source (q_g) cooled at the periphery with a uniform boundary temperature. Under the assumption of constant material thermal conductivity (K), the temperature difference (ΔT) from the center of the cross section to the periphery is analytically given by [3.4.3]:

$$\Delta T = 0.29468 \frac{q_g L^2}{K}$$

This analytical formula is applied to determine the effective material conductivity from a known quantity of heat generation applied in the FLUENT model (smeared as a uniform heat source, q_g), basket opening size and ΔT calculated in the first step.

As discussed earlier, the effective fuel space conductivity is a function of the temperature coordinate. The above two step analysis is carried out for a number of reference temperatures. In this manner, the effective conductivity as a function of temperature is established.

In Table 3.4.25, 10×10 array type BWR fuel assembly effective thermal conductivity results from a simplified analysis are presented to determine the most resistive fuel assembly in this class. Using the simplified analysis procedure discussed earlier, the Atrium-10 fuel type is determined to be the most resistive in this class of fuel assemblies. A detailed finite-element model of this assembly type was developed to rigorously quantify the heat dissipation characteristics. The results of this study are presented in Table 3.4.26 and compared to the bounding BWR fuel assembly effective thermal conductivity depicted in Figure 3.4.13. The results of this study demonstrate that the bounding BWR fuel assembly effective thermal conductivity is conservative with respect to the 10×10 class of BWR assemblies. Table 3.4.34 summarizes plant specific fuel types' effective conductivities. From these analytical results, the SPC-5 is determined to be the most resistive fuel assembly in this group of fuel types. A rigorous finite element model of SPC-5 fuel assembly was developed to confirm that its in-plane heat dissipation characteristics are bounded from below by the design basis BWR fuel conductivities used in the HI-STAR thermal analysis.

Temperature-dependent effective conductivities of PWR and BWR design basis fuel assemblies (most resistive SNF types) are shown in Figure 3.4.13. The finite-volume results are also compared to results reported from independent technical sources. From this comparison, it is readily apparent that FLUENT-based fuel assembly conductivities are conservative. The FLUENT computed values (not the published literature data) are used in the MPC thermal analysis presented in this document.

3.4.1.1.3 Effective Thermal Conductivity of Sheathing/Boral/Cell Wall Sandwich

Each MPC basket cell wall (except outer periphery MPC-68 & mpc-32 cell walls) is manufactured with a Boral neutron absorbing plate for criticality control. Each Boral plate is sandwiched in a sheathing-to-basket wall pocket. A schematic of the "Box Wall-Boral-Sheathing" sandwich geometry of an MPC basket is illustrated in Figure 3.4.5. During fabrication, a uniformly applied normal pressure on each sheathing-Boral-cell wall sandwich prior to stitch welding of the sheathing periphery to the box wall ensures adequate surface-to-surface contact for elimination of any macroscopic gaps. The mean coefficient of linear expansion of Boral is higher than the basket materials thermal expansion coefficients. Consequently, basket heat-up from the contained SNF will further ensure a tight fit of the Boral plate in the sheathing-to-cell wall pocket. The presence of small microscopic gaps due to less than perfect surface finish characteristics requires consideration of an interfacial contact resistance between the Boral and the box and sheathing surfaces. A conservative contact resistance resulting from a 2 mils Boral-to-pocket gap is applied to the analysis. Note that this gap would actually be filled with helium. In other words, no credit is taken for the interfacial pressure between Boral and stainless plate/sheet stock produced by the fixturing and welding process.

Heat conduction properties of a composite "Box Wall-Boral-Sheathing" sandwich in the two principal basket cross sectional directions as illustrated in Figure 3.4.5 (i.e., lateral "out-of-plane" and longitudinal "in-plane") are unequal. In the lateral direction, heat is transported across layers of sheathing, helium-gap, Boral (B_4C and cladding layers) helium-gap, and cell wall resistances that are in series (except for the small helium filled end regions shown in Figure 3.4.6). Heat conduction in the longitudinal direction, in contrast, is through an array of essentially parallel resistances comprised of these same layers. For the ANSYS based MPC basket thermal model, corresponding non-isotropic effective thermal conductivities in the two orthogonal directions are determined and applied in the analysis.

The non-isotropic conductivities are determined by constructing ANSYS models of the composite "Box Wall-Boral-Sheathing" sandwich for the "in-plane" and "out-of-plane" directions. For determining the effective conductivity (K_{eff}), a heat flux is applied to the to one end of the sandwich and an ANSYS numerical solution to the sandwich temperature differential obtained. From Fourier equation for one-dimensional conduction heat transfer, the following equation for K_{eff} is obtained:

$$K_{eff} = \frac{qL}{\Delta T}$$

where:

q = Sandwich heat flux
L = Sandwich length in the direction of heat transfer
□T = Sandwich temperature differential (obtained from ANSYS solution)

In the equation above, L is the width or thickness of the sandwich, respectively, for in-plane or out-of-plane heat transfer directions.

3.4.1.1.4 Modeling of Basket Conductive Heat Transport

Conduction of heat in a fuel basket is a combination of planar and axial contributions. These component contributions are individually calculated for each MPC basket design and combined (as described later in this subsection) to obtain an equivalent isotropic thermal conductivity . The heat rejection capability of each MPC design (i.e., MPC-24, MPC-24E, MPC-32 and MPC-68) is evaluated by developing a thermal model of the combined fuel assemblies and composite basket walls geometry on the ANSYS finite element code. The ANSYS model includes a geometric layout of the basket structure in which the "Box Wall-Boral-Sheathing" sandwich is replaced by a "homogeneous wall" with an equivalent thermal conductivity. Since the thermal conductivity of the Alloy X material is a weakly varying function of temperature, the equivalent "homogeneous wall" must have a temperature-dependent effective conductivity. Similarly, as illustrated in Figure 3.4.6, the conductivities in the in-plane and through-thickness direction of the equivalent "homogeneous wall" are different. Finally, as discussed earlier, the fuel assemblies occupying the basket cell openings are modeled as homogeneous heat generating regions with effective temperature dependent in-plane conductivities. The methodology used to reduce the heterogeneous MPC basket - fuel

assemblage to an equivalent homogeneous region with effective thermal properties is discussed in the following.

Consider a cylinder of height L and radius r_o with a uniform volumetric heat source term q_g, with insulated top and bottom faces and its cylindrical boundary maintained at a uniform temperature T_c. The maximum centerline temperature (T_h) to boundary temperature difference is readily obtained from classical one-dimensional conduction relationships (for the case of a conducting region with constant thermal conductivity K_s):

$$(T_h - T_c) = q_g r_o^2/(4 K_s)$$

Noting that the total heat generated in the cylinder (Q_t) is $\pi r_o^2 L q_g$, the above temperature rise formula can be reduced to the following simplified form in terms of the total heat generation per unit length (Q_t/L):

$$(T_h - T_c) = (Q_t / L)/ (4 \pi K_s)$$

This simple analytical approach is employed to determine an effective basket cross-sectional conductivity by applying an equivalence between the ANSYS finite element model of the basket and the analytical case. The equivalence principle employed in the HI-STAR System thermal analysis is depicted in Figure 3.4.2. The 2-dimensional ANSYS finite element model of the MPC basket is solved by applying a uniform heat generation per unit length in each basket cell region and a constant basket periphery boundary temperature, T_c'. Noting that the basket region with uniformly distributed heat sources and a constant boundary temperature is equivalent to the analytical case of a cylinder with uniform volumetric heat source discussed earlier, an effective MPC basket conductivity (K_{eff}) is readily derived from the analytical formula and the ANSYS solution leading to the following relationship:

$$K_{eff} = N (Q_f'/L) / (4 \pi [T_h' - T_c'])$$

where:

N = number of fuel assemblies

(Q_f'/L) = each fuel assembly heat generation per unit length applied in ANSYS model

T_h' = peak basket cross-section temperature from ANSYS model

Cross sectional views of MPC basket ANSYS models are illustrated in Figures 3.4.10 and 3.4.11 for a PWR and BWR MPC. Notice that many of the basket supports and all shims have been conservatively neglected in the models. This conservative geometry simplification, coupled with the conservative neglect of thermal expansion which would minimize the gaps, yields conservative gap thermal resistances. Temperature dependent equivalent thermal conductivities of the fuel region and composite basket walls, as determined from analysis procedures described earlier, are applied to the ANSYS model. The planar ANSYS conduction model is solved by applying a constant basket periphery temperature with uniform heat generation in the fuel region. Table 3.4.6 summarizes

effective thermal conductivity results of each basket design obtained from the ANSYS models. It is recalled that the equivalent thermal conductivity values presented in Table 3.4.6 are lower bound values because, among other elements of conservatism, the effective conductivity of the most resistive SNF type (Tables 3.4.4 and 3.4.5) is used in the MPC finite-element simulations.

The axial conductivity of a fuel basket is determined by calculating a cross-sectional area-weighted sum of the component conductivities (Helium, Alloy-X, Boral and fuel cladding). In accordance with NUREG-1536 guidelines, credit for fuel rod axial heat conduction is conservatively limited to cladding.

Having obtained planar and axial thermal conductivities as described above, an equivalent isotropic conductivity (defined as the Square Root of the Mean Sum of Squares (SRMSS[†])) is obtained as shown below:

$$k_{iso} = \sqrt{\frac{k_{rad}^{\ 2} + k_{ax}^{\ 2}}{2}}$$

where:

k_{iso} = equivalent isotropic thermal conductivity
k_{rad} = equivalent planar thermal conductivity
k_{ax} = equivalent axial thermal conductivity

The equivalent isotropic conductivities are employed in the HI-STAR thermal modeling as discussed in Subsection 3.4.2.

3.4.1.1.5 Heat Transfer in MPC Basket Peripheral Regions

Each of the MPC designs for storing PWR or BWR fuel are provided with relatively large helium filled regions formed between the relatively cooler MPC shell and hot basket peripheral panels. For a horizontally oriented cask under normal transport conditions, heat transfer in these helium-filled regions is similar to heat transfer in closed cavities under three cases listed below:

i. differentially heated short vertical cavity

ii. horizontal channel heated from below

iii. horizontal channel heated from above

In a closed cavity (case i scenario), an exchange of hot and cold fluids occurs near the top and bottom ends of the cavity, resulting in a net transport of heat across the gap.

The case (ii) scenario is similar to the classical Rayleigh-Benard instability of a layer of fluid heated from below [3.4.6]. If the condition for onset of fluid motion is satisfied, then a multi-cellular natural

† This formulation has been benchmarked for specific application to the MPC basket designs and confirmed to yield conservative results.

convection pattern is formed. The flow pattern results in upward motion of heated fluid and downward motion of relatively cooler fluid from the top plate, resulting in a net transport of heat across the heated fluid channel.

The case (iii) is a special form of case (ii) with an inverted (stably stratified) temperature profile. No fluid motion is possible in this circumstance and heat transfer is thus limited to fluid (helium) conduction only.

The three possible cases of closed cavity natural convection are illustrated in Figure 3.4.3 for an MPC-68 basket geometry. Peripheral spaces labeled B and B' illustrate the case (i) scenario, the space labeled D illustrates the case (ii) scenario, and the space labeled D' illustrates the case (iii) scenario. The basket is oriented to conservatively maximize the number of peripheral spaces having *no* fluid motion. A small alteration in the basket orientation will result in a non-zero gravity component in the x-direction which will induce case (i) type fluid motion in the D' space. The rate of natural convection heat transfer is characterized by a Rayleigh number for the cavity defined as follows:

$$R_{a_L} = \frac{C_p \rho^2 g \beta \Delta T L^3}{\mu K}$$

where:

C_p	=	fluid heat capacity
ρ	=	average fluid density
g	=	acceleration due to gravity
β	=	coefficient of thermal expansion (equal to reciprocal of absolute temperature for gases)
ΔT	=	temperature difference between hot and cold surfaces
L	=	spacing between hot and cold surfaces
μ	=	fluid viscosity
K	=	fluid conductivity

Hewitt et al. [3.4.5] report Nusselt number correlations for the closed cavity natural convection cases discussed earlier. A Nusselt number equal to unity implies heat transfer by fluid conduction only. A higher than unity Nusselt number is due to the so-called "Rayleigh" effect, which monotonically rises with increasing Rayleigh number. Nusselt numbers applicable to helium filled PWR and BWR MPCs in the peripheral voids are provided in Table 3.4.1. For conservatism, the heat dissipation enhancement due to Rayleigh effect is ignored.

3.4.1.1.6 Effective Conductivity of Multi-Layered Intermediate Shell Region

Fabrication of the layered overpack intermediate shells is discussed in Section 1.2 of this SAR. In the thermal analysis, each intermediate shell metal-to-metal interface presents an additional resistance to heat transport. The contact resistance arises from microscopic pockets of air trapped between surface irregularities of the contacting surfaces. Since air is a relatively poor conductor of heat, this results in a reduction in the ability to transport heat across the interface compared to that of the base metal. Interfacial contact conductance depends upon three principal factors, namely: (i) base material conductivity, (ii) interfacial contact pressure, and (iii) surface finish.

Rohsenow and Hartnett [3.2.2] have reported results from experimental studies of contact conductance across air entrapped stainless steel surfaces with a typical 100 μ-inch surface finish. A minimum contact conductance of 350 Btu/ft-hr-°F is determined from extrapolation of results to zero contact pressure.

The thermal conductivity of carbon steel is about three times that of stainless steel. Thus the choice of carbon steel as the base material in a multi-layered construction significantly improves heat transport across interfaces. The fabrication process guarantees interfacial contact. Contact conductance values extrapolated to zero contact pressures are therefore conservative. The surface finish of hot-rolled carbon steel plate stock is generally in the range of 250-1000 μ-inch [3.2.1]. The process of forming hot-rolled flat plate stock to cylindrical shapes to form the intermediate shells by rolling will result in a smoother surface finish. This results from the large surface pressures exerted by the hardened roller faces that flatten out any surface irregularities.

In the HI-STAR thermal analysis, a conservatively bounding interfacial contact conductance value is determined based on the following assumptions:

1. No credit is taken for high base metal conductivity.
2. No credit is taken for interfacial contact pressure.
3. No credit is taken for a smooth surface finish resulting from rolling of hot-rolled plate stock to cylindrical shapes.
4. Contact conductance is based on a uniform 2000 μ-inch (1000 μ-inch for each surface condition) interfacial air gap at all interfaces.
5. No credit for radiation heat exchange across this hypothetical inter-surface air gap.
6. Bounding low thermal conductivity at 200°F.

These assumptions guarantee a conservative assessment of heat dissipation characteristics of the multi-layered intermediate shell region. The resistances of the five carbon steel layers along with the associated interfacial resistances are combined as resistances in series to determine an effective conductivity of this region leading to the following relationship:

$$K_{gs} = r_o \ell n\left[\frac{r_5}{r_o}\right]\left[\sum_{i=1}^{5} \frac{\delta}{K_{air}} \frac{r_o}{r_i} + \frac{r_o \ell n\left[\frac{r_5}{r_o}\right]}{K_{cst}}\right]^{-1}$$

where (in conventional U.S. units):

K_{gs}	=	effective intermediate shell region thermal conductivity
r_o	=	inside radius of inner gamma shield layer
r_i	=	outer radius of i^{th} intermediate shell layer
δ	=	interfacial air gap (2000 μ-inch)
K_{air}	=	air thermal conductivity
K_{cst}	=	carbon steel thermal conductivity

3.4.1.1.7 Heat Rejection from Overpack and Impact Limiter Outside Surfaces

Jakob and Hawkins [3.2.9] recommend the following correlations for natural convection heat transfer to air from heated vertical surfaces (flat impact limiter ends) and from single horizontal cylinders (overpack and impact limiter curved surfaces):

Turbulent range:

$$h = 0.19\,(\Delta T)^{1/3} \text{ (Vertical, } GrPr > 10^9)$$

$$h = 0.18\,(\Delta T)^{1/3} \text{ (Horizontal Cylinder, } GrPr > 10^9)$$

(in conventional U.S. units)

Laminar range:

$$h = 0.29\left(\frac{\Delta T}{L}\right)^{1/4} \text{ (Vertical, } GrPr < 10^9)$$

$$h = 0.27\left(\frac{\Delta T}{D}\right)^{1/4} \text{ (Horizontal Cylinder, } GrPr < 10^9)$$

(in conventional U.S. units)

where ΔT is the temperature differential between the system exterior surface and ambient air. During normal transport conditions, the surfaces to be cooled are the impact limiter and overpack cylindrical surfaces, and the flat vertical faces of the impact limiters. The corresponding length scales for these surfaces are the impact limiter diameter, overpack diameter, and impact limiter diameter, respectively. Noting that Gr×Pr is expressed as $L^3\Delta TZ$, where Z (from Table 3.2.7) is at least 2.6×10^5 at a conservatively high upper bound system exterior surface temperature of 340°F, it is apparent that the turbulent condition is always satisfied for ΔT in excess of a few degrees Fahrenheit. Under turbulent conditions, the more conservative heat transfer correlation for horizontal cylinders (i.e., $h = 0.18\,\Delta T^{1/3}$) is utilized for thermal analyses on all exposed system surfaces.

Including both convective and radiative heat loss from the system exterior surfaces, the following relationship for surface heat flux is developed:

$$q_s = 0.18(T_s - T_A)^{4/3} + \sigma \times \varepsilon \times [(T_s + 460)^4 - (T_A + 460)^4]$$

where:

T_s, T_A = surface, ambient temperatures (°F)
q_s = surface heat flux (Btu/ft^2-hr)
ε = surface emissivity (see Table 3.2.4)
σ = Stefan-Boltzman Constant (0.1714×10^{-8} Btu/ft^2-hr-°R^4)

3.4.1.1.8 Determination of Solar Heat Input

The intensity of solar radiation incident on an exposed surface depends on a number of time varying parameters. The solar heat flux strongly depends upon the time of the day as well as on latitude and day of the year. Also, the presence of clouds and other atmospheric conditions (dust, haze, etc.) can significantly attenuate solar intensity levels. Rapp [3.4.2] has discussed the influence of such factors in considerable detail.

The HI-STAR System thermal analysis is based upon insolation levels specified in 10CFR71, Subpart F, which are for a 12-hour daytime period. During normal transport conditions, the HI-STAR System is cyclically subjected to solar heating during the 12-hour daytime period followed by cooling during the 12-hour nighttime. However, due to the large mass of metal and the size of the system, the inherent dynamic time lag in the temperature response is substantially larger than the 24-hour heating-cooling time period. Accordingly, the HI-STAR System cask model includes insolation at exposed surfaces averaged over a 24-hour time period. A bounding solar absorption coefficient of 1.0 is applied to cask exterior surfaces. The 10CFR71 mandated 12-hour average incident solar radiation levels are summarized in Table 3.4.7. The combined incident insolation heat flux absorbed by exposed cask surfaces and decay heat load from the MPC is rejected by natural convection and radiation to ambient air.

3.4.1.1.9 Effective Thermal Conductivity of Radial Channels - Holtite Region

In order to minimize heat transfer resistance limitations due to the poor thermal conductivity of the Holtite-A neutron shield material, a large number of thick radial channels formed from high strength and conductivity carbon steel material are embedded in the neutron shield region. These radial channels form highly conductive heat transfer paths for efficient heat removal. Each channel is welded to the outside surface of the outermost intermediate shell and at the overpack enclosure shell, thereby providing a continuous path for heat removal to the ambient environment.

The effective thermal conductivity of the composite neutron shielding and radial channels region is determined by combining the heat transfer resistance of individual components in a parallel network. In determining the heat transfer capability of this region to the outside ambient environment for normal transport conditions, no credit is taken for conduction through the neutron shielding material.

Thus, heat transport from the outer intermediate shell surface to the overpack outer shell is conservatively based on heat transfer through the carbon steel radial channel legs alone. Thermal conductivity of the parallel neutron shield and radial channel leg region is given by the following formula:

$$K_{ne} = \frac{K_R N_R t_R \ln\left[\frac{r_B}{r_A}\right]}{2\pi L_R} + \frac{K_{ns} N_R t_{ns} \ln\left[\frac{r_B}{r_A}\right]}{2\pi L_R}$$

where (in consistent U.S. units):

K_{ne}	=	effective thermal conductivity of neutron shield region
r_A	=	inner radius of neutron shielding
r_B	=	outer radius of neutron shielding
K_R	=	effective thermal conductivity of carbon steel radial channel leg
N_R	=	total number of radial channel legs (also equal number of neutron shield sections)
t_R	=	minimum (nominal) thickness of each radial channel leg
L_R	=	effective radial heat transport length through radial channel leg
K_{ns}	=	neutron shield thermal conductivity
t_{ns}	=	neutron shield circumferential thickness (between two radial channel legs)

The radial channel leg to outer intermediate shell surface weld thickness is equal to half the plate thickness. The additional weld resistance is accounted for by reducing the plate thickness in the weld region for a short radial span equal to the weld size. Conductivity of the radial carbon steel channel legs based on the full thickness for the entire radial span is correspondingly reduced. Figure 3.4.4 depicts a resistance network developed to combine the neutron shield and radial channel legs resistances to determine an effective conductivity of the neutron shield region. Note that in the resistance network analogy only the annulus region between overpack outer enclosure inner surface and intermediate shells outer surface is considered in this analysis. The effective thermal conductivity of neutron shield region is provided in Table 3.4.8.

3.4.1.1.10 Effective Thermal Conductivity of the Eccentric MPC to Overpack Gap

During horizontal shipment of the HI-STAR System under normal transport conditions, the MPC will rest on the inside surface of the overpack. In the region of line contact, the resistance to heat transfer across the gap will be negligibly small due to a vanishingly small gap thickness. The resistance to heat transfer at other regions along the periphery of the MPC will, however, increase in direct proportion to the thickness of the local gap. This variation in gap thickness can be accounted for in the thermal model by developing a relation for the total heat transferred across the gap as given below:

$$Q_E = 2\int_0^{\pi} \frac{K_{He}}{g(\theta)} L R_o \Delta T \, d\theta$$

where:

Q_E	=	total heat transfer across the gap (Btu/hr)
K_{He}	=	helium conductivity Btu/ft-hr-°F
L	=	length of MPC (ft.)
R_o	=	MPC radius (ft.)
θ	=	angle from point of line contact
g(θ)	=	variation of gap thickness with angle (ft.)
ΔT	=	temperature difference across the gap (°F)

A corresponding relationship for heat transferred across a uniform gap is given by:

$$Q_c = \frac{K_{eff}}{(R_I - R_O)} 2\pi R_O L \Delta T$$

where R_1 is the inside radius of the overpack and K_{eff} is the effective thermal conductivity of an equivalent concentric MPC/overpack gap configuration. From these two relationships, the ratio of effective gap conductivity to helium thermal conductivity in the MPC/overpack region is shown below:

$$\frac{K_{eff}}{K_{He}} = \frac{R_I - R_O}{\pi} \int_0^{\pi} \frac{1}{g(\theta)} d\theta$$

Based on an analysis of the geometry of a thin gap between two eccentrically positioned cylinders, the following relationship is developed for variation of the gap thickness with position:

$$g(\theta) = (R_I - R_O)(1 - \cos\theta) + \varepsilon \cos\theta$$

The above equation conservatively accounts for imperfect contact by postulating a minimum gap ε at the point where the two surfaces would ideally form a line of perfect contact. The relatively thin MPC shell is far more flexible than the much thicker overpack inner shell, and will ovalize to yield greater than line contact. The substantial weight of the fuel basket and contained fuel assemblies will also cause the MPC shell to conform to the overpack inner shell. An evaluation based on contact along a line would therefore be reasonable and conservative. However, a minimum gap is assumed to further increase conservatism in this calculation.

Based on an applied gap of 0.02-inch, which is conservative compared to contact along a line, the effective gap thermal conductivity determined from analytical integration [3.4.7] is in excess of 200% of the conductivity of helium gas. In the HI-STAR analysis, a conservative effective gap conductivity equal to twice the helium gas conductivity is applied to the performance evaluation.

3.4.1.1.11 Effective Thermal Conductivity of MPC Basket-to-Shell Aluminum Heat Conduction Elements

The HI-STAR MPCs feature an option to install full-length heat conduction elements fabricated from aluminum alloy 1100 in the large MPC basket-to-shell gaps. Due to the high aluminum alloy 1100 thermal conductivity (about 15 times that of Alloy X), a significant rate of net heat transfer is possible along the thin plates. For conservatism, heat dissipation by the Aluminum Heat Conduction Elements (AHCEs) is ignored in normal transport analyses. This overstates the initial fuel temperature for hypothetical fire accident evaluation. To conservatively compute heating of MPC contents in a hypothetical fire condition, the presence of heat conduction elements in AHCE equipped MPCs is duly recognized.

Figure 3.4.12 shows a mathematical idealization of a heat conduction element inserted between basket periphery panels and the MPC shell. The aluminum insert is shown to cover the MPC basket Alloy X peripheral panel and MPC shell surfaces (Regions I and III depicted in Figure 3.4.12) along the full-length of the basket. Heat transport to and from the aluminum insert is conservatively postulated to occur across a thin helium gap as shown in the figure (i.e., no credit is considered for aluminum insert to Alloy X metal-to-metal contact). Aluminum surfaces inside the hollow region are sandblasted prior to fabrication to result in a rough surface finish which has a significantly higher emissivity compared to smooth surfaces of rolled aluminum. The untreated aluminum surfaces directly facing Alloy X panels have a smooth finish to minimize contact resistance.

Net heat transfer resistance from the hot basket periphery panel to the relatively cooler MPC shell along the aluminum heat conduction element pathway is a sum of three individual resistances in regions labeled I, II, and III. In Region I, heat is transported from the basket to the aluminum insert surface directly facing the basket panel across a thin helium resistance gap. Longitudinal transport of heat (in the z direction) in the aluminum plate (in Region I) will result in an axially non-uniform temperature distribution. Longitudinal one-dimensional heat transfer in the Region I aluminum plate is analytically formulated to result in the following ordinary differential equation for the non-uniform temperature distribution:

$$t\,K_{Al}\frac{\partial^2 T}{\partial z^2} = -\frac{K_{He}}{h}(T_h - T) \qquad \text{(Equation a)}$$

Boundary Conditions

$$\frac{\partial T}{\partial z} = 0 \text{ at } z = 0$$
$$T = T_h' \text{ at } z = P \qquad \text{(Equation b)}$$

where (see Figure 3.4.12):

$T(z)$	=	non-uniform aluminum metal temperature distribution
t	=	conduction element thickness
K_{Al}	=	conduction element conductivity
K_{He}	=	helium conductivity
h	=	helium gap thickness
T_h	=	hot basket temperature
T_h'	=	conduction element Region I boundary temperature at $z = P$
P	=	conduction element Region I length

Solution of this ordinary differential equation subject to the imposed boundary condition is:

$$(T_h - T) = (T_h - T_h') \left[\frac{e^{\frac{z}{\sqrt{\alpha}}} + e^{\frac{z}{\sqrt{\alpha}}}}{e^{\frac{P}{\sqrt{\alpha}}} + e^{\frac{P}{\sqrt{\alpha}}}} \right] \qquad \text{(Equation c)}$$

where α is a dimensional parameter equal to htK_{Al}/K_{He}. The net heat transfer (Q_I) across the Region I helium gap can be determined by the following integrated heat flux to a conduction element of length L as:

$$Q_I = \int_0^P \frac{K_{He}}{h} (T_h - T)(L)\, dz \qquad \text{(Equation d)}$$

Substituting the analytical temperature distribution result obtained in Equation c into Equation d and then integrating, the following expression for net heat transfer is obtained:

$$Q_I = \frac{K_{He} L \sqrt{\alpha}}{h} \left(1 - \frac{1}{e^{\frac{P}{\sqrt{\alpha}}} + e^{\frac{P}{\sqrt{\alpha}}}} \right) (T_h - T_h') \qquad \text{(Equation e)}$$

Based on this result, an expression for Region I resistance is obtained as shown below:

$$R_I = \frac{T_h - T_h'}{Q_I} = \frac{h}{K_{He} L \sqrt{\alpha}} \left(1 - \frac{1}{e^{\frac{P}{\sqrt{\alpha}}} + e^{\frac{P}{\sqrt{\alpha}}}} \right)^{-1} \qquad \text{(Equation f)}$$

Similarly, a Region III resistance expression can be analytically determined as shown below:

$$R_{III} = \frac{(T_c' - T_c)}{Q_{III}} = \frac{h}{K_{He} L \sqrt{\alpha}} \left(1 - \frac{1}{e^{\frac{P}{\sqrt{\alpha}}} + e^{\frac{P}{\sqrt{\alpha}}}} \right)^{-1} \qquad \text{(Equation g)}$$

A Region II resistance expression can be developed from the following net heat transfer equation in the vertical leg of the conduction element as shown below:

$$Q_{II} = \frac{K_{Al} L t}{W} (T_h' - T_c') \qquad \text{(Equation h)}$$

Hence,

$$R_{II} = \frac{T_h' - T_c'}{Q_{II}} = \frac{W}{K_{Al} L t} \qquad \text{(Equation i)}$$

This completes the analysis for the total thermal resistance attributable to the heat conduction elements equal to sum of the three individual resistances. The total resistance is smeared across the basket-to-MPC shell region as an effective uniform annular gap conductivity (see Figure 3.4.2). Note that heat transport along the conduction elements is an independent conduction path in parallel with conduction and radiation mechanisms in the large helium gaps. Helium conduction and radiation between the MPC basket and the MPC shell is accounted for separately in the ANSYS MPC models described earlier in this section. Therefore, the total MPC basket-to-MPC shell peripheral gaps conductivity will be the sum of the conduction elements effective conductivity and the helium conduction-radiation gap effective conductivity.

3.4.1.1.12 FLUENT Model for HI-STAR Temperature Field Computation

In the preceding subsections, the series of analytical and numerical models to define the thermal characteristics of the various elements of the HI-STAR System are presented. The thermal modeling begins with the replacement of the SNF cross section and surrounding fuel cell space by a solid lamina with an equivalent conductivity. Since radiation is an important constituent of the heat transfer process in the SNF/storage cell space and the rate of radiation heat transfer is a strong function of the surface temperatures, it is necessary to treat the equivalent lamina conductivity as a function of temperature. In fact, because of the relatively large range of temperatures which will exist in a loaded HI-STAR System under the design basis heat loads, it is necessary to include the effect of variation in the thermal conductivity of materials with temperature throughout the system finite volume model. The presence of significant radiation effect in the storage cell spaces adds to the imperative to treat the equivalent lamina conductivity as temperature-dependent.

FLUENT finite volume simulations have been performed to establish the equivalent thermal conductivity as a function of temperature for the limiting (thermally most resistive) BWR and PWR spent fuel types. By utilizing the most limiting SNF (established through a simplified analytical process for comparing conductivities) the numerical idealization for the fuel space conductivity is ensured to be conservative for all non-limiting fuel types.

Having replaced the interior of the cell spaces by solid prismatic (square) columns possessing a temperature-dependent conductivity essentially renders the basket into a non-homogeneous three-dimensional solid where the non-homogeneity is introduced by the honeycomb basket structure. The basket panels themselves are a composite of Alloy X cell wall, Boral neutron absorber, and Alloy X sheathing metal. A conservative approach to replace this composite section with an equivalent "solid wall" is described in a preceding subsection.

In the next step, a planar section of the MPC is considered. The MPC, externally radially symmetric, contains a non-symmetric basket lamina wherein the equivalent fuel space solid squares are separated by the "equivalent" solid metal walls. The space between the basket and the MPC, called the peripheral gap, is filled with helium gas and optionally aluminum heat conduction elements. The equivalent thermal conductivity of this MPC section is computed using a finite element procedure on ANSYS, as described previously. For hypothetical fire conditions the "helium-conduction-radiation" based peripheral gap conductivity and the effective conductivity of aluminum conduction elements are added to obtain a combined effective conductivity. At this stage in the thermal analysis, the SNF/basket/MPC assemblage has been replaced with a two-zone (Figure 3.4.2) cylindrical solid whose thermal conductivity is a strong function of temperature.

The idealization for the overpack is considerably more straightforward. The overpack is radially symmetric except for the Holtite region (discussed in Subsection 3.4.1.1.9). The procedure to replace the multiple shell layers, Holtite-A and radial connectors with an equivalent solid utilizes classical heat conduction analogies, as described in the preceding subsections.

In the final step of the analysis, the equivalent two-zone MPC cylinder, the equivalent overpack shell, the top and bottom plates, and the impact limiters are assembled into a comprehensive finite volume model. A cross section of this axisymmetric model implemented on FLUENT is shown in Figure 3.4.14. A summary of the essential features of this model is presented in the following:

- The overpack shell is represented by 840×9 elements. The effective thermal conductivity of the overpack shell elements is set down as a function of temperature based on the analyses described earlier.

- The overpack bottom plate and bolted closure plate are modeled by 312×9 axisymmetric elements.

- The two-zone MPC "solid" is represented by 1,144×9 axisymmetric elements.

- The space between the MPC "solid" and the overpack interior space is assumed to contain helium.

- Heat input due to insolation is applied to the impact limiter surfaces and the cylindrical surface of the overpack.

- The heat generation in the MPC solid basket region is assumed to be uniform in each horizontal plane, but to vary in the axial direction to correspond to the axial burnup distribution in the active fuel region postulated in Chapter 1.

The finite volume model constructed in this manner will produce an axisymmetric temperature distribution. The peak temperature will occur near the centerline and is expected to correspond to the axial location of peak heat generation. As is shown later, the results from the finite element solution bear out these observations.

3.4.1.1.13 Effect of Fuel Cladding Crud Resistance

In this subsection, a conservatively bounding estimate of the temperature drop across a crud film adhering to a fuel rod during dry storage conditions is determined. The evaluation is performed for a BWR fuel assembly based on an upper bound crud thickness obtained from PNL-4835 report ([3.3.5], Table 3). The crud present on fuel assemblies is predominantly iron oxide mixed, with small quantities of other metals such as cobalt, nickel, chromium, etc. Consequently, the effective conductivity of the crud mixture is expected to be in the range of typical metal alloys. Metals have thermal conductivities several orders of magnitude larger than that of helium. In the interest of extreme conservatism, however, a film of helium with the same thickness replaces the crud layer. The calculation is performed in two steps. In the first step, a crud film resistance is determined based on bounding maximum crud layer thickness replaced as a helium film on the fuel rod surfaces. This is followed by a peak local cladding heat flux calculation for the smaller GE 7×7 fuel assembly postulated to emit a conservatively bounding decay heat equal to 0.5kW. The temperature drop across the crud film obtained as a product of the heat flux and crud resistance terms is determined to be less than 0.1°F. The calculations are presented below:

Bounding Crud Thickness (δ)= 130μm (4.26×10^{-4} ft)
(PNL-4835)

Crud Conductivity (K) = 0.1 Btu/ft-hr-°F (conservatively assumed as helium)

GE 7×7 Fuel Assembly:

Rod O.D. = 0.563"
Active Fuel Length = 150"

Heat Transfer Area	=	$(7\times7)\,(\pi\times0.563)\times150/144$
	=	$90.3\ ft^2$
Axial Peaking Factor	=	1.195 (Burnup distribution Table 1.2.15)
Decay Heat	=	500W (conservative assumption)

$$\text{Crud Resistance} = \frac{\delta}{K} = \frac{4.26\times10^{-4}}{0.1} = 4.26\times10^{-3}\,\frac{ft^2\text{-}hr\text{-}^\circ F}{Btu}$$

$$\text{Peak Heat Flux} = \frac{(500\times3.417)\,Btu/hr}{90.3\,ft^2}\times1.195$$

$$= 18.92\times1.195 = 22.6\,\frac{Btu}{ft^2\text{-}hr}$$

Temperature drop (ΔT_c) across crud film:

$$= 4.26\times10^{-3}\,\frac{ft^2\text{-}hr\text{-}^\circ F}{Btu}\times22.6\,\frac{Btu}{ft^2\text{-}hr}$$

$$= 0.096^\circ F$$

(i.e., less than $0.1^\circ F$)

Therefore, it is concluded that deposition of crud does not materially change the SNF cladding temperature.

3.4.1.1.14 Maximum Time Limit During Wet Transfer

While loading an empty HI-STAR System for transport directly from a spent fuel pool, water inside the MPC cavity is not permitted to boil. Consequently, uncontrolled pressures in the de-watering, purging, and recharging system that may result from two-phase condition, are completely avoided. This requirement is accomplished by imposing a limit on the maximum allowable time duration for fuel to be submerged in water after a loaded HI-STAR cask is removed from the pool and prior to the start of vacuum drying operations.

When the HI-STAR overpack and the loaded MPC under water-flooded conditions are removed from the pool, the combined mass of the water, the fuel, the MPC, and the overpack will absorb the decay heat emitted by the fuel assemblies. This results in a slow temperature rise of the entire system with time, starting from an initial temperature of the contents. The rate of temperature rise is limited by the thermal inertia of the HI-STAR system. To enable a bounding heat-up rate determination for the HI-STAR system, the following conservative assumptions are imposed:

i. Heat loss by natural convection and radiation from the exposed HI-STAR surfaces to the pool building ambient air is neglected (i.e., an adiabatic temperature rise calculation is performed).

ii. Design Basis maximum decay heat input from the loaded fuel assemblies is imposed on the HI-STAR system.

iii. The smallest of the *minimum* MPC cavity-free volumes between the two MPC types is considered for flooded water mass determination.

iv. Fifty percent of the water mass in the MPC cavity is credited towards water thermal inertia evaluation.

Table 3.4.19 summarizes the weights and thermal inertias of several components in the loaded HI-STAR system. The rate of temperature rise of the HI-STAR and its contents during an adiabatic heat-up is governed by the following equation:

$$\frac{dT}{d\tau} = \frac{Q}{C_h}$$

where:

Q = decay heat load (Btu/hr) [equal to Design Basis maximum (between the two MPC types) 20.0 kW (i.e., 68,260 Btu/hr)]

C_h = combined thermal inertia of the loaded HI-STAR system (Btu/°F)

T = temperature of the contents (°F)

□ = time after HI-STAR system is removed from the pool (hr)

A bounding heat-up rate for the HI-STAR system contents is determined to be equal to 2.19°F/hr. From this adiabatic rate of temperature rise estimate, the maximum allowable time duration (t_{max}) for fuel to be submerged in water is determined as follows:

$$t_{max} = \frac{T_{boil} - T_{initial}}{dT/d\tau}$$

where:

T_{boil} = boiling temperature of water (equal to 212°F at the water surface in the MPC cavity)

$T_{initial}$ =initial temperature of the HI-STAR contents when removed from the pool

Table 3.4.20 provides a summary of t_{max} at several initial HI-STAR contents temperatures.

As set forth in Section 7.4, in the unlikely event where the maximum allowable time provided in Table 3.4.20 is found to be insufficient to complete all wet transfer operations, a forced water circulation shall be initiated and maintained to remove the decay heat from the MPC cavity. In this case, relatively cooler water will enter via the MPC lid drain port connection and heated water will

exit from the vent port. The minimum water flow rate required to maintain the MPC cavity water temperature below boiling with an adequate subcooling margin is determined as follows:

$$M_W = \frac{Q}{C_{pw}(T_{max} - T_{in})}$$

where:

M_W = minimum water flow rate (lb/hr)

C_{pw} = water heat capacity (Btu/lb-°F)

T_{max} = maximum MPC cavity water mass temperature

T_{in} = temperature of water supply to MPC

With the MPC cavity water temperature limited to 150°F, MPC inlet water maximum temperature equal to 125°F and at the design basis maximum heat load, the water flow rate is determined to be 2,731 lb/hr (5.5 gpm).

3.4.1.1.15 Cask Cooldown and Reflood Analysis During Fuel Unloading Operation

Before a loaded HI-STAR System can be unloaded (i.e., fuel removed from the MPC) the cask must be cooled from the operating temperatures and reflooded with water†. Past industry experience generally supports cooldown of cask internals and fuel from hot storage conditions by direct water quenching. However, the extremely rapid cooldown rates that are typical during water injection, to which the hot cask internals and fuel cladding are subjected to, may result in uncontrolled thermal stresses and failure in the structural members. Moreover, water injection results in large amounts of steam generation and unpredictable transient two-phase flow conditions inside the MPC cavity, which may result in over-pressurization of the MPC helium retention boundary and a potentially unacceptable reduction in the safety margins to prevent criticality. To avoid potential safety concerns related to rapid cask cooldown by direct water quenching, the HI-STAR MPCs are designed to be cooled in a gradual manner, thereby eliminating thermal shock loads on the cask internals and fuel cladding.

In the unlikely event that a HI-STAR system is required to be unloaded, it will be transported back to the fuel handling building. Prior to reflooding the MPC cavity with water, a forced flow helium recirculation system with adequate flow capacity shall be operated to remove the decay heat and initiate a slow cask cooldown lasting for several days. The operating procedures in Section 7.2 provide a detailed description of the steps involved in the cask unloading. In this section, an analytical evaluation is presented to provide the basis for helium flow rates and time of forced cooling to meet the objective of eliminating thermal shock when the MPC cavity is eventually flooded with water.

† Certain fuel configurations in PWR MPCs require Borated water for criticality control (Chapter 6). Such MPCs are reflooded with Borated water.

Under a closed loop forced helium circulation condition, the helium gas is cooled via an external chiller, down to 100°F, and then introduced inside the MPC cavity from the drain line near the bottom baseplate. The helium gas enters the MPC basket from the bottom oversized flow holes and moves upward through the hot fuel assemblies, removing heat and cooling the MPC internals. The heated helium gas exits from the basket top and collects in the top plenum, from where it is expelled through the MPC lid vent connection to the helium recirculation and cooling system. The bulk average temperature reduction of the MPC contents as a function of time is principally dependent upon the rate of helium circulation. The temperature transient is governed by the following heat balance equation:

$$C_h \frac{dT}{d\tau} = Q_D - m C_p (T - T_i) - Q_c$$

Initial Condition: $T = T_o$ at $\tau = 0$

where:

T = MPC bulk average temperature (°F)

T_o = initial MPC bulk average temperature in the HI-STAR system (483°F†)

τ = time after start of forced circulation (hr)

Q_D = decay heat load (Btu/hr)
(equal to Design Basis maximum 20.0 kW (i.e., 68,260 Btu/hr))

m = helium circulation rate (lb/hr)

C_p = helium heat capacity (Btu/lb-°F)
(equal to 1.24 Btu/lb-°F)

Q_c = heat rejection from cask exposed surfaces to ambient (Btu/hr)
(conservatively neglected)

C_h = thermal capacity of the loaded MPC (Btu/°F)
(For a bounding upper bound 100,000 lb loaded MPC weight, and heat capacity of Alloy X equal to 0.12 Btu/lb-°F, the heat capacity is equal to 12,000 Btu/°F)

T_i = MPC helium inlet temperature (°F)

† Bounding for HI-STAR normal transport.

The differential equation is analytically solved, yielding the following expression for time-dependent MPC bulk temperature:

$$T(t) = (T_i + \frac{Q_D}{mC_p})(1 - e^{\frac{mC_p}{C_h}t}) + T_o e^{\frac{mC_p}{C_h}t}$$

This equation is used to determine the minimum helium mass flow rate that would cool the MPC cavity down from initially hot conditions to less than 200°F. For example, to cool the MPC to less than 200°F in 72 hours would required a helium mass flow rate of 574 lb/hr (i.e., 859 SCFM).

Once the helium gas circulation has cooled the MPC internals to less than 200°F, water can be injected to the MPC without risk of boiling and the associated thermal stress concerns. Because of the relatively long cooldown period, the thermal stress contribution to the total cladding stress would be negligible, and the total stress would therefore be bounded by the normal (dry) condition. The elimination of boiling eliminates any concern of over-pressurization due to steam production.

3.4.1.1.16 MPC Evaluation Under Drying Conditions

The initial loading of SNF in the MPC requires that the water within the MPC be drained, residual moisture removed and MPC filled with helium. This operation on the HI-STAR MPCs will be carried out using a Forced Helium Dehydrator (FHD) for a "load-and-go" operation. A "load-and-go" operation is defined as an activity wherein an MPC is loaded for direct off-site shipment in a HI-STAR transport cask. MPCs prepared via other competent methods for MPC drying as approved by the NRC on other dockets (1008 and 1014) are duly recognized for transport under this docket.

To reduce moisture to trace levels in the MPC using a Forced Helium Dehydration (FHD) system, a closed loop system consisting of a condenser, a demoisturizer, a compressor, and a pre-heater is utilized to extract moisture from the MPC cavity through repeated displacement of its contained helium, accompanied by vigorous flow turbulation. Appendix 3.B contains detailed discussion of the design and operation criteria for the FHD system.

The FHD system provides concurrent fuel cooling during the moisture removal process through forced convective heat transfer. The attendant forced convection-aided heat transfer occurring during operation of the FHD system ensures that the fuel cladding temperature will remain below the applicable peak cladding temperature limit for normal conditions of transport (752°F) for all combinations of SNF type, burnup, decay heat, and cooling time. Because the FHD operation induces a state of forced convection heat transfer in the MPC, (in contrast to the quiescent mode of natural convection in transport), it is readily concluded that the peak fuel cladding temperature under the latter condition will be greater than that during the FHD operation phase. In the event that the FHD system malfunctions, the forced convection state will degenerate to natural convection, which corresponds to the conditions of normal transport. As a result, the peak fuel cladding temperatures will approximate the values reached during normal transport as described elsewhere in this chapter.

3.4.1.1.17 Effects of Helium Dilution from Fuel Rod Gases

In this subsection, the generic cask transportation accident issue raised in a USNRC Spent Fuel Project Office (SFPO) staff guidance letter[†] is addressed. This issue directs cask designers to evaluate the impact of fission gas release into the canister, from a 100% fuel rods rupture accident, on the cask component temperatures and pressures when the MNOP[††] is within 10% of the design pressure. To determine whether the HI-STAR System falls within the stipulated criteria, the MNOP results from Table 3.4.15 are provided below:

Canister	MNOP (psig)	Threshold Criteria[†††] for Accident Evaluation (psig)
MPC-24	88.8	90
MPC-68	86.9	90
MPC-24E	88.9	90
MPC-32	89.3	90

As shown above the MNOPs are below the threshold and an accident evaluation is not required. Nevertheless, for illustrative purposes, a 100% rods rupture accident for a HI-STAR package with an MPC-24 canister is evaluated.

Under a severe hypothetical accident scenario 100% of the fuel rods may rupture, releasing the rod fill gas (helium) and a portion of the gaseous fission products (^{3}H, ^{85}Kr, ^{129}I and ^{131}Xe). The gaseous fission products release fractions are stipulated in NUREG-1536. The released gases will mix with the MPC backfill gas and reduce its thermal conductivity. This reduction in conductivity will result in a small increase in MPC temperatures and pressures.

Appendix C of NUREG/CR-0497 [3.4.13] describes a method for calculating the effective thermal conductivity of a mixture of gases. The same method is also described by Rohsenow and Hartnett [3.2.2]. The following expression is provided by both references:

$$k_{mix} = \sum_{i=1}^{n} \left(\frac{k_i x_i}{x_i + \sum_{\substack{j=1 \\ j \neq i}}^{n} \varphi_{ij} x_j} \right)$$

---

† SFPO Director's Interim Staff Guidance Letter(s), W.F. Kane, (Interim Staff-Guidance-7), October 8, 1998.

†† MNOP is a regulatory term defined in NUREG-1617 as the maximum gauge pressure that would develop in the containment in a period of 1 year under the heat condition specified in 10 CFR 71.71(c)(1) in the absence of venting, external ancillary cooling or operational controls.

††† Accident evaluation required when MNOP is within 10% of the design pressure. This translates to a pressure that is between 100 psig (HI-STAR design pressure (Table 2.1.1)) and 90 psig.

where:

k_{mix} = thermal conductivity of the gas mixture (Btu/hr-ft-°F)
n = number of gases
k_i = thermal conductivity of gas component i (Btu/hr-ft-°F)
x_i = mole fraction of gas component i

In the preceding equation, the term φ_{ij} is given by the following:

$$\varphi_{ij} = \phi_{ij}\left[1+2.41\frac{(M_i - M_j)(M_i - 0.142 \cdot M_j)}{(M_i + M_j)^2}\right]$$

where M_i and M_j are the molecular weights of gas components i and j, and ϕ_{ij} is:

$$\phi_{ij} = \frac{\left[1+\left(\frac{k_i}{k_j}\right)^{\frac{1}{2}}\left(\frac{M_i}{M_j}\right)^{\frac{1}{4}}\right]^2}{2^{\frac{3}{2}}\left(1+\frac{M_i}{M_j}\right)^{\frac{1}{2}}}$$

Table 3.4.30 presents a summary of the gas mixture thermal conductivity calculations for an MPC-24 containing design basis PWR fuel assemblies.

Having calculated the gas mixture thermal conductivity, the effective thermal conductivity of the design basis PWR fuel assembly is calculated using the finite-volume model described in Subsection 3.4.1.1.2. Only the helium gas conductivity is changed, all other modeling assumptions are the same. The fuel assembly effective thermal conductivity with diluted helium is compared to that with undiluted helium in Table 3.4.31.

Next, the effective thermal conductivities of the MPC fuel basket and basket periphery regions are determined as described in Subsections 3.4.1.1.3 and 3.4.1.1.4. This calculation incorporates both the diluted helium thermal conductivity and the effective thermal conductivity of the fuel assembly with diluted helium. The Rayleigh effect thermal conductivity multipliers are unchanged in this analysis. This is conservative because the released rod gases will increase the average fluid density and decrease the gas thermal conductivity, consequently increasing the Rayleigh number. The effective thermal conductivities with diluted helium are compared to those with undiluted helium in Table 3.4.31.

The MPC fuel basket effective thermal conductivities are input to a finite-volume model of the HI-STAR System arranged for transport. The cask system temperature distribution with diluted MPC helium is determined using the finite-volume model, as described in Subsection 3.4.1.1.12. Design basis normal environmental conditions are applied to the model and a temperature field solution obtained. Cask system temperatures with diluted MPC helium are summarized in Table 3.4.32.

The slightly higher MPC cavity temperature with MPC helium dilution will result in a small perturbation in MPC internal pressure. Based on the temperature field obtained with helium dilution, the MPC internal pressure is determined using the Ideal Gas Law. The calculated MPC internal pressure with helium dilution is presented in Table 3.4.33.

The results of analyses presented in this subsection are performed to illustrate the effect of a hypothetical 100% rods rupture on a HI-STAR package with an MPC-24.. Even under the extreme postulated conditions, the MPC component temperatures and pressures remain substantially below the design limits.

3.4.1.1.18 HI-STAR Temperature Field With Low Heat Emitting Fuel

The HI-STAR 100 thermal evaluations for BWR fuel are divided in two groups of fuel assemblies proposed for storage in MPC-68. These groups are classified as Low Heat Emitting (LHE) fuel assemblies and Design Basis (DB) fuel assemblies. The LHE group of fuel assemblies are characterized by low burnup, long cooling time, and short active fuel lengths. Consequently, their heat loads are dwarfed by the DB group of fuel assemblies. The Dresden-1 (6x6 and 8x8), QUAD+, and Humboldt Bay (7x7 and 6x6) fuel characteristics warrant their classification as LHE fuel. These characteristics, including burnup and cooling time limits imposed on this class of fuel, are presented in Table 2.1.6. This fuel (except Quad+) is permitted to be loaded when encased in Damaged Fuel Containers (DFCs). As a result of interruption of radiation heat exchange between the fuel assembly and the fuel basket by the DFC boundary, this loading configuration is bounding for thermal evaluation. In Subsection 3.4.1.1.2, two canister designs for encasing LHE fuel are evaluated – a previously approved Holtec Design (Figure 1.2.10) and an existing canister in which some of the Dresden-1 fuel is currently stored (Transnuclear D-1 Canister). The most resistive fuel assembly determined by analytical evaluation is considered for thermal evaluation (see Table 4.4.6). The MPC-68 basket effective conductivity, loaded with the most resistive fuel assembly from the LHE group of fuel (encased in a canister) is provided in Table 4.4.7. To this basket, LHE fuel decay heat load, is applied and a HI-STAR 100 System temperature field obtained. The low heat load burden limits the initial peak cladding temperature to less than 579°F which is substantially below the cladding temperature limit (Table 3.3.1) .

A thoria rod canister designed to hold a maximum of 20 fuel rods arrayed in a 5x4 configuration is currently stored at the Dresden-1 spent fuel pool. The fuel rods contain a mixture of enriched UO_2 and Thorium Oxide in the fuel pellets. The fuel rods were originally constituted as part of an 8x8 fuel assembly and used in the second and third cycle of Dresden-1 operation. The maximum fuel burnup of these rods is quite low (~13,100 MWD/MTU). The thoria rod canister internal design is a honeycomb structure formed from 12 gage stainless steel plates. The rods are loaded in individual square cells and are isolated from each other by the cell walls. The few number of rods (18 per assembly) and very low burnup of fuel stored in these Dresden-1 canisters render them as miniscule sources of decay heat. The canister all-metal internal honeycomb construction serves as an additional means of heat dissipation in the fuel cell space. In accordance with preferential fuel loading requirements, low burnup fuel shall be loaded toward the basket periphery (i.e., away from the hot

central core of the fuel basket). All these considerations provide ample assurance that these fuel rods will be stored in a benign thermal environment and therefore remain protected during transport.

3.4.1.2 Test Model

A detailed analytical model for evaluating the thermal design of the HI-STAR System was developed using the FLUENT CFD code and the industry standard ANSYS modeling system as discussed in Subsection 3.4.1.1. Furthermore, the analysis incorporates many conservative assumptions in order to demonstrate compliance with specified temperature limits for operation with adequate margins. In view of these considerations, the HI-STAR thermal design complies with the thermal criteria set forth in the design basis for normal transport conditions. Additional experimental verification of the thermal design is therefore not required. Acceptance and periodic thermal testing for the HI-STAR System is discussed in Sections 8.1 and 8.2.

3.4.2 Maximum Temperatures Under Normal Transport Conditions

Both MPC-basket designs developed for the HI-STAR System have been analyzed to determine temperature distributions under normal transport conditions. In the HI-STAR System thermal analysis models developed on FLUENT, the overpack impact limiters are included in the finite volume geometry. However, no credit is considered for the presence of heat conducting aluminum honeycomb material. In other words, heat transmission through the ends is conservatively neglected in the analysis. The thermal results are therefore bounding with respect to impact limiter design. The MPC baskets are considered to be loaded at design-basis maximum heat load with PWR or BWR fuel assemblies, as appropriate.

As discussed in Subsection 3.4.1.1.1, the thermal analysis is performed using a submodeling process where the results of an analysis on an individual component are incorporated into the analysis of a larger set of components. Specifically, the submodeling process yields directly computed fuel temperatures from which fuel basket temperatures are indirectly calculated. This modeling process differs from previous analytical approaches wherein the basket temperatures were evaluated first and then a basket-to-cladding temperature difference calculation by Wooten-Epstein or other means provided a basis for cladding temperatures. Subsection 3.4.1.1.2 describes the calculation of an effective fuel assembly thermal conductivity for an equivalent homogenous region. It is important to note that the result of this analysis is a function for thermal conductivity versus temperature. This function for fuel thermal conductivity is then input to the fuel basket effective thermal conductivity calculation described in Subsection 3.4.1.1.4. This calculation uses a finite-element methodology, wherein each fuel cell region containing multiple finite-elements has temperature varying thermal conductivity properties. The resultant temperature varying fuel basket thermal conductivity computed by this basket-fuel composite model is then input to the fuel basket region of the FLUENT cask model.

Because the FLUENT cask model incorporates the results of the fuel basket submodel, which in turn incorporates the fuel assembly submodel, the peak temperature reported from the FLUENT model is the peak temperature in any component. In a dry storage cask, the hottest components are the fuel assemblies. It should be noted that, because the fuel assembly models described in Subsection

3.4.1.1.2 include the fuel pellets, the FLUENT calculated peak temperatures reported in Tables 3.4.10 and 3.4.11 are actually peak pellet centerline temperatures which bound the peak cladding temperatures. We conservatively assume that the peak clad temperature is equal to the peak pellet centerline temperature.

From a thermal/hydraulic standpoint, the HI-STAR transport cask must cover two scenarios:

i. MPCs equipped with AHCEs
ii. MPCs without AHCEs

In the thermal analysis submitted in support of HI-STAR's original transport certification, which we now refer to as the Baseline Thermal Model (BTM), the AHCEs are included in the thermal models and the basket thermal model is constructed in an exceedingly conservative manner. In particular, the axial conductance of the basket fuel assemblage is assumed to be equal to the in-plane conductance (in reality, the in-plane conductance is much smaller than the axial conductance due to the presence of physical gaps between the fuel and the cell and within the fuel assemblies). For the Scenario (ii) analysis, such an overarching conservatism is removed while certain other less sweeping conservatisms are retained. The revised model, which we refer to as the Refined Thermal Model (RTM), forms the licensing basis for thermal evaluation. The conservatisms germane to the RTM are summarized in Appendix 3.A. To summarize, the principal difference between the BTM and RTM are as follows:

Item	*Description*	*BTM Assumption*	*RTM Assumption*
1	AHCE heat dissipation	Included	Excluded
2	Rayleigh effect	Included	Excluded
3	Basket Axial Conductivity	Grossly Understated	Realistic modeling of axial conductivity (See discussion in Subsection 3.4.1.1.4)

For representative PWR (MPC-24) and BWR (MPC-68) MPC-basket configurations with AHCEs installed, the temperature contours obtained with the Baseline Thermal Model (BTM) corresponding to steady-state hot conditions (100°F ambient, maximum design basis maximum decay heat and full insolation) are shown in Figures 3.4.16 and 3.4.17. Figures 3.4.19 and 3.4.20 show the axial temperature variation of the hottest fuel rod in the MPC-24 and MPC-68 basket designs, respectively. Figures 3.4.22 and 3.4.23 show the radial temperature profile in the MPC-24 and MPC-68 basket designs, respectively, in the horizontal plane where maximum fuel cladding temperature is indicated. Tables 3.4.10 and 3.4.11 summarize maximum calculated temperatures in different parts of the HI-STAR System at design-basis maximum decay heat loads. Tables 3.4.28 and 3.4.29 summarize the peak fuel cladding temperatures with heat loads lower than the design basis maximum. In Tables 3.4.22 and 3.4.23, maximum calculated temperatures in different parts of the HI-STAR System under steady-state cold conditions (-40°F ambient, maximum design basis maximum decay heat and no insolation) are summarized. To confirm the BTM fuel temperatures provided herein are bounding for all MPCs without the AHCEs option (MPC-24, MPC-24E, MPC-32 and MPC-68) a Refined Thermal Model (RTM) is articulated as discussed in the preceding

paragraph. As shown next, the results of the refined calculations confirm the BTM results are bounding.

Maximum Cladding Temperatures		
MPC Type	BTM [°F]	RTM [°F]
PWR	701	671 (MPC-24) 668 (MPC-24E) 699 (MPC-32)
BWR	713	642 (MPC-68)

The following additional observations can be derived by inspecting the temperature field obtained from the finite element analysis:

- The maximum fuel cladding temperature is well within the PNL recommended temperature limit.
- The maximum temperature of basket structural material is well within the stipulated design temperatures.
- The maximum temperature of the Boral neutron absorber is below the material supplier's recommended limit.
- The maximum temperatures of the MPC helium retention boundary materials are well below their respective ASME Code limits.
- The maximum temperatures of the aluminum heat conduction elements are well below the stipulated design temperature limits.
- The maximum temperature of the HI-STAR containment boundary materials is well below their respective ASME Code limits.
- The neutron shielding material (Holtite-A) will not experience temperatures in excess of its qualified limit.

The above observations lead us to conclude that the temperature field in the HI-STAR System with a fully loaded MPC containing design-basis heat emitting SNF complies with all regulatory and industry thermal requirements for normal conditions of transport. In other words, the thermal environment in the HI-STAR System will be conducive to safe transport of spent nuclear fuel.

3.4.2.1 Maximum Accessible Surface Temperatures

Access to the HI-STAR overpack cylindrical surface is restricted by the use of a personnel barrier (See Holtec Drawing 1809 in Chapter 1). Therefore, the HI-STAR System surfaces accessible during normal transport are the exposed impact limiter surfaces outside the personnel barrier. In this subsection, the exposed impact limiter surface temperatures are computed by including heat

transmission from the hot overpack ends through the impact limiters. A conservatively bounding analysis is performed by applying the thermal conductivity of aluminum to the encased aluminum-honeycomb material in the impact limiter shells to the normal condition thermal model discussed earlier in this chapter. In this manner heat transport to the exposed surfaces from the hot overpack is maximized and accessible surface temperatures over estimated. The maximum exposed cask surface temperatures for a PWR MPC (MPC-24) and a BWR MPC (MPC-68) at design maximum heat loads are 142°F and 139°F respectively. In Figure 3.4.28, a color contour map of the regions of HI-STAR System less than 185°F (358°K) is depicted for the hotter MPC-24 basket design. From this map, it is apparent that the accessible (impact limiter) surface temperatures are below the 10CFR71.43(g) mandated limit by a significant margin.

3.4.3 Minimum Temperatures

As specified in 10CFR71, the minimum ambient temperature conditions for the HI-STAR System are -20°F and a cold environment at -40°F. The HI-STAR System design does not have any minimum decay heat load restrictions for transport. Therefore, under zero decay heat load in combination with no solar input conditions, the temperature distribution will be uniformly equal to the imposed minimum ambient conditions. All HI-STAR System materials of construction would satisfactorily perform their intended function in the transport mode at this minimum postulated temperature condition. Evaluations in Chapter 2 demonstrate the acceptable structural performance of the overpack and MPC steel materials at low temperature. Shielding and criticality functions of the HI-STAR System materials (Chapters 5 and 6) are unaffected by exposure to this minimum temperature.

3.4.3.1 Post Rapid Ambient Temperature Drop Overpack Cooldown Event

In this section, the thermal response of the HI-STAR overpack to a rapid ambient temperature drop is analyzed and evaluated. The ambient temperature is postulated to drop from the maximum to minimum temperature under normal condition of transport in a very short time (100°F to –40°F during a 1 hour period) and is assumed to hold steady at –40°F thereafter. The initial overpack condition prior to this rapid temperature drop corresponds to normal steady state transport with maximum design basis heat load. During this postulated cooldown event, the outer surface of the overpack will initially cool more rapidly than the bulk of metal away from the exposed surfaces. Consequently, it is expected that the through-thickness temperature gradients will increase for a period of time, reach a maximum and follow an asymptotic return to the initial steady condition through thickness temperature gradients as the overpack temperature field approaches the –40°F ambient steady condition. The results of the transient analysis reported in this sub-section verify these observations.

Noting that the state of thermal stress is influenced by changes in the overpack temperature field during the cooldown transient, a number of critical locations in the containment boundary depicted in Figure 3.4.24 are identified as pertinent to a structural integrity evaluation discussed in Subsection 2.6.2.3 of this SAR. Locations (1) and (2) are chosen to track the through-thickness temperature gradients in the overpack top forging which is directly exposed to the ambient. Locations (3) and (4) are chosen to track the overpack inner containment shell through-thickness temperature gradient in a

plane of maximum heat generation (i.e. active fuel mid-height) where the heat fluxes and corresponding temperature gradients are highest. Locations (A) and (B) are similarly chosen to track the temperature differential in the multi-layered shells (outer-to-inner shells).

The normal transport condition thermal model discussed previously in this chapter is employed in the overpack cooldown transient analysis. This analysis is carried out by applying time-dependent thermal boundary conditions to the model and starting the transient solution in the FLUENT program. In the cooldown event, the ambient temperature is decreased from 100°F to –40°F in 10°F steps every 4 minutes (i.e. a total of 14 steps lasting 56 minutes). The ambient temperature is held constant thereafter. The maximum design basis heat load cask (i.e. the MPC-24 design) was selected to maximize the thermal gradients (by Fourier's Law, thermal gradient is proportional to heat flow). The overpack cooldown event is tracked by the thermal model for a period of 24 hours and results are reported in Figures 3.4.25 through 3.4.27 as discussed below.

In Figure 3.2.25, the overpack containment through-thickness temperature gradient responses are plotted. From this figure, it is evident that the exposed surface of the overpack forging (location (2)) initially cools at a faster rate than the recessed location (1). A similar but less pronounced result is observed in the multi-layered shells temperature changes depicted in Figure 3.4.26. This out-of-phase rate of cooling results in an increasing temperature gradient through the overpack metal layers. The thermal response of deeply recessed locations (3) and (4) show gradual temperature changes that follow each other closely. In other words, while through-thickness temperature gradients in the forging are somewhat altered the overpack inner shell gradients are essentially unchanged during the cooldown period. A closer examination of the forging temperature gradient is therefore warranted.

In Figure 3.4.27, the time dependent forging through thickness temperature differential is depicted. The gradient increases to a maximum in a short time period followed by a slow return towards the starting state. In absolute terms, both the steady state and transient temperature gradients in the forging are quite modest. In the steady state the forging through thickness temperature gradient is approximately 3°F. This value reaches a maximum plateau of 7°F during the transient event (Figure 3.4.27). The incremental thermal stress arising from this short-term gradient elevation is computed and discussed in Subsection 2.6.2.3 of this SAR.

3.4.4 Maximum Internal Pressures

The MPC is initially filled with dry helium after fuel loading and prior to sealing the MPC lid port cover plates and closure ring. During normal transport conditions, the gas temperature within the MPC rises to its maximum operating temperature as determined by the thermal analysis methodology described earlier (see Subsection 3.4.1). The gas pressure inside the MPC will increase with rising temperature. The pressure rise is determined using the Ideal Gas Law which states that the absolute pressure of a fixed volume of entombed gas is proportional to its absolute temperature.

The HI-STAR Maximum Normal Operating Pressure (MNOP) is calculated for10 CFR71.71(c)(1) heat condition (100°F ambient & insolation) and the HI-STAR Overpack passively cooled at design maximum heat load. For other lower than design maximum heat load scenarios, (e.g. transport with Trojan fuel) the MNOP results are confirmed to be bounding. . In Tables 3.4.13 and 3.4.14, summary

calculations for determining net free volume in the PWR and BWR canisters are presented. Based on a 30% release of the significant radioactive gases, a 100% release of the rod fill gas from postulated cladding breaches, the net free volume and the initial fill gas pressure (see Table 3.3.2), the MNOP results are given in Table 3.4.15. The overpack containment boundary MNOP for a hypothetical MPC breach condition is bounded by the MPC pressure results reported in this table.

3.4.5 Maximum Thermal Stresses

Thermal expansion induced mechanical stresses due to imposed non-uniform temperature distributions have been determined and reported in Chapter 2. Tables 3.4.17 and 3.4.18 summarize the HI-STAR System components temperatures, under steady-state hot conditions, for structural evaluation.

Additionally, Table 3.4.24 provides a summary of MPC helium retention boundary temperatures during normal transport conditions (steady state hot). Structural evaluations in Section 2.6 reference these temperature results to demonstrate the MPC helium retention boundary integrity.

3.4.6 Evaluation of System Performance for Normal Conditions of Transport

The HI-STAR System thermal analysis is based on detailed and complete heat transfer models that properly account for radiation, conduction and natural convection modes of heat transfer. The thermal models incorporate many conservative assumptions that are listed below. A quantitative evaluation of HI-STAR conservatisms is provided in Appendix 3.A.

1. No credit for gap reduction between the MPC and overpack due to differential thermal expansion under hot condition is considered.

2. No credit is considered for MPC basket internal thermosiphon heat transfer. Under a perfectly horizontal transport condition, axial temperature gradients with peaking at active fuel mid-height induces buoyancy flows from both ends of the basket in each MPC cell. Buoyancy flow in shallow horizontal channels has been widely researched and reported in the technical literature [3.4.10 to 3.4.12]. An additional mode of heat transport due to thermosiphon flow within the basket cells is initiated for any cask orientation other than a perfectly horizontal condition. In practice this is a highly likely scenario. However, in the interest of conservatism, no credit is considered for this mode of heat transfer.

3. An upper bound solar absorbtivity of unity is applied to all exposed surfaces.

4. No credit considered for radiative heat transfer between the Boral neutron absorber panels and the Boral pocket walls, or for the presence of helium in the pocket gaps.

5. No credit is considered for conduction through the neutron shielding materials.

6. No credit is considered for contact between fuel assemblies and the MPC basket wall or between the MPC basket and the MPC basket supports. The fuel assemblies and MPC basket are conservatively considered to be in concentric alignment.

7. No credit considered for presence of highly conducting aluminum honeycomb material inside impact limiters.

8. The fuel assembly contribution to MPC basket axial conductivity is conservatively limited to the fuel cladding only (i.e. axial heat transfer through fuel pellets is neglected).

9. The MPC is assumed to be loaded with the SNF type which has the maximum equivalent thermal resistance of all fuel types in its category (BWR or PWR), as applicable.

10. The design basis maximum decay heat loads are used for all thermal-hydraulic analyses. For casks loaded with fuel assemblies having decay heat generation rates less than design basis, additional thermal margins of safety will exist.

11. Interfacial contact conductance of multi-layered intermediate shell contacting layers was conservatively determined to bound surface finish, contact pressure, and base metal conductivity conditions.

12. Flow turbulation in the MPC space neglected.

Temperature distribution results obtained from a conservatively developed thermal model show that maximum fuel cladding temperature limits are met with adequate margins. Margins during actual normal transport conditions are expected to be greater due to the many conservative assumptions incorporated in the analysis. The maximum local temperatures in the neutron shield and overpack seals are lower than design limits. The maximum local MPC basket temperature level is below the recommended limits for structural materials in terms of susceptibility to stress, corrosion and creep induced degradation. Furthermore, structural evaluation (Chapter 2) has demonstrated that stresses (including those induced due to imposed temperature gradients) are within ASME B&PV Code limits. Section 3.6 provides a discussion of compliance with the regulatory requirements and acceptance criteria listed in Section 3.0. As a result of the above-mentioned considerations, it is concluded that the HI-STAR thermal design is in compliance with 10CFR71 requirements for normal conditions of transport.

Table 3.4.1

CLOSED CAVITY NUSSELT NUMBER†
RESULTS FOR HELIUM FILLED MPC PERIPHERAL VOIDS

	Case (i) Nusselt Number		Case (ii) Nusselt Number	
Temperature (°F)	MPC-24, MPC-24E, MPC-32	MPC-68	MPC-24, MPC-24E, MPC-32	MPC-68
200	6.93	4.72	5.45	3.46
450	5.44	3.71	4.09	2.58
700	4.60	3.13	3.36	2.12

† For conservatism, the heat dissipation enhancement due to Rayleigh effect discussed in Sub-section 3.4.1.1.5 is ignored

Table 3.4.2

RELATIONSHIP BETWEEN HI-STAR SYSTEM REGIONS
AND MATHEMATICAL MODEL DESCRIPTIONS

HI-STAR System Region	Mathematical Model	Subsections
Fuel Assembly	Fuel Region Effective Thermal Conductivity	3.4.1.1.2
MPC	Effective Thermal Conductivity of Boral/Sheathing/Box Wall Sandwich	3.4.1.1.3
	Basket In-Plane Conductive Heat Transport	3.4.1.1.4
	Heat Transfer in MPC Basket Peripheral Region	3.4.1.1.5
	Effective Thermal Conductivity of MPC Basket-to-Shell Aluminum Heat Conduction Elements	3.4.1.1.11
Overpack	Effective Conductivity of Multi-Layered Intermediate Shell Region	3.4.1.1.6
	Effective Thermal Conductivity of Holtite Neutron Shielding Region	3.4.1.1.9
Ambient Environment	Heat Rejection from Overpack Exterior Surfaces	3.4.1.1.7
	Solar Heat Input	3.4.1.1.8
Assembled Cask Model	Overview of the Thermal Model	3.4.1.1.1
	Effective Conductivity of MPC to Overpack Gap	3.4.1.1.10
	FLUENT Model for HI-STAR	3.4.1.1.12

Table 3.4.3

THIS TABLE IS INTENTIONALLY DELETED.

Table 3.4.4

SUMMARY OF PWR FUEL ASSEMBLIES
EFFECTIVE THERMAL CONDUCTIVITIES

No.	Fuel	@ 200°F (Btu/ft-hr-°F)	@ 450°F (Btu/ft-hr-°F)	@ 700°F (Btu/ft-hr-°F)
1	W 17×17 OFA	0.182	0.277	**0.402**
2	W 17×17 Std	0.189	0.286	0.413
3	W 17×17 Vantage-5H	0.182	0.277	0.402
4	W 15×15 Std	0.191	0.294	0.430
5	W 14×14 Std	0.182	0.284	0.424
6	W 14×14 OFA	**0.175**	**0.275**	0.413
7	B&W 17×17	0.191	0.289	0.416
8	B&W 15×15	0.195	0.298	0.436
9	CE 16×16	0.183	0.281	0.411
10	CE 14×14	0.189	0.293	0.435
11	HN† 15×15 SS	0.180	0.265	0.370
12	W 14×14 SS	0.170	0.254	0.361
13	B&W 15x15 Mark B-11	0.187	0.289	0.424
14	CE 14x14 (MP2)	0.188	0.293	0.434

Note: Boldface values denote the lowest thermal conductivity in each column (excluding stainless steel clad fuel assemblies).

† Haddam Neck B&W or Westinghouse stainless steel clad fuel assemblies.

Table 3.4.5

SUMMARY OF BWR FUEL ASSEMBLIES EFFECTIVE THERMAL CONDUCTIVITIES

No.	Fuel	@ 200°F (Btu/ft-hr-°F)	@ 450°F (Btu/ft-hr-°F)	@ 700°F (Btu/ft-hr-°F)
1	Dresden 1 8×8†	0.119	0.201	0.319
2	Dresden 1 6×6	0.126	0.215	0.345
3	GE 7×7	0.171	0.286	0.449
4	GE 7×7R	0.171	0.286	0.449
5	GE 8×8	0.168	0.278	0.433
6	GE 8×8R	**0.166**	0.275	0.430
7	GE-10 8×8	0.168	0.280	0.437
8	GE-11 9×9	0.167	**0.273**	**0.422**
9	AC†† 10×10 SS	0.152	0.222	0.309
10	Exxon 10×10 SS	0.151	0.221	0.308
11	Damaged Dresden 1 8×8 in a DFC†	0.107	0.169	0.254
12	Dresden-1 Thin Clad 6x6†	0.124	0.212	0.343
13	Humboldt Bay-7x7†	0.127	0.215	0.343
14	Damaged Dresden-1 8x8 (in TND-1 canister)†	0.107	0.168	0.252
15	8x8 QUAD+ Westinghouse†	0.164	0.278	0.435

Note: Boldface values denote the lowest thermal conductivity in each column (excluding Dresden and LaCrosse clad fuel assemblies).

† Low heat emitting fuel assemblies excluded from list of fuel assemblies (zircaloy clad) evaluated to determine the most resistive SNF type

†† Allis-Chalmers stainless steel clad fuel assemblies

Table 3.4.6

MPC BASKET EFFECTIVE THERMAL CONDUCTIVITY RESULTS
FROM ANSYS MODELS

Basket	@200°F (Btu/ft-hr-°F)	@450°F (Btu/ft-hr-°F)	@700°F (Btu/ft-hr-°F)
MPC-24 (Zircaloy Clad Fuel)	1.127	1.535	2.026
MPC-68 (Zircaloy Clad Fuel)	1.025	1.257	1.500
MPC-24 (Stainless Steel Clad Fuel) (Note 1)	0.901	1.230	1.615
MPC-68 (Stainless Steel Clad Fuel) (Note 1)	0.987	1.180	1.360
MPC-68 (Dresden-1 8x8 in canisters)	0.921	1.118	1.306
MPC-32 (Zircaloy Clad Fuel)	0.964	1.214	1.486
MPC-32 (Stainless Steel Clad Fuel) (Note 1)	0.762	0.936	1.104
MPC-24E (Zircaloy Clad Fuel)	1.211	1.635	2.137
MPC-24E (Stainless Steel Clad Fuel) (Note 1)	0.988	1.348	1.766

Note-1: Evaluated for a conservatively bounding configuration (fuel in a damaged fuel canister)

Table 3.4.7

INSOLATION DATA SPECIFIED BY 10CFR71, SUBPART F

Surface Type	12-Hour Total Insolation Basis	
	(g-cal/cm^2)	(Watts/m^2)
Horizontally Transported Flat Surfaces		
- Base	None	None
- Other Surfaces	800	774.0
Non-Horizontal Flat Surfaces	200	193.5
Curved Surfaces	400	387.0

Table 3.4.8

EFFECTIVE THERMAL CONDUCTIVITY OF THE NEUTRON SHIELD/RADIAL CHANNELS REGION

Condition/Temperature (°F)	Thermal Conductivity (Btu/ft-hr-°F)
Normal Condition:	
200	1.953
450	1.812
700	1.645
Fire Condition:	
200	3.012
450	2.865
700	2.689

Table 3.4.9

THIS TABLE IS INTENTIONALLY DELETED.

Table 3.4.10

HI-STAR SYSTEM NORMAL TRANSPORT[†] MAXIMUM TEMPERATURES
(PWR MPCs)

	Bounding Temperature [°F]	Normal Condition Temperature Limit [°F]
Fuel Cladding	701	752
MPC Basket Centerline	667	725
MPC Basket Periphery	430	725
MPC Outer Shell Surface	315	450
MPC/Overpack Helium Gap Outer Surface	291	400
Radial Neutron Shield Inner Surface	271	300
Overpack Enclosure Shell Surface	222	350
Axial Neutron Shield	292	300
Impact Limiter Exposed Surface	121	176
Overpack Closure Plate[††]	163	400
Overpack Bottom Plate[††]	295	350

[†] Steady-state hot (100°F ambient) with maximum decay heat and insolation.

[††] Overpack closure plate and vent/drain port plug seals normal condition design temperature is 400°F. The maximum seals temperatures are bounded by the reported closure plate and bottom plate maximum temperatures. Consequently, a large margin of safety exists to permit safe operation of seals in the overpack helium retention boundary.

Table 3.4.11

HI-STAR SYSTEM NORMAL TRANSPORT† MAXIMUM TEMPERATURES
(MPC-68)

	Bounding Temperature [°F]	Normal Condition Temperature Limit [°F]
Fuel Cladding	713	752
MPC Basket Centerline	697	725
MPC Basket Periphery	365	725
MPC Outer Shell Surface	306	450
MPC/Overpack Gap Outer Surface	282	400
Radial Neutron Shield Inner Surface	264	300
Overpack Enclosure Shell Surface	217	350
Axial Neutron Shield	255	300
Impact Limiter Exposed Surface	121	176
Overpack Closure Plate††	162	400
Overpack Bottom Plate††	256	350

† Steady-state hot (100°F ambient) with maximum decay heat and insolation.

†† Overpack closure plate and vent/drain port plug seals normal condition design temperature is 400°F. The maximum seals temperatures are bounded by the reported closure plate and bottom plate maximum temperatures. Consequently, a large margin of safety exists to permit safe operation of seals in the overpack helium retention boundary.

Table 3.4.12

THIS TABLE IS INTENTIONALLY DELETED.

Table 3.4.13

SUMMARY OF BOUNDING MINIMUM
FREE VOLUME CALCULATIONS (PWR MPCs)

Item	MPC-24 Volume (ft^3)	MPC-24E Volume (ft^3)	MPC-32 Volume (ft^3)
Cavity Volume	367	367	367
Basket Metal Volume	45	52	25
Bounding Fuel Assemblies Volume	79	79	106
Basket Supports and Fuel Spacers Volume	7	7	9
Aluminum Conduction Elements†	6	6	6
Net Free Volume	230 (6512 liters)	223 (6314 liters)	221 (6258 liters)

† Bounding 1,000 lbs aluminum weight.

Table 3.4.14

SUMMARY OF BOUNDING MINIMUM
MPC-68 FREE VOLUME CALCULATIONS

Item	Volume (ft^3)
Cavity Volume	367
Basket Metal Volume	35
Bounding Fuel Assemblies Volume	93
Basket Supports and Fuel Spacers Volume	12
Aluminum Conduction Elements†	6
Net Free Volume	221 (6258 liters)

† Bounding 1,000 lbs aluminum weight.

Table 3.4.15

SUMMARY OF MAXIMUM NORMAL OPERATING PRESSURE (MNOP)[†]
FOR HORIZONTAL TRANSPORT CONDITIONS

Condition	Pressure (psig)	Bounding MPC Cavity Bulk Temperature (°F)
MPC-24:		
Initial Backfill (at 70°F)	42.8	483
Normal Condition	87.7	
With 3% Rods Rupture(Note 1)	88.8	
MPC-68:		
Initial Backfill (at 70°F)	42.8	468
Normal Condition	86.0	
With 3% Rods Rupture(Note 1)	86.9	
MPC-24E:		
Initial Backfill (at 70°F)	42.8	483
Normal Condition	87.7	
With 3% Rods Rupture(Note 1)	88.9	
MPC-32:		
Initial Backfill (at 70°F)	42.8	483
Normal Condition	87.7	
With 3% Rods Rupture(Note 1)	89.3	

Note 1: NUREG-1617 requires an assumption for normal transport that 3% of the rods are breached with release of 100% fill gas and 30% fission gas to containment.

[†] Pressure analysis in accordance with heat condition specified in 10 CFR 71.71(c)(1) in the absence of venting, external ancillary cooling or operational controls.

Table 3.4.16

THIS TABLE IS INTENTIONALLY DELETED.

Table 3.4.17

PWR MPCs NORMAL HORIZONTAL TRANSPORT CONDITION
HI-STAR SYSTEM COMPONENTS BOUNDING TEMPERATURE SUMMARY

	MPC Basket Axial Mid-Length [°F]	MPC Basket Axial Ends [°F]
Overpack enclosure shell	222	147
Overpack inner shell	291	163
MPC shell	315	164
Basket periphery	430	166
Basket center	667	177

Table 3.4.18

MPC-68 NORMAL HORIZONTAL TRANSPORT CONDITION
HI-STAR SYSTEM COMPONENTS TEMPERATURE [°F] SUMMARY

	MPC Basket Axial Mid-Length	**MPC Basket Axial Ends**
Overpack enclosure shell	217	146
Overpack inner shell	282	161
MPC shell	306	163
Basket periphery	365	164
Basket center	697	175

Table 3.4.19

SUMMARY OF LOADED HI-STAR SYSTEM
BOUNDING COMPONENT WEIGHTS AND THERMAL INERTIAS

Component	Weight (lbs)	Heat Capacity (Btu/lb-°F)	Thermal Inertia (Btu/°F)
Holtite-A	11,000	0.39	4,290
Carbon Steel	140,000	0.1	14,000
Alloy-X MPC (empty)	35,000	0.12	4,200
Fuel	40,000	0.056	2,240
MPC Cavity Water[†]	6,500	1.0	6,500
			31,230 (Total)

† Based on smallest MPC-68 cavity net free volume with 50% credit for flooded water mass.

Table 3.4.20

MAXIMUM ALLOWABLE TIME DURATION
FOR WET TRANSFER OPERATIONS

Initial Temperature (°F)	Time Duration (hr)
115	44.3
120	42.0
125	39.7
130	37.4
135	35.2
140	32.9
145	30.6
150	28.3

Table 3.4.21

THIS TABLE IS INTENTIONALLY DELETED.

Table 3.4.22

HI-STAR SYSTEM BOUNDING TEMPERATURES [°F]
UNDER STEADY-STATE COLD† CONDITIONS (PWR MPCs)

Fuel Cladding	620
MPC Basket Centerline	586
MPC Basket Periphery	329
MPC Outer Shell Surface	190
MPC/Overpack Gap Outer Surface	165
Radial Neutron Shield Inner Surface	141
Overpack Enclosure Shell Surface	96
Axial Neutron Shield	165
Impact Limiter Exposed Surface	-40

† -40°F ambient temperature with maximum decay heat and no insolation.

Table 3.4.23

HI-STAR SYSTEM MAXIMUM TEMPERATURES [°F]
UNDER STEADY-STATE COLD† CONDITIONS (MPC-68)

Fuel Cladding	621
MPC Basket Centerline	605
MPC Basket Periphery	254
MPC Outer Shell Surface	178
MPC/Overpack Gap Outer Surface	153
Radial Neutron Shield Inner Surface	130
Overpack Enclosure Shell Surface	88
Axial Neutron Shield	123
Impact Limiter Exposed Surface	-40

† -40°F ambient temperature with maximum decay heat and no insolation.

Table 3.4.24

SUMMARY OF MPC HELIUM RETENTION BOUNDARY BOUNDING TEMPERATUREDISTRIBUTION DURING NORMAL STORAGE CONDITIONS

Location	Figure 2.6.20 Designation	PWR MPCs [°F]	MPC-68 [°F]
MPC Lid Inside Surface at Centerline	A	176	173
MPC Lid Outside Surface at Centerline	B	171	169
MPC Lid Inside Surface at Periphery	C	164	163
MPC Lid Outside Surface at Periphery	D	162	161
MPC Baseplate Inside Surface at Centerline	E	301	260
MPC Baseplate Outside Surface at Centerline	F	295	256
MPC Baseplate Inside Surface at Periphery	G	267	239
MPC Baseplate Outside Surface at Periphery	H	267	239
MPC Shell Maximum	I	315	306

Table 3.4.25

SUMMARY OF 10×10 ARRAY BWR FUEL ASSEMBLY TYPES
EFFECTIVE THERMAL CONDUCTIVITIES†

Fuel	k_{eff} at 200°F [Btu/(ft-hr-°F)]	k_{eff} at 450°F [Btu/(ft-hr-°F)]	k_{eff} at 700°F [Btu/(ft-hr-°F)]
GE-12/14	0.166	0.269	0.412
Atrium-10	0.164	0.266	0.409
SVEA-96	0.164	0.269	0.416

† The conductivities reported in this table are obtained by the simplified method described in the beginning of Subsection 3.4.1.1.2.

Table 3.4.26

COMPARISON OF ATRIUM-10[†] AND BOUNDING[††] BWR FUEL ASSEMBLY EFFECTIVE THERMAL CONDUCTIVITIES

Temperature	Atrium-10 Assembly		Bounding BWR Assembly	
°F	Btu/(ft-hr-°F)	W/m-K	Btu/(ft-hr-°F)	W/m-K
200	0.225	0.389	0.171	0.296
450	0.345	0.597	0.271	0.469
700	0.504	0.872	0.410	0.710

† The reported effective thermal conductivity has been obtained from a rigorous finite-element modeling of the Atrium-10 assembly.

†† The bounding BWR fuel assembly effective thermal conductivity applied in the MPC-68 basket thermal analysis.

Table 3.4.27

THIS TABLE IS INTENTIONALLY DELETED.

Table 3.4.28

PWR MPCs BOUNDING PEAK FUEL CLADDING TEMPERATURE
AS A FUNCTION OF TOTAL HEAT LOAD

Total MPC Decay Heat Load (kW)	Peak Fuel Cladding Temperature (°F)
20.0†	700.6
19.0	678.9
17.0	633.9
15.5	598.8

† Design Basis Maximum.

Table 3.4.29

MPC-68 PEAK FUEL CLADDING TEMPERATURE
AS A FUNCTION OF TOTAL HEAT LOAD

Total MPC Decay Heat Load (kW)	Peak Fuel Cladding Temperature (°F)
18.5†	712.7
17.0	674.0
15.5	634.1

† Design Basis Maximum.

Table 3.4.30

SUMMARY OF THERMAL CONDUCTIVITY CALCULATIONS
FOR MPC HELIUM DILUTED BY RELEASED ROD GASES

Component Gas	Molecular Weight (g/mole)	Mole Fraction	Thermal Conductivity* (Btu/hr-ft-°F)
MPC and Fuel Rod Backfill Helium	4	0.817	0.098 @ 200°F 0.129 @ 450 °F 0.158 @ 700°F
Rod Tritium	3	8.007×10^{-5}	0.119 @ 200 0.148 @ 450°F 0.177 @ 700°F
Rod Krypton	85	0.016	6.76×10^{-3} @ 200°F 8.782×10^{-3} @ 450°F 0.011 @ 700°F
Rod Xenon	131	0.160	3.987×10^{-3} @ 200°F 5.258×10^{-3} @ 450°F 6.471×10^{-3} @ 700°F
Rod Iodine	129	6.846×10^{-3}	2.496×10^{-3} @ 200°F 3.351×10^{-3} @ 450°F 4.201×10^{-3} @ 700°F
Mixture of Gases (diluted helium)	N/A	1.000	0.053 @ 200°F 0.069 @ 450°F 0.085 @ 700°F

* References [3.2.2], [3.4.18] & [3.4.19] consulted for fission gases (Tritium, Krypton, Xenon and Iodine) conductivities.

Table 3.4.31

COMPARISON OF COMPONENT EFFECTIVE THERMAL CONDUCTIVITIES WITH AND WITHOUT MPC HELIUM DILUTION

	Effective Thermal Conductivity (Btu/hr-ft-°F)		
	Value at 200°F	**Value at 450°F**	**Value at 700°F**
Fuel Assembly with Undiluted Helium	0.257	0.406	0.604
Fuel Assembly with Diluted Helium	0.160	0.278	0.458
MPC Fuel Basket with Undiluted Helium	1.127	1.535	2.026
MPC Fuel Basket with Diluted Helium	0.948	1.338	1.829

Table 3.4.32

MPC-24 HYPOTHETICAL 100% RODS RUPTURE ACCIDENT
MAXIMUM TEMPERATURES*

	Calculated Maximum Temperature (°F)	Accident Condition Temperature Limit (°F)
Fuel Cladding	743	1058
MPC Basket Centerline	709	950
MPC Basket Periphery	444	950
MPC Outer Shell Surface	314	775
MPC/Overpack Helium Gap Outer Surface	291	500
Radial Neutron Shield Inner Surface	271	N/A
Overpack Enclosure Shell Surface	222	1350
Overpack Closure Plate	176	700
Overpack Bottom Plate	296	700

* The results reported herein are obtained from thermal models employing grossly understated fuel basket conductivities.

Table 3.4.33

MPC-24 HYPOTHETICAL 100% RODS RUPTURE ACCIDENT PRESSURES

Calculated Accident Pressure (psig)	Accident Condition Design Pressure (psig)
134	200

Table 3.4.34

PLANT SPECIFIC BWR FUEL TYPES EFFECTIVE THERMAL CONDUCTIVITY*

Fuel	@200°F [Btu/ft-hr-°F]	@450°F [Btu/ft-hr-°F]	@700F° [Btu/ft-hr-°F]
Oyster Creek (7x7)	0.165	0.273	0.427
Oyster Creek (8x8)	0.162	0.266	0.413
TVA Browns Ferry (8x8)	0.160	0.264	0.411
SPC-5 (9x9)	0.149	0.245	0.380

* The conductivities reported in this table are obtained by a simplified analytical method described in Subsection 3.4.1.1.2.

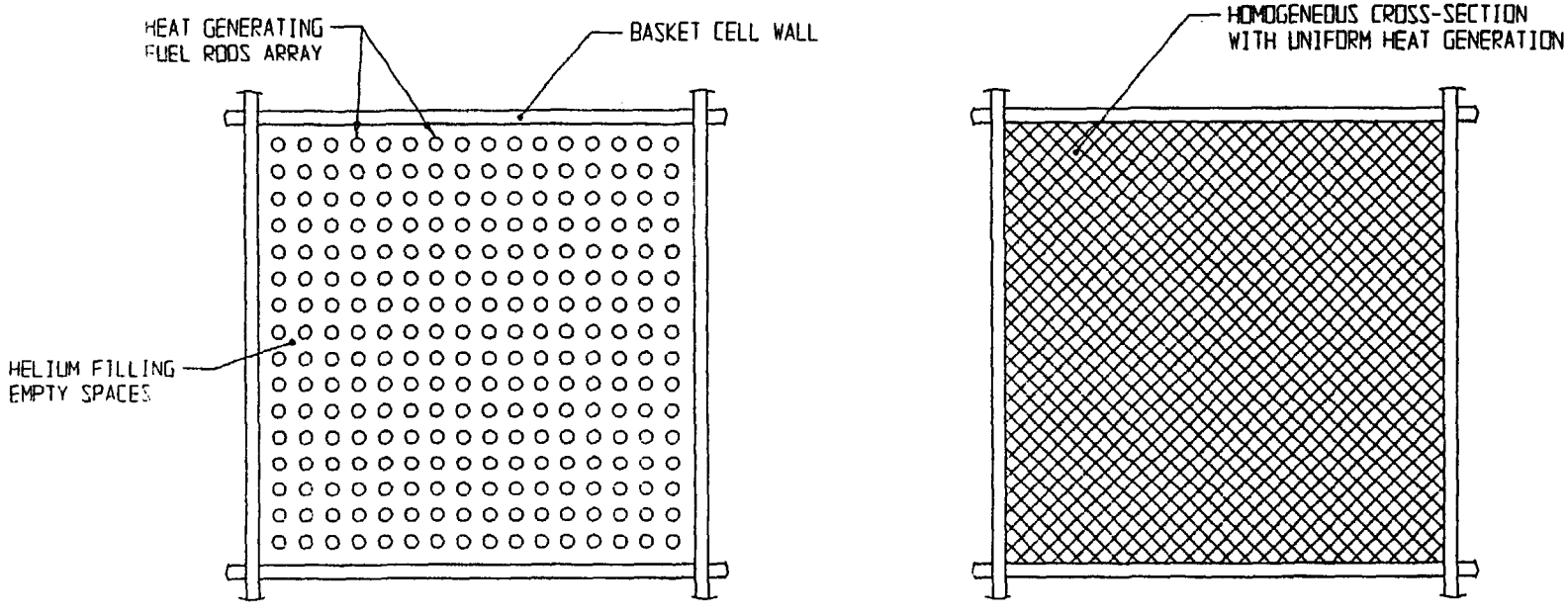

(a) TYPICAL FUEL CELL

(b) SOLID REGION OF
EFFECTIVE CONDUCTIVITY

FIGURE 3.4.1; HOMOGENIZATION OF THE STORAGE CELL CROSS-SECTION

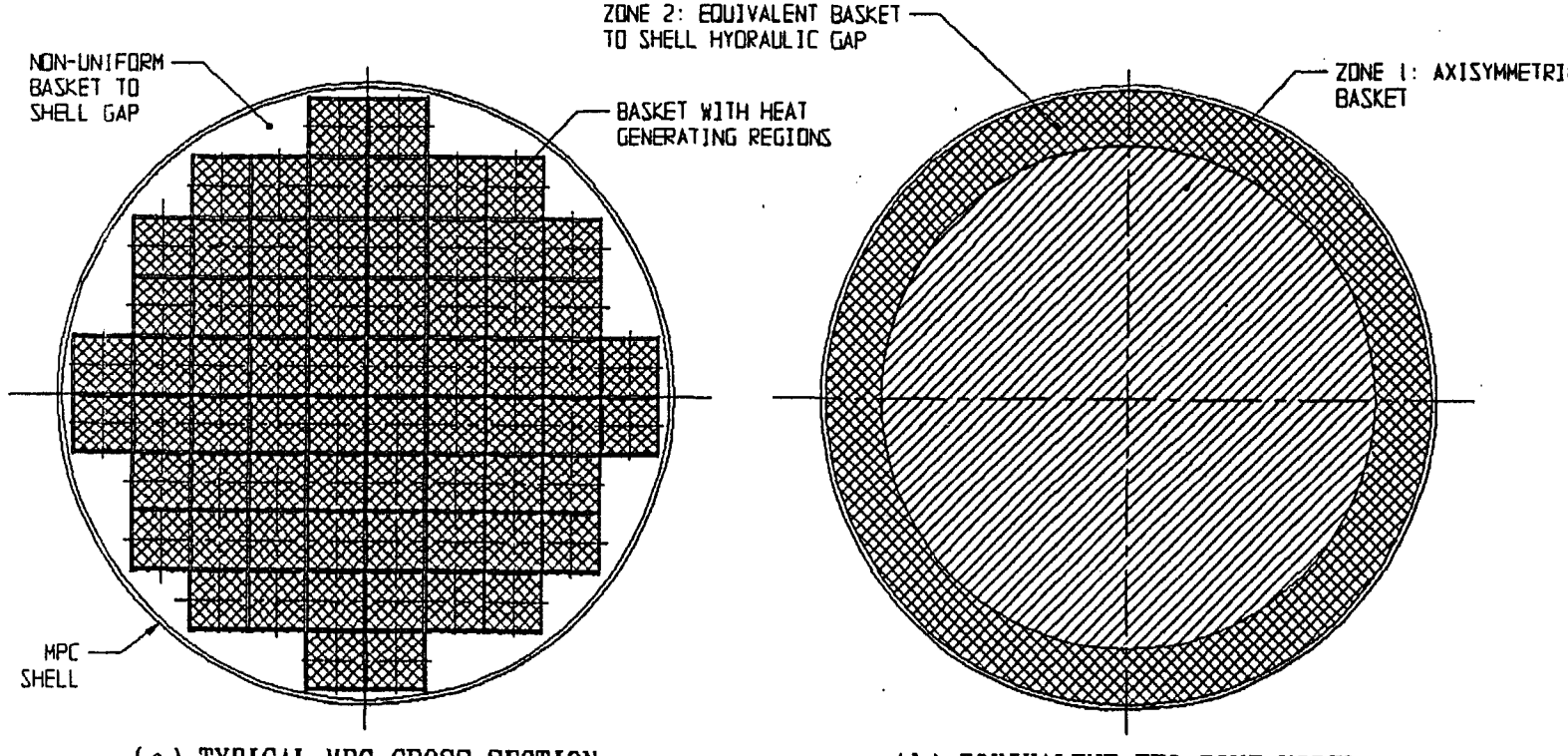

(a) TYPICAL MPC CROSS-SECTION

(b) EQUIVALENT TWO ZONE MODEL

FIGURE 3.4.2; MPC CROSS-SECTION REPLACED WITH AN EQUIVALENT TWO ZONE AXISYMMETRIC BODY

\PROJECTS\5014\HI951251\CH_3\3_4_2

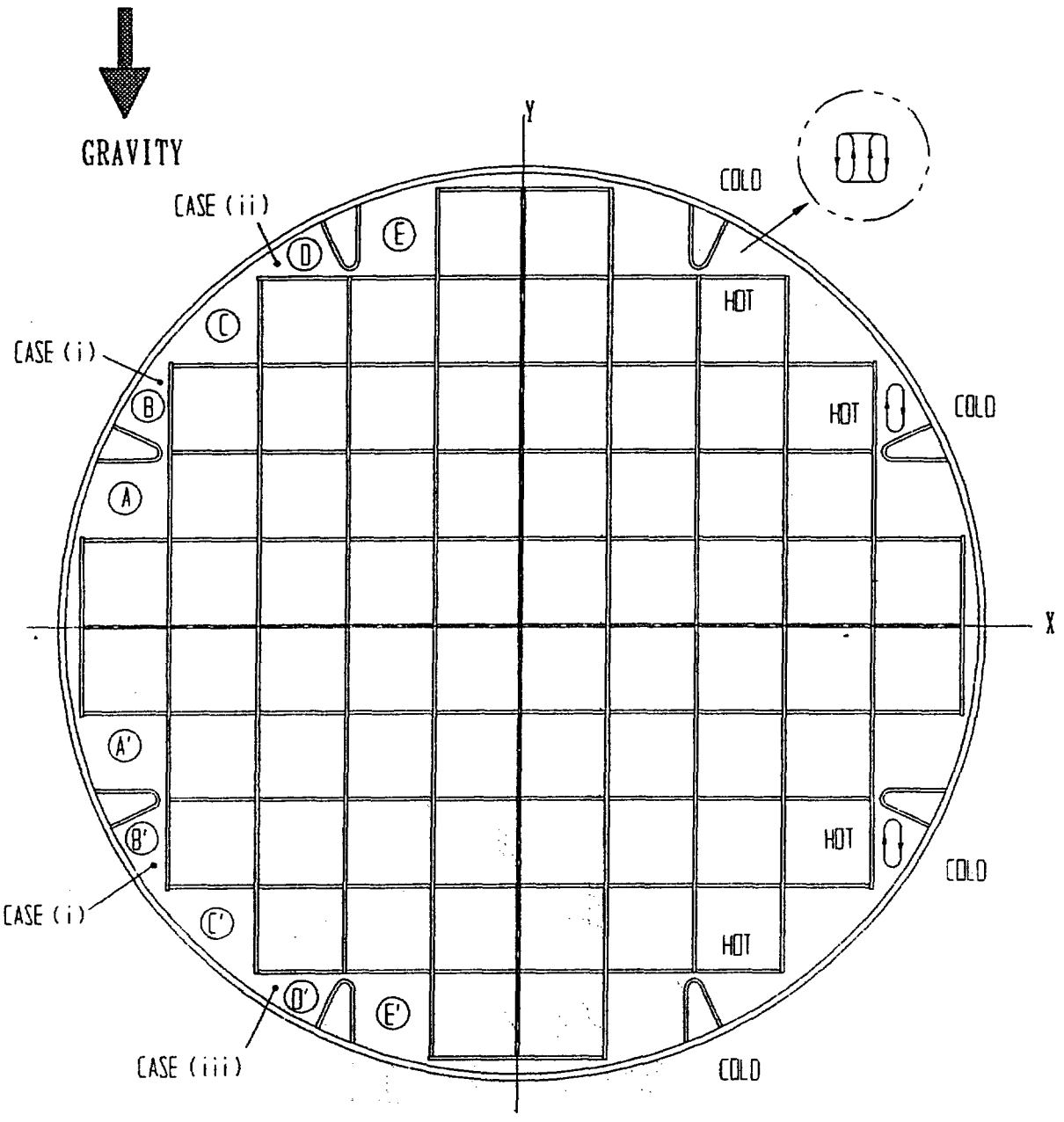

FIGURE 3.4.3; NATURAL CONVECTION IN MPC BASKET PERIPHERY REGION

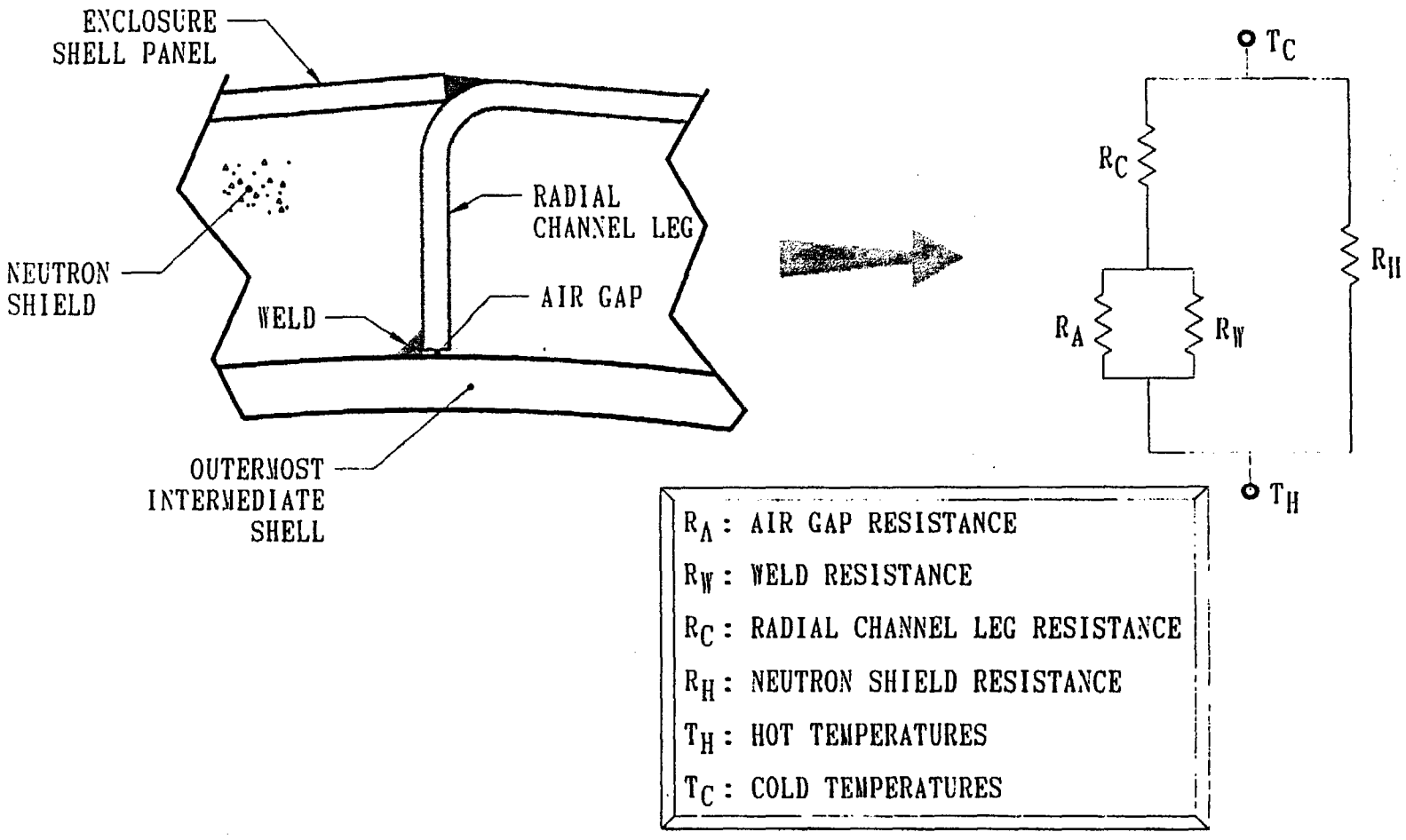

FIGURE 3.4.4; NEUTRON SHIELD REGION RESISTANCE NETWORK ANALOGY FOR EFFECTIVE CONDUCTIVITY CALCULATION

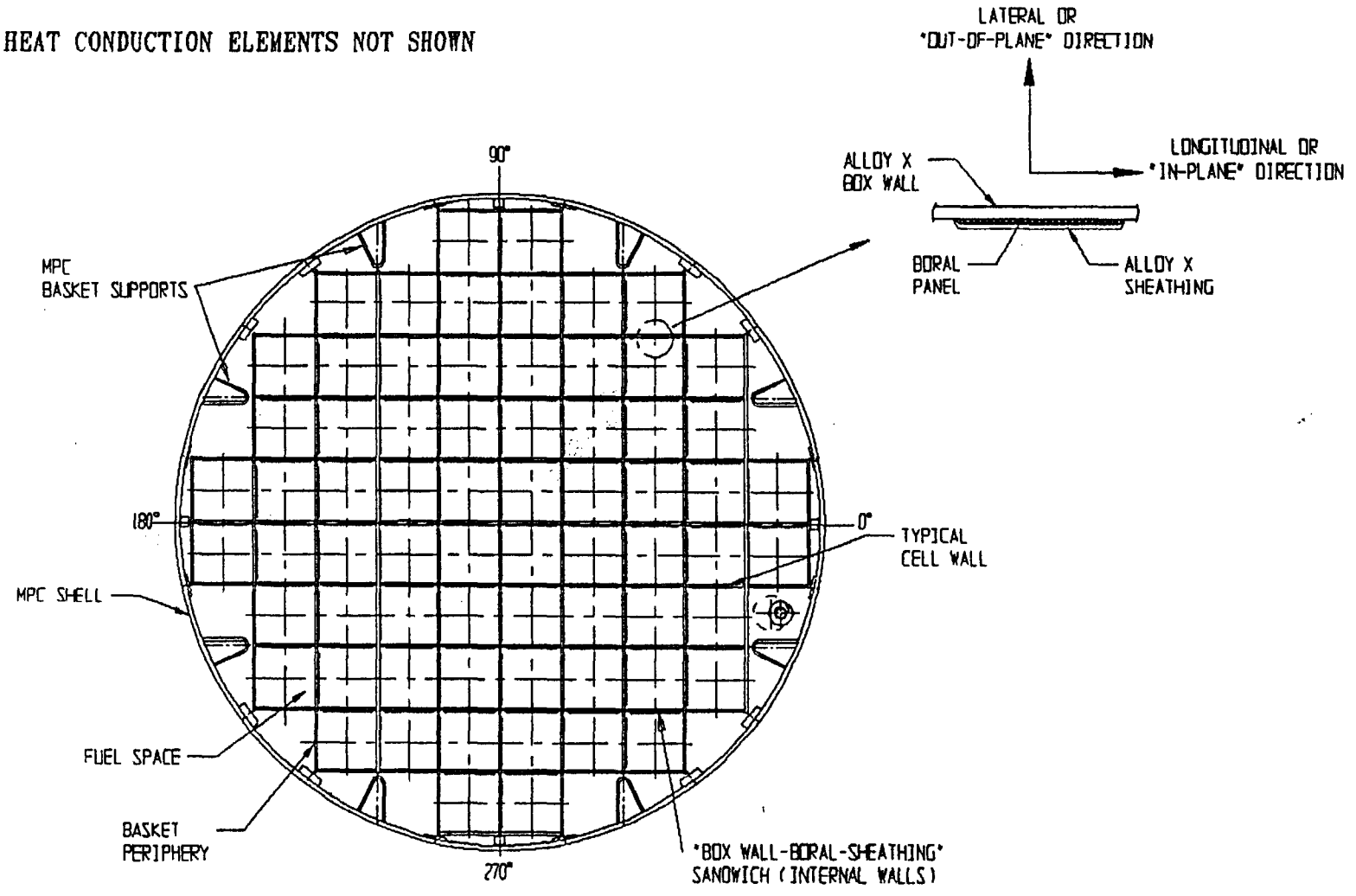

FIGURE 3.4.5; TYPICAL MPC BASKET PARTS IN A CROSS-SECTIONAL VIEW

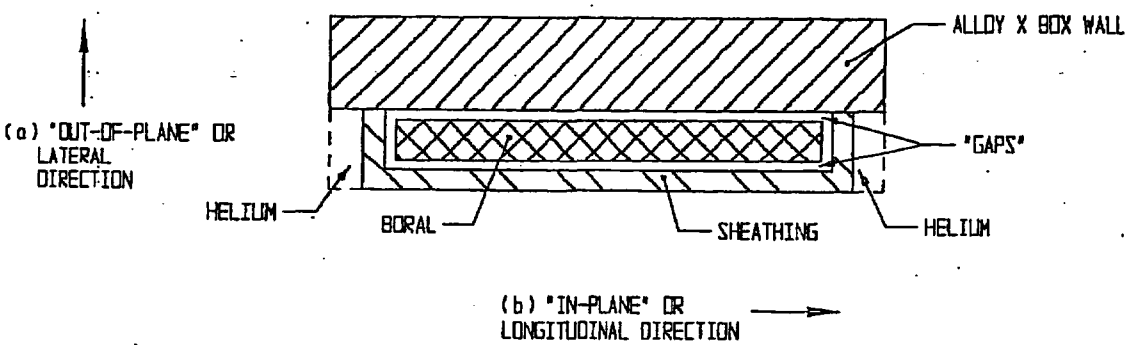

FIGURE 3.4.6: "BOX WALL-BORAL-SHEATHING" SANDWICH

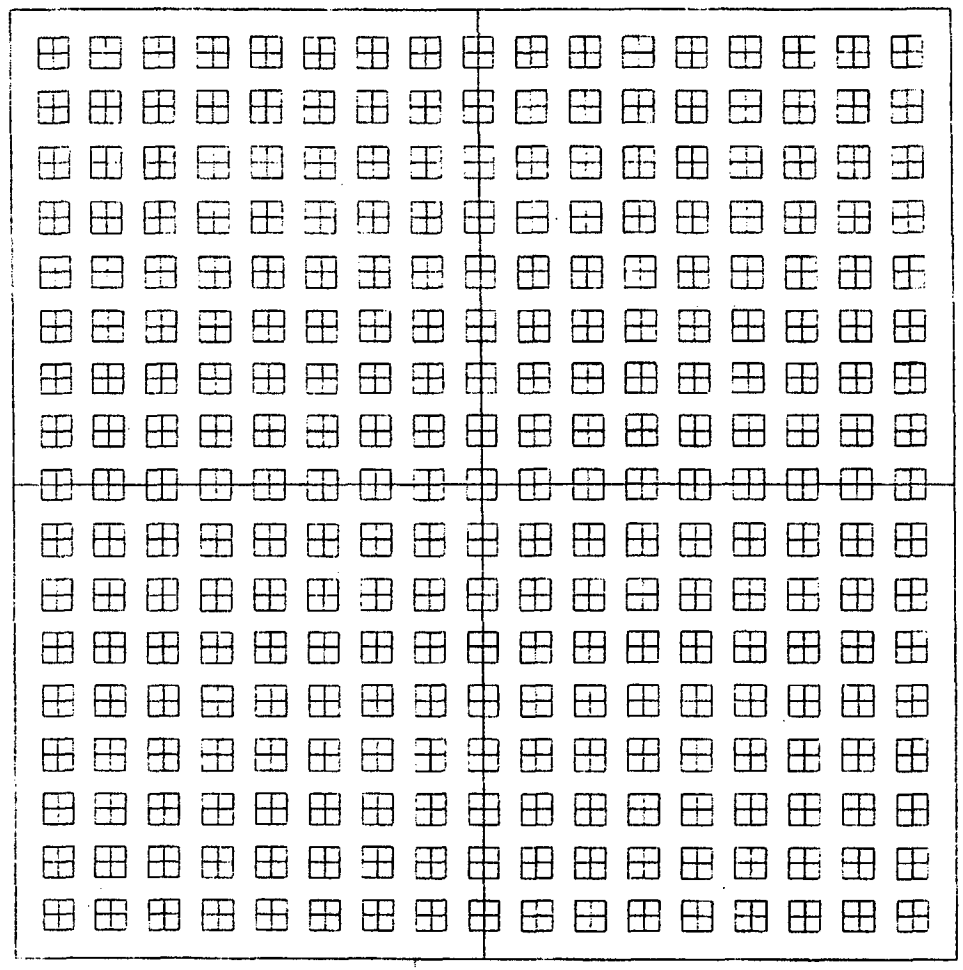

Y Z X	W17X17 OFA FUEL ASSEMBLY MODEL	Nov 11 1997 Fluent 4.32 Fluent Inc.

FIGURE 3.4.7: WESTINGHOUSE 17x17 OFA PWR FUEL ASSEMBLY MODEL

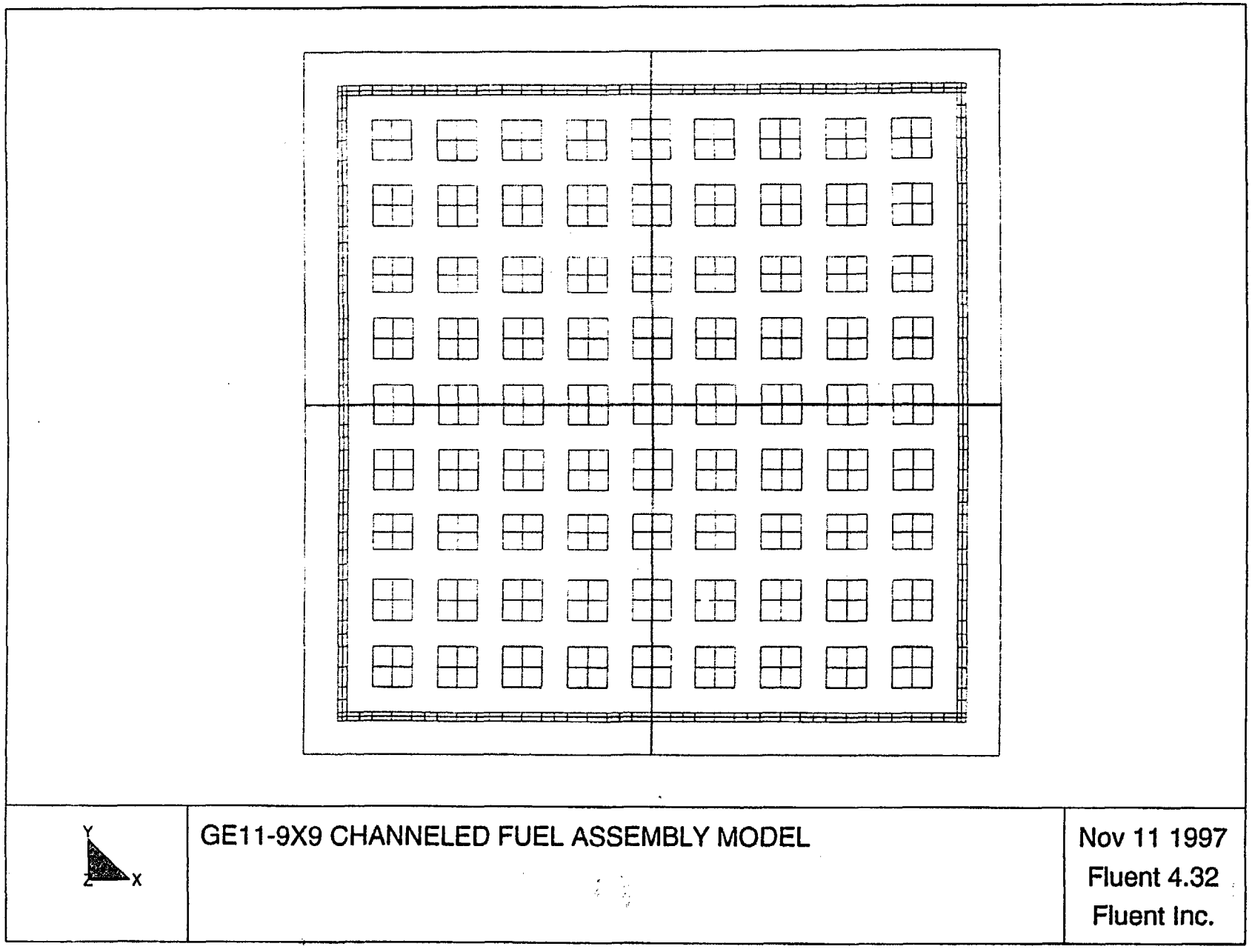

FIGURE 3.4.8: GENERAL ELECTRIC 9x9 BWR FUEL ASSEMBLY MODEL

FIGURE 3.4.9

THIS FIGURE IS INTENTIONALLY DELETED.

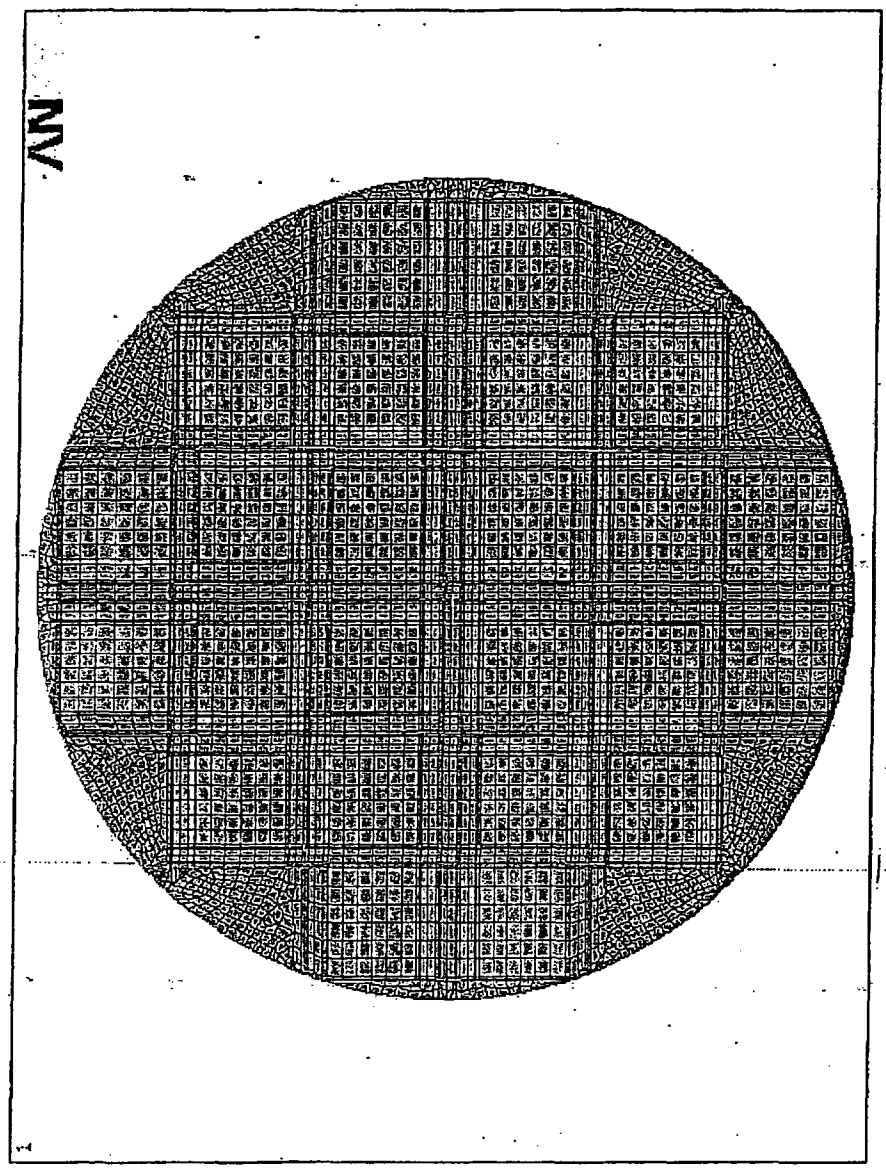

FIGURE 3.4.10: MPC-24 BASKET CROSS-SECTION ANSYS FINITE ELEMENT MODEL

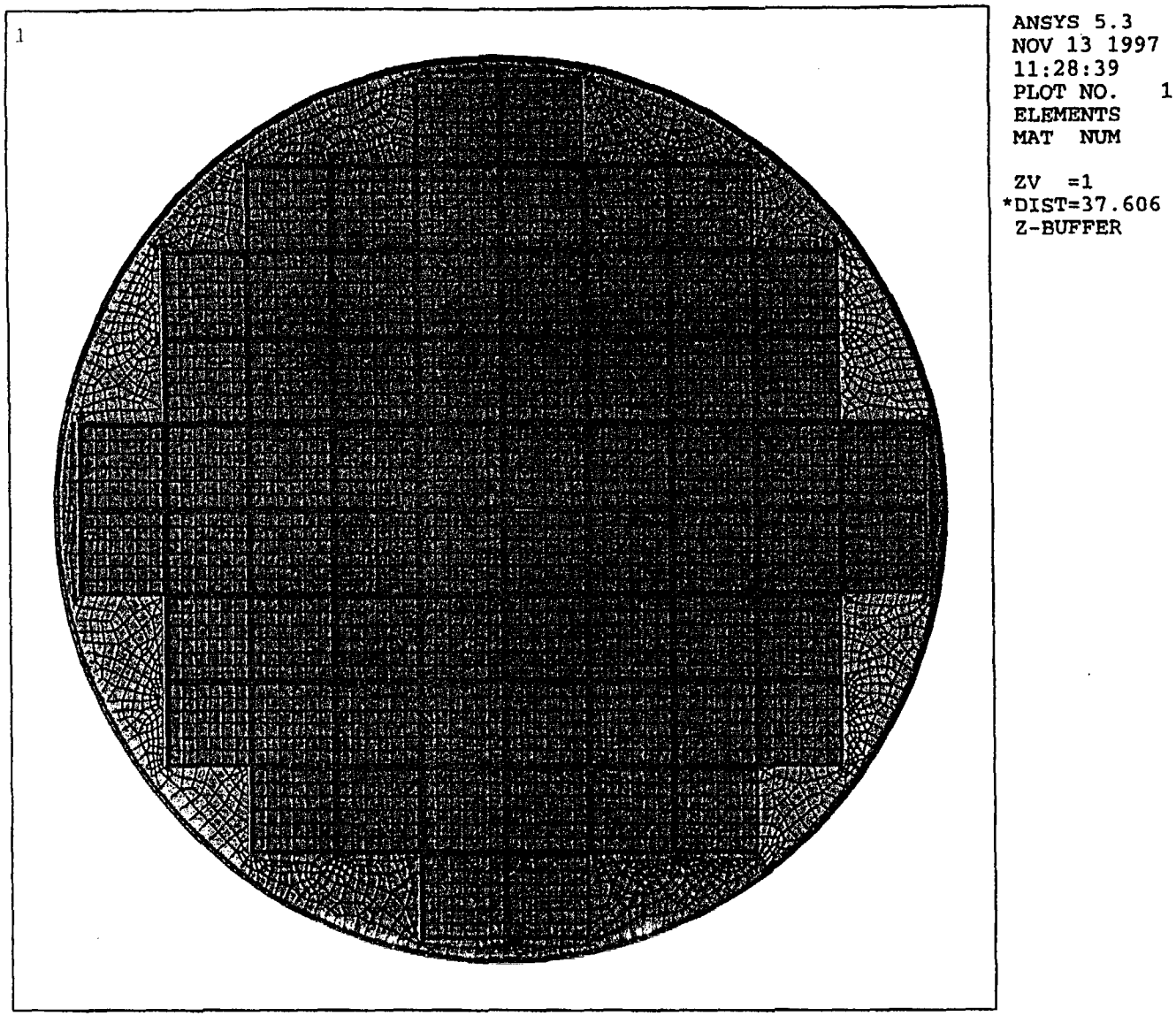

FIGURE 3.4.11; MPC-68 BASKET CROSS-SECTION ANSYS FINITE ELEMENT MODEL

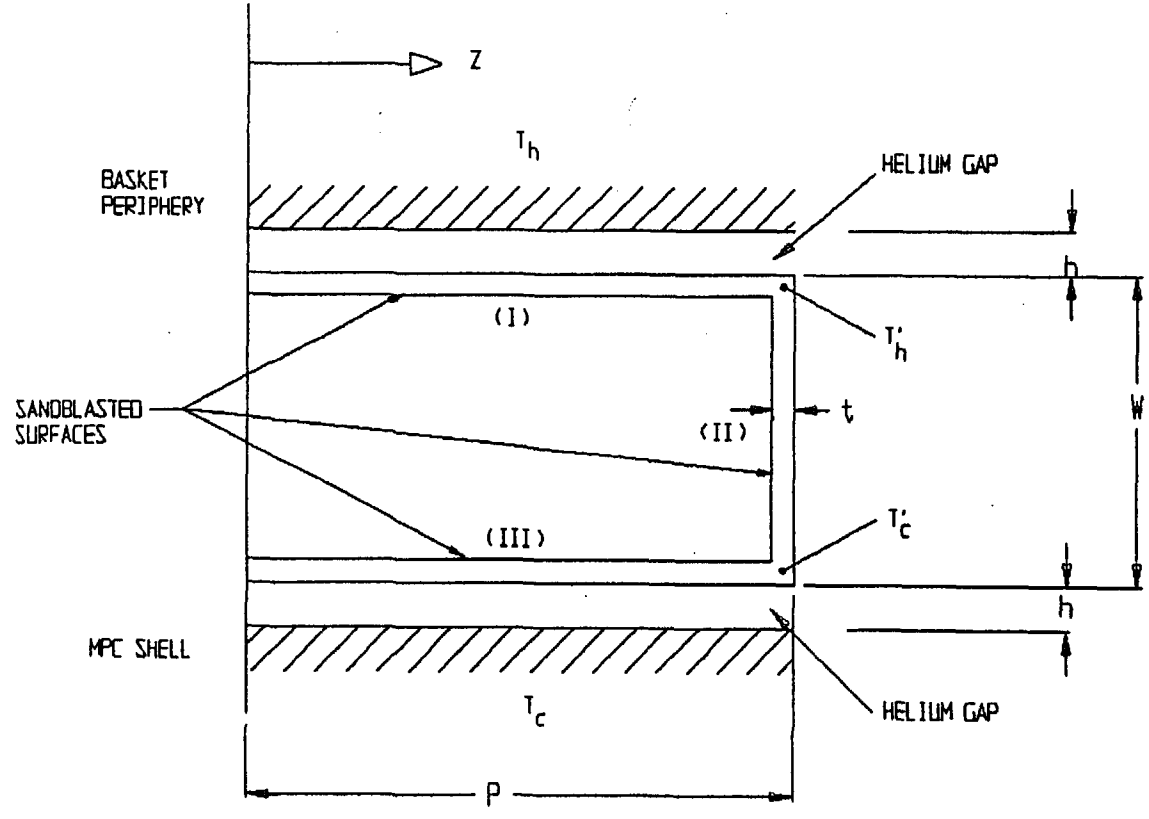

FIGURE 3.4.12; ILLUSTRATION OF AN MPC BASKET TO SHELL ALUMINUM HEAT CONDUCTION ELEMENT

\5014\HI951251\CH 3\3.4_12

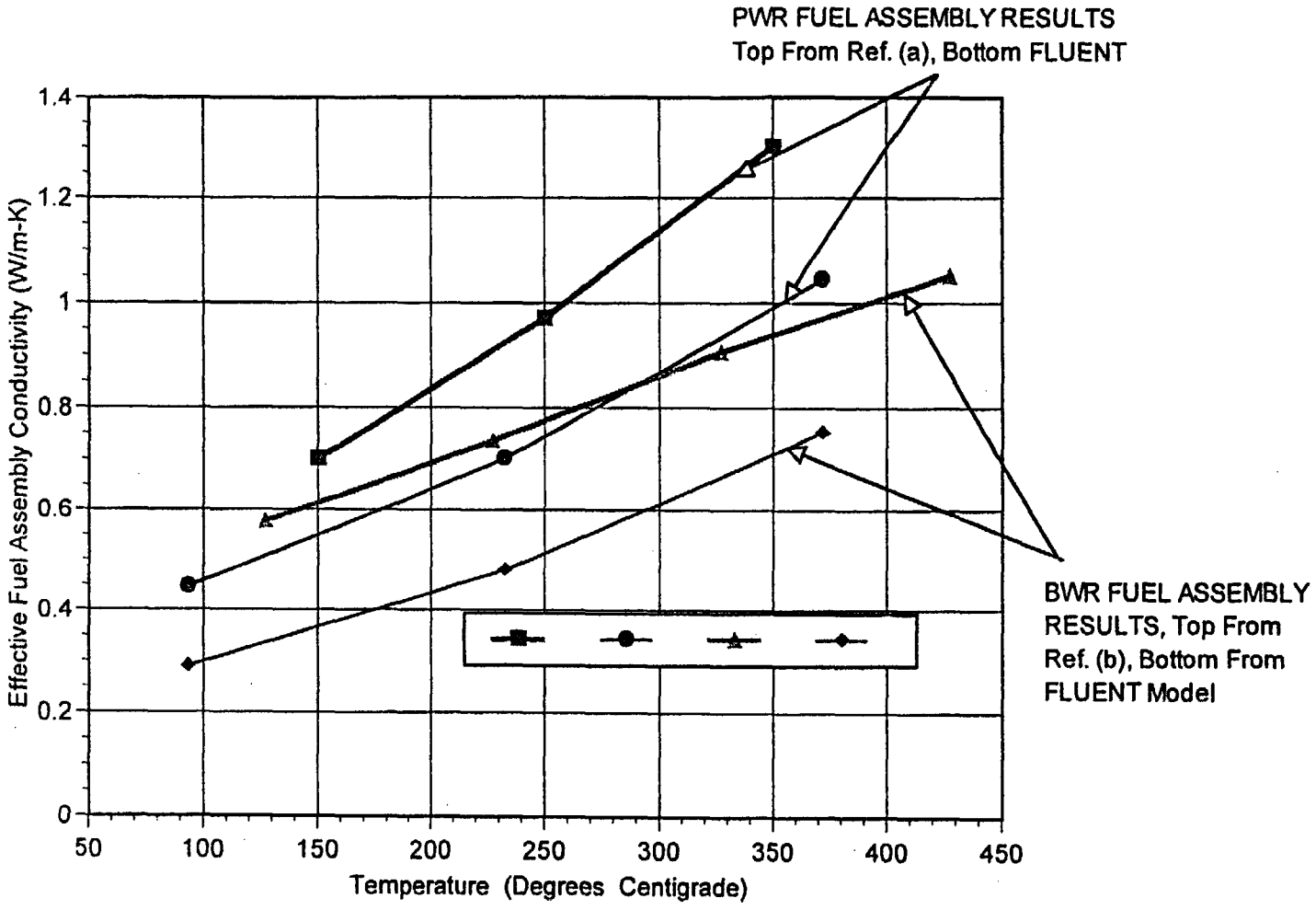

(a) "Determination of SNF Peak Temperatures in the Waste Package", Bahney & Doering, *HLRWM Sixth Annual Conf.*, Pages 671-673, (April 30 - May 5, 1995)
(b) "A Method for Determining the Spent-Fuel Contribution to Transport Cask Containment Requirements", *Sandia Report SAND90-2406*, page II-132, (1992)

FIGURE 3.4.13: COMPARISON OF FLUENT BASED FUEL ASSEMBLY EFFECTIVE CONDUCTIVITY RESULTS WITH PUBLISHED TECHNICAL DATA

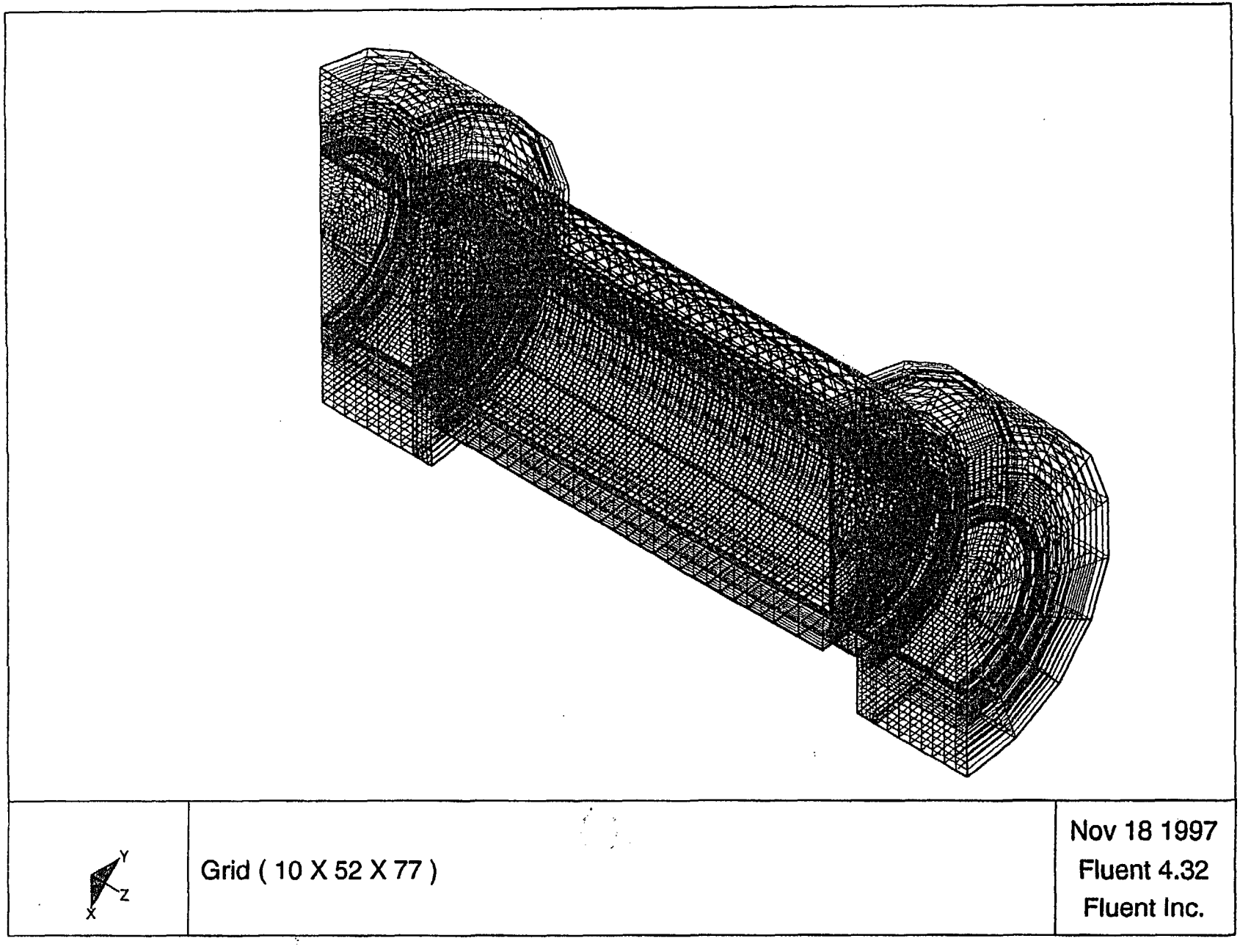

FIGURE 3.4.14: HI-STAR 100 SYSTEM FINITE ELEMENT MESH FOR THERMAL ANALYSIS

FIGURE 3.4.15

THIS FIGURE IS INTENTIONALLY DELETED.

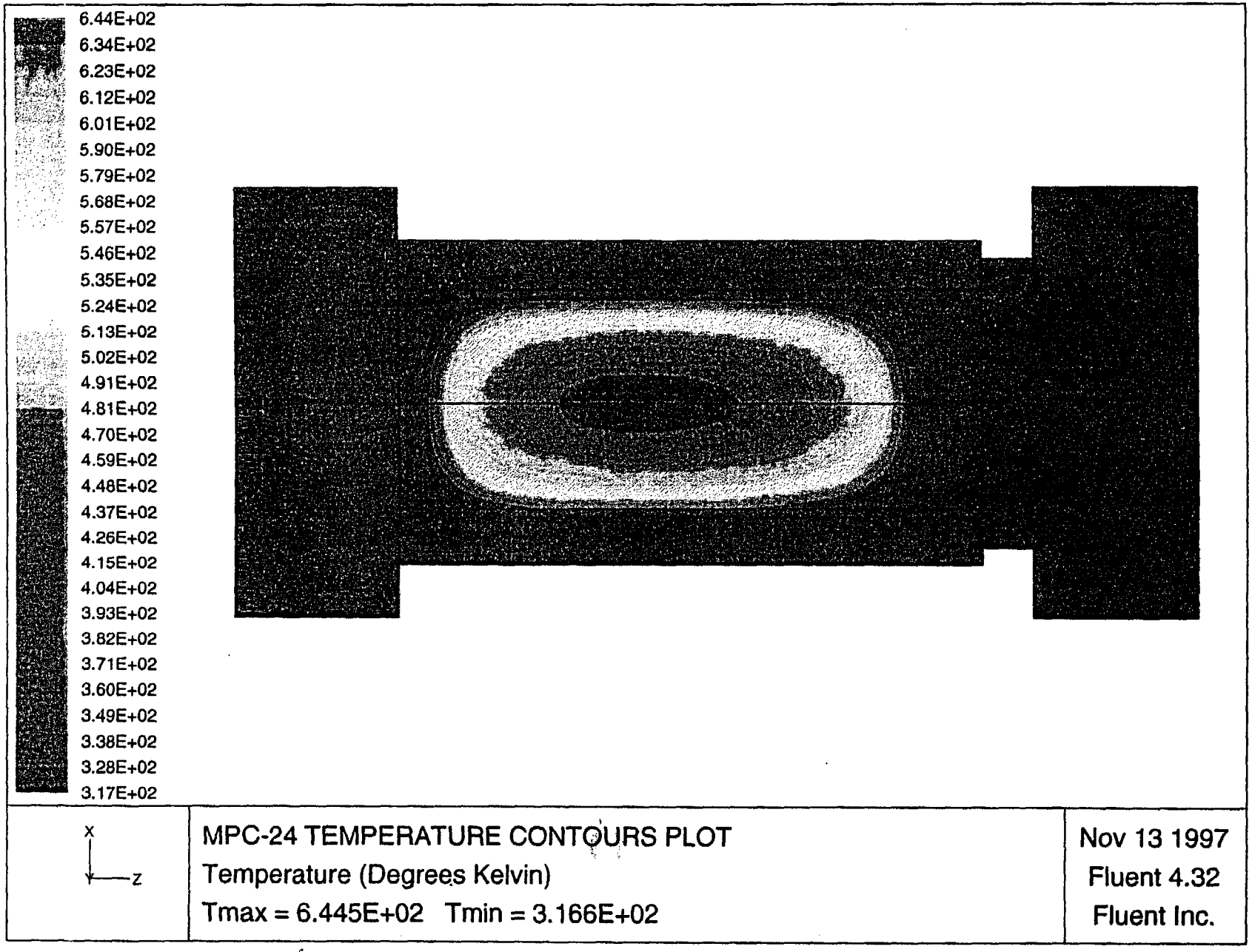

FIGURE 3.4.16: HI-STAR 100 SYSTEM NORMAL TRANSPORT CONDITION TEMPERATURE CONTOURS PLOT (MPC-24 BASKET)

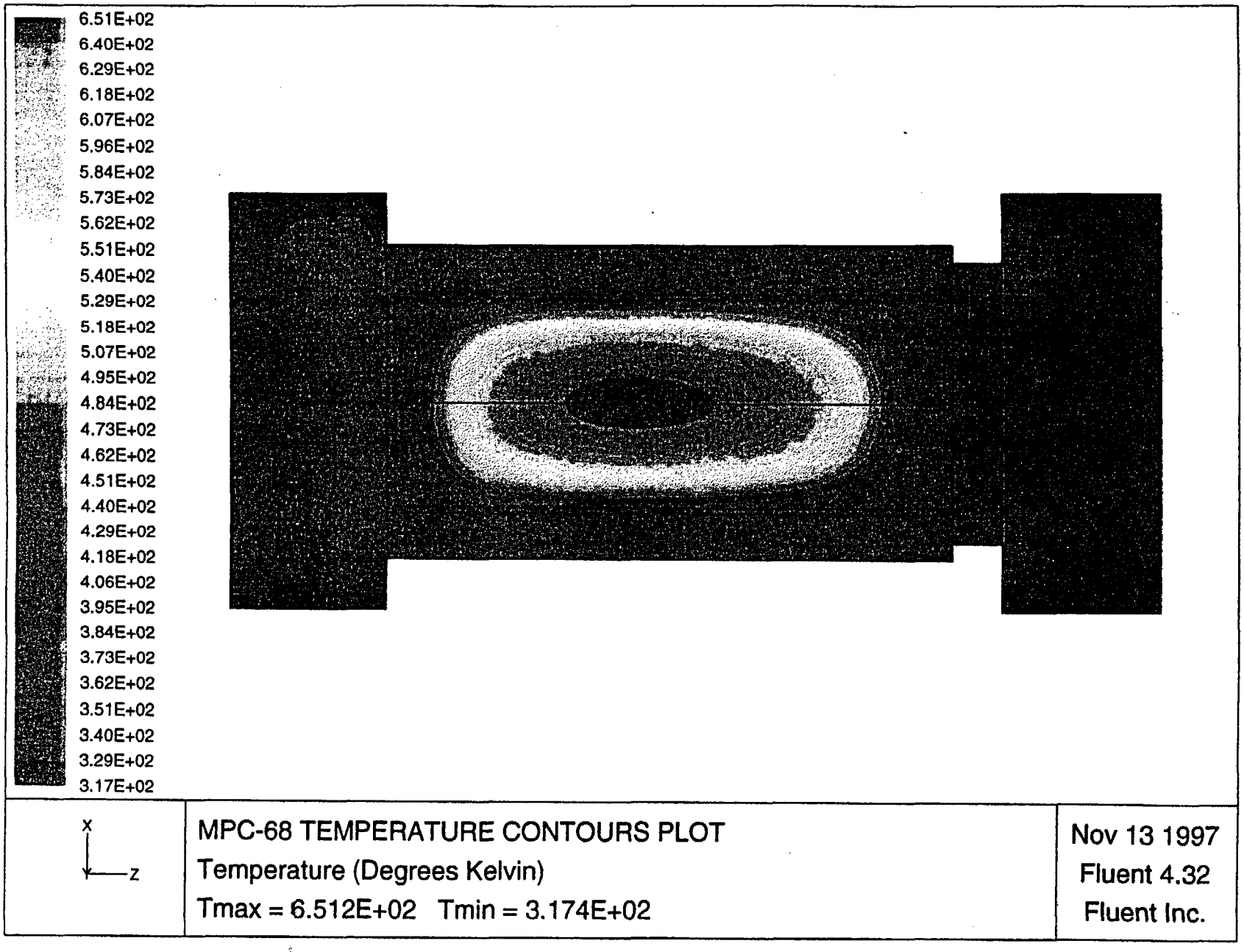

FIGURE 3.4.17: HI-STAR 100 SYSTEM NORMAL TRANSPORT CONDITION TEMPERATURE CONTOURS PLOT (MPC-68 BASKET)

FIGURE 3.4.18

THIS FIGURE IS INTENTIONALLY DELETED.

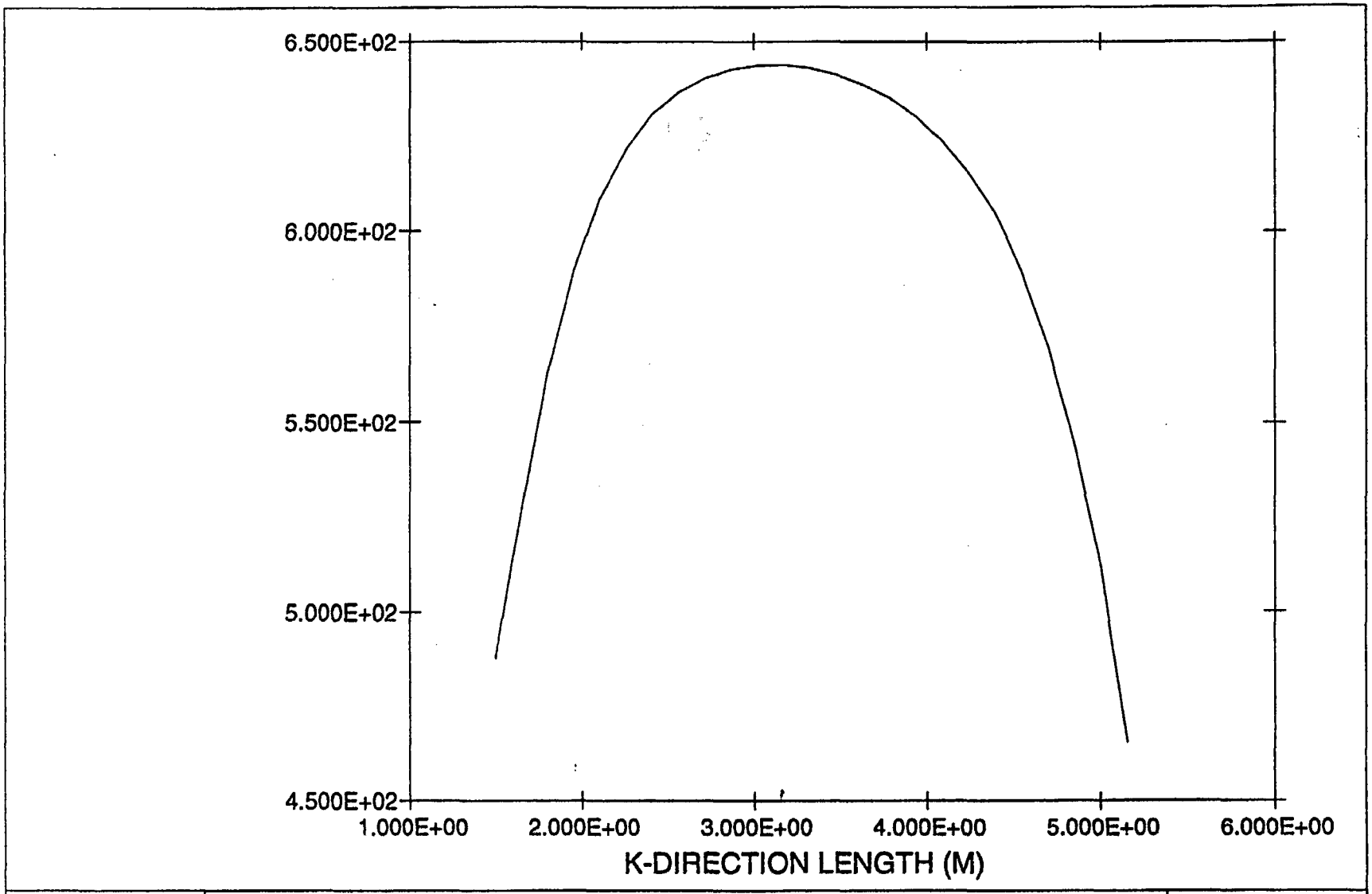

FIGURE 3.4.19: MPC-24 HOTTEST ROD TEMPERATURE PROFILE

Temperature (Kelvin) Vs. Axial Length (Meters)

May 24 1998
Fluent 4.32
Fluent Inc.

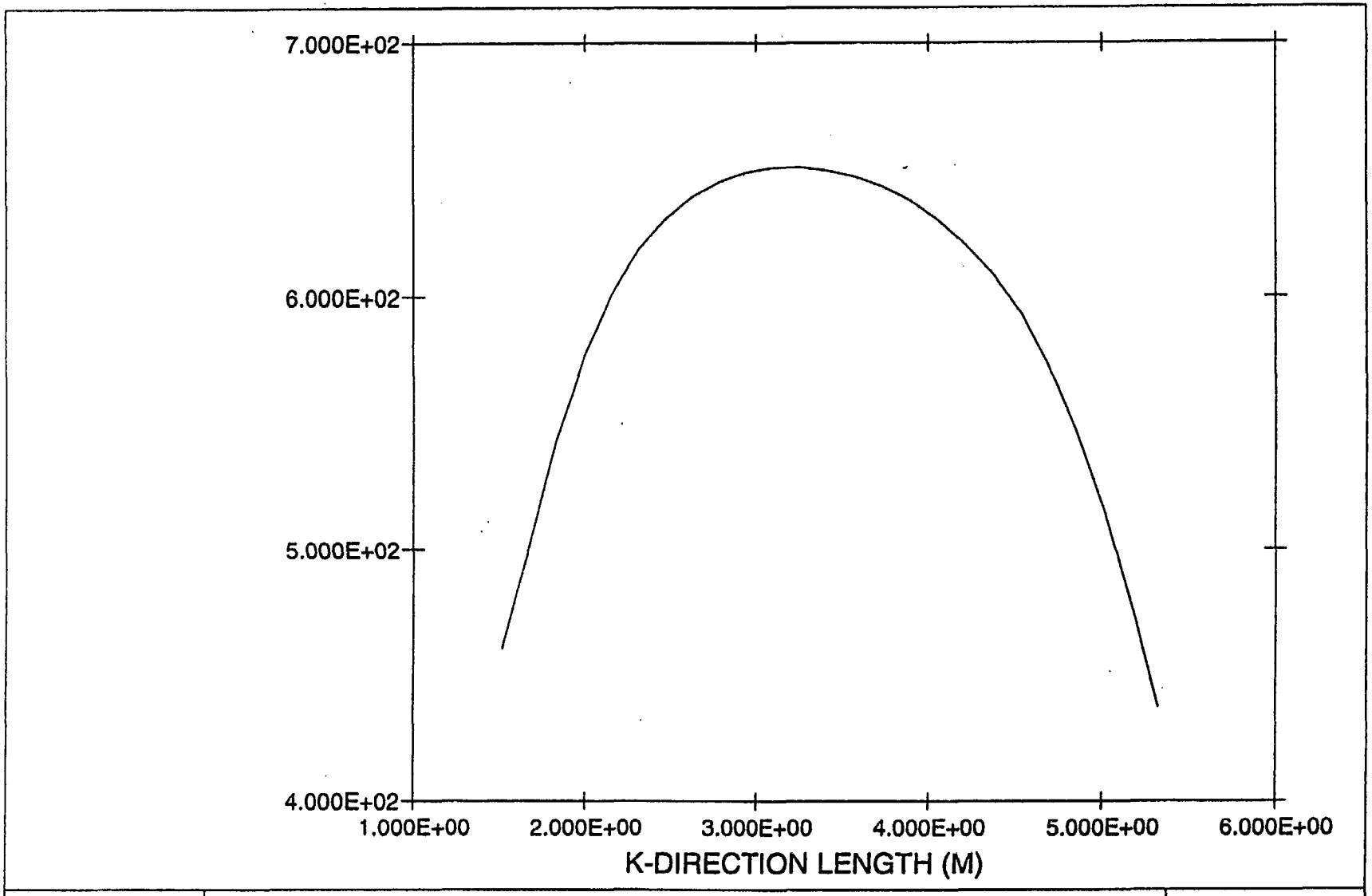

	FIGURE 3.4.20: MPC-68 HOTTEST ROD TEMPERATURE PROFILE Temperature (Kelvin) Vs. Axial Length (Meters)	May 24 1998 Fluent 4.32 Fluent Inc.

FIGURE 3.4.21

THIS FIGURE IS INTENTIONALLY DELETED.

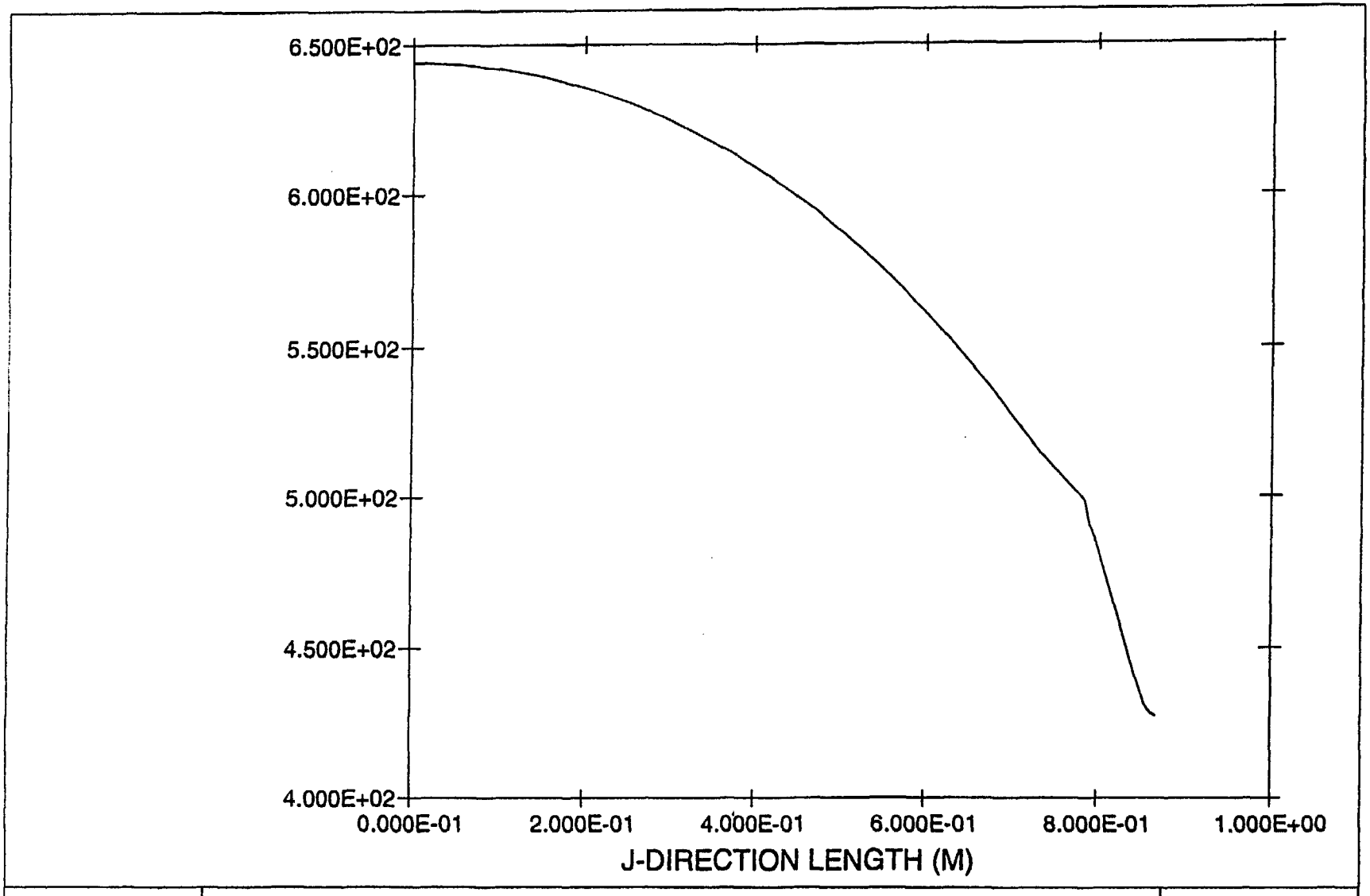

FIGURE 3.4.22: MPC-24 RADIAL TEMPERATURE PROFILE

Temperature (Kelvin) Vs. Radial Distance (Meters)

May 24 1998
Fluent 4.32
Fluent Inc.

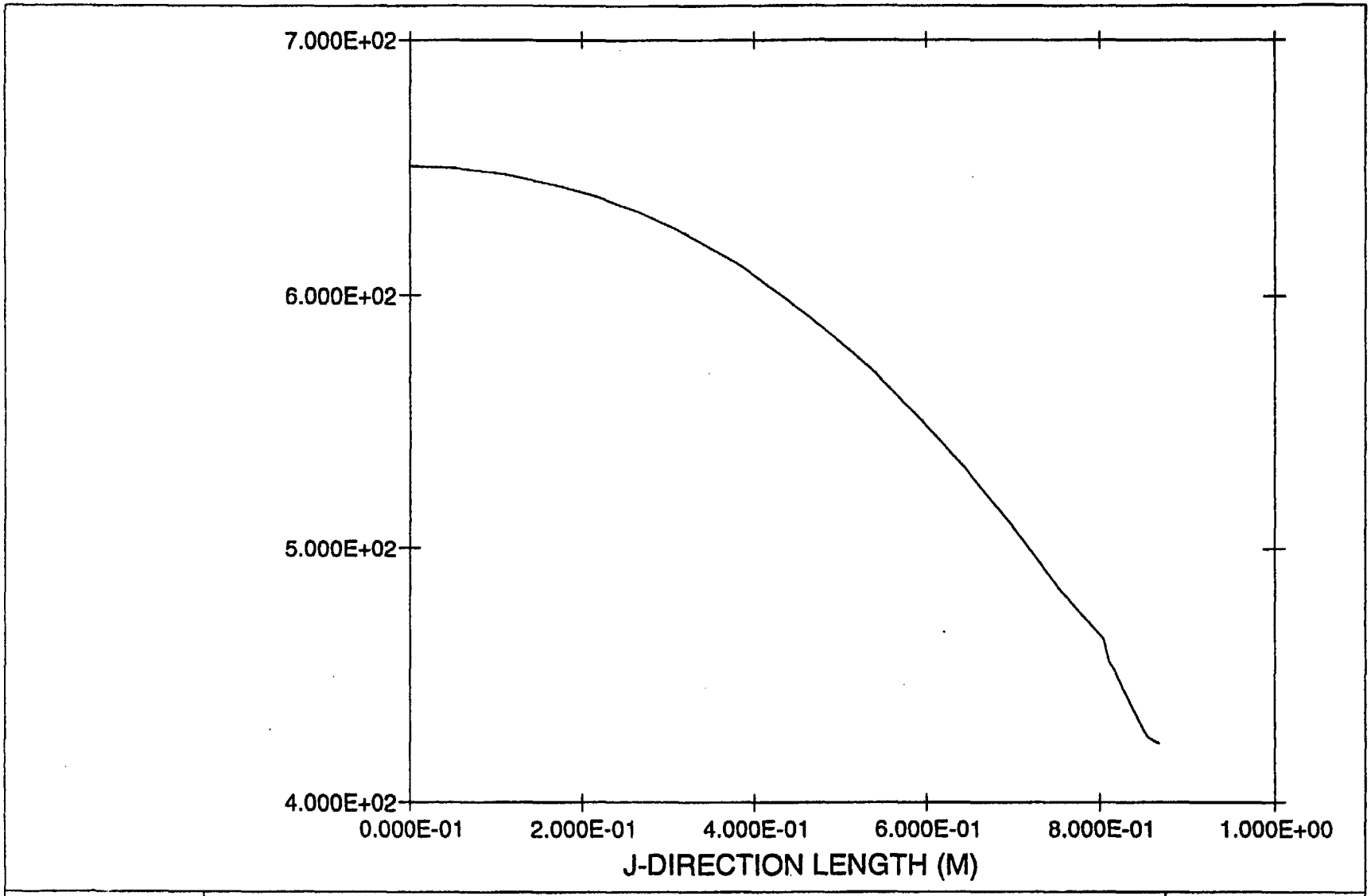

FIGURE 3.4.23: MPC-68 RADIAL TEMPERATURE PROFILE

Temperature (Kelvin) Vs. Radial Position (Meters)

May 24 1998
Fluent 4.32
Fluent Inc.

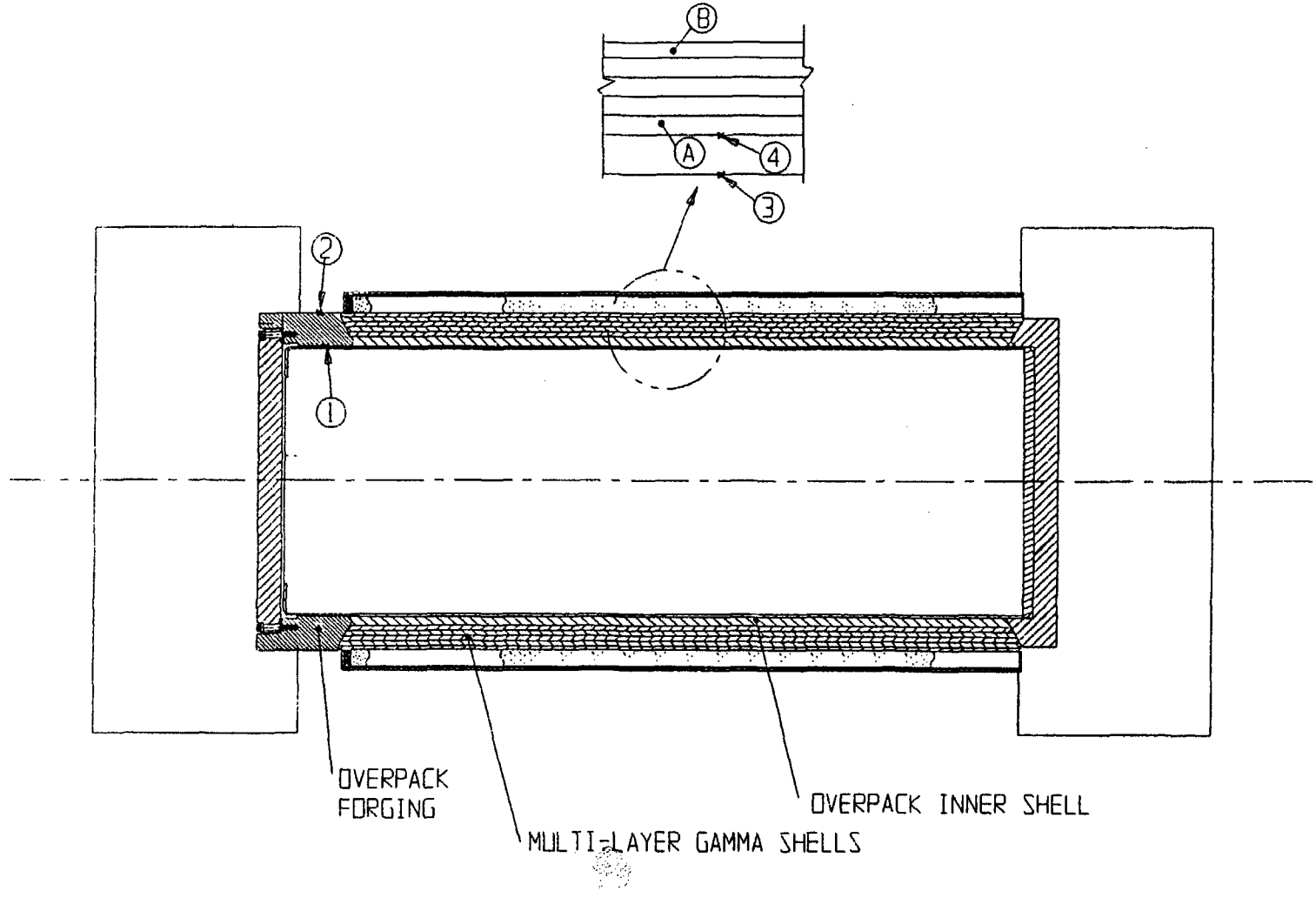

FIGURE 3.4.24; HI-STAR 100 PACKAGE CONTROL LOCATIONS TRACKED IN THE COOLDOWN EVENT

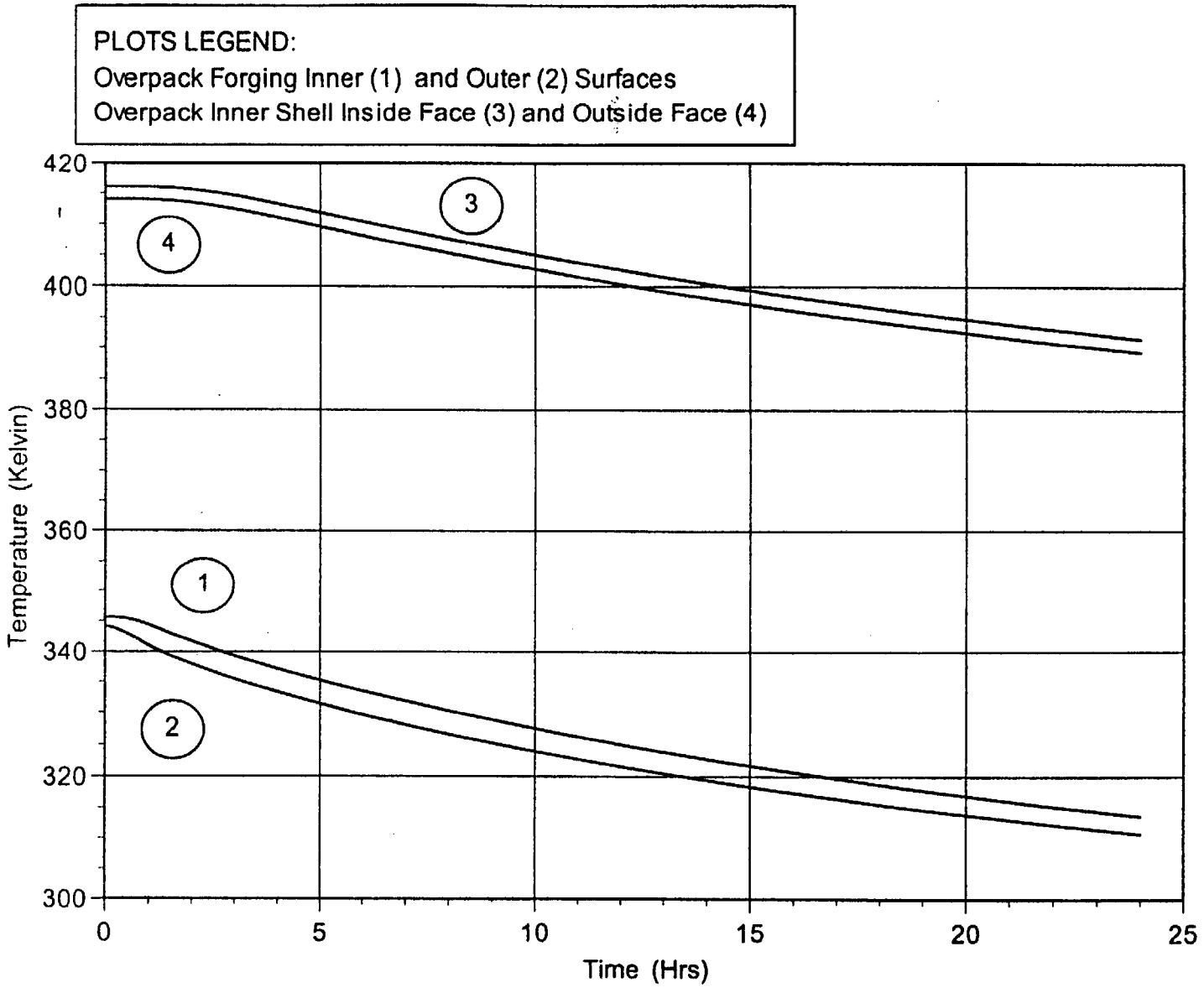

FIGURE 3.4.25: CONTAINMENT BOUNDARY COOLDOWN TEMPERATURE PROFILES

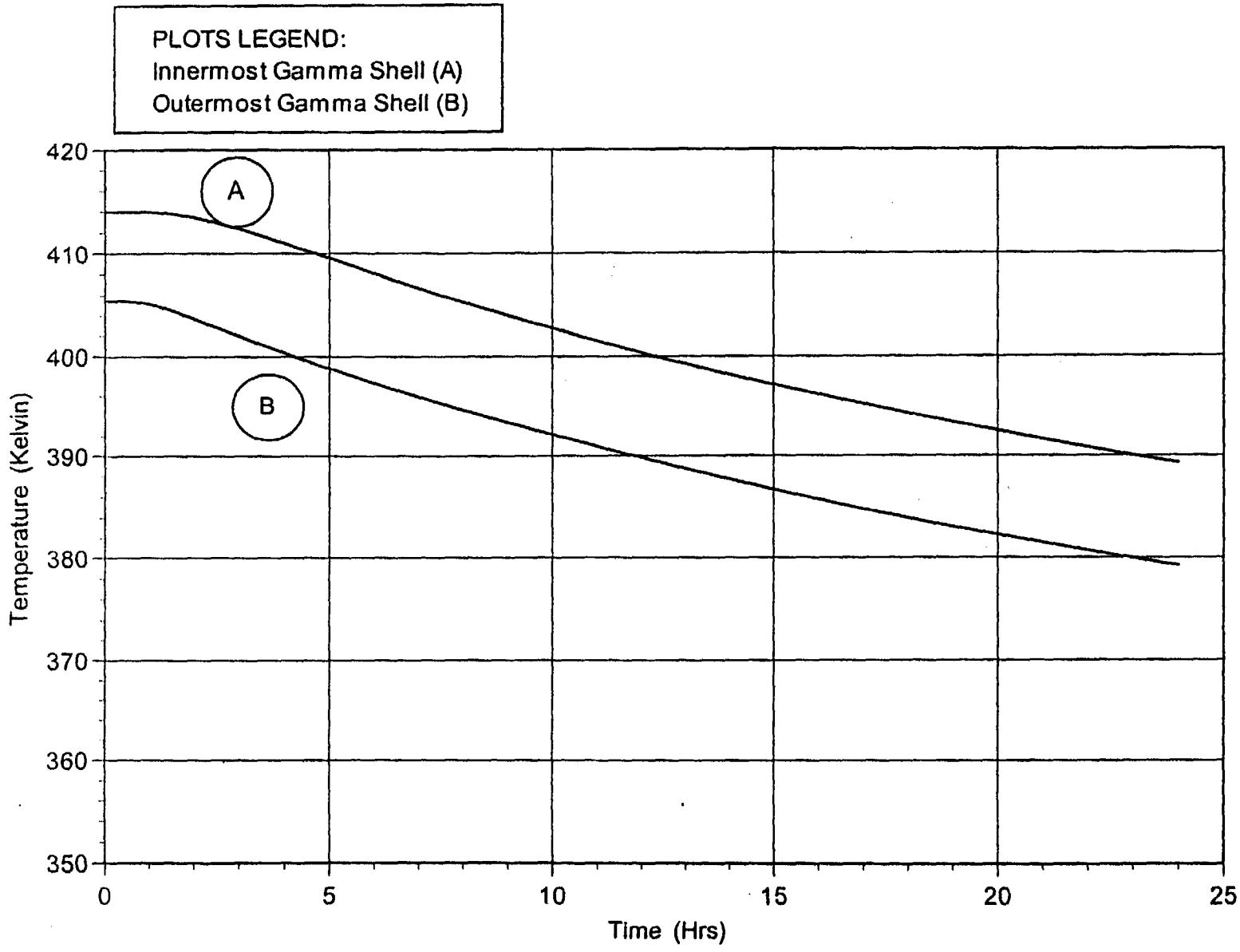

FIGURE 3.4.26: MULTI-LAYERED SHELLS COOLDOWN TEMPERATURE PROFILES

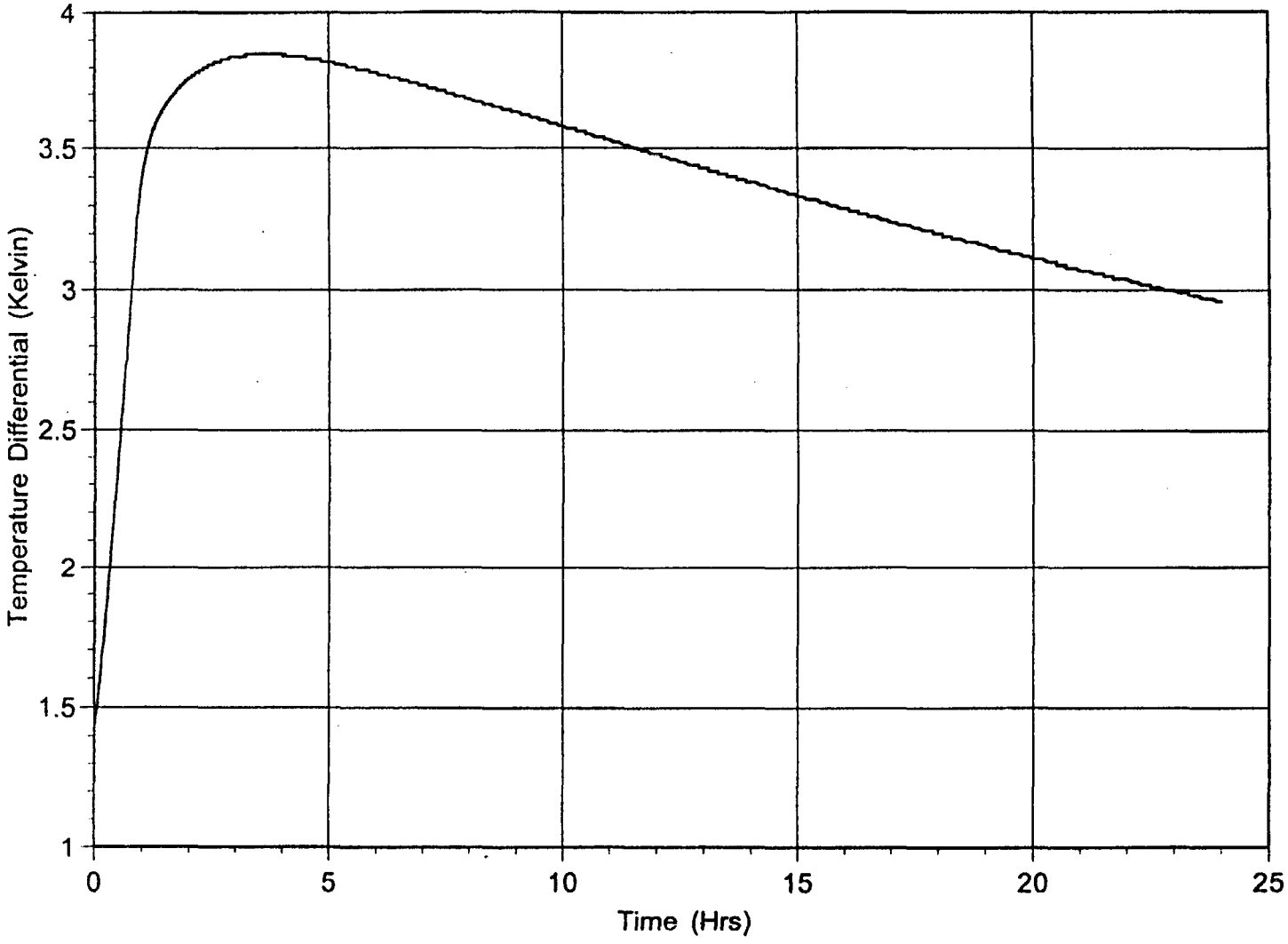

FIGURE 3.4.27: OVERPACK FORGING THROUGH THICKNESS TEMPERATURE GRADIENT DURING COOLDOWN TRANSIENT

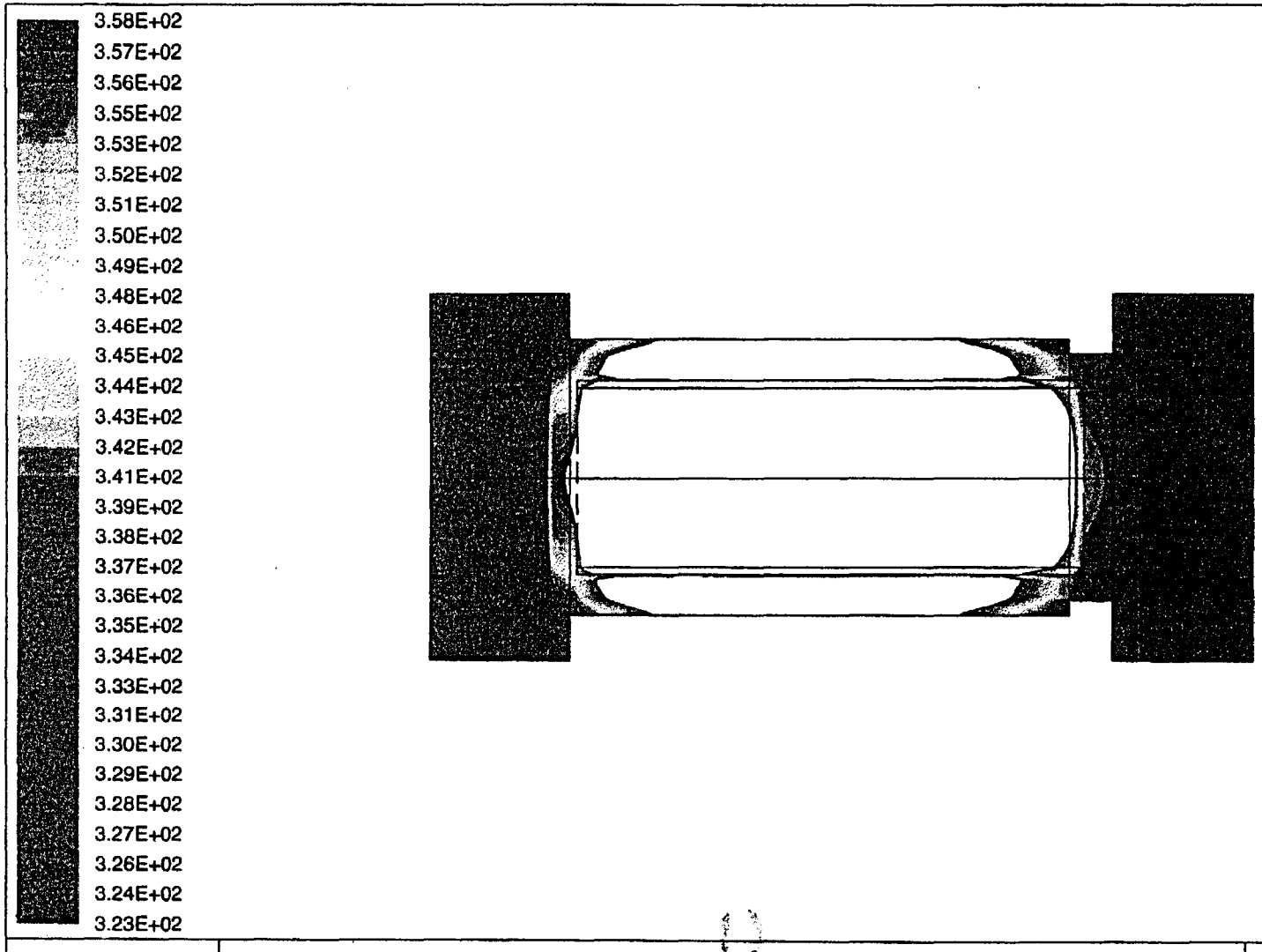

FIGURE 3.4.28: IMPACT LIMITERS SURFACE TEMPERATURE MAP
Temperature (Degrees Kelvin)
Tmax = 3.580E+02 Tmin = 3.232E+02

Feb 04 1999
Fluent 4.32
Fluent Inc.

3.5 HYPOTHETICAL ACCIDENT THERMAL EVALUATION

As mandated by 10CFR71 requirements, the HI-STAR System is subjected to a sequence of hypothetical accident conditions. The objective is to determine and assess the cumulative damage sustained by the system. The accident scenarios specified in order are: (1) a 30 foot free drop onto an unyielding surface; (2) a 40-inch drop onto a mild steel bar; and (3) exposure to a 30-minute fire at 1475°F. The initial conditions for the fire accident specify steady state at an ambient temperature between -20°F and 100°F [3.5.1]. In the HI-STAR System hypothetical fire accident evaluation, full effects of insolation before, during, and after the fire are considered. The effects of the first two drop accidents are evaluated in Chapter 2. In this section, the transient thermal response of the HI-STAR System to a 30-minute fire followed by a post-fire cooldown is determined. The fire accident evaluation is performed by consideration of a worst case combination of factors which conservatively overestimate heat input to the HI-STAR System during the fire followed by an underestimation of the ability of the cask to reject heat to the environment after the fire.

The impact limiters are designed to crush and absorb energy during the hypothetical drops. In the hypothetical fire accident evaluation, the impact limiter is assumed to be crushed to the bounding maximum condition of a solid block of highly conducting aluminum, resulting in increased heat input to the overpack ends through the reduced impact limiter thickness during the fire. The fire condition thermal analysis results are therefore bounding with respect to impact limiter design and amount of crush experienced during a hypothetical drop accident.

A puncture event may locally buckle some of the radial connector plates through the neutron shielding, thereby reducing the ability of the system to reject heat after the fire. As described in Section 2.7, the puncture bar is 6 inches in diameter and correspondingly has a face area of approximately 28.3 in^2. The enclosure shell area is greater than 52,200 in^2. Therefore, while the puncture bar would directly impact less than 0.06% of the exposed area, a conservative 10% reduction in the neutron shield region effective thermal conductivity is considered during the post-fire cooldown phase.

During the initial 30-minute fire event, some of the neutron shield will be exposed to high temperatures. Therefore, in determining heat input to the system, a conservative value maximizing the heat input is utilized for the neutron shield thermal conductivity. During the post-fire cooldown phase, no credit is considered for conduction through the neutron shield material. During the fire, a 10CFR71 mandated cask surface emissivity is considered to maximize radiant heat input to the cask. Destruction of the painted surfaces due to exposure to intense heat during the fire event is a credible possibility. Therefore, the lower emissivity of exposed carbon steel is conservatively considered for post-fire cooldown analysis.

The initial condition prior to the start of the fire accident is based on the bounding normal transport condition MPC basket temperature distribution. The smallest of the four baskets (MPC-24, MPC-24E, MPC-32 and MPC-68) average density and heat capacity are applied to the fire transient analysis. Thus, maximum basket heat load coincident with minimum thermal inertia provides a conservatively bounding response of the HI-STAR System to a fire accident condition.

In the fire event, analyzed in this Section of the SAR, the aim of the analysis is to bound two HI-STAR cask scenarios namely (a) MPCs installed with AHCEs and (b) MPCs without AHCEs. To achieve this objective, the analysis to characterize the response of the HI-STAR package in enveloping a Part 71 fire event assumes that the AHCE heat transfer bridge is present while the fire is raging so that the computed heat flow to the fuel is maximized. Further, the absorptivity of the overpack is increased from its normal operating condition value of 0.85 to the Part 71 value of 0.9. To account for the "no-AHCE" scenario, the emissivity of the overpack is reduced below its normal operating condition value (Table 3.5.2), as soon as the fire event ends, thus retarding the rejection of heat to the environment.

The temperature history of a number of critical control points in the HI-STAR System are monitored during the 30-minute fire and the subsequent relaxation of temperature profiles during the post-fire cooldown phase. The impact of transient temperature excursions on HI-STAR System materials is assessed in this section.

3.5.1 Thermal Model

3.5.1.1 Analytical Model

A thermal transient simulation model to determine the fire condition temperature response is developed on the FLUENT CFD code [3.1.2]. The basic underlying finite volume model is based on the steady-state FLUENT model developed and described in Section 3.4. This basic model is modified by incorporating time dependent thermal loads on the exposed surfaces of the HI-STAR System for determining transient responses at every computational cell defined in the FLUENT model.

The HI-STAR System configuration during a hypothetical fire accident is schematically depicted in Figure 3.5.1. The initial thermal condition of the HI-STAR System prior to the accident condition is the normal transport steady-state temperature distribution. The HI-STAR System is then subjected to a 1475°F fire environment for 30 minutes. During this fire event, the impact limiters installed on both ends are assumed to be in a fully crushed state. This is a conservative assumption which results in an increased heat input to the overpack due to the higher thermal conductivity and reduced thickness of the crushed impact limiter. After 30 minutes, the ambient temperature is restored to 100°F and the HI-STAR System is allowed to proceed through a post-fire cooldown phase. During this entire transient event (fire and post-fire cooldown), the temperature history of several control points in the HI-STAR System is monitored. These points are schematically depicted in Figure 3.5.1.

Heat input to the HI-STAR System while it is engulfed in a fire is from a combination of radiation and forced convection heat transfer to all overpack/impact limiter exposed surfaces. This can be expressed by the following equation:

$$q_F = h_{fc}(T_F - T_s) + \sigma \varepsilon [(T_F + 460)^4 - (T_s + 460)^4]$$

where:

q_F = surface heat input flux (Btu/ft^2-hr)

T_F = fire condition temperature (1475°F)
T_S = transient surface temperature (°F)
h_{fc} = forced convection heat transfer coefficient [Btu/ft-hr-°F]
ε = surface emissivity = 0.9 (per 10CFR71)
σ = Stefan-Boltzmann Constant (0.1714×10^{-8} Btu/ft^2-hr-°R^4)

The forced convection heat transfer coefficient is calculated to bound the convective heat flux contribution to the exposed cask surfaces due to a fire induced air flow velocity of 15 m/s. For the case of air flow past a heated cylinder, Jakob [3.5.2] recommends the following correlation for convective heat transfer, obtained from experimental data:

$$Nu_{fc} = 0.028\, Re^{0.8} \left[1 + 0.4 \left(\frac{L_{st}}{L_{tot}} \right)^{2.75} \right]$$

where:
L_{tot} = length traversed by flow
L_{st} = length of unheated section
K_f = thermal conductivity of air evaluated at the average film temperature
Re = flow Reynolds Number based on L_{tot}
Nu_{fc} = Nusselt Number ($h_{fc}\, L_{tot}/K_f$)

Consideration of the wide range of temperatures to which the exposed surfaces are subjected to during the fire and the temperature dependent trend of air properties requires a careful selection of parameters to determine a conservatively large bounding value of the convective heat transfer coefficient. In Table 3.5.1, a summary of the parameter selections with justifications provides an appropriate basis for application of this correlation to determine forced convection heating of the HI-STAR System during the short-term fire event.

After the 30-minute fire event, the ambient temperature is restored to 100°F. The HI-STAR System cools down during this post-fire cooldown phase. Heat loss from outside exposed surfaces of the overpack is determined by the following equations:

$$q_S = 0.18\,(T_S - T_A)^{4/3} + \sigma\,\varepsilon\,[(T_S + 460)^4 - (T_A + 460)^4]$$

where:
q_s = surface heat loss flux (Btu/ft^2-hr)
T_S = transient surface temperature (°F)
T_A = ambient temperature (100°F)
ε = surface emissivity
σ = Stefan-Boltzmann Constant (0.1714×10^{-8} Btu/ft^2-hr-°R^4)

During the fire event, some region of Holtite will be overheated and thus lose its ability to conduct heat. In the fire transient analysis, full credit is given to conduction through Holtite to conservatively increase heat input to the overpack. In the post-fire cooldown phase, all of the Holtite is conservatively assumed to be lost (no conduction through Holtite material).

During the 30-foot drop and puncture accident events, the mechanical integrity of the HI-STAR System is maintained. From a thermal analysis standpoint, the impact limiters are crushed and there is at most localized damage to radial channels. While the resulting localized damage would not significantly degrade the heat transfer ability of the Holtite region, a 10% effective conductivity reduction is conservatively (as described earlier in Section 3.5) applied during the post-fire cooldown phase. In Table 3.5.2, a summary of inputs used in the determination of the effect of a hypothetical fire accident is provided.

3.5.1.2 Test Model

For determining the transient response of the HI-STAR System under a hypothetical fire accident condition, a detailed finite volume model has been developed on the validated and benchmarked FLUENT code. The dynamic model features several conservative assumptions to bound temperature excursions during the heat up and cooldown phases of the accident. Accordingly, development of a separate test model to verify the results is not considered necessary. Evaluation of the HI-STAR System thermal design in the event of a hypothetical fire event is shown to be in compliance with 10CFR71 requirements.

3.5.2 System Conditions and Environment

The HI-STAR System is shown to maintain its mechanical integrity following a 30 foot drop and puncture accident with stresses within applicable ASME Code requirements. The impact limiters absorb the impact forces and are crushed in the drop event. Completely crushed impact limiters provide a conservatively limiting situation for increased heat absorption during the 30-minute fire. The effect of a puncture accident results in localized damage to the radial connectors embedded in Holtite neutron shielding. This will *not* reduce the heat transfer capability of the region containing Holtite by a significant factor. The fire is specified to be at a temperature of 1475°F and last for 30 minutes. Emissivity of all exposed surfaces is set to 0.9. Some of the Holtite will decompose and lose its ability to conduct heat during the fire event due to exposure to severe temperature conditions. Thermal analysis of the HI-STAR System is performed by postulating worst case conditions whereby increased heat absorption takes place during the 30-minute fire and a reduced ability of the HI-STAR System to reject heat takes place during the post-fire cooldown phase.

3.5.3 System Temperatures

The hypothetical fire accident condition is evaluated by imposing a 1475°F fire temperature for 30 minutes followed by a post-fire equilibrium phase that is followed for more than 30 hours. The temperature-time history of several control points is monitored. These points are selected because of their importance relating to safety evaluation. In Figures 3.5.2 to 3.5.4, the transient temperature profiles of the monitored points shown in Figure 3.5.1 are plotted. From these plots, the temperature of exposed surfaces is seen to increase rapidly and peak at about 1348°F at the end of the fire (i.e., 30 minutes). Figure 3.5.5 shows the peak axial fuel cladding temperature profile during post-fire cooldown. In the post-fire equilibrium phase, there is an initial rapid cooldown of the peak surface temperature followed by an asymptotic approach to the final steady-state condition. The closure bolts and mechanical seals peak temperatures are below short-term limits. The MPC basket center

temperature rises sluggishly to a broad peak and then slowly decays to a final steady-state condition. Portions of Holtite neutron shielding material near the overpack enclosure shell experience a short duration high temperature excursion. The crushed aluminum alloy inside the impact limiter begins to melt at 1105°F. The latent heat of melting of aluminum alloy during the melting phase would absorb the incident heat flux from the fire. This ablation mechanism will protect the cask by limiting the surface temperature excursion and restricting the amount of heat input to the overpack lid. In the HI-STAR System fire transient evaluation, credit for this protective feature is not considered.

The HI-STAR fire event model is depicted in Figure 3.5.6. Fire condition containment boundary through thickness temperature profiles are presented in Figures 3.5.7, 3.5.8, and 3.5.9 across Sections A-A, B-B, and C-C, as shown in Figure 3.5.6. The figures present through-thickness temperature profiles at the end of the 30-minute fire and 60 minutes after the start of the fire (30 minutes into the post-fire cooldown period).

In the fire event, the dominant heat input source is located on the outside of the cask. The temperature gradient, as seen in Figures 3.5.7, 3.5.8, and 3.5.9, is reversed from the normal condition, with the maximum temperature occurring at the outermost layer. From Figure 3.5.7, it is apparent that the overpack inner shell remains below the 500°F short-term design basis temperature limit. At the end of the 30-minute fire, the outermost layer of the multi-layered shells is heated to approximately 540°F. During the post-fire cooldown phase the temperature of this outer layer rapidly drops below 500°F, as shown on the 60-minute profile.

An examination of the overpack forging temperature profile (Section B-B, Figure 3.5.8) shows that the outer layers of the forging, directly adjacent to the surface exposed to the fire, are heated to in excess of 700°F during the fire. The bulk of the forging metal mass (in excess of 6 inches out of the total 8.5 inches) remains below the 700°F short-term design basis temperature limit. The portion of the overpack forging which is covered by the impact limiters remains below 700°F both during and after the fire. This is illustrated by the temperature profiles presented in Figure 3.5.9.

The following observations can be drawn from an examination of Figures 3.5.6 through 3.5.9:

- The containment boundary regions that are within the confines of the multi-layered shells remain below 500°F.

- The containment boundary regions that are within the confines of the impact limiters remain below 700°F.

- The bulk of the containment boundary in the regions that are directly exposed to the fire remain below 700°F.

The outer region of the HI-STAR 100 overpack consists of forty sector shaped annular spaces enclosed in half inch thick carbon steel plates. These annular spaces contain Holtite-A neutron absorber material. Holtite-A is a stable material under the environmental and thermal conditions corresponding to normal operation. Under a fire condition, the temperature in the enclosure shell

cavity rises resulting in loosening of the water intermolecular bonds to the neutron shield material leading to liberation of water vapor. For conservatism, a 6% weight loss factor for the neutron shield when exposed to a direct fire is assumed. . Under a conservatively postulated scenario wherein all of the radial neutron shield material (approximately 12,850 lbs required to completely fill the forty spaces) is exposed to a direct fire, 771 lbs of water vapor (i.e 6% of neutron shield) generation in 30 minutes is required to be expelled from the neutron shield cavities. To protect the enclosure shell from overpressure, two rupture discs (each having the required vapor expulsion capacity) are incorporated in the HI-STAR overpack design. The rupture discs have a relatively low set pressure (30 psig) to relieve water vapor if the generation is rapid during a fire condition.

3.5.4 Maximum Internal Pressure

Based on bounding transient temperature excursions calculated for the HI-STAR System during a hypothetical fire accident condition, maximum calculated cask internal pressures are reported in Table 3.5.3. Maximum pressure calculations assume 100% of the fuel rods rupture, releasing conservatively determined rod fill gas and fission gases volumes into the MPC cavity.

3.5.5 Maximum Thermal Stresses

Maximum thermal stresses generated during transient temperature excursions within the HI-STAR System are reported in Chapter 2.

3.5.6 Evaluation of System Performance for the Hypothetical Accident Thermal Conditions

The HI-STAR System was subjected to a hypothetical fire accident condition with the impact limiters crushed and enclosure shell punctured as a result of previously imposed drop and puncture accidents. However, mechanical integrity of the overpack intermediate and inner shells, mechanical seals, and MPC shell is retained. During the fire accident event, portions of neutron shielding material in the overpack enclosure shell experience high transient temperature excursions and thus partially lose the ability to conduct heat and shield neutrons. Portions of aluminum alloy inside the crushed impact limiters near the exposed surfaces melt, but do not ignite.

For assessing the impact of transient temperature excursions on the integrity of the HI-STAR System, the significant components and quantities of interest are the closure plate bolts temperatures, the mechanical seals temperatures, the neutron shield temperature, the peak pressure and the peak fuel cladding temperature. The closure plate bolts maintain their ability to hold the seals. The neutron shield material in the post-accident shielding analysis is conservatively assumed to be completely lost. The peak system pressure remains below the design basis accident pressure. The fuel cladding temperature peak does not exceed short-term accident limits. Consequently, the HI-STAR System integrity during the most severe fire event followed by a post-fire cooldown phase is not compromised. In Table 3.5.4, a summary of peak HI-STAR System component temperatures during fire and post-fire accident conditions is provided. The calculated results demonstrate that the HI-STAR System is in compliance with 10CFR71 thermal requirements for hypothetical accident conditions of transport.

Table 3.5.1

SUMMARY OF TEMPERATURE-DEPENDENT FORCED CONVECTION HEAT TRANSFER CORRELATION PARAMETERS FOR AIR

Parameter	Trend with Increasing Temperatures	Criteria to Maximize h_{fc}	Conservative Parameter Value	Evaluated At
Temperature Range	100°F-1475°F	NA	NA	NA
Density	Decreases	Reynolds Number	High	100°F
Viscosity	Increases	Reynolds Number	Low	100°F
Conductivity (K_f)	Increases	h_{fc} Proportional to K_f	High	1475°F

Table 3.5.2

SUMMARY OF HYPOTHETICAL FIRE ACCIDENT INPUTS

		Steady-State Initial† Condition	30-minute Fire	Post-Fire Equilibrium
1.	Conduction through Holtite	No	Yes	No
2.	Holtite Region Conductivity Reduction (Loss of Radial Connectors)	No	No	Yes
3.	Insolation	Yes	Yes	Yes
4.	Radiation Heat Transfer	Yes	Yes	Yes
5.	Surface Convection	Natural	Forced	Natural
6.	Impact Limiters Installed††	Yes	Yes (crushed)	Yes (crushed)
7.	Surface Emissivity	0.85	0.9	0.66

† A bounding initial temperature condition is imposed for fire transient analysis.

†† Based on minimum 15,000 lbs impact limiter weight modeled as a solid aluminum cap to maximize heat input to cask.

Table 3.5.3

MAXIMUM HI-STAR SYSTEM HYPOTHETICAL FIRE CONDITION EVENT PRESSURES[†]

Condition	Pressure (psig)			
	MPC-24	MPC-68	MPC-24E	MPC-32
Without fuel rods rupture	99.6	98.0	99.6	99.6
With 100% fuel rods rupture	143.8	128.5	145.2	160.9

† Pressure analysis is based on release of 100% of the rods fill gas and 30% of the significant radioactive gases from a ruptured rod.

Table 3.5.4

MAXIMUM HI-STAR SYSTEM COMPONENTS AND MATERIALS
TEMPERATURES DURING AND AFTER HYPOTHETICAL FIRE CONDITION

Material/Component	Initial Condition (°F)	During Fire (°F)	Post Fire Cooldown (°F)	Accident Limit (°F)
Fuel cladding	708	708	751	1058
Overpack closure bolts	159	415	514	600
Overpack closure plate seals	160	392	490	1200
Drain port plug seal	259	645	662	932
Vent port plug seal	160	283	443	932
Holtite outer surface	223	1232	1232	N/A†
Holtite inner surface	259	604	604	N/A
MPC shell	309	313	419	775
Impact limiter surface	127	983	983	1105
Overpack outer enclosure	226	1348	1348	1350

† Holtite is conservatively assumed to be completely lost during the fire accident.

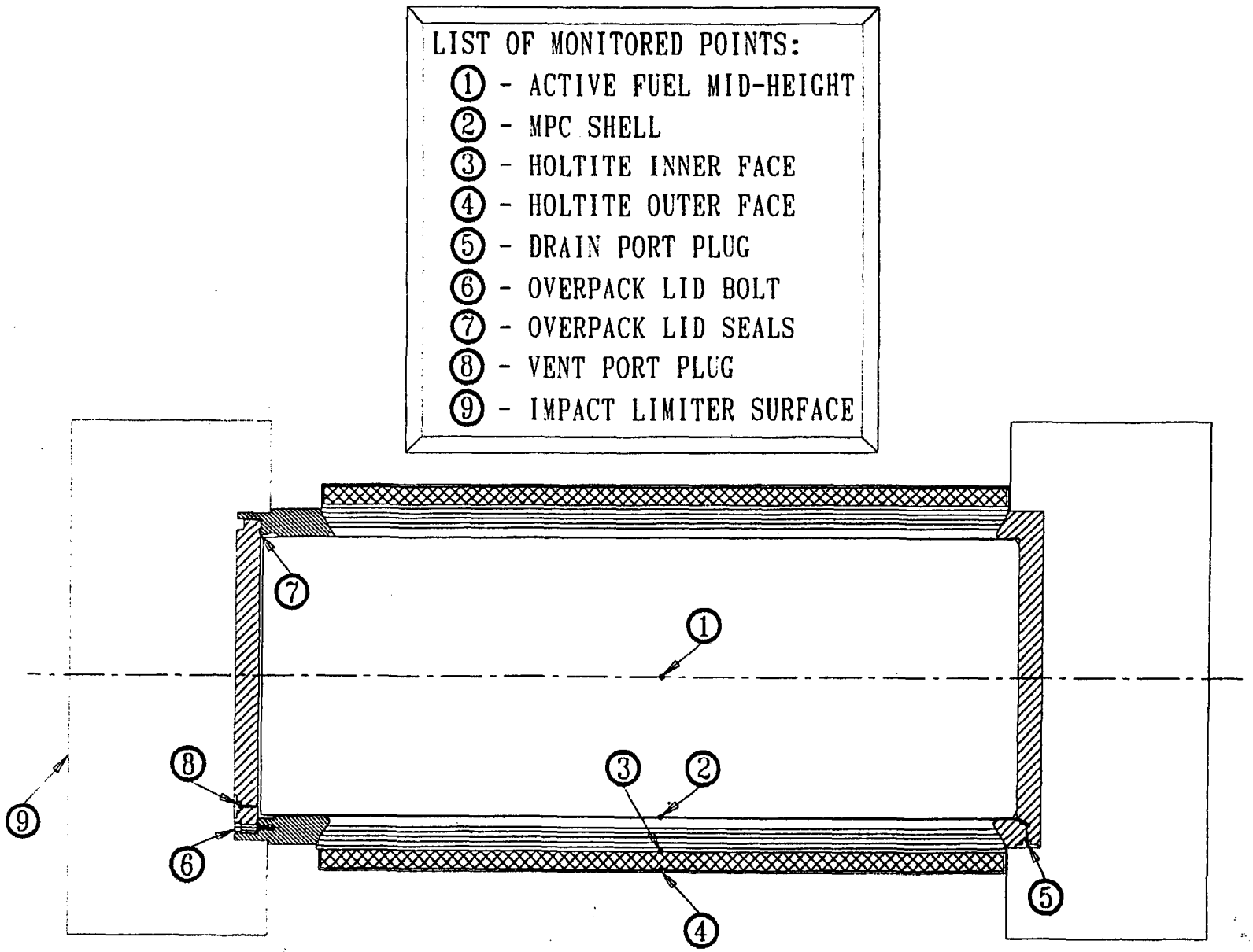

FIGURE 3.5.1; LOCATION OF HI-STAR 100 PACKAGE CONTROL POINTS MONITORED DURING HYPOTHETICAL FIRE ACCIDENT CONDITION

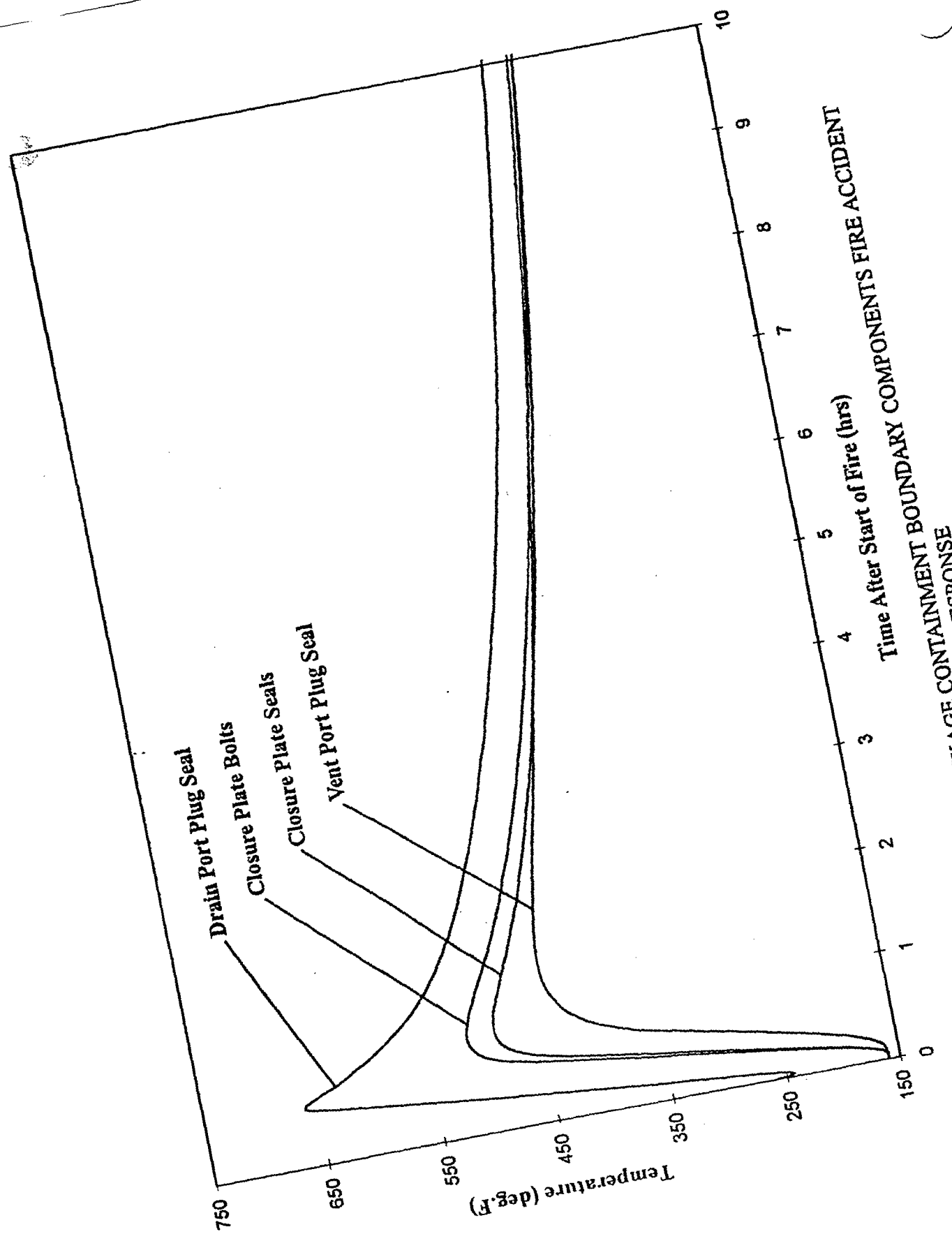

FIGURE 3.5.2; HI-STAR 100 PACKAGE CONTAINMENT BOUNDARY COMPONENTS FIRE ACCIDENT TRANSIENT TEMPERATURE RESPONSE

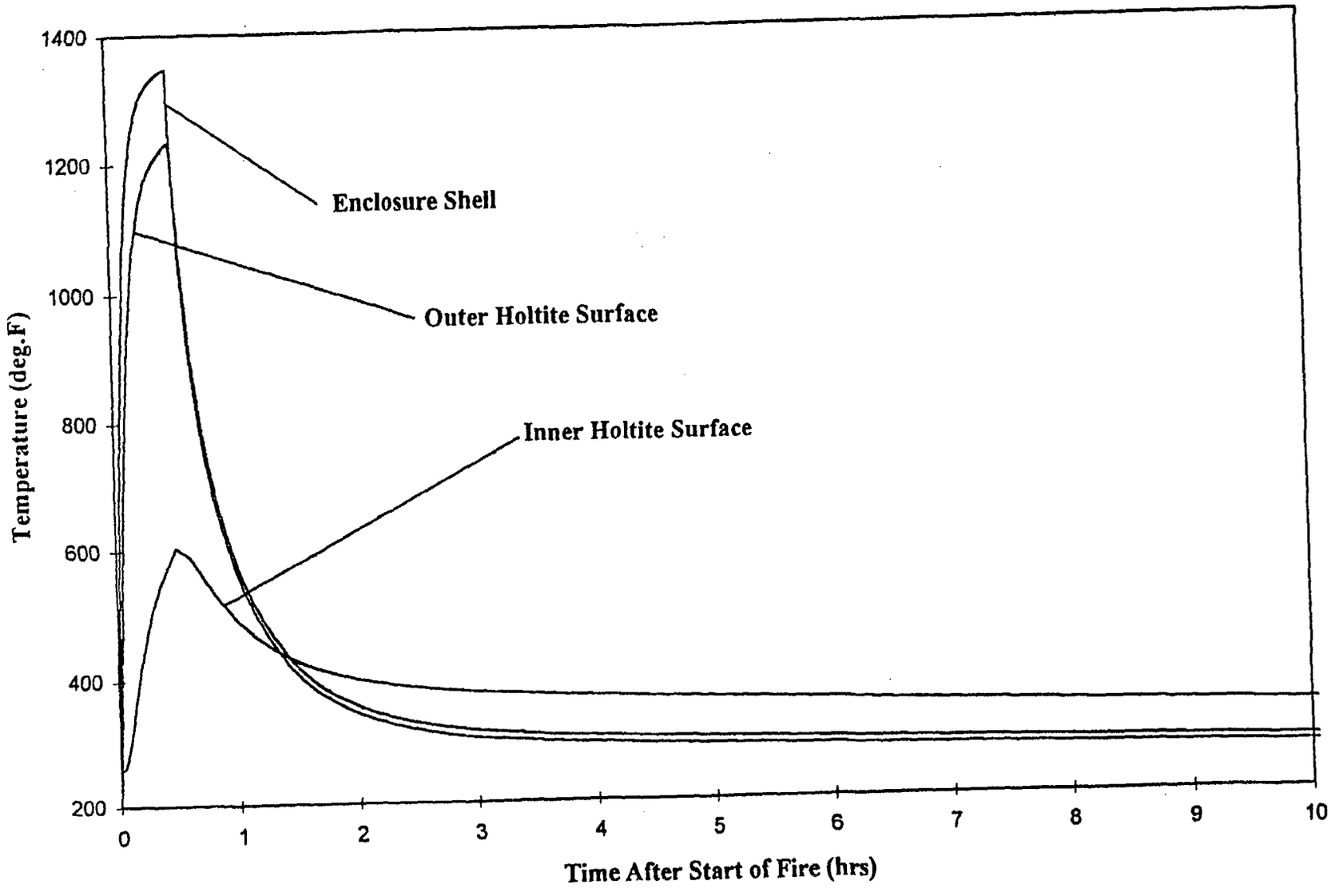

FIGURE 3.5.3; HI-STAR 100 PACKAGE NEUTRON SHIELDING REGION FIRE ACCIDENT TRANSIENT TEMPERATURE RESPONSE

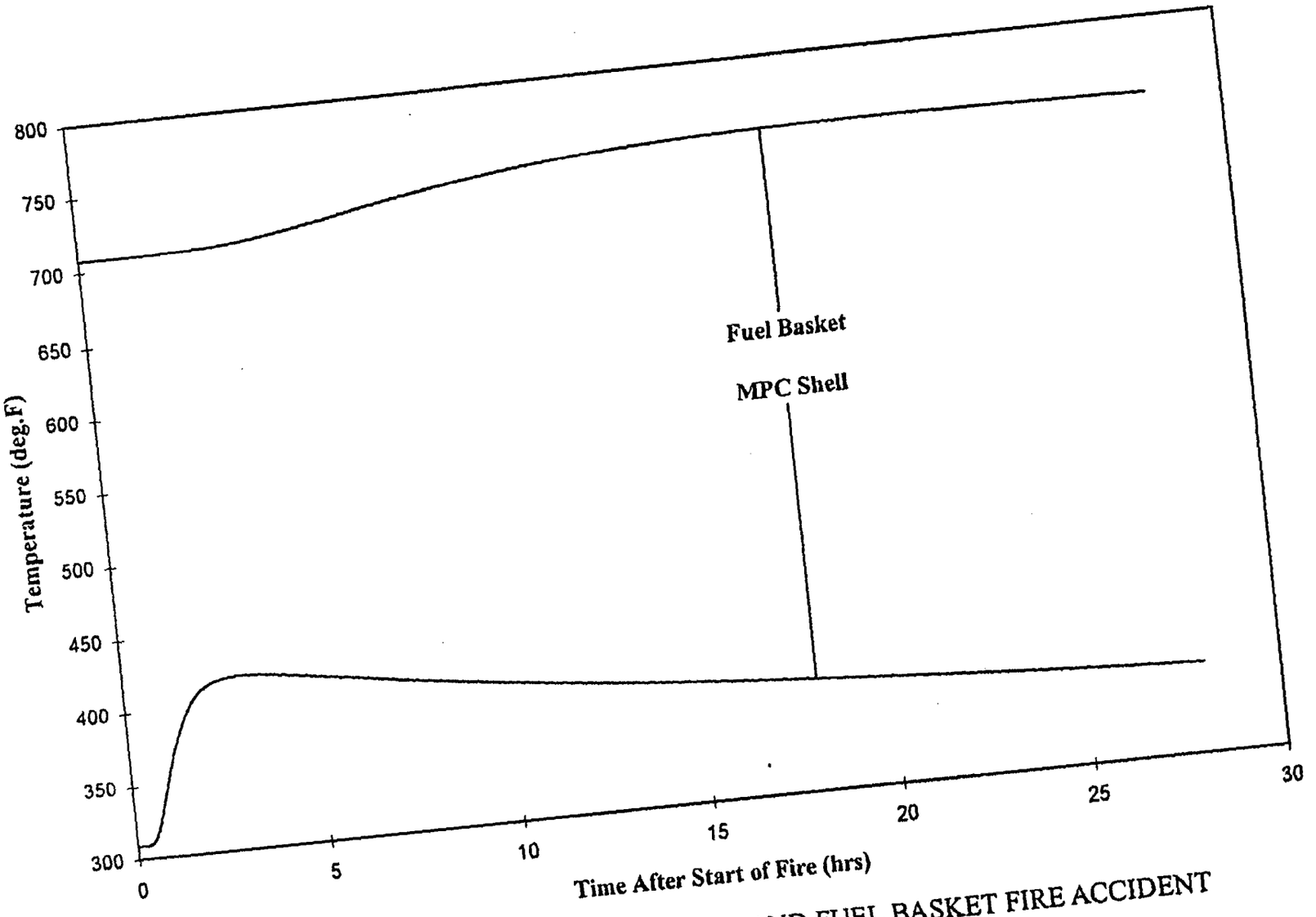

FIGURE 3.5.4; HI-STAR 100 PACKAGE MPC SHELL AND FUEL BASKET FIRE ACCIDENT TRANSIENT TEMPERATURE RESPONSE

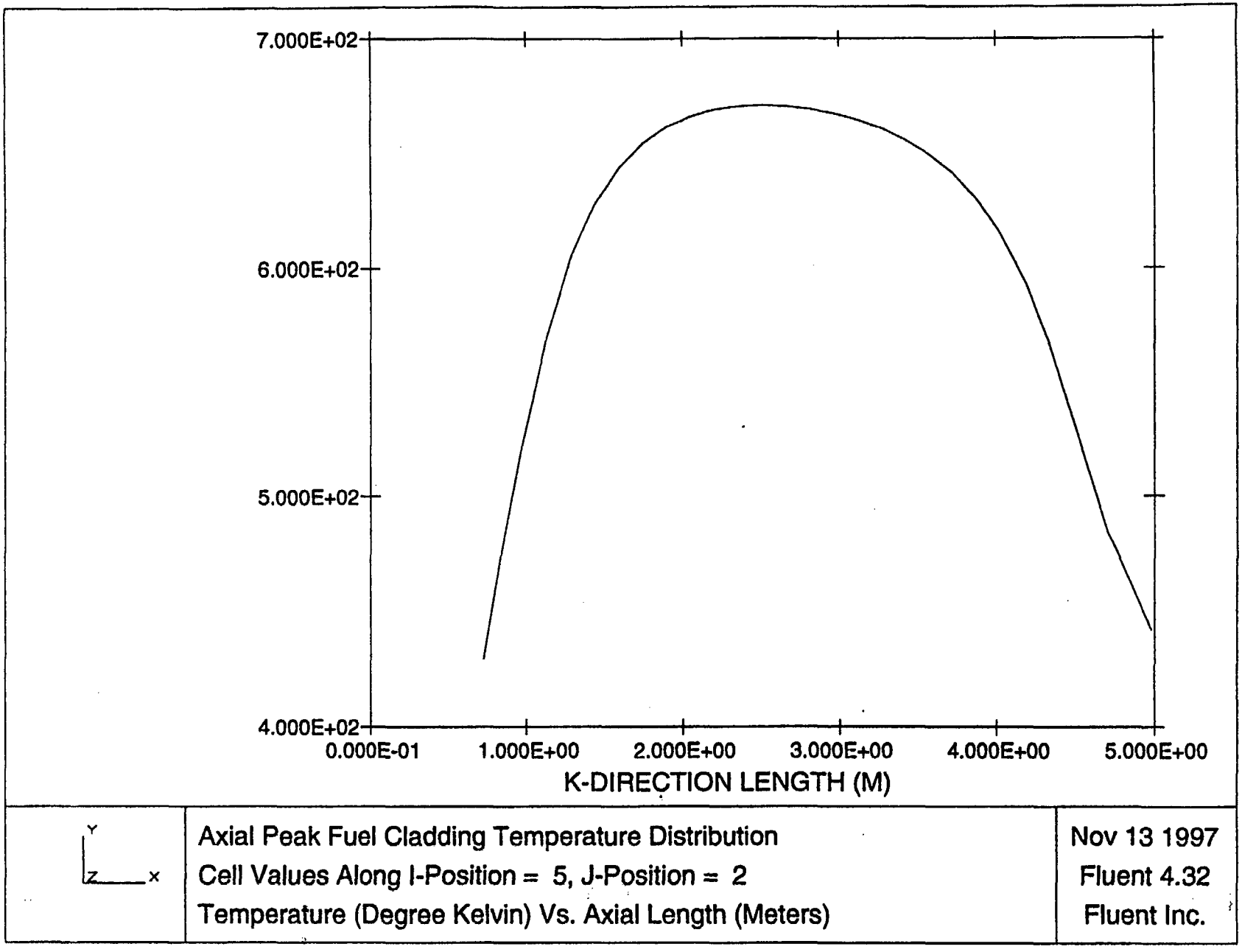

FIGURE 3.5.5: FUEL CLADDING PEAK AXIAL TEMPERATURE DISTRIBUTION DURING POST FIRE COOLDOWN

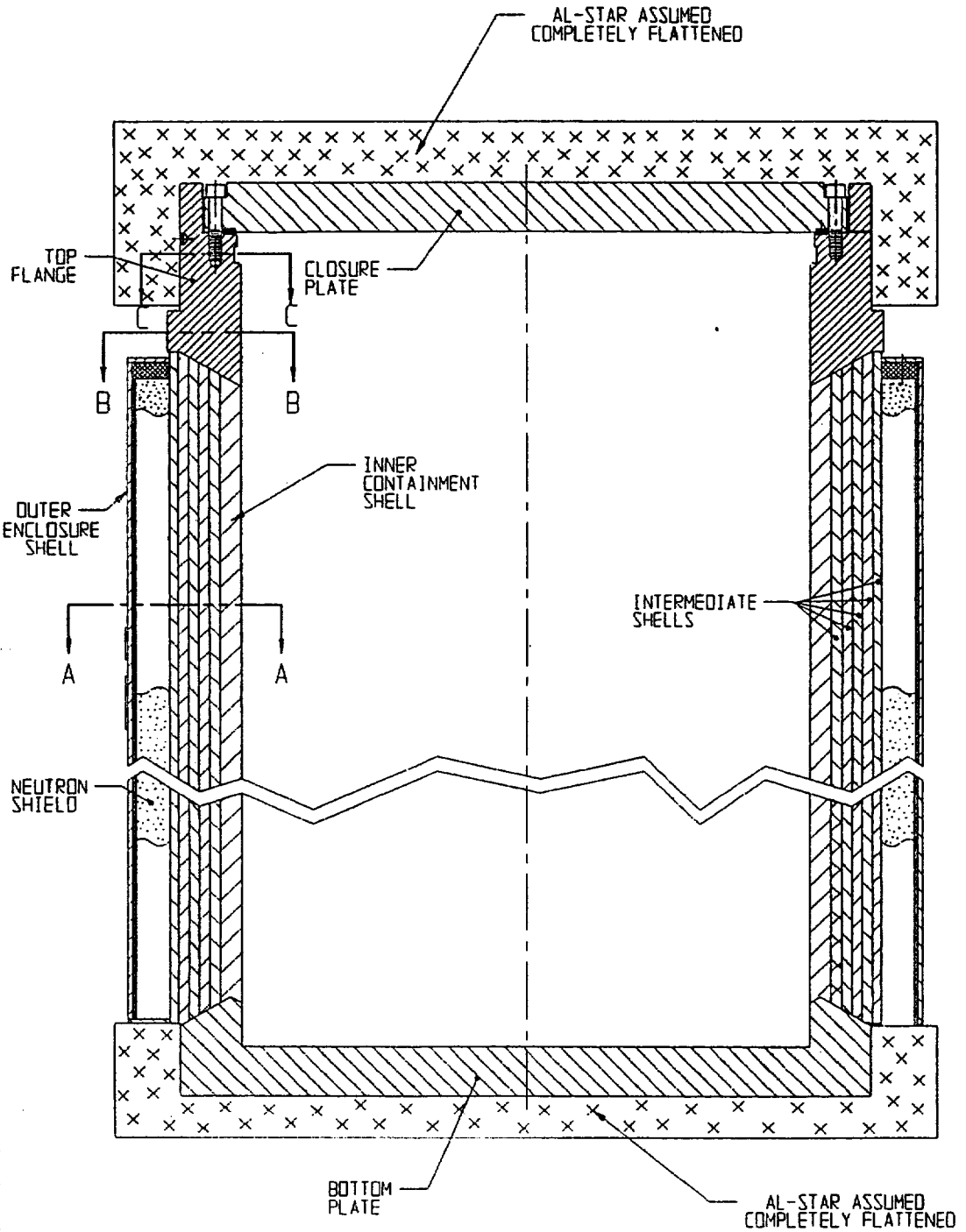

FIGURE 3.5.6; HI-STAR MODEL FOR TRANSPORT FIRE

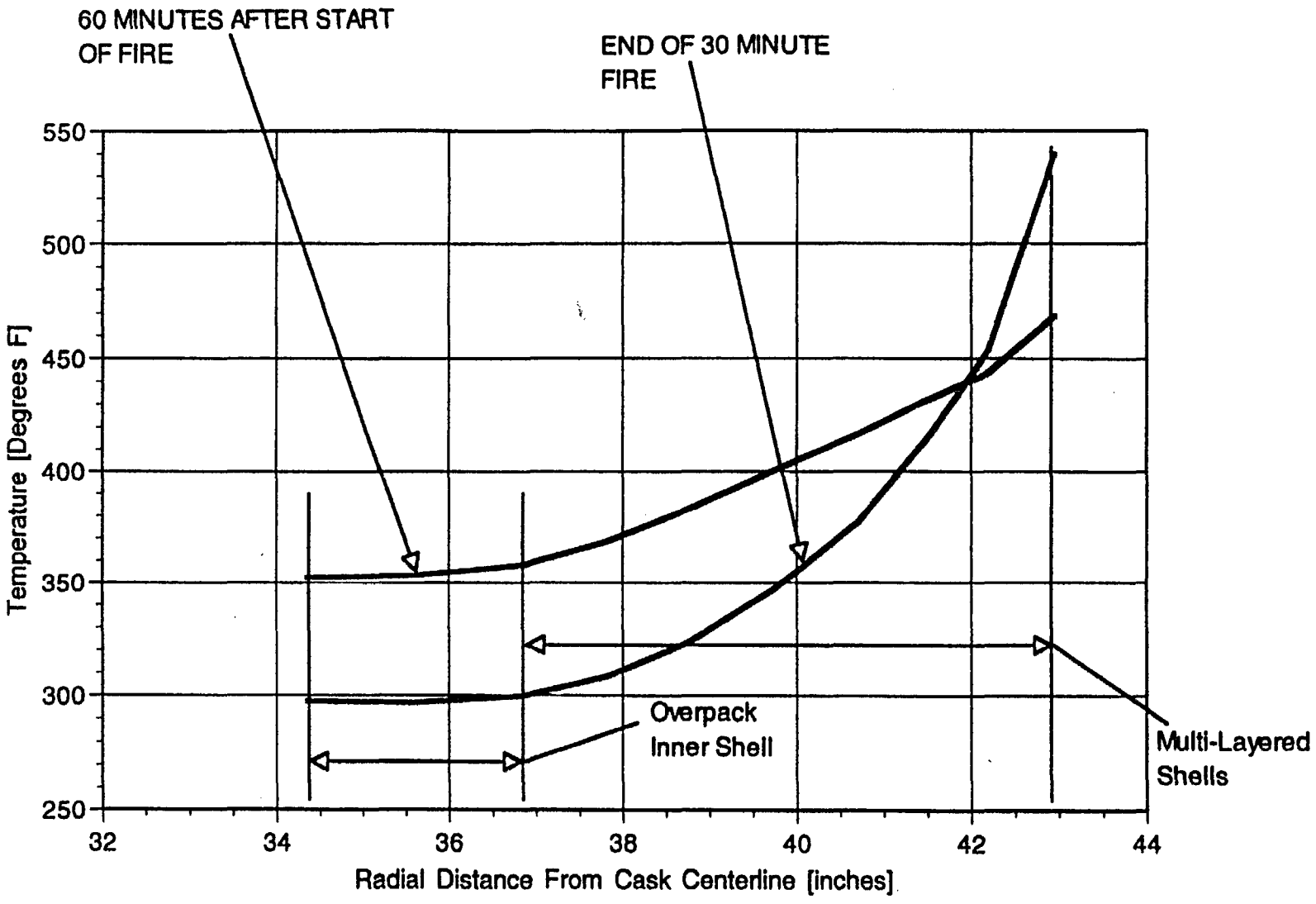

FIGURE 3.5.7: TRANSPORT FIRE CONDITION CONTAINMENT BOUNDARY AND LAYERED SHELLS TEMPERATURE DISTRIBUTIONS (SECTION A-A)

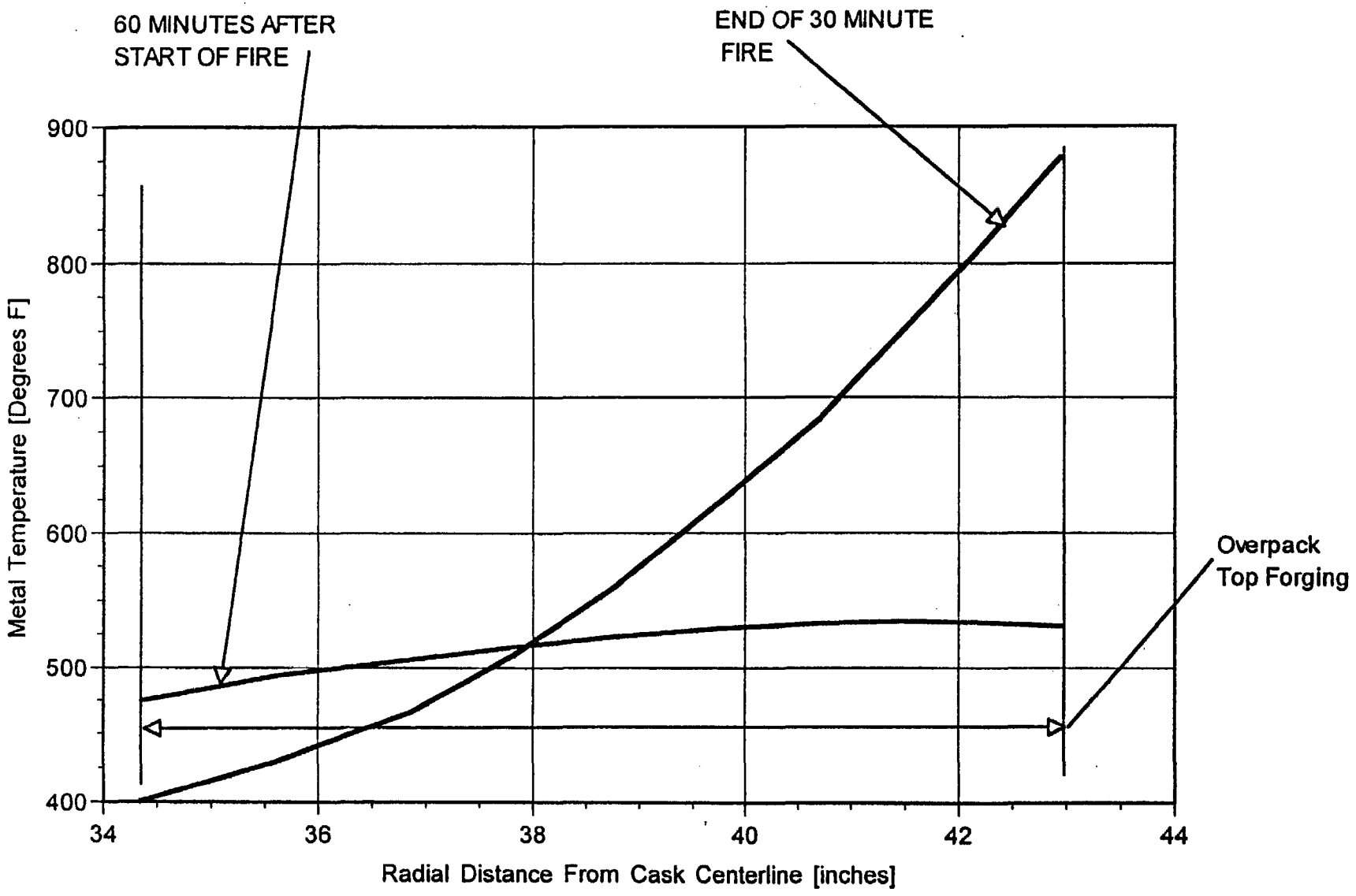

FIGURE 3.5.8: TRANSPORT FIRE CONDITION OVERPACK TOP FORGING TEMPERATURE DISTRIBUTIONS (SECTION B-B)

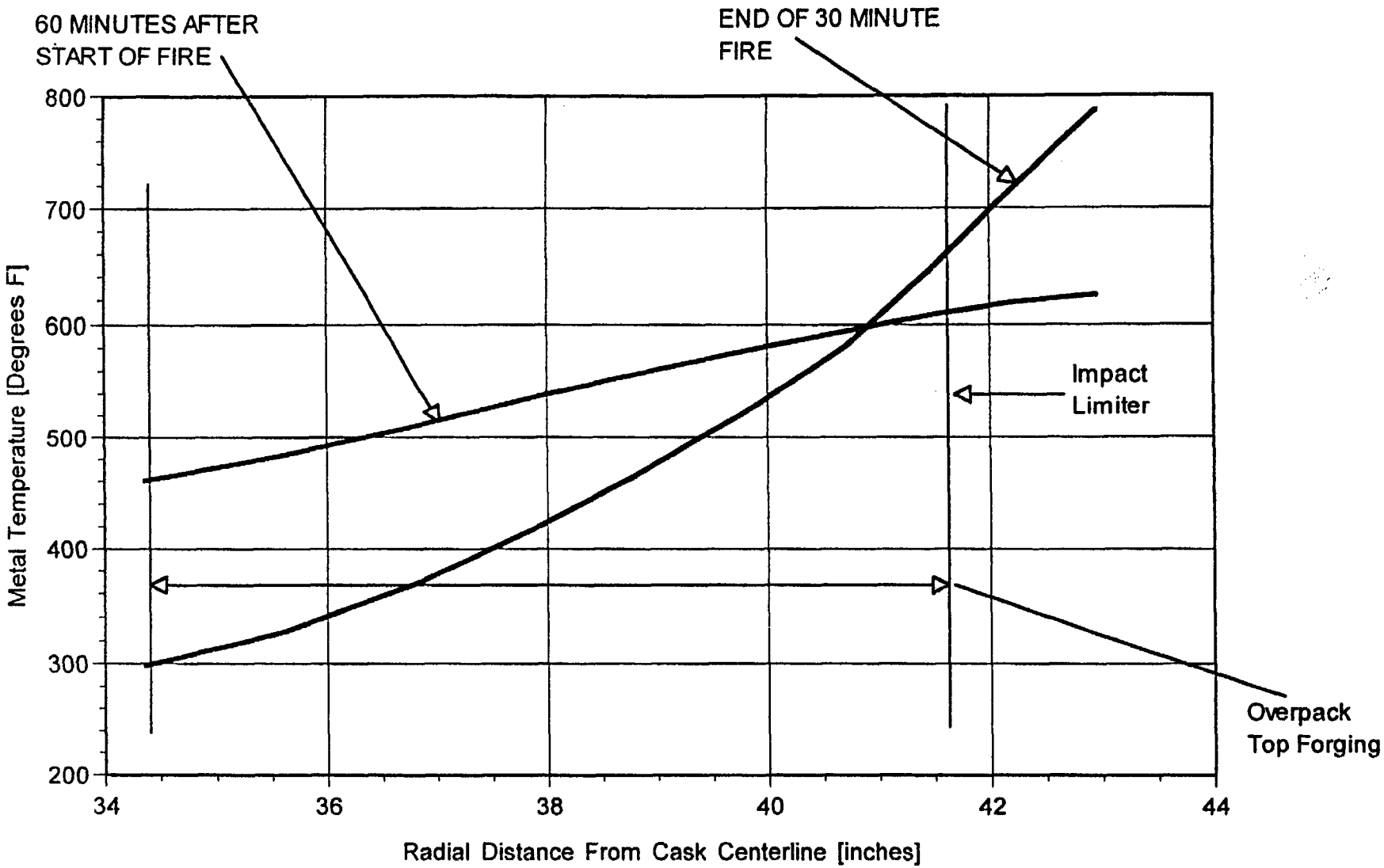

FIGURE 3.5.9: TRANSPORT FIRE CONDITION OVERPACK TOP FORGING TEMPERATURE DISTRIBUTIONS (SECTION C-C)

3.6 REGULATORY COMPLIANCE

Section 3.1 defines the requirements of 10CFR71 and ISG-11, Rev. 2 [3.1.5]) that must be met by the HI-STAR cask thermal design. The cask thermal evaluations in support of these requirements are provided in Sections 3.1 through 3.5. In this Section, a summary of the requirements and results of the evaluations are provided.

1. The applicant must include a description of the proposed package in sufficient detail to identify the package accurately and provide a sufficient basis for the evaluation of the package. The description must include, with respect to the packaging: specific materials of construction, weights, dimensions, and fabrication methods of materials specifically used as non-fissile neutron absorbers or moderators; and structural and mechanical means for the transfer and dissipation of heat. The description must include, with respect to the contents of the package: chemical and physical form; maximum normal operating pressure; maximum amount of decay heat; and identification and volumes of any coolants.

   A general description of the HI-STAR System is included in Chapter 1. Descriptions of cask materials are presented in Subsection 1.2.1, Section 1.4 and Appendices 1.A, 1.B and 1.C. Shielding materials are specifically addressed in Subsection 1.2.1.4. Cask component weights are presented in Subsections 1.2.1.1 and 2.2. Cask component dimensions are presented in Subsection 1.2.1.2 and in engineering drawings included in Section 1.4. The transfer and dissipation of heat are discussed generally in Subsection 1.2.1.6, and in detail in this chapter.

   General descriptions of and requirements for fuel assemblies for transport are presented in Subsection 1.2.3, including design basis maximum decay heat load specifications in Subsection 1.2.3.5. Maximum normal operating pressures are reported in Subsection 3.4.4. As stated in Subsection 1.2.1.7, there are no coolant volumes (reservoirs) in the HI-STAR System.

2. A package must be designed, constructed, and prepared for shipment so that under normal conditions of transport there would be no substantial reduction in the effectiveness of the packaging.

   The results of thermal evaluations presented in Section 3.4 demonstrate that the HI-STAR System performs as designed under all normal conditions of transport.

3. A package must be designed, constructed, and prepared for shipment so that in still air at 100°F and in the shade, no accessible surface of the package would have a temperature exceeding 185°F in an exclusive use shipment.

   Maximum exposed surface temperatures for the HI-STAR System are reported in Subsection 3.4.2. All impact limiter surface temperatures are shown to be below 185°F. The personnel barrier, described in Chapter 7, renders the hot overpack enclosure shell surfaces inaccessible.

4. Compliance with the permitted activity release limits for a Type B package may not depend on filters or on a mechanical cooling system.

   As stated in Section 3.1, all cooling mechanisms in the HI-STAR System are completely passive.

5. With respect to the initial conditions for the events of normal conditions of transport and hypothetical accident conditions, the demonstration of compliance with the requirements of 10CFR71 must be based on the ambient temperature preceding and following the event remaining constant at that value between -20°F and 100°F which is most unfavorable for the feature under consideration. The initial internal pressure within the containment system must be considered to be the maximum normal operating pressure (MNOP), unless a lower internal pressure consistent with the ambient temperature considered to precede and follow the event is more unfavorable.

   Hypothetical fire accident transient calculations for the HI-STAR System are described in Section 3.5. The initial condition for this event corresponds to the most severe steady-state solution for normal conditions of transport, which correspond to a 100°F ambient temperature with full insolation. These same environmental conditions are applied during the post-accident phase of the evaluation as well. All calculated temperatures for this event are below the specified design temperature limits.

   Maximum calculated normal condition internal pressures (MNOPs) are reported in Subsection 3.4.4. Maximum calculated hypothetical accident condition internal pressures are reported in Subsection 3.5.4. All calculated MNOPs are below the design pressure limits for the MPC helium retention boundary and the overpack containment boundary.

6. For normal conditions of transport, a heat event consisting of an ambient temperature of 100°F in still air and prescribed insolation must be evaluated.

   The maximum temperatures in the HI-STAR System reported in Subsection 3.4.2 correspond to the heat event. All calculated temperatures for this event are below the appropriate design temperature limits. As stated in Subsection 3.4.5, thermal stresses are determined and reported in Chapter 2.

7. For normal conditions of transport, a cold event consisting of an ambient temperature of –40°F in still air and shade must be evaluated.

The minimum temperatures in the HI-STAR System reported in Subsection 3.4.3 correspond to the cold event. All calculated temperatures for this event are below the appropriate design temperature limits. As stated in Subsection 3.4.5, thermal stresses are determined and reported in Chapter 2.

8. Evaluation for hypothetical accident conditions is to be based on sequential application of the specified events, in the prescribed order, to determine their cumulative effect on a package.

   As described in Section 3.5, the HI-STAR System hypothetical accident thermal condition (hydrocarbon fuel/air fire) evaluation incorporates bounding representations of the results of the preceding accident conditions. Specifically, the impact limiters are assumed to be completely crushed (drop event) and the heat transfer effectiveness of the radial channels region is reduced (puncture event). All calculated temperatures for this event are below the appropriate design temperature limits.

9. For hypothetical accident conditions, a thermal event consisting of a fully engulfing hydrocarbon fuel/air fire with an average emissivity coefficient of at least 0.9, with an average flame temperature of at least 1475°F for a period of 30 minutes.

   The description of the HI-STAR System hypothetical accident thermal event model (Subsection 3.5.1.1) specifies the fire condition input parameters. All input parameters are in accordance with the requirements of 10CFR71.73(c)(4). All calculated temperatures for this event are below the appropriate design temperature limits.

The thermal evaluations in Sections 3.4 and 3.5 demonstrate compliance with the ISG-11, Rev. 2 [3.1.5] temperature limits. Specifically, the maximum cladding temperatures for normal transport and accident conditions are below the prescribed limits (normal (752°F) and accident (1058°F)). The thermal evaluations provided in this SAR demonstrate that the HI-STAR System description and evaluation satisfy the thermal requirements of 10 CFR Part 71. Specifically:

- The material properties and component specifications used in the thermal evaluation are sufficient to provide a basis for evaluation of the HI-STAR System against the thermal requirements of 10 CFR Part 71.

- The methods used in the thermal evaluation are described in sufficient detail to permit an independent review, with confirmatory calculations, of the HI-STAR System thermal design.

- The accessible surface temperatures of the HI-STAR System as it will be prepared for shipment satisfy 10 CFR 71.43(g) for exclusive use shipments.

- The HI-STAR System design, construction, and preparations for shipment ensure that the material and component temperatures will not extend beyond the specified allowable limits during normal conditions of transport consistent with 10 CFR 71.71.

- The HI-STAR System design, construction, and preparations for shipment ensure that the material and component temperatures will not exceed the specified allowable temperature limits during hypothetical accident conditions consistent with 10 CFR 71.73.

It is therefore concluded that the thermal design of the HI-STAR System is in compliance with 10 CFR Part 71, and that the applicable design and acceptance criteria have been satisfied. The evaluation of the thermal design provides reasonable assurance that the HI-STAR System will allow safe transport of spent fuel. This conclusion is based on the technical data and analyses presented in this chapter in conjunction with provisions of 10 CFR Part 71, appropriate regulatory guides, applicable codes and standards, and accepted engineering practices.

3.7 REFERENCES

[3.1.1] ANSYS Finite Element Modeling Package, Swanson Analysis Systems, Inc., Houston, PA, 1993.

[3.1.2] FLUENT Computational Fluid Dynamics Software (Fluent, Inc., Centerra Resource Park, 10 Cavendish Court, Lebanon, NH 03766).

[3.1.3] Greer et al., "The TN-24P Spent Fuel Storage Cask: Testing and Analyses," EPRI NP-5128, PNL-6054, UC-85, (April 1987).

[3.1.4] Deleted.

[3.1.5] "Cladding Considerations for the Transportation and Storage of Spent Fuel", Interim Staff Guidance – 11, Revision 2, (7/30/02).

[3.2.1] Baumeister, T., Avallone, E.A. and Baumeister III, T., "Marks' Standard Handbook for Mechanical Engineers", 8th Edition, McGraw Hill Book Company, 1978.

[3.2.2] Rohsenow, W.M. and Hartnett, J.P., "Handbook of Heat Transfer," McGraw Hill Book Company, New York, 1973.

[3.2.3] Greer et al., "The TN-24P Spent Fuel Storage Cask: Testing and Analyses," EPRI NP-5128, PNL-6054, UC-85, (April 1987).

[3.2.4] Rust, J.H., "Nuclear Power Plant Engineering," Haralson Publishing Company, (1979).

[3.2.5] Kern, D.Q., "Process Heat Transfer," McGraw Hill Kogakusha, (1950).

[3.2.6] "A Handbook of Materials Properties for Use in the Analysis of Light Water Reactor Fuel Rod Behavior", NUREG/CR-0497, (August 1981).

[3.2.7] "Safety Analysis Report for the NAC Storable Transport Cask," Docket No. 71-9235.

[3.2.8] ASME Boiler and Pressure Vessel Code, Section II, Part D, (1995).

[3.2.9] Jakob, M. and Hawkins, G.A., "Elements of Heat Transfer," John Wiley & Sons, New York, 1957.

[3.3.1] "Handbook of Aluminum," Alcan Aluminum Corporation, 3rd Edition, page 170, (1970).

[3.3.2] Levy, I.S. et al., "Recommended Temperature Limits for Dry Storage of Spent Light Water Reactor Zircaloy Clad Fuel Rods in Inert Gas," PNL-6189, (May 1987).

[3.3.3] Deleted.

[3.3.4] "Characteristics of Spent Fuel, High-Level Waste, and Other Radioactive Wastes Which May Require Long-Term Isolation," DOE/RW-0184, (December 1987).

[3.3.5] Johnson, Jr., A.B. and Gilbert, E.R., "Technical Basis for Storage of Zircaloy-Clad Spent Fuel in Inert Gases," PNL-4835, (September 1983).

[3.3.6] Cunningham et. al., "Evaluation of Expected Behavior of LWR Stainless Steel-Clad Fuel in Long-Term Dry Storage," EPRI TR-106440, (April 1996).

[3.3.7] "Temperature Limit Determination for the Inert Dry Storage of Spent Nuclear Fuel," EPRI TR-103949, (May 1994).

[3.4.1] Wooton, R.O. and Epstein, H.M., "Heat Transfer from a Parallel Rod Fuel Element in a Shipping Container," Battelle Memorial Institute, 1963.

[3.4.2] Rapp, D., "Solar Energy," Prentice-Hall, Inc., Englewood Cliffs, NJ, 1981.

[3.4.3] Sanders et al., "A Method for Determining the Spent-Fuel Contribution to Transport Cask Containment Requirements," Sandia Report SAND90-2406-TTC-1019UC-820, page II-127, (November 1992).

[3.4.4] Holman, J.P., "Heat Transfer," 6th ed., McGraw Hill Book Company, 1986.

[3.4.5] Hewitt, G.F., Shires, G.L., and Bott, T.R., "Process Heat Transfer," CRC Press, (1994).

[3.4.6] Chandrasekhar, S., "Hydrodynamic and Hydromagnetic Stability," Dover, (1961).

[3.4.7] Gradshteyn, I.S. and Ryzhik, I.M., "Table of Integrals Series and Products," Academic Press, Fourth Edition, page 366, (1965).

[3.4.8] Deleted.

[3.4.9] Deleted.

[3.4.10] Cormack, D.E., L.G. Leal and J. Imberger, "Natural Convection in a Shallow Cavity With Differentially Heated End Walls. Part 1 Asymptotic Theory," J. Fluid Mechanics, 65, 209-229, (1974).

[3.4.11] Cormack, D.E., L.G. Leal and J.H. Seinfeld, "Natural Convection in a Shallow Cavity With Differentially Heated End Walls. Part 2 Numerical Solutions," J. Fluid Mechanics, 65, 231-246, (1974).

[3.4.12] Imberger, J., "Natural Convection in a Shallow Cavity with Differentially Heated End Walls. Part 3 Experimental Results," J. Fluid Mechanics, 65, 247-260, (1974).

[3.4.13] Hagrman, Reymann and Mason, "MATPRO-Version 11 (Revision 2) A Handbook of Materials Properties for Use in the Analysis of Light Water Reactor Fuel Rod Behavior," NUREG/CR-0497, Tree 1280, Rev. 2, EG&G Idaho, August 1981.

[3.4.14] Deleted.

[3.4.15] Deleted.

[3.4.16] Deleted.

[3.4.17] Deleted.

[3.4.18] Perry and Green, "Perry's Chemical Engineers' Handbook", 6th Edition, McGraw-Hill, 1984.

[3.4.19] Reid, Prauznitz and Poling, "The Properties of Gases and Liquids", Fourth Edition, McGraw-Hill, 1987.

[3.5.1] 10CFR Part 71, Paragraph 71.73, (January 1, 1998).

[3.5.2] Jakob, M., "Heat Transfer," John Wiley & Sons, Inc., page 555, (1967).

APPENDIX 3.A: CONSERVATISMS IN THE THERMAL ANALYSIS OF THE HI-STAR SYSTEM

3.A.1 INTRODUCTION

The HI-STAR 100 overpack is a thick walled, multi-layered cylindrical vessel with an internal cavity suited for emplacement of a cylindrical canister containing spent nuclear fuel (SNF). The canister rests on the inside surface of a horizontally oriented overpack during transport. One principal safety function of the cask is to ensure that the Spent Nuclear Fuel (SNF) cladding temperatures remain below prescribed regulatory limits. For this purpose a thermal model is articulated with modeling assumptions that overstate the temperature of cask contents and provide a conservative upperbound to cladding temperature field that would be obtained inside the canister. In this appendix, the underlying modeling assumptions are evaluated and an assessment of thermal margins reported.

Storage of SNF in casks is characterized by relatively large temperature elevations above the ambient. The cladding temperature rise is the cumulative sum of temperature increments arising from individual elements of thermal resistance. To assure that cladding temperatures are below regulatory limits with robust margins, analytical assumptions adversely impacting heat transfer are chosen with particular attention given to those temperature increments which form the bulk of the temperature rise. In this appendix, a quantitative estimate of some of the principal conservatisms in the thermal model of the HI-STAR 100 System are presented to provide an insight into the extent of overall conservatism in the predicted peak cladding temperatures.

3.A.2 CONSERVATISM IN REPRESENTING HEAT DISSIPATION TO AMBIENT

Heat dissipation from a HI-STAR cask occurs principally by convection and radiation heat transfer to ambient air. The rate of decay heat dissipation from the external surfaces is, of course, influenced by several factors, some of which aid the process (e.g. wind), and others (radiation heating by sun) that oppose it. In the HI-STAR modeling, factors aiding heat transfer are neglected (still air) and those opposing it (insolation) are included. A concomitant effect of assuming no wind is that heat transfer is limited to natural convection cooling. To represent heat transfer from the HI-STAR cask, natural convection correlations for heat transfer (h) from heated surfaces are reported in Chapter 3 (Sub-section 3.4.1.1.7). The numerical values obtained for the HI-STAR cask modeling are in the neighborhood of 1 Btu/ft^2-hr-°F. As we show in the following, these h values are extremely conservative when the effects of wind are considered.

For considering the effects of wind, we present a heat transfer correlation from Jakob [3.A.1] for air flow past a heated cylinder [3.A.1].

$$Nu = 0.028\ Re^{0.8}\ [1 + 0.4\ (L_h/L)^{2.75}] \qquad \text{[Eq. 1]}$$

where:

L = Length of cylinder

L_h = Length of heated section

Re = Reynolds number ($LV\rho/\mu$)
V = Air velocity
ρ = Air density
μ = Air viscosity
Nu = Nusselt number (hL/k)
k = Air conductivity

For illustrative purposes, let us consider a slight wind (10 MPH) and representative air properties (ρ = 0.075 lbm/ft^3, k = 0.015 Btu/ft-hr-°F and μ = 180 μP). The length (L) of the HI-STAR overpack cylinder is 203.125 inch (Section 1.4 HI-STAR Drawings). The length of overpack heating (L_h) is assumed to be equal to a representative height of active fuel zone (12 ft). Employing consistent units, Re is computed as:

$$Re = 16.92 \text{ ft} * 14.66 \text{ ft/s} * 0.075 \text{ lbm/ft}^3 / 1.2\text{x}10^{-5} \text{ lbm/ft-s}$$
$$= 1.5\text{x}10^6$$

The Nusselt number is computed by substituting numerical values for Re, L and L_h in Eq. 1. The numerical value is 2822. From the definition of Nu (=hL/k), h is computed as 2.5 Btu/ft^2-hr-°F. In other words, the principal mode of heat transfer – convection cooling of the HI-STAR cask – is approximately 150% greater than the values used in the thermal analysis.

3.A.3 CONSERVATISM IN REPRESENTING BASKET AXIAL RESISTANCE

Much of the elevation in fuel cladding temperatures in a HI-STAR cask occurs within the MPC[1]. Therefore, it stands to reason that conservatism in the basket thermal simulation would have a pronounced effect on the conservatism in the final solution. The thermal model of the fuel basket in the HI-STAR was accordingly constructed with a number of conservative assumptions to ensure robust margins. Most notable assumptions in this regard are:

a) Axial heat dissipation in the fuel pellets ignored
b) Convection heat transfer in the MPC space ignored

We illustrate these conservatisms by examining one of them (item a) in some detail in the following. It is recognized that the heat emission from a fuel assembly is axially non-uniform. The maximum heat generation occurs at about the mid-height region of the enriched uranium column, and tapers off toward its extremities. The axial heat conduction in the fuel basket would act to diffuse and levelize the temperature field in the basket. The axial conductivity of the basket, quite clearly, is the key determinant in how well the thermal field in the basket would be homogenized. In the interest of conservatism, axial heat dissipation in the fuel pellets is ignored. This assumption has the direct effect of throttling the axial flow of heat and thus of elevating the computed value of mid-height cladding temperature (where the peak temperature occurs) above its actual value. In actuality, the axial conductivity of the fuel basket is greater than used in the analysis. Had the axial conductivity of

1 See for example temperature results Table 3.4.10 for PWR MPCs wherein the cladding is elevated 386°F above the MPC shell temperature. This elevation is 64% of the cladding temperature rise above ambient (601°F).

the basket been modeled less conservatively in the thermal analysis, the temperature peaking would be depressed and the temperature field would be more uniform.

To estimate the conservatism in restricting the basket axial resistance, we perform a numerical exercise using mathematical perturbation techniques. The axial conductivity (K_z) of the MPC is, as explained previously, is higher than used in the analysis (K). The thermal solution to the higher axial conductivity problem (i.e. $K_z > K$) is mathematically expressed as a sum of a baseline solution T_o at K and a perturbation T^* which accounts for the higher axial conductivity. From Fourier's Law of heat conduction in solids, a perturbation equation for T* is articulated below:

$$K_z \frac{d^2T^*}{dz^2} = -\Delta K \frac{d^2T_o}{dz^2}$$

Where, ΔK is a perturbation parameter (axial conductivity offset $\Delta K = K_z - K$). The boundary conditions for the perturbation solution are zero slope at peak cladding temperature location ($dT^*/dz = 0$) (which occurs at about the active fuel mid- height) and $T^* = 0$ at the ends of the active fuel length. The object of this calculation is to compute T* where the peak fuel cladding temperature is reached. To this end, the baseline thermal solution T_o is employed to characterize d^2T_o/dz^2 for the hottest fuel cell. This is computed as $(-\Delta T_{ax}/L^2)$ where ΔT_{ax} is the cladding temperature rise from the ends of the active fuel length to mid-height and L is half the active fuel length (~6 ft). Conservatively postulating a lower bound ΔT_{ax} of 300°F d^2T_o/dz^2 is computed as $-8.33°F/ft^2$. Integrating the perturbation equation shown above, the following formula for T* is obtained:

$$T^* = \left(\frac{\Delta K}{K_z}\right) \frac{d^2T_o}{dz^2} \frac{L^2}{2}$$

Employing a conservative low value for the $(\Delta K/K_z)$ parameter of 0.05, T* is computed as – 7.5°F. In other words, the baseline HI-STORM solution over predicts the peak cladding temperature by over 7°F, because of the conservatism in the value of axial conductivity.

3.A.4 CONSERVATISM IN REPRESENTING FUEL BASKET CONFIGURATION

The HI-STAR System is designed for normal transport in a horizontal orientation. This orientation ensures physical contact between: (i) Fuel assemblies and the fuel basket, (ii) Fuel basket and MPC (iii) MPC and HI-STAR overpack. From a heat transfer perspective, this is an optimal orientation because (a) Gap resistances are minimized and (b) Heat dissipation is maximized through physical contact. In the MPC modeling, we assume a physical configuration that is opposite of (a) and (b) for the MPC space. This configuration assumes:

I. Each fuel assembly is levitating coaxially in it's storage cell
II. Fuel basket is levitating coaxially in the MPC shell

The assumptions described in I and II maximize gap resistance and completely ignore physical contact. In the thermal analysis of the HI-STAR system the fuel storage cell space is modeled with a uniform gap between the fuel assembly envelope and the cell walls (See Figure 3.4.7). The fuel basket-to-MPC space is modeled as a helium filled concentric annular gap (See Figure 3.4.2). Because gaps depress heat transfer, it follows that deliberately postulating gaps between physically contacting parts considerably elevates the MPC planar resistance and the computed fuel and basket temperatures. In the MPC-to-overpack space, the thermal modeling includes partial recognition of

gap reduction (See Sub-section 3.4.1.1.10 for eccentric gap evaluation) and completely ignores physical contact between the MPC and overpack.

3.A.5 OTHER CONSERVATISMS

Section 3.4.6 of the SAR lists an array of conservatisms, of which certain unobvious and individually significant items are discussed in detail in this appendix. These conservatisms are primarily intrinsic to the solution methodology or are product of assumptions in the input data. Examples in the latter category are values assumed in the thermal analysis for key inputs such as insolation heat and ambient temperature. Apart from the input data and methodology related conservatisms, the modeling includes assumptions to under represent heat transfer. A listing of such conservatisms is summarized below:

i) Insolation heating assumed with a bounding absorbtivity of 1.0
ii) Heat dissipation from the HI-STAR overpack ends ignored
iii) Conduction heat transfer in Holtite is neglected.
iv) MPCs are assumed to be loaded with the most thermally resistive fuel type in its category (BWR or PWR) as applicable

The assumptions inherent in the FLUENT methodology, in the thermal modeling and in the input data, are estimated to have an aggregate effect of overestimating cladding temperatures by a considerable amount, as estimated in Table 3.A.1.

3.A.6 CONCLUSIONS

The foregoing narrative provides a physical description of the many elements of conservatism in the HI-STORM 100 thermal model. The conservatisms may be broadly divided into two categories:

1. Those intrinsic to the FLUENT methodology.

2. Those arising from the input data and thermal modeling.

The conservatism in Category (1) may be identified by reviewing the Holtec International Benchmark Report [3.A.2], which shows that the FLUENT solution methodology, when applied to the prototype cask (TN 24P) over-predicts the peak cladding temperature by as much as 79 °F. and as much as 37°F relative to the PNNL results (see Attachment 1 to Reference [3.A.2]) from their COBRA SFS solution as compared against Holtec's FLUENT solution.

Category (2) conservatisms are those that we have deliberately embedded in the HI-STAR thermal models to ensure that the computed value of the peak fuel cladding temperature is further exaggerated. Table 3.A.1 contains a listing of the major conservatisms in the HI-STAR thermal model, along with an estimate of the effect (increase) of each on the computed peak cladding temperature. Finally, we note that the computed peak cladding temperatures for all MPCs are also lower than the 400°C limit by varying amounts, which can be viewed as an additional thermal margin in the system.

The cumulative effect of conservatisms listed in Table 3.A.1 would be additive if the thermal resistances were all arrayed in series. In reality some resistances are in series and others in parallel. For obtaining a reasonable estimate of the cumulative effect, a square root of sum of squares of the individual conservatisms is computed and reported in the last row of the Table 3.A.1.

Table 3.A.1

Estimated Conservatisms in the Computed Peak Cladding Temperature
for the HI-STAR 100 System

MODELING ASSUMPTION	CONSERVATISM [°F]
1. Wind effects neglected	45
2. Axial heat dissipation understated	7
3. MPC convection heat transfer neglected	40
4. Holtite conduction neglected	10
5. Miscellaneous	20
Cumulative Effect[2] of 1 thru 5:	64.6

3.A.6 REFERENCES

[3.A.1] Jakob, M., "Heat Transfer", John Wiley & Sons, Inc., (1967).

[3.A.2] "Topical Report on the HI-STAR/HI-STORM Thermal Model and its Benchmarking with Full-Size Cask Test Data", Holtec Report HI-992252, Rev. 1.

2 See cumulative effect discussion in the last paragraph of 3.A.6.

APPENDIX 3.B: THE FORCED HELIUM DEHYDRATION (FHD) SYSTEM

3.B.1 System Overview

The Forced Helium Dehydration (FHD) system is used to remove the remaining moisture in the MPC cavity after all of the water that can practically be removed through the drain line using a hydraulic pump or an inert gas has been expelled in the water blowdown operation. Expelling the water from the MPC using a conventional pump or a water displacement method using inert gas would remove practically all of the contained water except for the small quantity remaining on the MPC baseplate below the bottom of the drain line and an even smaller adherent amount wetting the internal surfaces. A skid-mounted, closed loop dehydration system will be used to remove the residual water from the MPC such that the partial pressure of the trace quantity of water vapor in the MPC cavity gas is brought down to $\leq$ 3 torr. The FHD system, engineered for this purpose, shall utilize helium gas as the working substance.

The FHD system, schematically illustrated in Figure 3.B.1, can be viewed as an assemblage of four thermal modules, namely, (i) the condensing module, (ii) the demoisturizer module, (iii) the helium circulator module and (iv) the pre-heater module. The condensing module serves to cool the helium/vapor mixture exiting the MPC to a temperature well below its dew point such that water may be extracted from the helium stream. The condensing module is equipped with suitable instrumentation to provide a direct assessment of the extent of condensation that takes place in the module during the operation of the FHD system. The demoisturizer module, engineered to receive partially cooled helium exiting the condensing module, progressively chills the recirculating helium gas to a temperature that is well below the temperature corresponding to the partial pressure of water vapor at 3 torr.

The motive energy to circulate helium is provided by the helium circulator module, which is sized to provide the pressure rise necessary to circulate helium at the requisite rate. The last item, labeled the pre-heater module, serves to pre-heat the flowing helium to the desired temperature such that it is sufficiently warm to boil off any water present in the MPC cavity.

The pre-heater module, in essence, serves to add supplemental heat energy to the helium gas (in addition to the heat generated by the stored SNF in the MPC) so as to facilitate rapid conversion of water into vapor form. The heat input from the pre-heater module can be adjusted in the manner of a conventional electric heater so that the recirculating helium entering the MPC is sufficiently dry and hot to evaporate water, but not unduly hot to place unnecessary thermal burden on the condensing module.

The FHD system described in the foregoing performs its intended function by continuously removing water entrained in the MPC through successive cooling, moisture removal and reheating of the working substance in a closed loop. In a classical system of the FHD genre, the moisture removal operation occurs in two discrete phases. In the beginning of the FHD system's operation (Phase 1), the helium exiting the MPC is laden with water vapor produced by boiling of the entrained bulk water. The condensing module serves as the principal device to condense out the water vapor from the helium stream in Phase 1. Phase 1 ends when all of the bulk water in the MPC cavity is

vaporized. At this point, the operation of the FHD system moves on to steadily lowering the relative humidity and bulk temperature of the circulating helium gas (Phase 2). The demoisturizer module, equipped with the facility to chill flowing helium, plays the principal role in the dehydration process in Phase 2.

3.B.2 Design Criteria

The design criteria set forth below are intended to ensure that design and operation of the FHD system will drive the partial pressure of the residual vapor in the MPC cavity to ≤ 3 torr if the temperature of helium exiting the demoisturizer has met the value and duration criteria provided in the HI-STORM technical specifications. The FHD system shall be designed to ensure that during normal operation (i.e., excluding startup and shutdown ramps) the following criteria are met:

i. The temperature of helium gas in the MPC shall be at least 15°F higher than the saturation temperature at coincident pressure.

ii. The pressure in the MPC cavity space shall be less than or equal to 60.3 psig (75 psia).

iii. The recirculation rate of helium shall be sufficiently high (minimum hourly throughput equal to ten times the nominal helium mass backfilled into the MPC for fuel storage operations) so as to produce a turbulated flow regime in the MPC cavity.

iv. The partial pressure of the water vapor in the MPC cavity will not exceed 3 torr if the helium temperature at the demoisturer outlet is ≤ 21°F for a period of 30 minutes.

In addition to the above system design criteria, the individual modules shall be designed in accordance with the following criteria:

i. The condensing module shall be designed to de-vaporize the recirculating helium gas to a dew point of 120°F or less.

ii. The demoisturizer module shall be configured to be introduced into its helium conditioning function after the condensing module has been operated for the required length of time to assure that the bulk moisture vaporization in the MPC (defined as Phase 1 in Section 2.B.1) has been completed.

iii. The helium circulator shall be sized to effect the minimum flow rate of circulation required by the system design criteria described above.

iv. The pre-heater module shall be engineered to ensure that the temperature of the helium gas in the MPC meets the system design criteria described above.

3.B.3 Analysis Requirements

The design of the FHD system shall be subject to the confirmatory analyses listed below to ensure that the system will accomplish the performance objectives set forth in this FSAR.

i. System thermal analysis in Phase 1: Characterize the rate of condensation in the condensing module and helium temperature variation under Phase 1 operation (i.e., the scenario where there is some unevaporated water in the MPC) using a classical thermal-hydraulic model wherein the incoming helium is assumed to fully mix with the moist helium inside the MPC.

ii. System thermal analysis in Phase 2: Characterize the thermal performance of the closed loop system in Phase 2 (no unvaporized moisture in the MPC) to predict the rate of condensation and temperature of the helium gas exiting the condensing and the demoisturizer modules. Establish that the system design is capable to ensure that partial pressure of water vapor in the MPC will reach $\leq$ 3 torr if the temperature of the helium gas exiting the demoisturizer is predicted to be at a maximum of 21°F for 30 minutes.

iii. Fuel Cladding Temperature Analysis: A steady-state thermal analysis of the MPC under the forced helium flow scenario shall be performed using the methodology described in SAR Subsections 3.4.1.1.1 through 3.4.1.1.4 with due recognition of the forced convection process during FHD system operation. This analysis shall demonstrate that the peak temperature of the fuel cladding under the most adverse condition of FHD system operation (design maximum heat load, no moisture, and maximum helium inlet temperature), is below the peak cladding temperature limit for normal conditions of storage for the applicable fuel type (PWR or BWR) and cooling time at the start of dry storage.

3.B.4 Acceptance Testing

The first FHD system designed and built for the MPC drying function required by HI-STORM's technical specifications shall be subject to confirmatory testing as follows:

a. A representative quantity of water shall be placed in a manufactured MPC (or equivalent mock-up) and the closure lid and RVOAs installed and secured to create a hermetically sealed container.

b. The MPC cavity drying test shall be conducted for the worst case scenario (no heat generation within the MPC available to vaporize water).

c. The drain and vent line RVOAs on the MPC lid shall be connected to the terminals located in the pre-heater and condensing modules of the FHD system, respectively.

d. The FHD system shall be operated through the moisture vaporization (Phase 1) and subsequent dehydration (Phase 2). The FHD system operation will be stopped after the temperature of helium exiting the demoisturizer module has been at or below 21°F for thirty minutes (nominal). Thereafter, a sample of the helium gas from the MPC will be extracted and tested to determine the partial pressure of the residual water vapor in it. The FHD system will be deemed to have passed the acceptance testing if the partial pressure in the extracted helium sample is less than or equal to 3 torr.

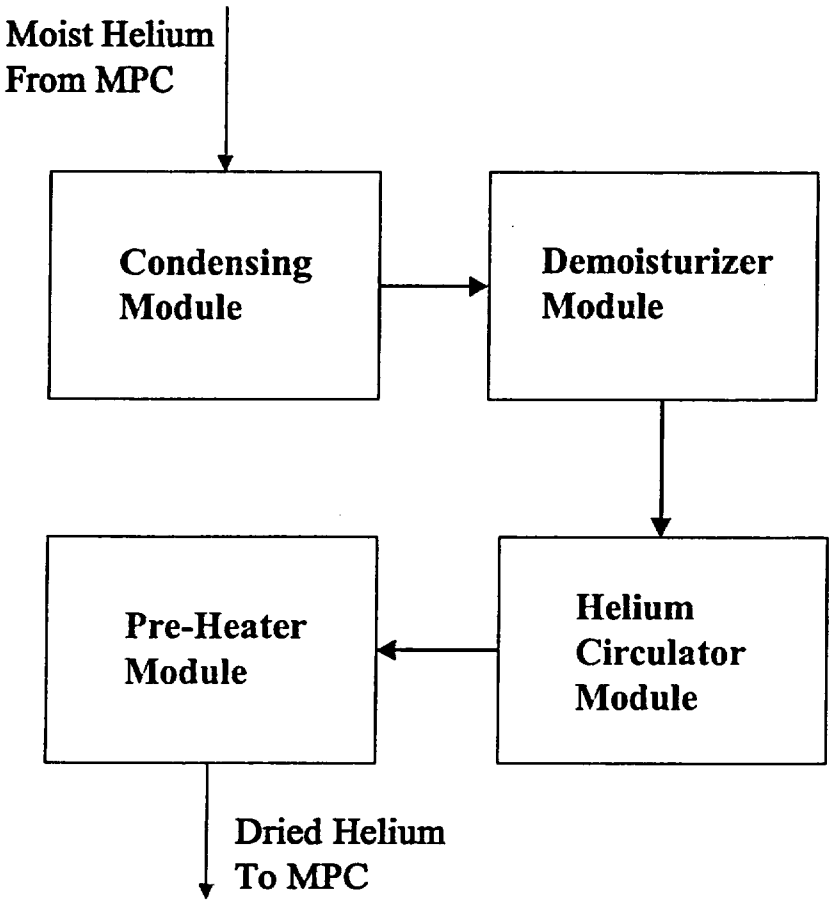

FIGURE 3.B.1: SCHEMATIC OF THE FORCED HELIUM DEHYDRATION SYSTEM

CHAPTER 4: CONTAINMENT

4.0 INTRODUCTION

This chapter demonstrates the HI-STAR 100 containment boundary compliance with the permitted activity release limits specified in 10CFR71, 71.51(a)(1) and 71.51(a)(2) for both normal and hypothetical accident conditions of transport [4.0.1]. Satisfaction of the containment criteria, expressed as the leakage rate acceptance criterion (atm-cm^3/sec, Helium), ensures that the HI-STAR 100 package will not exceed the specified allowable radionuclide release rates. Leakage rates are determined in accordance with the recommendations of ANSI N14.5 [4.0.2], and utilizing NUREG/CR-6487, *Containment Analysis for Type B Packages Used to Transport Various Contents* [4.0.3], Regulatory Guide 7.4, *Leakage Tests on Packages for Shipment of Radioactive Materials* [4.0.4] as content guides, and Draft NUREG-1617, *Standard Review Plan for Transportation Packages for Spent Nuclear Fuel* [4.0.5].

The HI-STAR 100 packaging allowable leakage rates established herein ensures that the requirements of 10CFR71.51 and 10CFR71.63(b) are met. The primary containment system boundary for the HI-STAR 100 packaging consists of the overpack inner shell, the bottom plate, the top flange, the top closure plate, closure bolts, the overpack vent and drain port plugs, and their respective mechanical seals. The secondary containment system boundary for a HI-STAR 100 packaging containing BWR fuel debris in the MPC-68F or Trojan PWR fuel debris in the MPC-24EF consists of the MPC enclosure vessel including the MPC shell, the MPC bottom plate, the MPC lid, closure ring, and vent and drain port cover plates. The MPC-24EF and MPC-68F each provide the separate inner container per 10CFR71.63(b) for the HI-STAR 100 System transporting fuel classified as fuel debris. The other MPC designs (MPC-24, MPC-24E, MPC-32 and MPC-68) are not currently evaluated for secondary containment requirements.

Chapter 2 of this SAR shows that all primary and secondary containment boundary components are maintained within their code-allowable stress limits during all normal and hypothetical accident conditions of transport as defined in 10CFR71.71 and 10CFR71.73. Chapter 3 of this SAR shows that the peak containment component temperatures and pressures are within the design basis limits for all normal and hypothetical accident conditions of transport as defined in 10CFR71.71 and 10CFR71.73. Since both the primary and secondary containment boundaries are shown to remain intact, and the temperature and pressure design bases are not exceeded, the design basis leakage rates are not exceeded during normal or hypothetical accident conditions of transport.

The HI-STAR overpack is subjected to a containment system fabrication verification test before the first use as described in Chapter 8. The containment system fabrication verification test is performed at the factory as part of the HI-STAR 100 acceptance testing. The welds of the primary containment boundary, the closure plate inner seal, and the vent and drain port plug seals are helium leakage tested in accordance with ANSI N14.5. A containment system periodic verification test as described in Chapter 8, will be performed prior to each loaded transport. The mechanical seals of the HI-STAR 100 overpack will be replaced and retested each time the HI-STAR 100 is loaded. The

secondary containment boundary system (MPC-24EF or MPC-68F) will be subjected to the fabrication verification leakage testing at the fabrication facility as described in Chapter 8 of this SAR. Prior to transport of an MPC containing fuel debris, a secondary containment boundary periodic verification leakage test will be performed as described in Chapter 8 to ensure that the measured leakage rates are below the limit specified in this chapter.

As the containment system periodic verification leakage test shall be performed on each containment boundary separately prior to each loaded transport, this test takes the place of and is performed in lieu of the assembly verification.

4.1 CONTAINMENT BOUNDARIES

The primary containment system boundary for the HI-STAR 100 packaging consists of the overpack inner shell, the bottom plate, the top flange, the top closure plate, closure bolts, the overpack vent and drain port plugs, and their respective mechanical seals. The primary containment boundary system components for the HI-STAR 100 system are designed and fabricated in accordance with the requirements of ASME Code, Section III, Subsection NB [4.1.1], to the maximum extent practicable. Chapter 1 provides design criteria for the containment design. Section 1.3 provides applicable Code requirements. Exceptions to specific Code requirements with complete justifications are presented in Table 1.3.2. The primary containment boundary components are shown on Figure 4.1.1 with additional details provided in Figures 4.1.2 and 4.1.3.

The secondary containment system boundary for a HI-STAR 100 packaging containing fuel debris in the MPC-24EF or the MPC-68F consists of the enclosure vessel including the MPC shell, the MPC bottom plate, the MPC lid, vent and drain port cover plates and MPC closure ring. The secondary containment boundary system components for the HI-STAR 100 system are designed and fabricated in accordance with the requirements of ASME Code, Section III, Subsection NB, to the maximum extent practicable. Chapter 2 provides design criteria for the containment design. Section 1.3 provides applicable Code requirements. Alternatives to specific Code requirements with complete justifications are presented in Table 1.3.2. The secondary containment boundary components are shown in Figure 4.1.4. The use of two independent and testable containment boundaries provides the capability to load and transport the specified fuel debris in accordance with the requirements of 10CFR71.63(b) [4.0.1]. The MPC-24EF or MPC-68F each provide the separate inner container per 10CFR71.63(b) for the HI-STAR 100 System transporting fuel classified as fuel debris. The other MPC designs (MPC-24, MPC-24E, MPC-32 and MPC-68) are not currently evaluated for secondary containment requirements.

4.1.1 Containment Vessel

The primary containment vessel for the HI-STAR 100 packaging consists of the overpack components which form the inner cavity volume used to house any of the MPC designs which contain spent nuclear fuel. The primary containment vessel is represented by the overpack inner shell, bottom plate, the top flange, and the closure plate. These components create an enclosed cylindrical cavity sufficient for insertion and enclosure of an MPC. The materials of construction for the packaging primary containment vessel are specified in the drawings in Section 1.4.

The secondary containment vessel for the HI-STAR 100 packaging consists of either the MPC-24EF or the MPC-68F enclosure vessel complete with field-installed MPC lid, closure ring, vent and drain port cover plates. The enclosure vessel components create an enclosed cylindrical cavity sufficient for insertion and enclosure of fuel debris. The materials of construction for the secondary containment vessel are specified in the drawings in Section 1.4.

Table 4.1.1 provides a summary of the containment boundary design specifications.

4.1.2 Containment Penetrations

The primary containment system boundary penetrations for the HI-STAR 100 package include the closure plate test port plug, the vent port plug, the drain port plug, and their respective mechanical seals. Each penetration has redundant mechanical seals. The vent port is located in the closure plate and the drain port is located in the bottom plate. The closure configuration of the vent and drain ports is essentially identical (See Figure 4.1.3). The primary containment penetrations are designed and tested to ensure that the radionuclide release rates specified in 10CFR71.51 will not be exceeded.

The secondary containment boundary for the HI-STAR 100 packaging is the either the MPC-24EF or the MPC-68F. The penetrations on the MPC include the MPC vent and drain port cover plates. The MPC penetrations are designed to prevent the release of radionuclides. Two penetrations (the MPC vent and drain ports) are provided in the MPC lid for MPC draining, vacuum drying and backfilling during MPC loading operations, and for fuel cool-down and MPC flooding during unloading operations. No other confinement penetrations exist in the MPC. The MPC vent and drain ports are equipped with metal-to-metal seals to minimize leakage and withstand the long-term effects of temperature and radiation. No containment credit is taken for the vent and drain mechanical seals. The vent and drain connectors allow the vent and drain ports to be operated like valves and prevent the need to hot tap into the penetrations during unloading operations. The vent and drain port covers are sealed with the fully welded vent and drain port cover plates. The MPC closure ring covers the vent and drain port cover plate welds, and the MPC lid-to-shell weld providing redundant closure of the MPC vessel. Both the MPC-24EF and MPC-68F are designed and tested to ensure that the radionuclide release rates specified in 10CFR71.63(b) will not be exceeded.

4.1.3 Seals and Welds

The HI-STAR 100 primary containment vessel uses a combination of seals and welds designed and tested during normal transport conditions, and during and after the hypothetical transport accident conditions. The secondary containment boundary utilizes a fully welded vessel to prevent the release of radioactive materials. Seals and welds are individually discussed below.

The seals and welds discussed below provide containment systems which are securely closed, cannot be opened unintentionally or by an internal pressure within the package as required in 10CFR71.43(c).

4.1.3.1 Containment Seals

The HI-STAR 100 closure plate uses two concentric metallic seals to form the closure between the top flange surface and the closure plate. To protect the sealing surfaces against corrosion, a stainless steel weld inlay is provided during manufacturing on both the closure plate and mating overpack surfaces. The closure plate inner seal is tested for leakage through a small test port in the overpack closure plate (See Figure 4.1.2). The test port provides access to the volume between the two mechanical lid seals for leakage testing of the closure plate inner seal. Following leakage testing, a threaded plug with a metallic seal is installed in the test port hole to provide redundant closure.

Primary closure of the vent and drain ports is achieved via a threaded plug with a single metallic seal. The metallic seal is compressed between the underside of the threaded plug head and the overpack body to form the seal. The sealing surfaces are not subject to corrosion due to the presence of the cover plates and their seals preventing exposure of the seal surfaces to the elements. Each port plug seal is independently tested for leakage to verify containment performance. A bolted cover plate, with a machined seal groove, is installed over the vent and drain ports. A metallic seal, installed in the cover plate groove, is compressed between the cover plate and the overpack body during cover plate bolt torquing. These cover plates provide redundant closure of the drain and vent port penetrations.

Details on the seals are provided in the drawings in Section 1.4 and in Appendix 4.B. Table 4.1.1 contains reference information for the seals from the selected supplier. Note that the seals selected are designed and fabricated to meet the design requirements of the HI-STAR 100 System. The Chapter 7 procedures require replacement of any used seal after closure opening except for transportation of an empty overpack.

There are no seals on the secondary containment boundary.

4.1.3.2 Containment Welds

The primary containment boundary welds of the HI-STAR 100 overpack body include the welds forming the inner closure shell, the weld connecting the inner shell to the top flange, and the weld connecting the bottom plate to the inner shell. All primary containment boundary welds are fabricated and inspected in accordance with ASME Code Section III, Subsection NB (no stamp required). Full-penetration welds are specified for the plates that form the overpack inner shell. Full-penetration welds are also specified for the inner shell to the top flange and bottom plate welds. The weld details are shown in the drawings in Section 1.4. The containment boundary welds are volumetrically examined by radiography (RT) as described in Chapter 8.

The secondary containment boundary welds of the MPC-24EF and MPC-68F include the welds forming the MPC shell, the weld connecting the shell to the MPC baseplate, and the final field closure welds described in Section 4.1.4.2. All secondary containment welds are fabricated and inspected in accordance with ASME Code Section III, Subsection NB, except for the field installed closure welds. The alternatives to the ASME Code for the secondary containment are detailed in Table 1.3.2. The weld details are shown on the MPC-24EF and MPC-68F drawings in Section 1.4. The secondary containment boundary welds are volumetrically examined by radiography (RT) or ultrasonic (UT) inspection methods as described in Chapter 8.

4.1.4 Closure

4.1.4.1 Primary Closure

The HI-STAR 100 packaging closure plate is secured using multiple closure bolts around the perimeter. Torquing of the closure plate bolts compresses the closure plate concentric mechanical seals between the closure plate and the overpack flange forming the closure plate seal.

Closure of the overpack vent and drain ports is provided by a single threaded plug installed in each penetration (see Figure 4.1.3). The mechanical seal is compressed between the underside of the port plug head and the overpack body forming the primary port closure. A cover plate, containing a single metallic seal, is installed over each of the ports forming the redundant closure of the vent and drain port penetrations. The cover plate is secured by bolts. The closure plate test port is sealed using a port plug and mechanical seal in the same manner as the vent and drain port penetrations (see Figure 4.1.2).

The installation procedures, bolt torquing patterns, required lubrication, and torque values are provided in Table 7.1.3. The torque values are established to maintain containment during normal and accident conditions of transport. Torque values for the closure plate bolts were determined to preclude separation of the closure plate from the overpack flange. Appendix 4.A contains the calculations for the test, vent and drain port plugs and the vent and drain port cover plates bolt torques.

Table 4.1.2 provides a summary of the containment closure bolting for the HI-STAR 100 overpack penetrations.

4.1.4.2 Secondary Closure

The secondary closure of the HI-STAR 100 packaging is provided by the MPC lid which is welded to the MPC shell. Following fuel loading and MPC lid welding, the MPC lid to shell weld may be examined by either volumetric or multi-layer liquid penetrant examination. If volumetric examination is used, it shall be the ultrasonic method and shall include a PT of the root and final weld layers. If PT alone is used, at a minimum, it must include the root and final weld layers and sufficient intermediate layers to detect critical weld flaws. The lid to shell weld is also volumetrically examined, helium leakage tested, and hydrostatic tested. If the MPC lid weld is acceptable, the vent and drain port cover plates are welded in place, examined by the liquid penetrant method (root and final), and a leakage rate test is performed. Finally, the MPC closure ring is installed, welded and inspected by the liquid penetrant method (root and final).

4.1.5 Damaged Fuel Container

Fuel assemblies classified as damaged fuel or fuel debris (assembly array/class 6x6A, 6x6B, 6x6C, 7x7A, and 8x8A for BWR fuel as specified in Table 1.2.11 and Trojan damaged fuel and fuel debris for PWR fuel as specified in Table 1.2.10) have been evaluated.

The MPC is designed to transport damaged fuel, fuel debris, or intact fuel. The sole additional requirement imposed on an MPC to load fuel debris is an additional leakage rate criteria test just prior to shipment. Therefore, an MPC which is to transport fuel debris will be designated to ensure the proper leakage rate test criteria is applied. To distinguish an MPC which is fabricated to transport fuel debris, the MPC will be designated with an "F" after the MPC designation (i.e. MPC-68F or MPC-24EF)

To aid in loading and unloading, damaged fuel assemblies and fuel debris will be loaded into stainless steel DFCs prior to placement in the HI-STAR 100 System. The damaged fuel container (DFC) is shown in the drawings in Section 1.4. The DFC is designed to provide SNF loose component retention and handling capabilities. The DFC consists of a smooth-walled, welded stainless steel square canister with a removable lid. The canister lid provides the means of DFC closure and handling. The DFC is provided with stainless steel wire mesh screens in the top and bottom for draining, vacuum drying and helium backfill operations. The screens are specified as a 250-by-250-mesh with an effective opening of 0.0024 inches. There are no other openings in the DFC. Chapter 1 specifies the fuel assembly characteristics for damaged fuel acceptable for loading in the MPC-68, MPC-68F, or MPC-24EF and for fuel debris acceptable for loading in the MPC-68F or MPC-24EF.

Up to four (4) DFCs containing specified fuel debris may be placed in a custom-designed Trojan MPC-24EF (Trojan PWR fuel debris) or an MPC-68F (BWR fuel debris). Up to 4 PWR damaged fuel assemblies in DFCs may be transported in a custom-designed Trojan MPC-24EF or up to 68 BWR damaged fuel assemblies in DFCs may be transported in an MPC-68 or MPC-68F, respectively. The quantity of fuel debris is limited to meet the off-site transportation requirements of 10CFR71, specifically, 10CFR71.63(b). Analyses provided in this chapter conservatively assume 100% of the rods of the fuel debris are breached under normal conditions of transport. Therefore, 100% of the contents of the DFCs are available for release.

Table 4.1.1

SUMMARY OF CONTAINMENT BOUNDARY DESIGN SPECIFICATIONS

Design Attribute	Design Rating	
	Primary (Overpack) 10CFR71.51	Secondary (MPC) 10CFR71.63(b)
Closure Plate Mechanical Seals:††		
Design Temperature	1200°F	N/A
Pressure Rating	1,000 psig	
Design Leakage Rate	$1x10^{-6}$ cm^3/s, Helium	
Overpack Vent and Drain Port Cover Plate Mechanical Seals: †,††		N/A
Design Temperature	1200°F	
Pressure Rating	1,000 psig	
Design Leakage Rate	$1x10^{-6}$ cm^3/sec, Helium	
Overpack Vent and Drain Port Plug Mechanical Seals: ††		N/A
Design Temperature	1200°F	
Pressure Rating	1,000 psig	
Design Leakage Rate	$1x10^{-6}$ cm^3/sec, Helium	
Leakage Rate Acceptance Criterion	4.3×10^{-6} atm cm^3/s, He	5.0×10^{-6} atm cm^3/s, He
Leakage Rate Test Sensitivity	2.15×10^{-6} atm cm^3/s, He	2.5×10^{-6} atm cm^3/s, He

† No credit is taken for the overpack vent and drain port cover plate seals as part of the containment boundary. Specifications are provided for information.

†† Per manufacturer's recommended operating limits.

Table 4.1.2

CONTAINMENT CLOSURE BOLTING SUMMARY

Item	Qty	Type	Material
Closure Plate Bolt (Long)	52	1-5/8"-8 UNC x 7-3/8" LG Cap Screw	SB-637-N07718
Closure Plate Bolt (Short)	2	1-5/8"-8 UNC x 7-1/8" LG Cap Screw	SB-637-N07718
Vent/Drain Port Cover Plate Bolt	4 ea	3/8 -16 UNC x 5/8" LG Cap Screw	SA-193 GRADE B7
Vent/Drain/Closure Plate Test Port Plugs	1 ea	7/8" diameter Fabricated Plug	SA-193 GRADE B8

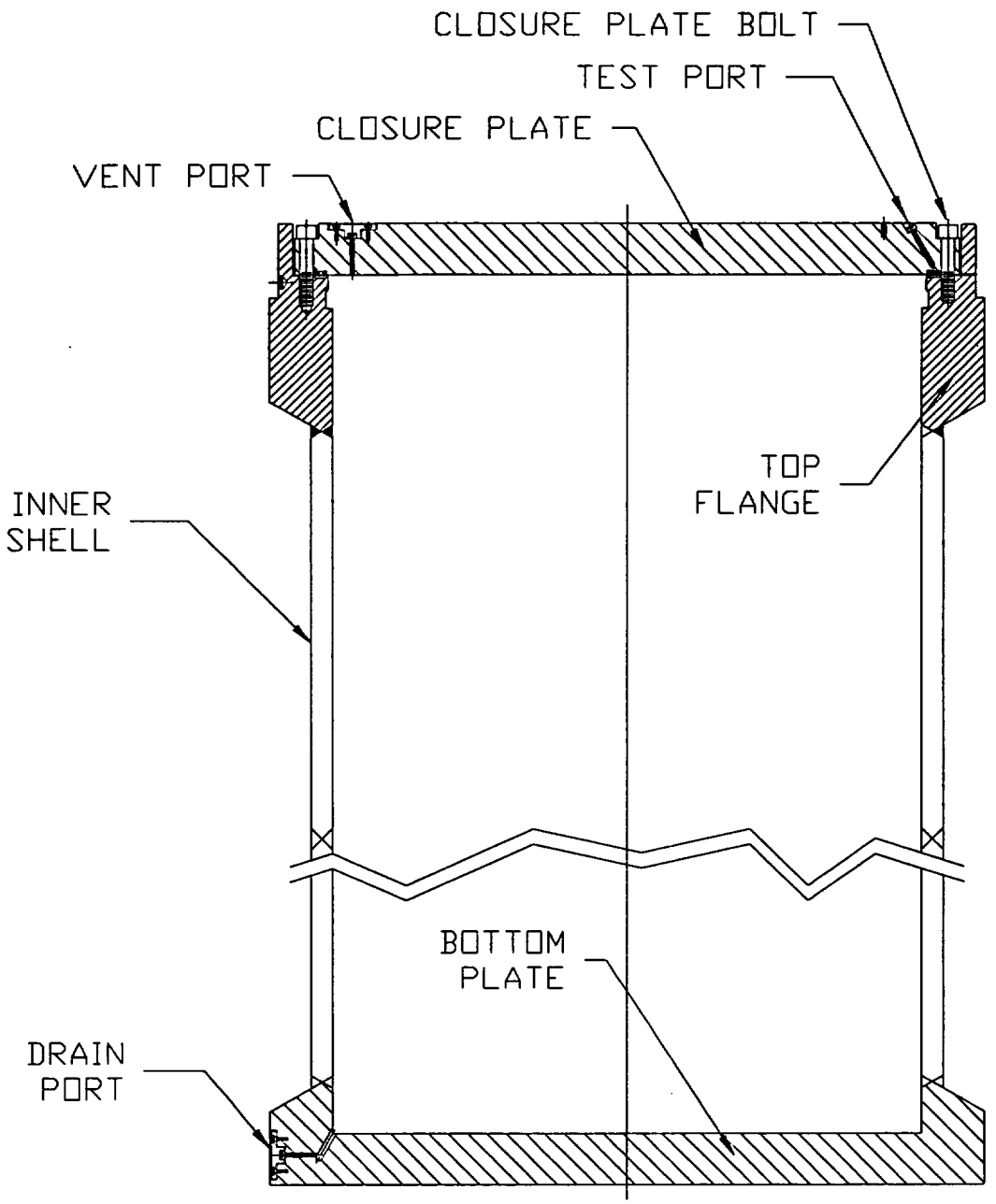

FIGURE 4.1.1; HI-STAR 100 OVERPACK PRIMARY CONTAINMENT BOUNDARY COMPONENTS

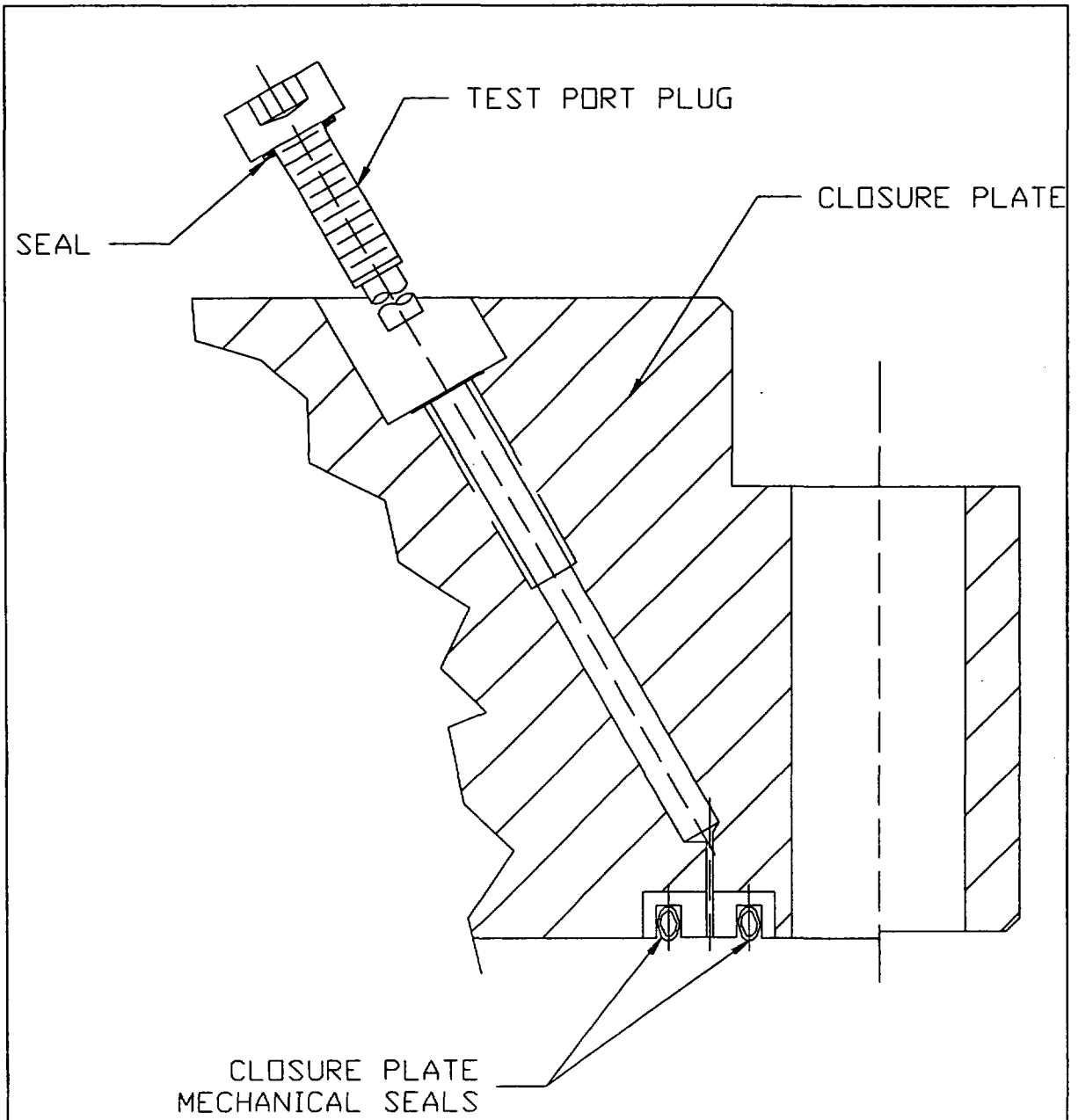

FIGURE 4.1.2; HI-STAR 100 CLOSURE PLATE CONTAINMENT DETAILS

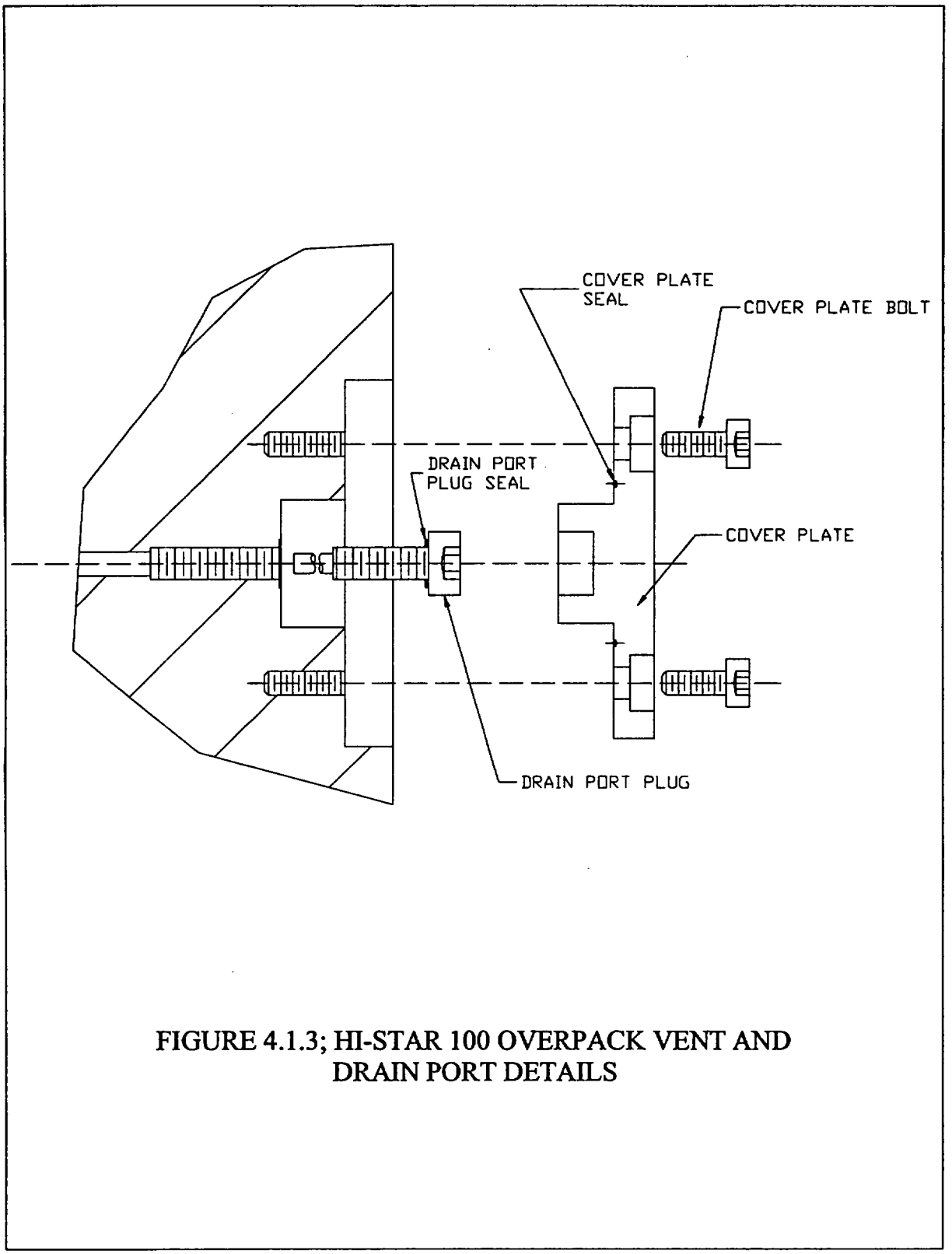

FIGURE 4.1.3; HI-STAR 100 OVERPACK VENT AND DRAIN PORT DETAILS

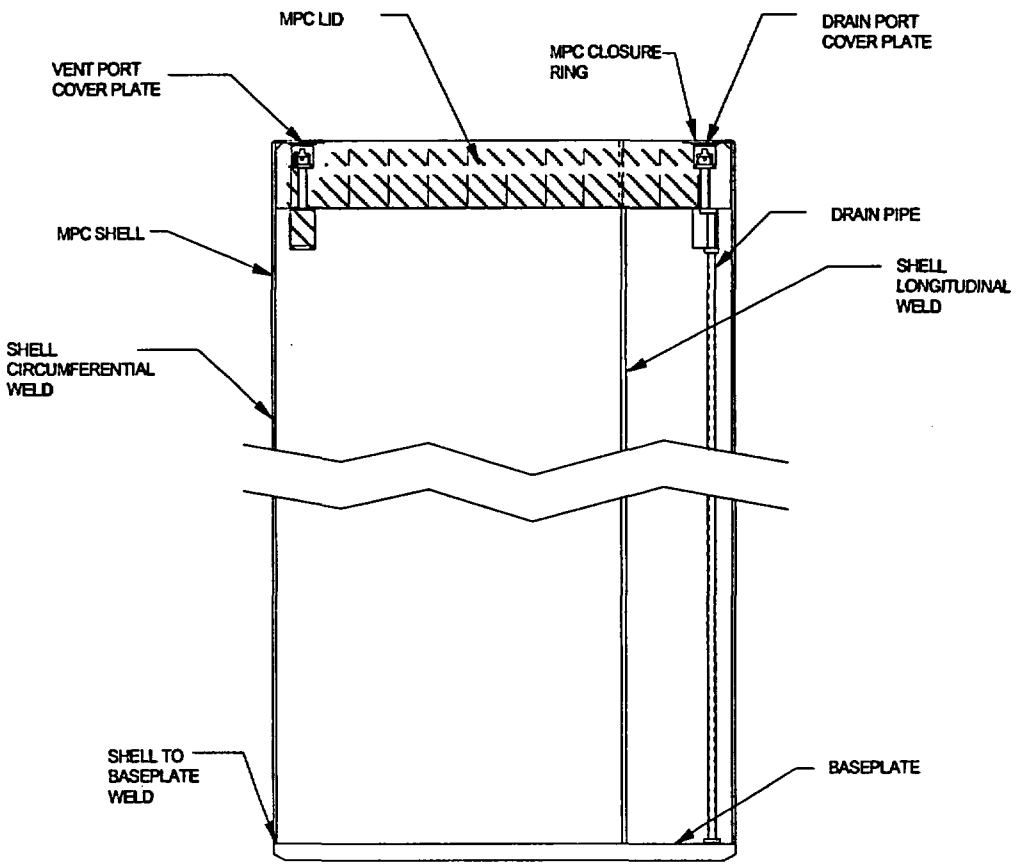

FIGURE 4.1.4; MPC SECONDARY CONTAINMENT BOUNDARY

4.2 REQUIREMENTS FOR NORMAL AND HYPOTHETICAL ACCIDENT CONDITIONS OF TRANSPORT

Chapter 2 shows that all primary and secondary containment components are maintained within their code-allowable stress limits during all normal and hypothetical accident conditions of transport as defined in 10CFR71.71 and 10CFR71.73 [4.0.1]. Chapter 3 shows that the peak containment component temperatures and pressure are within the design basis limits for all normal and hypothetical accident conditions of transport as defined in 10CFR71.71 and 10CFR71.73. Since the primary and secondary containment vessels remain intact, and the temperature and pressure design bases are not exceeded, the design basis leakage rate (see Table 4.1.1) will not be exceeded during normal or hypothetical accident conditions of transport.

4.2.1 Containment Criteria

The allowable leakage rates presented in this chapter were determined in accordance with ANSI N14.5-1997 [4.0.2] and shall be used for containment system fabrication verification and containment system periodic verification tests of the HI-STAR 100 containment boundaries. Measured leakage rates shall not exceed the values presented in Table 4.1.1. Compliance with these leakage rates ensures that the radionuclide release rates specified in 10CFR71.51 and 10CFR71.63(b) will not be exceeded during normal or hypothetical accident conditions of transport.

4.2.2 Containment of Radioactive Material

The HI-STAR 100 packaging allowable leakage rate (See Table 4.1.1) ensures that the requirements of 10CFR71.51 and 10CFR71.63(b) are met. Section 4.2.5 determines the maximum leakage rate for normal and hypothetical accident conditions of transport and the allowable leakage rate criterion for the HI-STAR 100 packaging containing each of the MPC types. The maximum calculated leakage rates for normal transport conditions assume a full complement of design basis fuel assembly types with bounding radiological source terms. The calculations also assume 3% fuel rod rupture for normal conditions. This bounds all possible MPC fuel loading configurations. For calculating the maximum leakage rates for normal conditions of transport, the internal pressure is conservatively assumed to be greater than the MPC internal pressure for the most limiting MPC type determined in Chapter 3. Following testing, no credit is taken for the MPC as a containment boundary for the transport of intact fuel. The MPC enclosure vessel is identified as the secondary containment boundary for the transport of the specified fuel debris in accordance with the 10CFR71.63(b) requirements for a separate inner container.

The allowable leakage rate is then conservatively chosen to be less than the calculated maximum leakage rates from all MPC types for normal conditions of transport. This ensures that the 10CFR71.51(a)(1) and 71.63(b) limits for radionuclide release are not exceeded.

4.2.3 Pressurization of Containment Vessel

The HI-STAR 100 overpack contains a sealed MPC during normal conditions of transport. Except for the small space between the MPC and overpack, the overpack internal cavity is essentially filled. This space (annulus) is drained, dried, evacuated and backfilled with helium gas prior to final closure of the overpack; therefore, no vapors or gases are present which could cause a reaction or explosion inside the overpack. Procedural steps (Chapter 7) prevent overpack over-pressurization during closure operations. The enclosed MPC is also drained, dried, and backfilled with helium gas prior to final closure; therefore, any MPC leak would not introduce any explosive gases into the overpack cavity. Since the exterior of the MPC is entirely composed of stainless steel, there is no possibility of chemical reaction that would produce gas or vapor. The overpack accident condition design basis internal pressure analysis assumes a non-mechanistic event resulting in the loss of MPC closure welds, a full-complement of design basis fuel with 100% fill gas and 30% of significant fission gas release, and the hypothetical 10CFR71.73(c)(4) fire condition. Even in this event, structural integrity and containment of the HI-STAR 100 packaging are maintained.

As the MPC is drained, dried, evacuated and backfilled with helium gas, no vapors or gases are present which could cause a reaction or explosion inside the MPC. Procedural steps (Chapter 7) prevent MPC over-pressurization during closure operations. The interior of the MPC contains stainless steel, Boral, and optional aluminum heat conductive inserts. There is no possibility of chemical reaction that would produce gas or vapor.

4.2.4 Assumptions

The HI-STAR 100 System is designed to meet the radioactive release limit requirements of 10CFR71.51 and 10CFR71.63(b). Allowable leakage rates are determined in accordance with the requirements of ANSI N14.5, and utilizing NUREG/CR-6487, *Containment Analysis for Type B Packages Used to Transport Various Contents* [4.0.3] and Regulatory Guide 7.4, *Leakage Tests on Packages for Shipment of Radioactive Materials* [4.0.4] as guides.

The following assumptions have been used in determining the allowable leakage rates:

1. For MPCs other than the MPC-24EF with Trojan fuel debris and MPC-68F, three percent of the fuel rods are assumed to have failed during normal conditions of transportation. One-hundred percent of the fuel rods are assumed to have failed during hypothetical accident conditions.

2. Thirty percent of the radioactive gases are assumed to escape each failed fuel rod.

3. Fifteen percent of the ^{60}Co from the crud on the surface of the fuel rods is released as an aerosol in normal conditions of transport. One-hundred percent of the ^{60}Co is released as an aerosol from the surfaces of the fuel assemblies during accident conditions.

4. Since the overpack internals are never exposed to contaminants, the residual activity on the overpack interior surface and the MPC exterior surface is negligible compared to crud

deposits on the fuel and is neglected as a source term.

5. Up to four (4) DFCs containing specified fuel debris may be placed in an MPC-24EF (only the custom-designed Trojan MPC-24EF) or an MPC-68F.

6. Crud spallation and cladding breaches occur instantaneously after fuel loading and container closure operations.

7. The calculation for normal transport conditions of an MPC containing fuel debris assumes 100% of the rods of the fuel debris are breached.

8. For containment analysis purposes, the MPC-24, MPC-24E or MPC-24EF contain up to 24 PWR assemblies, of which 4 of these in the custom-designed Trojan MPC-24EF may be DFCs with Trojan fuel debris, the MPC-32 contains up to 32 PWR assemblies, the MPC-68 contains up to 68 BWR assemblies, and the MPC-68F contains up to 68 intact BWR fuel assemblies, of which 4 of those may be specified BWR fuel debris in damaged fuel containers.

9. 0.003% of the total fuel mass contained in a rod is assumed to be released as fines if the cladding on the rod ruptures (i.e., $f_f=3x10^{-5}$).

10. Bounding values for the crud surface activity for PWR rods is $140x10^{-6}$ Ci/cm^2 and for BWR rods is $1254x10^{-6}$ Ci/cm^2.

11. The rod surface area per assembly is $3x10^5$ cm^2 for PWR and $1x10^5$ cm^2 for BWR fuel assemblies. These surface areas are also conservatively used for the surface area of damaged fuel or fuel debris..

12. The release fractions for volatiles (^{89}Sr, ^{90}Sr, ^{103}Ru, ^{106}Ru, ^{134}Cs, ^{135}Cs, and ^{137}Cs) are all assumed to be $2x10^{-4}$ ($f_V=2x10^{-4}$).

13. In the analysis of the primary containment boundary, the MPC is assumed to rupture. In the analysis of the secondary containment boundary, the primary containment is assumed to fail.

14. In calculating the leakage rates of the primary containment for normal conditions of transport, the internal pressure of the overpack is conservatively assumed to be larger than the maximum internal pressure of all MPC types determined in Chapter 3.

15. The average cavity temperature for all analyses is conservatively assumed to be the design basis peak cladding temperature.

16. All of the activity associated with crud is assumed to be Cobalt-60.

17. It is assumed that the flow is unchoked for all leakage analyses.

18. In the evaluation to demonstrate compliance with 10CFR71.63(b), the source activity due to Plutonium was determined by conservatively assuming that all of the rods develop cladding breaches during normal transportation and hypothetical accident conditions (i.e., f_B=1.0).

19. In the evaluation to demonstrate compliance with 10CFR71.63(b), the assumption was also made that roughly 0.003% of the plutonium is released from a fuel rod (i.e., $f_{Pu}=3x10^{-5}$).

4.2.5 Analysis and Results

The allowable leakage rates for the primary and secondary containment boundaries under normal and hypothetical accident conditions of transport at operating conditions for the HI-STAR 100 packaging containing each of the MPC types were determined and are presented in this chapter. To calculate the leakage rates for a particular contents type and transportation condition, the following were determined: the source term concentration for the releasable material; the effective A_2 of the individual contributors; the releasable activity; the effective A_2 for the total source term; the allowable radionuclide release rates; and the allowable leakage rates at transport (operating) conditions. Using the equations for continuum and molecular flow, the corresponding leakage hole diameters were calculated. Then, using these leak hole diameters, the corresponding allowable leakage rates at test conditions were calculated. Parameters were utilized in a way that ensured conservatism in the final leakage rates for the conditions, contents, and package arrangements considered.

The methodology and analysis results are summarized below.

4.2.5.1 Volume in the Containment Vessel

As discussed above, the primary containment system boundary for the HI-STAR 100 packaging consists of the overpack inner shell and associated components and the secondary containment system boundary consists of the MPC enclosure vessel and associated components. The MPC provides the separate inner container per 10CFR71.63(b) for the HI-STAR 100 System transporting fuel classified as fuel debris.

Except for a small volume between the MPC and the overpack (the annulus), the overpack internal cavity is essentially filled. Therefore, the free gas volume for the primary containment boundary includes the free gas volume for the MPC plus the overpack annulus volume. The free gas volume in each of the MPC types is presented in Chapter 3. The free gas volumes of the primary and secondary containment are repeated in Table 4.2.1 for completeness. The MPC-24E and MPC-24EF basket designed for Trojan are shorter to allow for storage in their overpacks. These shorter baskets are designated as the Trojan MPC-24E and Trojan MPC-24EF, respectively, where necessary. For calculating the free volume in the primary containment (overpack) with either of the Trojan MPCs, the annulus space is assumed to be the same as that for the larger generic MPCs (i.e. the larger annulus space between the Trojan MPC and HI-STAR overpack is neglected). This will conservatively underestimate the free volume inside the primary containment.

4.2.5.2 Source Terms For Spent Nuclear Fuel Assemblies

In accordance with NUREG/CR-6487 [4.0.3], the following contributions are considered in determining the releasable source term for packages designed to transport irradiated fuel rods: (1) the radionuclides comprising the fuel rods, (2) the radionuclides on the surface of the fuel rods, and (3) the residual contamination on the inside surfaces of the vessel. NUREG/CR-6487 goes on to state that a radioactive aerosol can be generated inside a vessel when radioactive material from the fuel rods or from the inside surfaces of the container become airborne. The sources for the airborne material are (1) residual activity on the cask interior, (2) fission and activation-product activity associated with corrosion-deposited material (crud) on the fuel assembly surface, and (3) the radionuclides within the individual fuel rods. In accordance with NUREG/CR-6487, contamination due to residual activity on the cask interior surfaces is negligible as compared to crud deposits on the fuel rods themselves and therefore may be neglected. The source term considered for this calculation results from the spallation of crud from the fuel rods and from the fines, gases and volatiles which result from cladding breaches.

The inventory for isotopes other than ^{60}Co is calculated with the SAS2H and ORIGEN-S modules of the SCALE 4.3 system as described in Chapter 5. The inventory for the MPC-24, MPC-24E, MPC-24EF, and MPC-32 was conservatively based on the B&W 15x15 fuel assembly with a burnup of 45,000 MWD/MTU, 5 years of cooling time, and an enrichment of 3.6%. The inventory for the Trojan MPCs (Trojan MPC-24E, Trojan MPC-24EF) was based on the Westinghouse 17x17 fuel assembly with a burnup of 42,000 MWD/MTU, 9 years cooling time, and an enrichment of 3.09%. The inventory for the MPC-68 was based the GE 7x7 fuel assembly with a burnup of 45,000 MWD/MTU, 5 years of cooling time, and 3.2% enrichment. The inventory for the MPC-68F was based on the GE 6x6 fuel assembly with a burnup of 30,000 MWD/MTU, 18 years of cooling time, and 1.8% enrichment. Additionally, an MPC-68F was analyzed containing 67 GE 6x6 assemblies and a DFC containing 18 thorium rods. Finally, an Sb-Be source stored in one fuel rod in one assembly with 67 GE 6x6 assemblies was analyzed. The isotopes which contribute greater than 0.01% to the total curie inventory for the fuel assembly are considered in the evaluation as fines. Additionally, isotopes with A_2 values less than 1.0 in Table A-1, Appendix A, 10CFR71 are included as fines. Isotopes which contribute greater than 0.01% but which do not have an assigned A_2 value in Table A-1 are assigned an A_2 value based on the guidance in Table A-2, Appendix A, 10CFR71. Isotopes which contribute greater than 0.01% but have a radiological half life less than 10 days are neglected. Table 4.2.2 presents the isotope inventory used in the calculation.

A. Source Activity Due to Crud Spallation from Fuel Rods

The majority of the activity associated with crud is due to ^{60}Co [4.0.3]. The inventory for ^{60}Co was determined by using the crud surface activity for PWR rods (140×10^{-6} Ci/cm^2) and for BWR rods (1254×10^{-6} Ci/cm^2) provided in NUREG/CR-6487 [4.0.3] multiplied by the surface area per assembly (3×10^5 cm^2 and 1×10^5 cm^2 for PWR and BWR, respectively, also provided in NUREG/CR-6487).

The source terms were then decay corrected (5 years for the MPC-24, MPC-24E, MPC-24EF, MPC-32 and the MPC-68; 18 years for the MPC-68F; 9 years for the Trojan MPCs) using the basic

radioactive decay equation:

$$A(t) = A_0 e^{-\lambda t} \quad \textbf{(4-1)}$$

where:

A(t) is activity at time t [Ci]
A_o is the initial activity [Ci]
λ is the $\ln 2/t_{1/2}$ (where $t_{1/2}$ = 5.272 years for ^{60}Co)
t is the time in years (5 years for the MPC-24, MPC-24E, MPC-24EF, MPC-32 and the MPC-68; 18 years for the MPC-68F; 9 years for the Trojan MPCs)

The inventory for ^{60}Co was determined using the methodology described above with the following results:

PWR
Surface area per Assy = 3.0E+05 cm^2
140 $\mu Ci/cm^2$ x 3.0E+05 cm^2 = 42.0 Ci/assy

BWR
Surface area per Assy = 1.0E+05 cm^2
1254 $\mu Ci/cm^2$ x 1.0E+05 cm^2 = 125.4 Ci/assy

$^{60}Co(t) = {}^{60}Co_0\, e^{-(\lambda t)}$, where $\lambda = \ln 2/t_{1/2}$, t = 5 years (for the MPC-24, MPC-24E, MPC-24EF, MPC-32 and MPC-68), t = 18 years (MPC-68F), t = 9 years (Trojan MPCs), $t_{1/2}$ = 5.272 years for ^{60}Co [4.2.4]

MPC-24, MPC-24E, MPC-24EF, MPC-32
$^{60}Co(5) = 42.0\ Ci\ e^{-(\ln 2/5.272)(5)}$
$^{60}Co(5)$ = 21.77 Ci/assy

MPC-68
$^{60}Co(5) = 125.4\ Ci\ e^{-(\ln 2/5.272)(5)}$
$^{60}Co(5)$ = 64.98 Ci/assy

Trojan MPC-24E, Trojan MPC-24EF
$^{60}Co(5) = 42.0\ Ci\ e^{-(\ln 2/5.272)(9)}$
$^{60}Co(5)$ = 12.86 Ci/assy

MPC-68F
$^{60}Co(18) = 125.4\ Ci\ e^{-(\ln 2/5.272)(18)}$
$^{60}Co(18)$ = 11.76 Ci/assy

A summary of the ^{60}Co inventory available for release is provided in Table 4.2.2.

The activity density that results inside the containment vessel as a result of crud spallation from spent fuel rods can be formulated as:

$$C_{crud} = \frac{f_C M_A N_A}{V} \quad \textbf{(4-2)}$$

where:

C_{crud} is the activity density inside the containment vessel as a result of crud spallation [Ci/cm^3],
M_A is the total crud activity inventory per assembly [Ci/assy],
f_C is the crud spallation fraction,
N_A is the number of assemblies, and
V is the free volume inside the containment vessel [cm^3].

NUREG/CR-6487 states that measurements have shown 15% to be a reasonable value for the percent of crud spallation for both PWR and BWR fuel rods under normal transportation conditions. For hypothetical accident conditions, it is assumed that there is 100% crud spallation [4.0.3].

B. Source Activity Due to Releases of Fines from Cladding Breaches

A breach in the cladding of a fuel rod may allow radionuclides to be released from the resulting cladding defect into the interior of the MPC. If there is a leak in the primary or secondary containment vessels, then the radioisotopes emitted from a cladding breach that were aerosolized may be entrained in the gases escaping from the package and result in a radioactive release to the environment.

NUREG/CR-6487 suggests that a bounding value of 3% of the rods develop cladding breaches during normal transportation (i.e., f_B=0.03). For hypothetical accident conditions, it is assumed that all of the rods develop a cladding breach (i.e., f_B=1.0). These values were used for both PWR and BWR fuel rods. As described in NUREG/CR-6487, roughly 0.003% of the fuel mass contained in a rod is released as fines if the cladding on the rod ruptures (i.e., $f_f=3\times10^{-5}$).

The calculation for normal transport conditions of either a Trojan MPC-24EF or an MPC-68F containing four (4) DFCs containing fuel debris assumes that for the four DFCs, 100% of the rods of the fuel debris are breached. The remaining 20 or 64 assemblies in either the Trojan MPC-24EF or the MPC-68F, respectively, were assumed to have a 3% cladding rupture. Therefore, f_B for a Trojan MPC-24EF or an MPC-68F containing fuel debris is:

$$f_B = (0.03)\frac{20}{24} + (1.0)\frac{4}{20}$$
$$f_B = 0.192 \qquad \textbf{(4-3a)}$$

$$f_B = (0.03)\frac{64}{68} + (1.0)\frac{4}{68}$$
$$f_B = 0.087 \qquad \textbf{(4-3b)}$$

The activity concentration inside the containment vessel due to fines being released from cladding breaches is given by:

$$C_{fines} = \frac{f_f\, I_{fines}\, N_A\, f_B}{V} \qquad \textbf{(4-4)}$$

where:

C_{fines} is the activity concentration inside the containment vessel as a result of fines released from cladding breaches [Ci/cm^3],

f_f is the fraction of a fuel rod's mass released as fines as a result of a cladding breach ($f_f=3x10^{-5}$),
I_{fines} is the total activity inventory [Ci/assy],
N_A is the number of assemblies,
f_B is the fraction of rods that develop cladding breaches, and
V is the free volume inside the containment vessel [cm^3].

C. Source Activity from Gases due to Cladding Breaches

If a cladding failure occurs in a fuel rod, a large fraction of the gap fission gases will be introduced into the free volume of the system. Tritium and Krypton-85 are typically the major sources of radioactivity among the gases present [4.0.3]. NUREG/CR-6487 suggests that a bounding value of 30% of the fission product gases escape from a fuel rod as a result of a cladding breach (i.e., $f_g=0.3$).

The activity concentration due to the release of gases form a cladding breach is given by:

$$C_{gases} = \frac{f_g I_{gases} N_A f_B}{V} \quad (4\text{-}5)$$

where:

C_{gases} is the releasable activity concentration inside the containment vessel due to gases released from cladding breaches [Ci/cm^3],
f_g is the fraction of gas that would escape from a fuel rod that developed a cladding breach,
I_{gases} is the gas activity inventory [^3H, ^{129}I, ^{85}Kr, ^{81}Kr, ^{127}Xe] [Ci/assy],
N_A is the number of assemblies,
f_B is the fraction of rods that develop cladding breaches, and
V is the free volume inside the containment vessel [cm^3].

D. Source Activity from Volatiles due to Cladding Breaches

Volatiles such as cesium, strontium, and ruthenium, can also be released from a fuel rod as a result of a cladding breach. NUREG/CR-6487 estimates that $2x10^{-4}$ is a conservative bounding value for the fraction of the volatiles released from a fuel rod (i.e., $f_V=2x10^{-4}$).

The activity concentration due to the release of volatiles is given by:

$$C_{vol} = \frac{f_v I_{vol} N_A f_B}{V} \quad (4\text{-}6)$$

where:

C_{vol} is the releasable activity concentration inside the containment vessel due to volatiles released from cladding breaches [Ci/cm^3],
f_V is the fraction of volatiles that would escape from a fuel rod that developed a cladding breach,

I_{vol} is the volatile activity inventory [^{89}Sr, ^{90}Sr, ^{134}Cs, ^{135}Cs, ^{137}Cs, ^{134}Cs, ^{103}Ru, ^{106}Ru] [Ci/assy], |
N_A is the number of assemblies,
f_B is the fraction of rods that develop cladding breaches, and
V is the free volume inside the containment vessel [cm^3].

E. Total Source Term for the HI-STAR 100 System

The total source term was determined by combining Equations 4-2, 4-4, 4-5, and 4-6:

$$C_{total} = C_{crud} + C_{fines} + C_{gases} + C_{vol} \quad \textbf{(4-7)}$$

where C_{total} has units of Ci/cm^3.

Table 4.2.3 presents the total source term determined using the above methodology. Table 4.2.4 summarizes the parameters from NUREG/CR-6487 used in this analysis.

4.2.5.3 Effective A_2 of Individual Contributors (Crud, Fines, Gases, and Volatiles)

The A_2 of the individual contributions (i.e., crud, fines, gases, and volatiles) were determined in accordance with NUREG/CR-6487. As previously described, the majority of the activity due to crud is from Cobalt-60. Therefore, the A_2 value of 10.8 Ci used for crud for both PWR and BWR fuel is the same as that for Cobalt-60 found in 10CFR71, Appendix A.

In accordance with 10CFR71.51(b) the methodology presented in 10CFR71, Appendix A for mixtures of different radionuclides was used to determine the A_2 values for the gases, fines and volatiles.

$$A_2 \text{ for a mixture} = \frac{1}{\sum_{i=1}^{I} \frac{f_i}{(A_2)_i}} \quad \textbf{(4-8)}$$

Where f(i) is the fraction of activity of nuclide I in the mixture and $A_2(i)$ is the appropriate A_2 value for the nuclide I.

10CFR71.51(b) also states that for Krypton-85, an effective A_2 value equal to 10 A_2 may be used. Table 4.2.5 summarizes the effective A_2 for all individual contributors.

4.2.5.4 Releasable Activity

The releasable activity is the product of the respective activity concentrations (C_{fines}, C_{gas}, C_{crud}, and C_{vol}) and the respective MPC volume. The releasable activity of fines, volatiles, gases, and crud were determined using this methodology.

$$\text{Releasable Activity [Ci]} = \text{Activity Concentration } [\frac{\text{Ci}}{\text{cm}^3}] \text{ x Volume } [\text{cm}^3] \qquad \textbf{(4-9)}$$

4.2.5.5 Effective A_2 for the Total Source Term

Using the releasable activity and the effective A_2 values from the individual contributors (i.e., crud, fines, gases, and volatiles), the effective A_2 for the total source term was calculated for each MPC type, for normal transportation and hypothetical accident conditions. The methodology used to determine the effective A_2 is the same as that used for a mixture, which is provided in Equation 4-8.

The results are summarized in Table 4.2.6. As stated in 4.2.5.3, the effective A_2 used for Krypton-85 is 10 A_2 (2700 Ci).

4.2.5.6 Allowable Radionuclide Release Rates

The containment criterion for the HI-STAR 100 System under normal conditions of transport is given in 10CFR71.51(a)(1). This criterion requires that a package have a radioactive release rate less than $A_2 \times 10^{-6}$ in one hour, where A_2 is the effective A_2 for the total source term in the packaging determined in 4.2.5.5. Additionally, 10CFR71.51(b)(2) specifies that for hypothetical accident conditions, the quantity that may be released in one week is A_2 (effective A_2 for the total source term determined in 4.2.5.5).

NUREG/CR-6487 and ANSI N14.5 provides the following equations for the allowable release rates.

Release rate for normal conditions of transport:

$$R_N = L_N C_N \leq A_2 \times 2.78\text{x}10^{-10}/\text{second} \qquad \textbf{(4-10)}$$

where:

R_N is the release rate for normal transport [Ci/s]
L_N is the volumetric gas leakage rate [cm^3/s]
C_N is the total source term activity concentration [Ci/cm^3]
A_2 is the appropriate effective A_2 value [Ci].

Release rate for hypothetical accident conditions:

$$R_A = L_A C_A \leq A_2 \times 1.65\text{x}10^{-6}/\text{second} \qquad \textbf{(4-11)}$$

where:

R_A is the release rate for hypothetical accident conditions [Ci/s]
L_A is the volumetric gas leakage rate [cm^3/s]
C_A is the total source term activity concentration [Ci/cm^3]
A_2 is the appropriate effective A_2 value [Ci].

Equations 4-10 and 4-11 were used to determine the allowable radionuclide release rates for each MPC type and transport condition. The release rates are summarized in Table 4.2.7.

4.2.5.7 Allowable Leakage Rates at Operating Conditions

The allowable leakage rates at operating conditions were determined by dividing the allowable release rates by the appropriate source term activity concentration (modifying Equations 4-10 and 4-11).

$$L_N = \frac{R_N}{C_N} \text{ or } L_A = \frac{R_A}{C_A} \quad \textbf{(4-12)}$$

where,

L_N or L_A is the allowable leakage rate at the upstream pressure for normal (N) or accident (A) conditions [cm^3/s],
R_N or R_A is the allowable release rate for normal (N) or accident (A) conditions [Ci/s], and
C_N or C_A is the allowable release rate for normal (N) or accident (A) conditions [Ci/cm^3].

The allowable leakage rates determined using Equation 4-12 are the allowable leakage rates at the upstream pressure. Table 4.2.9 summarizes the allowable leakage rates at the upstream pressures. The most limiting allowable leakage rate presented in Table 4.2.9 was conservatively selected and used to determine the leakage rate acceptance criterion .

Equation deleted **(4-13)**

4.2.5.8 Leakage Rate Acceptance Criteria for Test Conditions

The leakage rates discussed thus far were determined at operating conditions (see normal and accident conditions in Table 4.2.12). The following provides details of the methodology used to convert the allowable leakage rate at operating conditions to a leakage rate acceptance criterion at reference test conditions.

For conservatism, unchoked flow correlations were used as the unchoked flow correlations better approximate the true measured flow rate for the leakage rates associated with transportation packages. Using the equations for molecular and continuum flow provided in NUREG/CR-6487, the corresponding leak hole diameter was calculated by solving Equation 4-14a for D, the leak hole diameter. The capillary length required for Equation 4-14a for the primary containment was

conservatively chosen as the closure plate inner seal seating width which is 0.25 cm; for the secondary containment, the capillary length was conservatively chosen to be the MPC lid closure weld thickness which is 1.25 inches thick (3.175 cm).

$$L_{@P_u} = \left[\frac{2.49 \times 10^6 \, D^4}{a \, u} + \frac{3.81 \times 10^3 \, D^3 \sqrt{\frac{T}{M}}}{a \, P_a} \right] [P_u - P_d] \frac{P_a}{P_u} \qquad \textbf{(4-14a)}$$

where:

$L_{@Pu}$ is the allowable leakage rate at the upstream pressure for normal and accident conditions [cm^3/s],
a is the capillary length [cm],
T is the temperature for normal and accident conditions [K],
M is the gas molecular weight [g/mole] = 4.0 from ANSI N14.5, Table B1 [4.0.2],
u is the fluid viscosity for helium [cP] from Rosenhow and Hartnett [4.2.3]
P_u is the upstream pressure [ATM],
D leak hole diameter [cm],
P_d is the downstream pressure for normal and accident conditions [ATM], and
P_a is the average pressure; $P_a = (P_u + P_d)/2$ for normal and accident conditions [ATM].

The actual leakage tests performed on the primary and secondary confinement boundary welds are typically not performed under exactly the same conditions every time. Therefore, reference test conditions are specified to provide a consistent comparison of the measured leakage rate to the leakage rate acceptance criterion. For example, the MPC Lid-to-Shell weld is performed with an elevated pressure (85 psig min) inside the MPC cavity to magnify the leakage rate in the event of a leak. The reference test conditions, and approximate actual test conditions are specified in Table 4.2.12.

The corresponding leak hole diameter at operating conditions was determined by solving Equation 4-14a for 'D' where $L_{@Pu}$ is equal to 1.03×10^{-5} cm^3/s and using the parameters for normal conditions of transport presented in Table 4.2.12.

Using this leak hole diameter and the temperature and pressure specified for reference test conditions provided in Table 4.2.12, Equation 4-14a was solved for the volumetric leakage rate at reference test conditions.

Equation B-1 of ANSI N14.5-1997 [4.0.2] is used to express this volumetric leakage rate into a mass-like helium flow rate (Q_u) as follows:

$$Q_u = L_u * P_u \ (\text{atm-cm}^3/\text{sec}) \qquad \textbf{(4-14b)}$$

where:

L_u is the upstream volumetric leakage rate [cm^3/sec],
Q_u is the mass-like helium leak rate [atm-cm^3/sec], and
P_u is the upstream pressure [atm].

Using Equation 4-14b to convert the volumetric flow rate into a mass-like flow, the leakage rate acceptance criteria is calculated to be 5.41×10^{-6} atm-cm^3/sec, which has been conservatively reduced and is presented in Table 4.1.1.

Table 4.2.12 provides additional parameters used in the analysis.

4.2.5.9 10CFR71.63(b) Plutonium Leakage Verification

The HI-STAR 100 System configured to transport fuel debris must meet the criteria of 10CFR71.63(b) for plutonium shipments. This criteria specifies that for normal conditions of transport, the separate inner container must not release plutonium as demonstrated to a sensitivity of $A_2 \times 10^{-6}$ in one hour, where A_2 is the effective A_2 for the plutonium inventory in the damaged fuel (up to four DFCs containing specified fuel debris). Additionally, 10CFR71.63(b) specifies that for hypothetical accident conditions, the separate inner container must restrict the loss of plutonium to not more than A_2 in one week (effective A_2 for the plutonium inventory determined using the methodology described in Section 4.2.5.3).

To demonstrate compliance with this requirement, the leakage rate acceptance criterion was determined following the basic methodology described above. To determine this leakage rate, the plutonium inventory for the GE 6x6 MOX fuel assembly and the plutonium inventories for the assemblies described in Section 4.2.5.2 was analyzed. Table 4.2.11 contains the plutonium inventory for the MOX fuel used in this evaluation.

As discussed in 4.2.5.2, Equation 4-3a and Equation 4-3b presents the methodology to determine f_B for a Trojan MPC-24EF and an MPC-68F containing fuel debris, respectively. This f_B was applied in determining the source activity due to Plutonium. The calculation for normal transport conditions of an MPC containing four (4) DFCs containing fuel debris assumes that for the four DFCs, 100% of the rods of the fuel debris are breached. The remaining assemblies in the MPC were assumed to have a 3% cladding rupture. The source activity due to Plutonium was determined by conservatively assuming that all of the rods develop cladding breaches during hypothetical accident conditions (i.e., f_B=1.0). The assumption was also made that roughly 0.003% of the plutonium is released from a fuel rod (i.e., $f_{Pu}=3 \times 10^{-5}$). Therefore, the activity concentration inside the containment vessel due to plutonium is given by:

$$C_{Pu} = \frac{f_{Pu} I_{Pu} N_A f_B}{V} \qquad \textbf{(4-15)}$$

where:

C_{Pu} is the activity concentration inside the containment vessel from Plutonium [Ci/cm^3],
f_{Pu} is the fraction of a fuel rod's mass released as Plutonium ($f_f = 3x10^{-5}$),
I_{Pu} is the total Plutonium inventory of one assembly [Ci/assy],
N_A is the number of assemblies,
f_B is the fraction of rods that develop cladding breaches (f_B=0.087 for BWR fuel and f_B=0.192 for PWR fuel under normal conditions of transport and f_B=1.0 for accident conditions), and
V is the free volume inside the containment vessel [cm^3] from Table 4.2.1.

The methodology described in 4.2.5.3 for mixtures was used to calculate the effective A_2 for Plutonium. The methodology in 4.2.5.4 was used to determine the releasable activity. The allowable radionuclide release rates were determined using the methodology presented in 4.2.5.6 and are summarized in Table 4.2.13. The allowable leakage rates at the upstream pressure were determined as discussed in 4.2.5.7 (using Equation 4-12). The allowable leakage rates are presented in Table 4.2.14. As in 4.2.5.7, the most limiting allowable leakage rate presented in Table 4.2.14 was conservatively selected and used to determine the leakage rate acceptance criterion for the MPC.

As discussed in 4.2.5.8, the allowable leakage rate was then converted to a leakage rate acceptance criterion at test conditions using the equations for molecular and continuum flow provided in NUREG/CR-6487 (Equation 4-14a). The capillary length required for Equation 4-14a for the secondary containment was conservatively chosen to be the MPC lid closure weld thickness which is assumed to be 1.25 inches thick (3.175 cm). Equation 4-14a was solved for D, the leak hole diameter and then using this leak hole diameter, and the temperature and pressures for test conditions (Table 4.1.12), Equation 4-14a was solved for the volumetric leakage rate acceptance criterion at test conditions. Equation 4-14b is used to convert the volumetric flow rate into the mass-like flow rate, resulting in an acceptance criterion leakage rate of $8.94x10^{-6}$ atm-cm^3/sec. For additional conservatism to ensure compliance with 10CFR71.63(b), this leakage rate acceptance criterion was conservatively reduced and is presented in Table 4.1.1.

4.2.5.10 Leak Test Sensitivity

The sensitivity for the overpack leakage test procedures is equal to one-half of the allowable leakage rate. The HI-STAR 100 containment packaging tests in Chapter 8 incorporate the appropriate leakage test procedure sensitivity. The leakage rates for the HI-STAR 100 containment packaging with its corresponding sensitivity are presented in Table 4.1.1.

Table 4.2.1

FREE GAS VOLUME OF THE PRIMARY AND SECONDARY CONTAINMENT

MPC Type	Primary Containment Volume (overpack) (cm^3)	Secondary Containment Volume (MPC) (cm^3)
MPC-24	6.70×10^6	N/A
MPC-24E MPC-24EF	6.55×10^6	N/A
Trojan MPC-24E Trojan MPC-24EF	6.12×10^6	5.96×10^6
MPC-32	6.35×10^6	N/A
MPC-68	6.15×10^6	N/A
MPC-68F	6.15×10^6	5.99×10^6

Table 4.2.2

ISOTOPE INVENTORY
Ci/Assembly

Nuclide	PWR MPCs Ci/Assembly	MPC-68 Ci/Assembly	MPC-68F Ci/Assembly	Trojan MPCs Ci/Assembly
Gases				
^{3}H	2.76E+02	1.09E+02	1.78E+01	1.75E+02
^{129}I	2.17E-02	8.66E-03	3.49E-03	1.93E-02
^{85}Kr	4.69E+03	1.79E+03	2.37E+02	2.76E+03
^{81}Kr	7.97E-08	3.50E-08	1.19E-08	6.80E-08
^{127}Xe	5.95E-11	2.05E-11	1.62E-17	3.39E-29
Crud				
^{60}Co	2.18E+01	6.50E+01	1.18E+01	1.29E+01
Volatiles				
^{90}Sr	4.53E+04	1.76E+04	4.29E+03	3.36E+04
^{106}Ru	4.97E+04	1.74E+04	2.30E-01	7.99E+02
^{134}Cs	4.43E+04	1.66E+04	3.16E+01	5.14E+03
^{137}Cs	6.76E+04	2.68E+04	7.21E+03	5.20E+04
^{89}Sr	1.25E-01	3.47E-02	2.41E-35	1.01E-14
^{103}Ru	3.65E-03	1.13E-03	0.00E+00	5.47E-20
^{135}Cs	2.79E-01	1.11E-01	4.54E-02	2.16E-01
Fines				
^{225}Ac*	3.05E-08	2.14E-08	9.69E-09	9.89E-13
^{227}Ac*	2.36E-06	1.18E-06	1.45E-06	2.56E-08
^{110m}Ag	1.73E+02	6.58E+01	4.97E-06	2.04E-07
^{241}Am	4.76E+02	1.61E+02	2.52E+02	1.17E+00

Table 4.2.2 (continued)
ISOTOPE INVENTORY

	MPC-24 Ci/Assembly	MPC-68 Ci/Assembly	MPC-68F Ci/Assembly	Trojan MPCs Ci/Assembly
^{242M}Am*	5.60E+00	1.94E+00	9.35E-01	5.06E-03
^{243}Am*	2.23E+01	9.42E+00	3.30E+00	2.53E-02
^{137m}Ba	6.39E+04	2.53E+04	6.81E+03	0.00E+00
^{210M}Bi*	0.00E+00	0.00E+00	0.00E+00	1.38E-10
^{247}Bk*	2.82E-08	1.32E-08	5.94E-08	7.06E-24
^{144}Ce	4.77E+04	1.45E+04	7.33E-03	2.62E-04
^{248}Cf*	0.00E+00	0.00E+00	0.00E+00	0.00E+00
^{249}Cf*	8.01E-05	4.47E-05	3.62E-06	7.20E-08
^{250}Cf*	2.92E-04	1.86E-04	6.69E-06	7.73E-08
^{251}Cf*	3.40E-06	2.06E-06	1.36E-07	2.84E-09
^{252}Cf*	4.11E-04	3.14E-04	3.64E-07	1.52E-08
^{254}Cf*	1.19E-13	1.05E-13	0.00E+00	5.32E-28
^{240}Cm*	0.00E+00	0.00E+00	0.00E+00	0.00E+00
^{242}Cm*	3.21E+02	1.26E+02	7.71E-01	8.42E-05
^{243}Cm*	1.61E+01	6.51E+00	1.54E+00	9.51E-03
^{244}Cm	3.26E+03	1.43E+03	2.17E+02	1.42E+00
^{245}Cm*	3.25E-01	1.23E-01	2.48E-02	3.21E-04
^{246}Cm*	1.06E-01	5.40E-02	1.01E-02	1.14E-04
^{247}Cm*	7.07E-07	3.72E-07	5.26E-08	7.01E-10
^{248}Cm*	4.20E-06	2.43E-06	2.53E-07	1.56E-08

Table 4.2.2 (continued)

ISOTOPE INVENTORY

Ci/Assembly

	MPC-24 Ci/Assembly	MPC-68 Ci/Assembly	MPC-68F Ci/Assembly	Trojan MPCs Ci/Assembly
^{253}Es*	6.35E-20	4.62E-20	0.00E+00	0.00E+00
^{254}Es*	1.93E-08	1.96E-08	8.05E-16	5.24E-15
^{154}Eu	4.03E+03	1.47E+03	1.44E+02	1.01E-03
^{155}Eu	1.34E+03	5.46E+02	2.23E+01	6.06E-05
^{55}Fe	6.98E+01	3.23E+01	2.94E-01	1.11E-07
^{257}Fm*	4.26E-07	1.69E-07	0.00E+00	2.35E-26
^{148}Gd*	0.00E+00	0.00E+00	0.00E+00	0.00E+00
^{182}Hf*	0.00E+00	0.00E+00	0.00E+00	0.00E+00
^{236}Np*	9.77E-06	3.29E-06	7.30E-07	1.78E-09
^{237}Np*	2.33E-01	8.07E-02	2.55E-02	2.33E-04
^{239}Np	2.23E+01	9.42E+00	3.30E+00	1.01E-05
^{231}Pa*	1.82E-05	8.17E-06	3.16E-06	3.26E-08
^{210}Pb*	4.30E-09	2.17E-09	1.17E-08	3.77E-13
^{147}Pm	4.28E+04	1.52E+04	1.18E+02	2.17E-03
^{208}Po*	0.00E+00	0.00E+00	0.00E+00	0.00E+00
^{209}Po*	0.00E+00	0.00E+00	0.00E+00	0.00E+00
^{210}Po*	3.92E-09	1.98E-09	1.08E-08	1.49E-13
^{144}Pr	4.77E+04	1.45E+04	7.33E-03	0.00E+00
^{144m}Pr	6.68E+02	2.04E+02	1.03E-04	0.00E+00
^{236}Pu*	2.04E-01	6.32E-02	3.66E-04	1.26E-05

Table 4.2.2 (continued) ISOTOPE INVENTORY Ci/Assembly				
	MPC-24 Ci/Assembly	MPC-68 Ci/Assembly	MPC-68F Ci/Assembly	Trojan MPCs Ci/Assembly
^{238}Pu	2.56E+03	9.55E+02	2.50E+02	2.37E+00
^{239}Pu	1.91E+02	6.24E+01	2.95E+01	2.00E-01
^{240}Pu	3.27E+02	1.34E+02	6.81E+01	3.70E-01
^{241}Pu	7.55E+04	2.47E+04	5.16E+03	1.21E+00
^{242}Pu*	1.65E+00	7.05E-01	3.06E-01	1.97E-03
^{244}Pu*	1.11E-13	6.58E-14	3.73E-14	2.87E-16
^{223}Ra*	2.37E-06	1.18E-06	1.45E-06	1.70E-11
^{225}Ra*	3.05E-08	2.14E-08	9.69E-09	4.94E-13
^{226}Ra*	2.82E-08	1.32E-08	5.94E-08	1.38E-12
^{106}Rh	4.97E+04	1.74E+04	2.30E-01	0.00E+00
^{222}Rn*	2.82E-08	1.32E-08	5.94E-08	6.89E-12
^{125}Sb	2.87E+03	1.15E+03	8.02E+00	1.59E-04
^{151}Sm	2.60E+02	7.92E+01	2.53E+01	1.24E-05
^{119m}Sn	5.46E+02	3.08E+02	1.07E-06	4.23E-05
^{125m}Te	6.99E+02	2.82E+02	1.96E+00	1.89E-03
^{227}Th*	2.33E-06	1.16E-06	1.43E-06	5.05E-11
^{228}Th*	8.56E-03	3.40E-03	1.71E-03	8.06E-06
^{229}Th*	3.05E-08	2.14E-08	9.69E-09	3.29E-10
^{230}Th*	2.16E-05	8.26E-06	1.29E-05	5.40E-08
^{230}U*	1.33E-23	4.74E-24	0.00E+00	0.00E+00

Table 4.2.2 (continued) ISOTOPE INVENTORY Ci/Assembly				
	MPC-24 Ci/Assembly	MPC-68 Ci/Assembly	MPC-68F Ci/Assembly	Trojan MPCs Ci/Assembly
^{232}U*	1.51E-02	5.58E-03	1.69E-03	1.21E-05
^{233}U*	1.41E-05	4.20E-06	3.03E-06	3.94E-09
^{234}U*	4.97E-01	1.70E-01	7.26E-02	1.08E-04
^{236}U*	1.60E-01	5.85E-02	1.84E-02	3.18E-05
^{90}Y	4.53E+04	1.76E+04	4.29E+03	4.13E-02

Note: The isotopes which contribute greater than 0.01% to the total curie inventory for the fuel assembly are considered in the evaluation as fines. Additionally, isotopes with A_2 values less than 1.0 in Table A-1, Appendix A, 10CFR71 are included as fines and are designated in the table by an "*".

Table 4.2.3

TOTAL SOURCE TERM FOR THE HI-STAR 100 SYSTEM (Ci/cm^3)

	C_{crud} (Ci/cm^3)	C_{fines} (Ci/cm^3)	C_{vol} (Ci/cm^3)	C_{gas} (Ci/cm^3)	Total (Ci/cm^3)
Normal Transport Conditions					
MPC-24	1.17E-05	1.26E-07	4.45E-06	1.60E-04	1.77E-04
MPC-24E, MPC-24EF	1.20E-05	1.29E-07	4.55E-06	1.64E-04	1.82E-04
Trojan MPC-24E	7.56E-06	5.31E-07	2.15E-06	1.04E-04	1.14E-04
Trojan MPC-24EF Secondary	7.77E-06	3.49E-06	1.42E-05	6.81E-04	7.06E-04
Trojan MPC-24EF Primary	7.56E-06	3.40E-06	1.38E-05	6.63E-04	6.88E-04
MPC-32	1.64E-05	1.77E-07	6.26E-06	2.25E-04	2.50E-04
MPC-68	1.08E-04	1.36E-07	5.20E-06	1.89E-04	3.03E-04
MPC-68F Secondary	2.00E-05	5.16E-07	2.28E-06	7.55E-05	9.83E-05
MPC-68F Primary	1.95E-05	5.02E-08	2.22E-06	7.35E-05	9.58E-05
Accident Conditions					
MPC-24	7.79E-05	4.20E-05	1.48E-04	5.34E-03	5.60E-03
MPC-24E, MPC-24EF	7.97E-05	4.29E-05	1.52E-04	5.46E-03	5.73E-03
Trojan MPC-24E	5.04E-05	1.77E-05	7.18E-05	3.45E-03	3.59E-03
Trojan MPC-24EF Secondary	5.18E-05	1.82E-05	7.37E-05	3.55E-03	3.69E-03
Trojan MPC-24EF Primary	5.04E-05	1.77E-05	7.18E-05	3.45E-03	3.59E-03
MPC-32	1.10E-04	5.90E-05	2.09E-04	7.51E-03	7.88E-03
MPC-68	7.18E-04	4.52E-05	1.73E-04	6.30E-03	7.23E-03
MPC-68F Secondary	1.34E-04	5.93E-06	2.62E-05	8.68E-04	1.03E-03
MPC-68F Primary	1.30E-04	5.77E-06	2.55E-05	8.45E-04	1.01E-03

Table 4.2.4

VARIABLES FOUND IN NUREG/CR-6487 USED IN THE LEAKAGE RATE ANALYSIS

Variable	PWR		BWR	
	Normal	Accident	Normal	Accident
Fraction of crud that spalls, f_C	0.15	1.0	0.15	1.0
Crud surface activity (Ci/cm^2)	$140x10^{-06}$	$140x10^{-06}$	$1254x10^{-06}$	$1254x10^{-06}$
Surface area per assembly, cm^2	$3x10^5$	$3x10^5$	$1x10^5$	$1x10^5$
Fraction of rods that develop cladding breach, f_B†	0.03	1.0	0.03	1.0
Fraction of fines that are released, f_f	$3x10^{-5}$	$3x10^{-5}$	$3x10^{-5}$	$3x10^{-5}$
Fraction of gases that are released, f_G	0.3	0.3	0.3	0.3
Fraction of volatiles that are released, f_V	$2x10^{-04}$	$2x10^{-04}$	$2x10^{-04}$	$2x10^{-04}$

† The calculation for normal transport conditions of the Trojan MPC-24EF and MPC-68F each containing four (4) DFCs with fuel debris assumes that for the four DFCs, 100% of the rods of the fuel debris are breached. The remaining 20 or 64 assemblies in the Trojan MPC-24EF and MPC-68F, respectively, were assumed to have a 3% cladding rupture. Therefore, f_B for the Trojan MPC-24EF and the MPC-68F containing fuel debris is 0.192 and 0.087, respectively.

Table 4.2.5

INDIVIDUAL CONTRIBUTOR EFFECTIVE A_2
FOR GASES, CRUD, FINES, AND VOLATILES

MPC Type	A_2 (Ci)
Gases	
PWR MPCs	282
MPC-68	282
MPC-68F	285
Trojan MPCs	478
Crud	
All MPCs	10.8
Fines	
PWR MPCs	0.308
MPC-68	0.284
MPC-68F	0.115
Trojan MPCs	0.147
Volatiles	
PWR MPCs	6.04
MPC-68	6.05
MPC-68F	5.43
Trojan MPCs	5.44

Table 4.2.6

TOTAL SOURCE TERM EFFECTIVE A_2 FOR NORMAL AND HYPOTHETICAL ACCIDENT CONDITIONS

Normal Transport Conditions	
	Effective A_2 (Ci)
MPC-24	27.4
MPC-24E MPC-24EF	27.4
Trojan MPC-24E	23.1
Trojan MPC-24EF	24.7
MPC-32	27.4
MPC-68	18.6
MPC-68F	14.0
Accident Conditions	
MPC-24	30.0
MPC-24E MPC-24EF	30.0
Trojan MPC-24E	24.6
Trojan MPC-24EF	24.6
MPC-32	30.0
MPC-68	26.2
MPC-68F	14.4

Table 4.2.7

RADIONUCLIDE RELEASE RATES

	Allowable Release Rate (R_N or R_A) (Ci/s)
Normal Conditions	
MPC-24	7.62E-09
MPC-24E, MPC-24EF	7.62E-09
Trojan MPC-24E	6.41E-09
Trojan MPC-24EF	6.87E-09
MPC-32	7.62E-09
MPC-68	5.18E-09
MPC-68F	3.88E-09
Accident Conditions	
MPC-24	4.94E-05
MPC-24E, MPC-24EF	4.94E-05
Trojan MPC-24E	4.06E-05
Trojan MPC-24EF	4.06E-05
MPC-32	4.94E-05
MPC-68	4.32E-05
MPC-68F	2.37E-05

Table 4.2.8

Table Deleted

Table 4.2.9

ALLOWABLE LEAKAGE RATES AT UPSTREAM PRESSURE

	C_{total} (Ci/cm^3)	Allowable Leakage Rate at P_u L_N or L_A (cm^3/s)
Normal Transport Conditions		
MPC-24	1.77E-04	4.29E-05
MPC-24E, MPC-24EF	1.82E-04	4.20E-05
Trojan MPC-24E	1.14E-04	5.63E-05
Trojan MPC-24EF Secondary	7.06E-04	9.73E-06
Trojan MPC-24EF Primary	6.88E-04	1.00E-05
MPC-32	2.50E-04	3.05E-05
MPC-68	3.03E-04	1.71E-05
MPC-68F Secondary	9.83E-05	3.95E-05
MPC-68F Primary	9.58E-05	4.05E-05
Accident Conditions		
MPC-24	5.60E-03	8.82E-03
MPC-24E, MPC-24EF	5.73E-03	8.62E-03
Trojan MPC-24E	3.59E-03	1.13E-02
Trojan MPC-24EF Secondary	3.69E-03	1.10E-02
Trojan MPC-24EF Primary	3.59E-03	1.13E-02
MPC-32	7.88E-03	6.27E-03
MPC-68	7.23E-03	5.96E-03
MPC-68F Secondary	1.03E-03	2.29E-02
MPC-68F Primary	1.01E-03	2.35E-02

Table 4.2.10

Table Deleted

Table 4.2.11

PLUTONIUM INVENTORY
(Ci/assembly)

Nuclide	MPC-68F MOX fuel Ci/Assy	MPC-68F UO_2 fuel Ci/Assy	Trojan MPC-24EF UO_2 fuel Ci/Assy
Pu-236	4.92E-04	3.66E-04	2.04E-01
Pu-237	0.00E+00	0.00E+00	3.04E-07
Pu-238	1.11E+03	2.50E+02	2.56E+03
Pu-239	3.29E+01	2.95E+01	1.91E+02
Pu-240	7.83E+01	6.81E+01	3.27E+02
Pu-241	6.15E+03	5.16E+03	7.55E+04
Pu-242	3.44E-01	3.06E-01	1.65E+00
Pu-244	0.0	3.73E-14	1.11E-13
Total	**7.37E+03**	**5.51E+03**	**7.86E+04**

Table 4.2.12

PARAMETERS FOR NORMAL, HYPOTHETICAL ACCIDENT AND TEST CONDITIONS

Parameter	Normal Conditions	Hypothetical Accident Conditions	Reference Test Conditions	Actual Test Conditions
P_u	104 psia[1] (7.07 ATM)	214.7 psia (14.61 ATM)	Primary: 1.68 ATM	Primary: 1.68 ATM (min)
			Secondary: 2.0 ATM	Secondary: 6.78 ATM (min)
P_d	14.7 psia (1 ATM)	14.7 psia (1 ATM)	14.7 psia (1 ATM)	14.7 psia (1 ATM)
T	495°F (530 K)	1058°F (843 K)	373 K	373 K (max)
M	4 g/mol	4 g/mol	4 g/mol	4 g/mol
u	0.0293 cP	0.0397 cP	0.0231 cP	0.0231 cP
a	Primary: 0.25 cm	Primary: 0.25 cm	Primary: 0.25 cm	Primary: 0.25 cm
	Secondary: 3.175 cm	Secondary: 3.175 cm	Secondary: 3.175 cm	Secondary: 3.175 cm

[1] The maximum upstream pressure for normal operating conditions in the Trojan MPCs is 83.2 psia (5.66 ATM). This value has been used to determine the maximum allowable leakage rate from the Trojan MPCs.

Table 4.2.13

RADIONUCLIDE RELEASE RATES
FOR PLUTONIUM (SECONDARY CONTAINMENT)

	Effective A_2 (Ci)	Allowable Release Rate (R_N or R_A) (Ci/s)
Normal Transport Conditions		
MPC-68F MOX Fuel	0.0297	8.24E-12
MPC-68F UO_2 Fuel	0.0660	1.84E-11
Trojan MPC-24EF UO_2 Fuel	0.0926	2.57E-11
Accident Conditions		
MPC-68F	0.0297	4.89E-08
MPC-68F UO_2 Fuel	0.0660	1.09E-07
Trojan MPC-24EF UO_2 Fuel	0.0926	1.53E-07

Table 4.2.14

ALLOWABLE LEAKAGE RATES AT UPSTREAM PRESSURE FOR PLUTONIUM (SECONDARY CONTAINMENT)

	C_{Pu} (Ci/cm^3)	Allowable Leakage Rate at P_u L_N or L_A (cm^3/s)
Normal Transport Conditions		
MPC-68F MOX Fuel	2.18E-07	3.77E-05
MPC-68F UO_2 Fuel	1.63E-07	1.12E-04
Trojan MPC-24EF UO_2 Fuel	1.82E-06	1.41E-05
Accident Conditions		
MPC-68F	2.51E-06	1.95E-02
MPC-68F UO_2 Fuel	1.88E-06	5.81E-02
Trojan MPC-24EF UO_2 Fuel	9.49E-06	1.61E-02

4.3 REGULATORY COMPLIANCE

Chapter 4 of this SAR has been prepared to summarize the containment features and capabilities of the HI-STAR 100 packaging. The containment boundaries of the HI-STAR 100 packaging are designed and tested to ensure that the radionuclide release rates specified in 10CFR71.51 and 10CFR71.63(b) [4.0.1] will not be exceeded.

Leakage rates presented in Chapter 4 are determined in accordance with the requirements of ANSI N14.5 [4.0.2], and utilizing NUREG/CR-6487, *Containment Analysis for Type B Packages Used to Transport Various Contents* [4.0.3], Regulatory Guide 7.4, *Leakage Tests on Packages for Shipment of Radioactive Materials* [4.0.4] as content guides, and NUREG-1617, Standard Review Plan for Transportation Packages for Spent Nuclear Fuel [4.0.5].

The containment features and capabilities of the HI-STAR 100 packaging can be summarized in the following evaluation statements:

1. The HI-STAR 100 packaging, as presented in Chapter 4, complies with all applicable codes and standards for the containment system as identified in the chapter.

2. The primary containment boundary is securely closed by using multiple bolts and plugs. The secondary containment boundary is closed using multi-pass welds. The closure of both containment boundaries is sufficient to prevent unintentional opening or opening by pressure that may arise in the package as required by 10CFR71.43(c).

3. The materials of construction for the packaging primary and secondary containment are specified in the Bills-of-Material in Section 1.4. All materials and construction assure that there will be no significant chemical, galvanic, or other reaction as required by 10CFR71.43(d).

4. The overpack and MPC penetrations are designed to prevent leakage and protect against unauthorized operation by using cover plates to provide redundant closure as required by 10CFR71.43(e).

5. The primary containment system boundary for the HI-STAR 100 packaging consists of the overpack inner shell, the bottom plate, the top flange, the top closure plate, closure bolts, the overpack vent and drain port plugs, and their respective mechanical seals. The secondary containment system boundary for a HI-STAR 100 packaging containing fuel debris consists of the MPC enclosure vessel including the MPC shell, the MPC bottom plate, the MPC lid, closure ring, and vent and drain port cover plates. The use of two independent containment boundaries provides the capability to load and transport specified fuel debris in accordance with the requirements of 10CFR71.63(b).

6. The HI-STAR 100 packaging is design, constructed, and prepared for shipment so that under the tests specified in 10CFR71.71 (normal conditions of transport), the package satisfies the containment requirement of 10CFR71.43(f) and 10CFR71.51(a)(1) for normal conditions of transport and 10CFR71.51(a)(2) for hypothetical accident conditions with no dependence on filters or a mechanical cooling system as required by 10CFR71.51(c).

7. The HI-STAR 100 packaging satisfies the requirements of 10CFR71.63(b) for transport related to fuel debris with plutonium in excess of 20 Ci per package.

8. The HI-STAR 100 packaging satisfies the containment requirements of 10CFR71, and the packaging meets the containment criteria of ANSI N14.5.

4.4 REFERENCES

[4.0.1] 10CFR71. "Packaging and Transportation of Radioactive Material."

[4.0.2] ANSI N14.5-1997. "American National Standard for Radioactive Materials-Leakage Tests on Packages for Shipment."

[4.0.3] B.L. Anderson et al. *Containment Analysis for Type B Packages Used to Transport Various Contents.* NUREG/CR-6487, UCRL-ID-124822. Lawrence Livermore National Laboratory, November 1996.

[4.0.4] U.S. Nuclear Regulatory Commission, Regulatory Guide 7.4, *Leakage Tests on Packages for Shipment of Radioactive Materials*, June 1975.

[4.0.5] NUREG-1617, "Standard Review Plan for Transportation Packages for Spent Nuclear Fuel", Draft Report for Comment, March 1998.

[4.1.1] American Society of Mechanical Engineers (ASME), Boiler and Pressure Vessel Code, Section III, Division 1, Subsection NB, Class 1 Components, 1995 Edition.

[4.2.1] Deleted.

[4.2.2] Deleted.

[4.2.3] Rosenhow, W.M. and Hartnett, J.P., *Handbook of Heat Transfer*, Hemisphere Publishing Corporation, New York, 1973.

[4.2.4] Shleien, B., *The Health Physics and Radiological Health Handbook*, Scinta, Inc. Silver Spring, MD, 1992.

APPENDIX 4.A: BOLT AND PLUG TORQUES

This appendix provides the calculations used to determine the torque values for the vent and drain port plugs and cover plate bolts.

4.A.1 HI-STAR 100 Vent and Drain Port Plug Torques†

The HI-STAR 100 vent and drain port are sealed with plugs under which a mechanical seal is compressed. The objective of this calculation is to determine the torque required on the plug and to provide the required compressive load.

Given:

O-Ring (Mechanical Seal) Diameter: D_{OR} =0.683 in

O-Ring Compression: q_{OR} =800 lbf/in (pound force per linear inch)

Internal Pressure: p_i =100 psi

Plug Diameter: D_B =0.5 inch

Load due to internal overpack pressure: $q_i = p_i \pi D_B^2/4 =$ 19.6 lbf

Determine the required seating load:

The circumference of the O-Ring is: $C_{OR}=\pi D_{OR}$ C_{OR}= 2.14 in

The required seating load is: $F_i = q_i + P_{OR}$

$P_{OR}=C_{OR}q_{OR}$ P_{OR}= 1712 lbf

F_i=1732 lbf

The procedure presented here is taken from Shingley, Joseph Edward and Mischke, Charles R., Mechanical Engineering Design, Fifth Edition, McGraw Hill, p. 344-346.

---

† Since the closure plate test port plug is the same material, diameter and uses the same seal, this calculation also applies to the closure plate test port plug.

Given a torque factor K= 0.30 (for non-plated, non-lubricated plug).

Determine the required torque:

$T= KFiD_B$

T=0.30 (1732 lbf)0.5 in T=259 in-lbf T=22 ft-lbf

4.A.2 HI-STAR 100 Vent and Drain Port Cover Plate Bolt Torques

The HI-STAR 100 vent and drain port cover plates are sealed with a mechanical seal that is compressed under a bolted cover plate. The objective of this calculation is to determine the torque required on the bolts and to provide the required compressive load.

Given:

O-Ring (Mechanical Seal) Diameter: D_{OR} =2.5 in

Required O-Ring Compression: q_{OR} =1150 lbf/in (pound force per linear inch)

Internal Pressure: p_i =100 psi (assumed)

Bolt Diameter:D_B =0.375 inch

Number of Bolts: n= 4 bolts

Determine the required seating load:

The circumference of the O-Ring is: $C_{OR}=\pi D_{OR}$ C_{OR}= 7.85 in

The required seating load per bolt is: $F_i = q_i + P_{OR}/n$

$qi= p_i \pi D_{OR}^2/4$ qi= 491 lbf
$P_{OR}=C_{OR}q_{OR}$ P_{OR}= 9028 lbf

F_i=9516 lbf/4 F_i=2380 ft-lbf

The procedure presented here is taken from Shingley, Joseph Edward and Mischke, Charles R., Mechanical Engineering Design, Fifth Edition, McGraw Hill, p. 344-346.

Given a torque factor K= 0.15 (See technical Bulletin for FELPRO N-5000 in Appendix 1.C).

For conservatism, the torque factor is increased by an additional 5 percent in the following calculation.

Determine the required torque:

$T = KFiD_B$

T=0.1575 (2380 lbf)0.375 in T=141 in-lbf T=11.8 ft-lbf

APPENDIX 4.B: Manufacturer Seal Information
(Total of 5 Pages Including This Page)

The information provided in this appendix provides additional details on the mechanical seals specified to ensure containment. The following is a listing of the drawings provided in this appendix.

- ASE Drawing No. 050038-TAB, Rev B, ".375 C-Ring, Spring Ener., Internal Pressure" (Detail of Closure Plate Mechanical Seals, Holtec Dwg. 1397 and Bill-of-Material 1476, Items 26 and 27)
- ASE Drawing No. 050033, Rev. B, "C-Ring, .062 Spring Energized, Internal Pressure" (Detail of Port Plug Mechanical Seal, Holtec Dwg. 1397 and Bill-of-Material 1476, Item 19)
- ASE Drawing No. 050118, Rev. A, ".062 C-Ring, Spring Ener., Internal Pressure" (Detail of Port Cover Mechanical Seal, Holtec Dwg. 1398 and Bill-of-Material 1476, Item 30)

The detailed dimensions, materials, and groove requirements are provided below for each mechanical seal.

Closure Plate Outer Seal:

Holtec Item No.	27
ASE Part No.	ASE050038-TAB-1
Seal Type	Spring energized C-ring, internal pressure
Seal Size	72.50 OD x 3/8 free height
Material	Jacket Alloy X750
	Spring Alloy X750
Plating	Silver
Groove OD	72.545 inches nominal
Groove ID	71.685 inches nominal
Groove Depth	0.300 inches nominal

Closure Plate Inner Seal:

Holtec Item No.	26
ASE Part No.	ASE050038-TAB-2
Seal Type	Spring energized C-ring, internal pressure
Seal Size	71.00 OD x 3/8 free height
Material	Jacket Alloy X750
	Spring Alloy X750
Plating	Silver
Groove OD	71.045 inches nominal
Groove ID	70.175 inches nominal
Groove Depth	0.300 inches nominal

Port Plug Seal:

Holtec Item No.	19
ASE Part No.	ASE050033
Seal Type	Spring energized C-ring, internal pressure
Seal Size	0.75 OD x 0.062 free height
Material	Jacket Alloy X750
	Spring Alloy X750
Plating	Silver
Groove OD	0.760 inches nominal
Groove Depth	0.052 inches nominal

Port Cover Seal:

Holtec Item No.	30
ASE Part No.	ASE050118
Seal Type	Spring energized C-ring, internal pressure
Seal Size	2.50 OD x 0.062 free height
Material	Jacket Alloy X750
	Spring Alloy X750
Plating	Silver
Groove OD	2.52 inches nominal
Groove ID	2.31 inches nominal
Groove Depth	0.052 inches nominal

FIGURE WITHHELD UNDER 10 CFR 2.390

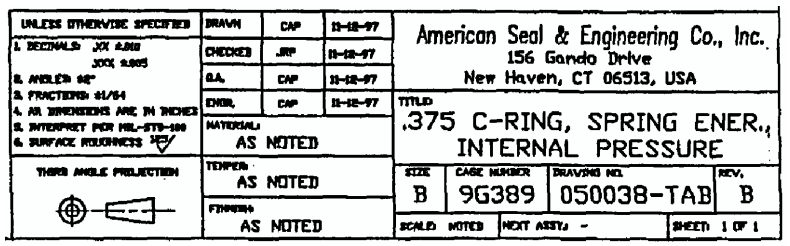

FIGURE WITHHELD UNDER 10 CFR 2.390

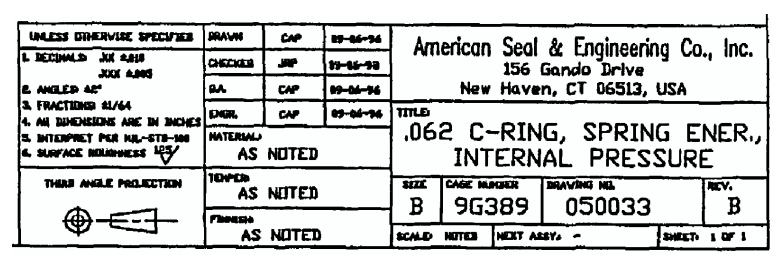

FIGURE WITHHELD UNDER 10 CFR 2.390